



## Degradation of diclofenac and 4-chlorobenzoic acid in aqueous solution by cold atmospheric plasma source



Amit Kumar<sup>a,b,\*</sup>, Nikola Škoro<sup>a</sup>, Wolfgang Gernjak<sup>c,d</sup>, Olivera Jovanović<sup>a</sup>, Anđelija Petrović<sup>a</sup>, Suzana Živković<sup>e</sup>, Elisabeth Cuervo Lumbaque<sup>c</sup>, Maria José Farré<sup>c</sup>, Nevena Puač<sup>a</sup>

<sup>a</sup> Institute of Physics, University of Belgrade, Pregrevica 118, 11080 Belgrade, Serbia

<sup>b</sup> Universitat de Girona, 17003 Girona, Spain

<sup>c</sup> Catalan Institute for Water Research (ICRA), 17003 Girona, Spain

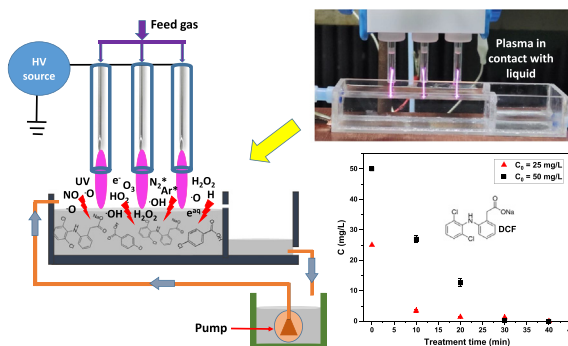
<sup>d</sup> Catalan Institution for Research and Advanced Studies (ICREA), 08010 Barcelona, Spain

<sup>e</sup> Institute for Biological Research "Siniša Stanković", University of Belgrade, Bulevar despota stefana 142, 11060, Serbia

### HIGHLIGHTS

- Multi-pin APPJ utilized to treat DCF and pCBA in aqueous solution.
- Shown efficient removal of contaminants with large plasma/contaminant surface ratio
- Energy yield determined using power deposited to discharge in contact with sample
- A multi-pin APPJ with recirculation system allows for scalability.

### GRAPHICAL ABSTRACT



### ARTICLE INFO

Editor: Yifeng Zhang

#### Keywords:

Cold atmospheric plasma  
Plasma characterization  
Degradation of pharmaceutical and industrial chemical

### ABSTRACT

In this study, cold atmospheric plasma (CAP) was explored as a novel advanced oxidation process (AOP) for water decontamination. Samples with high concentration aqueous solutions of Diclofenac sodium (DCF) and 4-Chlorobenzoic acid (pCBA) were treated by plasma systems. Atmospheric pressure plasma jets (APPJs) with a 1 pin-electrode and multi-needle electrodes (3 pins) configurations were used. The plasma generated using argon as working gas was touching a stationary liquid surface in the case of pin electrode-APPJ while for multi-needle electrodes-APPJ the liquid sample was flowing during treatment. In both configurations, a commercial RF power supply was used for plasma ignition. Measurement of electrical signals enabled precise determination of power delivered from the plasma to the sample. The optical emission spectroscopy (OES) of plasma confirmed the appearance of excited reactive species in the plasma, such as hydroxyl radicals and atomic oxygen which are considered to be key reactive species in AOPs for the degradation of organic pollutants. Treatments were conducted with two different volumes (5 mL and 250 mL) of contaminated water samples. The data acquired allowed calculation of degradation efficiency and energy yield for both plasma sources. When treated with pin-APPJ, almost complete degradation of 5 mL DCF occurred in 1 min with the initial concentration of 25 mg/L and 50 mg/L, whereas 5 mL pCBA almost degraded in 10 min at the initial concentration of 25 mg/L and 40 mg/L. The treatment results with multi-needle electrodes system confirmed that DCF almost completely degraded in 30 min and pCBA degraded about 24 % in 50 min. The maximum

\* Corresponding author at: Institute of Physics, University of Belgrade, Pregrevica 118, 11080 Belgrade, Serbia.  
E-mail address: [amit@ipb.ac.rs](mailto:amit@ipb.ac.rs) (A. Kumar).

<http://dx.doi.org/10.1016/j.scitotenv.2022.161194>

Received 5 October 2022; Received in revised form 21 December 2022; Accepted 21 December 2022

Available online 27 December 2022

0048-9697/© 2022 The Authors. Published by Elsevier B.V. This is an open access article under the CC BY-NC license (<http://creativecommons.org/licenses/by-nc/4.0/>).

calculated energy yield for 50 % removal was 6465 mg/kWh after treatment of 250 mL of DCF aqueous solution utilizing the plasma recirculation technique. The measurements also provided an insight to the kinetics of DCF and pCBA degradation. Degradation products and pathways for DCF were determined using LC-MS measurements.

## 1. Introduction

Many pharmaceutical and other industrial organic chemical substances have been recognized as emerging persistent organic micropollutants (OMPs) and are frequently found in trace concentrations (ranging from  $\text{ngL}^{-1}$  and  $\mu\text{gL}^{-1}$ ) in aquatic bodies (Arslan et al., 2017; Ebele et al., 2017; Patel et al., 2019). It is estimated that several tons of pharmaceuticals, for example, >100,000 tons of pharmaceutical items, are consumed globally each year, inflicting harm to our ecosystem (Kot-Wasik et al., 2007; Wilkinson et al., 2022). Pharmaceutical and other industrial chemicals are discharged to the environment from a wide range of sources, including industry, hospitals and households. Pharmaceuticals are detected in the environment through a variety of channels due to a lack of proper wastewater treatment technologies; they all share the characteristics of providing a considerable threat to public health or the environment, as well as being extremely resistant to traditional wastewater treatment techniques (Arslan et al., 2017; Eggen et al., 2014; Khan et al., 2020). Certain organizations, such as the European Union (EU) and the United States Environmental Protection Agency (USEPA), establishing strict quality criteria for wastewater discharge; yet, various nations and industries are following that (Sathishkumar et al., 2020; Schellenberg et al., 2020). The previous review article by various authors offers thorough information regarding pharmaceutical classification, source and regulations, as well as the impact of pharmaceuticals on the environment and human health. and (Khan et al., 2020; Lonappan et al., 2016; Schwarzenbach et al., 2006).

In this work, DCF sodium and pCBA were chosen as model test pollutants and treated with two plasma sources with different reactor geometry under a variety of experimental conditions. DCF non-steroidal anti-inflammatory drug (NSAID) is used on a global scale to treat inflammatory diseases and reduce pain and fever (Rodrigues et al., 2021; Sathishkumar et al., 2020). According to the authors' statistics, a large amount of DCF, approximately >1000 tons, is used globally each year (Lonappan et al., 2016). As a consequence, DCF is regularly observed in high concentrations in sewage treatment plant effluents that are persistent enough to be found in surface, ground and even drinking water. and (Heberer and Feldmann, 2005; Lonappan et al., 2016). The presence of DCF in water can play a toxic influence on aquatic life, plants and human health (Deng et al., 2021; Sathishkumar et al., 2020). This also led to the unprecedented decline of vultures in India (Taggart et al., 2009). Consumption of DCF has been banned by various countries (e.g. India, Nepal, Bangladesh, etc.) in order to reduce the further decline of the vulture population (Markandya et al., 2008). The pCBA was the second compound that was chosen for the treatment as it is used in various chemical syntheses. The pCBA was found as a by-product in the treatment of various organic chemicals (Bing et al., 2012). The pCBA is an industrial chemical that is commonly used in the pharmaceutical industry. Since it has strong reactivity with  $\text{HO}\cdot$ , pCBA was also utilized as a probe compound in several water treatment procedures to determine  $\text{HO}\cdot$  levels (Bing et al., 2012; Pi et al., 2005).

Since conventional wastewater treatment plants (WWTPs) do not completely decompose a large number of OMPs of anthropogenic origin due to unfavorable properties such as poor biodegradability, they are released into natural water bodies (Sathishkumar et al., 2020). For example, conventional WWTPs are reported to remove just 30–70 % of DCF from wastewater streams (Deng et al., 2021; Lonappan et al., 2016). As a result, untreated DCF effluents from WWTPs enters the environment and pollutes ecosystems. Previous research has also stated that DCF can interact with other organic molecules in the environment, leading to the production of other harmful contaminants (Mukherjee et al., 2022).

AOPs have been used successfully as a tertiary treatment method and are regarded as a promising method in the field of wastewater treatment to eliminate OMPs (pharmaceuticals, organic dyes, pesticides, etc.) (Cuerda-Correa et al., 2019; Garrido-Cardenas et al., 2020). The primary feature of AOPs is the generation of  $\text{HO}\cdot$  radicals (high oxidizing potential), which are particularly reactive with a wide variety of organic contaminants and then degrade them, resulting in effective mineralization of organic pollutants into  $\text{H}_2\text{O}$  and  $\text{CO}_2$  (An et al., 2010; Wang and Xu, 2012). The goal of generating  $\text{HO}\cdot$  radicals, different AOPs based on chemical admixture ( $\text{O}_3/\text{H}_2\text{O}_2$ ,  $\text{O}_3/\text{UV}$ ,  $\text{O}_3/\text{UV}/\text{H}_2\text{O}_2$ ), photocatalysis ( $\text{UV}/\text{TiO}_2$ ,  $\text{UV}/\text{TiO}_2/\text{H}_2\text{O}_2$ ), Fenton ( $\text{Fe}_2^+/\text{H}_2\text{O}_2$ ,  $\text{Fe}_2^+/\text{UV}/\text{H}_2\text{O}_2$ ) and application of electric energy (electrochemical oxidation: Anodic, Electro-Fenton) have been addressed and shown in past study (Amor et al., 2019; Kumar et al., 2021; Macias-Quiroga et al., 2021; Wang and Xu, 2012). The majority of AOPs rely on external chemicals and catalysts to create  $\text{HO}\cdot$  radicals. There are some reviews where authors revealed possible possibilities and limitations related with various AOPs for OMPs degradation (Hijosa-Valsero et al., 2014; Ma et al., 2021).

Cold atmospheric plasmas have been shown to effectively decompose OMPs effectively and are a promising innovative AOP that has been explored for water decontamination (Hijosa-Valsero et al., 2014; Kumar et al., 2022; Li et al., 2014; Magureanu et al., 2015; Malik, 2010; Topolovec et al., 2022). Gaseous plasma can be a very complex mixture of electrons, ions, metastables, UV lights, electromagnetic fields, electric fields, etc. (Bruggeman and Brandenburg, 2013; Chen, 2016; Foster, 2017; Jaiswal et al., 2020). The interaction of cold plasma with an open or controlled environment can produce a plethora of reactive species that can be used for a variety of beneficial chemical reactions in applications such as agriculture, medicine, sterilization, disinfection, material synthesis, electronics and so on (Barjasteh et al., 2021; Domonkos et al., 2021; Fridman, 2008; Tomić et al., 2021).

Plasma-liquid interactions have grown in popularity in recent years due to crucial characteristics such as the simultaneous production of many powerful chemical reactive oxidants at low temperatures, which has the ability to have a large impact on a variety of prospective applications. For example, the APPJ source which was used in this study for plasma formation in the gas phase above the liquid surface can cause a variety of chemical and physical effects, including the generation of reactive oxygen and nitrogen species (RONS:  $\text{HO}\cdot$ ,  $\text{O}\cdot$ ,  $\text{HO}_2$ ,  $\text{H}_2\text{O}_2$ ,  $\text{O}_3$ ,  $\text{NO}_3^-$ ,  $\text{NO}_2^-$ ,  $\text{NO}\cdot$ ,  $\text{ONOO}^-$ , etc.), UV photons, as well as hydrated electrons (free electrons in the solution) without the usage of chemical agents (Bradu et al., 2020; Bruggeman et al., 2016; Foster et al., 2012; Lukes et al., 2014). The APPJ has a high potential for transporting highly concentrated reactive species from the gas phase to the liquid phase via the jet's gas flow (Bruggeman et al., 2016; Du et al., 2018). As a consequence, such a plasma source can be used as a green approach of destroying complex non-biodegradable organic contaminants. Previous studies attempted to use certain CAPs with various reactor configurations, powered by different electrical signals (AC, DC, RF sources), different working gases (argon, helium, oxygen, nitrogen) and several process parameters to decontaminate water (Hijosa-Valsero et al., 2014; Kumar et al., 2021; Malik, 2010). It was also noted that there have been a few earlier experiments that used CAPs to generate large plasma and surface contacts to remove organic contaminants from water.

The purpose of this study was to investigate the degradation of pCBA and DCF in aqueous solutions utilizing CAPs (pin-APPJ and multi-needle electrodes-APPJ with recirculation), as well as to compare the performance of both plasma reactors in terms of pollutants removal and energy yield. The pin-APPJ, which has 1 jet, was utilized to treat 5 mL of polluted water. The multi-needle electrodes-APPJ, which have 3 jets and continuous

recirculation, were utilized to treat a quarter liter of contaminated water. The approach of increasing the number of jets aims to increase the mass transfer of reactive species and consequently the kinetics of pollutant breakdown in water. The continuous recirculation approach improves the mixing of reactive species in the liquid and hence increases reactivity. The plasma source with multi-needle electrodes can lead to an easily scalable plasma source for treatment of large volumes of contaminated water. The efficient application of plasma pin-APPJs to the flowing contaminated sample, with large plasma/liquid surface area ratio, brings an advantage compared to large area Dielectric Barrier Discharge plasmas that are more complicated to sustain.

In this paper, we will present electrical characterization, Optical Emission Spectroscopy and ICCD (Intensified Charged Coupled Device) imaging of 1-pin APPJ and 3-pin APPJ. The measurements were made during the removal of pollutants from contaminated water samples. These two plasma devices are used for DCF and pCBA removal. The HPLC analytical instrument was used to study the degradation kinetics of DCF and pCBA. The obtained data was used to determine the energy yield and compared to the

literature. The oxidation transformation products generated during the degradation of the DCF were detected using Orbitrap-LC-MS and possible degradation mechanisms were proposed.

## 2. Materials and methods

### 2.1. Experimental setup

Two plasma sources are used for the treatment of DCF and pCBA-containing aqueous solutions. The reactor geometry and the instrumental devices that were used are described in the following section.

#### 2.1.1. Pin-electrode-APPJ

The schematic of the experimental setup of pin-APPJ and the picture of the plasma jet contacting the liquid sample is shown in Fig. 1a. The plasma source consists of a concentrically placed glass tube, a ceramic tube and a stainless steel wire as an electrode. The outer and inner diameters of the glass tube are 6 mm and 4 mm, respectively. The stainless steel wire with

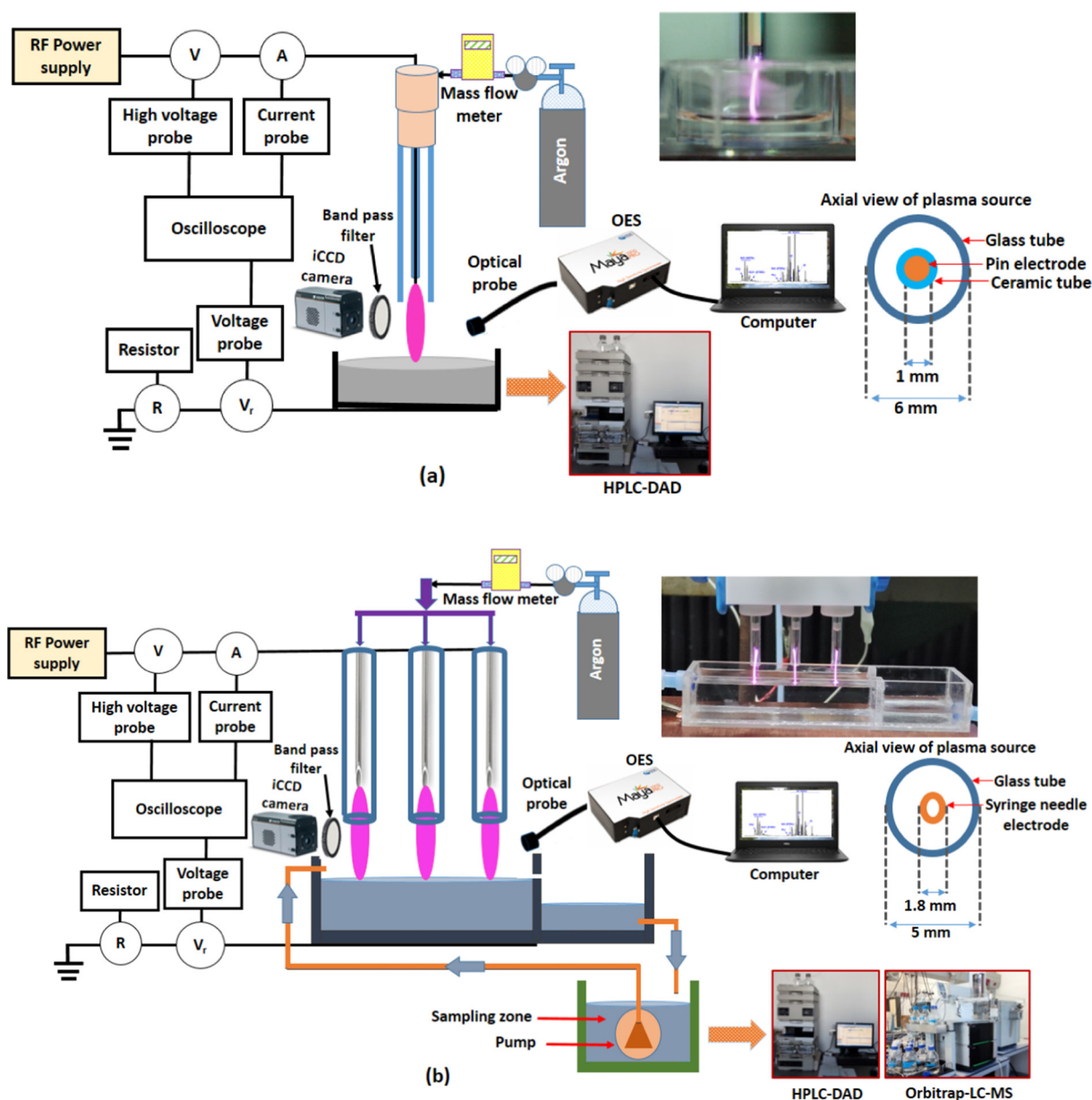


Fig. 1. The schematic diagram of experimental, (a) setup-pin-APPJ (left) with an image of plasma solution treatment (upper right), (b) multi-needle electrodes-APPJ with continuous flow treatment system (left) with plasma solution treatment (right).

a diameter of 1 mm with a sharpened tip is used as a high-voltage electrode and while the rest of the wire was covered with a ceramic tube. The electrode is powered by a high voltage radio frequency (RF) power supply with a frequency of 332 kHz. The other grounded electrode is the solution placed in a vessel with copper tape glued to the outer bottom side of the vessel and connected to the ground. In this configuration, plasma was generated between the electrode tip and stagnant liquid surface using argon as a working gas.

### 2.1.2. Multi-needle electrodes-APPJ

The schematic diagram of the experimental setup of multi-needle electrodes-APPJ is shown in Fig. 1b. The atmospheric pressure plasma jet over the flowing liquid surface was generated through a multi-syringe needle electrode type configuration. The inner and outer diameter of each needle was about 1 mm and 1.8 mm, respectively. The needles were inserted inside the glass tubes, where the inner diameter, outer diameter and length of each tube were about 3.7, 5 and 45 mm, respectively. The distance between the tip of each needle and the end of each tube was 7 mm. The distance between the two adjacent needle electrodes was 20 mm. The distance between needle tips and solution was set at 15 mm. Similarly as for a single-pin system, the copper tape was wrapped over the bottom of the sample vessel while the electrodes were supplied by a sine signal at a frequency of 351 kHz. Since the same power supply was used for the pin-electrode jet, the difference in the electrical impedance of the circuit causes a change in the signal frequency. Argon gas with a total flow rate of 2 slm (standard liter per minute) was used as a feed gas, distributed evenly between 3 pin electrodes.

In both configurations, the voltage ( $v$ ) at the powered electrode was determined by a high voltage probe (Tektronix 6015A). The current at the powered electrode was measured with a current probe (Agilent N2783B). The voltage drop ( $v_r$ ) across the 1 k $\Omega$  resistor used to establish the current in the grounded part ( $i_g$ ) was recorded using a voltage probe (Agilent 10073C). The time variable voltage and current signals were monitored by using a 4-channel, 200 MHz, 2.5 GSPS digital oscilloscope (Tektronix MDO3024). Simultaneously, the data from the oscilloscope was transferred to a laptop for further analysis. The power delivered from the power supply to the plasma source and the power in the grounded line, i.e. the power deposited from the plasma passing through the sample, was calculated.

## 2.2. Treatment of solution

In the configuration of pin-electrode APPJ, 5 mL of solution was exposed to the jet with different treatment times. In each experiment, 2 mL of plasma-treated samples were taken for further analysis. In the assembly of the flow system, a total volume of 250 mL of solution was treated, where around 12 % of the solution was continuously exposed to the treatment zone. The solution was circulated by a pump (kept inside the solution reservoir) at a flow rate of 300 mL/min and a corresponding Reynolds number of 1349. The Reynolds number determines the flow pattern, hence at this value, the flow was in the laminar flow regime (Xiong et al., 2012). The total treatment times were 30 min for DCF and 50 min for pCBA, where 2 mL of samples were taken at specific intervals for analysis. In the event of the treatment of 5 mL using pin-APPJ (1 jet), each sample corresponded to a single experiment. In the case of treatment using a plasma (3 jets) recirculation system (volume 250 mL), there was continuous sampling at various time intervals.

In both experimental systems, there were minor reductions in volume due to heating and gas flow (always <0.4 % for 3 jets and 36 % for 1 jet, longer treatment time). The volume reduction was always recorded and incorporated into the final calculation of degradation removal. It shall also be noted that volatilization of the target contaminants is not expected due to their low volatility.

## 2.3. Solution characterization

DCF (chemical formula:  $C_{14}H_{10}C_{12}NNaO_2$ , molecular weight: 318.13 g/mol, purity  $\geq 98$  %, CAS number: 15307-79-6) and pCBA (chemical

formula:  $C_7H_5ClO_2$ , molecular weight: 156.57 g/mol, purity  $\geq 98$  %, CAS number: 74-11-3) were purchased from Sigma Aldrich.

In this investigation, DCF with initial concentrations of 25 mg/L and 50 mg/L and pCBA with initial concentrations of 25 mg/L and 40 mg/L were used in the treatment. First, a stock solution with a high initial concentration was prepared by dissolving each compound in distilled water. The lower concentration was obtained by diluting the concentrated solution with distilled water. Both DCF and pCBA are soluble in water to a considerable extent. For example, DCF and pCBA solubility in distilled water have been reported to be 2425 mg/L (Jankunaite et al., 2017) and 80 mg/L (Phatak and Gaikar, 1996), respectively. The initial concentrations chosen are greater than those found in the water bodies (ng/L to g/L). The higher initial concentrations evaluated allowed for proper examination of the degradation pattern. The authors claimed that prior studies on the degradation of OMPs by AOPs were also conducted in similar, higher initial concentration ranges (Kumar et al., 2021; Lesage et al., 2013; Rong et al., 2014).

Chromatographic analysis of the samples was carried out on an Agilent HPLC instrument, series 1100 (Agilent Technologies, Waldronn, Germany), with a photodiode array detector, using Hypersil BDS-C18 column (125  $\times$  2 mm) with 5  $\mu$ m particle size (Phenomenex, Torrance, USA), thermostated at 30  $^{\circ}$ C. All samples were filtered through a 0.2  $\mu$ m cellulose filters (Agilent technologies, Santa Clara, CA, USA) prior to analysis. The mobile phase consisted of a 1 % (v/v) solution of orthophosphoric acid in ultrapure water (solvent A) and acetonitrile (solvent B). Acetonitrile and orthophosphoric acid were LC-MS grade (Fisher Scientific, Leics, UK) and ultra-pure water was generated by using the Water Purification System (New Human Power I Integrate, Human Corporation, Seoul, Republic of Korea). The flow rate of the mobile phase was 0.5 mL/min and the injection volume was 10  $\mu$ L. A gradient program was used as follows: 80–30 % A, 0–7 min; 30–80 % A, 7–12 min (DCF) and 80–60 % A, 0–8 min; 60–80 % A, 8–12 min (pCBA). The detection wavelengths were set at 240 nm and 276 nm for pCBA and DCF, respectively. Quantification was performed using standardized calibration curves. The content of products in the samples was determined by calculation of peak area and expressed as milligrams per liter. Chromatographic data were recorded and processed by using HP ChemStation Chromatographic Software (Palo Alto, CA, USA).

The byproducts derived from the degradation of DCF were analyzed by using Orbitrap Exploris 120 high-resolution LC-MS (Thermo Fisher Scientific). A reverse-phase column (Hypersil GOLD-Selectivity C18, 3  $\mu$ m, 2.1 mm  $\times$  50 mm) was used for the separation of the component in the mixture. The column temperature was set at 30  $^{\circ}$ C. The injection volume and flow rate was 10  $\mu$ L and 0.4 mL/min, respectively. The analysis was carried out in a negative ion and positive ion mode with ionization voltages of 2500 V and 3500 V, respectively. Heated electrospray ionization (H-ESI) system was used as an ion source. The mass spectra were acquired in full scan mode in the mass range of 40 to 5000. In the positive ion mode, the mobile phase composition was HPLC water with 0.1 % formic acid and methanol. In the negative mode, the mobile phase consists of HPLC water with 5 mM ammonium acetate (at pH 8) and methanol. Variation in composition, first started with 98:2 % and increased up to 2:98 % in 4.7 min and remained constant for 6 min and decreased up to 98:2 % in 9 min. The extracted data was transferred to Thermo Scientific<sup>TM</sup> Compound Discoverer software for further processing. The software also provided an excel based report containing details of the compound, isotopes, retention time, mass to charge ratio, fragment ion, intensity, mass error (ppm), etc. The chemical structure and fragmentation pattern for each possible transformation product were drawn by using ChemSketch software (ACD/ChemSketch Freeware).

DCF and pCBA removal efficiency was defined as Eq. (1).

$$\text{Removal (\%)} = \frac{C_o - C \times d}{C_o} \times 100 \quad (1)$$

where  $C_o$  (mg/L) is the initial concentration before plasma treatment,  $C$  (mg/L) is the final concentration after plasma treatment and  $d$  is the evaporation coefficient.

The energy yield of the removal of DCF and pCBA is determined by the following Eq. (2).

$$\text{Energy yield} \left( \frac{\text{mg}}{\text{kWh}} \right) = \frac{C_o \left( \frac{\text{mg}}{\text{L}} \right) \times V_o (\text{L}) \times \frac{1}{100} \times \text{Removal} (\%)}{P_{\text{mean at the sample}} (\text{kW}) \times t (\text{h})} \quad (2)$$

where  $C_o$  (mg/L) is initial concentration of the plasma treated compound,  $V_o$  (L) indicates the initial volume of plasma treated compound,  $P_{\text{mean}}$  (kW) is discharge power at the sample and  $t$  (h) is the treatment time.

In all plasma treatment processes, the solution pH was determined by a pH meter (HANNA-HI1330).

#### 2.4. Optical characterization

Plasma emission spectra was captured by using Maya2000 Pro-UV-NIR (Ocean Insight-High Sensitive Spectrometer) with an optical resolution of 0.18 nm full width at half maximum. The optical fiber (M114L02) length of 2 m and core diameter of 600  $\mu\text{m}$  was placed perpendicular to the plasma jet in order to capture the emission from the whole volume of the plasma jet. The emission was recorded with an exposure time of 50 ms. The raw OES data was transferred to a laptop and analyzed in OriginPro data analysis software. Plasma emission is measured with and without plasma (background). The background spectra were subtracted from the plasma emission spectra to achieve the exact spectrum. The spectral intensity was corrected for the optical system efficiency.

The plasma emission profiles were characterized by using an Andor iStar DH7341 ICCD camera with a Nikon UV-105 mm f/4.5 lens mounted. The lens of the ICCD camera was set perpendicular and in front of the plasma jet. During the analysis, the sample was filled in a quartz-type petri dish (to avoid the blockage of light having a lower wavelength (e.g. UV)) and placed under APPJ. There was no sample flow during ICCD imaging. In order to capture the spatial emission distribution of various reactive species ( $\text{HO}^\bullet$ ,  $\text{O}^\bullet$ ,  $\text{H}^\bullet$ ,  $\text{N}_2$  (SPS: second positive system & FNS: First negative system),  $\text{Ar}^*$ ), band pass filters (attached with holder) were used and placed in the front of the lens. The transmittance percentage of each filter was calculated by spectrophotometer (Beckman Coulter DU 720 UV/Visible). A MATLAB script was used to estimate the geometry of the plasma jet and to process ICCD camera images.

### 3. Results and discussions

#### 3.1. Electrical measurements

The electrical measurements were implemented to investigate the discharge parameters (voltage, current, power deposition). The discharge

voltage and current are the critical parameters that are used to obtain dissipated power in the plasma system. The high voltage was applied to the electrodes (to pin and multi-needles). The sharp edge electrode configuration was selected because it creates a high electric field around the tip. When the applied voltage is strong enough this electric field is enough for the breakdown to occur followed by the production of a conduction channel in the discharge gap.

The voltage-current parameters were investigated and the power deposition to the plasma system for both plasma sources was estimated. Fig. 2 displays the relationship between RMS voltage vs RMS current and power deposition at sample vs RMS voltage for 3-jets.

The mean power deposition at the sample was calculated using eq. 3, by averaging the instantaneous power (product of time-varying voltage  $v(t)$  and time-varying current  $i(t)$  waveforms) over a time interval of  $n = 6$  periods.

$$P_{\text{mean at sample}} = \frac{1}{nT} \int_{T_1}^{T_2} v(t) \times i_g(t) \times dt \quad (3)$$

where,  $P_{\text{mean at sample}}$ : mean power at the sample;  $v_R(t)$ : voltage drop at the resistor; resistance  $R = 1 \text{ k}\Omega$ ;  $i_g(t)$ : current at the ground (sample);  $nT = T_2 - T_1$ .

$$i_g(t) = v_R(t)/R \quad (4)$$

The plasma system was electrically described in two modes: when the plasma was ignited and when it was not. When there was no plasma ignition, voltage and current changed linearly, but voltage decreased after plasma discharge began (Fig. 2a). The power delivered to the sample after plasma ignition, which is essential in our investigation, was in the range of 5.8 W–16 W (Fig. 2b).

#### 3.2. Optical characterization of plasma

##### 3.2.1. OES measurements

The recorded spectra during the treatment of DCF by a multi-needle electrodes-flow system, shown in Fig. 3. The spectra between 200 and 427 nm, mainly correspond to various emission bands, such as the vibrational transition of  $\text{HO}^\bullet$  ( $\text{A}^2\Sigma^+ \rightarrow \text{X}^2\Pi$ ),  $\text{N}_2$  SPS ( $\text{C}^3\Pi_u \rightarrow \text{B}^3\Pi_g$ ),  $\text{N}_2^+$  FNS ( $\text{B}^2\Sigma_u \rightarrow \text{X}^2\Sigma_g$ ) and nitric oxide  $\text{NO}_\gamma$  ( $\text{A}^2\Sigma^+ \rightarrow \text{X}^2\Pi$ ). The spectrum lines between 697 and 965 nm are dominated by the excited argon atoms ( $4p \rightarrow 4s$ ) and  $\text{O}^\bullet$  ( $3p^3P \rightarrow 3s^3S$  and  $3p^3P \rightarrow 3s^3S$ ). The spectra of  $\text{N}_2$  SPS,  $\text{N}_2^+$  FNS,  $\text{O}^\bullet$  and  $\text{NO}_\gamma$  are typical for open-air-argon plasma discharges operating above a water sample (Lamichhane et al., 2022).

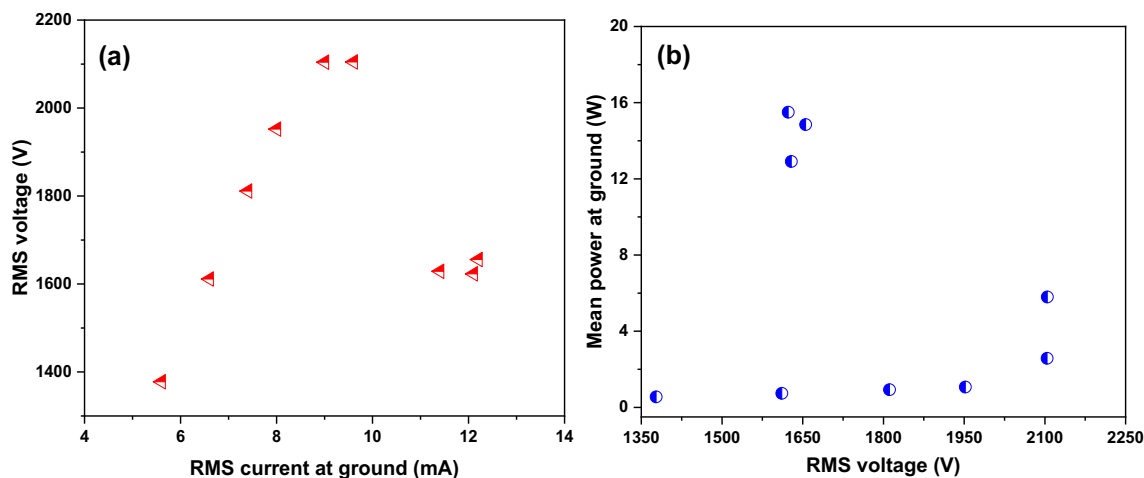


Fig. 2. (a) V-A characteristics (RMS voltage as a function of RMS current at sample/ground), (b) variation of mean power (delivered at the sample/ground) as a function of RMS voltage.

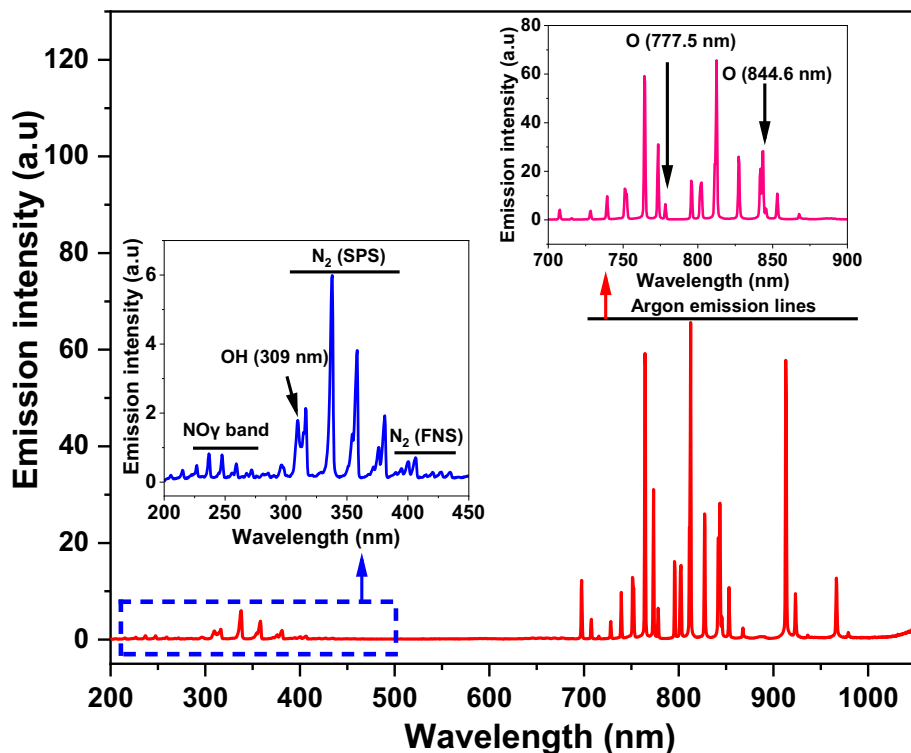


Fig. 3. The emission spectrum of argon – atmospheric pressure plasma jet in contact with ambient air and over the liquid surface, integration time 50 ms. Experimental conditions:  $C_0 = 25$  mg/L (DCF),  $V_0 = 250$  mL,  $P_{\text{mean}}$  at the sample 8 W, argon flow of 2 slm. Inset graphs depict the zoomed-in portion.

The collision of energetic species with  $H_2O$  molecules may be the primary source of  $HO\cdot$  production (Eqs. (5) & (6)) (Invernizzi et al., 2020; Jaiswal and Aguirre, 2021). Water molecules in the gas phase are formed mainly through evaporation, plasma species bombardment, gas movement and air (Ghimire et al., 2021; Liu et al., 2016). The threshold energy required to dissociate  $H_2O$  by electron impact dissociation is approximately 4.4 eV. As a result, the reaction necessitates a lower electron temperature, which is easily attained in argon-APPJ.



In general, argon metastables have energies ranging from 11.5 to 11.8 eV, which is high enough to react with  $H_2O$  as well as excite  $N_2$  ( $C^3\pi_u \rightarrow B^3\pi_g$ , 11.03 eV) (Soler-Arango et al., 2018), as explained by the following reactions (7) and (8).



Excited molecular nitrogen and its metastables have enough energy to react with and dissociate  $H_2O$  molecules (Eq. (9)) (Adhikari et al., 2021; Uhm et al., 2018).



The threshold energy for  $N_2^+$  ion generation is substantially greater (18.8 eV) than for excitation, hence the FNS band appeared with much lower intensity (Cullen and Milosavljević, 2015; Gazeli et al., 2015). One possibility for the FNS generation reaction is that argon metastables with high energy can ionize  $N_2$  via impact excitation and ionization (Eq. (10)).



Atomic O can originate after the dissociation of molecular  $O_2$  by energetic electrons and argon metastables via collisional dissociation (Eqs. (11) & (12)). The process reaction requires lower threshold energy (below 11 eV) (Adhikari et al., 2021).



The emission from the  $NO_y$  system was observed.  $NO_y$  production is caused by admixing air within the plasma (Yousfi et al., 2011), described by the following equations.



The presence of UV emission in the APPJ can also generate strong oxidants, such as  $HO\cdot$  and  $O\cdot$  by photolysis of  $H_2O$  and  $O_2$  (Attri et al., 2015; Invernizzi et al., 2020).

From the point of water decontamination, the presence of  $HO\cdot$  and  $O\cdot$  in the plasma is found to be major short-lived oxidants having high oxidative potential that can break down almost most non-biodegradable refractory organic substances by the following reaction mechanism: hydrogen atom abstraction, electrophilic addition and electron transfer reactions. Abundant excited argon and other RONS can also play an important role in water decontamination (García et al., 2017; Yehia et al., 2020). The reactive species produced by the plasma-gas-liquid-interface can transfer/diffuse/penetrate in the liquid phase and form secondary reactive species in the bulk solution, which can further drive degradation and change the pH and conductivity of the solution (Bruggeman et al., 2016; Foster et al., 2012; Kumar et al., 2022; Lukes et al., 2014).

We have also performed OES for pin-APPJ, which can be found in our prior published work (Kumar et al., 2022) and it was found that the emission spectra were almost identical. In case of pin-APPJ, a weak  $H_\alpha$  line

was present in the spectra, but the  $H_{\alpha}$  emission line was absent in multi-needle electrodes-APPJ, which might be created and promptly quenched.

The production of RONS in liquid phase is directly connected to the plasma chemistry in gas phase and gas/liquid interface (Bruggeman et al., 2016; Lukes et al., 2012; Pawlat et al., 2019). The presence of reactive species in the gaseous phase of plasma discharge responsible for further reactions at plasma gas/liquid interface can be determined by OES. In our previous work, we have used several methods for the quantification of long lived RONS in the plasma treated liquid (Kumar et al., 2022; Tomić et al., 2021). Several long-lived RONS (e.g.,  $H_2O_2$ ,  $NO_3^-$  and  $NO_2^-$ ) were detected and quantified in the aqueous phase.

### 3.2.2. ICCD imaging of pin and multi-needle electrodes-APPJ

**3.2.2.1. ICCD imaging of pin-APPJ.** The ICCD imaging with filters was performed to investigate the spatial resolution emission of reactive species produced by argon-APPJ when it interacts with liquid in the presence of ambient air. Various optical filters (310 nm, 425 nm, 660 nm and 780 nm) were employed to identify certain lines/bands inside the plasma. Each filter's bandwidth (bandpass region) was around 10 nm. Acquisition parameters such as gate pulse width, exposure time and gain remained constant during ICCD imaging with filters. Fig. 4 shows the spatially resolved ICCD images.

The emission of  $HO\cdot$  and vibrationally excited  $N_2$  (SPS, 315.8 nm) was monitored using a filter with a center wavelength of 310 nm. The emission from mostly  $O\cdot$  was measured at 777.5 nm in combination with excited argon (since excited argon also emits near 780 nm) using a 780 nm-centered filter. The filter with a central wavelength of 660 nm is primarily employed to record  $H_{\alpha}$  emission at a wavelength of 656 nm. The emission of excited  $N_2$  (SPS) and ionic nitrogen  $N_2^+$  (FNS) was monitored using a 425 nm filter.

Fig. 4a shows an image captured using a 310 nm filter. Fig. 4b shows the images associated with the remaining filters, such as 780, 425 and 660 nm; the intensity level in these images was kept constant. In the case of the 310 nm filter, the emission from  $HO\cdot$  (containing  $N_2$  SPS) was extensively dispersed across the active plasma. It should be noted that the images with the highest emission intensity were obtained using 310 nm filters. The emission profiles recorded at 425 nm, 660 nm and 780 nm were nearly identical. Nevertheless, intense emission occurred in the case of the 780 nm filter (mainly owing to plasma interaction with the ambient air) and dominated at close to the liquid surface. Overall, ICCD time-integrated images demonstrated the presence of several reactive species in the plasma that could be responsible for the degradation of chosen OMPs in this investigation.

**3.2.2.2. ICCD imaging of multi-needle electrodes-APPJ.** The ICCD time-integrated imaging of multi-needle electrodes-APPJ was also done. The

camera and filters were placed in such a way that they captured emissions from all three jets. Fig. 5 displays images captured with 310 nm and 780 nm filters, with the intensity scale constant for both filters for comparison. The spatially resolved emission intensity in all three jets was observed to fluctuate in both filters. For example, one jet's intensity was higher while the intensity in the other two jets was different at the same time. The variation in emission intensities could be related to a different level of excitation in the jets.

The emission intensity profile of  $HO\cdot$  and  $N_2$  (SPS) was brighter all along the jets but more intense in the middle jet, which could be owing to an intense concentrated electric field and excitation.  $O\cdot$  and excited argon were observed in the jets, but strong emission was noticed in the middle of all three jets and the intensity was significantly reduced downstream at the jets' top.

### 3.3. Treatment of pharmaceuticals with pin-APPJ and multi-needle electrodes-APPJ

#### 3.3.1. Pin-APPJ

The treatment studies were carried out by directly exposing the pin-APPJ to an aqueous solution containing DCF and PCBA while taking into account various experimental parameters that influence the degradation of both compounds. The parameters, such as initial pollutant concentration and treatment time, were adjusted and the resulting degradation results were thoroughly explained.

Fig. 6a depicts the degradation of pCBA in solution as a function of plasma treatment time. The degradation profile revealed that more than half of the initial pCBA concentration was eliminated in the first 5 min. The greatest degradation occurred in the first 3 min, with degradation efficiency values of approximately 63 % for 25 mg/L and 56 % for 40 mg/L. The initial concentration has a considerable impact on the behavior of the oxidation curves during the first 3 min of plasma treatment. After 10 min of treatment, both degradation curves merged, resulting in the complete removal of pCBA.

We fitted the data displayed in Fig. 6a to obtain pCBA degradation kinetics. The kinetics of pCBA decay demonstrate that it is well suited to the first order:

$$\ln \frac{C}{C_0} = -kt \quad (15)$$

where  $k$  is the kinetic rate constant.

The calculated  $R^2$  (correlation coefficients) was evidence that the degradation of pCBA fitted well with first-order kinetics. Lower initial pCBA concentration promoted the highest degrading first-order rate constant, while larger initial pCBA concentrations reduced the rate constant. Higher concentration of pCBA represents more pCBA molecules in the

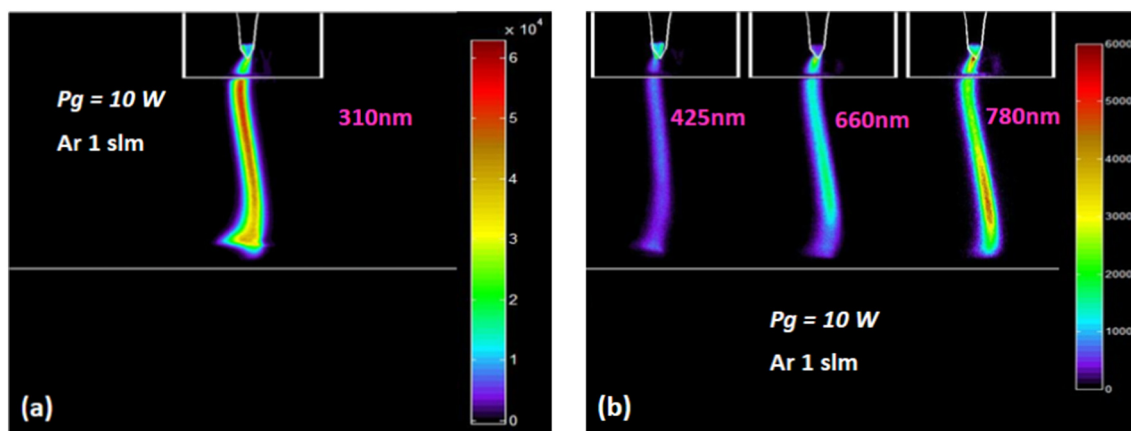


Fig. 4. The ICCD images with filters, (a) 310 nm, (b) 425 nm, 660 nm and 780 nm. Acquisition parameters: exposure time 20 ms, gate pulse width 5 ms and gain 50.

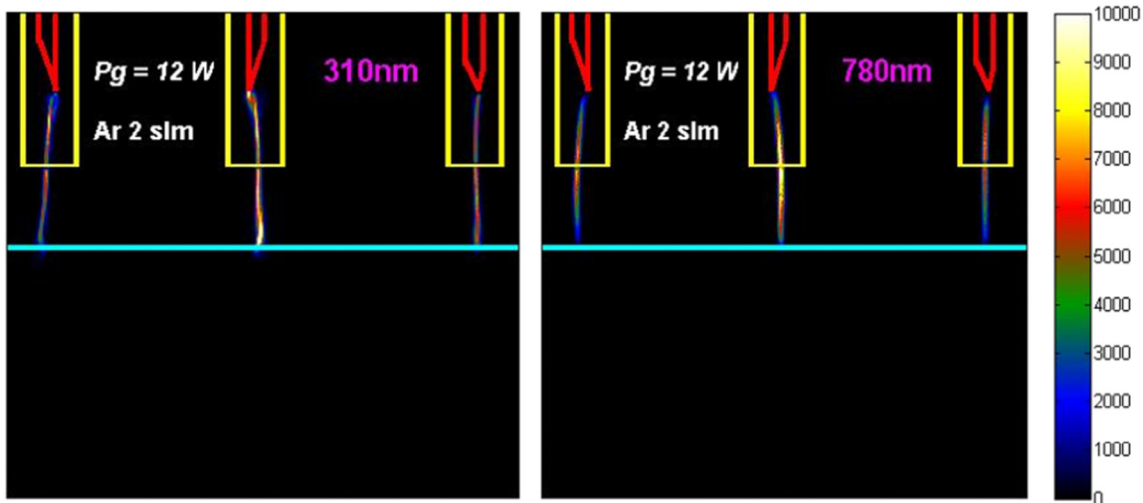


Fig. 5. The ICCD images with filters (310 nm and 780 nm). Acquisition parameters: exposure time 20 ms, gate pulse width 3 ms and gain 80.

solution resulting in more reaction sites for plasma species. Moreover, during the treatment by-products of pCBA are formed so not all introduced plasma species continue reacting with the original pCBA molecules. Taking

into account that the rate of plasma species production remains relatively constant in time this can lead to lower degradation rate at higher concentrations.

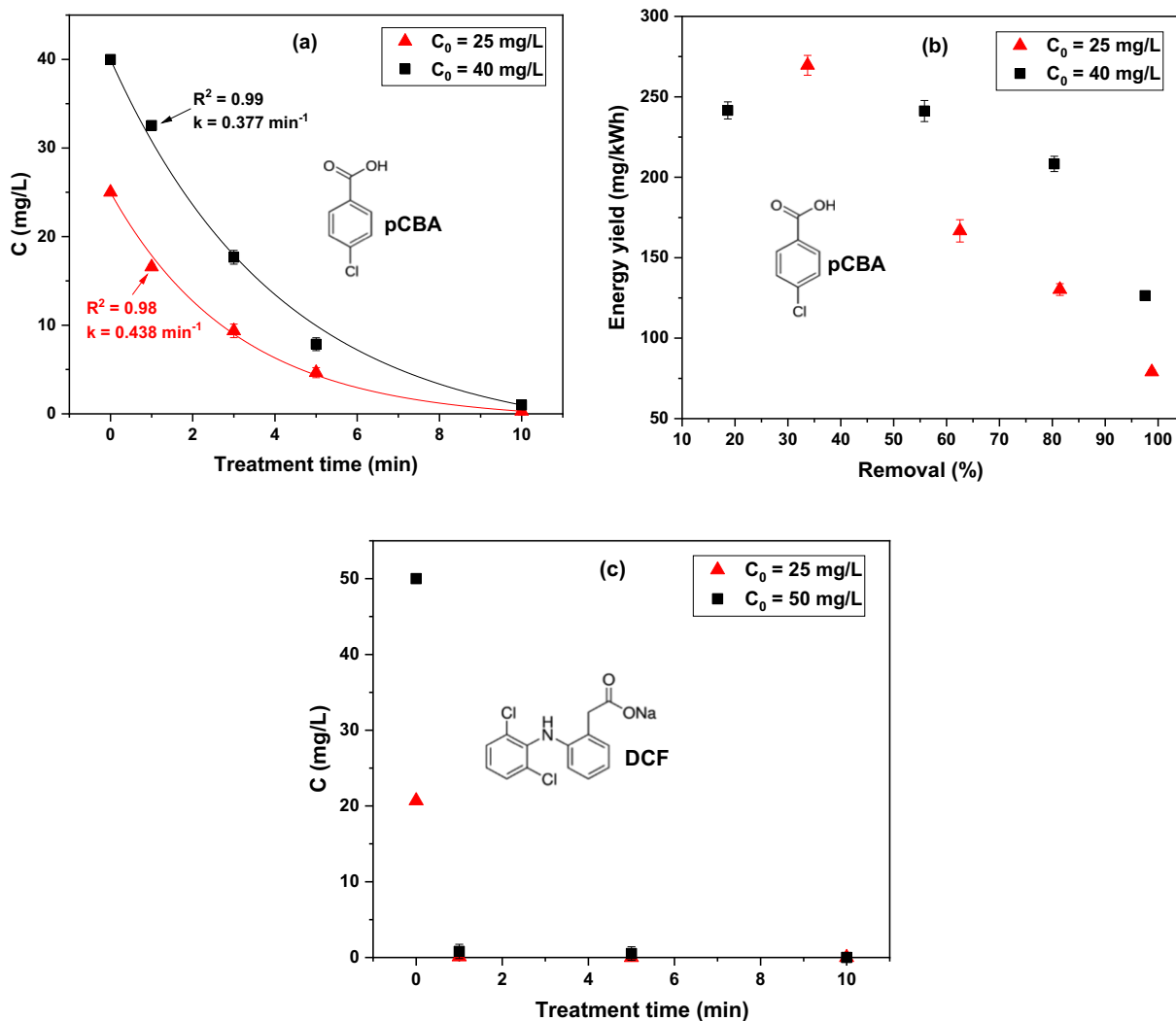


Fig. 6. (a) Change in pCBA concentration with treatment time, (b) energy yield vs removal %, (pCBA,  $C_0 = 25$  mg/L and  $C_0 = 40$  mg/L) and (c) change in DCF concentration with treatment time (DCF,  $C_0 = 25$  mg/L and  $C_0 = 50$  mg/L). Experimental conditions:  $V_0 = 5$  mL, argon flow of 1 slm,  $P_{mean}$  at the sample 10 W.



Consequently, the half-life ( $t_{1/2}$ ) pCBA decomposition time was determined as:

$$t_{1/2} = \frac{0.693}{k} \quad (16)$$

The time required to remove 50 % of the pCBA was 1.58 min for 25 mg/L and 1.83 min for 40 mg/L.

Aside from degradation, energy yield is a significant factor to consider in investigating the energy effectiveness of the plasma source. The energy yield for removing pCBA was calculated. Fig. 6b depicts the energy yield for removing pCBA as a function of removal %. Because of the longer treatment duration, the energy yield was lower at higher removal. For a longer treatment, power deposition may become increasingly concentrated in unproductive processes (e.g., the interaction of byproducts with plasma-induced species), resulting in a drop in energy yield. In the literature on plasma-based treatment, the energy yield is typically reported in terms of 50 % elimination for comparison. As a result, the amount of energy required to decompose 50 % of contaminants was calculated. Energy yield at 50 % pCBA elimination was 253 mg/kWh for 25 mg/L and 354 mg/kWh for 40 mg/L, respectively. More detailed comparison of the data on energy yield collected from the literature for pCBA removal by plasma was given at the end of Section 3.3.2.

DCF was treated with plasma while the same experimental conditions were considered as pCBA. As the solution was subjected to plasma, DCF decayed rapidly, as shown in Fig. 6c. The rapid degradation in the early stages of the process suggests that the majority of plasma-induced reactive species interacted and oxidized DCF. The chemical nature of organic substances (e.g. structural features/chemical reactivity) influences degradation. It has been found, for example, that DCF is strongly reactive not only with HO•, but also with other oxidants. As a result, HO• and other reactive species may play a significant role in the rapid degradation of DCF.

The degradation kinetics of DCF was not established because DCF practically vanished in 1 min and there were just a few points available to analyze the kinetic behavior. So, in our paper, we just reported the DCF degradation pattern.

The energy yield for DCF removal could not be determined precisely from the obtained measurements since DCF degraded quickly during the shortest sampling interval of 1 min for both initial concentrations. From these measurements, we can only conclude that the energy yield for DCF was higher than pCBA.

The pH of plasma-treated pCBA and DCF solutions was found to be lower after treatment. After 10 min of plasma treatment, the pH of pCBA decreased from 4 to 2.57 at 25 mg/L and to 2.65 at 40 mg/L. In the instance of DCF, the initial pH of the DCF solution was 6, but after 10 min of plasma treatment, the pH dropped to 2.66 at 25 mg/L and 2.69 at 50 mg/L. In both cases, the final pH was reduced to similar values after 10 min of plasma treatment. Additional experiments were conducted to treat distilled water without contamination with the same system of pin-APPJ. After 10 min of treatment, the pH of distilled water was reduced from 6.5 to 2.62. So, the reduction of pH is not related to contaminants but probably to plasma-induced nitrogen-based species. Changes in pH demonstrated the existence of acidogenic species (inorganic acids) in the liquid after plasma liquid interaction with ambient air (Judée et al., 2018; Rezaei et al., 2019). The authors found that the principal acidic species formed in the liquid are HNO<sub>3</sub> and HNO<sub>2</sub> (Thirumdas et al., 2018; Wenjuan and Xiangli, 2007). In water, these strong acids dissociate to their respective anion and a hydronium ion. Researchers determined that the pH value influences the degradation kinetics of OMPs in water -lower pH results in faster degradation. Rong et al., 2014, for example, investigated DCF degradation using an air DBD plasma source and reported that DCF removal was greater at pH 2.9 and 6.15 as compared to an alkaline environment at pH 10.1. Similar effect of low pH on pCBA degradation was reported in a study conducted by He et al., 2011. According to these results, we presume that lowering the pH value in the plasma treatment in our experiments contributed to the degradation of DCF and pCBA.

### 3.3.2. Multi-needle electrodes-APPJ

Another approach for treating significant amounts of polluted water, at least a quarter liter, was tested. Treatments were carried out using a continuous flow system with varying treatment times. The plasma source with multi-needle electrode geometry was employed to create plasma over the recirculated DCF and pCBA solutions. The goal of generating multi plasma jets over the recirculation solutions was to increase the plasma-liquid contact area and introduce more reactive species into the liquid, which can enhance the degradation.

The DCF degradation curve as a function of treatment time is depicted in Fig. 7a. DCF decayed significantly in the first 10 min at both initial DCF concentrations, although the rate of degradation was faster at the lower initial concentration. The complete removal of DCF was seen with both initial concentrations in 30 min. The quicker degradation could be explained by plasma-generated reactive components participating in DCF removal.

To undertake the kinetic analysis and determine the reaction order and rate constant, the experimental results were evaluated. When the treatment was performed at an initial concentration of 25 mg/L, the decay of DCF was well-matched with a first-order equation with a rate constant of 0.145 min<sup>-1</sup>. The first order revealed that plasma-generated reactive species not only interacted with DCF, but also with intermediate products. DCF degradation is governed by a zero-order equation for rich initial concentrations, such as 50 mg/L and the rate of degradation was 1.636 mgL<sup>-1</sup> min<sup>-1</sup>, as indicated by provided Eq. (17). Zero-order decay (Eq. (17)) demonstrates that the reaction rate is steady and independent of DCF concentration.

$$C = C_0 - kt \quad (17)$$

The time required to degrade 50 % of DCF was assessed and the half-life ( $t_{1/2}$ ) for zeroth-order decay was calculated using the given Eq. (18). It took roughly 5 min for lower initial concentrations of DCF to degrade 50 % and three times longer for higher concentrations.

$$t_{1/2} = \frac{C_0}{2k} \quad (18)$$

Fig. 7b depicts the calculated energy yield as a function of DCF removal for two initial concentrations. DCF concentration has a substantial impact on energy yield. The high energy yield for DCF elimination is most likely owing to a greater contribution of plasma-induced reactive species to the oxidation process. At 25 mg/L and 50 mg/L, the energy yield values were approximately 1542 mg/kWh and 3084 mg/kWh for complete degradation of DCF, respectively.

Multi-needle electrodes-APPJ was also explored for the treatment of pCBA, the degradation result can be seen in Fig. 7c. During the treatment of pCBA, slow degradation was observed, about 24 % removal of pCBA after 50 min of plasma treatment. A kinetic study was conducted to explore the kinetic behavior of pCBA. The investigation was carried out with only three treatment times in consideration. The degradation of pCBA corresponded closely to a first-order equation. The kinetic constant for pCBA was 0.00497 min<sup>-1</sup>, which was lower than the kinetic constant for DCF.

The slow decomposition of pCBA in a case of 3-pin APPJ can be attributed to the different experimental setup compared to 1-pin APPJ. In case of 3-pin jet, although the effective plasma-liquid contact is larger than in case of 1-pin APPJ here we had a better mixing of the contaminated sample. This could lead to a higher competition for the reactive oxygen species (HO• radicals for example), which plays important role in interactions with pCBA byproducts and with the original compound. Also, increment of treated volume is reducing the efficiency of the treatment as with DCF compound.

The obtained energy yields at 50 % removal of DCF and pCBA by both plasma sources are estimated and compared to previous plasma-based DCF and pCBA removal. As previously stated, DCF was the most efficiently degraded pollutant in both plasma sources in our investigation. However, when the plasma sources were compared, the resulting energy yields were

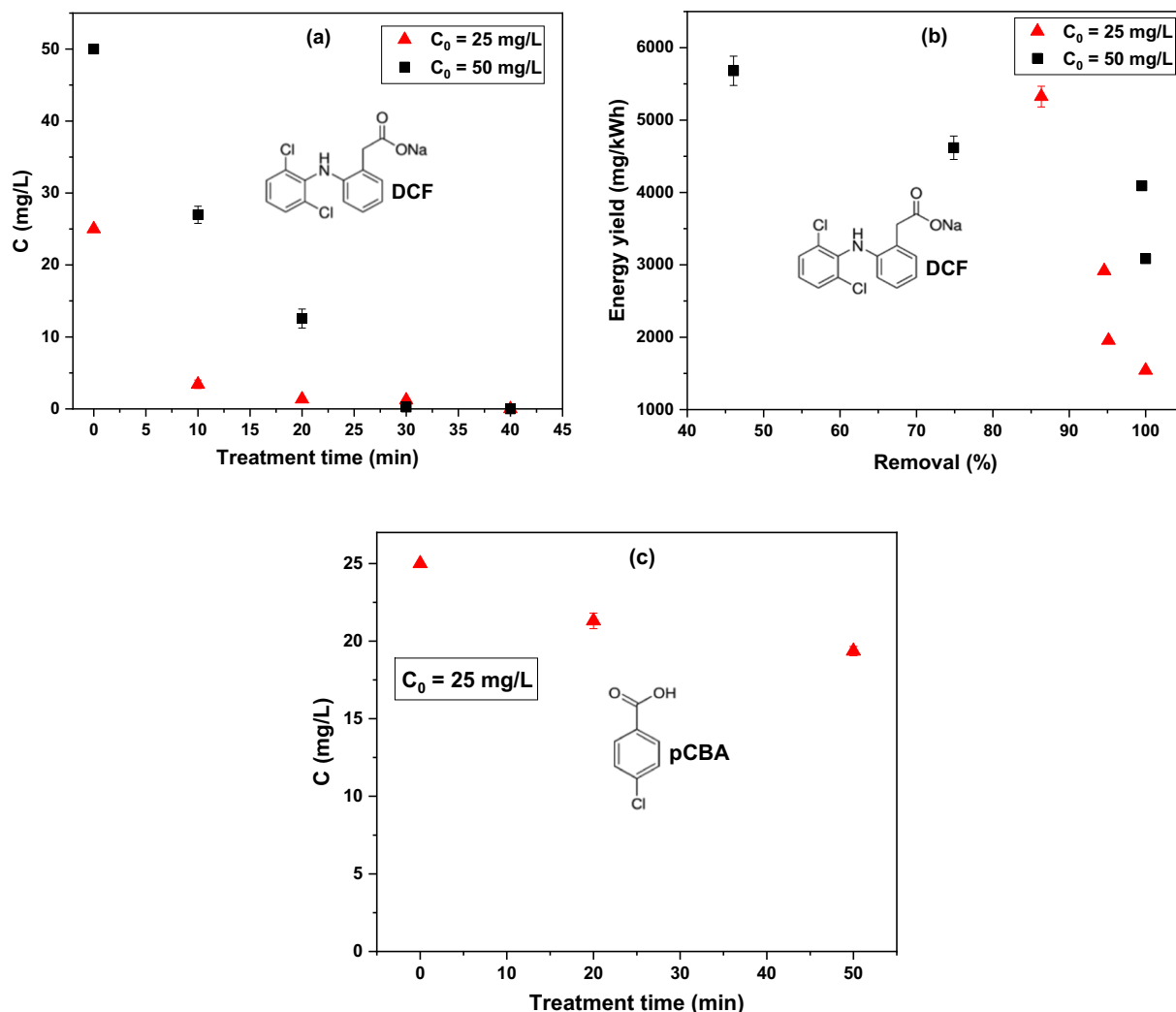


Fig. 7. (a) Change in DCF concentration with treatment time, (b) energy yield vs removal %, (DCF,  $C_0 = 25$  mg/L and  $C_0 = 50$  mg/L) and (c) change in pCBA concentration with treatment time (pCBA,  $C_0 = 25$  mg/L). Experimental conditions:  $V_0 = 250$  mL, argon flow of 2 slm,  $P_{\text{mean}}$  at the sample 8 W.

approximately one order of magnitude higher in multi-needle electrodes-APPJ than in pin-APPJ. This can be attributed to the increased plasma-liquid contact caused by three jets and a large initial volume, which results in a larger energy yield. In case of pCBA removal, the difference in energy output obtained with both plasma sources was not statistically significant.

Authors, for example, Dobrin et al., 2013 reported 1000 mg/kWh for 50 % and 760 mg/kWh for energy yield 90 % removal during the degradation of DCF by using pulsed corona discharge, where the plasma was formed over a liquid surface. Deng et al., 2021 used dielectric barrier discharge (DBD) plasma and obtained 2458 mg/kWh for 50 % and 1332 mg/kWh for 90 % DCF removal. According to Back et al., 2018, after the treatment of DCF with DBD, energy yield values varied from 20 to 715 mg/kWh for removal up to 90 %. When compared to our work, where DCF treatment was performed with the three jets-recirculation system, published data show relatively low DCF removal energy yield. In case of pCBA treatment, Lesage et al., 2014 explored the DBD-recirculation system and plasma was generated over the thin falling film, they found 624 mg/kWh of energy yield for 50 % removal. In the study of Schönekerl et al., 2020, degradation of pCBA was carried out with a plasma-multi electrodes system, as a result, 320 mg/kWh energy yield was obtained for 50 % removal. The reported energy yield associated with pCBA removal in the literature was not significantly different from our results.

If we look at the results, we can see that efficient removal of pollutants with a high energy yield suggests that treatment of some pollutants by

plasma with recirculation could be considered a potential method for wastewater treatment and the technology can also be scaled up for large polluted water treatment.

### 3.3.3. Degradation products and mechanism of DCF

The use of full-scan ultra-high performance liquid chromatography coupled to Orbitrap MS (UHPLC-Orbitrap-MS) allows the identification of seven TPs (see supplementary, Table S1) during the plasma treatment (by plasma recirculation system): DCF-154 ( $C_8H_{10}O_3$ ), DCF-166 ( $C_8H_6O_4$ ), DCF-202 ( $C_8H_{10}O_6$ ), DCF-241 ( $C_{14}H_{11}NO_3$ ), DCF-259 ( $C_{14}H_{10}ClNO_2$ ), DCF-277 ( $C_{14}H_9Cl_2NO$ ) and DCF-308 ( $C_{14}H_9Cl_2NO_3$ ). The TP analysis data was processed with Compound Discoverer software (Thermo Scientific). Elemental composition and double-bond equivalent (RDB) were selected. In all cases, possible elemental compositions for ions with a deviation of  $\pm 5$  ppm of error were assigned (see supplementary, Fig. S1-S7). On the basis of the TPs identified, tentatively DCF degradation pathways were proposed (Fig. 8).

Due to APPJ-liquid-interactions, abundant ROS can be produced such as including hydroxyl radicals ( $HO\cdot$ ), hydrogen peroxide ( $H_2O_2$ ), singlet oxygen ( $^1O_2$ ) and ozone ( $O_3$ ) (Cheng et al., 2020; Foster, 2017). Thereby,  $HO\cdot$  radicals can cleave DCF in the aqueous solution, leading to the formation of TPs, which could be further degraded and mineralized (Deng et al., 2021; Dobrin et al., 2013; Liu et al., 2019). Fig. 8 shows different reactions mechanisms  $HO\cdot$ -mediated such as hydroxylation, dechlorination,

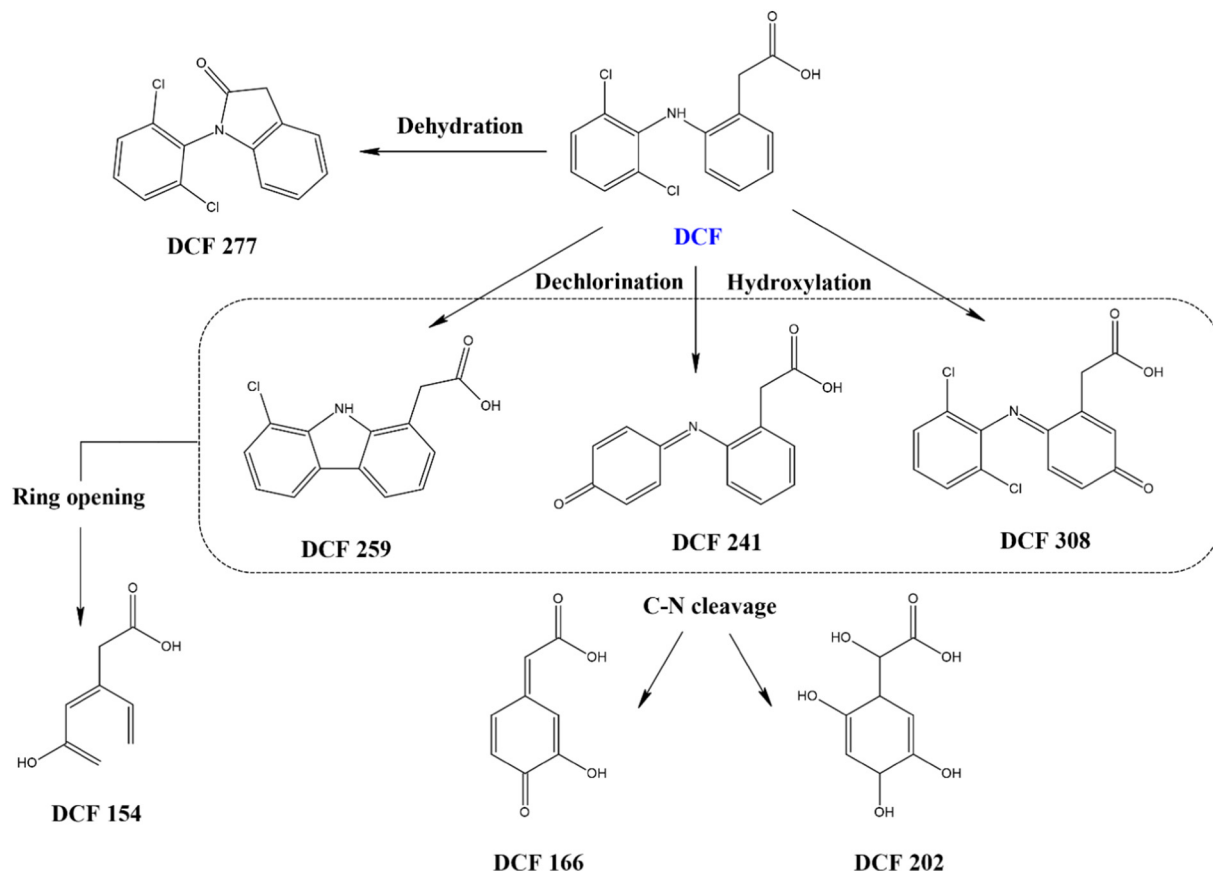


Fig. 8. Proposed possible reaction pathways for degradation of DCF.

cyclization and C—N cleavage, these tentative mechanisms are in agreement with the literature (Banaschik et al., 2018; Peng et al., 2021; Zhang et al., 2020).

The initial reaction of DCF with  $\text{HO}\cdot$  to lead to either the abstraction of a hydrogen or the addition of the hydroxyl radical in the electron-donating position of the aromatic ring, DCF could undergo hydroxylation and lead to the production of  $\text{C}_{14}\text{H}_{11}\text{NO}_3$  (DCF-241) and  $\text{C}_{14}\text{H}_9\text{Cl}_2\text{NO}_3$  (DCF-308), it is known that  $\text{HO}\cdot$  addition to benzene ring is kinetically more favored than H abstraction from the ring carbons (Agopcan Cinar et al., 2017). The presence of a Cl-benzyl bond in the aromatic ring of DCF resulted in fast dechlorination under plasma conditions and led to the release of chloride ions with reaction Gibbs free energies around 84–88 kcal/mol (Agopcan Cinar et al., 2017). Two dechlorination TPs were identified,  $\text{C}_{14}\text{H}_{11}\text{NO}_3$  (DCF-241) and  $\text{C}_{14}\text{H}_{10}\text{ClNO}_2$  (DCF-259). DCF-259 showed a transformation route involved the cyclisation into a carbazole derivative and loss of Cl (Salgado et al., 2013).

The mechanism suggested for the formation of DCF-277 ( $\text{C}_{14}\text{H}_9\text{Cl}_2\text{NO}$ ) starts with cyclization and is followed by water elimination. According to Agopcan Cinar et al., 2017, nitrogen attack on the carbonyl carbon results in formation of the cyclic intermediate. DCF-277 was also identified in Sono-activated persulfate oxidation (Monteagudo et al., 2018).

Subsequently, the cleavage of C—N bonds could occur and form low molecular weight byproducts including  $\text{C}_8\text{H}_{10}\text{O}_3$  (DCF-154),  $\text{C}_8\text{H}_6\text{O}_4$  (DCF-166) and  $\text{C}_8\text{H}_{10}\text{O}_6$  (DCF-202). The cleavage of the C—N bond can be facilitated by the attack of reactive species at the amino group in DCF and breaking the bridge of aromatic rings. Degradation of DCF could continue by cleavage of the ring and the formation of small molecules.

#### 4. Conclusion

In this study pin-APPJ and multi-needle electrodes-APPJ sources were utilized as chemical free AOPs approaches for degradation of DCF and

pCBA in water. We have constructed the 3-pin APPJ to be able to treat larger volumes and in flow regime. Both plasma sources operated in argon as a working gas and plasma was in contact with contaminated samples during the treatments. We have performed electrical characterization and obtained power deposited in the plasma in contact with liquid. This was necessary because power given by the power supply is not the same as power actually deposited in the discharges due to the losses in the system. The power deposited in the part of the discharge in contact with sample was needed for more precise calculation of energy yield. OES and ICCD imaging showed the presence and spatial distribution of excited species (for example  $\text{HO}\cdot$ ,  $\text{O}\cdot$ ,  $\text{N}_2$  (SPS), argon excited species etc.) that are major initiators of the reactions in the liquid phase.

Pollutant degradation was efficient by using both plasma sources with DCF degrading much faster than pCBA. For both contaminants, the degradation was more efficient with 1-pin APPJ due to the much smaller volume of the contaminated sample. The results showed that the multi-needle electrodes-APPJ treatment was more energy-efficient and the energy yield varied by the magnitude difference. The maximum energy yield values at 50 % elimination were 6465 mg/kWh and 4036 mg/kWh for DCF concentrations of 25 mg/L and 50 mg/L, respectively. The energy yield for pCBA removal was much lower. With the introduction of recirculation of contaminant, plasma created RONS had more time to react. As a result, the plasma-recirculation system has the most substantial impact to the degradation process.

The elemental composition of transformation products of DCF was identified by high-resolution Orbitrap-LC-MS. The tentative molecular structure of transformation products was analyzed and compared to the literature. The DCF oxidation routes are described and products that formed after various reaction processes including hydroxylation, dechlorination and cyclization are reported based on the chemical formula and molecular weight.

Overall, the findings of this study indicate that cold plasma technology can be efficient option for removing organic pollutants from water that are

extremely difficult to degrade in conventional WWTPs. A multi-needle electrodes-APPJ recirculating system implemented in the research has the ability to enhance plasma and liquid interaction.

### CRedit authorship contribution statement

Conceptualization A.K. N.P., W.G., N.S.; writing – original draft preparation A.K., review and editing A.K., N.S., N.P., W.G., O.J., A.P., S.Z., E.C.L., M.J.F.; supervision N.P., W.G.; project administration N.P., W.G. All authors have read and agreed to publish the manuscript.

### Data availability

Data will be made available on request.

### Declaration of competing interest

The authors state that they have no known competing financial interests or personal ties that could have seemed to affect the work reported in this study.

### Acknowledgments

This work was carried out under NOWELTIES project. NOWELTIES received funding from the European Union's Horizon 2020 research and innovation programme under the Marie Skłodowska-Curie grant agreement No. 812880. N.S., A.P., O. J. and N.P. are funded by the Ministry of Science, Technological Development and Innovation, grant number 451-03-68/2022-14/200024. This article is based upon work from COST Action PIAgri, CA19110, supported by COST (European Cooperation in Science and Technology).

### Appendix A. Supplementary data

Supplementary data to this article can be found online at <https://doi.org/10.1016/j.scitotenv.2022.161194>.

### References

Adhikari, B.C., Lamichhane, P., Lim, J.S., Nguyen, L.N., Choi, E.H., 2021. Generation of reactive species by naturally sucked air in the ar plasma jet. *Results in Physics* 30, 104863. <https://doi.org/10.1016/j.rinp.2021.104863>.

Agopcan Cinar, S., Ziyilan-Yavas, A., Catak, S., Ince, N.H., Aviyente, V., 2017. Hydroxyl radical-mediated degradation of diclofenac revisited: a computational approach to assessment of reaction mechanisms and by-products. *Environ. Sci. Pollut. Res.* 24, 18458–18469. <https://doi.org/10.1007/s11356-017-9482-7>.

Amor, C., Marchão, L., Lucas, M.S., Peres, J.A., 2019. Application of advanced oxidation processes for the treatment of recalcitrant agro-industrial wastewater: a review. *Water* 11, 205. <https://doi.org/10.3390/w11020205>.

An, T., Yang, H., Li, G., Song, W., Cooper, W.J., Nie, X., 2010. Kinetics and mechanism of advanced oxidation processes (AOPs) in degradation of ciprofloxacin in water. *Appl. Catal. B Environ.* 94, 288–294. <https://doi.org/10.1016/j.apcatb.2009.12.002>.

Arslan, M., Ullah, I., Müller, J.A., Shahid, N., Afzal, M., 2017. Organic micropollutants in the environment: ecotoxicity potential and methods for remediation. *Enhancing Cleanup of Environmental Pollutants*. Springer International Publishing, Cham, pp. 65–99. [https://doi.org/10.1007/978-3-319-55426-6\\_5](https://doi.org/10.1007/978-3-319-55426-6_5).

Attri, P., Kim, Y.H., Park, D.H., Park, J.H., Hong, Y.J., Uhm, H.S., Kim, K.N., Fridman, A., Choi, E.H., 2015. Generation mechanism of hydroxyl radical species and its lifetime prediction during the plasma-initiated ultraviolet (UV) photolysis. *Sci. Rep.* 5, 1–8. <https://doi.org/10.1038/srep09332>.

Back, J.O., Obholzer, T., Winkler, K., Jabornig, S., Rupprich, M., 2018. Combining ultrafiltration and non-thermal plasma for low energy degradation of pharmaceuticals from conventionally treated wastewater. *J. Environ. Chem. Eng.* 6, 7377–7385. <https://doi.org/10.1016/j.jece.2018.07.047>.

Banaschik, R., Jablonowski, H., Bednarski, P.J., Kolb, J.F., 2018. Degradation and intermediates of diclofenac as instructive example for decomposition of recalcitrant pharmaceuticals by hydroxyl radicals generated with pulsed corona plasma in water. *J. Hazard. Mater.* 342, 651–660. <https://doi.org/10.1016/j.jhazmat.2017.08.058>.

Barjasteh, A., Dehghani, Z., Lamichhane, P., Kaushik, N., Choi, E.H., Kaushik, N.K., 2021. Recent Progress in applications of non-thermal plasma for water purification, bio-sterilization, and decontamination. *Appl. Sci.* 11, 3372. <https://doi.org/10.3390/app11083372>.

Bing, J., Li, L., Lan, B., Liao, G., Zeng, J., Zhang, Q., Li, X., 2012. Synthesis of cerium-doped MCM-41 for ozonation of p-chlorobenzoic acid in aqueous solution. *Appl. Catal. B Environ.* 115–116, 16–24. <https://doi.org/10.1016/j.apcatb.2011.12.017>.

Bradu, C., Kutasi, K., Magureanu, M., Puač, N., Živković, S., 2020. Reactive nitrogen species in plasma-activated water: generation, chemistry and application in agriculture. *J. Phys. D: Appl. Phys.* 53, 223001. <https://doi.org/10.1088/1361-6463/ab795a>.

Bruggeman, P., Brandenburg, R., 2013. Atmospheric pressure discharge filaments and microplasmas: physics, chemistry and diagnostics. *J. Phys. D: Appl. Phys.* 46, 464001. <https://doi.org/10.1088/0022-3727/46/46/464001>.

Bruggeman, P.J., Kushner, M.J., Locke, B.R., Gardieniers, J.G.E., Graham, W.G., Graves, D.B., Hofman-Caris, R.C.H.M., Maric, D., Reid, J.P., Ceriani, E., Fernandez Rivas, D., Foster, J.E., Garrick, S.C., Gorbanev, Y., Hamaguchi, S., Iza, F., Jablonowski, H., Klimova, E., Kolb, J., Krema, F., Lukes, P., Machala, Z., Marinov, I., Mariotti, D., Medvedovic Thagard, S., Minakata, D., Neyts, E.C., Pawlat, J., Petrovic, Z.L., Pflieger, R., Reuter, S., Schram, D.C., Schröter, S., Shiraiwa, M., Tarabová, B., Tsai, P.A., Verlet, J.R.R., von Woedtko, T., Wilson, K.R., Yasui, K., Zvereva, G., 2016. Plasma-liquid interactions: a review and roadmap. *Plasma Sources Sci. Technol.* 25, 053002. <https://doi.org/10.1088/0963-0252/25/5/053002>.

Chen, F.F., 2016. Introduction to plasma physics and controlled fusion. Third Edit. ed. Springer International Publishing, Cham <https://doi.org/10.1007/978-3-319-22309-4>.

Cheng, J.-H., Lv, X., Pan, Y., Sun, D.-W., 2020. Foodborne bacterial stress responses to exogenous reactive oxygen species (ROS) induced by cold plasma treatments. *Trends Food Sci. Technol.* 103, 239–247. <https://doi.org/10.1016/j.tifs.2020.07.022>.

Cuerda-Correa, E.M., Alexandre-Franco, M.F., Fernández-González, C., 2019. Advanced oxidation processes for the removal of antibiotics from water: An Overview. *Water* 12, 102. <https://doi.org/10.3390/w12010102>.

Cullen, P.J., Milosavljević, V., 2015. Spectroscopic characterization of a radio-frequency argon plasma jet discharge in ambient air. *Prog. Theor. Exp. Phys.* 2015, 1–17. <https://doi.org/10.1093/ptep/ptv070>.

Deng, R., He, Q., Yang, D., Dong, Q., Wu, J., Yang, X., Chen, Y., 2021. Enhanced synergistic performance of nano-FeO-CeO<sub>2</sub> composites for the degradation of diclofenac in DBD plasma. *Chem. Eng. J.* 406, 126884. <https://doi.org/10.1016/j.cej.2020.126884>.

Dobrin, D., Bradu, C., Magureanu, M., Mandache, N.B., Parvulescu, V.I., 2013. Degradation of diclofenac in water using a pulsed corona discharge. *Chem. Eng. J.* 234, 389–396. <https://doi.org/10.1016/j.cej.2013.08.114>.

Domonkos, M., Tichá, P., Trejbal, J., Demo, P., 2021. Applications of cold atmospheric pressure plasma technology in medicine, agriculture and food industry. *Applied Sciences* 11, 4809. <https://doi.org/10.3390/app11114809>.

Du, J., Liu, Z., Bai, C., Li, L., Zhao, Y., Wang, L., Pan, J., 2018. Concentration distributions and reaction pathways of species in the mass transfer process from atmospheric pressure plasma jet to water. *Eur. Phys. J. D* 72, 179. <https://doi.org/10.1140/epjd/e2018-90138-3>.

Ebele, A.J., Abou-Elwafa Abdallah, M., Harrad, S., 2017. Pharmaceuticals and personal care products (PPCPs) in the freshwater aquatic environment. *Emerg. Contam.* 3, 1–16. <https://doi.org/10.1016/j.emcon.2016.12.004>.

Eggen, R.L.L., Hollender, J., Joss, A., Schärer, M., Stamm, C., 2014. Reducing the discharge of micropollutants in the aquatic environment: the benefits of upgrading wastewater treatment plants. *Environ. Sci. Technol.* 48, 7683–7689. <https://doi.org/10.1021/es500907n>.

Foster, J., Sommers, B.S., Gucker, S.N., Blankson, I.M., Adamovsky, G., 2012. Perspectives on the interaction of plasmas with liquid water for water purification. *IEEE Trans. Plasma Sci.* 40, 1311–1323. <https://doi.org/10.1109/TPS.2011.2180028>.

Foster, J.E., 2017. Plasma-based water purification: challenges and prospects for the future. *Phys. Plasmas* 24, 055501. <https://doi.org/10.1063/1.4977921>.

Fridman, A., 2008. *Plasma Chemistry*. 1st Edition. ed. Cambridge University Press, Cambridge <https://doi.org/10.1017/CBO9780511546075>.

García, M.C., Mora, M., Esquivel, D., Foster, J.E., Rodero, A., Jiménez-Sanchidrián, C., Romero-Salguero, F.J., 2017. Microwave atmospheric pressure plasma jets for wastewater treatment: degradation of methylene blue as a model dye. *Chemosphere* 180, 239–246. <https://doi.org/10.1016/j.chemosphere.2017.03.126>.

Garrido-Cardenas, J.A., Esteban-García, B., Agüera, A., Sánchez-Pérez, J.A., Manzano-Agugliaro, F., 2020. Wastewater treatment by advanced oxidation process and their worldwide research trends. *Int. J. Environ. Res. Public Health* 17, 170. <https://doi.org/10.3390/ijerph17010170>.

Gazeli, K., Svarnas, P., Held, B., Marlin, L., Clément, F., 2015. Possibility of controlling the chemical pattern of He and Ar “guided streamers” by means of N<sub>2</sub> or O<sub>2</sub> additives. *J. Appl. Phys.* 117, 093302. <https://doi.org/10.1063/1.4914035>.

Ghimire, B., Szili, E.J., Patenall, B.L., Lamichhane, P., Gaur, N., Robson, A.J., Trivedi, D., Thet, N.T., Jenkins, A.T.A., Choi, E.H., Short, R.D., 2021. Enhancement of hydrogen peroxide production from an atmospheric pressure argon plasma jet and implications to the antibacterial activity of plasma activated water. *Plasma Sources Sci. Technol.* 30, 035009. <https://doi.org/10.1088/1361-6595/abe0c9>.

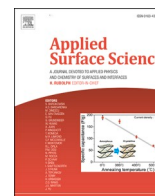
He, Y., Grieser, F., Ashokkumar, M., 2011. Kinetics and mechanism for the sonophotocatalytic degradation of p-chlorobenzoic acid. *J. Phys. Chem. A* 115, 6582–6588. <https://doi.org/10.1021/jp203518s>.

Heberer, T., Feldmann, D., 2005. Contribution of effluents from hospitals and private households to the total loads of diclofenac and carbamazepine in municipal sewage effluents - modeling versus measurements. *J. Hazard. Mater.* 122, 211–218. <https://doi.org/10.1016/j.jhazmat.2005.03.007>.

Hijosa-Valsero, M., Molina, R., Monràs, A., Müller, M., Bayona, J.M., 2014. Decontamination of waterborne chemical pollutants by using atmospheric pressure nonthermal plasma: a review. *Environ. Technol. Rev.* 3, 71–91. <https://doi.org/10.1080/21622515.2014.990935>.

Invernizzi, L., Muja, C., Sainct, F.P., Guillot, P., 2020. Investigation of RONS production and complex molecules degradation induced by an APPJ generated by two different sources. *IEEE Trans. Radiat. Plasma Med. Sci.* 4, 121–129. <https://doi.org/10.1109/TRPMS.2019.2918623>.

- Jaiswal, A.K., Ananthanarasimhan, J., Shivapuji, A.M., Dasappa, S., Rao, L., 2020. Experimental investigation of a non-catalytic cold plasma water-gas shift reaction. *J. Phys. D: Appl. Phys.* 53, 465205. <https://doi.org/10.1088/1361-6463/aba92d>.
- Jaiswal, S., Aguirre, E.M., 2021. Comparison of atmospheric pressure argon producing O(1S) and helium plasma jet on methylene blue degradation. *AIP Adv.* 11, 045311. <https://doi.org/10.1063/5.0046948>.
- Jankunaite, D., Tichonovas, M., Buivydiene, D., Radziuniene, I., Racys, V., Krugly, E., 2017. Removal of diclofenac, ketoprofen, and carbamazepine from simulated drinking water by advanced oxidation in a model reactor. *Water Air Soil Pollut.* 228, 1–15. <https://doi.org/10.1007/s11270-017-3517-z>.
- Judée, F., Simon, S., Bailly, C., Dufour, T., 2018. Plasma-activation of tap water using DBD for agronomy applications: identification and quantification of long lifetime chemical species and production/consumption mechanisms. *Water Res.* 133, 47–59. <https://doi.org/10.1016/j.watres.2017.12.035>.
- Khan, N.A., Ahmed, S., Farooqi, I.H., Ali, I., Vambol, V., Changani, F., Yousefi, M., Vambol, S., Khan, S.U., Khan, A.H., 2020. Occurrence, sources and conventional treatment techniques for various antibiotics present in hospital wastewaters: a critical review. *TrAC Trends Anal. Chem.* 129, 115921. <https://doi.org/10.1016/j.trac.2020.115921>.
- Kot-Wasik, A., Debska, J., Namieśnik, J., 2007. Analytical techniques in studies of the environmental fate of pharmaceuticals and personal-care products. *TrAC, Trends Anal. Chem.* 26, 557–568. <https://doi.org/10.1016/j.trac.2006.11.004>.
- Kumar, A., Skoro, N., Gernjak, W., Povrenović, D., Puač, N., 2022. Direct and indirect treatment of organic dye (Acid blue 25) solutions by using cold atmospheric plasma jet. *Front. Phys.* 10, 1–14. <https://doi.org/10.3389/fphy.2022.835635>.
- Kumar, A., Skoro, N., Gernjak, W., Puač, N., 2021. Cold atmospheric plasma technology for removal of organic micropollutants from wastewater—a review. *Eur. Phys. J. D* 75, 1–26. <https://doi.org/10.1140/epjd/s10053-021-00283-5>.
- Lamichhane, P., Acharya, T.R., Kaushik, N., Nguyen, L.N., Lim, J.S., Hessel, V., Kaushik, N.K., Choi, E.H., 2022. Non-thermal argon plasma jets of various lengths for selective reactive oxygen and nitrogen species production. *J. Environ. Chem. Eng.* 10, 107782. <https://doi.org/10.1016/j.jece.2022.107782>.
- Lesage, O., Falk, L., Tatoulian, M., Mantovani, D., Ognier, S., 2013. Treatment of 4-chlorobenzoic acid by plasma-based advanced oxidation processes. *Chem. Eng. Process. Process Intensif.* 72, 82–89. <https://doi.org/10.1016/j.cep.2013.06.008>.
- Lesage, O., Roques-Carmes, T., Commenge, J.M., Duten, X., Tatoulian, M., Cavadias, S., Mantovani, D., Ognier, S., 2014. Degradation of 4-chlorobenzoic acid in a thin falling film dielectric barrier discharge reactor. *Ind. Eng. Chem. Res.* 53, 10387–10396. <https://doi.org/10.1021/ie403772t>.
- Li, S., Ma, X., Jiang, Y., Cao, X., 2014. Acetamidoprid removal in wastewater by the low-temperature plasma using dielectric barrier discharge. *Ecotoxicol. Environ. Saf.* 106, 146–153. <https://doi.org/10.1016/j.ecoenv.2014.04.034>.
- Liu, F., Liang, J., Chen, L., Tong, M., Liu, W., 2019. Photocatalytic removal of diclofenac by Ti-doped BiOI microspheres under visible light irradiation: kinetics, mechanism, and pathways. *J. Mol. Liq.* 275, 807–814. <https://doi.org/10.1016/j.molliq.2018.11.119>.
- Liu, J., He, B., Chen, Q., Li, J., Xiong, Q., Yue, G., Zhang, X., Yang, S., Liu, H., Liu, Q.H., 2016. Direct synthesis of hydrogen peroxide from plasma-water interactions. *Sci. Rep.* 6, 1–7. <https://doi.org/10.1038/srep38454>.
- Lonappan, L., Brar, S.K., Das, R.K., Verma, M., Surampalli, R.Y., 2016. Diclofenac and its transformation products: environmental occurrence and toxicity - a review. *Environ. Int.* 96, 127–138. <https://doi.org/10.1016/j.envint.2016.09.014>.
- Lukes, P., Dolezalova, E., Sisrova, I., Clupek, M., 2014. Aqueous-phase chemistry and bactericidal effects from an air discharge plasma in contact with water: evidence for the formation of peroxyxynitrite through a pseudo-second-order post-discharge reaction of H<sub>2</sub>O<sub>2</sub> and HNO<sub>2</sub>. *Plasma Sources Sci. Technol.* 23, 015019. <https://doi.org/10.1088/0963-0252/23/1/015019>.
- Lukes, P., Locke, B.R., Brisset, J., 2012. Aqueous-phase chemistry of electrical discharge plasma in water and in gas-liquid environments. *Plasma Chemistry and Catalysis in Gases and Liquids*. Wiley, pp. 243–308. <https://doi.org/10.1002/9783527649525.ch7>.
- Ma, D., Yi, H., Lai, C., Liu, X., Huo, X., An, Z., Li, L., Fu, Y., Li, B., Zhang, M., Qin, L., Liu, S., Yang, L., 2021. Critical review of advanced oxidation processes in organic wastewater treatment. *Chemosphere* 275, 130104. <https://doi.org/10.1016/j.chemosphere.2021.130104>.
- Macías-Quiroga, I.F., Henao-Aguirre, P.A., Marín-Flórez, A., Arredondo-López, S.M., Sanabria-González, N.R., 2021. Bibliometric analysis of advanced oxidation processes (AOPs) in wastewater treatment: global and ibero-american research trends. *Environ. Sci. Pollut. Res.* 28, 23791–23811. <https://doi.org/10.1007/s11356-020-11333-7>.
- Magureau, M., Mandache, N.B., Parvulescu, V.I., 2015. Degradation of pharmaceutical compounds in water by non-thermal plasma treatment. *Water Res.* 81, 124–136. <https://doi.org/10.1016/j.watres.2015.05.037>.
- Malik, M.A., 2010. Water purification by plasmas: which reactors are most energy efficient? *Plasma Chem. Plasma Process.* 30, 21–31. <https://doi.org/10.1007/s11090-009-9202-2>.
- Markandya, A., Taylor, T., Longo, A., Murty, M.N., Murty, S., Dhavala, K., 2008. Counting the cost of vulture decline—an appraisal of the human health and other benefits of vultures in India. *Ecol. Econ.* 67, 194–204. <https://doi.org/10.1016/j.ecolecon.2008.04.020>.
- Monteagudo, J.M., El-taliawy, H., Durán, A., Caro, G., Bester, K., 2018. Sono-activated persulfate oxidation of diclofenac: degradation, kinetics, pathway and contribution of the different radicals involved. *J. Hazard. Mater.* 357, 457–465. <https://doi.org/10.1016/j.jhazmat.2018.06.031>.
- Mukherjee, A.G., Wanjar, U.R., Eladl, M.A., El-Sherbiny, M., Elsherbiny, D.M.A., Sukumar, A., Kannampuzha, S., Ravichandran, M., Renu, K., Vellingiri, B., Kandasamy, S., Gopalakrishnan, A.V., 2022. Mixed contaminants: occurrence, interactions, toxicity, detection, and remediation. *Molecules* 27, 2577. <https://doi.org/10.3390/molecules27082577>.
- Patel, M., Kumar, R., Kishor, K., Mlsna, T., Pittman, C.U., Mohan, D., 2019. Pharmaceuticals of emerging concern in aquatic systems: chemistry, occurrence, effects, and removal methods. *Chem. Rev.* 119, 3510–3673. <https://doi.org/10.1021/acs.chemrev.8b00299>.
- Pawlat, J., Terebun, P., Kwiatkowski, M., Tarabová, B., Kovalová, Z., Kučerová, K., Machala, Z., Janda, M., Hensel, K., 2019. Evaluation of oxidative species in gaseous and liquid phase generated by mini-gliding arc discharge. *Plasma Chem. Plasma Process.* 39, 627–642. <https://doi.org/10.1007/s11090-019-09974-9>.
- Peng, Y., Shi, H., Wang, Z., Fu, Y., Liu, Y., 2021. Kinetics and reaction mechanism of photochemical degradation of diclofenac by UV-activated peroxymonosulfate. *RSC Adv.* 11, 6804–6817. <https://doi.org/10.1039/D0RA10178H>.
- Phatak, P.V., Gaikar, V.G., 1996. Solubilities of o-and p-chlorobenzoic acids and o-and p-nitroanilines in N,N-Dimethylformamide + Water. *J. Chem. Eng. Data* 41, 1052–1054. <https://doi.org/10.1021/je960082m>.
- Pi, Y., Schumacher, J., Jekel, M., 2005. The use of Para-chlorobenzoic acid (pCBA) as an ozone/hydroxyl radical probe compound. *Ozone Sci. Eng.* 27, 431–436. <https://doi.org/10.1080/01919510500349309>.
- Rezaei, F., Vanraes, P., Nikiforov, A., Morent, R., Geyter, N.De, 2019. Applications of plasma-liquid systems: a review. *Materials* 12, 2751. <https://doi.org/10.3390/ma12172751>.
- Rodrigues, J.A., Silva, S., Cardoso, V.V., Benoliel, M.J., Cardoso, E., Coelho, M.R., Martins, A., Almeida, C.M.M., 2021. Screening and seasonal behavior of analgesics, non-steroidal anti-inflammatory drugs, and antibiotics in two urban wastewater treatment plants. *Environ. Manag.* 68, 411–425. <https://doi.org/10.1007/s00267-021-01496-5>.
- Rong, S., Sun, Y., Zhao, Z., Wang, H., 2014. Dielectric barrier discharge induced degradation of diclofenac in aqueous solution. *Water Sci. Technol.* 69, 76–83. <https://doi.org/10.2166/wst.2013.554>.
- Salgado, R., Pereira, V.J., Carvalho, G., Soeiro, R., Gaffney, V., Almeida, C., Cardoso, V.V., Ferreira, E., Benoliel, M.J., Ternes, T.A., Oehmen, A., Reis, M.A.M., Noronha, J.P., 2013. Photodegradation kinetics and transformation products of ketoprofen, diclofenac and atenolol in pure water and treated wastewater. *J. Hazard. Mater.* 244–245, 516–527. <https://doi.org/10.1016/j.jhazmat.2012.10.039>.
- Sathishkumar, P., Meena, R.A.A., Palanisami, T., Ashokkumar, V., Palvannan, T., Gu, F.L., 2020. Occurrence, interactive effects and ecological risk of diclofenac in environmental compartments and biota - a review. *Sci. Total Environ.* 698, 134057. <https://doi.org/10.1016/j.scitotenv.2019.134057>.
- Schellenberg, T., Subramanian, V., Ganeshan, G., Tompkins, D., Pradeep, R., 2020. Wastewater discharge standards in the evolving context of urban sustainability—the case of India. *Front. Environ. Sci.* 8. <https://doi.org/10.3389/fenvs.2020.00030>.
- Schönekerl, S., Weigert, A., Uhlig, S., Wellner, K., Pörschke, R., Pfefferkorn, C., Backhaus, K., Lerch, A., 2020. Evaluating the performance of a lab-scale water treatment plant using non-thermal plasma technology. *Water* 12, 1956. <https://doi.org/10.3390/w12071956>.
- Schwarzenbach, R.P., Escher, B.I., Fenner, K., Hofstetter, T.B., Johnson, C.A., von Gunten, U., Wehrli, B., 2006. The challenge of micropollutants in aquatic systems. *Science* 313, 1072–1077. <https://doi.org/10.1126/science.1127291>.
- Soler-Arango, J., Brelles-Mariño, G., Rodero, A., Garcia, M.C., 2018. Characterization of an air-based coaxial dielectric barrier discharge plasma source for biofilm eradication. *Plasma Chem. Plasma Process.* 38, 535–556. <https://doi.org/10.1007/s11090-018-9877-3>.
- Taggart, M.A., Senacha, K.R., Green, R.E., Cuthbert, R., Jhala, Y.V., Meharg, A.A., Mateo, R., Pain, D.J., 2009. Analysis of nine NSAIDs in ungulate tissues available to critically endangered vultures in India. *Environ. Sci. Technol.* 43, 4561–4566. <https://doi.org/10.1021/es9002026>.
- Thirumdas, R., Kothakota, A., Annappure, U., Siliveru, K., Blundell, R., Gatt, R., Valdramidis, V.P., 2018. Plasma activated water (PAW): chemistry, physico-chemical properties, applications in food and agriculture. *Trends Food Sci. Technol.* 77, 21–31. <https://doi.org/10.1016/j.tifs.2018.05.007>.
- Tomčić, S., Petrović, A., Puač, N., Škoro, N., Bekić, M., Petrović, Z.L., Čolić, M., 2021. Plasma-activated medium potentiates the immunogenicity of tumor cell lysates for dendritic cell-based cancer vaccines. *Cancers* 13, 10–13. <https://doi.org/10.3390/cancers13071626>.
- Topolovec, B., Škoro, N., Puač, N., Petrović, M., 2022. Pathways of organic micropollutants degradation in atmospheric pressure plasma processing – a review. *Chemosphere* 294, 133606. <https://doi.org/10.1016/j.chemosphere.2022.133606>.
- Uhm, H.S., Ki, S.H., Baik, K.Y., Choi, E.H., 2018. Influence of oxygen on generation of reactive chemicals from nitrogen plasma jet. *Sci. Rep.* 8, 1–12. <https://doi.org/10.1038/s41598-018-27473-3>.
- Wang, J.L., Xu, L.J., 2012. Advanced oxidation processes for wastewater treatment: formation of hydroxyl radical and application. *Crit. Rev. Environ. Sci. Technol.* 42, 251–325. <https://doi.org/10.1080/10643389.2010.507698>.
- Wenjuaan, B., Xiangli, Y., 2007. Nitrogen fixation into HNO<sub>3</sub> and HNO<sub>2</sub> by pulsed high voltage discharge. *Plasma Sci. Technol.* 9, 288–291. <https://doi.org/10.1088/1009-0630/9/3/08>.
- Wilkinson, J.L., Boxall, A.B.A., Al, K., 2022. Pharmaceutical pollution of the world's rivers. *Proceedings of the National Academy of Sciences* 119, 1–10. <https://doi.org/10.1073/pnas.2113947119>.
- Xiong, R., Xiong, Q., Nikiforov, A.Y., Vanraes, P., Leys, C., 2012. Influence of helium mole fraction distribution on the properties of cold atmospheric pressure helium plasma jets. *J. Appl. Phys.* 112, 033305. <https://doi.org/10.1063/1.4746700>.
- Yehia, S.A., Zarif, M.E., Bit, B.I., Teodorescu, M., Carpen, L.G., Vizireanu, S., Petrea, N., Dinescu, G., 2020. Development and optimization of single filament plasma jets for wastewater decontamination. *Plasma Chem. Plasma Process.* 40, 1485–1505. <https://doi.org/10.1007/s11090-020-10111-0>.
- Yousfi, M., Merbahi, N.P.J., Eichwald, O., Ricard, A., Gardou, J.P., Ducasse, O., Benhenni, M., 2011. Non thermal plasma sources of production of active species for biomedical uses: analyses, optimization and prospect. *Biomedical Engineering - Frontiers and Challenges* <https://doi.org/10.5772/19129>.
- Zhang, L., Liu, Y., Fu, Y., 2020. Degradation kinetics and mechanism of diclofenac by UV/paracetic acid. *RSC Adv.* 10, 9907–9916. <https://doi.org/10.1039/D0ra00363h>.



Full Length Article

# Regeneration of the ciprofloxacin-loaded clinoptilolite by non-thermal atmospheric plasma

Barbara Kalebić<sup>a,\*</sup>, Nikola Škoro<sup>b</sup>, Janez Kovač<sup>c</sup>, Nevenka Rajić<sup>a</sup><sup>a</sup> Faculty of Technology and Metallurgy, University of Belgrade, Karnegijeva 4, 11120 Belgrade, Serbia<sup>b</sup> Institute of Physics, University of Belgrade, Pregrevica 118, 11080 Belgrade, Serbia<sup>c</sup> Jožef Stefan Institute, Jamova cesta 39, 1000 Ljubljana, Slovenia

## ARTICLE INFO

## Keywords:

Adsorption  
Clinoptilolite  
Ciprofloxacin  
Non-thermal plasma  
Regeneration

## ABSTRACT

Natural clinoptilolite (CLI) exhibited a high efficacy in ciprofloxacin (CIP) removal from aqueous solution by adsorption. However, the regeneration of the spent adsorbent was a challenge since the adsorption occurred via electrostatic interactions and ion-exchange reaction. Herein, the feasibility of non-thermal plasma (NTP) was studied for the regeneration of ciprofloxacin-containing clinoptilolite (CIP-CLI) in five successive adsorption/NTP regeneration cycles. The NTP treatments were performed using a surface dielectric barrier discharge (SDBD) operating at atmospheric pressure in air. Plasma discharge gap, sample mass, and electrode surfaces were varied to find optimal regeneration parameters. For the plasma source with an electrode surface of 37.2 cm<sup>2</sup>, the 2 mm electrode gap and 20 min of plasma treatment were found as optimal parameters (sample mass of 0.2 g). The plasma treatment did not affect clinoptilolite features which were concluded from a study of textural properties and powder X-ray diffraction (PXRD) analysis. X-ray photoelectron spectroscopy (XPS) showed a decrease of total carbon content with around 10% of carbon residual left on the surface. The CLI adsorption capacity can be regenerated to at least 90% of its initial capacity during the five successive cycles, showing the involvement of plasma reactive species in decomposition of adsorbed CIP.

## 1. Introduction

Antibiotics are a group of pharmaceuticals intensively used in not only human, but also in veterinary medicine, as well as a growth promoter in livestock. Due to the wide range of their applications, global production of antibiotics constantly increases. According to Klein et al. the antibiotic consumption increased for 65% between 2000 and 2015 worldwide, which indicates that the presence of antibiotics in the environment is growing and causing numerous problems [1]. Antibiotics easily reach the natural water bodies via wastewater effluents and although present in low concentrations, they could have adverse effects on both ecosystem and human health [2].

Ciprofloxacin (CIP) is one of the most consumed antibiotics. It is a fluoroquinolone (Fig. 1) and can be found in surface water in concentration range from ng dm<sup>-3</sup> to mg dm<sup>-3</sup> [3]. A particular feature of CIP present in water solutions is its strong pH dependence. The zwitterionic structure with pK<sub>a</sub> = 5.90 ± 0.15 and 8.89 ± 0.11 for carboxyl and amine groups, respectively [4,5], makes CIP removal from water media more complex.

Moreover, due to the complex structure and low biodegradability, CIP cannot be completely removed from water by conventional wastewater treatment processes.

Among different methods, adsorption has been found to be a promising technique since it has shown a satisfactorily efficiency in removal of different organic contaminants such as organic dyes [6], pesticides [7], as well as pharmaceuticals [8]. The main advantages of adsorption are availability of a wide range of different adsorbent materials, low operational costs, as well as a possibility to reuse the spent adsorbent in a large number of adsorption cycles. Minerals such as porous aluminosilicates – zeolites have shown a good efficacy in removal of organic and inorganic pollutants from water solutions [9].

The adsorption of pollutants species on natural zeolites has many advantages due to their availability, low cost, unique structural features, and thermal stability. Regeneration of the spent zeolite-based adsorbents are usually based on relatively simple procedures. Thus, adsorbed phosphate or ammonia can be removed from the spent clinoptilolite-based adsorbent by NaOH solution [10] or by combined chemical and biological treatment [11], respectively, while most of the adsorbed

\* Corresponding author.

E-mail addresses: [bkalebic@tmf.bg.ac.rs](mailto:bkalebic@tmf.bg.ac.rs) (B. Kalebić), [nskoro@ipb.ac.rs](mailto:nskoro@ipb.ac.rs) (N. Škoro), [janez.kovac@ijs.si](mailto:janez.kovac@ijs.si) (J. Kovač), [nenat@tmf.bg.ac.rs](mailto:nenat@tmf.bg.ac.rs) (N. Rajić).

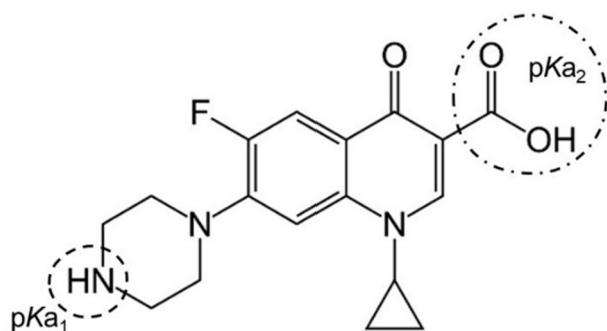


Fig. 1. Chemical structure of CIP molecule.

phenol can be released from the zeolite  $\beta$  (synthetic zeolite) by thermal desorption [12]. Generally, conventional regeneration methods are still the most applied ones so far, but they are not always effective due to complex adsorbate-adsorbent interactions. Thus, it has been previously investigated and determined that the regeneration efficacy of CIP-containing natural zeolite-clinoptilolite by ion-exchange reaction was low [13].

Recently, treatments based on non-thermal plasmas (NTPs) have been studied for regeneration and modification of different adsorbents. Plasma consists of excited molecules, ions, free radicals, and UV photons which provide enough energy for promoting different chemical reactions [14]. NTP has been used for the surface activation and modification of carbonaceous materials [15], clay minerals [16], and zeolites [14,17]. It has been reported that treatment of zeolite in NTP can increase the amount of oxygen functional groups on the zeolite surface and increase the pore openings by removal of captured organic species [17,18]. Namely, highly reactive species generated in NTP induce chemical bond cleavage on the surface layers of the adsorbent and thus restore the adsorption capacity. This is achieved in short treatment time, with a low energy consumption and without using any additional chemicals or producing toxic waste. Thus, the aforementioned features are the main advantages of the plasma treatments compared to commonly applied procedures.

However, NTP operating at atmospheric pressure are inevitably limited to small active plasma volumes, which restricts the effective treatment surface and the flux of reactive species. One way to overcome this limitation is to use a plane dielectric barrier discharge (DBD) type of plasma source which enables plasma formation in the gas at the surface of the electrode [19,20]. These sources named surface dielectric barrier discharge (SDBD) employ specific electrode geometry and dielectric insertion between electrodes, together with alternating high-voltage signals to form the plasma on large surfaces (in comparison to other NTP sources operating at atmospheric pressure) with limited discharge current.

NTP operating in air at atmospheric pressure is characterized by a diversity of generated reactive oxygen (ROS) and nitrogen species (RNS) such as radicals, ions, excited atoms, and molecules as well as neutral species ( $\cdot\text{O}$ ,  $\cdot\text{OH}$ ,  $\text{H}_2\text{O}_2$ ,  $\text{O}_3$ ,  $\text{N}_2^*$ ,  $\text{O}_2$ , etc.). The presence of short-lived OH radicals is primarily ascribed to water molecule dissociation through NTP [21]. Furthermore, the generation of long-lived reactive species of ozone and nitrogen ( $\text{NO}_x$  and  $\text{HNO}_x$ ) plays an important role in air DBD plasma, due to the generation of a sufficient amount of radicals and active species such as  $\text{N}_2$ ,  $\text{N}_2^+$ ,  $\text{O}_2$ ,  $\cdot\text{OH}$ , etc., which in turn induce a train of chemical reactions, resulting in the destruction of organic pollutant and intermediates molecules [22,23]. It is important to emphasize that plasma chemistry depends on plasma source parameters such as applied power density, and plasma conditions such as gas temperature, electron density, vibrational temperature, etc. [21,22]. An important asset of using SDBD sources is that it can operate in ambient air, avoiding the need for vacuum equipment. Moreover, it is possible to stack several sources to increase the effective surface, creating modular systems,

which allows a straightforward integration into the existing processing lines [24].

The aim of this study was to evaluate the ability of NTP technology for regeneration of a natural zeolite (clinoptilolite, CLI)-based adsorbent, that was used for the removal of antibiotic ciprofloxacin (CIP) from aqueous solutions. To investigate the CLI reusability and applicability of NTP, the adsorbent efficiency was investigated within five adsorption cycles with NTP as a regeneration step. Subsequently, the CLI before and after the NTP treatment, as well as the spent CLI was characterized in detail. Regeneration mechanisms considering the interaction between plasma and adsorbed CIP were discussed. To the best of our knowledge, natural clinoptilolite adsorbent regeneration by NTP technique has not been reported until now.

## 2. Materials and methods

### 2.1. Materials

The clinoptilolite-rich zeolitic tuff used in this study was obtained from the Serbian deposit Slanci, near the capital Belgrade. Major mineral phase of the zeolitic tuff was clinoptilolite (CLI) (>80 wt%) with quartz (<7.5 wt%) and feldspar (<13 wt%) as major satellite phases, which was revealed by quantitative PXRD analysis using the Rietveld refinement calculations and the Topas-Academic v.4 software package [25]. The cation exchange capacity (CEC) measured by a standard procedure [26] was 162.2 mmol  $\text{M}^+$ /100 g.

Prior to the adsorption experiments, the sample was sieved, washed with deionized water to remove impurities, and then dried in oven at 105 °C until a constant mass. The particle size used in the experiments was in the range of 0.063–0.125 mm for which previous experimental work showed the best adsorptive performance [27,28].

Two different concentrations of CIP were used. For preliminary optimization of the plasma treatment process, a solution of 200 mg  $\text{dm}^{-3}$  (CIP<sup>200</sup>-CLI) was used. For the reusability tests, a CIP solution of 25 mg  $\text{dm}^{-3}$  was used, since it is more of a realistic concentration found in natural waters and wastewaters.

All used chemicals were of analytical grade and deionized water was used in all adsorption experiments which were performed under controlled conditions. The CLI samples were weighted to four-digit accuracy, and the solution concentrations were determined with four-digit accuracy.

### 2.2. Adsorbent characterization

#### 2.2.1. Powder X-ray diffraction analysis (PXRD)

Clinoptilolite crystallinity was examined using a powder X-ray diffraction method (PXRD) and a Rigaku SmartLab powder diffractometer with  $\text{CuK}\alpha$  ( $\lambda = 1.54178 \text{ \AA}$ ) radiation at 40 kV and 30 mA. Scans were performed in the  $2\theta$  range from 5° to 65°, with 0.01° step and a scan rate of 5°  $\text{min}^{-1}$ .

#### 2.2.2. Textural properties

The specific surface area ( $S_{\text{BET}}$ ) and porosity were analyzed by nitrogen adsorption at  $-196 \text{ }^\circ\text{C}$  according to Brunauer Emmet Teller (BET) method [29] using a Surfer porosimeter (Thermo Fisher Scientific, USA). Prior to the analysis, the samples were degassed for 10 h at 150 °C under the vacuum. The pore size distribution (PSD) was calculated by Barrett, Joyner, and Halenda (BJH) method [30], and the data was extrapolated from desorption isotherm branch. The mesopore and micropore surfaces as well as the volume of micropore were calculated using the  $t$ -plot method [31].

#### 2.2.3. X-ray photoelectron spectroscopy (XPS)

The X-ray photoelectron spectroscopy (XPS) analyses were carried out on the PHI-TFA XPS spectrometer produced by Physical Electronics Inc and equipped with Al-monochromatic source. The analyzed area was

0.4 mm in diameter and the analyzed depth was about 3–5 nm. During data processing the spectra were aligned by setting the C 1 s peak at 284.8 eV, characteristic for C–C/C–H bonds. Quantification of surface composition was performed from XPS peak intensities considering relative sensitivity factors provided by instrument manufacturer [32]. The sensitivity of the method is about 0.5 at.%. To analyse in-depth distribution of elements in the sub-surface region up to 40 nm deep, the XPS depth profiling was performed in combination with ion sputtering. The Ar ions of energy 3 keV were used. The velocity of the ion sputtering was estimated to be  $2.0 \text{ nm min}^{-1}$  calibrated on the Ni/Cr multilayer structure of the known thickness.

### 2.3. CIP adsorption tests

Details of the adsorption experiments were given in our previous work [13]. Shortly, we found that the CLI has high affinity towards CIP at  $\text{pH} = 5$ . Accordingly, in this study the CIP adsorption experiments were performed at  $22 \pm 0.5 \text{ }^\circ\text{C}$  with a solid to liquid ratio of 1:100. Therefore, the adsorbent mass for the first adsorption cycle was 1.5 g for 150 ml of CIP solution. The mass loss per regeneration cycle was taken into account when calculating subsequent masses so that the above-mentioned ratio of 1:100 was maintained. The initial concentration of CIP solution was  $25 \text{ mg dm}^{-3}$  at  $\text{pH} = 5$  and the adsorption time was 5 min.

The CIP concentration ( $q$ ) on the CIP-containing CLI (CIP-CLI) was calculated using the following formula:

$$q = (25 - C_5) \times V/m \quad (1)$$

where  $C_5$  ( $\text{mg dm}^{-3}$ ) is the CIP concentration after 5 min,  $V$  ( $\text{dm}^3$ ) is the volume of the CIP solution, and  $m$  (g) is the adsorbent mass. The CIP concentration was measured in filtrate by a standard procedure using a UV–Vis spectrophotometer (Beckman Coulter DU®720, General Purpose) at 278 nm [33]. The CLI adsorption capacity for CIP was  $2.32 \text{ mg g}^{-1}$ .

After the adsorption experiment, adsorbent was separated from the liquid phase by vacuum filtration and then air-dried for around 2 h at room temperature.

### 2.4. Regeneration of CIP-CLI by plasma treatment

The regeneration experiments were performed by the NTP treatment

using a surface dielectric barrier discharge (SDBD) source. Electrical circuit and vertical cross section of the plasma source are schematically shown in Fig. 2a, while Fig. 2b shows a photograph of the plasma source with a CIP-CLI sample. Plasma source was composed of two parallel dielectrics barriers with electrodes – powered electrode facing the dielectric glass surface covering the grounded electrode. The round-shaped upper part consisted of Cu tape strips glued to both sides of a glass plate of 2 mm thickness forming a square with area of  $37.2 \text{ cm}^2$ . For scaling studies, a smaller version of the source with area of  $18.1 \text{ cm}^2$  was also used. Grid shaped electrodes from the lower side were powered while comb-shape electrodes from the upper side were grounded. The grounded stripe electrodes were positioned between powered electrode segments. The sample was put in a lower circular glass holder with side walls (ID: 108 mm, OD: 120 mm), which was standing on the grounded metal plate that served as a lower grounded electrode. The upper part was distanced  $d = 2 \text{ mm}$  from the lower dielectric. Sine high-voltage (HV) signal of 50 Hz was supplied to the powered electrode. Amplitude of the high-voltage signal was regulated by a voltage regulator at input of the AC signal to the primary coil of the HV transformer. In the grounded line  $R = 15 \text{ k}\Omega$  resistor was used to monitor the plasma current by measuring voltage drop on the resistor. In order to determine the gas temperature inside the active plasma volume during CIP-CLI sample treatment, an optical temperature sensor (opSense, OTG serie) placed inside the investigated volume was used.

Before treatments mass of each CIP-CLI sample were determined on a precise scale and then homogeneously spread on the glass holder in a very thin layer (less than 1 mm of thickness) to cover entire square are formed by the upper electrode. After plasma ignition, due to charging of the powder, it was drifting in electric field and conglomerating at certain points under the electrode grid. However, this had no influence on the treatment process which was assessed by repeating the treatment-adsorption cycle using the same parameters. The square-shaped electrode spacer was surrounding the active plasma zone, limiting the sample from drifting outside. After each treatment, very small amount of the sample was lost in manipulation so weighting at a precise scale was performed again before the adsorption step.

The efficiency of the regeneration treatment was measured in loss of the adsorption efficiency (LAE) which was calculated as a difference in CIP removal efficiency in the first and second adsorption cycle, after NTP treatment.

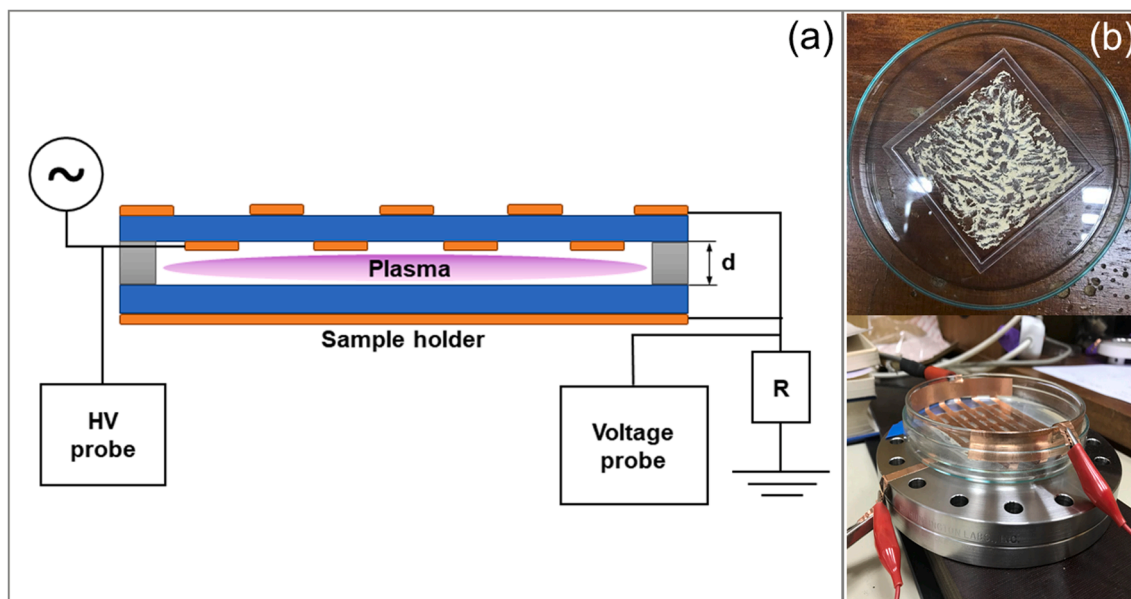


Fig. 2. Scheme of the plasma SDBD reactor (a) and image of the sample layer on the glass barrier and the used SDBD plasma source with the CIP-CLI sample (b).



## 2.5. Plasma characterization

### 2.5.1. Optical emission spectroscopy

To identify the excited species present in the plasma during treatment, optical emission spectroscopy (OES) of the surface dielectric barrier discharge in ambient air was performed. The OES measurements were attained using Maya 2000 Pro spectrometer (Ocean Optics Inc, FL, USA). Emission from the plasma region was collected and directed towards an entrance slit of the spectrometer by using a collimating lens in UV and VIS range (Ocean Optics UV74) and an optical fiber (Thorlabs, Newton, NJ, USA) with  $\varnothing 200 \mu\text{m}$  core.

### 2.5.2. Power measurement

Electric parameters were measured and recorded using a digital oscilloscope KEYSIGHT (InfiniiVision DSOX 1024A, USA), a high-voltage (HV) probe (P6015A, Tektronix Inc., Beaverton, OR, USA) and a voltage probe (N2863B, Agilent, Santa Clara, CA, USA). From the waveforms of voltage and current the instantaneous power  $P(t)$  was calculated, considering correction of the current signal belonging to the displacement current. Then, the mean power was calculated by averaging  $P(t)$  function for several signal periods. This setup allowed to monitor changes in the plasma with changing the treatment parameters and consequently to perform the optimization of the parameters. Moreover, we were able to monitor the stability of plasma during the treatment.

## 3. Results and discussion

### 3.1. Electrical measurements of the plasma source

Fig. 3 shows time varying signals of voltage at the powered electrode and plasma current recorded for  $V_p = 23 \text{ kV}$  (peak-to-peak), i.e., at conditions used for treatments. The plasma current signal is corrected to counterbalance the displacement current effect that appears due to the time-variation of the electric field. The displacement current is calculated assuming its fully capacitive origin – by taking a derivative of the applied voltage signal and using realistically determined capacitance of the source [19].

The voltage signal has sinusoidal shape while the current signal is periodical with distortions that appear both in the positive and negative part of the period and narrow spiry shape in maximum and minimum

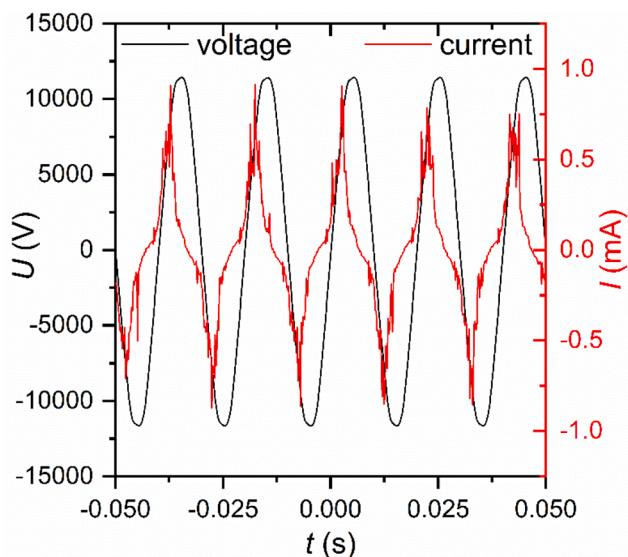


Fig. 3. Waveforms of electrode voltage (left axis) and plasma current (right axis) of the SDBD source in air at atmospheric pressure, recorded at 1.3 W. The current signal is shown without the displacement current.

values. At these values, especially for maxima, i.e. in the positive part of the signal, structures with peaks appear in the current signal. These current peaks appear due to occasional occurrence of filaments in diffuse surface discharge [19].

### 3.2. Optimization of the SDBD key operating parameters

This study investigates a range of operational parameters in order to determine the optimal ones for efficient regeneration of natural clinoptilolite after the ciprofloxacin adsorption. For this experiment the DBD source with the electrode surface of  $S = 18.1 \text{ cm}^2$  was used. The distance between electrodes ( $d$ ) and the sample as well as sample mass ( $m$ ) were varied. In all experiments the plasma treatment time was 20 min with maximum available voltage at the power supply. The treatment duration was selected as the longest possible considering the type of treatment as well as prior experiences. The three investigated combinations of parameters and associated plasma power are given in Table 1 together with the loss of adsorption efficiency after the plasma regeneration (LAE). LAE parameter is calculated as a difference in the CLI adsorption efficiency between the first and second adsorption cycle, where regeneration was made after the first cycle. The efficiencies of the regeneration process were measured as difference in adsorption efficiency before and after one regeneration treatment of CIP<sup>200</sup>-CLI.

The results showed that decrease of sample mass improved the adsorbent recovery. This was related to the effective area of sample particles exposed to the plasma. Moreover, decreasing the electrode gap also enhanced the adsorbent recovery process, i.e. decreased the LAE. Reduction in the electrode distance reduced active plasma volume which consequently increased the total plasma current, i.e. the density of reactive species. Consequently, a small increase in plasma power was obtained. Since the smallest reduction in adsorption efficiency was obtained with  $d = 2 \text{ mm}$ , this electrode gap was used for further investigation of atmospheric NTP treatment potential for the CLI regeneration after antibiotic adsorption.

To enable the treatment of a larger mass in one iteration, we expanded the electrode surface to approximately double of its size and increased the sample mass two times. Thus, the results obtained by using the source configuration with electrode surface of  $S = 37.2 \text{ cm}^2$  while treating the 0.20 g of CLI showed negligible difference in LAE, less than 1% in comparison to the most optimal configuration 2 (Table 1). The mean power in this case was 2.50 W. Thus, the obtained results support the fact that, for the range of parameters investigated, the plasma process is scalable with respect to active plasma area and treated sample mass. This is significant for potentially scaling up of the regeneration process.

After determination of the optimal conditions, the regeneration experiments were performed using the source with the electrode surface of  $37.2 \text{ cm}^2$ , at applied voltage of  $V_p = 23 \text{ kV}$  (peak-to-peak), i.e.  $V_{\text{RMS}} = 8 \text{ kV}$  and  $I_{\text{RMS}} = 0.30 \text{ mA}$ . In each treatment, 0.20 g of spent CLI was exposed to the plasma for 20 min. The mean power was calculated at several instances during each treatment and the value of  $2.50 \pm 0.06 \text{ W}$  was obtained.

Monitoring voltage and current during every plasma treatment also

Table 1

Parameters of the plasma treatment systems for regeneration process optimization.

Configuration	Plasma parameters		Sample	
	$d$ , mm	$P_{\text{mean}}$ , W	$m$ , g	LAE, %
1a	4	1.1	0.25	14.2
1b	4	1.1	0.10	12.3
2	2	1.3	0.10	10.0

Treatment time: 20 min.

$m$  – sample mass (g);  $d$  – plasma discharge gap (mm);  $P_{\text{mean}}$  – applied system power (W); LAE – loss of adsorption efficiency (%).

provided an additional insight into the amount of residual water in the samples. Namely, considerable change in the humidity levels in the active plasma volume is accompanied with reduction of the discharge current and power [34,35]. In our treatments these values proved to be unchanged so the amount of residual water in the samples was the same. Thus, all treatments were stable and reproducible.

### 3.3. Optical emission spectroscopy

The emission spectrum from the air SDBD plasma obtained in absence of CLI sample for a near ultraviolet–visible region (200–900 nm) is shown in Fig. 4. The spectrum gives a qualitative information regarding excited chemical species present in the plasma. The most intense lines recorded belong to the N<sub>2</sub> Second Positive System (SPS) band, as it was expected for an air plasma. Lower intensities of peaks can be observed for the First Negative System (FNS) of N<sub>2</sub>, and OH radicals since the plasma operates in ambient air of certain humidity. There were also very weak bands of the First Positive System (FPS) of N<sub>2</sub> in the visible part of the spectrum [36]. Furthermore, according to the literature data, the main active species present in such SDBD air plasma discharge (but not visible in the obtained OES spectrum) responsible for the degradation of organic molecules were found to be atomic oxygen (O), ozone (O<sub>3</sub>) [37,38], hydrogen peroxide (H<sub>2</sub>O<sub>2</sub>), hydroxyl radicals (OH), as well as peroxy nitrates and nitrogen oxides [39,40].

In order to perceive a possible emission from CIP decomposition products that were dispersed into the gas phase and excited in the plasma, the comparison between the spectra obtained without CLI sample and with CLI and CIP-CLI samples were performed. However, both obtained spectra had the same lines as in Fig. 4. So, no additional emission coming from the decomposition products of CIP (or eventually from CLI) could be detected in the investigated spectral range.

### 3.4. Plasma regeneration experiments

The reusability of CLI during the adsorption cycles was further investigated, and the results are shown in Fig. 5. The removal efficiency of CIP did not change significantly during the five adsorption cycles. The first cycle with the removal efficiency of 87 % included pristine CLI. After the first cycle, both removal efficiency and CLI adsorption capacity

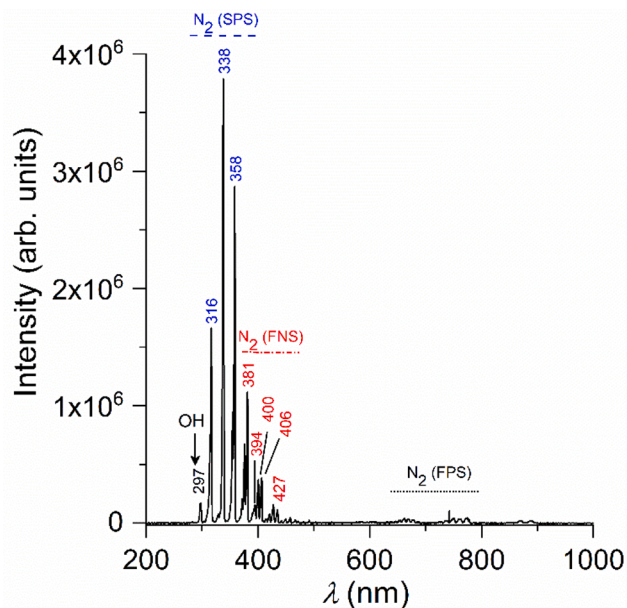


Fig. 4. The optical emission spectrum from the SDBD source in air at atmospheric pressure, recorded at 1.3 W. Line intensities are corrected for the spectral efficiency.

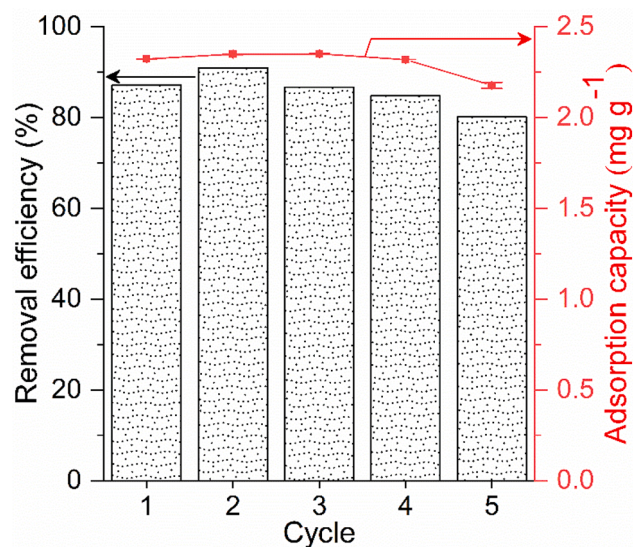


Fig. 5. Reusability tests of CLI for the removal of CIP through five cycles (bar graph – removal efficiency (%), symbol-line graph – adsorption capacity (mg g<sup>-1</sup>), C<sub>0</sub> = 25 mg dm<sup>-3</sup>, adsorbent dosage = 10 g dm<sup>-3</sup>, pH = 5, and contact time of 5 min).

stayed approximately constant during the next 3 cycles (87.5 ± 0.01 % and 2.34 ± 0.01 mg g<sup>-1</sup>, respectively). Subsequently, the removal efficiency of CIP decreased to 80% in the last cycle accompanied by a slightly decrease in CLI capacity (2.17 mg g<sup>-1</sup>).

Therefore, exposure of CIP-CLI sample to the plasma induced some mechanism of adsorbent regeneration. CIP is thermally stable in the temperature range 25–50 °C. Decomposition of the CIP starts at 50 °C and finishes at around 750 °C in three successive stages [41,42]. DBD plasma sources produce chemical reactive environment at nearly room-temperature since their construction prevents emergence of higher currents that can heat both the gas and the sample. In order to completely exclude the thermal effect of the plasma treatment, measurement of the gas temperature inside the plasma during sample treatment was performed. The measured temperature never exceeded 30 °C, with an average temperature increase of 2.5 °C during 20 min treatment. According to the abovementioned data about CIP thermal decomposition, the temperature that was achieved by SDBD plasma was not high enough to induce thermal degradation of CIP.

SDBD plasma source operating in air at atmospheric pressure generates different NO<sub>x</sub> species, ozone, hydroxyl radicals and hydrogen peroxide which can participate in the CIP degradation. Considering the presented results and literature data which mainly considered CIP degradation by plasma formed in a liquid phase, the main features of the CIP decomposition by air plasma most likely involve: 1) hydrogen attack on the piperidine ring followed by a recombination with OH, and 2) ozone attack on the carboxyl group of the quinolone moiety followed by subsequent attack of the piperazinyl substituent [40,43]. It seems likely that CIP was firstly degraded into different intermediates of masses between 300 and 420 Da. Then, some species were mineralized up to some extent under exposure to the NTP. Volatile by-products of these reactions were removed immediately during the plasma treatment while other probably remain at the CLI surface and detach in the following adsorption cycle. It was shown that some of the degradation products that appear resistant to further oxidation have highly polar nature which renders them water-soluble [43].

Preservation of zeolite crystallinity after plasma treatments has been confirmed by XRD measurements and is in accord with the literature data [14,18]. Crystallinity of the CLI was tested after the first (CIP-CLI\_PL1) and the fifth adsorption cycle (CIP-CLI\_PL5). The obtained PXRD diffractograms are shown in Fig. 6., showing that the plasma did

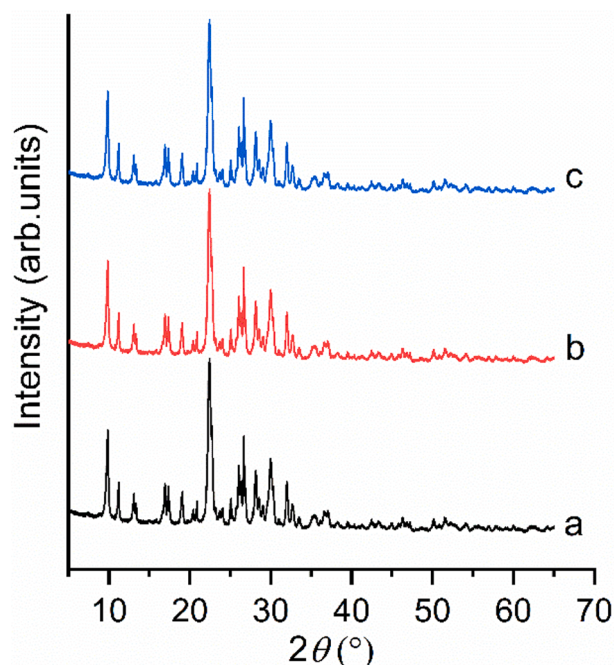


Fig. 6. PXRD patterns of CLI (a) and CIP-CLI\_PL1 (b) and CIP-CLI\_PL5 (c).

not affect structural feature of CLI through 5 cycles. The obtained XRD reflections are consistent with the natural clinoptilolite pattern [44]. Similar results were reported for the low-pressure oxygen plasma activation of zeolite-A [17] and clinoptilolite [18]. The plasma treatment increases the adsorption capacity of zeolite-A for cadmium ions and organic dyes [17].

The influence of NTP on textural properties of the spent adsorbent was studied using the adsorption/desorption experiments of  $N_2$  at  $-196^\circ C$ . The results are given at Fig. 7. According to IUPAC classification, the adsorption/desorption isotherms belong to the type IV, which is the characteristic of mesoporous solids [45]. The presence of hysteresis loops of type H3 is typical for clinoptilolite indicating that clinoptilolite is in the form of non-rigid aggregates of plate-like particles, generating slit-shaped pores [46]. Fig. 7 also shows a higher adsorption of  $N_2$  at  $-196^\circ C$  on CIP-CLI\_PL in comparison to the other two samples which

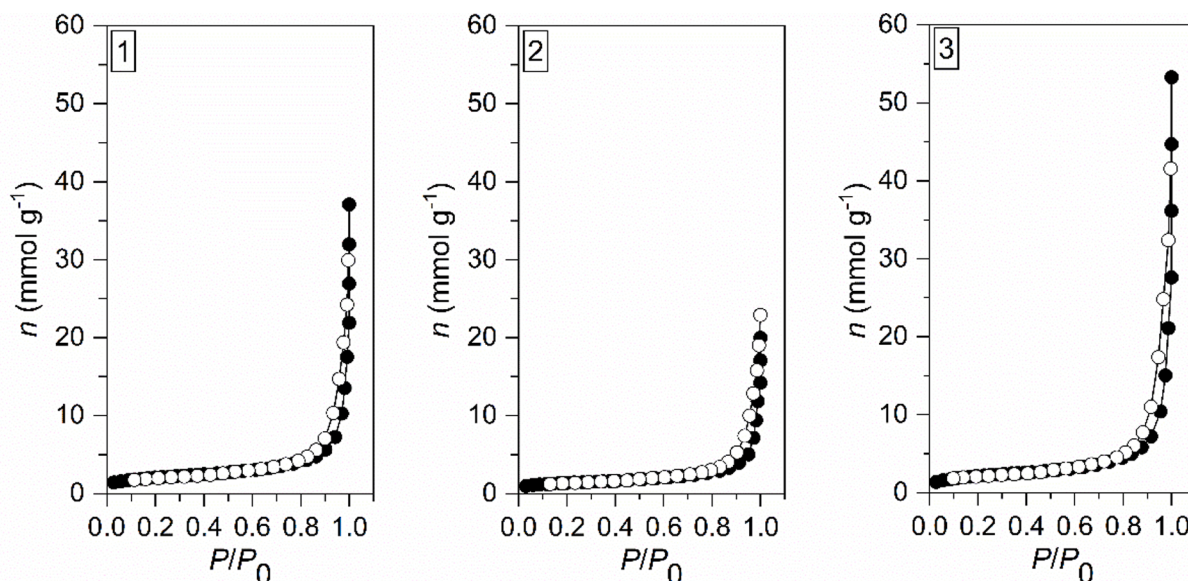


Fig. 7. Nitrogen adsorption isotherms plot for CLI (1), CIP-CLI (2), and CIP-CLI\_PL (3). Solid symbols – adsorption, open symbols – desorption.

could be assigned to a higher number of mesopores after the plasma regeneration treatment. This could be also attributed to slower  $N_2$  molecule diffusion through CLI and CIP-CLI lattice due to the presence of impurities that prevent the  $N_2$  molecules to access the clinoptilolite pore system.

The specific surface area ( $S_{BET}$ ) of CLI calculated by BET equation ( $32\text{ m}^2\text{ g}^{-1}$ ) was similar to that for raw clinoptilolite reported in literature [47,48]. The textural properties of CIP-CLI ( $2.32\text{ mg CIP g}^{-1}$ ) before and after NTP treatment (CIP-CLI\_PL) were similar to that of raw CLI (Table S1). Furthermore, plasma treatment did not significantly influence the pore size distribution (Fig. S1).

To get an insight into the surface properties after plasma treatment, XPS analysis was performed. Fig. 8 shows typical XPS survey spectra from the surface of CLI, CIP-CLI, CIP-CLI\_PL and CIP samples. The peaks of elements O, Fe, Si, Al, Ca, Mg and K were identified in XPS spectra originating from the CLI matrix. In addition, carbon present in CLI spectra (Fig. 8-1) originated from the contamination layer due to sample handling in air. The binding energy found in the carbon C 1s XPS spectra of CIP-CLI (Fig. 8-2) and CIP-CLI\_PL (Fig. 8-3) is  $284.7\text{ eV}$ , and that can be assigned to C-C and C-H bonds [49]. The XPS spectrum of pure CIP (Fig. 8-4) displayed F, N, C and O peaks. The F and N peaks are also evident in the spectra of CIP-CLI and CIP-CLI\_PL (Fig. 8-2 and 8-3) which confirming the presence of CIP. The intensity of F and N peaks were lower for CIP-CLI\_PL sample than for the CIP-CLI sample due to plasma treatment.

Moreover, Fig. 9 shows that the C concentration was significantly higher for CIP-CLI as well as for the CIP-CLI\_PL than for pristine CLI. These suggested three facts: 1) presence of CIP on the CLI results in an increase of C concentration onto CLI surface, 2) C concentration is lower for about 50% for the plasma treated CLI than for CLI-CIP, and 3) certain amount of C (about 10%) remained in the CLI lattice after the treatment suggesting that the NTP did not completely remove organic species present in CLI. We should note that the Ar-ion sputtering of powder samples does not remove uniformly the surface layer on all particles due to the shadowing effect, which is present due to uneven sample surface. This could be the main reason that carbon was present also after different sputtering time, which reflects the carbon-based coating of particles in the non-sputtered area among the particles. Anyhow, we believe that level of carbon concentration in the XPS profiles represents the residual level of CIP after NTP treatment. During XPS depth profiling, the concentration of F and N was not followed on the CIP-CLI and CIP-CLI\_PL samples due to their low concentrations.

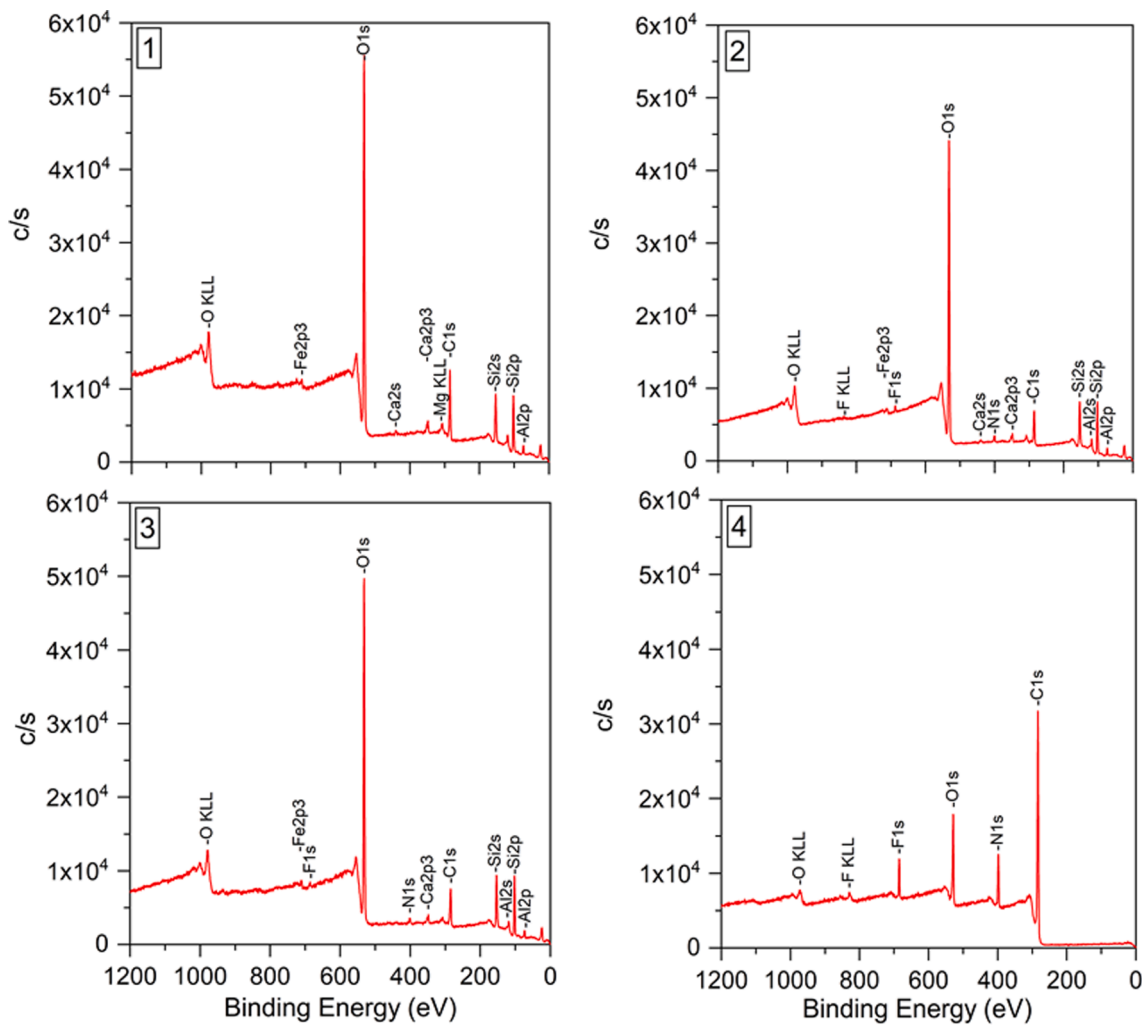


Fig. 8. XPS survey spectra from the surface of pristine CLI (1), CIP-CLI (2), CIP-CLI\_PL (3) and CIP (4).

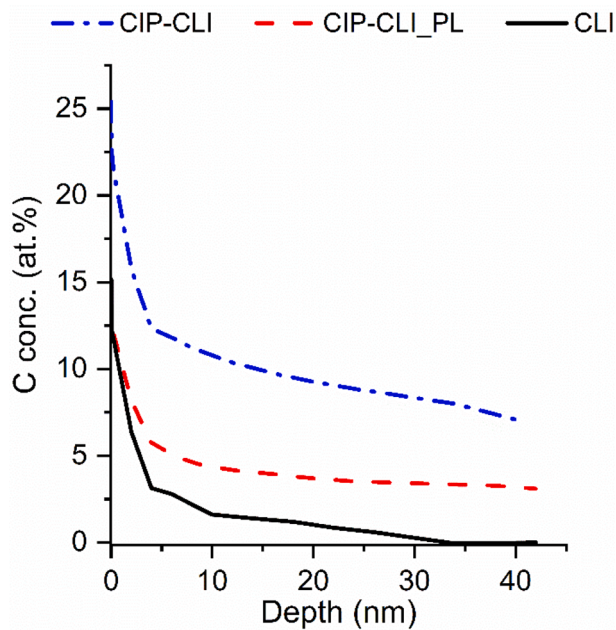


Fig. 9. XPS depth profile for C obtained on the samples CLI, CIP-CLI and CIP-CLI\_PL.

#### 4. Conclusions

Non-thermal plasma was used for the removal of antibiotic ciprofloxacin adsorbed by natural clinoptilolite. The plasma treatment operating at atmospheric pressure with air as the working gas regenerated the spent adsorbent in a high rate (about 90%). The adsorption capacity remains stable after the five adsorption/plasma regeneration cycles with the less than 7% difference in the adsorption efficiency of the first and fifth adsorption cycles.

The plasma treatment did not affect clinoptilolite crystallinity nor its specific surface area. XPS analysis showed that the treatment decomposed majority of the adsorbed ciprofloxacin with about 10% of carbon left immobilized on the surface.

Performed electrical characterization of the plasma source proved the stability of plasma properties in different treatments with a power consumption of 2.5 W. Optical emission measurements showed typical spectrum of an air plasma with OH radical and excited N<sub>2</sub> species. The obtained results of the scaling-up the plasma source showed that doubling the treatment area and sample mass gave repeatable result. All this proves the fact that innovative plasma treatment could be applicable on a larger scale (an industrial plant).

By using a non-thermal atmospheric pressure plasma treatment, the adsorption capacity of the spent clinoptilolite can be almost completely restored, preserving the initial crystalline structure and textural properties of clinoptilolite. All these leads to the conclusion that non-thermal plasma, as an innovative method for the regeneration of antibiotic-

containing natural clinoptilolite can be considered as perspective, economically and environmentally acceptable method.

## Funding

This research was supported by the European Union's Horizon 2020 research and innovation program under the Marie Skłodowska-Curie grant agreement, MSCA-ITN-2018 [grant number 812880] and the Ministry of Education, Science and Technological Development of the Republic of Serbia [grant numbers 451-03-68/2022-14/200135 and 451-03-68/2022-14/200024].

## CRedit authorship contribution statement

**Barbara Kalebić:** Methodology, Formal analysis, Investigation, Data curation, Writing – original draft, Visualization. **Nikola Škoro:** Conceptualization, Methodology, Validation, Investigation, Writing – review & editing. **Janez Kovač:** Formal analysis, Writing – review & editing. **Nevenka Rajić:** Conceptualization, Methodology, Validation, Resources, Writing – review & editing, Supervision, Project administration, Funding acquisition.

## Declaration of Competing Interest

The authors declare that they have no known competing financial interests or personal relationships that could have appeared to influence the work reported in this paper.

## Acknowledgments

The authors are very grateful to prof. dr. Branko Matović from the Institute of Nuclear Science "Vinča" (Belgrade, Serbia) for performance of BET and XRD analysis.

## Appendix A. Supplementary material

Supplementary data to this article can be found online at <https://doi.org/10.1016/j.apsusc.2022.153379>.


## References

- E.Y. Klein, T.P. van Boeckel, E.M. Martinez, S. Pant, S. Gandra, S.A. Levin, H. Goossens, R. Laxminarayan, Global increase and geographic convergence in antibiotic consumption between 2000 and 2015, *PNAS* 115 (2018) E3463–E3470, <https://doi.org/10.1073/pnas.1717295115>.
- M.C. Danner, A. Robertson, V. Behrends, J. Reiss, Antibiotic pollution in surface fresh waters: Occurrence and effects, *Sci. Total Environ.* 664 (2019) 793–804, <https://doi.org/10.1016/j.scitotenv.2019.01.406>.
- S. Rakshit, D. Sarkar, E.J. Elzinga, P. Punamiya, R. Datta, Mechanisms of ciprofloxacin removal by nano-sized magnetite, *J. Hazard. Mater.* 246–247 (2013) 221–226, <https://doi.org/10.1016/j.jhazmat.2012.12.032>.
- N. Genç, E.C. Dogan, Adsorption kinetics of the antibiotic ciprofloxacin on bentonite, activated carbon, zeolite, and pumice, *Desalin. Water Treat.* 53 (3) (2015) 785–793, <https://doi.org/10.1080/19443994.2013.842504>.
- S.A.C. Carabineiro, T. Thavorn-amornsri, M.F.R. Pereira, P. Serp, J.L. Figueiredo, Comparison between activated carbon, carbon xerogel and carbon nanotubes for the adsorption of the antibiotic ciprofloxacin, *Catal. Today* 186 (1) (2012) 29–34, <https://doi.org/10.1016/j.cattod.2011.08.020>.
- W. Xiao, X. Jiang, X. Liu, W. Zhou, Z.N. Garba, I. Lawan, L. Wang, Z. Yuan, Adsorption of organic dyes from wastewater by metal-doped porous carbon materials, *J. Cleaner Prod.* 284 (2021), <https://doi.org/10.1016/j.jclepro.2020.124773>.
- A. Mojiri, J.L. Zhou, B. Robinson, A. Ohashi, N. Ozaki, T. Kindaichi, H. Farraji, M. Vakili, Pesticides in aquatic environments and their removal by adsorption methods, *Chemosphere* 253 (2020), <https://doi.org/10.1016/j.chemosphere.2020.126646>.
- J.R. de Andrade, M.F. Oliveira, M.G.C. da Silva, M.G.A. Vieira, Adsorption of Pharmaceuticals from Water and Wastewater Using Nonconventional Low-Cost Materials: A Review, *Ind. Eng. Chem. Res.* 57 (9) (2018) 3103–3127, <https://doi.org/10.1021/acs.iecr.7b05137>.
- A. Lam, A. Rivera, Theoretical study of the interaction of surfactants and drugs with natural zeolite, *Microporous Mesoporous Mater.* 91 (1–3) (2006) 181–186, <https://doi.org/10.1016/j.micromeso.2005.11.035>.
- I. Kaplanec, A. Rečnik, G. Mali, N. Rajić, Study of the iron(III)-modified clinoptilolite in the adsorption of phosphate from aqueous medium: Mechanism and kinetics, *Desalin. Water Treat.* 78 (2017) 231–240, <https://doi.org/10.5004/dwt.2017.20875>.
- A. Hedström, L. Rastas Amofah, Adsorption and desorption of ammonium by clinoptilolite adsorbent in municipal wastewater treatment systems, *J. Environ. Eng. Sci.* 7 (1) (2008) 53–61, <https://doi.org/10.1139/S07-029>.
- L. Damjanović, V. Rakić, V. Rac, D. Stosić, A. Auroux, The investigation of phenol removal from aqueous solutions by zeolites as solid adsorbents, *J. Hazard. Mater.* 184 (1–3) (2010) 477–484, <https://doi.org/10.1016/j.jhazmat.2010.08.059>.
- B. Kalebić, J. Pavlović, J. Dikić, A. Rečnik, S. Gyergyek, N. Škoro, N. Rajić, Use of natural clinoptilolite in the preparation of an efficient adsorbent for ciprofloxacin removal from aqueous media, *Minerals* 11 (2021), <https://doi.org/10.3390/min11050518>.
- H. Mirzaei, M.R. Almasian, S.M.A. Mousavian, H. Sid Kalal, Plasma modification of a natural zeolite to improve its adsorption capacity of strontium ions from water samples, *Int. J. Environ. Sci. Technol.* 16 (10) (2019) 6157–6166, <https://doi.org/10.1007/s13762-018-2024-0>.
- P.S. de Velasco Maldonado, V. Hernández-Montoya, A. Concheso, M.A. Montes-Morán, Formation of cerussite and hydrocerussite during adsorption of lead from aqueous solution on oxidized carbons by cold oxygen plasma, *Appl. Surf. Sci.* 386 (2016) 381–388, <https://doi.org/10.1016/j.apsusc.2016.06.025>.
- Ö. Yavuz, C. Saka, Surface modification with cold plasma application on kaolin and its effects on the adsorption of methylene blue, *Appl. Clay Sci.* 85 (2013) 96–102, <https://doi.org/10.1016/j.clay.2013.09.011>.
- A. Fahmy, A. Elzeref, H. Youssef, H. Shehata, M. Wassel, J. Friedrich, F. Poncin-Epaillard, D. Debarnot, Plasma O<sub>2</sub> modifies the structure of synthetic zeolite-A to improve the removal of cadmium ions from aqueous solutions, *Turk. J. Chem.* 43 (2019) 172–184, <https://doi.org/10.3906/kim-1808-14>.
- P.S. de Velasco-Maldonado, V. Hernández-Montoya, M.A. Montes-Morán, N.A. R. Vázquez, M.A. Pérez-Cruz, Surface modification of a natural zeolite by treatment with cold oxygen plasma: Characterization and application in water treatment, *Appl. Surf. Sci.* 434 (2018) 1193–1199, <https://doi.org/10.1016/j.apsusc.2017.11.023>.
- R. Brandenburg, Corrigendum: Dielectric barrier discharges: progress on plasma sources and on the understanding of regimes and single filaments, *Plasma Sources Sci. Technol.* 27 (2018), <https://doi.org/10.1088/1361-6595/aaced9>.
- U. Kogelschatz, Dielectric-barrier discharges: Their history, discharge physics, and industrial applications, *Plasma Chem. Plasma Process.* 23 (2003) 1–46.
- P. Bruggeman, D.C. Schram, On OH production in water containing atmospheric pressure plasmas, *Plasma Sources Sci. Technol.* 19 (2010), <https://doi.org/10.1088/0963-0252/19/4/045025>.
- E. Simoncelli, J. Schulpen, F. Barletta, R. Laurita, V. Colombo, A. Nikiforov, M. Gherardi, UV-VIS optical spectroscopy investigation on the kinetics of long-lived RONS produced by a surface DBD plasma source, *Plasma Sources Sci. Technol.* 28 (2019), <https://doi.org/10.1088/1361-6595/ab3c36>.
- N. Jiang, R. Shang, S.G.J. Heijman, L.C. Rietveld, High-silica zeolites for adsorption of organic micro-pollutants in water treatment: A review, *Water Res.* 144 (2018) 145–161, <https://doi.org/10.1016/j.watres.2018.07.017>.
- R. Suresh, B. Rajoo, M. Chenniappan, M. Palanichamy, Treatment possibilities of electrical discharge non-thermal plasma for industrial wastewater treatment-review, *IOP Conference Series: Materials Science and Engineering* 1055 (2021), 012018, <https://doi.org/10.1088/1757-899X/1055/1/012018>.
- A. Coelho, TOPAS Academic 4.1; Coelho Software: Brisbane, Australia, 2007.
- D.W. Ming, J.B. Dixon, Quantitative determination of clinoptilolite in soils by a cation-exchange capacity method, *Clays Clay Miner.* 35 (1987) 463–468.
- N. Rajić, D. Stojaković, M. Jovanović, N.Z. Logar, M. Mazaj, V. Kaucic, Removal of nickel(II) ions from aqueous solutions using the natural clinoptilolite and preparation of nano-NiO on the exhausted clinoptilolite, *Appl. Surf. Sci.* 257 (5) (2010) 1524–1532.
- D. Stojaković, J. Milenković, N. Daneu, N. Rajić, A Study of the Removal of Copper Ions from Aqueous Solution Using Clinoptilolite from Serbia, *Clays Clay Miner* 59 (2012) 277–285, <https://doi.org/10.1346/CCMN.2011.0590305>.
- S. Brunauer, P.H. Emmett, E. Teller, Adsorption of Gases in Multimolecular Layers, *J. Am. Chem. Soc.* 60 (2) (1938) 309–319.
- O.F. Baugh, E.P. Barrett, L.G. Joyner, P.P. Halenda, The volume and area distributions in porous substances, *J. Am. Chem. Soc.* 73 (1951) 373–380.
- B.C. Lippens, B.G. Linsen, J.H. de Boer, Studies on pore systems in catalysts I. The adsorption of nitrogen; apparatus and calculation, *J. Catal.* 3 (1964) 32–37, [https://doi.org/10.1016/0021-9517\(64\)90089-2](https://doi.org/10.1016/0021-9517(64)90089-2).
- J.F. Moulder, W.F. Stickle, P.E. Sobol, K.D. Bomben, J. Chastain, Handbook of X-ray Photoelectron Spectroscopy, A Reference Book of Standard Spectra for Identification and Interpretation of XPS Data. (1992).
- S. Naveed, N. Waheed, Simple UV spectrophotometric assay of ciprofloxacin, *Mintage J. Pharm. Med. Sci.* 3 (2014) 10–13, <https://doi.org/10.1128/AAC.00306-13>.
- W.u. Zhou, Z. Ye, A. Nikiforov, J. Chen, J. Wang, L. Zhao, X. Zhang, The influence of relative humidity on double dielectric barrier discharge plasma for chlorobenzene removal, *J. Cleaner Prod.* 288 (2021) 125502, <https://doi.org/10.1016/j.jclepro.2020.125502>.
- A.A. Abdelaziz, T. Ishijima, T. Seto, Humidity effects on surface dielectric barrier discharge for gaseous naphthalene decomposition, *Phys. Plasmas* 25 (4) (2018) 043512, <https://doi.org/10.1063/1.5020271>.
- A. Lofthuis, P.H. Krupenie, The spectrum of molecular nitrogen, *J. Phys. Chem. Ref. Data.* 6 (1977), <https://doi.org/10.1063/1.555546>.

- [37] K. Shang, M. Wang, B. Peng, J. Li, N. Lu, N. Jiang, Y. Wu, Characterization of a novel volume-surface DBD reactor: Discharge characteristics, ozone production and benzene degradation, *J. Phys. D Appl. Phys.* 53 (2020), <https://doi.org/10.1088/1361-6463/ab538d>.
- [38] Y. Sakiyama, D.B. Graves, H.W. Chang, T. Shimizu, G.E. Morfill, Plasma chemistry model of surface microdischarge in humid air and dynamics of reactive neutral species, *J. Phys. D Appl. Phys.* 45 (2012), <https://doi.org/10.1088/0022-3727/45/42/425201>.
- [39] C. Sarangapani, G. O'toole, P. Bourke, Atmospheric cold plasma dissipation efficiency of atmospheric cold plasma dissipation efficiency of agrochemicals on blueberries agrochemicals on blueberries. 44 (2017) 235–241. 10.1016/j.ifset.2017.02.012.
- [40] C. Sarangapani, D. Ziuzina, P. Behan, D. Boehm, B.F. Gilmore, P.J. Cullen, P. Bourke, Degradation kinetics of cold plasma-treated antibiotics and their antimicrobial activity, *Sci. Rep.* 9 (2019) 3955, <https://doi.org/10.1038/s41598-019-40352-9>.
- [41] L. Valdés, I. Pérez, L.C. de Ménorval, E. Altshuler, J.O. Fossum, A. Rivera, A simple way for targeted delivery of an antibiotic: In vitro evaluation of a nanoclay-based composite, *PLoS ONE* 12 (2017), <https://doi.org/10.1371/journal.pone.0187879>.
- [42] S.A. Sadeek, W.H. El-Shwiniy, W.A. Zordok, A.M. El-Didamony, Spectroscopic, structure and antimicrobial activity of new Y(III) and Zr(IV) ciprofloxacin, *Spectrochimica Acta - Part A: Molecular and Biomolecular, Spectroscopy.* 78 (2) (2011) 854–867, <https://doi.org/10.1016/j.saa.2010.12.048>.
- [43] C.A. Aggelopoulos, M. Hatzisymeon, D. Tataraki, G. Rassias, Remediation of ciprofloxacin-contaminated soil by nanosecond pulsed dielectric barrier discharge plasma: Influencing factors and degradation mechanisms, *Chem. Eng. J.* 393 (2020), 124768, <https://doi.org/10.1016/j.cej.2020.124768>.
- [44] E.P. Favvas, C.G. Tsanaktsidis, A.A. Sapalidis, G.T. Tzilantonis, S.K. Papageorgiou, A.C. Mitropoulos, Clinoptilolite, a natural zeolite material: Structural characterization and performance evaluation on its dehydration properties of hydrocarbon-based fuels, *Microporous Mesoporous Mater.* 225 (2016) 385–391, <https://doi.org/10.1016/j.micromeso.2016.01.021>.
- [45] K.S.W. Sing, D.H. Everett, R.A.W. Haul, L. Moscou, R.A. Pierotti, J. Rouquerol, T. Siemieniowska, Reporting Physisorption Data for Gas/Solid Systems (1984) 1217–1230, <https://doi.org/10.1002/9783527610044.HETCAT0065>.
- [46] S. Lowell, J. Shields, M.A. Thomas, M. Thommes, Characterization of Porous Solids and Powders: Surface Area, Pore Size and Density, 42 (2006). 42-5288–42-5288. 10.5860/CHOICE.42-5288.
- [47] Y. Garcia-Basabe, I. Rodriguez-Iznaga, L.-C. de Menorval, P. Llewellyn, G. Maurin, D.W. Lewis, R. Binions, M. Autie, A.R. Ruiz-Salvador, Step-wise dealumination of natural clinoptilolite: Structural and physicochemical characterization, *Microporous Mesoporous Mater.* 135 (1-3) (2010) 187–196, <https://doi.org/10.1016/j.micromeso.2010.07.008>.
- [48] S. Jevtić, I. Arčon, A. Rečnik, B. Babić, M. Mazaj, J. Pavlović, D. Matijašević, M. Nikšić, N. Rajić, The iron(III)-modified natural zeolitic tuff as an adsorbent and carrier for selenium oxyanions, *Microporous Mesoporous Mater.* 197 (2014) 92–100, <https://doi.org/10.1016/j.micromeso.2014.06.008>.
- [49] N.T.M. Tam, Y. Liu, H. Bashir, Z. Yin, Y. He, X. Zhou, Efficient Removal of Diclofenac from Aqueous Solution by Potassium Ferrate-Activated Porous Graphitic Biochar: Ambient Condition Influences and Adsorption Mechanism, *Int. J. Environ. Res. Public Health* 17 (2019) 291, <https://doi.org/10.3390/IJERPH17010291>.

## Article

# Treatment of Chrysanthemum Synthetic Seeds by Air SDBD Plasma

Nikola Škoro <sup>1,\*</sup> , Suzana Živković <sup>2</sup>, Slađana Jevremović <sup>2,\*</sup>  and Nevena Puač <sup>1</sup> 

<sup>1</sup> Institute of Physics—National Institute of Republic of Serbia, University of Belgrade, Pregrevica 118, 11080 Belgrade, Serbia; nevena@ipb.ac.rs

<sup>2</sup> Institute for Biological Research “Siniša Stanković”—National Institute of Republic of Serbia, University of Belgrade, Despot Stefan Boulevard 142, 11000 Belgrade, Serbia; suzy@ibiss.bg.ac.rs

\* Correspondence: nskoro@ipb.ac.rs (N.Š.); sladja@ibiss.bg.ac.rs (S.J.)

**Abstract:** Herein, we present the effect of surface dielectric barrier discharge (SDBD) air cold plasma on regrowth of chrysanthemum synthetic seeds (synseeds) and subsequent plantlet development. The plasma system used in this study operates in air at the frequency of 50 Hz. The detailed electrical characterization of SDBD was shown, as well as air plasma emission spectra obtained by optical emission spectroscopy. The chrysanthemum synseeds (encapsulated shoot tips) were treated in air plasma for different treatment times (0, 5 or 10 min). Plasma treatment significantly improved the regrowth and whole plantlet development of chrysanthemum synseeds under aseptic (in vitro) and non-aseptic (ex vitro) conditions. We evaluated the effect of SDBD plasma on synseed germination of four chrysanthemum cultivars after direct sowing in soil. Germination of synseeds directly sowed in soil was cultivar-dependent and 1.6–3.7 fold higher after plasma treatment in comparison with untreated synseeds. The study showed a highly effective novel strategy for direct conversion of simple monolayer alginate chrysanthemum synseeds into entire plantlets by plasma pre-conversion treatment. This treatment reduced contamination and displayed a considerable ex vitro ability to convert clonally identical chrysanthemum plants.



**Citation:** Škoro, N.; Živković, S.; Jevremović, S.; Puač, N. Treatment of Chrysanthemum Synthetic Seeds by Air SDBD Plasma. *Plants* **2022**, *11*, 907. <https://doi.org/10.3390/plants11070907>

Academic Editors: Anna De Carlo and Waed Tarraf

Received: 7 March 2022

Accepted: 25 March 2022

Published: 29 March 2022

**Publisher’s Note:** MDPI stays neutral with regard to jurisdictional claims in published maps and institutional affiliations.



**Copyright:** © 2022 by the authors. Licensee MDPI, Basel, Switzerland. This article is an open access article distributed under the terms and conditions of the Creative Commons Attribution (CC BY) license (<https://creativecommons.org/licenses/by/4.0/>).

**Keywords:** artificial seeds; plasma treatment; chrysanthemum; dielectric barrier discharge; cold plasma

## 1. Introduction

Synthetic seed technology is one of the most promising tools in plant biotechnology and may represent an innovative method for massive plant production and sustainable agriculture in the future [1]. Synthetic seeds (artificial seeds or synseeds) have been defined as artificially encapsulated somatic embryos or other non-embryogenic vegetative parts of plants, mainly in alginate, that may be used for storage or sowing under in vitro or ex vitro conditions [2]. The term ‘synseeds’ was described by Murashige in 1977 [3] as ‘an encapsulated single somatic embryo’, but later, the definition of artificial seeds was extended to any artificially coated micropropagules that have capability to be sown as a seed and converted into a plant [4,5]. There is a growing trend in applications of synseed technology for medium- and long-term storage of plant material under aseptic conditions [6,7] or as an advanced procedure of cryopreservation by encapsulation–dehydration and encapsulation–vitrification method [8,9]. Synseed technology represents an efficient alternative technique for propagation and germplasm conservation of valuable forest, medicinal and vegetable plant species that reproduce mainly vegetatively or have a problem in seed propagation, i.e., plants that produce non-viable seeds or seedless plants [10].

In synseed technology, an alginate capsule has two roles: (i) it acts as physical barrier of shoot tips against mechanical damage, and (ii) it serves as an artificial endosperm, carbon source and reservoir of nutrients for better survival and supply of energy [9]. Alginates are a group of naturally occurring anionic polysaccharides derived from brown algae cell walls (*Macrocystis pyrifera*, *Limnaria hyperborea*, *Ascophyllum nodosum*) and several bacterial strains

(*Azotobacter*, *Pseudomonas*). Sodium alginate is soluble in water, but when the sodium is replaced with calcium, the ionic bond with calcium cross links the polymer chain in alginate, which results in the formation of an insoluble gel. Sodium alginate and calcium salt are reported to be the best combination for encapsulation, representing the most successful and widely accepted approach to synseed production [9]. Alginates can be formed into diverse semisolid or solid structures because of their ability of sol/gel transition and are commonly used as viscosity-increasing agents, thickeners and suspension and emulsion stabilizers in food and the pharmaceutical industry (code E400-E405) [11]. In addition, alginate gels are the basis for a variety of wound dressings that have showed variety of therapeutically effects, such as hemostatic and bacteriostatic properties [12,13]. On the other hand, in plants, sodium alginate is considered a potential elicitor that improves tolerance to plant environmental stresses, such as drought, inhibiting plant infections and reducing the toxic effect of heavy metals [14,15].

Chrysanthemums (*Chrysanthemum morifolium* Ramat. syn. *C. grandiflorum* Kitam) are, besides roses, the most important economically ornamental crop in the world [16]. They originate from east Asia, a center of their biodiversity; however, to date, many horticultural varieties and cultivars of chrysanthemums are produced using different biotechnological tools [17]. The name chrysanthemum means gold flower, but they are also called “autumn roses” because they were, in the past, used as cut flowers during late summer and autumn. Nowadays, there is constant demand on the market for new cultivars that are available during the whole year. Modern biotechnological tools, such as mutation breeding and micropropagation under in vitro conditions, allow for production of hundreds of new chrysanthemum cultivars every year [18]. Chrysanthemum cultivars are commonly propagated vegetatively by cuttings and suckers and stored as field, greenhouse or in vitro collections due to high spontaneous mutation rates and high levels of ploidy and self-incompatibility [19,20]. Micropropagation of chrysanthemum cultivars, as an in vitro way of vegetative multiplication in culture, was reported for the first time more than 50 years ago [21], and numerous reports about plantlet regeneration from various explants of chrysanthemum have been presented [16,22–24].

The application of synseed technology, accompanied by micropropagation, represents a perfect biotechnological approach that could be used for agricultural improvement of year-round plant production of chrysanthemums. There are several advantages of this approach, including large-scale production; easy handling; short and medium storage (4 °C) or low temperature (−196 °C) storage; easy transportation; and the genetically true-to-type nature of the plants produced from synseeds. On the other hand, there are some limitations of wider usage of synseed technology in commercial applications as published to date, such as implementation of labor-intensive procedures, which include double-layer encapsulation or several media changes to derived plantlets with well-developed shoot and roots at the same time. To date, the application of synseed technology of chrysanthemum cultivars has been investigated for in vitro storage and ex vitro planting (summarized in Table 1). In addition, synseed technology in chrysanthemums is widely used as a part of encapsulation–dehydration and encapsulation–vitrification protocols for long-term storage of chrysanthemum cultivars by cryopreservation in liquid nitrogen [25]. Considering the fact that chrysanthemums are susceptible to mutations, meristem explants (i.e., nodal segments or shoot tips) proved to be the best explant choice for the plant propagation of chrysanthemums, with a high degree of clonal fidelity as mother plants, as well as for synseed production [26–28].

Chrysanthemum synseeds are mainly produced under sterile conditions for short- and long-term storage [19], but sowing of chrysanthemum synthetic seeds under non-aseptic conditions has been also reported [29,30]. Chrysanthemum synseeds easily regrow from Na-alginate beads under sterile conditions, whereas for complete germination and whole-plantlet development (shoot and root), it is necessary to add indole-acetic acid to the encapsulation matrix [29] or, as separate step, in the medium for rooting after shoot regrowth [19]. For sowing under unsterile conditions, the results showed that presence



of organic compounds in the gelling matrix and commercial substrates caused microbial contamination in all synseeds and complete inhibition of further regrowth of the shoots or whole plantlet development. In general, difficulties of sowing artificial seeds directly in soil or in commercial substrates, such as compost, vermiculite, etc., under non-sterile conditions are considered to be one of the main limitations for the widescale practical application of synseed technology [2,31]. Some progress has been achieved by using chemical mixtures and antibiotics for preservation of synseeds before sowing [32], but more investigations and novel approaches are still needed to improve the capacity of synseed cultivation under non-sterile conditions.

**Table 1.** Application of synseed technology for storage and propagation of chrysanthemum cultivars.

Cultivar	Plant Material	Beads	Sowing	Germination (%)	Flowering	References
Clone 'PS 27'	Nodal segments (in vitro)	Monolayered (3% Na-alginate + 0.1 mg/L IAA)	Sterile, water–sand	50	no	[29]
		Double-layered (beads: 3% Na alginate, second layer: water)	Non-sterile, water–perlite	45	no	
Lady group	Shoot tips (in vitro)	Monolayered (3% Na-alginate)	Sterile, agar	52	no	[19]
cv. 'Royal Purple'	Shoot tips (ex vitro)	Monolayered (2.5% Na-alginate, sucrose, vitamin free)	Non-sterile, vermiculite	34	no	[30]

Atmospheric pressure plasma (non-thermal, “cold”) systems have been extensively used in biomedical applications for almost two decades [33–36]. In parallel, another field of plasma applications has been growing—plasma agriculture [37,38]. One of the first applications of cold plasmas was the treatments of conventional seeds [39,40]. This includes various applications in seed treatment with several purposes [41–43]. Many authors have shown that plasma treatments can increase seed germination and speed up the whole process of plantlet development [37–40]. The rich plasma chemistry (with reactive oxygen and nitrogen species) interacts with the seed coating and triggers various responses, such as increasing water uptake, changes in the surface of seeds' coating and elimination of pathogens on seed surfaces [44–53]. In this sense, cold plasma treatment can have a multiply positive impact on seed germination and subsequent plant development of conventional seeds without the addition of chemicals that can be harmful for the environment.

Nowadays, there is a plethora of plasma sources that operate at atmospheric pressure [54–57]. They differ in electrode design, type of applied voltage, feeding gas, etc. The variety of atmospheric pressure plasma sources enables a large number of possible applications, but at the same time, comparison between the results of treatment is difficult. Therefore, it is of the utmost importance to obtain detailed characteristics of the plasma device that is used in experiments. One of the first steps that is usually performed includes electrical characterization of the discharge, accompanied by optical emission spectroscopy, which can give insight into the plasma-excited species. These diagnostic techniques represent only the starting point for a detailed description of plasma characteristics and include mass spectrometry, fast imaging, laser-induced fluorescence, etc. [56].

In this paper, we present results of air plasma treatment of *Chrysanthemum* synseeds together with detailed plasma source diagnostics. We performed electrical characterization of the optical emission spectra (OES) of an SDBD system that operates in air at atmospheric pressure. Until now, we are not aware of any research data in the literature about the effect of cold atmospheric plasma treatment on the regrowth (germination) of artificial seeds of any plant species. The objective of this study related to synseed treatment was to:

(1) investigate the influence of cold plasma treatment on chrysanthemum synseed regrowth under in vitro conditions; (2) analyze the impact of cold plasma treatment on regrowth and further plantlet development from synseeds sowed directly in soil (ex vitro); and (3) evaluate the effect of plasma treatment on synseed germination of different chrysanthemum cultivars. In this pioneer work, we present a novel approach in synseed biotechnology and plasma agriculture cold plasma treatment of synseeds (encapsulated shoot tips) prior to sowing to prevent contamination and enhance plant growth.

## 2. Results

### 2.1. Regrowth of Plasma-Treated Synthetic Seeds under Aseptic Conditions (In Vitro)

We tested the regrowth rate of chrysanthemum synseeds after plasma treatment cultivated under in vitro (Figure 1) and ex vitro conditions (Figures 2–4). The regrowth and shoot development of plasma-treated and untreated chrysanthemum monolayered, simple synseeds were evaluated for two growing substrates without plant growth regulators under aseptic (in vitro) conditions (Figure 1).

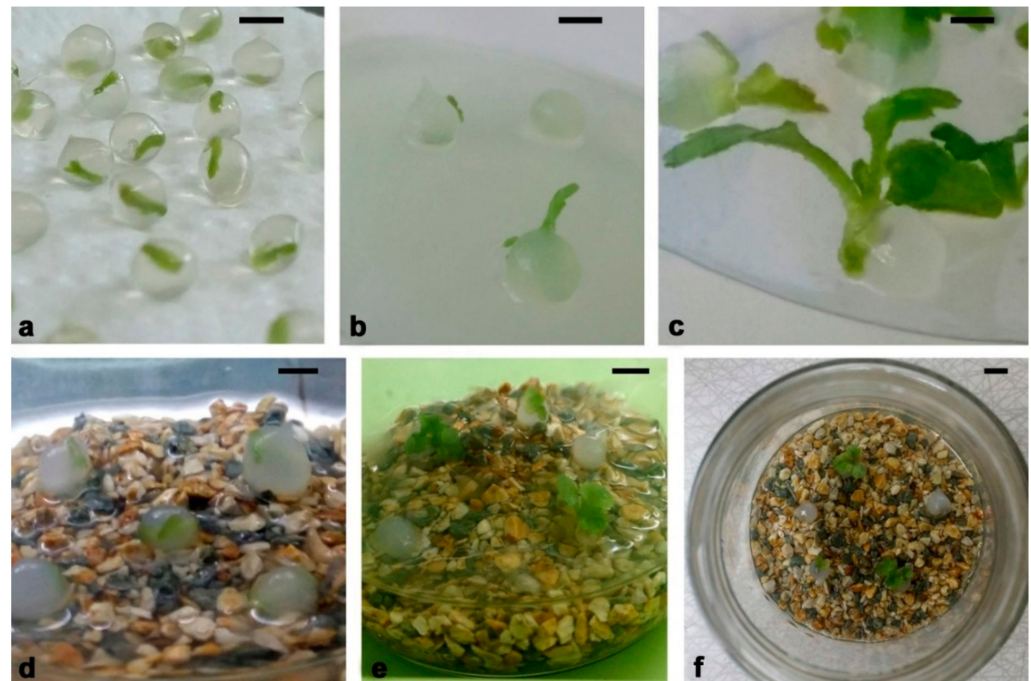


**Figure 1.** Chrysanthemum synseed germination under in vitro conditions. (a) Synseeds before plasma treatment; (b,c) plasma-treated synseeds grown on solid agar medium—leaf emergence after one week of culture (b) and shoot development after four weeks of culture (c); (d,f) plasma-treated synseeds grown on vermiculite + liquid medium—plasma-treated synseeds grown one week (d) and four weeks (e,f). Bars a–f, 5 mm.

After plasma treatment, one set of synseeds was grown on the solid agar medium (AM, Figure 1b,c), and the second set was placed on the vermiculite + liquid medium (VLM, Figure 1d–f). Untreated synseeds served as a control group and were grown on the same medium. Encapsulated chrysanthemum shoot tips cultivated on AM in vitro (Figure 1a) easily continued to grow after plasma treatment, and within the first week, leaf emergence was observed (Figure 1b). Full development of microshoots was established after four weeks of culture (Figure 1c). There was no apparent difference in regrowth between the control (untreated) and plasma-treated synseeds. Additionally, no contamination was observed among treated synseeds. All synseeds, including the control as well as plasma-treated synseeds, were fully developed in microshoots. We further evaluated shoot multiplication after plasma treatment, and no difference between plasma-treated and untreated synseeds was observed (Supplementary Data, Figure S1).

When chrysanthemum synseeds were grown on VLM (sterilized vermiculite moisture with liquid plant regulator free medium) under in vitro conditions (Figure 1d–f), a significant increase in regrowth of plasma-treated synseeds was achieved (Table 2).

**Table 2.** The effect of plasma treatment on germination of chrysanthemum synseeds grown in vitro on vermiculite + liquid medium.

Plasma Treatment (min)	Leaf Emergence (%) *	Shoot Regrowth (%) **
	1 Week	4 Weeks
0	20 ± 10 <sup>a ***</sup>	0 ± 0 <sup>a</sup>
1	47 ± 13 <sup>a,b</sup>	40 ± 13 <sup>b</sup>
5	67 ± 12 <sup>b</sup>	47 ± 13 <sup>b</sup>
10	67 ± 13 <sup>b</sup>	33 ± 12 <sup>b</sup>

\* Leaf emergence is evaluated as first sign of shoot appearance out of alginate beads after one week of growth; \*\* shoot regrowth was evaluated as fully developed shoot out of beads after four weeks of growth. \*\*\* values represent mean ± standard error. The data signed with different letter within the same column are significantly different according to Fisher's LSD test.

After one week of culture, only 20% of untreated synseeds broke out of the alginate capsule, and none of them continued their growth. On the other hand, among plasma-treated synseeds, leaf emergence, as a first sign of synseed germination, was two- to three-fold higher in comparison to untreated synseeds after one week of culture. The best results for shoot regrowth, more than three times higher than that of untreated synseeds, was achieved after plasma treatment for 5 min and 10 min before planting in VLM. After four weeks of cultivation, only plasma-treated chrysanthemum synseeds (33–47%) continued their growth and developed microshoots (Figure 1e,f), whereas the untreated (control) synseeds did not survive on VLM. For further experiments on chrysanthemum synseeds, we used 10 min plasma treatment.

## 2.2. Germination of Plasma-Treated Synthetic Seeds under Non-Aseptic Conditions (Ex Vitro)

We examined the germination of plasma-treated and untreated chrysanthemum synseeds, as well as the subsequent growth and development of plantlets after direct sowing in soil substrate (ex vitro conditions) (Table 3, Figure 2). Plasma-treated synseeds showed more vigorous survival, regrowth and germination in comparison to untreated synseeds (Table 3). After one week of ex vitro cultivation, shoots broke the Na-alginate bead, and the first leaf emerged from the synseeds (Figure 2a,b), which represented the main sign of shoot regrowth. The difference in survival between plasma-untreated (first column) and plasma-treated synseeds (second and third column) was evident (Figure 2a,c). Despite the fact that there was no statistically significant difference in shoot regrowth of plasma-treated (66%) and untreated synseeds (60%), after one week of growth under ex vitro conditions, we noticed that the developed leaves formed from plasma-treated synseeds were wider than those derived from untreated synseeds (Figure 2a). After one week of growth, some untreated synseeds were lost due to desiccation and contamination.

After three weeks of growing under ex vitro conditions, we observed two times higher survival and almost doubled percentage of shoot development of plasma-treated chrysanthemum synseeds in comparison to untreated samples. Namely, only 33.3% of untreated synseeds continued growth and developed very well-formed shoots, whereas more than 60% of plasma-treated chrysanthemum synseeds formed well-developed shoots (Figure 2c). Six weeks after sowing, whole chrysanthemum plantlets with well-formed shoots and roots were developed (Table 3). Only 17% of untreated synseeds fully germinated and developed whole plantlets, whereas 2.5 fold higher synseed germination (over 40%) and whole-plantlet development of plasma-treated synseeds was achieved.

**Table 3.** The effect of plasma treatment on germination of chrysanthemum synseeds grown ex vitro.

Plasma Treatment (min)	Synseed Germination		
	Leaf Emergence * (%)	Shoot Regrowth * (%)	Plantlet * (%)
0	60 ± 7 <sup>a</sup> **	33 ± 7 <sup>a</sup>	17 ± 5 <sup>a</sup>
10	66 ± 5 <sup>a</sup>	60 ± 5 <sup>b</sup>	41 ± 5 <sup>b</sup>

\* Leaf emergence is evaluated as first sign of shoot appearance out of alginate beads one week after sowing; shoot regrowth was evaluated as a fully developed shoot out of the bead three weeks after sowing; plantlet development was recorded as a fully developed plant with well-developed shoot and roots. \*\* Values represent mean ± standard error. The data signed with a different letter within the same column are significantly different according to Fisher's LSD test.

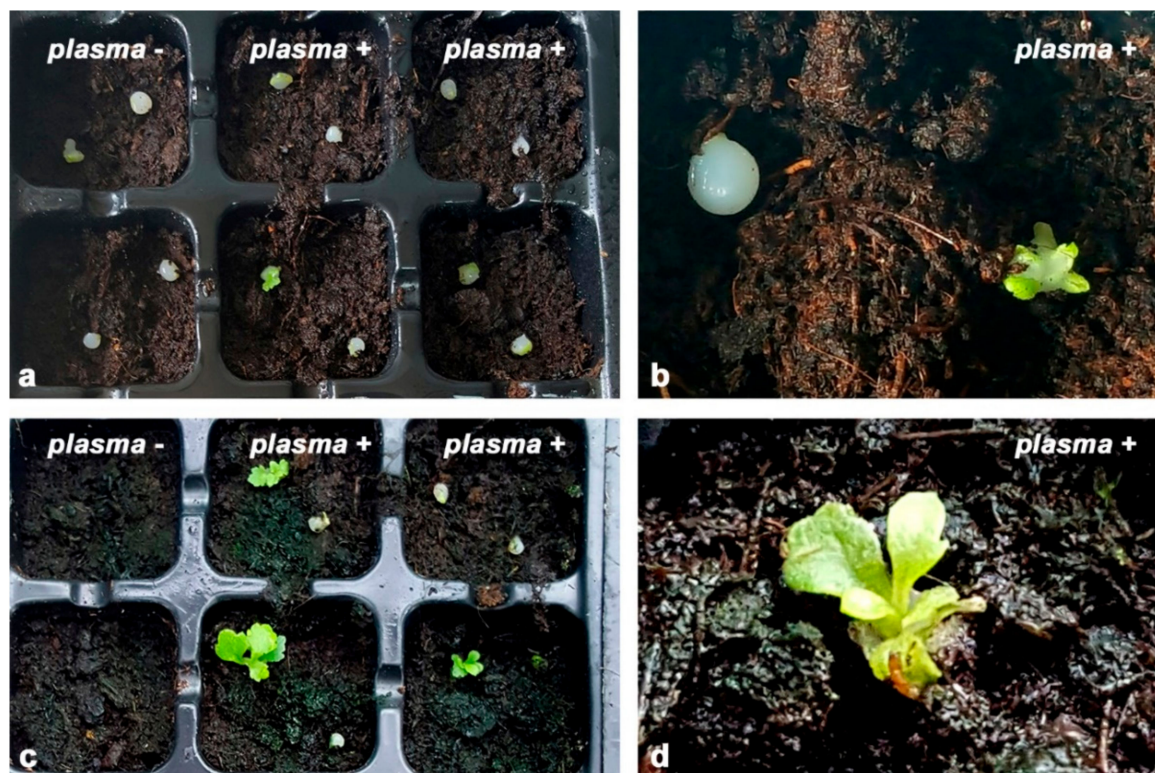


**Figure 2.** Chrysanthemum synseed germination under ex vitro conditions, cv. *Précocita carna*. (a) Control (first column) and plasma-treated synseeds (second and third column) after one week of growth; (b) first sign of germination (leaf emergence) of plasma-treated synseeds; (c) control (first column) and plasma-treated synseeds (second and third column) after three weeks of cultivation ex vitro; (d) detail of fully germinated plasma-treated chrysanthemum synseed four weeks after sowing.

We compared the total deterioration (%) of the chrysanthemum plasma-treated and untreated synseeds within the first 6 weeks of growth ex vitro (Figure 3). The values reached almost 85% in the case of untreated synseeds, whereas for the plasma-treated seeds, this percentage was around 60%. According to these results, we can conclude that the plasma treatment of synseeds before sowing under ex vitro conditions enables increased survival of the newly developed plants by 25%.

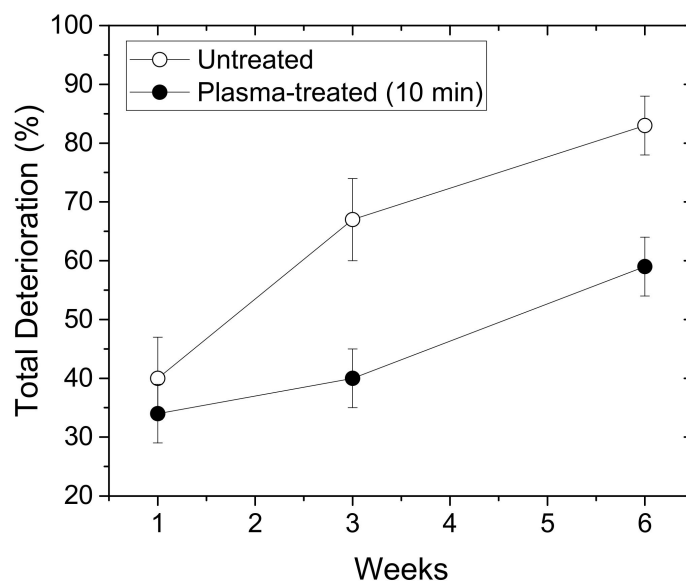


**Figure 3.** Total deterioration (%) of chrysanthemum synseeds grown ex vitro during 6-week period. Empty symbols: untreated synseeds; full symbols: plasma-treated synseeds.

### 2.3. Germination of Plasma-Treated Synthetic Seeds of Different Cultivars Ex Vitro

We evaluated the effect of plasma treatment (10 min) on synseed germination of different chrysanthemum cultivars (Table 4, Figure 4). We found that the plasma treatment significantly enhanced the process of synseed germination and conversion to plantlet after direct sowing in soil for all tested cultivars. This effect of plasma was cultivar-dependent (Table 4). Without plasma treatment of chrysanthemum synseeds, frequency of whole plantlet regeneration varied from 6% to 28% depending on the cultivar. On the other hand, plantlet regeneration from plasma-treated synseeds was 22–49%. The highest treatment effects on whole-plantlet development were recorded for cultivars BC and PP (~370% and ~350%, respectively) in comparison to control synseeds, whereas the lowest values were obtained for the PP cultivar (~160%).

**Table 4.** The effect of plasma treatment on synseed germination and plantlet development of different chrysanthemum cultivars.

Plasma Treatment (min)	Plantlet (%)			
	BC *	Q *	PC *	PP *
0	6 ± 1 <sup>a **</sup>	17 ± 2 <sup>a</sup>	28 ± 1 <sup>a</sup>	14 ± 1 <sup>a</sup>
10	22 ± 6 <sup>b</sup>	40 ± 3 <sup>b</sup>	44 ± 2 <sup>b</sup>	49 ± 3 <sup>b</sup>
Increment (%)	~370	~230	~160	~350

\* Chrysanthemum cultivars: Brandsound Liliac (BC), Queens (Q), Précocita Carna (PC) and Précocita Parme (PP); \*\* values represent mean ± standard error. The data signed with different letters within the same column are significantly different according to Fisher's LSD test.

Chrysanthemum plantlets derived from plasma-treated synseeds continued their growth until full physiological maturity and flowering (Figure 4). During further growth of the plantlets under greenhouse conditions, no morphological differences were observed between the plants developed from untreated (Figure 4a,c) and plasma-treated synseeds (Figure 4b,d). Some of the plants originated from synseeds flowered after six months of ex vitro growth (Figure 4f); during the next flowering season, no morphological or color changes in flowers were observed (Figure 4g–i).



**Figure 4.** Chrysanthemum plantlets derived from synseeds during growth under greenhouse conditions (ex vitro). (a–d) Plants derived from untreated (a,c) and plasma-treated (b,d) synseeds of chrysanthemum cv. PC (a,b) and Q (c,d) three months after sowing; (e,f) Plantlets derived from untreated (e) and plasma-treated (f) synseeds of cv. PC six months after sowing; (g–i) untreated (left) and plasma-treated (right) chrysanthemum plants twelve months after sowing, during next flowering season, cv. BL; (h,i) flowering of chrysanthemum plants derived from untreated (h) and plasma-treated synseeds (i), cv. BL.

#### 2.4. Characterization of DBD Plasma Source

Detailed plasma diagnostics was carried out prior to the treatments. After assessment of the range of plasma conditions that could be achieved with the DBD source, we selected one condition for the synseed treatment (part 4.3). The SDBD, previously used in treatments of flour [57], was characterized by using commercially available voltage probes. In order to properly assess the discharge current, one needs to subtract the displacement current. The first step was determination of the capacitance of the SDBD when the discharge was not ignited. This capacitance represents the passive capacitance of the plasma system, and it depends mainly on the geometry of the system, so it was determined for several interelectrode distances. The voltage at the powered electrode and current waveforms for one of the cases is represented in Figure 5. The peak-to-peak value of the voltage is 700 V (black line), whereas the peak-to-peak value of the current (red line) is  $\sim 12 \mu\text{A}$ .

The current measured when there is no discharge ignited is only the displacement current. It is represented by:

$$i_{disp}(t) = C_p \frac{dv(t)}{dt} \quad (1)$$

where  $C_p$  represents passive capacitance of the system, and  $v(t)$  represents instantaneous voltage measured at the powered electrode. As  $i_{nodischarge}(t) = i_{disp}(t)$ , the  $C_p$  value calculated as a parameter from Equation (1) for different electrode distances is given in Table 5.

An example of the voltage and current waveforms with the discharge ignited is shown in Figure 6. The voltage waveform was measured by HV probe at the powered electrode, whereas the current waveform represents the current through discharge. It was obtained by subtraction of the displacement current from the total current measured in the grounded branch of the electrical circuit. Variation of measured voltage and current were below 2% and 4%, respectively. Consequently, the root mean square (RMS) values were calculated

with the same uncertainties. We can see that the voltage waveform is a sine function with a dominant first harmonic (50 Hz). The shape of the current waveform reflects a discharge with microfilaments that can be seen through the appearance of current peaks superimposed on the waveform [58,59].

**Table 5.** Values of stray capacitance in the SDBD system.

Electrode Distance-d [mm]	Stray Capacitance— $C_p$ [pF]
2	20
3	35
4	41
5	45

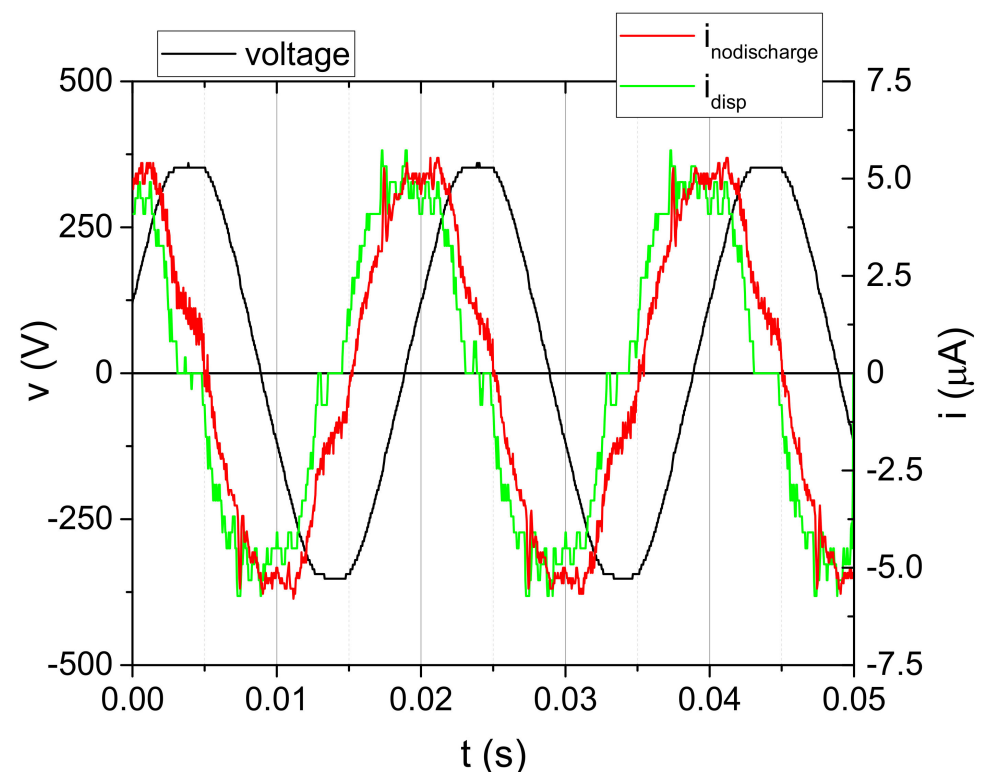


**Figure 5.** Waveforms of voltage (black line) and current (red line) obtained for  $d = 5$  mm without discharge (input voltage  $V_{\text{input}} = 6$  V). Displacement current (green line) is calculated by using voltage signal (Equation (1)).

The dependence of the output RMS voltage measured at the powered electrode on the input voltage is shown in Figure 7, left-hand axis. We can see that the dependence is linear, and it does not change significantly with an increase in the distance between electrodes.

The maximum operating voltage that could be obtained with this power supply system and the plasma source geometries was  $\sim 25$  kV<sub>peak-to-peak</sub> ( $\sim 8560$  V<sub>RMS</sub>). The dependence of the measured current on the input voltage is shown in Figure 7 on the right-hand axis. In this case, the dependence was not linear, and it changes with the distance between the powered electrode and the bottom plate, i.e., sample. For all distances presented here, the maximum current was 0.3 m A<sub>RMS</sub> obtained for  $d = 2$  mm.

The volt–ampere (V–A) characteristics (Figure 8) show that the system is not linear with constant impedance. The complex impedance changes with an increase in the applied voltage, and the non-linearity is the most pronounced for the distance of 2 mm. This can be explained by the number of microfilaments formed and the effective area that they covered. For the interelectrode distances of  $d = 3, 4$  and 5 mm, the V–A dependence is almost the

same up to the applied RMS voltage of 6.5 kV. Increasing of the interelectrode distance reduces the number of microfilaments that occur in one half-period, and the ones that are ignited operate totally with low conduction current.

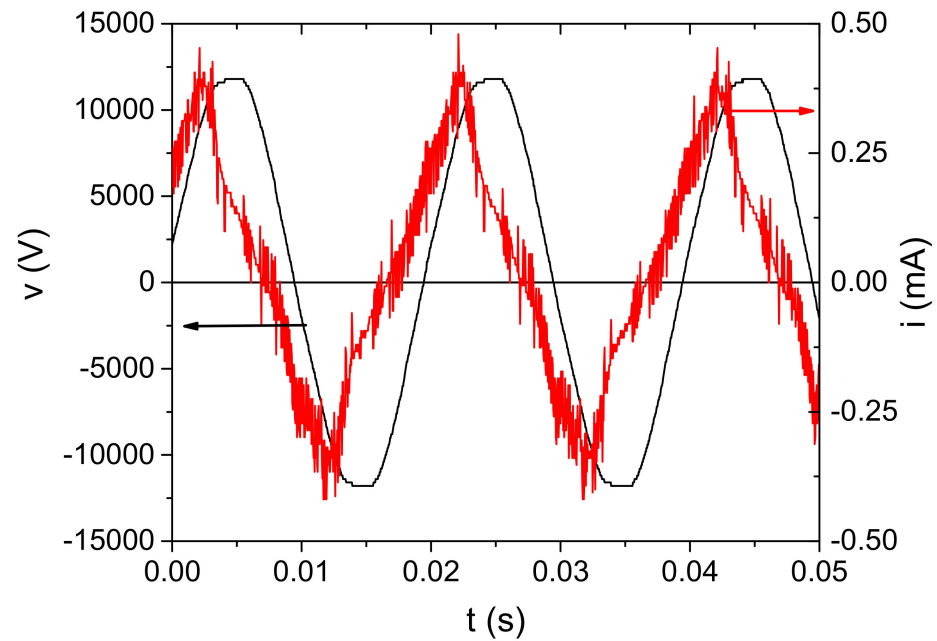


**Figure 6.** Time dependence of voltage and current signals at  $V_{\text{input}} = 220$  V and  $d = 5$  mm for the discharge operating in air.

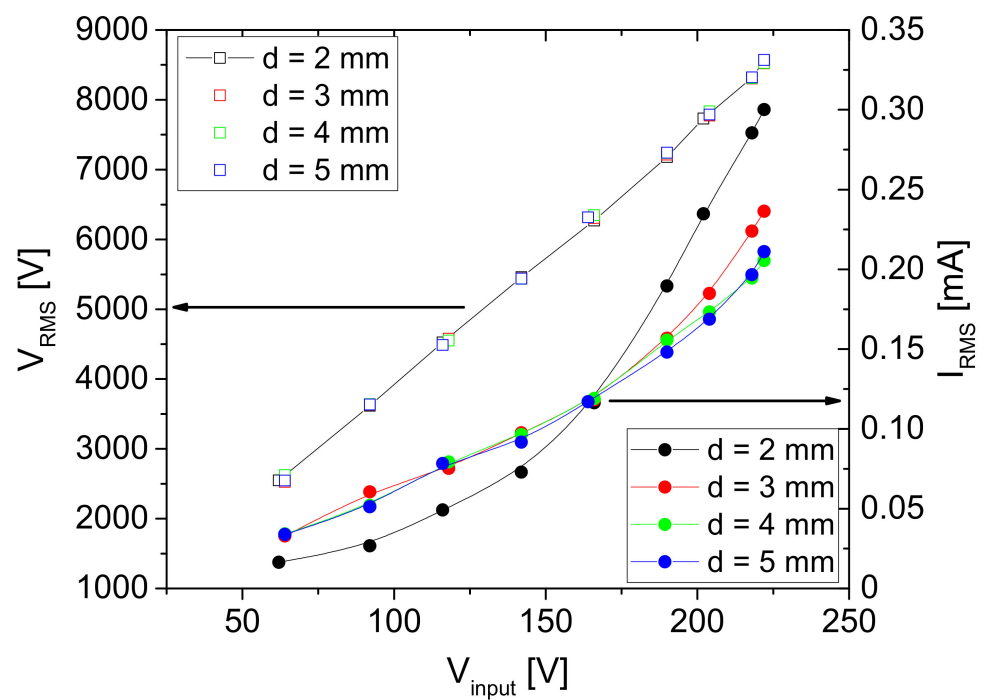


**Figure 7.** Dependence of the RMS voltage and current values on the input voltage  $V_{\text{input}}$  for four geometries. The discharge was operating in air.



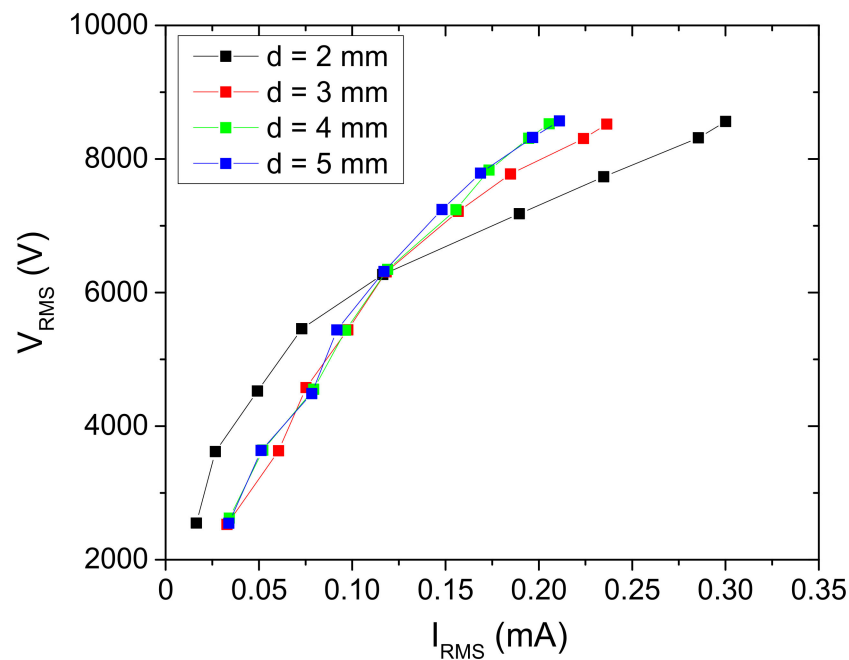


**Figure 8.** Volt–ampere characteristics of the SDBD obtained for the different distances between the powered electrode and the sample. The discharge was operating in air.

As expected, a similar change can be observed for the power transmitted to the discharge (Figure 9). Power is obtained as a mean value of instantaneous power calculated over several periods. The instantaneous power is obtained by direct multiplication of the waveforms of voltage and discharge current. We can see that the mean power transmitted to the discharge increases with the applied voltage. The maximum power that can be deposited to the discharge is around 1.5 W for the interelectrode distance of 2 mm. For voltages lower than 6.5 kV, the deposited power is similar for distances of  $d = 3, 4$  and 5 mm and lowest for  $d = 2$  mm.

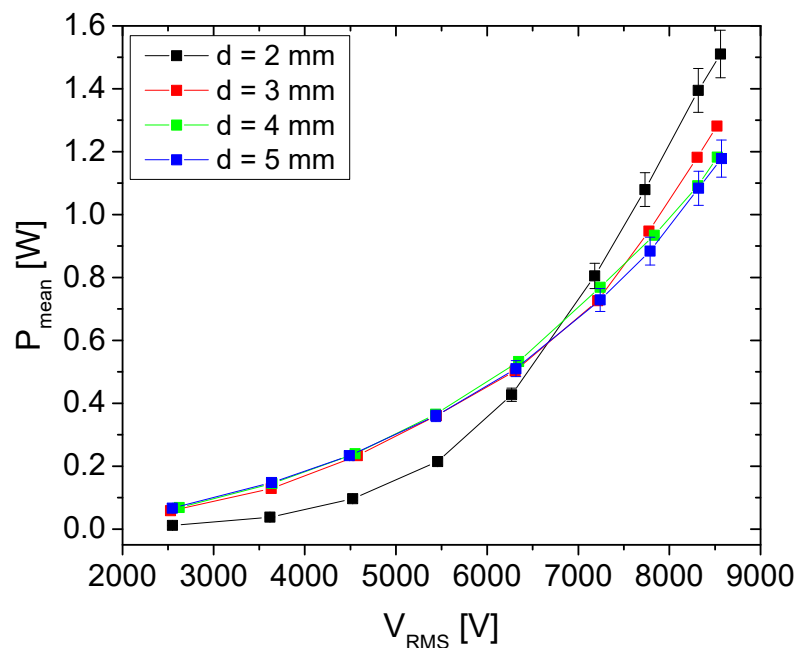


**Figure 9.** Mean power transmitted to the discharge as a function of the voltage at the powered electrode.

We recorded the emission spectra of the SDBD plasma source operating in air in the wavelength range from 275 nm to 850 nm. In Figure 10, we present the emission spectrum for  $d = 2$  mm up to 500 nm. Almost all lines visible in the spectrum belong to  $N_2$  Second Positive System (SPS): 313.67 nm, 315.93 nm, 337.13 nm (head of the band), 350.05 nm, 353.67 nm, 357.69 nm, 364.17 nm, 375.54 nm, 380.49 nm, 399.84 nm, 405.94 nm, 420.05 nm, 426.97 nm, 441.67 nm, 449.02 nm.

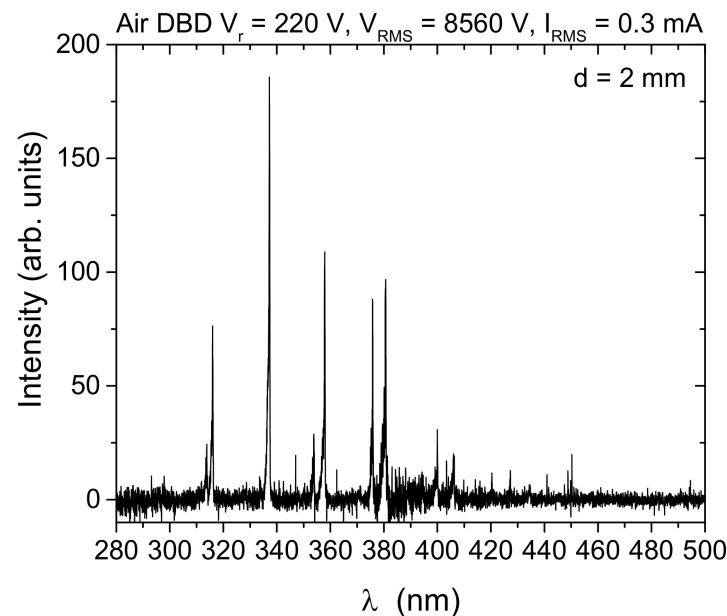


**Figure 10.** Optical emission spectrum from an air SDBD source obtained from side-on recording of spatially integrated emissions from the whole discharge volume (electrode gap,  $d = 2$  mm). The intensity signal is corrected for spectral efficiency of the optical system.

### 3. Discussion

First, we will discuss in detail the plasma characteristics used in the study. We used air SDBD because of the plane-parallel geometry, large effective plasma surface and possibility to operate with only air as a feeding gas. When the discharge was ignited, streamers were formed at temporary random points in the form of microfilaments, and they conducted higher discharge current than the rest of the discharge. Because we were not treating plant cells directly but the sodium-alginate-encapsulated plant material, the samples could withstand these local inhomogeneities in the active plasma volume without any damage. Nevertheless, due to the nature of an SDBD source, the total current of filaments was limited, preventing formation of current hot-spots. Another reason for choosing this type of plasma source was its simplicity, both in design and in application. It did not require the addition of feeding gas, and, as an important feature for the future technology, it has a potential for scaling up. Detailed electrical characterization of the SDBD and optical emission spectra was presented where the plasma source, with its plan-parallel geometry, served as a capacitance in the electrical circuit. Regarding this, we used a simple and reliable method to measure the stray capacitance,  $C_p$ , for different distances,  $d$ , between upper and lower electrode segments. Results showed that with the increase in the distance between the powered electrode and grounded bottom electrode, we had an increase in the system capacitance, which was expected (Table 5). The obtained  $C_p$  values allowed for determination of the displacement current of each input voltage. The measured current signals included both the displacement and discharge current. Thus, after subtracting the displacement current, all current waveforms represented only current through the discharge. The capacitance determined for each  $d$  enabled calculation of the discharge current for all possible configurations of the plasma source.

With respect to application, one of the most important macro parameters in plasma treatments is power deposited to the discharge. This macro parameter that can be easily monitored; it reflects the electron density and temperature and, to some extent, through these two parameters, plasma chemistry [60].  $P_{\text{mean}}$  (Figure 9) depends on the distance between electrodes, as well as formation of microfilaments. Thus, the highest increase and mean power values were achieved for  $d = 2$  mm. For this distance, we chose to treat the synseeds at a power of 1.1 W. This showed to be the optimal value with respect to the effect on the seeds for the three treatment times that we used.

Apart from power, the feeding gas (in this case air) and humidity can also play an important role in plasma chemistry [61]. Although humidity in the treatment environment was not controlled, all experiments were performed in a room with constant humidity. Additionally, measurements of discharge characterization, as well as all treatments, were repeated several times in order to verify the reproducibility of the measurements. All measurements were performed with and without synseed samples. One way to obtain an insight into the chemical reactions occurring in the discharge is optical emission spectroscopy, as it can show the existence of certain excited species. In our experiment, the spectra were recorded for different RMS voltages and interelectrode distances without samples, but all have the same lines belonging only to the  $N_2$  Second Positive System, SPS (Figure 10). Absence of the lines of, e.g., NO, OH and atomic oxygen, from the spectrum of an air DBD has been noted before and is related to dominant excitation and quenching reactions that favor  $N_2$  excitation in filamentary discharges [11,12,61,62]. Moreover, other important reactive species, such as  $O_3$ , do not have emissions in the spectral range investigated. Nevertheless, these kinds of plasma sources generate a large amount of ozone and  $N_2O$  that is important for treatments of alginate surfaces of synseeds [13,14,63,64].

The most important parameters determining the efficiency of the encapsulation and plant recovery of synseeds are survival, regrowth and capability of initial explants for further plantlet growth to complete plantlets [1]. Chrysanthemum synseeds used in this study (plasma-treated and untreated) easily established regrowth with the first leaf emergence after one week of cultivation. The presence of alginate capsules did not inhibit regrowth of chrysanthemum shoots grown on agar medium. In addition, shoots were developed on plant growth regulator free medium without any callus formation, similar to what was reported for chrysanthemum cultivars by the Lady group [19]. Our results are not surprising because regrowth of encapsulated shoot tips of chrysanthemums is possible on plant growth regulation free medium [19]. In the case of encapsulation of nodal segments, the addition of a small amount of IAA in the encapsulation complex is necessary and obligatory for better regrowth of shoots from synseeds [29]. When synseeds were grown on VLM only, plasma-treated chrysanthemum synseeds continued their regrowth and formed well-developed microshoots. It should be mentioned that microshoots established on VLM were smaller than those developed on standard solid agar medium, which could be related to accessibility of nutrients in this type of medium.

Data about application of synseed technology for short- and long-term storage in vitro or easy transport of valuable genetic resources are available [65,66], whereas data regarding synseed manipulations for ex vitro growth are quite scarce [67,68]. In chrysanthemum, plantlet development from synseeds formed in vitro and sowing ex vitro was successfully achieved from double-layered synseeds [29]. In the current work, we planted untreated and plasma-treated simple, one-layer chrysanthemum synseeds directly in soil substrate. After three weeks of ex vitro cultivation of chrysanthemum synseeds, two-fold higher shoot development was observed in the case of plasma-treated chrysanthemum synseeds in comparison to untreated synseeds. Additionally, after six weeks of growth under ex vitro conditions, plasma-treated chrysanthemum synseeds showed significantly higher plantlet conversion compared to the untreated control. The enhanced survival, regrowth and further complete plantlet formation of plasma-treated chrysanthemum synseeds shown in our work might be explained, besides by antimicrobial effect, by the prolonged effects of chemical changes in the alginate gels after plasma treatment and their antimicrobial properties.

Similar effects were reported for plasma treatment of alginate wound dressings [12]. Plasma treatment of alginate gels inactivated bacterial and fungal infection for a month, which was a long enough period for successful shoot development and complete conversion of synseeds to plantlets. On the other hand, continued growth of untreated chrysanthemum synseeds was significantly reduced due to contamination and lack of adventitious root formation for other plant species [9].

We found that the plasma treatment significantly enhanced synseed germination and complete plantlet development for all investigated chrysanthemum cultivars. The response to plasma treatment of chrysanthemum synseeds was cultivar-dependent. Observed differences could be attributed to the fact that different chrysanthemum cultivars have distinct nutritional requirements, as was reported earlier for other chrysanthemum cultivars [19,30]. According to our results, no morphological disorders were noticed among plantlets derived from untreated and plasma-treated synseeds. The absence of any morphological or flower color alterations in chrysanthemum plants may be explained as a consequence of the regeneration protocol used in this study. First, we used stock shoot cultures derived from one mother plant. In addition, initiation of shoot regeneration was mainly achieved by direct shoot induction on the initial explant, avoiding a callus phase and further shoot multiplication by axillary meristem activation, which minimized possibilities for genetic changes due to somaclonal variations [16,17]. According to available data, this research represents first data about complete chrysanthemum plantlet regeneration from synseeds to flowering plants.

During direct sowing of synseeds, contamination by microorganisms is one of the major hurdles for the commercialization of encapsulation technology for many plant species [9]. Besides that, one of the main limiting factors for plantlet conversion is low-nutrient availability due to inhibition of root growth. Numerous factors are involved in this process, such as poor rooting ability and survival due to the lack of nutrients and oxygen supply. Organic nutrients released by the beads are mainly responsible for severe contamination of synseeds [29,30]. Unfortunately, the depletion of nutritional compounds in beads may cause lower shoot regrowth or complete growth inhibition [28–30]. To date, there are two strategies to overcome this problem in chrysanthemum synseeds. The first strategy is to use double-layered synseeds to restrict contamination, where the second layer is formed by Ca-alginate made with water [29]. A recently reported strategy for both production and sowing of chrysanthemum synseeds in non-aseptic conditions proposes eliminating all carbon sources and organic additives both inside and outside the synseeds [30]. The reported strategy might be promising, but it was applied to one cultivar only, and it is questionable whether it is applicable to other cultivars. Therefore, it is necessary to build up a system that lowers contamination and keeps a nutrient reservoir within the encapsulated plant tissue, which is necessary for successful rooting. Considering the results of the present study, this problem may be successfully solved by plasma treatment of chrysanthemum synseeds before sowing.

There are many research data that demonstrate that cold plasma has a potent general antimicrobial effect through its generation of free radicals, reactive oxygen species (ROS) and reactive nitrogen species, such as hydrogen peroxide, superoxide, singlet oxygen, nitric oxide and ammonia [42]. The generated reactive species or their products are responsible for the antimicrobial effect and, in certain situations, have proven to be non-toxic to eukaryotic cells [69]. The chemical changes produced in the gel are relatively stable, and the anti-microbial properties of such a gel may last for close to one month, as reported after plasma treatment of alginate wound dressings [13]. The treated alginate gels inactivated all of the Gram-negative, Gram-positive and fungal pathogens by generated ROS inside bacterial cells, leading to their rapid death or triggering programmed cell death exhibiting characteristic features of apoptosis [12]. According to our results, we can conclude that treatment with non-thermal plasma generates chemical and physical responses in an alginate gel, producing changes that implicate not only biocidal effects but possibly growth-promoting effects.

## 4. Materials and Methods

### 4.1. Atmospheric Pressure Plasma Source

In the experiments, we used a circular surface dielectric barrier discharge (SDBD) source with an outer diameter of 90 mm. Side- and top-view schematics of the source are shown in Figure 11.

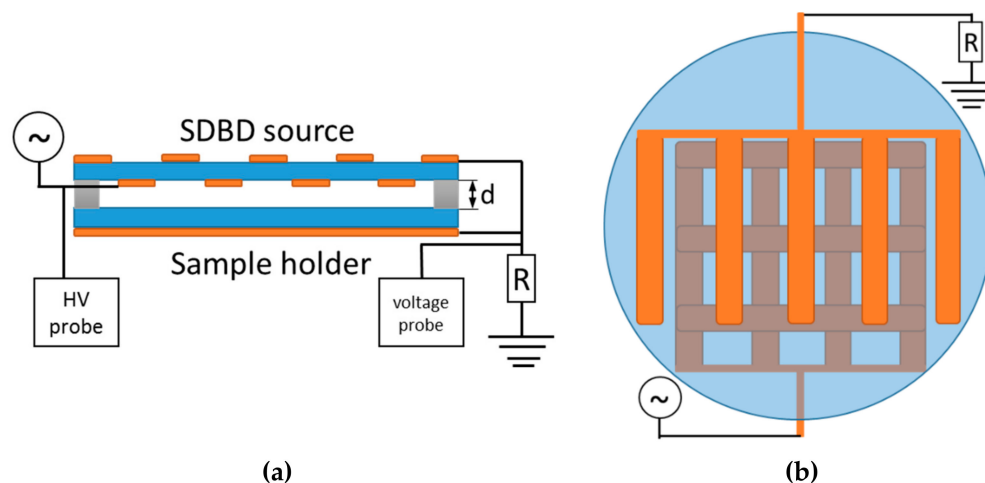


**Figure 11.** SDBD source schematics: (a) side view of the setup and schematics of electrical circuit; (b) top view of an upper electrode part. Dimensions of the source are given in the text.

The source consists of the two plane-parallel glass plates (2 mm thickness). The lower glass plate is positioned on a stainless-steel plate and serves as a sample holder. The upper glass plate is covered with conductive strips made of 5 mm wide copper tape. The strips are placed on both sides of the glass dielectric (Figure 11a). On the top side, they form a comb-like structure with gaps between the strips of 12 mm (Figure 11b). On the bottom side, the conductive strips form a grid structure making 12 mm side squares. The strip structures on opposite sides of the glass plate are shifted in such way that longer sides of the conductive strips are not overlapping (Figure 11b). The copper strips fixed to the upper part were grounded, whereas the strips on the bottom part of the top glass plate were powered with 50 Hz high-voltage (HV) sine signal. The outer edges of both powered and grounded electrode structures on the top part form a rectangle. Along the sides of this rectangle, plastic spacers were placed, keeping fixed distance in between the glass plates and bordering the active plasma volume of the SDBD source. Characterization of the device was performed by using spacers with thicknesses ( $d$ ) of 2, 3, 4 and 5 mm.

The HV signal at the powered electrode was supplied by a homemade HV transformer. The input voltage ( $V_{\text{input}}$ ) to the HV transformer was provided by a variable voltage regulator connected to the electrical power grid. The HV signal was monitored by a high-voltage probe (Tektronix 6015A, North Star High Voltage, Beaverton, OR, USA) connected to the circuit close to the powered electrode. Grounded electrodes on the top and bottom part of the source were connected to the same grounding point. In this grounded line, the probe (Agilent 10076A, Agilent Technologies, Beijing, China) allowed tracing of the voltage drop on the  $R = 15 \text{ k}\Omega$  resistor, thus monitoring of the total current in the discharge. Electrical signals were recorded by oscilloscope (Agilent DSO6052A, Agilent Technologies, Beijing, China) and saved on a computer for further processing.

### 4.2. Synthetic Seed Production

We used four chrysanthemum cultivars as starting plant material for the experiments: Brandsound Liliac (BL), Précocita Carna (PC), Précocita Parme (PP) and Queens (Q). Shoot cultures were established from one branch of the mother plant of each cultivar. Nodal and internodal stem (Figure 12a) and leaf segments (Figure 12b) of the mother plant were, after

surface sterilization, grown on Murashige and Skoog mineral solution and vitamins [70] solidified with 7% agar, with the addition of 3% sucrose and 100 mg/L myo-inositol (MS medium) supplemented with  $\alpha$ -naphthylacetic acid (0.1 mg/L NAA, Sigma-Aldrich, St. Luis, MO, USA) and 1.0 mg/L 6-benzylpurine (BAP, Sigma-Aldrich, St. Luis, MO, USA) for shoot induction. Initially regenerated shoots were further subcultured on the same medium, and stable stock cultures of chrysanthemum cultivars were established and subcultured in 4-week intervals (Figure 12c).

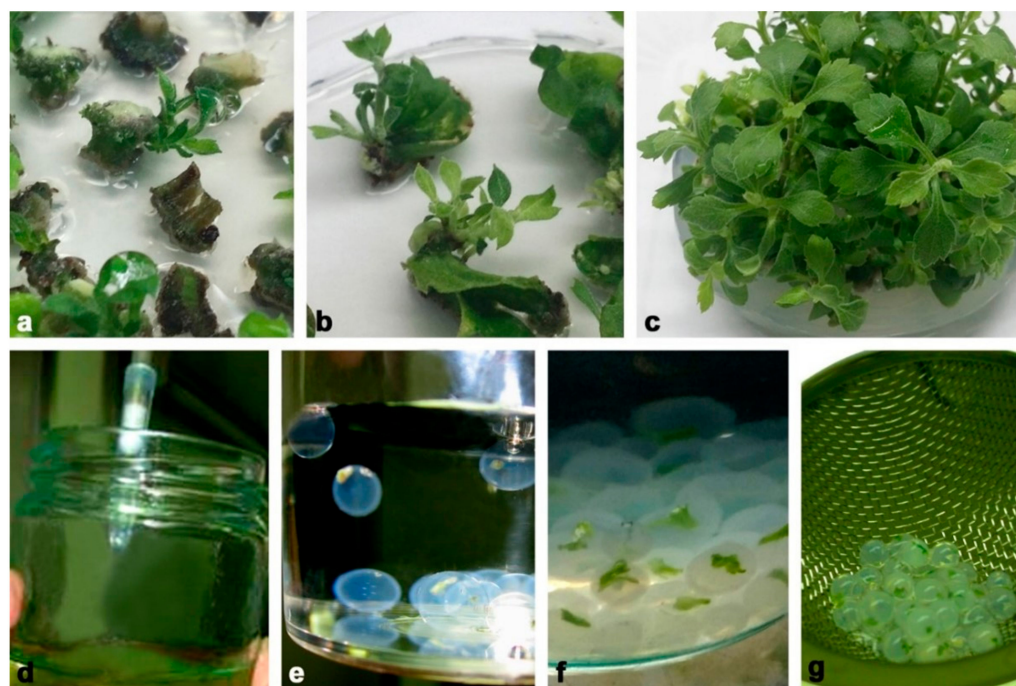


**Figure 12.** Chrysanthemum synthetic seed production. (a,b) Initiation of shoot regeneration in steam segment of cv. PC (a) and leaf culture of cv. BL (b); (c) stock shoot cultures used as primary explants for synthetic seed production; (d) sucking of shoot tips with sodium alginate; (e) formation of alginate beads in complex solution consisting of 100 mM  $\text{CaCl}_2 \times 2\text{H}_2\text{O}$ ; (f) well-formed alginate beads after 20 min in complex solution; (g) washed synseeds ready for treatment.

For production of synthetic seeds, we used axillary shoots developed from nodal stem segments (1 cm) grown for 3 weeks on plant regulator free MS medium described above. After 3 weeks of growth, shoot tips (2–3 mm) were excised from same-sized axillary shoots (2 cm) and washed for 20 min in MS liquid medium without  $\text{CaCl}_2 \times 2\text{H}_2\text{O}$ . Encapsulation was performed according to the following procedure: the explants were plunged into a solution of sodium alginate (2.5%, *w/v*, medium viscosity, Carlo Erba, Carnadero, Italy) made with MS liquid medium without  $\text{CaCl}_2 \times 2\text{H}_2\text{O}$ . Subsequently, droplets of the alginate solution containing one shoot tip were sucked into pipettes with shortened sterile plastic tips (Figure 12d) and dropped into a complex solution (Figure 12e) consisting of 100 mM  $\text{CaCl}_2 \times 2\text{H}_2\text{O}$  (Sigma-Aldrich, St. Louis, MO, USA). Formed alginate beads (5–6 mm in diameter) were maintained for 20 min in this solution with continuous slow agitation (Figure 12f). The encapsulated shoot tips (synseeds) were retrieved and rinsed three times in sterile distilled water in order to remove traces of  $\text{CaCl}_2 \times 2\text{H}_2\text{O}$  (Figure 12g). Finally, water was decanted, and synseeds were placed on sterile filter paper for a few minutes (Figure 1a).

All nutritional media were adjusted to pH 5.8 before sterilization. All media, sodium alginate and complexing solution were sterilized in an autoclave for 20 min at 114 °C. In vitro cultures were grown in a growth room at  $23 \pm 2$  °C, with a photoperiod of 16 h day/8 h night.

#### 4.3. Plasma Treatment of Synthetic Seeds

Chrysanthemum synseeds (Figure 1a) of the same size (5–6 mm in diameter) were exposed to an air SDBD. Twenty-five synseeds were gently placed onto a sterile glass Petri dish (diameter, 90 mm) and then placed below the powered electrode in unsterile conditions and exposed to the plasma all at the same time. The distance between the powered electrode and the synseed surface was ~2 mm. Due to the fact that seeds are ball-shaped and vary slightly in size, the distance could only be estimated. The treatment times were 1 min, 5 min and 10 min. The applied HV in all treatments was  $V_{\text{peak-to-peak}} = 22 \text{ kV}$  ( $V_{\text{RMS}} = 7.8 \text{ kV}$ ), which corresponded to a mean power of 1.1 W.

#### 4.4. Sowing of Synthetic Seeds

Untreated and plasma-treated synseeds were grown on three different sowing substrates as follows: (i) sterile agar MS medium (AM), grown under in vitro conditions; (ii) sterilized vermiculite + liquid MS medium (VLM), grown under in vitro conditions; (iii) direct sowing into unsterilized soil substrate, grown under ex vitro conditions (greenhouse).

For the in vitro experiment, untreated (control) and cold plasma-treated chrysanthemum synseeds were grown on solid plant regulator free MS medium (30 mL) filled in baby jars. Similarly, untreated and cold plasma-treated synseeds (5 per baby jar) were grown in baby jars (5) filled with 10 g vermiculite and moisture with 10 mL liquid plant regulator free MS medium. Baby jars filled with 10 g of vermiculite were sterilized in an autoclave for 20 min at 114 °C. In vitro cultures with synseeds grown on AM and VLM were grown in a growth room at  $23 \pm 2 \text{ °C}$ , with a photoperiod of 16 h day/8 h night. Germination of the synseeds under in vitro conditions was estimated as a frequencies of shoot regrowth from alginate beads at two steps: leaf emergence after one week and full shoot development after four weeks of cultivation.

For the ex vitro experiment, untreated (control) and cold plasma-treated synseeds were sowed directly in plastic containers with 18 places ( $3 \times 6$ ) filled with commercial substrate (Floradur® Seed, Floradur, Oldenburg, Germany) during April and May. Two synthetic seeds were placed on the top of the substrate, one in each place inside a plastic container. All containers were covered with transparent foil during the first four weeks of growing. The synseeds were sprayed weekly with unsterile MS mineral solution. Germination of synseeds under ex vitro conditions was estimated as a frequencies of leaf emergence from alginate beads after one week of cultivation, full shoot development was assigned as complete shoot regrowth from initial synseed after three weeks of cultivation and whole-plantlet formation was recorded when germinated synseeds developed roots after 6 weeks of culture. Total deterioration (%) was evaluated as a percentage of seeds that failed to regrow (germinate) and regenerate to plantlets with respect to the total number of planted synseeds. After twelve weeks of growth in containers, each synseed plantlet was potted in individual pots filled with a mix of peat and perlite (3:1) and grown under greenhouse conditions until flowering. Experiments with plasma treatment were repeated two to four times, and 15–25 synthetic synseeds were used per treatment depending on chrysanthemum cultivar. All data were subjected to statistical analysis using STATISTICA and analysis of variance (ANOVA) using least significance (LSD) tests.

## 5. Conclusions

Synseed technology may be a useful technique for a propagation systems in terms of fast reproduction of seedless plants, preservation of the genetic uniformity of plants, straight delivery to the field and, last but not least, low cost. The difficulties of sowing artificial seeds directly in soil or on commercial substrates under non-sterile conditions are considered to be one of the main limitations for the practical use of this technique. In this paper, we presented, in detail, the results of the electrical characterization of an SDBD that operates in air and its possible application in synthetic seed technology. According to our results, implementation of the SDBD plasma treatment before sowing represents a promising strategy for future investigations and sustainable use of cold plasma in synseed

biotechnology. Plasma-treated chrysanthemum synseeds showed a better survival rate and overall plantlet growth under greenhouse conditions in comparison to untreated synseeds.

In conclusion, to the best of our knowledge, this is the first report about the use of SDBD plasma for seed germination of synthetic seeds under aseptic or non-aseptic conditions. This study demonstrated a highly effective strategy for direct conversion of synseeds into entire plantlets by using plasma pre-conversion treatment. This treatment reduced contamination and displayed a considerable ex vitro ability to convert clonally identical chrysanthemum plants.

**Supplementary Materials:** The following are available online at <https://www.mdpi.com/article/10.3390/plants11070907/s1>, Figure S1: Shoot multiplication index in a control group (plasma –) and with plasma treated synseeds (plasma +).

**Author Contributions:** Conceptualization, N.Š., N.P., S.J. and S.Ž.; methodology, N.Š., N.P., S.J. and S.Ž.; software, N.Š., N.P. and S.J.; formal analysis, N.Š., N.P., S.J. and S.Ž.; investigation, N.Š., N.P., S.J. and S.Ž.; resources, N.Š., N.P., S.J. and S.Ž.; writing—original draft preparation, N.Š., S.J. and S.Ž.; writing—review and editing, N.Š. and N.P.; supervision, N.P.; project administration, N.P.; funding acquisition, N.P. All authors have read and agreed to the published version of the manuscript.

**Funding:** This research was funded by the Ministry of Education, Science, and Technological Development of the Republic of Serbia, grant numbers 451-03-68/2022-14/200007 and 451-03-68/2022-14/200024.

**Institutional Review Board Statement:** Not applicable.

**Informed Consent Statement:** Not applicable.

**Data Availability Statement:** All data are shown in the manuscript, and raw data are available from corresponding authors upon reasonable request.

**Acknowledgments:** Results represent a part of activity in COST action-Plasma applications for smart and sustainable agriculture (CA19110). The authors would like to thank chrysanthemum breeder Zlatko Nekić, Serbia, for providing plant material for the experiments. N.P. and N.Š. would like to thank Milica Bajić for performing measurements for electrical characterization.

**Conflicts of Interest:** The authors declare no conflict of interest.

## References

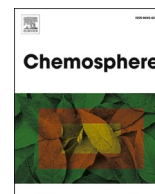
1. Rihan, H.Z.; Kareem, F.; El-Mahrouk, E.; Fuller, M.P. Artificial seeds (Principle, aspects and applications). *Agronomy* **2017**, *7*, 71. [CrossRef]
2. Yücesan, B. Synseed: A new trend in seed technology. In *Synthetic Seeds, Germplasm Regeneration, Preservation and Prospects*; Faisal, M., Alatar, A.A., Eds.; Springer Nature: Cham, Switzerland, 2019; pp. 61–75. [CrossRef]
3. Murashige, T. Plant cell and organ culture as horticultural practice. *Acta Hort.* **1977**, *78*, 17–30. [CrossRef]
4. Standardi, A.; Picconi, E. Recent perspectives on the synthetic seed technology using non-embryogenic in vitro-derived explants. *Int. J. Plant Sci.* **1998**, *159*, 968–978. [CrossRef]
5. Ara, H.; Jaiswal, U.; Jaiswal, V.S. Synthetic seed: Prospects and limitations. *Curr. Sci.* **2000**, *78*, 1438–1444. [CrossRef]
6. Benelli, C.; Micheli, M.; De Carlo, A. An improved encapsulation protocol for regrowth and conservation of four ornamental species. *Acta Soc. Bot. Pol.* **2017**, *86*, 3559. [CrossRef]
7. Phanornchai, S.; Bodhipadma, K.; Noichnda, S.; Leung, D.W.M. Short-term storability of alginate-encapsulated Persian violet microshoots for germplasm exchange. *Plants* **2022**, *11*, 185. [CrossRef]
8. Sakai, A.; Engelmann, F. Vitrification, encapsulation-vitrification and droplet-vitrification: A review. *Cryo Lett.* **2007**, *28*, 151–172.
9. Sharma, S.; Shahza, A.; Teixeira da Silva, J.A. Synseed technology—A complete synthesis. *Biotechnol. Adv.* **2013**, *31*, 186–207. [CrossRef]
10. Saxena, A.; Shukla, M.; Saxena, P. Synthetic seeds: Relevance to endangered germplasm conservation in vitro. In *Synthetic Seeds, Germplasm Regeneration, Preservation and Prospects*; Faisal, M., Alatar, A.A., Eds.; Springer Nature: Cham, Switzerland, 2019; pp. 21–59. [CrossRef]
11. Szekalska, M.; Puciłowska, A.; Szymańska, E.; Ciosek, P.; Winnicka, K. Alginate: Current use and future perspectives in pharmaceutical and biomedical applications. *Int. J. Polym. Sci.* **2016**, *2016*, 7697031. [CrossRef]
12. Wiegand, C.; Heinze, T.; Hipler, U.C. Comparative in vitro study on cytotoxicity, antimicrobial activity, and binding capacity for pathophysiological factors in chronic wounds of alginate and silver-containing alginate. *Wound Repair Regen.* **2009**, *17*, 511–521. [CrossRef]



13. Poor, A.E.; Ercan, U.K.; Yost, A.; Brooks, A.D.; Joshi, S.G. Control of multi-drug-resistant pathogens with non-thermal-plasma-treated alginate wound dressing. *Surg. Infect.* **2014**, *15*, 233–243. [[CrossRef](#)] [[PubMed](#)]
14. Salachna, P.; Grzeszczuk, M.; Miller, E.; Soból, M. Oligo-alginate with low molecular mass improves growth and physiological activity of *Eucomisa utumnalis* under salinity stress. *Molecules* **2018**, *23*, 812. [[CrossRef](#)] [[PubMed](#)]
15. Golkar, P.; Taghizadeh, M.; Noormohammadi, A. Effect of sodium alginate on secondary metabolites and antioxidant activity of safflower genotypes under in vitro salinity stress. *In Vitro Cell Dev. Biol.-Plant* **2019**, *55*, 527–538. [[CrossRef](#)]
16. Teixeira da Silva, J.A. Ornamental chrysanthemums: Improvement by biotechnology. *Plant Cell Tissue Organ Cult.* **2004**, *79*, 1–18. [[CrossRef](#)]
17. Teixeira da Silva, J.A.; Kulus, D. Chrysanthemum biotechnology: Discoveries from the recent literature. *Folia Hort.* **2014**, *26*, 67–77. [[CrossRef](#)]
18. Zalewska, M.; Lema-Rumińska, J.; Miler, N. In vitro propagation using adventitious buds technique as a source of new variability in chrysanthemum. *Sci. Hort.* **2007**, *113*, 70–73. [[CrossRef](#)]
19. Kulus, D.; Zalewska, M. In vitro plant recovery from alginate-encapsulated chrysanthemum  $\times$  grandiflorum (Ramat.) Kitam. shoot tips. *Propag. Orn. Plants* **2014**, *14*, 3–12.
20. Zalewska, M.; Tymoszek, A.; Miler, N. New Chrysanthemum cultivars as a result of in vitro mutagenesis with the application of different explant types. *Acta Sci. Pol. Hort. Cult.* **2011**, *10*, 109–123.
21. Hill, G.P. Shoot formation in tissue cultures of chrysanthemum *Chrysanthemum morifolium* Ramat. *JPN J. Breed.* **1968**, *42*, 386–389.
22. Jevremović, S.; Radojević, L. In vitro plant regeneration from stem segments of several cultivars of chrysanthemum (*Chrysanthemum morifolium* Ramat.) *Bull. Inst. Jard. Bot. Univ. Belgrade* **1995**, *29*, 107–114.
23. Jevremović, S.; Subotić, A.; Miljković, D.; Trifunović, M.; Petrić, M.; Cingel, A. Clonal fidelity of chrysanthemum cultivars after long term micropropagation by stem culture. *Acta Hort.* **2012**, *961*, 211–216. [[CrossRef](#)]
24. Jevremovic, S.; Subotic, A. Micropropagation of chrysanthemum cultivars in Serbia. In Proceedings of the IX International Scientific Agriculture Symposium, Agrosym 2018, Jahorina, Bosnia and Herzegovina, 4–7 October 2018; Kovacevic, D., Ed.; University of East Sarajevo, Faculty of Agriculture: Sarajevo, Bosnia and Herzegovina, 2018; pp. 408–413.
25. Teixeira da Silva, J.A.; Kim, H.; Engelmann, F. Chrysanthemum low-temperature storage and cryopreservation: A review. *Plant Cell Tissue Organ Cult.* **2015**, *120*, 423–440. [[CrossRef](#)]
26. Rout, G.R.; Das, P. Recent trends in the biotechnology of Chrysanthemum: A crucial review. *Sci. Hort.* **1997**, *69*, 239–257. [[CrossRef](#)]
27. Teixeira da Silva, J.A. Chrysanthemum: Advances in tissue culture, cryopreservation, postharvest technology, genetics and transgenic biotechnology. *Biotechnol. Adv.* **2003**, *21*, 715–766. [[CrossRef](#)]
28. Kulus, D. Application of synthetic seeds in propagation, storage, and preservation of Asteraceae plant species. In *Synthetic Seeds, Germplasm Regeneration, Preservation and Prospects*; Faisal, M., Alatar, A.A., Eds.; Springer Nature: Cham, Switzerland, 2019; pp. 155–179. [[CrossRef](#)]
29. Pinker, I.; Abdel-Rahman, S.S. Artificial seeds for propagation of *Dendranthema  $\times$  grandiflora* (Ramat.). *Propag. Orn. Plants* **2005**, *5*, 186–191.
30. Hung, C.D.; Dung, C.D. Production of chrysanthemum synthetic seeds under non-aseptic conditions for direct transfer to commercial greenhouses. *Plant Cell Tissue Organ Cult.* **2015**, *122*, 639–648. [[CrossRef](#)]
31. Reddy, M.C.; Rama Murthy, K.S.; Pullaiah, T. Synthetic seeds: A review in agriculture and forestry. *Afr. J. Biotechnol.* **2012**, *11*, 14254–14275. [[CrossRef](#)]
32. Rihan, H.Z.; Al-Issawi, M.; Al-Swedi, F.; Fuller, M.P. The effect of using PPM (Plant preservative mixture) on the development of cauliflower microshoots and the quality of the artificial seed produced. *Sci. Hort.* **2012**, *141*, 47–52. [[CrossRef](#)]
33. Adamovich, I.; Baalrud, S.D.; Bogaerts, A.; Bruggeman, P.J.; Cappelli, M.; Colombo, V.; Czarnetzki, U.; Ebert, U.; Eden, J.G.; Favia, P.; et al. The Plasma Roadmap: Low temperature plasma science and technology. *J. Phys. D Appl. Phys.* **2017**, *50*, 323001. [[CrossRef](#)]
34. Weltmann, K.-D.; von Woedtke, T. Plasma medicine—current state of research and medical application. *Plasma Phys. Control. Fusion* **2017**, *59*, 014031. [[CrossRef](#)]
35. Laroussi, M.; Kong, M.G.; Morfill, G.; Stolz, W. (Eds). *Plasma Medicine Applications of Low-Temperature Gas Plasmas in Medicine and Biology*; Cambridge University Press: Cambridge, UK, 2012.
36. Lazović, S.; Puač, N.; Miletić, M.; Pavlica, D.; Jovanović, M.; Bugarski, D.; Mojsilović, S.; Maletić, D.; Malović, G.; Milenković, P.; et al. The effect of a plasma needle on bacteria in planktonic samples and on peripheral blood mesenchymal stem cells. *New J. Phys.* **2010**, *12*, 083037. [[CrossRef](#)]
37. Puac, N.; Gherardi, M.; Shiratani, M. Plasma agriculture: A rapidly emerging field. *Plasma Proc. Polym.* **2018**, *15*, 1700174. [[CrossRef](#)]
38. Attri, P.; Ishikawa, K.; Okumura, T.; Koga, K.; Shiratani, M. Plasma agriculture from laboratory to farm: A review. *Processes* **2020**, *8*, 1002. [[CrossRef](#)]
39. Živković, S.; Puač, N.; Giba, Z.; Grubišić, D.; Petrović, Z.L. The stimulatory effect of non-equilibrium (low temperature) air plasma pretreatment on light-induced germination of *Paulownia tomentosa* seeds. *Seed Sci. Tech.* **2004**, *32*, 693–701. [[CrossRef](#)]
40. Sera, B.; Stranák, V.; Serý, M.; Tichý, M.; Spatenka, P. Germination of *Chenopodium album* in response to microwave plasma treatment. *Plasma Sci. Technol.* **2008**, *10*, 506. [[CrossRef](#)]
41. Lu, X.; Reuter, S.; Laroussi, M.; Liu, D. *Non Equilibrium Atmospheric Pressure Plasma Jets: Fundamentals, Diagnostics, and Medical Applications*, 1st ed.; CRC Press: Boca Raton, FL, USA, 2019; pp. 1–426.

42. Waskow, A.; Avino, F.; Howling, A.; Furno, I. Entering the plasma agriculture field: An attempt to standardize protocols for plasma treatment of seeds. *Plasma Process Polym.* **2022**, *19*, e2100152. [[CrossRef](#)]
43. Motyka-Pomagruk, A.; Dzimitrowicz, A.; Orłowski, J.; Babinska, W.; Terefinko, D.; Rychlowski, M.; Prusinski, M.; Pohl, P.; Lojkowska, E.; Jamroz, P.; et al. Implementation of a non-thermal atmospheric pressure plasma for eradication of plant pathogens from a surface of economically important seeds. *Int. J. Mol. Sci.* **2021**, *22*, 79256. [[CrossRef](#)]
44. Lu, X.; Naidis, G.V.; Laroussi, M.; Reuter, S.; Graves, D.B.; Ostrikov, K. Reactive species in non-equilibrium atmospheric-pressure plasmas: Generation, transport, and biological effects. *Phys. Rep.* **2016**, *630*, 1–84. [[CrossRef](#)]
45. Bradu, C.; Kutasi, K.; Magureanu, M.; Puač, N.; Živković, S. Reactive nitrogen species in plasma-activated water: Generation, chemistry and application in agriculture. *J. Phys. D Appl. Phys.* **2020**, *53*, 223001. [[CrossRef](#)]
46. Matthes, R.; Bender, C.; Schlüter, R.; Koban, I.; Bussiahn, R.; Reuter, S.; Lademann, J.; Weltmann, K.D.; Kramer, A. Antimicrobial efficacy of two surface barrier discharges with air plasma against in vitro biofilms. *PLoS ONE* **2013**, *8*, 70462. [[CrossRef](#)]
47. Bormashenko, E.; Grynyov, R.; Bormashenko, Y.; Driori, E. Cold radiofrequency plasma treatment modifies wettability and germination speed of plant seeds. *Sci. Rep.* **2012**, *2*, 741. [[CrossRef](#)] [[PubMed](#)]
48. Sivachandiran, L.; Khacef, A. Enhanced seed germination and plant growth by atmospheric pressure cold air plasma: Combined effect of seed and water treatment. *RSC Adv.* **2017**, *7*, 1822–1832. [[CrossRef](#)]
49. Mildažienė, V.; Aleknavičiūtė, V.; Žūkienė, R.; Giedrė, P.; Naučienė, Z.; Filatova, I.; Lyushkevich, V.; Haimi, P.; Tamošiūnė, I.; Baniulis, D. Treatment of Common Sunflower (*Helianthus annuus* L.) Seeds with radio-frequency electromagnetic field and cold plasma induces changes in seed phytohormone balance, seedling development and leaf protein expression. *Sci. Rep.* **2019**, *9*, 6437. [[CrossRef](#)] [[PubMed](#)]
50. Zahoranová, A.; Henselová, M.; Hudecová, D.; Kalináková, B.; Kováčik, D.; Medvecká, V.; Černák, M. Effect of cold atmospheric pressure plasma on the wheat seedlings vigor and on the inactivation of microorganisms on the seeds surface. *Plasma Chem. Plasma Process.* **2016**, *36*, 398–414. [[CrossRef](#)]
51. Waskow, A.; Betschart, J.; Butscher, D.; Oberbossel, G.; Klöti, D.; Büttner-Mainik, A.; Adamcik, J.; von Rohr, P.R.; Schuppler, M. Characterization of efficiency and mechanisms of cold atmospheric pressure plasma decontamination of seeds for sprout production. *Front. Microbiol.* **2018**, *9*, 3164. [[CrossRef](#)]
52. Liu, B.; Honnorat, B.; Yang, H.; Arancibia, J.; Rajjou, L.; Rousseau, A. Non-thermal DBD plasma array on seed germination of different plant species. *J. Phys. D Appl. Phys.* **2019**, *52*, 025401. [[CrossRef](#)]
53. Chen, H.H.; Chang, H.C.; Chen, Y.K.; Hung, C.L.; Lin, S.Y.; Chen, Y.S. An improved process for high nutrition of germinated brown rice production: Low-pressure plasma. *Food Chem.* **2016**, *191*, 120–127. [[CrossRef](#)]
54. Brandenburg, R. Dielectric barrier discharges: Progress on plasma. *Plasma Sources Sci. Technol.* **2017**, *26*, 053001. [[CrossRef](#)]
55. Winter, J.; Brandenburg, R.; Weltmann, K.D. Atmospheric pressure plasma jets: An overview of devices and new directions. *Plasma Sources Sci. Technol.* **2015**, *24*, 064001.
56. Bruggeman, P.; Brandenburg, R. Atmospheric pressure discharge filaments and microplasmas: Physics, chemistry and diagnostics. *J. Phys. D Appl. Phys.* **2013**, *46*, 464001. [[CrossRef](#)]
57. Janić Hajnal, E.; Vukić, M.; Pezo, L.; Orčić, D.; Puač, N.; Škoro, N.; Milidrag, A.; Šoronja Simović, D. Effect of atmospheric cold plasma treatments on reduction of alternaria toxins content in wheat flour. *Toxins* **2019**, *11*, 704. [[CrossRef](#)] [[PubMed](#)]
58. Brandenburg, R.; Navrátil, Z.; Jansky, J.; Stahel, P.; Trunec, D.; Wagner, H.E. The transition between different modes of barrier discharges at atmospheric pressure. *J. Phys. D Appl. Phys.* **2009**, *42*, 085208. [[CrossRef](#)]
59. Wang, C.; Zhang, G.; Wang, X. Comparison of discharge characteristics of a dielectric barrier discharge with different electrode structures. *Vacuum* **2012**, *86*, 960. [[CrossRef](#)]
60. Sakiyama, Y.; Graves, D.B.; Chang, H.-W.; Shimizu, T.; Morfill, G.E. Plasma chemistry model of surface microdischarge in humid air and dynamics of reactive neutral species. *J. Phys. D Appl. Phys.* **2012**, *45*, 425201. [[CrossRef](#)]
61. Tang, Q.; Jiang, W.; Cheng, Y.; Lin, S.; Lim, T.M.; Xiong, J. Generation of Reactive Species by Gas-Phase Dielectric Barrier Discharges. *Ind. Eng. Chem. Res.* **2011**, *50*, 9839–9846. [[CrossRef](#)]
62. Kozlov, K.V.; Brandenburg, R.; Wagner, H.-E.; Morozov, A.M.; Michel, P. Investigation of the filamentary and diffuse mode of barrier discharges in N<sub>2</sub>/O<sub>2</sub> mixtures at atmospheric pressure by cross-correlation spectroscopy. *J. Phys. D Appl. Phys.* **2005**, *38*, 518–529. [[CrossRef](#)]
63. Shang, K.; Wang, M.; Peng, B.; Li, J.; Lu, N.; Jiang, N.; Wu, Y. Characterization of a novel volume-surface DBD reactor: Discharge characteristics, ozone production and benzene degradation. *J. Phys. D Appl. Phys.* **2020**, *53*, 065201. [[CrossRef](#)]
64. Jiang, N.; Guo, L.; Qiu, C.; Zhang, Y.; Shang, K.; Lu, N.; Li, J.; Wu, Y. Reactive species distribution characteristics and toluene destruction in the three-electrode DBD reactor energized by different pulsed modes. *Chem. Eng. J.* **2018**, *350*, 12–19. [[CrossRef](#)]
65. Liberatore, C.M.; Rodolfi Beghèa, D.; Fabbri, A.; Ganino, T.; Chiancone, B. Adventitious shoot organogenesis and encapsulation technology in hop (*Humulus lupulus* L.). *Sci. Hortic.* **2020**, *270*, 109416. [[CrossRef](#)]
66. Benelli, C. Encapsulation of shoot tips and nodal segments for in vitro storage of “kober 5BB” grapevine rootstock. *Horticulturae* **2016**, *10*, 185. [[CrossRef](#)]
67. Hung, C.D.; Trueman, S.J. Encapsulation technology for short term preservation and germplasm distribution of the African mahogany *Khaya senegalensis*. *Plant Cell Tissue Organ. Cult.* **2011**, *107*, 397–405. [[CrossRef](#)]
68. Hung, C.D.; Trueman, S.J. Alginate encapsulation of shoot tips and nodal segments for short term storage and distribution of the eucalypt *Corymbia torelliana* × *C. citriodora*. *Acta Physiol. Plant.* **2012**, *34*, 117–128. [[CrossRef](#)]

- 
69. Dobrynin, D.; Fridman, G.; Friedman, G.; Fridman, A. Physical and biological mechanisms of direct plasma interaction with living tissue. *New J. Phys.* **2009**, *11*, 115020. [[CrossRef](#)]
  70. Murashige, T.; Skoog, F. A revised medium for rapid growth and bio assays with tobacco tissue cultures. *Physiol. Plant* **1962**, *15*, 473–497. [[CrossRef](#)]



# Pathways of organic micropollutants degradation in atmospheric pressure plasma processing – A review

Barbara Topolovec<sup>a,b</sup>, Nikola Škoro<sup>c</sup>, Nevena Puač<sup>c</sup>, Mira Petrovic<sup>a,d,\*</sup>

<sup>a</sup> Catalan Institute for Water Research (ICRA), Emili Grahit 101, 17003, Girona, Spain

<sup>b</sup> University of Girona, Girona, Spain

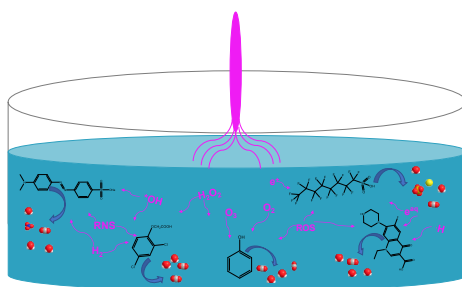
<sup>c</sup> Institute of Physics, University of Belgrade, Pregrevica 118, 11080, Belgrade, Serbia

<sup>d</sup> Catalan Institution for Research and Advanced Studies (ICREA), Passeig Lluís Companys 23, 08010, Barcelona, Spain

## HIGHLIGHTS

- Different applications of several types of non-equilibrium non-thermal plasma sources for wastewater treatment.
- Degradation mechanisms of organic micropollutants induced in plasma treatments.
- Challenges and future important steps in research for application of plasma technology in wastewater processing.

## GRAPHICAL ABSTRACT



## ARTICLE INFO

Handling Editor: Xiangru Zhang

### Keywords:

Organic micropollutants  
Non-equilibrium/non-thermal plasma types  
Degradation pathways  
Removal  
Advanced oxidation technologies  
Novel wastewater treatment processes

## ABSTRACT

Concern of toxic compounds and their, potentially more harmful degradation products, present in aquatic environment alarmed scientific community and research on the development of novel technologies for wastewater treatment had become of great interest. Up to this date, many papers pointed out the challenges and limitations of conventional wastewater treatment and of some advanced oxidation processes. Advanced technologies based on the use of non-equilibrium or non-thermal plasma had been recognized as a possible solution for, not only degradation, but for complete removal of recalcitrant organic micropollutants. While previous review papers have been focused on plasma physics and chemistry of different types of discharges for few organic micropollutants, this paper brings comprehensive review of current knowledge on the chemistry and degradation pathways by using different non-thermal plasma types for several micropollutants' classes, such as pharmaceuticals, perfluorinated compounds, pesticides, phenols and dyes and points out some major research gaps.

## 1. Introduction

During the last decades, an increasing number of emerging

contaminants (EC) have been detected in the aquatic environment. Among them, the main concern and awareness is about the presence of organic micropollutants (OMPs). OMPs represents wide group of

\* Corresponding author. Catalan Institute for Water Research (ICRA), Catalan Institution for Research and Advanced Studies (ICREA), Emili Grahit 101 17003, Girona, 08010, Spain.

E-mail address: [mpetrovic@icra.cat](mailto:mpetrovic@icra.cat) (M. Petrovic).

<https://doi.org/10.1016/j.chemosphere.2022.133606>

Received 8 October 2021; Received in revised form 28 December 2021; Accepted 11 January 2022

Available online 13 January 2022

0045-6535/© 2022 Elsevier Ltd. All rights reserved.

chemical compounds, including, but not limited to, pharmaceuticals, pesticides, personal care products, different household, and industrial chemicals, which can be found in wastewaters of urban, industrial, or agricultural origin. OMPs in water bodies are known to cause harmful effects on aquatic organisms and ultimately on humans (EEA (European Environment Agency), 2011; Rozas et al., 2016; Verlicchi et al., 2012). Various studies report that some OMPs are bioaccumulative and can cause growth inhibition and endocrine disruption in aquatic organisms (Caballero-Gallardo et al., 2016; Santos et al., 2010; Tijani et al., 2014).

Abundant research conducted in the past showed that conventional biological treatment, adopted at majority of wastewater treatment plants (WWTPs) is only partially able to mitigate OMPs contamination with highly variable performance (Falás et al., 2016; Gros et al., 2010). Poor elimination of more hydrophilic and poorly-to-moderately biodegradable OMPs is well documented (Luo et al., 2014). Advanced technologies to remove OMPs from the wastewater are available, but in many cases, they are too costly and/or energy unsustainable. In previous studies, different advanced oxidation processes (AOPs), such as ultraviolet (UV)/hydrogen peroxide ( $H_2O_2$ ) treatment, ozonation ( $O_3$ ), photo-Fenton have been recognized as successful for wastewater treatment with the ability to rapidly and efficiently degrade many different types of organic compounds (Giannakis et al., 2015; Kudlek, 2018; Wols and Hofman-Caris, 2012).

One of the novel highly-promising AOPs is based on the use of non-equilibrium or non-thermal plasma (NTP) which produce nitrogen-containing species, hydroxyl radical, hydroperoxyl radical, atomic hydrogen and oxygen, as well as other radicals and active chemical species that are generally required for an effective water treatment (Ghime and Ghosh, 2020; Miklos et al., 2018; Ribeiro et al., 2015). However, little is known about the feasibility of plasma treatment for the removal of more recalcitrant compounds from wastewater (i.e. OMPs) or regarding their degradation kinetics, as well as degradation by-products generated and their toxicity.

In previous reviews on water treatment which involve plasma technology, the focus was on plasma physics and chemistry of different types of discharges and modeling of plasma interaction with the liquid (Foster, 2017; Foster et al., 2012; Hijosa-Valsero et al., 2014; Jiang et al., 2014; Lindsay et al., 2015; Parvulescu et al., 2012; Reuter et al., 2018). This review summarizes the current knowledge on the chemistry and pathways of degradation of OMPs by using different NTP types.

## 2. Fundamentals of non-equilibrium plasma for water treatment

### 2.1. Plasma classification and technological aspects

Plasma is fully or partially ionized gas and is frequently called the fourth state of matter. Generally speaking, by applying energy to a gas, some amount of excited species and ions and electrons are produced in frequent collisions between the existing free electrons and neutral species eventually leading to the formation of plasma. Energy input required for the creation of plasma in majority of cases is realized by imposing sufficiently high electric field. Although it contains free charge carriers, from a macroscopic point of view, plasma is electrically neutral. In thermodynamic term plasma species (electrons, ions, and neutrals) can be characterized by their temperatures and in the respect to this description plasma can be classified into two categories: equilibrium or thermal and non-equilibrium plasma. In thermal plasmas characteristic temperatures of electrons and heavy particles (atoms, molecules, ions) are equal high, with temperature values of  $10^3$  K and above (Lieberman and Lichtenberg, 1994). Strictly speaking, at terrestrial conditions (i.e., in applications) these kinds of plasma are only in local thermodynamic equilibrium since the temperatures of all plasma species are the same only in a limited space volume. When comes to applications, thermal plasmas are realized as arcs and torches and typically used for applications where high temperatures are required, such as for cutting, spraying, welding or, as in the analytical devices, for the evaporation of

an analyte material (Tendero et al., 2006).

In non-equilibrium plasmas the temperature of the electrons is much higher than the temperatures of heavy particles. Depending on the type of the plasma, temperatures of the heavy particles can be few hundred degrees or much below and close to the room temperature. Thus, these plasmas are also referred as non-thermal plasma (NTP) or cold plasma. Due to pronounced non-equilibrium of particle energies, mainly electrons have sufficient energy to collide with the background gas particles and provide multiplication of charges necessary to sustain the plasma. Apart from production of charged particles, excited species (especially metastables), fast neutrals, radicals, photons are also produced in collisions. In comparison to thermal plasmas, non-equilibrium plasma is characterized by lower energy densities, have lower degree of ionization and consequently lower particle densities (Lieberman and Lichtenberg, 1994). Nevertheless, the fact that these plasmas operate at temperatures which are equal or close to room temperatures, allow their application in many different aspects (Becker et al., 2004; Makabe and Petrovic, 2014).

Non-equilibrium plasmas working at atmospheric pressure have an advantage compared to their low-pressure counterparts when comes to applications where samples cannot withstand exposures to pressures below atmospheric. Thus, many applications of plasma in fields of biology and medicine have been driving the development of atmospheric pressure non-equilibrium plasmas in the last 30 years (Fridman et al., 2008; Laroussi et al., 2017; Machala et al., 2012; Miletić et al., n. d.). Several types of electrical discharges at atmospheric pressure, such as corona, dielectric barrier discharge (DBD), gliding arc, glow discharge and streamer discharge, have been employed depending on particular treatment demands. Albeit the limited active volume of these plasmas versatility and success of their biomedical applications lies in production of suitable chemical species and their interaction with living cells (Lu et al., 2016; Privat-Maldonado et al., 2019; Tomić et al., 2021).

In recent years, the applications of non-equilibrium plasmas are expanded to the wastewater treatment. According to recent papers, applications of NTP for wastewater treatment are becoming more attractive and are recognized as technological solution for EC which are highly recalcitrant to conventional wastewater treatment technologies. Reactive chemical species created in the plasma have already proven their capability to decontaminate water by pulverizing molecules of the pollutant in various chemical reactions (Foster, 2017; Magureanu et al., 2018). However, before reaching the auspicious situation where plasma technology is used for wastewater treatment several major obstacles should be taken. The first one is related to determination of proper parameter related to the power consumption in plasma processes that will adhere to existing wastewater technology standards and enable comparison with conventional methods. Diversity of experimental setups for water treatment, which sometimes include additional power consumption (e.g., for sample recirculation), and plasma devices that require different approaches in power measurements make this a demanding task. Comparison of reported data in review papers shows the absence of standard for reporting of the treatment conditions (Jiang et al., 2014; Magureanu et al., 2018; Malik, 2010; Nzeribe et al., 2019). Therefore, a paper describing wastewater plasma treatment should contain the minimum information on: significant dimensions of the experimental setup, type of the discharge used, working gas flow (if present), power supply type, electrical parameters including the power delivered to plasma, volume of the treated sample (and the flow rate if in flowing regime), initial and final concentrations of the pollutant and duration of the treatment. Providing a detailed account on experimental conditions will enable analysis of and comparison of plasma treatments and can be a first step towards defining appropriate power-efficiency parameter.

Another difficulty for application of NTP as technology for water treatment come from the rather small volume of the active plasma region which, in turn, limit the out flux of reactive species created in the plasma. Since plasma is created at atmospheric pressure, mean free paths (the mean distance between two collisions) of all particles are in

the order of  $\mu\text{m}$ . Thus, to establish an effective interaction between the plasma and the water they should be in close contact while an increase in the transfer of reactive species requires increasing the effective interaction area. In the existing experimental setups, there are two different approaches – one option is to establish plasma inside the water while another way is to create plasma in the gas phase adjacent to the liquid sample.

In that view, we can divide atmospheric pressure non-equilibrium plasmas that can be used in wastewater treatment as discharges in liquids and in contact with liquids.

### 2.2. Non-equilibrium plasmas in liquids

This group of high non-equilibrium plasmas refers to the discharges where electrodes are completely immersed in liquid. There are two sub-groups:

- i. Discharges in liquids where no gas phase plasma is involved
- ii. Discharges in bubbles inside liquids.

The major challenges in these types of discharges are how to achieve a breakdown without subsequent transition into the thermal plasma, the appropriate power supply, the optimal geometry of the electrodes and their etching during the operation, heating of the liquid, the complexity of the chemical composition of the liquid etc. Until now several review papers have been published on the topics related to the discharges in liquids (Peter Bruggeman and Leys, 2009; Graham and Stalder, 2011; Locke et al., 2006; Malik et al., 2001).

The discharges with no gas phase involved can be created in the pin-to-pin, pin-to-plate or plate-to-plate electrode system with the pulsed (usually nanosecond) power supplies (Akiyama, 2000; An et al., 2007; Locke and Thagard, 2012; Petr Lukes et al., 2005; Schaper et al., 2011; Schoenbach et al., 2008; Šunka, 2001). There are several important parameters that will influence the formation and propagation of the discharge like the energy deposited in the pulse, frequency and duty cycle, inter-electrode distance, conductivity of the liquid. The discharges are streamer-like in case of non-equilibrium plasmas and the created streamers usually dissipate before reaching the grounded electrode.

The second sub-type of the discharges in water involves creation of bubbles and in this case, we are dealing with gas phase surface plasmas (inside bubble) with the liquid electrode. The bubbles can be created by bubbling systems, heat wave, in capillary systems etc. (Bruggeman et al., 2008; Gershman et al., 2007). The bubbles do not need to be introduced into the liquid (for example by bubbling system) in order to have this type of discharge. The appearance of the micro-bubbles can be related to the breakdown of the discharge where the initial Joule heating of the liquid leads to their creation (Ceccato et al., 2010; Korobeinikov and Yanshin, 1983).

### 2.3. Non-equilibrium plasmas in contact with liquid surfaces

In this case the powered electrode is not in direct contact with liquid which serves here as a grounded electrode. There are various geometries that are used in these type of discharges: pin-jet type, DBD-jet type, planar strip electrodes that can be in direct contact with surrounding gas or immersed in dielectric etc. (Boselli et al., 2014; Puač et al., 2012; Šimor et al., 2002; Škoro et al., 2018). The used power supplies range from nano-pulsed to a sine wave excitation voltage and the applied voltages depend on the excitation frequency, working gas used, electrode geometry and electrode gap. The applied frequencies can range from several Hz up to the MHz region. The discharge is created in the gas phase and the resulted chemistry inside the liquid is the result of gas phase and gas/liquid interface chemistry (Bruggeman et al., 2016; Parvulescu et al., 2012; Sunka et al., 1999). The gas temperature stays in the range 300 K–400 K and usually the energy per pulse is of order of  $\mu\text{J}$ . The electron temperature stays in the range of 1–3 eV and electron

concentration between  $10^{19}$ – $10^{21} \text{ m}^{-3}$ .

## 3. Application of plasma for removal of pollutants dissolved in water

### 3.1. Pharmaceuticals

Pharmaceuticals are OMPs which are widely investigated and the attention for further research is increasing due to the numerous reports of their presence in ground, surface and even drinking water. Despite low concentrations, the influence of continuous exposure to mixtures of different therapeutic groups has become of growing concern, not just to the aquatic species, but for human health as well (Arnold et al., 2014; Bernhardt et al., 2017). Some of these contaminants have been reported as very persistent, prone to accumulation and very hard to remove with conventional water treatment technologies. Therefore, alternative methods are being investigated and NTP, as a potent chemically active agent, has shown to be promising solution for degradation of highly resistant pharmaceuticals. Table 1 shows several plasma configurations most used for pharmaceuticals.

As it can be seen in Table 1, plasma configurations dominantly present in the papers are DBDs and corona. In the (Krause et al., 2011) rework, preceding corona discharge over water reactor (Krause et al., 2009) was further developed and used to study degradation of “CBZ” and clofibrac acid. Two electrodes with dielectric barrier were installed above rotating drum, which moved a test solution as a thin water film in an atmospheric DBD system. The results showed that the degradation after 60 min of single-solution treatment was 94% for CBZ in ultra-pure water. Clofibrac acid was degraded after 30 min of treatment. In a solution which contained landfill leachate, degradation after 90 min was 97% and 88% respectively, which showed that in the leachate the removal efficiency also depends on the type of the compound. The influence of corona discharge system on the degradation was discussed in the (Dobrin et al., 2013) for DCF. Tap water solution was treated with pulsed corona discharge above water system with addition of oxygen as working gas. Complete removal of DCF occurred after 15 min of treatment and after 30 min 50% of mineralization was achieved. The authors concluded that use of oxygen as a feeding gas improves energy efficiency as well as ozone and hydrogen peroxide formation in corona discharge that probably play important role in the degradation of the micro-pollutant. Similar conclusions are reached by other authors (Hama Aziz et al., 2017; Monica Magureanu et al., 2018). In a DBD reactor, with gaseous plasma-liquid system, degradation of DCF and IBP was investigated with application of different working gasses (Hama Aziz et al., 2017). The authors found that with argon, the degradation of DCF is less efficient than it was for the IBP. On the other hand, using working gas mixture of  $\text{Ar}/\text{O}_2$ , mineralization of only DCF was improved which implies that, even with the same DBD plasma system, the influence of gas mixture must be considered for each treated compound. Different gasses and gas mixtures produce different types of radicals which effect the break of compound bonds.

Several other authors discussed the influence of different gasses and radicals on the mineralization of pharmaceuticals in their papers (Banashchik et al., 2015; Singh et al., 2019; Wardenier et al., 2019; Zhang et al., 2018) where they evaluated degradation pathways. For the degradation of norfloxacin a DBD system was used with explanation of the degradation mechanisms by (Zhang et al., 2018). Different working gasses were used in experiments: pure nitrogen or oxygen and the mixture of both for the treatment of norfloxacin solution. They discovered that different types of radical species, reactive oxygen species (ROS) and reactive nitrogen species (RNS) produced in the plasma lead to different degradation pathways. Fig. 1 shows possible pathways for degradation of norfloxacin in DBD treatment with different gasses. The results showed that hydroxyl radicals may play important role in the degradation of the compound, to be precise, for the break of C–F bond in piperazine ring and formation of C–OH group. For the verification of the

**Table 1**  
Different plasma configurations used treatment of organic micropollutants.

OMPs	Plasma system/plasma type and configuration/working gas	Solution type/volume treated/ treatment time/initial concentration	Degradation	Reference
<b>Pharmaceuticals</b>				
Norfloxacin	DBD reactor/discharge above liquid/Oxygen (O <sub>2</sub> ), nitrogen (N <sub>2</sub> ) or air	Ultrapure aqueous solution 3 ml 2 min 200 mg/L	O <sub>2</sub> /air – 98% N <sub>2</sub> – 50%	Zhang et al. (2018)
Ofloxacin (OFX) and ciprofloxacin (CFX)	DBD reactor/discharge above liquid/air	Matrix solution 25 ml 5–25 min 10 mg/L	66% CFX 72% OFX	Sarangapani et al. (2019)
Paracetamol, Caffeine, Ceftriaxone	DBD reactor/tilted cylindrical configuration, discharge above liquid/air or O <sub>2</sub>	Ultrapure aqueous solution 100 ml 10–30 min 25 mg/L (parac.); 50 mg/L (caff.); 5 mg/L (ceft.)	>80% (caff.) 89% (parac.) >80% (ceft.)	Iervolino et al. (2019)
Amoxicillin, Oxacillin, Ampicillin	DBD reactor/coaxial configuration, thin falling water film/O <sub>2</sub>	Tap water 200 ml 10–30 min 100 mg/L	Degradation occurred but percentage not specified	(Magureanu et al., 2011)
Ibuprofen (IBP)	DBD reactor/discharge above falling water film/air	Ultrapure aqueous solution 350 ml 15 min 60 mg/L	85%	Marković et al. (2015)
Diclofenac (DCF), IBP	DBD reactor/planar configuration above falling water film/argon (Ar)	Ultrapure aqueous solution 500 ml 20–30 min 50 mg/L	Complete degradation occurred	Hama Aziz et al. (2017)
DCF, Carbamazepine (CBZ), CFX	Corona discharge/pulsed needle-to-plane continuous flow reactor/air	Distilled, lake and river water 10–40 ml/min 24 min 1 ml (in mix added in equal ratio)	>99% in distilled and lake water >91% in river water	Singh et al. (2019)
Paracetamol	Corona discharge/pulsed above liquid/air or O <sub>2</sub>	Ultrapure aqueous solution 40 000 ml 30 min 100 mg/L	Complete degradation with partial mineralization	Panorel et al. (2013)
CBZ, diatrizoate, diazepam, DCF, IBP, 17 $\alpha$ -ethinylestradiol, trimethoprim	Corona discharge/coaxial geometry/discharge inside water in surrounding air	Ultrapure aqueous solution 300 ml 60 min 500 mg/L	45–99%	Banaschik et al. (2015)
<b>Perfluorinated compounds</b>				
perfluorooctanoic acid (PFOA), perfluorooctane sulfonate (PFOS)	DC-plasma generated within gas bubbles/O <sub>2</sub> , helium (He), Ar	Ultrapure aqueous solution 50 mL 240 min 50 mg/L	92% - decomposition ratio of fluorine ions 57% decomposition ratio of sulfate ions	Yasuoka et al. (2010)
PFOA, PFOS	DC-plasma generated within gas bubbles/O <sub>2</sub>	Ultrapure aqueous solution 20 mL PFOA: 3 h 41,4 mg/L PFOS: 8 h 60 mg/L	PFOA: 94,5% defluorination ratio PFOS: 70% defluorination ratio	Hayashi et al. (2015)
PFOA	DC-plasma generated within gas bubbles/O <sub>2</sub>	Ultrapure aqueous solution (single and mix with other PFAS) 20 mL 150 min 156 $\mu$ M	Complete degradation in single solution; 80% in mix solution	(Takeuchi et al., 2014)
PFOA	Laminar jet with bubbling (LJB)/Ar	Ultrapure aqueous solution 1,4 L 30 min 20 $\mu$ M	90% (high removal rate process) 25% (high removal efficiency process)	Stratton et al. (2017)
PFOA, PFOS	Discharge above the liquid with bubbling/argon	Ultrapure aqueous solution 1,5 L 30–120 min 8,3 mg/L	90% of PFOA in 60 min and PFOS in 40 min	Singh et al. (2019)
<b>Pesticides</b>				
Lindane	DBD a) conventional batch reactor (R1)/He b) falling water film reactor (R2)	Distilled and wastewater 175 mL 5 min 1 mg/ml	87% in R1 and 79% in R2 for distilled water 50% in R1 for wastewater	Hijosa-Valsero et al. (2013)
Atrazine				Vanraes et al. (2015)

(continued on next page)

Table 1 (continued)

OMPs	Plasma system/plasma type and configuration/working gas	Solution type/volume treated/ treatment time/initial concentration	Degradation	Reference
	pDBD, gas phase above liquid/with or without membrane/air	Water matrix 100 ml 45 min 30 µg/L	Without membrane 61,0% With membrane 84,7%	
	Pulsed DBD reactor with Continuous flow falling water film over activated carbon textile/air	Deionized water 2,5 L 2500 ml 30 min 200 µg/L	93,9%	Wardenier et al. (2019)
2,4 - D	Corona discharge, needle to plane/air	Distilled, lake and river water Not defined 24 min 0,2–2 mg/L	>99% in distilled and lake water >91% in river water	Singh et al. (2019)
	Pulsed corona discharge/O <sub>2</sub>	Tap water 330 ml 60 min 25 mg/L	93%	Bradu et al. (2017)
	DBD reactor with planar falling water film/ pure Ar, Ar/O <sub>2</sub> (80:20), and air	Deionized water solution 0,5 L 90 min 100 mg/L	Degradation occurred but percentage not specified	Hama Aziz et al. (2018)
	Multiple pin-plate corona discharge/air	Aqueous solution Not defined 6 min 1 mg/L	100%	Singh et al. (2017)
Alachlor	Continuous flow pulsed DBD/O <sub>2</sub>	Deionized water solution Single pass through reactor 30 min 1 mg/L	78,4%	Wardenier et al. (2019)
	DBD/plasma gas bubbled/combined with activated carbon/air	Ultrapure aqueous solution 30 min 500 ml 57 µg/L	75,1%	Vanraes et al. (2017)
Carbofuran	Corona discharge, needle to plane/air	Distilled, lake and river water Not defined 24 min 0,2–2 mg/L	>99% in distilled and lake water >91% in river water	Singh et al. (2019)
<b>Phenols and phenolic compounds</b>				
2,4 dibromophenol	DBD a) conventional batch reactor (R1)/He b) falling water film reactor, surface discharge (R2)	Ultrapure aqueous solution a) 4 mlb) 174 ml 5 min 1 mg/L	a) 98% b) 73,5%	Hijosa-Valsero et al. (2013)
Bisphenol A (BPA)	Pulsed DBD reactor with Continuous flow falling water film over activated carbon textile/air	Synthetic aqueous solution in mix 2500 ml 30 min 200 µg/L	98,8%	Wardenier et al. (2019)
Phenol	DBD reactor, surface discharge/air	Ultrapure aqueous solution 70 ml 240 min 47,05 mg/L	Almost complete removal	Ceriani et al. (2018)
	Cylindrical DBD reactor/O <sub>2</sub>	Ultrapure aqueous solution 100 ml 15 min 50 mg/L	Complete mineralization after 15 min	Iervolino et al. (2019)
	DBD reactor, surface discharge/air	Ultrapure aqueous solution 70 ml 120, 240 min 47,05 mg/L	80% in 4 h (Ni/Cr wire) Complete degradation in 2 h (SS wire)	Marotta et al. (2011)
2,4 – dichlorophenol	DBD reactor with planar falling water film/ pure Ar, Ar/O <sub>2</sub> (80:20), and air	Ultrapure aqueous solution 500 ml 15 min 100 mg/L	Complete degradation	Hama Aziz et al. (2018)
<b>Dyes</b>				
Methylene blue	DBD reactor/cylindrical configuration/air, oxygen	Ultrapure aqueous solution 100 mL 5 min; 10 mg/L	96% (O <sub>2</sub> ) 76% (air)	Iervolino et al. (2019)
	DC plasma, in slug flow/gas -liquid interface with bubbles/O <sub>2</sub> , Ar, He	Synthetic wastewater 5 mL time specified as one-time (one lap) 15 mg/L	94.5% O <sub>2</sub> 89.3% Ar 75.8% He	Yamada et al. (2020)
	Pulsed corona discharge in multiwire-plate/air			

(continued on next page)



Table 1 (continued)

OMPs	Plasma system/plasma type and configuration/working gas	Solution type/volume treated/treatment time/initial concentration	Degradation	Reference
Methyl orange	Surface glow discharge/air	Ultrapure aqueous solution 35 mL 10 min 50 mg/L	Almost complete degradation (decolorization)	Monica Magureanu et al. (2013)
		Ultrapure aqueous solution 50 ml 15 min 10 mg/L	93%	Liu et al. (2016)
	DBD reactor/air	Aqueous solution 10 mL 60–180 s 50, 75, 100 mg/L	Degradation occurred but percentage not specified	Sarangapani et al. (2017)
Methyl red	DBD reactor/air	Aqueous solution 200 ml 30 min 20 mg/L	Degradation occurred but percentage not specified	He et al. (2018)
		Solution in deionized water 25 ml 5 min 100 mg/L	Complete degradation after 5 min at 80 kV	Pankaj et al. (2017)
Crystal violet	DBD reactor/air	Solution in deionized water 25 ml 5 min 100 mg/L	Complete degradation after 5 min at 80 kV	Pankaj et al. (2017)
		DBD reactor/cylindrical configuration/air	Ultrapure aqueous solution Not available 25 min 50–100 mg/L	>89%
Acid orange 7	Two formed modes- corona like discharge and streamer channels/air	Deionized water 200 ml Time not defined 20 mg/L	Degradation occurred but percentage not specified	Ruma et al. (2013)

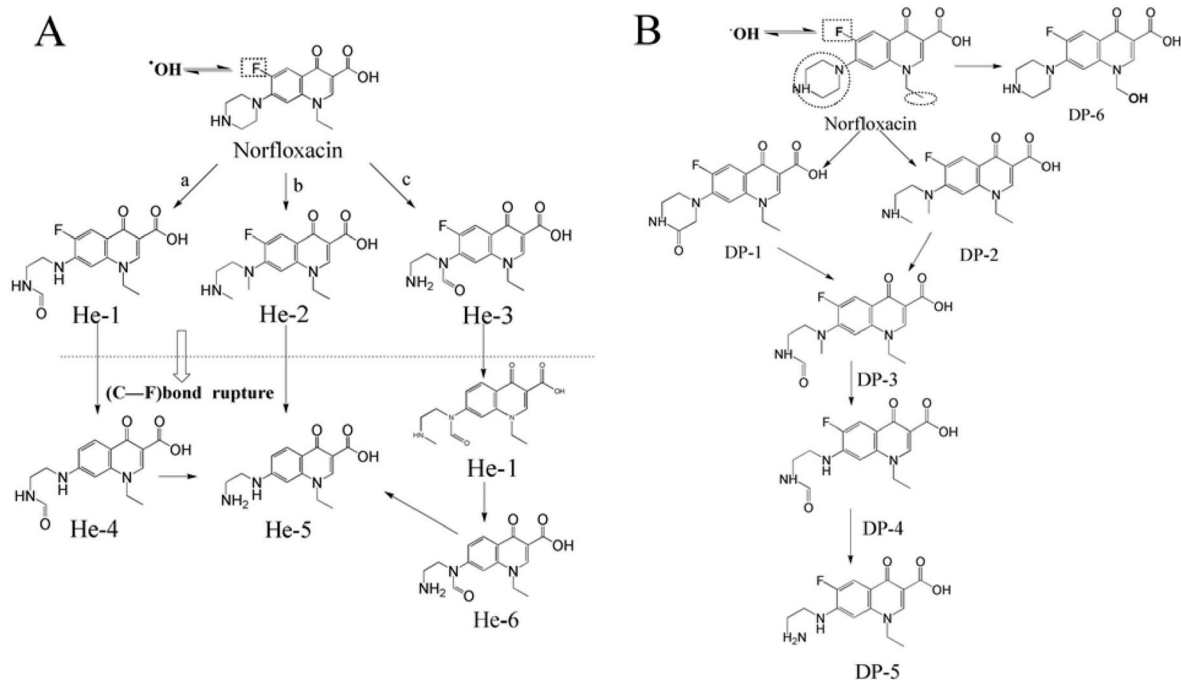


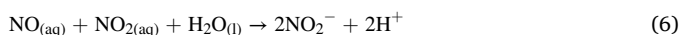
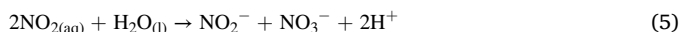
Fig. 1. Possible pathways for degradation of norfloxacin in DBD treatment: (A) treated by DBD in helium; (B) treated by DBD in air or nitrogen. Reprinted with permission from (Zhang et al., 2018). Copyright (2018) Elsevier.

results, mass spectrometry analysis was used and confirmed that the products with expected masses were found. It is important to note that the solution was made with pure water and the effects may be different in the real wastewater samples.

In the work by (Singh et al., 2019) for three pharmaceuticals (DCF,

CBZ, CPF), degradation was much faster in distilled water than in the river and lake water due to the presence of other compounds, such as carbonates and ions which can act as scavengers of  $\cdot\text{OH}$  radicals. Also, in the presence of the nitrates, phosphates and sulfates, removal efficiency is not changed significantly which indicate that the alkalinity of the

water effects on the % of degradation. Indeed, the  $\text{CO}_3^{2-}$  and  $\text{HCO}_3^-$  ions which are associated with the alkalinity are major scavengers for  $\cdot\text{OH}$  radicals and other oxidants and in the presence of high concentrations of those ions, removal efficiency can decrease significantly. For the water pH, corona discharge in air above liquid configuration played important role since in that system, different reactive oxygen and nitrogen species are produced which can decrease the pH with the formation of  $\text{H}^+$  ions (Eqs. (1)–(6)).



The results given by the TOC analysis indicated that there is the presence of transformation products. The reduction in TOC was around 70%, 65% and 50% in distilled, lake and river water, respectively, but also decreasing in TOC with time indicated their mineralization. In the study by (Monica Magureanu et al., 2018) a plasma-ozonation system was employed for the treatment of IBP. It was concluded that complete removal occurred within 15–20 min and after 60 min complete mineralization was confirmed with high TOC reduction. Also, they confirmed the importance of oxygen for the degradation of OMPs and discussed importance of the discharge pulses.

In the recent work (Iervolino et al., 2019), assessed the removal of paracetamol and ceftriaxone in DBD reactor. With oxygen as a feeding gas, results showed that the complete mineralization for the paracetamol sample can be achieved after 15 min of treatment instead of 60 min in air. (Sarangapani et al., 2019) investigated influence of different radical scavengers on removal efficiency of antibiotics OFX and CFX. What was interesting is that in the presence of carbon tetrachloride ( $\text{CCl}_4$ ), degradation of antibiotics increased. It is possible that reactions between  $\cdot\text{H}$  radical and  $\text{CCl}_4$  may occur faster and reactions between  $\cdot\text{H}$  radical and hydroxyl radical is inhibited consequently giving more possibilities to hydroxyl radical and target compound (or its intermediates) reactions. Generally, when the target compound is in a matrix solution, it can affect the degradation degree induced by plasma due to other molecules and compounds that can react with oxidant radicals. Authors also suggested the degradation mechanisms for antibiotics depending on the working gas in the plasma system. The mechanisms can include the formation of ozone as most important active species, but also peroxy radicals that can lead further to formation of other oxidants and superoxide radicals which can hydrolyze to final products. It was concluded that ozone and hydroxyl radicals can affect the carboxyl group of the quinolone part and piperazinyl substituent and oxazinyl substituent.

### 3.2. Perfluorinated compounds

Perfluorinated compounds are wide group of chemicals which are used in many industrial applications, as surfactants in non-stick cookware, packaging, textiles, firefighting foams production etc. Their characteristic C–F bonds are one of the strongest known bonds which makes those compounds environmentally persistent. In recent years, per- and polyfluoroalkyl substances (PFAS) had become of growing concern, especially long-chained compounds, such as perfluorooctanoic acid (PFOA) and perfluorooctane sulfonate (PFOS) due to their recalcitrant behavior (Lindstrom et al., 2011). In 2009, PFOS was listed as a Persistent Organic Pollutant (POP) in Stockholm Convention and by the United States Environmental Protection Agency (USEPA) PFOA listed as possible carcinogenic compound (Council, 2020; OECD, 2018; US EPA,

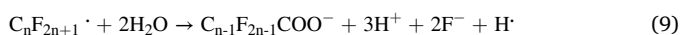
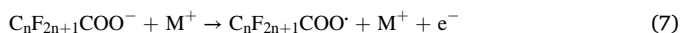
2016). Under the EU Water Framework Directive (2015/495 & 2015, 2015) PFOS and its derivatives are included as a priority hazardous substances with Environmental Quality Standard (AA-EQS) limit value of 0.65 ng/L in inland surface waters and 0.13 ng/L in seawater (ECHA, 2013; European Commission, 2000; Stockholm, 2019; UNEP, 2009). Therefore, global production of PFOA and PFOS started to be restricted or banned while new substances, as substitutes, were developed. In terms of wastewater treatment processes, many studies and practice had shown that most PFAS are highly recalcitrant to conventional wastewater treatment, but also to many AOPs. In the review paper by (Nzeribe et al., 2019) several physico-chemical processes, such as electrochemical oxidation, ultrasonication, plasma-based technology, advanced reduction processes (ARPs) for PFAS degradation have been compared and summarized. In general, the aim of those processes is complete mineralization of the compounds or at least degradation to non-toxic, biodegradable products. As shown, in terms of energy efficiency, treatment time and cost, plasma-based technology showed one of the most promising results and can be suitable for PFAS degradation.

Several authors have reported application of NTP for PFAS degradation. In (Yasuoka et al., 2011) degradation of PFOA and PFOS in solution by DC-plasma generated within gas bubbles was studied, using different gases. In oxygen plasma fluorine concentration after treatment was the highest while with helium plasma was the lowest. With argon plasma bubbles, the energy efficiency was the highest because of larger expansion along inner bubble surface, as authors suggested. Similar configuration was used in (Hayashi et al., 2015) where results showed degradation of PFOA after 3 h of treatment, and 8 h of treatment of PFOS. The evaluation of degradation efficiency was performed by measuring fluorine ions which were part of PFOA and PFOS molecules. Defluorination ratio of 94,5% confirmed almost complete degradation for PFOA. As for the PFOS, ratio of 70% can be explained with the existence of  $\text{SO}_3\text{H}$  sulfo-group which makes PFOS less degradable. (Takeuchi et al., 2014) investigated degradation of PFOA using generated plasma inside oxygen bubbles. Initial concentration of 156  $\mu\text{M}$  of PFOA was degraded after 2.5 h treatment. Also, the authors investigated degradation of PFOA in a mix solution with perfluoroheptanoic acid (PFHpA), another perfluorocarboxylic acids (PFCA). In that case, rate constants decreased to about 80% compared to those in solutions containing single pollutant. Authors also pointed out that PFOA molecules behave differently in liquid-phase reactions then at the gas-liquid interface due to their surfactant characteristics which affects their degradation (Nozomi Takeuchi et al., 2011). (Stratton et al., 2017) applied laminar plasma jet with bubbling reactor which was used for degradation of PFOA and PFOS in solutions and in groundwater samples. PFOA was removed by 90% in a 30-min plasma treatment with 76.5 W input power in high removal rate process. With input power of 4.1 W up to 25% of the pollutant was removed (high removal efficiency process). For the treatment of groundwater, the high removal efficiency process was used. Groundwater contained PFOA and several co-contaminants, such as PFOS, perfluorohexane sulfonate (PFHxS) and some non-fluorinated co-contaminants, trichloroethene and tetrachloroethene. To compare degradation efficiency results between the samples, the same process was used for treatment of prepared solution without other non-fluorinated co-contaminants and PFHxS. Degradation of PFOA had similar rate in both cases (within 2.5%) which can prove that there is no significant effect of other non-PFAS co-contaminants for PFOA degradation.

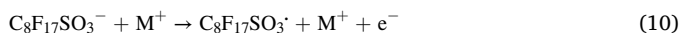
Possible degradation pathways for PFAS in a plasma-based water treatment have been proposed by several papers (Hayashi et al., 2015; Singh et al., 2019; Stratton et al., 2017; Takeuchi et al., 2014; Yasuoka et al., 2010). (Takeuchi et al., 2014) suggested the following degradation pathway: PFAS can adsorb on the gas-liquid interface since they have surfactant characteristics. Then, the C–C bond may break because of the interaction with electrons and ions but also as a result of a direct thermal degradation. Generated fluorocarbon radicals that are located in the bubbles may reduce and oxidize to H and O radicals, HF,  $\text{CO}_2$  and

CO gases. The authors indicated that there is more than one possible parallel pathway during degradation of PFAS, therefore, it is difficult to choose the exact degradation mechanism.

Decomposition of PFOA and PFOS was also investigated by (Hayashi et al., 2015). In the degradation process of PFOA, the by-products which are detected and measured were PFCAs ( $C_nF_{2n+1}COOH$ ,  $n = 1$  to 6) with carboxyl group (COOH) like PFOA. Reaction formulas were suggested (Eqs. (7)–(9)) where  $M^+$  stands for ions with the highest energy in the plasma (Hayashi et al., 2015).



The hypothesis is that the PFCA are present as negative ions on the surface, and they can collide with ions with the highest energy. Similar by-products may occur after degradation of PFOS in the treatment, but since PFOS has a sulfo-group ( $SO_3H$ ), it is less likely decomposed than PFOA. Also, the formation of PFOA as a by-product of PFOS is possible by reactions (Eqs.(10)–(12)) (Hayashi et al., 2015).



In the study by (Yasuoka et al., 2010) it was reported that the decomposition of PFOA/PFOS may be significantly affected by the applied voltage polarity at the discharge electrode(s) in case of all working gases. Since PFOA/PFOS is an anion in the solution, concentrated close to bubble-water interface, in case of applied positive voltage to the powered electrode, it may react with some positive plasma species which come near the surface ( $M^+$ ). Reactions involving these species were proposed (Yasuoka et al., 2010). The ionized PFOS molecules reacts with  $M^+$  which leads to formed shorter carbon chains than PFOS and fluoride and sulfate ions are generated. The PFOA reacts in similar way as PFOS where fluorinated radical reacts with  $H_2O$  yielding shorter-chain PFCA. Fluoride ions and carbon dioxide can be generated during PFCA degradation. Contrarily, if negative voltage is applied to

the powered electrode, generation of oxygen and hydrogen occurs in the gas phase which may influence decomposition. Moreover, in this paper it was concluded that hydrated electrons are not significant for PFAS degradation. However, in the paper by (Stratton et al., 2017) where PFOA/PFOS degradation was studied, the hydrated electrons were reported as an important species in addition to argon ions and high-energy free electrons produced in the plasma. In this investigation, the shorter-chain by-products were quantified: PFHpA, perfluorohexanoic acid (PFHxA) and perfluoropentanoic acid (PFpNA). Although by-products were identified, it was shown that up to 10% of PFOA and PFOS is converted into shorter-chain PFAAs. Experiments with scavenger showed that hydroxyl and superoxide radicals play no significant role. Several by-products in plasma-based PFOA/PFOS solution treatments were also quantified by (Singh et al., 2019). PFOA, PFHxA and perfluorobutane sulfonate (PFBS) were found as by-products from PFOS degradation. Also, some fluoride ions, inorganic carbon, and smaller organic acids (trifluoroacetic acid, acetic acid, and formic acid) were identified with significant concentrations. The short chain PFCAs were detected as well, which suggests that some step-wise reduction of the parent compounds has occurred. Concentrations of all by-products increased in the first 60 min of treatment but by the end of experiment decreased. The authors suggested that the main species responsible for PFAS degradation are electrons from plasma/gas phase, aqueous electrons, and argon ions. Fig. 2 from study shows proposed pathway for PFOA and PFOS degradation.

### 3.3. Pesticides

Pesticides are group of chemicals that are applied on the crops and soil against pest species. The huge variety of herbicides and insecticides are used worldwide in high quantities which makes them a group of contaminants with the highest potential to enter the environment. Recent studies have shown the potential of using NTP in liquid and gas-liquid environment for the remediation of pesticide manufacturing wastewater.

Plasma systems used in published studies for the pesticide removal are different types NTP, either discharges directly inside liquid or discharges in contact with liquid. Regarding the type of discharge, in most cases pulsed corona discharge and DBD with falling water film are used,

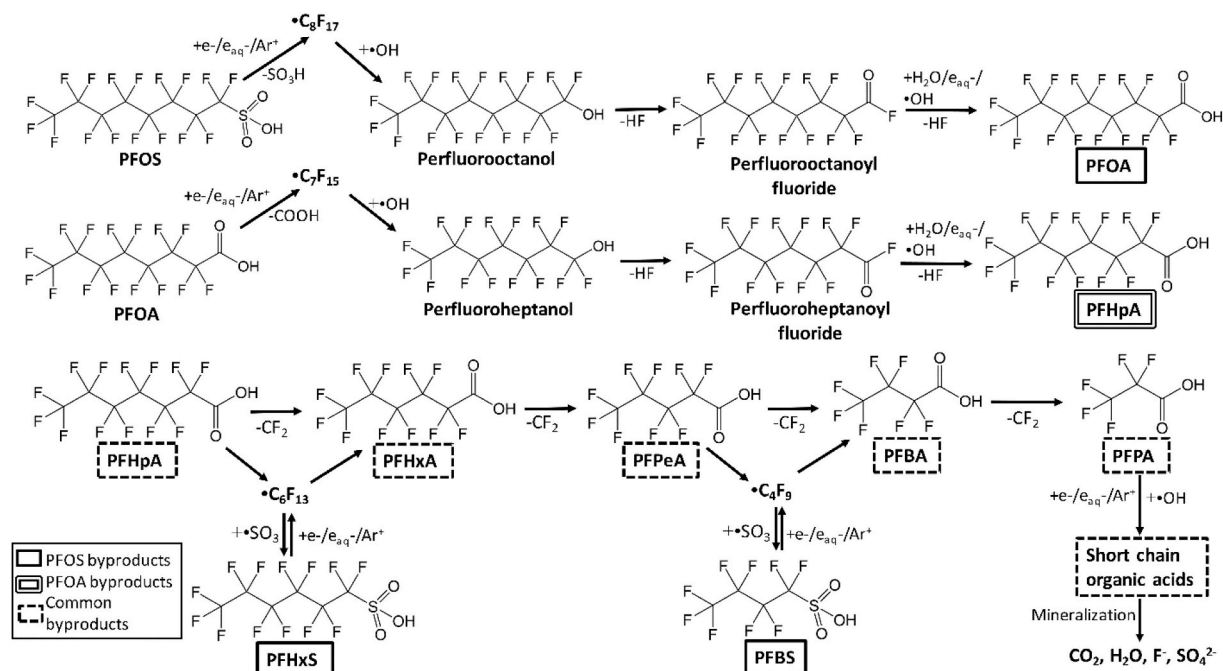


Fig. 2. Proposed pathway for PFOA and PFOS degradation Reprinted with permission from (Singh et al., 2019). Copyright (2019) American Chemical Society.

some of them in combination with another AOPs (e.g., ozonation).

(Hijosa-Valsero et al., 2013) reported two different NTP reactors at atmospheric pressure, one operating as a thin-falling water film reactor and the other as conventional batch reactor, both producing discharge between dielectric barriers. The study compared degradation efficiencies for several pesticides: atrazine, lindane and chlorfenvinfos. For both reactors a first order degradation kinetics was proposed for all reactions. It was calculated that achieved relative removal rates for all pollutants in both reactors were around 70% after 5 min of treatment. In comparison to the batch DBD reactor above the liquid, energy efficiency (G-values, expressed in  $\text{mol J}^{-1}$ ) were higher by one order of magnitude. That can be explained with the fact that in the coaxial reactor the electrode surface is larger allowing higher concomitantly treated volume of the sample. Similar configurations were reported in other studies (Hama Aziz et al., 2018; Vanraes et al., 2017; Wardenier et al., 2019). (Vanraes et al., 2017) utilized a DBD reactor system with addition of activated carbon textile over the grounded inner electrode which caused better removal of all the pollutants. Indeed, depending on the molecular structure of a pollutant, plasma treatment can improve process of its degradation through adsorption. A DBD reactor with falling water film over activated carbon textile was also studied by (Wardenier et al., 2019) for the degradation of pesticide mixture (atrazine, alachlor, diuron, dichlorvos and pentachlorophenol) where removal efficiencies between 57 and 88% were reported (56.9% atrazine, 57.8% alachlor, 62.4% diuron, 69.3% pentachlorophenol, 70.2% dichlorvos). Many of the studies for the pesticide removal were performed by using one of the simplest plasma configurations - pulsed corona discharge above water (Bradu et al., 2017; Gerrity et al., 2010; Singh et al., 2016, 2017; Singh et al., 2019). In a multiple needle-to-plane corona discharge reactor degradation of carbofuran from aqueous solution has been tested. Almost complete degradation occurred within 10 min of treatment and

the degradation rate could be enhanced by increasing voltage and frequency (Singh et al., 2016). Similar configuration was reported in another study by (Singh et al., 2017) for the almost complete mineralization of 2,4-dichlorophenoxyacetic acid (2,4-D). For the same OMP (Bradu et al., 2017) generated NTP in a pulsed corona discharge combined with ozonation process. In this work, complete mineralization of 2,4-D after 30 min of treatment was demonstrated. Although the plasma treatment with corona discharge configurations have showed promising results, all of them worked with small treatment volume and in configurations where large-volume to plasma surface ratio have been preferred. However, a possible pilot-scale NTP device, with corona discharge in ambient air placed above the liquid surface was evaluated by (Gerrity et al., 2010). Experiments were conducted in different types of solution (wastewater and surface water). Promising removal efficiency was found for each type of water solution. Even though based on the results the oxidation is probably the dominant mechanism, more future studies are needed in the field of NTP for wastewater treatment applications with real samples type solution.

Several studies had proposed degradation pathways since the cognition of the mechanism and detection of intermediates is important step for pesticides plasma treatment optimization and practical applications. (Vanraes et al., 2015) detected ammelide and deethylatrazine as by-products in the degradation process of atrazine by a DBD in contact with liquid. The same intermediates were also reported by (Hijosa-Valsero et al., 2013). According to the literature, the main species responsible for the degradation of atrazine is hydroxyl radical and for plasma treatments this was confirmed in (Locke and Thagard, 2012). In some recent papers, decomposition mechanisms were also proposed for pesticide 2,4-D, common used herbicide in agriculture (Bradu et al., 2017; Hama Aziz et al., 2018; Singh et al., 2017). In (Singh et al., 2017) the by-products were identified and several possible routes of breaking

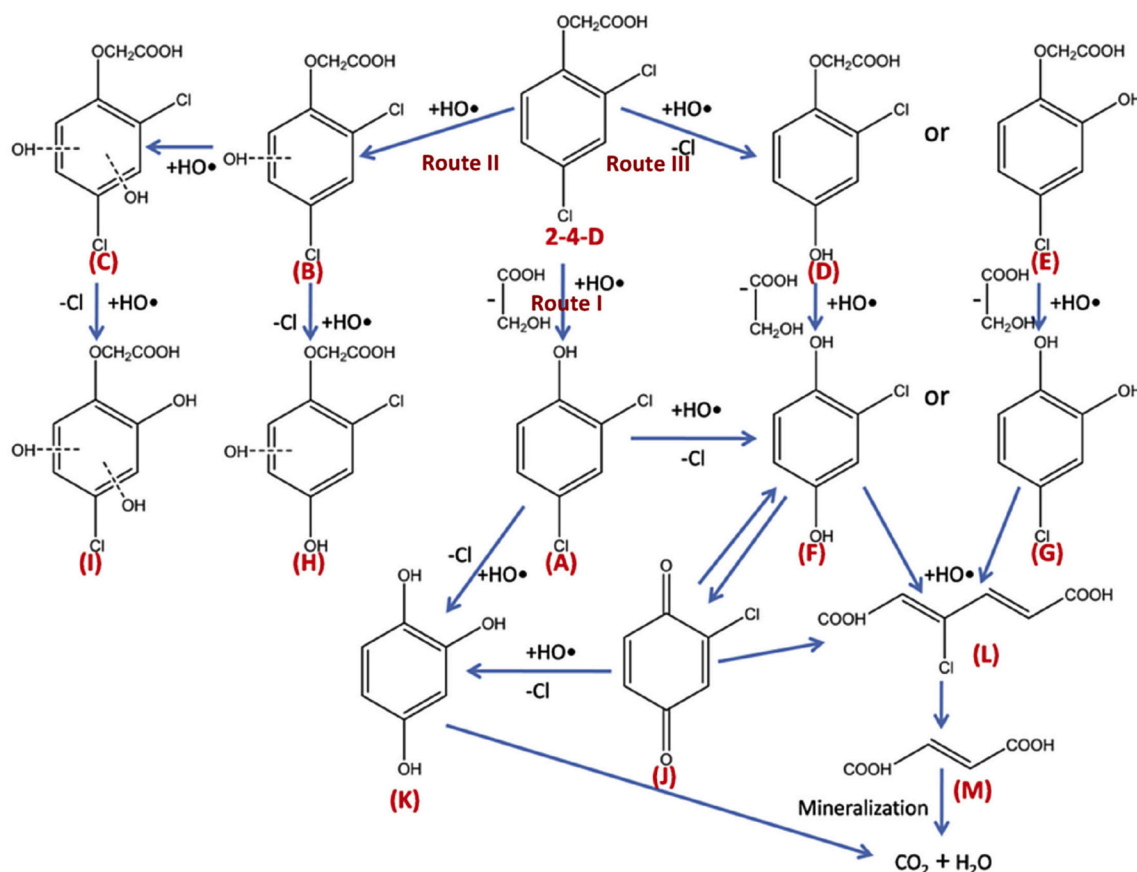


Fig. 3. Degradation pathway of 2,4-D during plasma treatment. Reprinted with permission from (Singh et al., 2017) Copyright (2017) American Chemical Society.

C–O bond on the benzene ring were described (Fig. 3). Their conclusion again was that the main radical responsible for the degradation of the parent compound is  $\cdot\text{OH}$ . The pathways were later confirmed by (Hama Aziz et al., 2018).

In similar conditions, degradation of carbofuran was reported where seven intermediates were identified and reductive/oxidative pathways were proposed (Singh et al., 2016).

### 3.4. Phenols

Most common used models for comparing and testing plasma-based AOP are phenol and its derivatives (e.g. bisphenol A, nitrophenols, chlorophenols, hydroxyphenols). This group of chemicals are known to be used in many industrial applications as pesticides, disinfectants, antioxidants, etc. Their presence in ground, surface and drinking water has been of great concern due to the toxicity and estrogenic nature. As for the properties and oxidation pathways, they have been studied and well described in previous studies, but because of their very low biodegradability they still represent a challenge and more investigations of novel technologies for the improved removal of phenol and phenolic compounds are needed. According to the regulations of European Union Directives (2006/11/EC, 2013, 2008/105/EC, 2013), maximum allowable concentrations of phenols are 2,0  $\mu\text{g/L}$  in inland surface waters and 0,3  $\mu\text{g/L}$  for other surface waters.

In (Marotta et al., 2011) the degradation of phenol was investigated by application of DBD in air or in pure oxygen plasma above the liquid. The results showed that with the decreasing the air flow rate of phenol decomposition increases. The authors concluded that for phenol decomposition the most responsible are reactive species produced in the gas phase and then transferred into the solution. So, contact time between phenols and reactive species is of great importance since they have short lifetime. Regarding the influence of the electrode material on the treatment process, results has shown that after 4 h treatment, the decomposition rate of phenol is about 3.2 times larger with stainless steel than Ni/Cr wires. The same experimental plasma configuration has been applied in (Marotta et al., 2012), where degradation rates of phenol in tap water and deionized water have been compared. The results shown significant increase of the degradation rate of phenol in tap water when compared to the one in deionized water. The authors suggested that possible reason is due to the specific effects of some other chemical species which can be found in tap water solution. Authors also investigated effects of the pH, bicarbonate ions, chlorine species, iron ions, etc. in the water on phenol degradation.

Bicarbonate ions had shown a positive effect on the degradation of phenols since they behave as a buffer and keep the pH of the solution around 7 during the plasma treatment. (Ceriani et al., 2018), is one of the first studies which reported complete mineralization of phenol, including mineralization of produced intermediates. It was found that after 30 min of treatment, phenol was completely removed, while mineralization of solution was achieved after 4 h. In another experiment, with different initial concentration, after 5.5 h complete mineralization was achieved. These results had shown that the initial concentration of OMP has effect on the degradation rate. On the other side, an electrical discharge generated directly inside water, based on a DC diaphragm discharge excited in a vapor bubble, was applied in (Lukes et al., 2013). About 50% degradation of phenol in  $\text{NaH}_2\text{PO}_4$  solution after 50 min was achieved. Authors suggested that hydroxyl radicals formed by plasma led to the production of hydroxylated phenol products. Thus, hydroxyl radicals were found to be the main active components for the oxidation of phenol.

(Hijosa-Valsero et al., 2013) reported the degradation of 2,4 – dibromophenol in two different plasma reactors, one as a conventional batch (R1) reactor and other one as a coaxial thin-falling water film (R2), with a helium as a working gas. It was reported that relative degradation rate was around 98% in R1 after 5 min of treatment. Also, the kinetic constant ( $0.802 \text{ min}^{-1}$ ) was slightly faster in R1 and

first-order degradation kinetics was proposed. (Hama Aziz et al., 2018) evaluated degradation of 2,4 – dichlorophenol (2,4 – DCP) in DBD planar falling water film reactor. In the study, comparable studies with ozonation and photocatalysis had also been reported. The authors concluded that in pure argon, after 15 min, complete degradation of 2,4 – DCP occurred in aqueous solution. The main reason is that hydrogen peroxide was produced under argon atmosphere in deionized water solution of 2,4 – DCP and high concentration of generated  $\cdot\text{OH}$  radical. Several other papers (Banaschik et al., 2015; Chen et al., 2019; Iervolino et al., 2019) had also reported phenol degradation during plasma treatment and they evaluate the degradation effects depending on different types of discharge, working gas and the plasma reactor setup.

Several studies discussed possible mechanisms and pathways of the phenol and phenolic compounds degradation. In (Banaschik et al., 2015) high concentration of hydrogen peroxide was detected indicating that the production of hydroxyl radicals was significant. According to the authors, in Fig. 4 possible degradation mechanism of phenol can be shown (Banaschik et al., 2015).

Few phenol intermediates, such as benzoquinone (BQ), hydroxybenzoquinone (HBQ), catechol (CC) and hydroquinone (HQ) were detected. Results also shown that there is no trace of muconic acid or nitrated products of phenol. With that, it can be concluded that the ozone concentration was very low or absent. As for the intermediate, hydroxyhydroquinone (HHQ), the reaction product, HBQ was found, but not the HHQ himself. In (Lukes et al., 2013) phenol intermediates HQ, BQ, CC and HBQ were also detected. As for the other phenol products, the authors concluded that since in the diaphragm discharge was a present thermal mechanism it is possible that thermal decomposition occurred together with oxidative decomposition. (Ceriani et al., 2018) reported hydroxyl radical and ozone as the reactive species for the phenol degradation in miliQ water and formation of the intermediates: maleic acid, fumaric acid, *cis*, *cis*- and *trans*, *trans*- muconic acids, 1,2 – dihydroxybenzene, 1,4 – dihydroxybenzen, formic acid, acetic acid, oxalic acid. For all the intermediates, except maleic acid, it was found that they are no longer detected after 4 h of plasma treatment. The results had shown that the concentration of formic and oxalic acids was increasing during the treatment while acetic acid reached  $2.5 \times 10^{-5} \text{ M}$  concentration and remained stable during 4 h treatment. In (Chen et al., 2019) phenol and *p*-nitrophenol (PNP) were analyzed by both HPLC and UV-VIS quantitative methods for different concentrations and different treatment times. With the increasing time, results had shown that concentrations of phenol and PNP decreased and decomposed into other intermediates under the influence of atmospheric pressure plasma jets (APPJs) in deionized water solution. Because of the presence of gas-liquid interfaces and the bubble motions, active species have been able to interact more with the phenol and PNP molecules. The degradation efficiency can also be enhanced by changing the pH value, according to the authors. There was no detailed study related to the degradation pathways, but the authors suggested the main reactions for both plasma configurations: inside and in contact with water. The analysis of the 2,4-DCP was performed after plasma treatment by high performance liquid chromatography (HPLC) in (Hama Aziz et al., 2018). It was found that chloride ion and other low chain anionic by-products occurred during the degradation process. Other by-products were identified such as oxalic acid, glyoxylic acid and glycolic acid. In most cases, the concentrations of the formed by-products increased during the beginning of degradation, but then decreased over time of the treatment, except oxalate ion which remain as a by-product even after completing the treatment.

### 3.5. Dyes

Dyes are OMP mainly used in textile industry, paper, plastic, and leather industry. The discharge of the dyes has been considered as great problem since most of these compounds show high resistance to the conventional wastewater treatment processes. Also, their toxicity and

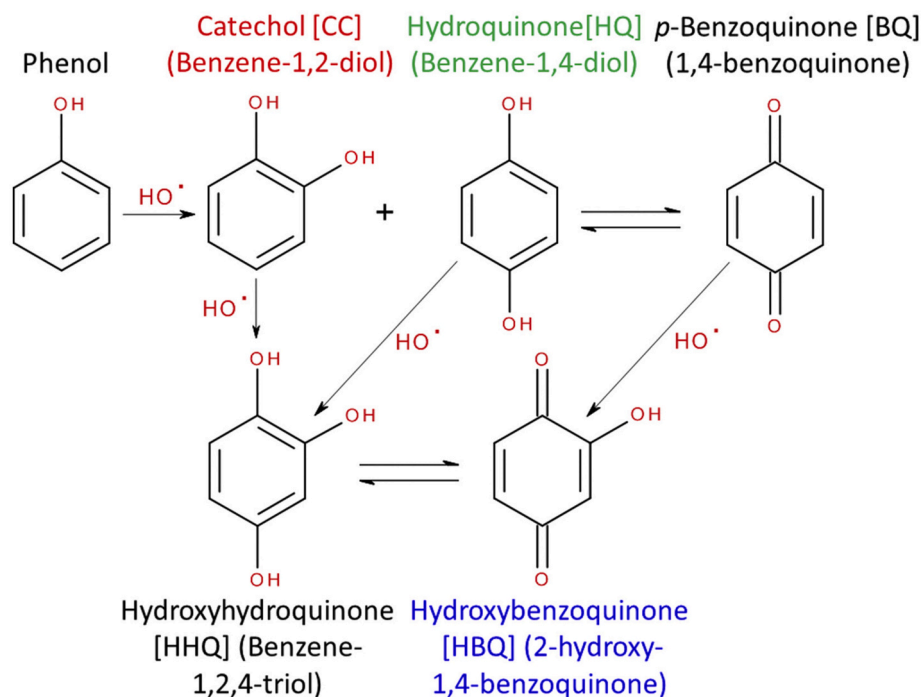


Fig. 4. Possible reaction pathways of phenol with hydroxyl radicals. Reprinted with permission from (Banaschik et al., 2015). Copyright (2015) Elsevier.

potential carcinogenicity raise concern for the aquatic ecosystem. Therefore, development of an effective wastewater treatment process for dye elimination had been in the focus of interest of many researchers. Recently, several plasma systems using different type of working gas (argon, air, oxygen) have been evaluated: DBD discharge with cylindrical configuration (He et al., 2018; Iervolino et al., 2019), pin to surface configuration (Kasih et al., 2019; Mitrović et al., 2020), flow reactor system (Yamada et al., 2020), corona discharge (Ruma et al., 2013), parallel plane type DBD reactor (Reddy and Subrahmanyam, 2012).

The degradation of methylene blue (MB) in a pulsed corona discharge, generated above the liquid surface in multiwire-plate was investigated by (Monica Magureanu et al., 2013). After about 10 min of plasma treatment, the MB solution decolorized rapidly and the formation of nitrate, formate, sulfate, and chlorine ions have been detected. Also, a colorimetric method was used to determine the presence of  $\text{H}_2\text{O}_2$ , main active species for the degradation of MB. It was found that during plasma exposure, concentration of  $\text{H}_2\text{O}_2$  increased after 30 min treatment. Also, the presence of the  $\text{NO}_3^-$  was detected, which can be prescribed to the air admixture and dissolved in water as the authors suggested since the oxygen was used as a working gas. The same compound was also investigated by (Kasih et al., 2019) and (Yamada et al., 2020). A pin to surface configuration plasma system at atmospheric pressure was used for decolorization of MB in water solution. After 120 min, decolorization efficiency was around 93%. In (Yamada et al., 2020), based on the results, decolorization efficiency of MB was around 90%. The experiments were performed using a gas-liquid pulsed discharge plasma with oxygen and argon as working gases. The concentrations of the active species were not tested but the results suggested that in the MB decolorization process, oxygen-based active species and  $\cdot\text{OH}$  radicals were involved, especially in the case of argon gas. (Liu et al., 2016) suggested using atmospheric pressure DBD plasma system for the degradation of methyl orange (MO). The aim of this study was to evaluate new treatment method with glow discharge generated above the water surface. After 15 min, decolorization rate was 93%. In (He et al., 2018), experiments were performed in the cylinder-like reactor, with a home-made direct current power source. It was concluded that the active species responsible for decolorization of MO are the

short-lived ones instead of long-lived species such as  $\text{H}_2\text{O}_2$ . Nevertheless, the presence of  $\text{H}_2\text{O}_2$  can affect the production of  $\cdot\text{OH}$  radicals when in combination with Fenton process ( $\text{Fe}_2^+$  ions). Several other authors evaluated different plasma configurations for dyes removal and up to this date, most of them concluded that the best efficiency is usually achieved when oxygen is used as a working gas. The details can be found in the reports (Iervolino et al., 2019; Jiang et al., 2012; Mitrović et al., 2020; Pankaj et al., 2017; Reddy and Subrahmanyam, 2012; Ruma et al., 2013; Sarangapani et al., 2017).

(Jiang et al., 2012) evaluated degradation mechanism for the decomposition of methyl orange and degradation efficiency depending on different initial concentrations. It was found that increasing initial concentration of MO decoloration efficiency ( $\eta$ ) decreased through time. The authors suggested possible degradation pathway for the MO shown in Fig. 5.

Based on the dissociation energies (BDEs), authors suggested that the C–N–C bond BDE is the lowest and therefore breaking that bond results with two demethylation reactions which are the first ones taking place in plasma treatment. As for the C–N bond in the intermediate group ( $\text{C}_6\text{H}_5\text{--N}_2\text{C}_6\text{H}_5$ ), the cleavage effect occurs because of the presence of the high reactive oxygen species,  $\text{O}_3$  and  $\cdot\text{OH}$  radical which are produced in a gas phase of the discharge. The authors also found the presence of  $\text{SO}_4^{2-}$  ions and  $\text{NO}_3^-$  which can be explained with possible mineralization of MO and the intermediates, into  $\text{CO}_2$ ,  $\text{H}_2\text{O}$ ,  $\text{SO}_4^{2-}$  and  $\text{NO}_3^-$ . Monica Magureanu et al. (2013) detected formic acid as an intermediate during MB plasma treatment. It is possible that the formation of acid resulted as a side chain oxidation. Also, small amounts of sulfate ( $\text{SO}_4^{2-}$ ) were found. As in previous work, authors concluded a cleavage effect of the C–S bond in heterocyclic system. The generation of  $\text{H}_2\text{O}_2$  has also been studied as important compound for the formation of  $\cdot\text{OH}$  radicals. Comparing the concentration of  $\text{H}_2\text{O}_2$  generated in water and in the MB solution through time, it was founded that higher concentration of  $\text{H}_2\text{O}_2$  was generated in water. This can be related to the reactions between MB compound and its by-products with  $\cdot\text{OH}$  radicals, influencing the less formation of  $\text{H}_2\text{O}_2$ . Kasih et al. (2019) analyzed formation of MB functional groups through FTIR analysis. Some important MB functional groups were detected: NH/OH (overlapped vibration at  $3417\text{ cm}^{-1}$ ), –CH– (aromatic group at  $2889\text{ cm}^{-1}$ ), C–N (from amid II, at  $1456\text{ cm}^{-1}$ ),

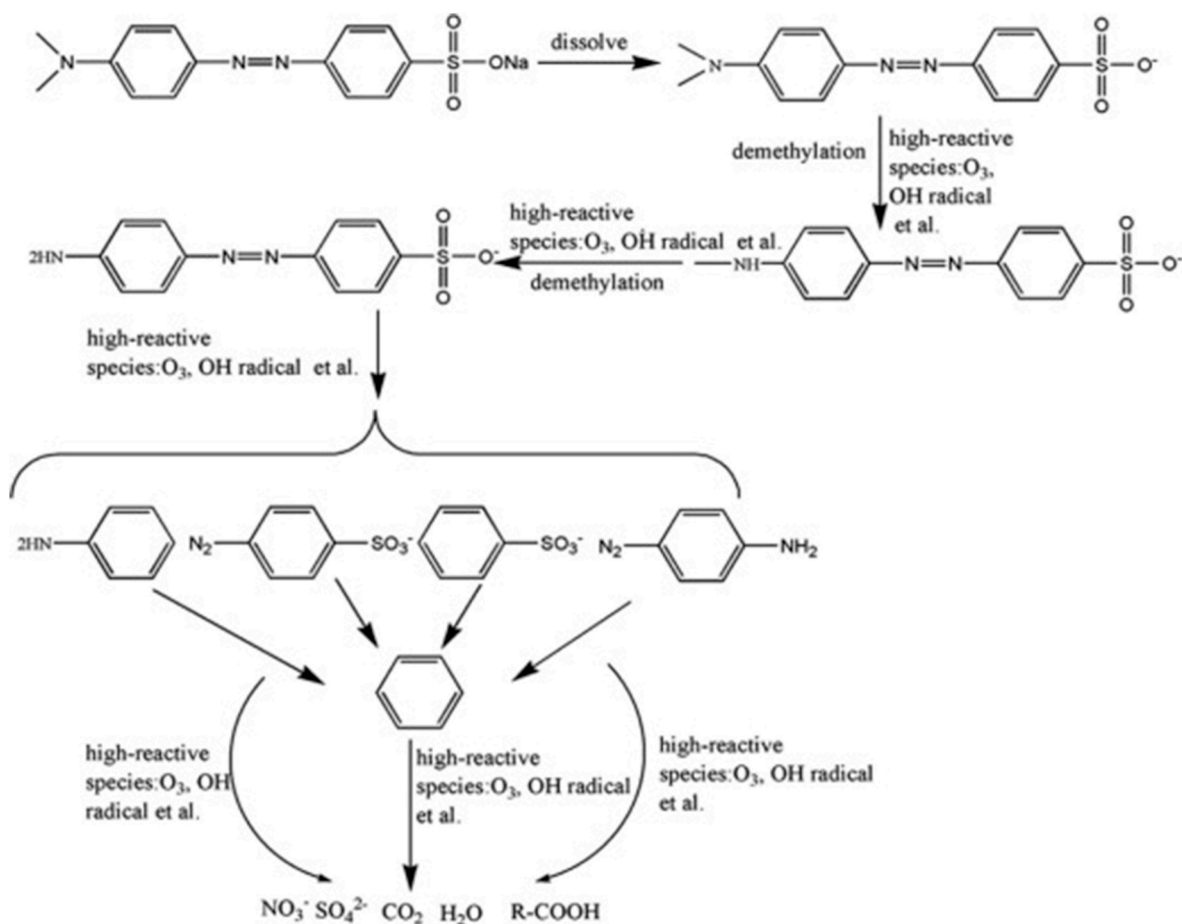


Fig. 5. Proposed pathways for the degradation of MO using non-thermal plasma. Reprinted with permission from (Jiang et al., 2012). Copyright (2012) Elsevier.

N–H (from amide III,  $1112\text{ cm}^{-1}$ ), C–N (from amide III,  $852\text{ cm}^{-1}$ ). From the spectrum, it can be seen that after 20 min of plasma treatment, a broad band in the range of  $3000\text{--}3700\text{ cm}^{-1}$  appears that can represent O–H stretching and a strong peak at  $1643\text{ cm}^{-1}$  as O–H–O bending scissors. The authors concluded that the high removal of 93% resulted after 120 min treatment.

Formation of reactive species during plasma treatment has been more investigated in some studies providing possible reaction sets for different working gases used (He et al., 2018; Jiang et al., 2012; Reddy and Subrahmanyam, 2012; Yamada et al., 2020). When in plasma system the oxygen was used as a working gas, as a result, there is a large generation of ozone. With dissociation of  $H_2O$ ,  $H_2O_2$  can be produced. Both ozone and  $H_2O_2$  can be consumed for organic degradation. OH, H, O $\cdot$  and  $HO_2\cdot$  radicals can be generated from various gases.  $\cdot OH$  radicals can also be derived from  $H_2O$  molecules which have been confirmed and evaluated by several authors as an important active species for the degradation (decolorization) of dyes.

#### 4. Combining plasma technology and other advanced treatments

Several studies report application of NTP in a combination with other treatments. For example, (Mitrović et al., 2020), combined NTP with titanium dioxide ( $TiO_2$ ) catalyst for the Reactive orange 16 (RO 16) dye degradation. The authors investigated the processes separately and in combination to compare energy efficiency of all systems. As a result, when NTP is enhanced with  $TiO_2$  nanopowders, the degradation efficiency has improved since in the process the radicals are generated in the gas phase by the plasma and transported into the liquid, but also in the liquid on the surface of the catalyst. The influence of different flow

rates and gas composition was also evaluated. In (Hama Aziz et al., 2017), ozonation, photocatalysis and DBD were compared for DCF and IBP in aqueous solution. The same reactor design was used in all experiments which allowed more valid comparison of the efficiency. For both pharmaceuticals, after DBD treatment, removal efficiency was higher than when treated with other methods, but also important note is that the degradation depended on the type of gas during treatment. Overall, the combination of two AOPs showed the most promising results. Similar conclusions were reported in (Hama Aziz et al., 2018) for pesticides. Other interesting reports can be found in (Vanraes et al., 2015), where degradation of atrazine was investigated by combination of NTP and nanofiber membrane and in (Vanraes et al., 2017), where NTP was combined with activated carbon. In both reports, results had shown that decomposition of atrazine was higher when NTP was used. Very detailed evaluation of physico-chemical processes for the PFAS treatment can be found in (Nzeribe et al., 2019). The authors investigated and compared efficiency such as cost, energy use, removal and proposed possible degradation pathway for several types of chemical oxidation and chemical reduction processes, ultrasonication and plasma technology. In general, as a proposed conclusion is that technologies which include persulfate and photochemical oxidation are less efficient than electrochemical oxidation technology. Based on the defluorination yield, energy use and cost, plasma treatment is one of the most efficient process for the PFAS treatment.

#### 5. Outlook/conclusion

This paper gives a broad review on degradation mechanisms, pathways, removal efficiency of treatments by NTP for several groups of OMPs as well as the effects of different parameters on the degradation

processes of pharmaceuticals, perfluorinated compounds, pesticides, phenols and phenolic compounds and dyes. For those OMPs which are known to be recalcitrant and difficult to remove with other types of AOP and conventional treatment, successful removal, and degradation up to 95% has been demonstrated with application of different types of discharges. In majority of cases plasma is generated in the air or other working gas or gas mixture above the liquid sample surface with the reactive species transferred from the gaseous to the liquid phase. Plasma sources used in these kinds of setups are different DBD geometries: coaxial, parallel plate, or thin falling water film, then (multi) pin-to-plane corona and streamer discharges operating mostly in pulsed mode. In fewer cases, the discharge is formed directly inside the liquid phase usually using pulsed power supplies. In some studies authors employed recirculation of the sample and showed that this results in enhancement of the decontamination in all cases. Most studies are done by studying an individual OMP present in the aqueous solution or, in some cases, in a synthetic mix solution with few other contaminants. It should be pointed out that these types of experimental set-ups are useful to study interaction between plasma-generated reactive species inside the liquid and pollutant molecules to better understand the degradation mechanisms for each contaminant. Once the mechanisms are identified, one can perceive the possibility of employment of the plasma technology for an efficient treatment of certain type of compound to be treated in polluted water. However, at this point little is known on how OMPs behave in real (waste)water samples when plasma is applied and what degradation pathways they would follow. As it can be seen from the review of the studies, depending on the type of OMP in water, different radical can play important role on its degradation. However, with other co-contaminants present in the water, the mechanism of the target OMP degradation can change easily since there is possibility that one or more of those co-contaminants have scavenger affect towards the radicals. An example for this is mixture of few different EC (pharmaceuticals and pesticides) in river water where presence of carbonates and bicarbonates, known as scavengers of  $\cdot\text{OH}$  radicals, decreased degradation rate of EC. The results of most of the studies involving one or several contaminants had shown promising removal efficiency and even mineralization in some cases. Nevertheless, since most dominant reaction mechanisms are shown in “the best case” scenario, i.e. without the influence of co-contaminants, more research is needed with realistic samples of wastewater treated by plasma in order to apprehend the complete potential of the plasma technology. Because of this research gaps, further studies are recommended: (i) at laboratory scale – experiments using matrix solutions and real wastewater to understand optimal conditions and to elucidate degradation mechanisms for such complex matrix, (ii) at pilot scale – experiments using real matrix to investigate how to scale-up parameters for optimal energy/economic costs. According to the literature, most of the studies have been performed at laboratory scale and in such systems high degradation rates have been achieved. However, future studies should be also focused on the investigation of possibilities to scale-up the plasma systems and make application of the plasma technology at water volumes that are  $10^4$ – $10^6$  times higher than existing. Among other treatment parameters, this also affects the treatment duration; thus, the scaling-up of the systems should comprehend the changes in all related parameters. That is not a straightforward task and even though at laboratory scale plasma treatment showed numerous advantages compared to other AOP – such as no use of chemical reagents and better output of cost-efficiency, these assets should be also demonstrated at a large-scale in order to move the scientific advances towards new technology.

Moreover, the next important step in plasma degradation studies is further investigation degradation mechanisms and by-products formed both in the liquid phase and gas phase. In this research phase, it is very difficult to give proper general degradation mechanism for the organics due to the variations in given results by the research done up to this date. Possible degradation mechanisms and proper conclusions can be done per group of OMPs. Still, in some group of OMPs, those mechanisms can

change based on the type of compound and working parameters, for example, by using different type of working gases, it is possible that different types of reactive species are produced, and possible reaction pathways can be changed. Therefore, the study of by-products is important. In recent years many new protocols have been reported for detection of those by-products after the AOP treatment and degradation of a parent compound. While some authors have investigated and studied the formation of by-products, but only few have evaluated and discussed the toxicity of those compounds. In some cases, they prove to be even more toxic and not biodegradable, for example PFAS. Therefore, this is an important step that should be investigated along with the decontamination process. Having said that, one possible way to resolve this issue is to focus the future studies towards reaching possible mineralization of treated compounds in plasma systems, especially for compounds where currently there is lack of findings of complete degradation and/or mineralization.

In terms of comparison between plasma and other AOPs, few studies were reported. Since the degradation efficiency depends on experimental conditions, i.e., many different treatment parameters (volume, initial concentration, characteristics of solution, reactor type, gas type, etc.), general comparison of this type is very difficult to obtain, and direct comparisons have been obtained only for specific cases. To have the reliable results for comparison, the combination of experimental conditions should be the same for all types of AOPs. Nevertheless, it was clearly shown when NTP is combined with other AOPs, better removal efficiency can be achieved, with reduced treatment time. Considering the necessity for scaling-up the plasma decontamination systems, combining plasma with another AOP seems a promising option to achieve large-scale reactors.

#### Author contribution statement

**Barbara Topolovec:** Conceptualization, Investigation, Resources, Writing – original draft, Visualization. **Nikola Škoro:** Investigation, Resources, Writing– review and editing. **Nevena Puac:** Investigation, resources, Writing–review and editing. **Mira Petrovic:** Validation, Resources, Writing – review and editing, Supervision, Project administration, Funding acquisition.

#### Declaration of competing interest

The authors declare that they have no known competing financial interests or personal relationships that could have appeared to influence the work reported in this paper.

#### Acknowledgements

This work was supported by the European Union’s Horizon 2020 research and innovation programme under the Marie Skłodowska-Curie grant agreement – MSCA-ITN-2018 (grant number 812880). ICRA researchers thank funding from CERCA program.

#### References

- 2006/11/EC, D., 2013. Directive 2006/11/EC of the European parliament and of the council. Off. J. Eur. Union L 64, 52–59, 4 March 2006. [revised Oct 2013].
- 2008/105/EC, D., 2013. Directive 2008/105/EC of the European Parliament and of the Council. Official Journal of the European Union L 348/84, 24 Dec 2008 [revised Oct 2013].
- 2015/495, 2015/2015/495, C. I. D. (Eu), 2015, of 20 M., 2015. COMMISSION IMPLEMENTING DECISION (EU) 2015/495 of 20 March 2015 Establishing a Watch List of Substances for Union-wide Monitoring in the Field of Water Policy Pursuant to Directive 2008/105/EC of the European Parliament and of the Council. Official Journal of the European Union, L78/40(C(2015) 1756), pp. 20–30.
- Akiyama, H., 2000. Streamer discharges in liquids and their applications. IEEE Trans. Dielectr. Electr. Insul. 7, 646–653.
- An, W., Baumung, K., Bluhm, H., 2007. Underwater streamer propagation analyzed from detailed measurements of pressure release. J. Appl. Phys. 101 (5), 53302. <https://doi.org/10.1063/1.2437675>.






- Arnold, K.E., Brown, A.R., Ankley, G.T., Sumpter, J.P., 2014. Medicating the environment: assessing risks of pharmaceuticals to wildlife and ecosystems. *Phil. Trans. Biol. Sci.* 369 (1656), 20130569. <https://doi.org/10.1098/rstb.2013.0569>.
- Banaschik, R., Lukes, P., Jablonowski, H., Hammer, M.U., Weltmann, K.D., Kolb, J.F., 2015. Potential of pulsed corona discharges generated in water for the degradation of persistent pharmaceutical residues. *Water Res.* 84, 127–135. <https://doi.org/10.1016/j.watres.2015.07.018>.
- Becker, K.H., Kogelschatz, U., Schoenbach, K.H., Barker, R.J. (Eds.), 2004. *Non-Equilibrium Air Plasmas at Atmospheric Pressure*. CRC Press. <https://doi.org/10.1201/9781482269123>.
- Bernhardt, E.S., Rosi, E.J., Gessner, M.O., 2017. Synthetic chemicals as agents of global change. *Front. Ecol. Environ.* 15 (2), 84–90. <https://doi.org/10.1002/fee.1450>.
- Boselli, M., Colombo, V., Ghedini, E., Gherardi, M., Laurita, R., Liguori, A., Sanibondi, P., Stancampiano, A., 2014. Schlieren high-speed imaging of a nanosecond pulsed atmospheric pressure non-equilibrium plasma jet. *Plasma Chem. Plasma Process.* 34, 853–869. <https://doi.org/10.1007/s11090-014-9537-1>.
- Bradu, C., Magureanu, M., Parvulescu, V.I., 2017. Degradation of the chlorophenoxyacetic herbicide 2,4-D by plasma-ozonation system. *J. Hazard Mater.* 336, 52–56. <https://doi.org/10.1016/j.jhazmat.2017.04.050>.
- Bruggeman, Peter, Leys, C., 2009. Non-thermal plasmas in and in contact with liquids. *J. Phys. Appl. Phys.* 42 (5), 53001. <https://doi.org/10.1088/0022-3727/42/5/053001>.
- Bruggeman, P., Degroote, J., Vierendeels, J., Leys, C., 2008. DC-excited discharges in vapour bubbles in capillaries. *Plasma Sources Sci. Technol.* 17, 25008.
- Bruggeman, P.J., Kushner, M.J., Locke, B.R., Gardieniers, J.G.E., Graham, W.G., Graves, D.B., Hofman-Caris, R.C.H.M., Maric, D., Reid, J.P., Ceriani, E., Fernandez Rivas, D., Foster, J.E., Garrick, S.C., Gorbanev, Y., Hamaguchi, S., Iza, F., Jablonowski, H., Klimova, E., Kolb, J., et al., 2016. Plasma-liquid interactions: a review and roadmap. *Plasma Sources Sci. Technol.* 25 (5) <https://doi.org/10.1088/0963-0252/25/5/053002>.
- Caballero-Gallardo, K., Olivero-Verbel, J., L Freeman, J., 2016. Toxicogenomics to evaluate endocrine disrupting effects of environmental chemicals using the Zebrafish model. *Curr. Genom.* 17 (6), 515–527. <https://doi.org/10.2174/1389202917666160513105959>.
- Ceccato, P., Guaitella, O., Gloahec, M., Rousseau, A., 2010. Time-resolved nanosecond imaging of the propagation of a corona-like plasma discharge in water at positive applied voltage polarity. *J. Phys. D: Appl. Phys. J. Phys. D: Appl. Phys.* 43(20) <https://doi.org/10.1088/0022-3727/43/17/175202>.
- Ceriani, E., Marotta, E., Shapoval, V., Favaro, G., Paradisi, C., 2018. Complete mineralization of organic pollutants in water by treatment with air non-thermal plasma. *Chem. Eng. J.* 337 (December 2017), 567–575. <https://doi.org/10.1016/j.cej.2017.12.107>.
- Chen, B., Zhu, C., Fei, J., Jiang, Y., Yin, C., Su, W., He, X., Li, Y., Chen, Q., Ren, Q., Chen, Y., 2019. Reaction kinetics of phenols and p-nitrophenols in flowing aerated aqueous solutions generated by a discharge plasma jet. *J. Hazard Mater.* 363, 55–63. <https://doi.org/10.1016/j.jhazmat.2018.09.051>.
- Council, O. F. T. H. E., 2020. Directive 2013/11/EU of the European parliament and of the council. In: *Fundamental Texts on European Private Law*, vol. 2013. Issue July, pp. 1–17. <https://doi.org/10.5040/9781782258674.0032>.
- Dobrin, D., Bradu, C., Magureanu, M., Mandache, N.B., Parvulescu, V.I., 2013. Degradation of diclofenac in water using a pulsed corona discharge. *Chem. Eng. J.* 234, 389–396. <https://doi.org/10.1016/j.cej.2013.08.114>.
- ECHA, 2013. Echa - European chemical agency. Inclusion of substances of very high concern in the candidate list (decision of the European chemicals agency) - document ED/69/2013-SVHC article 57d.June 17, 2013. [https://echa.europa.eu/candidate-list-table?p\\_p\\_id=disslists\\_WAR\\_disslistsportlet&p\\_lifecycle=0&p\\_s\\_state=normal&p\\_mode=view&p\\_col\\_id=column-1&p\\_col\\_pos=2&p\\_col\\_count=3&disslists\\_WAR\\_disslistsportlet\\_keywords=&disslists\\_WAR\\_disslistsportlet\\_or](https://echa.europa.eu/candidate-list-table?p_p_id=disslists_WAR_disslistsportlet&p_lifecycle=0&p_s_state=normal&p_mode=view&p_col_id=column-1&p_col_pos=2&p_col_count=3&disslists_WAR_disslistsportlet_keywords=&disslists_WAR_disslistsportlet_or)
- EEA (European Environment Agency), 2011. Hazardous substances in Europe's fresh and marine waters - news - EEA (Issue 8). <https://doi.org/10.2800/78305>.
- European Commission, 2000. European commission. EU water Framework directive - integrated river basin management in europe. Directive 2000/60/EC. European Commission October 23, 2000. [https://ec.europa.eu/environment/water/water-framework/index\\_en.html](https://ec.europa.eu/environment/water/water-framework/index_en.html).
- Falás, P., Wick, A., Castronovo, S., Habermacher, J., Ternes, T.A., Joss, A., 2016. Tracing the limits of organic micropollutant removal in biological wastewater treatment. *Water Res.* 95, 240–249. <https://doi.org/10.1016/j.watres.2016.03.009>.
- Foster, J., 2017. Plasma-based water purification: challenges and prospects for the future. *Phys. Plasmas* 24, 55501. <https://doi.org/10.1063/1.4977921>.
- Foster, J., Sommers, B., Gucker, S., Blankson, I., Adamovsky, G., 2012. Perspectives on the interaction of plasmas with liquid water for water purification. *Plasma Sci., IEEE Transact. On* 40, 1311–1323. <https://doi.org/10.1109/TPS.2011.2180028>.
- Fridman, G., Friedman, G., Gutsol, A., Shekhter, A.B., Vasilets, V.N., Fridman, A., 2008. Applied plasma medicine. *Plasma Process. Polym.* 5 (6), 503–533. <https://doi.org/10.1002/ppap.200700154>.
- Gerrity, D., Stanford, B.D., Trenholm, R.A., Snyder, S.A., 2010. An evaluation of a pilot-scale nonthermal plasma advanced oxidation process for trace organic compound degradation. *Water Res.* 44 (2), 493–504. <https://doi.org/10.1016/j.watres.2009.09.029>.
- Gershman, S., Mozhina, O., Belkind, A., Becker, K., Kunhardt, E., 2007. Pulsed electrical discharge in bubbled water. *Contrib. Plasma Phys.* 47, 19–25. <https://doi.org/10.1002/ctpp.200710004>.
- Ghime, D., Ghosh, P., 2020. Advanced oxidation processes: a powerful treatment option for the removal of recalcitrant organic compounds. *Advanced Oxidation Processes - Appl., Trends, Prospects* 1–12. <https://doi.org/10.5772/intechopen.90192>.
- Giannakis, S., Gamarrá Vives, F.A., Grandjean, D., Magnet, A., De Alencastro, L.F., Pulgarin, C., 2015. Effect of advanced oxidation processes on the micropollutants and the effluent organic matter contained in municipal wastewater previously treated by three different secondary methods. *Water Res.* 84, 295–306. <https://doi.org/10.1016/j.watres.2015.07.030>.
- Graham, W.G., Stalder, K.R., 2011. Plasmas in liquids and some of their applications in nanoscience. *J. Phys. Appl. Phys.* 44 (17), 174037. <https://doi.org/10.1088/0022-3727/44/17/174037>.
- Gros, M., Petrović, M., Ginebreda, A., Barceló, D., 2010. Removal of pharmaceuticals during wastewater treatment and environmental risk assessment using hazard indexes. *Environ. Int.* 36 (1), 15–26. <https://doi.org/10.1016/j.envint.2009.09.002>.
- Hama Aziz, K.H., Miessner, H., Mueller, S., Kalass, D., Moeller, D., Khorshid, I., Rashid, M.A.M., 2017. Degradation of pharmaceutical diclofenac and ibuprofen in aqueous solution, a direct comparison of ozonation, photocatalysis, and non-thermal plasma. *Chem. Eng. J.* 313, 1033–1041. <https://doi.org/10.1016/j.cej.2016.10.137>.
- Hama Aziz, K.H., Miessner, H., Mueller, S., Mahyar, A., Kalass, D., Moeller, D., Khorshid, I., Rashid, M.A.M., 2018. Comparative study on 2,4-dichlorophenoxyacetic acid and 2,4-dichlorophenol removal from aqueous solutions via ozonation, photocatalysis and non-thermal plasma using a planar falling film reactor. *J. Hazard Mater.* 343, 107–115. <https://doi.org/10.1016/j.jhazmat.2017.09.025>.
- Hayashi, R., Obo, H., Takeuchi, N., Yasuoka, K., 2015. Decomposition of perfluorinated compounds in water by DC plasma within oxygen bubbles. *Electr. Eng. Jpn.* 190 (3), 9–16. <https://doi.org/10.1002/eej.22499>.
- He, B., Gong, X., Wang, X., Li, J., Xiong, Q., Chen, Q., Liu, Q.H., 2018. What are the effective reactants in the plasma-induced wastewater treatment? *J. Electrochem. Soc.* 165 (10), E454–E459. <https://doi.org/10.1149/2.0241810jes>.
- Hijosa-Valsero, M., Molina, R., Schikora, H., Müller, M., Bayona, J.M., 2013. Removal of priority pollutants from water by means of dielectric barrier discharge atmospheric plasma. *J. Hazard Mater.* 262, 664–673. <https://doi.org/10.1016/j.jhazmat.2013.09.022>.
- Hijosa-Valsero, M., Molina, R., Monràs, A., Müller, M., Bayona, J.M., 2014. Decontamination of waterborne chemical pollutants by using atmospheric pressure nonthermal plasma: a review. *Environ. Technol. Rev.* 3 (1), 71–91. <https://doi.org/10.1080/21622515.2014.990935>.
- Iervolino, G., Vaiano, V., Palma, V., 2019. Enhanced removal of water pollutants by dielectric barrier discharge non-thermal plasma reactor. *Separ. Purif. Technol.* 215 (October 2018), 155–162. <https://doi.org/10.1016/j.seppur.2019.01.007>.
- Jiang, B., Zheng, J., Liu, Q., Wu, M., 2012. Degradation of azo dye using non-thermal plasma advanced oxidation process in a circulating airtight reactor system. *Chem. Eng. J.* 204 (205), 32–39. <https://doi.org/10.1016/j.cej.2012.07.088>.
- Jiang, B., Zheng, J., Qiu, S., Wu, M., Zhang, Q., Yan, Z., Xue, Q., 2014. Review on electrical discharge plasma technology for wastewater remediation. *Chem. Eng. J.* 236, 348–368. <https://doi.org/10.1016/j.cej.2013.09.090>.
- Kasih, T.P., Faghlafi, M.A., Radjagukguk, R., Murphiyanto, R.D.J., 2019. Organic pollutant model of methylene blue dye decoloration by non-thermal plasma advanced oxidation processes (AOPs) with pin to surface configuration. *Rasayan J. Chem.* 12 (3), 1375–1382. <https://doi.org/10.31788/RJC.2019.1235366>.
- Korobeinikov, S.M., Yanshin, E.V., 1983. Dynamics of the electrostriction pressure in a fluid near a spherical electrode. *Sov. Phys. Tech. Phys.* 28, 1288.
- Krause, H., Schweiger, B., Schuhmacher, J., Scholl, S., Steinfeld, U., 2009. Degradation of the endocrine disrupting chemicals (EDCs) carbamazepine, clofibric acid, and ipromide by corona discharge over water. *Chemosphere* 75 (2), 163–168. <https://doi.org/10.1016/j.chemosphere.2008.12.020>.
- Krause, H., Schweiger, B., Prinz, E., Kim, J., Steinfeld, U., 2011. Degradation of persistent pharmaceuticals in aqueous solutions by a positive dielectric barrier discharge treatment. *J. Electrostat.* 69 (4), 333–338. <https://doi.org/10.1016/j.elstat.2011.04.011>.
- Kudlek, E., 2018. Decomposition of contaminants of emerging concern in advanced oxidation processes. *Water (Switzerland)* 10 (7). <https://doi.org/10.3390/w10070955>.
- Laroussi, M., Lu, X., Keidar, M., 2017. Perspective: the physics, diagnostics, and applications of atmospheric pressure low temperature plasma sources used in plasma medicine. *J. Appl. Phys.* 122 (2), 20901. <https://doi.org/10.1063/1.4993710>.
- Lieberman, M.A., Lichtenberg, A.J., 1994. *Principles of plasma discharges and materials processing*. *MRS Bull.* 30 (12), 899–901.
- Lindsay, A., Anderson, C., Slikboer, E., Shannon, S., Graves, D., 2015. Momentum, heat, and neutral mass transport in convective atmospheric pressure plasma-liquid systems and implications for aqueous targets. *J. Phys. Appl. Phys.* 48 (42), 424007. <https://doi.org/10.1088/0022-3727/48/42/424007>.
- Lindstrom, A.B., Strynar, M.J., Libelo, E.L., 2011. Polyfluorinated compounds: past, present, and future. *Environ. Sci. Technol.* 45 (19), 7954–7961. <https://doi.org/10.1021/es2011622>.
- Liu, W., Zhao, Q., Wang, T., Duan, X., Li, C., Lei, X., 2016. Degradation of organic pollutants using atmospheric pressure glow discharge plasma. *Plasma Chem. Plasma Process.* 36 (4), 1011–1020. <https://doi.org/10.1007/s11090-016-9714-5>.
- Locke, B., Thagard, S., 2012. Analysis and review of chemical reactions and transport processes in pulsed electrical discharge plasma formed directly in liquid water. *Plasma Chem. Plasma Process.* 32 <https://doi.org/10.1007/s11090-012-9403-y>.
- Locke, B.R., Sato, M., Sunka, P., Hoffmann, M.R., Chang, J.-S., 2006. Electrohydraulic discharge and nonthermal plasma for water treatment. *Ind. Eng. Chem. Res.* 45 (3), 882–905. <https://doi.org/10.1021/ie050981u>.
- Lu, X., Naidis, G.V., Laroussi, M., Reuter, S., Graves, D.B., Ostrikov, K., 2016. Reactive species in non-equilibrium atmospheric-pressure plasmas: generation, transport, and biological effects. *Phys. Rep.* 630, 1–84. <https://doi.org/10.1016/j.physrep.2016.03.003>.

- Lukes, Petr, Clupek, M., Babicky, V., Janda, V., Sunka, P., 2005. Generation of ozone by pulsed corona discharge over water surface in hybrid gas-liquid electrical discharge reactor. *J. Phys. Appl. Phys.* 38 (3), 409–416. <https://doi.org/10.1088/0022-3727/38/3/010>.
- Lukes, P., Clupek, M., Babicky, V., Spetlikova, E., Sisrova, I., Marsalkova, E., Marsalek, B., 2013. High power DC diaphragm discharge excited in a vapor bubble for the treatment of water. *Plasma Chem. Plasma Process.* 33 (1), 83–95. <https://doi.org/10.1007/s11090-012-9432-6>.
- Luo, Y., Guo, W., Ngo, H.H., Nghiem, L.D., Hai, F.I., Zhang, J., Liang, S., Wang, X.C., 2014. A review on the occurrence of micropollutants in the aquatic environment and their fate and removal during wastewater treatment. *Sci. Total Environ.* 473–474, 619–641. <https://doi.org/10.1016/j.scitotenv.2013.12.065>.
- Machala, Z., Hensel, K., Akishev, Y. (Eds.), 2012. *Plasma for Bio-Decontamination, Medicine and Food Security*. Springer Netherlands. <https://doi.org/10.1007/978-94-007-2852-3>.
- Magureanu, M., Piroi, D., Mandache, N.B., David, V., Medvedovici, A., Bradu, C., Parvulescu, V.I., 2011. Degradation of antibiotics in water by non-thermal plasma treatment. *Water Res.* 45 (11), 3407–3416. <https://doi.org/10.1016/j.watres.2011.03.057>.
- Magureanu, Monica, Bradu, C., Piroi, D., Mandache, N.B., Parvulescu, V., 2013. Pulsed corona discharge for degradation of methylene blue in water. *Plasma Chem. Plasma Process.* 33 (1), 51–64. <https://doi.org/10.1007/s11090-012-9422-8>.
- Magureanu, M., Bradu, C., Parvulescu, V.I., 2018. Plasma processes for the treatment of water contaminated with harmful organic compounds. *J. Phys. Appl. Phys.* 51 (31) <https://doi.org/10.1088/1361-6463/aacd9c>.
- Magureanu, Monica, Mandache, N.B., Bradu, C., Parvulescu, V.I., 2018. High efficiency plasma treatment of water contaminated with organic compounds. Study of the degradation of ibuprofen. *Plasma Process. Polym.* 15 (6), 1–9. <https://doi.org/10.1002/ppap.201700201>.
- Makabe, T., Petrovic, Z.L., 2014. *Plasma Electronics*. CRC Press. <https://doi.org/10.1201/b17322>.
- Malik, M.A., 2010. Water purification by plasmas: which reactors are most energy efficient? *Plasma Chem. Plasma Process.* 30 (1), 21–31. <https://doi.org/10.1007/s11090-009-9202-2>.
- Malik, M., Ghaffar, A., Malik, S., 2001. Water purification by electrical discharge. *Plasma Sources Sci. Technol.* 10, 82. <https://doi.org/10.1088/0963-0252/10/1/311>.
- Marković, M., Jovičić, M., Stanković, D., Kovacević, V., Roglić, G., Gojčić-Cvijović, G., Manojlović, D., 2015. Application of non-thermal plasma reactor and Fenton reaction for degradation of ibuprofen. *Sci. Total Environ.* 505, 1148–1155. <https://doi.org/10.1016/j.scitotenv.2014.11.017>.
- Marotta, E., Schiorlin, M., Ren, X., Rea, M., Paradisi, C., 2011. Advanced oxidation process for degradation of aqueous phenol in a dielectric barrier discharge reactor. *Plasma Process. Polym.* 8 (9), 867–875. <https://doi.org/10.1002/ppap.201100036>.
- Marotta, E., Ceriani, E., Schiorlin, M., Ceretta, C., Paradisi, C., 2012. Comparison of the rates of phenol advanced oxidation in deionized and tap water within a dielectric barrier discharge reactor. *Water Res.* 46 (19), 6239–6246. <https://doi.org/10.1016/j.watres.2012.08.022>.
- Miklos, D.B., Remy, C., Jekel, M., Linden, K.G., Drewes, J.E., Hübner, U., 2018. Evaluation of advanced oxidation processes for water and wastewater treatment – a critical review. *Water Res.* 139, 118–131. <https://doi.org/10.1016/j.watres.2018.03.042>.
- Miletić, M., Milenković, P., Mojsilović, S., Okić Đorđević, I., Bugarski, D., Maletić, D., Puač, N., Lazović, S., Malović, G., & Lj Petrović, Z. (n.d.). Effects of non-thermal atmospheric plasma on human periodontal ligament mesenchymal stem cells. *J. Phys. Appl. Phys.*, 46(34), 9. <https://doi.org/DOI:10.1088/0022-3727/46/34/345401>.
- Mitrović, T., Tomić, N., Djukić-Vuković, A., Dohčević-Mitrović, Z., Lazović, S., 2020. Atmospheric plasma supported by TiO<sub>2</sub> catalyst for decolourisation of reactive orange 16 dye in water. *Waste and Biomass Valorization* 11 (12), 6841–6854. <https://doi.org/10.1007/s12649-019-00928-y>.
- Nzeribe, B.N., Crimi, M., Mededovic Thagard, S., Holsen, T.M., 2019. Physico-chemical processes for the treatment of per- and polyfluoroalkyl substances (PFAS): a review. *Crit. Rev. Environ. Sci. Technol.* 49 (10), 866–915. <https://doi.org/10.1080/10643389.2018.1542916>.
- OECD, 2018. 033-066-C609-51.pdf. Series on risk management, No. 39 (39), 1–24. [http://www.oecd.org/officialdocuments/publicdisplaydocumentpdf/?cote=ENV-JM-MONO\(2018\)7&doclanguage=en](http://www.oecd.org/officialdocuments/publicdisplaydocumentpdf/?cote=ENV-JM-MONO(2018)7&doclanguage=en).
- Pankaj, S.K., Wan, Z., Colonna, W., Keener, K.M., 2017. Degradation kinetics of organic dyes in water by high voltage atmospheric air and modified air cold plasma. *Water Sci. Technol.* 76 (3), 567–574. <https://doi.org/10.2166/wst.2017.169>.
- Panorel, I., Preis, S., Kornev, I., Hatakka, H., Louhi-Kultanen, M., 2013. Oxidation of aqueous paracetamol by pulsed corona discharge. *Ozone Sci. Eng.* 35 (2), 116–124. <https://doi.org/10.1080/01919512.2013.760415>.
- Parvulescu, V.I., Magureanu, M., Lukes, P., 2012. Plasma chemistry and catalysis in gases and liquids. <https://doi.org/10.1002/9783527649525>.
- Privat-Maldonado, A., Schmidt, A., Lin, A., Weltmann, K.-D., Wende, K., Bogaerts, A., Bekeschus, S., 2019. ROS from physical plasmas: redox chemistry for biomedical therapy. *Oxid. Med. Cell. Longev.* 2019, 9062098. <https://doi.org/10.1155/2019/9062098>.
- Puač, N., Maletić, D., Lazović, S., Malović, G., Đorđević, A., Petrović, Z.L., 2012. Time resolved optical emission images of an atmospheric pressure plasma jet with transparent electrodes. *Appl. Phys. Lett.* 101 (2), 24103. <https://doi.org/10.1063/1.4735156>.
- Reddy, P.M.K., Subrahmanyam, C., 2012. Green approach for wastewater treatment-degradation and mineralization of aqueous organic pollutants by discharge plasma. *Ind. Eng. Chem. Res.* 51 (34), 11097–11103. <https://doi.org/10.1021/ie301122p>.
- Reuter, S., von Woedtk, T., Weltmann, K.-D., 2018. The kINPen—a review on physics and chemistry of the atmospheric pressure plasma jet and its applications. *J. Phys. Appl. Phys.* 51 (23), 233001. <https://doi.org/10.1088/1361-6463/aab3ad>.
- Ribeiro, A.R., Nunes, O.C., Pereira, M.F.R., Silva, A.M.T., 2015. An overview on the advanced oxidation processes applied for the treatment of water pollutants defined in the recently launched Directive 2013/39/EU. *Environ. Int.* 75, 33–51. <https://doi.org/10.1016/j.envint.2014.10.027>.
- Rozas, O., Vidal, C., Baeza, C., Jardim, W.F., Rossner, A., Mansilla, H.D., 2016. Organic micropollutants (OMPs) in natural waters: oxidation by UV/H<sub>2</sub>O<sub>2</sub> treatment and toxicity assessment. *Water Res.* 98, 109–118. <https://doi.org/10.1016/j.watres.2016.03.069>.
- Ruma, Lukes, P., Aoki, N., Spetlikova, E., Hosseini, S.H.R., Sakugawa, T., Akiyama, H., 2013. Effects of pulse frequency of input power on the physical and chemical properties of pulsed streamer discharge plasmas in water. *J. Phys. Appl. Phys.* 46 (12) <https://doi.org/10.1088/0022-3727/46/12/125202>.
- Santos, L.H.M.L.M., Araújo, A.N., Fachini, A., Pena, A., Delerue-Matos, C., Montenegro, M.C.B.S.M., 2010. Ecotoxicological aspects related to the presence of pharmaceuticals in the aquatic environment. *J. Hazard Mater.* 175 (1–3), 45–95. <https://doi.org/10.1016/j.jhazmat.2009.10.100>.
- Sarangapani, C., Dixit, Y., Milosavljevic, V., Bourke, P., Sullivan, C., Cullen, P.J., 2017. Optimization of atmospheric air plasma for degradation of organic dyes in wastewater. *Water Sci. Technol.* 75 (1), 207–219. <https://doi.org/10.2166/wst.2016.471>.
- Sarangapani, C., Zuzina, D., Behan, P., Boehm, D., Gilmore, B.F., Cullen, P.J., Bourke, P., 2019. Degradation kinetics of cold plasma-treated antibiotics and their antimicrobial activity. *Sci. Rep.* 9 (1), 1–15. <https://doi.org/10.1038/s41598-019-40352-9>.
- Schaper, L., Stalder, K.R., Graham, W.G., 2011. Plasma production in electrically conducting liquids. *Plasma Sources Sci. Technol.* 20 (3), 34004. <https://doi.org/10.1088/0963-0252/20/3/034004>.
- Schoenbach, K., Kolb, J., Xiao, S., Katsuki, S., Minamitani, Y., Joshi, R., 2008. Electrical breakdown of water in microgaps. *Plasma Sources Sci. Technol.* 17 (2), 24010. <https://doi.org/10.1088/0963-0252/17/2/024010>.
- Šimor, M., Ráhel, J., Vojtek, P., Černák, M., Brablec, A., 2002. Atmospheric-pressure diffuse coplanar surface discharge for surface treatments. *Appl. Phys. Lett.* 81 (15), 2716–2718. <https://doi.org/10.1063/1.1513185>.
- Singh, R.K., Philip, L., Ramanujam, S., 2016. Rapid removal of carbofuran from aqueous solution by pulsed corona discharge treatment: kinetic study, oxidative, reductive degradation pathway, and toxicity assay. *Ind. Eng. Chem. Res.* 55 (26), 7201–7209. <https://doi.org/10.1021/acs.iecr.6b01191>.
- Singh, R.K., Philip, L., Ramanujam, S., 2017. Removal of 2,4-dichlorophenoxyacetic acid in aqueous solution by pulsed corona discharge treatment: effect of different water constituents, degradation pathway and toxicity assay. *Chemosphere* 184, 207–214. <https://doi.org/10.1016/j.chemosphere.2017.05.134>.
- Singh, R.K., Fernando, S., Baygi, S.F., Multari, N., Thagard, S.M., Holsen, T.M., 2019a. Breakdown products from perfluorinated alkyl substances (PFAS) degradation in a plasma-based water treatment process [Research-article]. *Environ. Sci. Technol.* 53 (5), 2731–2738. <https://doi.org/10.1021/acs.est.8b07031>.
- Singh, R.K., Philip, L., Ramanujam, S., 2019b. Continuous flow pulse corona discharge reactor for the tertiary treatment of drinking water: insights on disinfection and emerging contaminants removal. *Chem. Eng. J.* 355 (July 2018), 269–278. <https://doi.org/10.1016/j.cej.2018.08.109>.
- Škoro, N., Puač, N., Živković, S., Krstić-Milošević, D., Cvelbar, U., Malović, G., Petrović, Z.L., 2018. Destruction of chemical warfare surrogates using a portable atmospheric pressure plasma jet. *European Phys. J. D* 72 (1), 2. <https://doi.org/10.1140/epjd/e2017-80329-9>.
- Stockholm, C., on P. O. P., 2019. Amend acceptable purposes and specific exemptions of perfluorooctane sulfonic acid, its salts and perfluorooctane sulfonyl fluoride in Annex B (decision SC-9/4). *New POPs under Stock. Conv.* 9–10.
- Stratton, G.R., Dai, F., Bellona, C.L., Holsen, T.M., Dickenson, E.R.V., Mededovic Thagard, S., 2017. Plasma-based water treatment: efficient transformation of perfluoroalkyl substances in prepared solutions and contaminated groundwater. *Environ. Sci. Technol.* 51 (3), 1643–1648. <https://doi.org/10.1021/acs.est.6b04215>.
- Šunka, P., 2001. Pulse electrical discharges in water and their applications. *Phys. Plasmas* 8 (5), 2587–2594. <https://doi.org/10.1063/1.1356742>.
- Sunka, P., Babický, V., Clupek, M., Lukes, P., Šimek, M., Schmidt, J., Černák, M., 1999. Generation of chemically active species by electrical discharges in water. *Plasma Sources Sci. Technol.* 8 (2), 258–265. <https://doi.org/10.1088/0963-0252/8/2/006>.
- Takeuchi, Nozomi, Oishi, R., Kitagawa, Y., Yasuoka, K., 2011. Adsorption and efficient decomposition of perfluoro compounds at plasma-water interface. *IEEE Trans. Plasma Sci.* 39 (12 PART 2), 3358–3363. <https://doi.org/10.1109/TPS.2011.2171374>.
- Takeuchi, N., Kitagawa, Y., Kosugi, A., Tachibana, K., Obo, H., Yasuoka, K., 2014. Plasma-liquid interfacial reaction in decomposition of perfluoro surfactants. *J. Phys. Appl. Phys.* 47 (4) <https://doi.org/10.1088/0022-3727/47/4/045203>.
- Tendero, C., Tixier, C., Tristant, P., Desmaison, J., Leprince, P., 2006. Atmospheric pressure plasmas: a review. *Spectrochim. Acta B Atom Spectrosc.* 61 (1), 2–30. <https://doi.org/10.1016/j.sab.2005.10.003>.
- Tijani, J.O., Fatoba, O.O., Madzivire, G., Petrik, L.F., 2014. A review of combined advanced oxidation technologies for the removal of organic pollutants from water. *Water Air Soil Pollut.* 225 (9) <https://doi.org/10.1007/s11270-014-2102-y>.
- Tomić, S., Petrović, A., Puač, N., Škoro, N., Bekić, M., Petrović, Z.L., Čolić, M., 2021. Plasma-activated medium potentiates the immunogenicity of tumor cell lysates for dendritic cell-based cancer vaccines. *Cancers* 13 (7), 1626. <https://doi.org/10.3390/cancers13071626>.

- UNEP, 2009. Listing of perfluorooctane sulfonic acid (PFOS), its salts and perfluorooctane sulfonyl fluoride (PFOSF) in Annex B of the Stockholm Convention on Persistent Organic Pollutants. *Unep/Pops/Cop. 4/17*, 15–18.
- US EPA, 2016. Drinking water health advisory for perfluorooctane sulfonate (PFOS). *EPA 822-R-16-004. May, 1–88*. [https://www.epa.gov/sites/production/files/2016-05/documents/pfoa\\_health\\_advisory\\_final-plain.pdf](https://www.epa.gov/sites/production/files/2016-05/documents/pfoa_health_advisory_final-plain.pdf).
- Vanraes, P., Willems, G., Daels, N., Van Hulle, S.W.H., De Clerck, K., Surmont, P., Lynen, F., Vandamme, J., Van Durme, J., Nikiforov, A., Leys, C., 2015. Decomposition of atrazine traces in water by combination of non-thermal electrical discharge and adsorption on nanofiber membrane. *Water Res.* 72, 361–371. <https://doi.org/10.1016/j.watres.2014.11.009>.
- Vanraes, P., Ghodbane, H., Davister, D., Wardenier, N., Nikiforov, A., Verheust, Y.P., Van Hulle, S.W.H., Hamdaoui, O., Vandamme, J., Van Durme, J., Surmont, P., Lynen, F., Leys, C., 2017. Removal of several pesticides in a falling water film DBD reactor with activated carbon textile: energy efficiency. *Water Res.* 116, 1–12. <https://doi.org/10.1016/j.watres.2017.03.004>.
- Verlicchi, P., Al Aukidy, M., Zambello, E., 2012. Occurrence of pharmaceutical compounds in urban wastewater: removal, mass load and environmental risk after a secondary treatment-A review. *Sci. Total Environ.* 429, 123–155. <https://doi.org/10.1016/j.scitotenv.2012.04.028>.
- Wardenier, N., Gorbanev, Y., Van Moer, I., Nikiforov, A., Van Hulle, S.W.H., Surmont, P., Lynen, F., Leys, C., Bogaerts, A., Vanraes, P., 2019a. Removal of alachlor in water by non-thermal plasma: reactive species and pathways in batch and continuous process. *Water Res.* 161, 549–559. <https://doi.org/10.1016/j.watres.2019.06.022>.
- Wardenier, N., Vanraes, P., Nikiforov, A., Van Hulle, S.W.H., Leys, C., 2019b. Removal of micropollutants from water in a continuous-flow electrical discharge reactor. *J. Hazard Mater.* 362 (August 2018), 238–245. <https://doi.org/10.1016/j.jhazmat.2018.08.095>.
- Wols, B.A., Hofman-Caris, C.H.M., 2012. Review of photochemical reaction constants of organic micropollutants required for UV advanced oxidation processes in water. *Water Res.* 46 (9), 2815–2827. <https://doi.org/10.1016/j.watres.2012.03.036>.
- Yamada, M., Wahyudiono, Machmudah, S., Kanda, H., Goto, M., 2020. Nonthermal atmospheric pressure plasma for methylene blue dye decolorization by using slug flow reactor system. *Plasma Chem. Plasma Process.* 40 (4), 985–1000. <https://doi.org/10.1007/s11090-020-10066-2>.
- Yasuoka, K., Sasaki, K., Hayashi, R., Kosugi, A., Takeuchi, N., 2010, 2. Degradation of Perfluoro Compounds and F - Recovery in Water Using Discharge Plasmas Generated within Gas Bubbles, vol. 4, pp. 113–117.
- Yasuoka, K., Sasaki, K., Hayashi, R., 2011. An energy-efficient process for decomposing perfluorooctanoic and perfluorooctane sulfonic acids using dc plasmas generated within gas bubbles. *Plasma Sources Sci. Technol.* 20 (3) <https://doi.org/10.1088/0963-0252/20/3/034009>.
- Zhang, Q., Zhang, H., Zhang, Q., Huang, Q., 2018. Degradation of norfloxacin in aqueous solution by atmospheric-pressure non-thermal plasma: mechanism and degradation pathways. *Chemosphere* 210, 433–439. <https://doi.org/10.1016/j.chemosphere.2018.07.035>.

## Article

# Plasma-Activated Medium Potentiates the Immunogenicity of Tumor Cell Lysates for Dendritic Cell-Based Cancer Vaccines

Sergej Tomić <sup>1,\*</sup>, Anđelija Petrović <sup>2</sup>, Nevena Puač <sup>2,\*</sup>, Nikola Škoro <sup>2</sup>, Marina Bekić <sup>1</sup>, Zoran Lj. Petrović <sup>3,4</sup> and Miodrag Čolić <sup>1,3,5</sup>

- <sup>1</sup> Department for Immunology and Immunoparasitology, Institute for the Application of Nuclear Energy, University of Belgrade, 11080 Belgrade, Serbia; marina.bekic@inep.co.rs (M.B.); miocolic@gmail.com (M.Č.)  
<sup>2</sup> Institute of Physics, University of Belgrade, 11080 Belgrade, Serbia; andjelija@ipb.ac.rs (A.P.); nskoro@ipb.ac.rs (N.Š.)  
<sup>3</sup> Serbian Academy for Sciences and Arts, 11000 Belgrade, Serbia; zoran@ipb.ac.rs  
<sup>4</sup> School of Engineering, Ulster University, Jordanstown, Co. Antrim BT37 0QB, UK  
<sup>5</sup> Medical Faculty Foca, University of East Sarajevo, 73 300 Foča, Bosnia and Herzegovina  
\* Correspondence: sergej.tomic@inep.co.rs (S.T.); nevena@ipb.ac.rs (N.P.); Tel.: +381-11-2610-126 (S.T.); +381-11-3713-143 (N.P.)



**Citation:** Tomić, S.; Petrović, A.; Puač, N.; Škoro, N.; Bekić, M.; Petrović, Z.L.; Čolić, M. Plasma-Activated Medium Potentiates the Immunogenicity of Tumor Cell Lysates for Dendritic Cell-Based Cancer Vaccines. *Cancers* **2021**, *13*, 1626. <https://doi.org/10.3390/cancers13071626>

Academic Editors: Annemie Bogaerts, Katharina Stapelmann and Abraham Lin

Received: 3 February 2021  
Accepted: 17 March 2021  
Published: 1 April 2021

**Publisher's Note:** MDPI stays neutral with regard to jurisdictional claims in published maps and institutional affiliations.



**Copyright:** © 2021 by the authors. Licensee MDPI, Basel, Switzerland. This article is an open access article distributed under the terms and conditions of the Creative Commons Attribution (CC BY) license (<https://creativecommons.org/licenses/by/4.0/>).

**Simple Summary:** Dendritic cells (DCs)-based anti-cancer vaccines displayed limited efficacy in clinical trials, mostly due to a lack of protocols for preparing immunogenic tumor antigens used in the vaccine. Here, a unique atmospheric pressure plasma jet was used to prepare a plasma-activated medium (PAM) which induced immunogenic cell death in tumor cells. This procedure increased the efficacy of tumor lysates in enhancing the immunogenicity of DCs according to their increased maturation, production of IL-12, and the capacity to induce cytotoxic CD8 T cells able to kill tumor cells. In contrast to the tumor lysates commonly used in DC vaccines, PAM-tumor lysates lacked the capacity to increase IL-10 production by DCs, and their potential to induce protumorigenic Th2 and regulatory T cells. Cumulatively, these results suggest that the novel method for preparing immunogenic tumor lysates with PAM could be suitable for improved DC-based immunotherapy of cancer patients.

**Abstract:** Autologous dendritic cells (DCs)-based vaccines are considered quite promising for cancer immunotherapy due to their exquisite potential to induce tumor antigen-specific cytotoxic T cells. However, a lack of efficient protocols for inducing immunogenic tumor antigens limits the efficacy of DC-based cancer vaccines. Here, we found that a plasma-activated medium (PAM) induces immunogenic cell death (ICD) in tumor cells but not in an immortalized L929 cell line or human peripheral blood mononuclear cells. PAM induced an accumulation of reactive oxygen species (ROS), autophagy, apoptosis, and necrosis in a concentration-dependent manner. The tumor lysates prepared after PAM treatment displayed increased immunogenicity in a model of human monocyte-derived DCs, compared to the lysates prepared by a standard freezing/thawing method. Mature DCs loaded with PAM lysates showed an increased maturation potential, as estimated by their increased expression of CD83, CD86, CD40, IL-12/IL-10 production, and attenuated PDL1 and ILT-4 expression, compared to the DCs treated with control tumor lysates. Moreover, in co-culture with allogeneic T cells, DCs loaded with PAM-lysates increased the proportion of cytotoxic IFN- $\gamma$ + granzyme A+ CD8+ T cells and IL-17A-producing T cells and preserved the Th1 response. In contrast, control tumor lysates-treated DCs increased the frequency of Th2 (CD4+IL-4+), CD4, and CD8 regulatory T cell subtypes, none of which was observed with DCs loaded with PAM-lysates. Cumulatively, these results suggest that the novel method for preparing immunogenic tumor lysates with PAM could be suitable for improved DC-based immunotherapy of cancer patients.

**Keywords:** plasma activated medium; dendritic cells; tumor vaccines; Th polarization

## 1. Introduction

Cold atmospheric plasma (CAP), also called non-equilibrium atmospheric-pressure plasma (NEAPP), is a partially ionized gas generated under normal atmospheric pressure and ambient temperature [1]. Achieving non-equilibrium conditions at atmospheric pressure proved to be possible in only a limited number of cases. Just recently, CAP sources have become more diversified and are being developed with specific applications in mind. CAP is a source of reactive species, ions, neutral particles and molecules, electrons, and other physical factors such as electromagnetic fields, metastable and excited molecules, weak ultraviolet radiation, etc., while producing only a very weak or negligible heating effect [2]. CAP has been widely used in various fields of modern medicine, such as promoting wound healing, blood coagulation, stem cell differentiation and the treatment of some skin diseases, as an anti-bacterial, anti-viral and sterilization agent [3]. In particular, CAP has recently been tested for cancer treatment [2,4–6]. The therapeutic effect of low-temperature plasma is based on the production of various reactive oxygen and nitrogen species (RONS) [7], such as nitric oxide ( $\bullet\text{NO}$ ) and hydroxyl ( $\bullet\text{OH}$ ) radicals [8]. In contact with the cancer tissue, CAP produced RONS are capable of inducing cell death and this approach has been extensively explored for the treatment of tumor because malignant cells are extremely vulnerable to the effect of RONS and die by necrosis, apoptosis, or necroptosis. In contrast, normal cells are less sensitive to CAP [9]. An indirect approach to using CAP in medicine is the production of a plasma-activated medium (PAM). The gas phase plasma chemistry and the plasma chemistry in the gas/liquid (i.e., cell culture medium) interface induce chemical reactions in the liquid phase. As a result, specific compounds are created in the liquid phase which are responsible for the effects on cells (bacteria, plant cells, human cells, cancer cells, stem cells, etc.). The chemistry, both in a gas phase and liquid phase, depends on the plasma parameters (type of gas mixture, gas flow, concentration of electrons, temperature of electrons, deposited power etc.), and on the type of liquid medium that is being treated by plasma. PAM may be prepared by treating aqueous solutions, including cell culture media, with CAP. In this process, RONS are transported from the gas phase into the liquid surface, dissolved into the medium, and undergo further reactions with dissolved molecules in the aqueous solution. Mixing of the gas-phase RONS with the medium is promoted (in this paper as well) by a strong flow of gas/plasma into the liquid whereby “bubbles” of plasma effluent are formed within the top layer of the liquid.

The interaction of gas-phase RONS with aqueous organics produces other relatively long-lived RONS, such as hydrogen peroxide ( $\text{H}_2\text{O}_2$ ), nitrates, nitrites and organic peroxides ( $\text{RO}_2$ ) [8]. Due to the long-lived RONS, PAM has been shown to be as effective in killing cancer cells as direct treatment with CAP, and the effect of both treatments is enhanced by intracellular ROS production [10]. The “treatment dose” depends on the source of the plasma, the time of plasma exposure of the liquid, as well as the period for which the cells or tissue is allowed to remain in contact with PAM [11]. The efficacy of plasma in the treatment of malignant tumors is based on two general principles. The first includes a direct cytotoxic effect caused by RONS-mediated intracellular oxidative stress followed by inactivation by anti-oxidative mechanisms. This phenomenon is of special relevance, knowing that the increase of pro-oxidative mechanisms in the tumor could be beneficial for tumor therapy [12]. The second pathway involves activation of the anti-tumor immune response by molecules released from CAP- and PAM-dependent immunogenic cell death (ICD) [13].

ICD is a type of cell death, also referred to as immunogenic apoptosis, which is characterized by a release or display of damage-associated molecular patterns (DAMPs). The most important DAMPs released from cancer cells during ICD are calreticulin, adenosine triphosphate (ATP), heat-shock proteins, and high mobility group protein B1 (HMGB1). DAMPs are a potent adjuvant for antigen-presenting cells (APCs), especially dendritic cells (DCs), inducing their migration to the regional lymphoid tissue, maturation, and stimulation of a specific anti-tumor immune response [14]. DCs are specialized APCs

playing a key role in the initiation and regulation of innate and adaptive immune responses. Due to their unique properties, DCs have been extensively investigated and used to improve cancer immunotherapy. In this context, many strategies have been developed to target DCs in cancer [15]. One of them is the *in vitro* generation of DCs from monocytes (MoDCs), loading of these APCs with autologous tumor lysates together with maturation stimuli, and inoculation of thus prepared DCs vaccines in cancer patients [16]. The use of DC vaccines for cancer therapy has been extensively investigated, with more than 200 completed clinical trials to date. The injected MoDCs migrate to the regional lymph nodes where they efficiently induce CD4+ T cell- and CD8+ T cell-mediated anti-tumor responses. MoDCs can be also recruited into the tumor microenvironment (TME) following treatment with ICD inducers, including CAP, with the potency to the prime anti-tumor T-cell responses [15]. The clinical benefit of DC-based vaccines is not as efficient as expected due to the presence of many inhibitory molecules and mechanisms in TME. Therefore, an immunotherapy approach based on improved DC vaccines together with the blockade of inhibitory molecules in TME sounds promising for future tumor therapy [15,17]. Optimization of DC vaccines implies the use of better protocols for preparing tumor antigens, designing new strategies for antigen loading, as well as selection of optimal adjuvants and maturation stimuli. In this context, the use of lysates from tumor cells subjected to ICD could be beneficial, as already well documented [14,18–20]. PAM treatment of tumor cells has not been explored up to the date for the stimulation of MoDCs. This was the reason why we tested the hypothesis that a lysate prepared from PAM-treated tumor cells is superior to the induction of immunogenic DCs than the tumor lysates prepared under the conventional freezing-thawing protocol, commonly employed in clinics.

## 2. Materials and Methods

### 2.1. Experimental Setup-Plasma Treatments

Figure 1 illustrates the schematics of the dielectric barrier discharge (DBD) atmospheric pressure plasma jet (APPJ) setup and the plasma treatment of a medium placed in the well of a 24-well plate. The DBD jet consists of a glass tube with an inner diameter of 4 mm and an outer diameter of 6 mm. The two electrodes placed around the tube are 15 mm wide and made of copper tape. The surface of the target grounded through a resistor served as the third electrode. The electrode positioned at 5 mm from the edge of the glass tube was connected to the power supply. Another grounded electrode was placed at a distance of 10 mm from the powered electrode. This electrode was grounded over a second resistor to the same point of the electrical circuit as the ground line of the target. The power supply of the APPJ consists of a function generator (PeakTech DDS Function Generator, PeakTech GmbH, Ahrensburg, Germany), a home-made amplifier, and a high-voltage transformer operating at its resonance frequency of 81 kHz. A sine-wave high-voltage signal was provided to power the APPJ. One high-voltage (HV) probe (P6015A HV probe, Tektronix Inc., Beaverton, OR, USA) and two voltage probes (N2863B voltage probe, Agilent, Santa Clara, CA, USA) were used to record voltage and current waveforms. The current waveforms were obtained at the resistors ( $R = 1\text{k}\Omega$ ) in the grounded branches of the electrical circuit. They were used to monitor the stability of plasma and calculate the power delivered from the plasma to the sample. This power was 1.2 W in all experiments. The RMS voltage was 1.9 kV and the RMS current was 2.2 mA. The APJ was operating with 2 slm of He as the working gas. The distance between the ending of the APPJ tube and the surface of the sample was 5 mm in all experiments. After the sample treatment, the production of RONS in PAM was investigated by spectrophotometry and colorimetric methods and the concentrations of nitrite ions, nitrate ions and hydrogen peroxide were determined. The pH value of the PAM-RPMI 1640 was not changed after the plasma treatment.

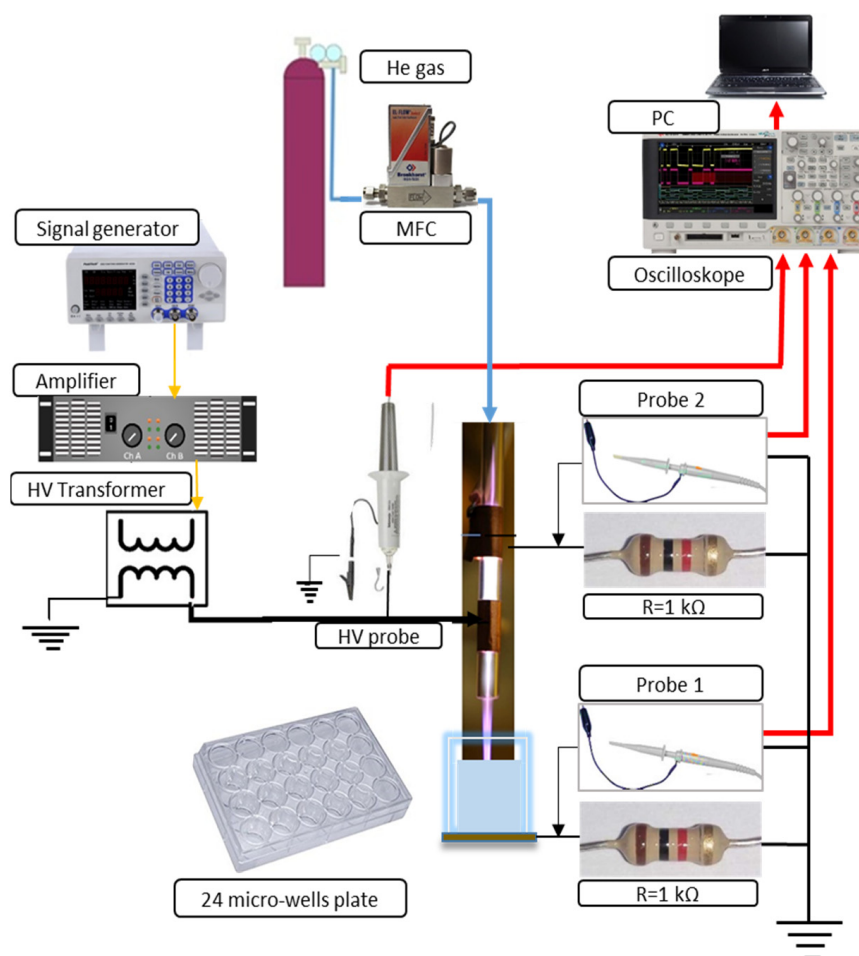


**Figure 1.** Schematic diagram of the experimental setup.

## 2.2. Measurement of RONS in the Plasma-Activated Medium

Immediately after the plasma treatment PAM was placed in vials and frozen in liquid  $N_2$ . RONS ( $H_2O_2$ ,  $NO_2^-$ ,  $NO_3^-$ ) were measured by using colorimetric measurements. The measurements were performed immediately after the plasma treatment and, as a control, after defrosting the PAM. No differences in RONS concentrations were noticed between these samples (data not shown). This is in accordance with the previously reported results. The good stability of PAM properties in room conditions has been shown to be preserved for 8 to 18 h [21]. Moreover, freeze-thaw procedures for different PAM were studied and it reportedly retains the properties when kept at low temperatures [22].

The  $H_2O_2$  and  $NO_3^-$  concentrations of the treated medium were analyzed by using commercial  $H_2O_2$  test stripes (Merckoquant 110011, Merck, Darmstadt, Germany) and commercial  $NO_3^-$  test stripes (Merckoquant 110020, Merck, Darmstadt, Germany). The test stripes were scanned by a scanner (Perfection V370 Photo, Epson, Nagano, Japan) in order to analyze their color value. A calibration procedure was performed before the experiments. Six different  $H_2O_2$  concentrations ranging from 0 to 25 mg/L were made by diluting 30%  $H_2O_2$  stock solution in distilled  $H_2O$ . The same process of calibration was used for the nitrate concentration. Seven different nitrate concentrations ranging from 0 to 250 mg/L were made by diluting a nitrate stock solution (Nitrate standard solution 200 mg/L  $NO_3^-$ -N in  $H_2O$ , 125040, Merck, Darmstadt, Germany) in distilled  $H_2O$ . The sum of the color values of the red, green, and blue channel (grey value) for different  $H_2O_2$  and  $NO_3^-$  concentrations were plotted in their respective calibration graphs. The exponential fit of the calibration data allows the determination of an unknown  $H_2O_2$  and  $NO_3^-$  concentration deposited in the sample during the plasma treatment. Aliquots of 10  $\mu$ L PAM were taken

immediately after 5 min of plasma treatment time. The plasma treatment was done in triplicate and each time concentration of  $\text{H}_2\text{O}_2$  and  $\text{NO}_3^-$  was determined.

To detect nitrite ions ( $\text{NO}_2^-$ ), Griess reagent was added to the PAM (Spectroquant Nitrite test 1.14776.0001, Merck, Darmstadt, Germany). In an acidic solution, nitrite ions react with sulfanilic acid to form a diazonium salt, which in turn reacts with N-(1-naphthyl) ethylenediamine dihydrochloride to form a red-violet azo dye. This dye was determined spectrophotometrically and the absorbance was measured at  $\lambda = 540$  nm. For the calibration curve, seven different nitrite concentrations ranging from 0 to 1 mg/L  $\text{NO}_2^-$ -N were produced by diluting a nitrite stock solution (Nitrate standard solution 40 mg/L  $\text{NO}_2^-$ -N in  $\text{H}_2\text{O}$ , 125042, Merck, Darmstadt, Germany) in distilled water. Similarly to  $\text{NO}_3^-$  and  $\text{H}_2\text{O}_2$ , the concentration of  $\text{NO}_2^-$  was determined after 5 min plasma treatments. The experiment was done in triplicate.

### 2.3. Cells

Human melanoma A375, laryngeal carcinoma Hep2, and immortalized mouse fibroblast L929 cell lines were obtained from ATCC (American Type Cell Culture, Manassas, WV, USA) and were stored in 10% DMSO/Fetal calf serum (FCS, Sigma, St. Louis, MO, USA) in liquid nitrogen before the experiments. The cells were thawed in 20x volume of complete RPMI medium, containing basal RPMI 1640, 10% FCS, 2 mM L-glutamine (Sigma, St. Louis, MO, USA), 50  $\mu\text{M}$  2-mercaptoethanol (2-ME, Sigma, St. Louis, MO, USA), and antibiotics (gentamicin, streptomycin, penicillin) and after washing by centrifugation, they were cultivated at 37 °C, 5%  $\text{CO}_2$  up to 80% confluence. After reaching the confluence, the cells were passaged via trypsinization in 0.2% trypsin/0.02% NaEDTA (Sigma, St. Louis, MO, USA) according to standard laboratory procedures.

Peripheral blood mononuclear cells (PBMCs) were obtained from healthy volunteers who signed consent forms and isolated by using Lymphoprep (Nycomed, Oslo, Norway). All studies involving the usage of human cells were approved by the Ethics committee of the Institute for the Application of Nuclear Energy, University of Belgrade (No. 02/765/2). PBMC were used in direct cytotoxicity assay or as a source for the isolation of monocytes and T cells as negative fractions of Magnetic-activated cell sorting (MACS) using Monocyte isolation kit II and Pan-T cell isolation kits (Miltenyi Biotec, Bergisch Gladbach, Germany), respectively.

MACS-sorted monocytes were used for the generation of monocyte-derived dendritic cells (DCs) according to a protocol described previously [23]. Briefly,  $1 \times 10^6$  monocytes were plated in low-adherent 6-well plates (Sarstedt AG & Company, Sarstedt, Germany) and cultivated for 4 days in CellGenix<sup>®</sup> GMP DC medium (CellGenix, Freiburg im Breisgau, Germany) in the presence of a recombinant human granulocyte-macrophage colony-stimulating factor (GM-CSF) and interleukin (IL)-4 (both at 20 ng/mL, R & D Systems, Minneapolis, MN, USA) to obtain immature (im)DCs. Tumor lysates derived from A375 or Hep2 cells, as described in Section 2.4, were added to the DC cultures on day 4. To obtain mature (m)DC, the cells were treated with LPS from *E. coli* 0.111:B4 (200 ng/mL, Sigma, St. Louis, MO, USA) and human recombinant IFN- $\gamma$  (20 ng/mL), 4 h after the treatment of DCs with tumor lysates, for the next 16–18 h. Afterward, the DCs were collected and used for phenotype characterization and functional assays with MACS-purified T cells.

### 2.4. Cytotoxicity Study

PAM was prepared by treating a basic RPMI 1640 medium with CAP. The components for a complete RPMI medium were added immediately afterwards and serial dilutions of PAM were prepared in the complete RPMI medium.

To evaluate the cytotoxic effects of PAM on A375, Hep2, L929 cells (each at  $5 \times 10^4$  cells per well of a flat 96-well plate) and PBMCs ( $2 \times 10^5$  cells per well of 96-wells plate) were cultivated in complete RPMI medium with serial dilutions of PAM (100%, 50%, 25%, 12.5%, 6.25%, 0%) for 24 h. Supernatants of these cell-cultures were collected and stored at  $-80$  °C for cytokines analysis. The MTT assay was performed on the remaining cells to determine



the metabolic activity of the cells treated with PAM. The corresponding cell-free cultures containing PAM were used as blank controls. After the cultivation, all cultures were washed in phenol red-free RPMI medium twice and MTT (3-(4,5-dimethylthiazol-2-yl)-2,5-diphenyltetrazolium bromide (1 mg/mL), Sigma) in phenol red-free RPMI was added for the next 4 h. The formazan crystals were dissolved by using 10% sodium dodecyl sulphate (SDS, Sigma, St. Louis, MO, USA) in 0.01N HCl (Sigma, St. Louis, MO, USA) overnight, and the absorbance was read at 570 nm with a spectrophotometer (ELx800, Biotek, Winooski, VT, USA). The absorbance in cell-free blank controls was subtracted from the absorbance of corresponding experimental cultures. Each of the three experiments performed was carried out in six-plicates. The metabolic activity (MTT%) detected in the treated cultures was expressed as the percentage of the absorbance in non-treated control cultures (100%).

Oxidative stress in the A375 cells treated with different concentrations of PAM (6.25–100%) for 4 h or 24 h was analyzed after trypsinization of cells, by using a Muse<sup>®</sup> Oxidative Stress Kit (Luminex, Austin, TX, USA), which is based on the reactive oxygen species-sensitive dye dihydroethidium (DHE), according to manufacturer's instruction. Autophagy flux in the A375 cells treated with different concentrations of PAM was evaluated using a Muse<sup>®</sup> Autophagy LC3 Antibody-based kit, according to the manufacturer's instructions. The method relies on the detection of membrane-bound LC3 after selective permeabilization of cells which extracts cytoplasmic LC3 but not membrane-bound LC3, and the blockage of lysosomal degradation of LC3 in autophagosomes. Apoptosis of the A375 cells treated with PAM for 24 h was detected with a Muse<sup>®</sup> Annexin V & Dead Cell kit, which is based on Annexin V/7AAD staining in Ca<sup>2+</sup>-containing buffer. The analysis of oxidative stress, autophagy, and apoptosis was performed on a Guava<sup>®</sup> Muse<sup>®</sup> Cell Analyzer (Luminex, Austin, TX, USA). The expression of heat-shock protein (HSP) 60 and heat-shock complex (HSC) 70 on the surface of A375 and Hep2 cells was analyzed after 4h exposure of cells to different doses of PAM. After harvesting the cells by trypsinization, the cells were incubated with primary mouse anti-HSP 60 (Clone 24, 1 µg/mL BD Biosciences, San Jose, CA, USA) or mouse anti-HSC 70 (Clone sc-7298, 1 µg/mL Santa Cruz Biotechnology, Inc., Dallas, TX, USA) in PBS/NaN<sub>3</sub>/5%FCS for 30 min, washed, and then incubated with a secondary anti-mouse IgG-FITC antibody (Sigma St. Louis, MO, USA) for 20 min, followed by fixation and analysis by flow cytometry (BD LSR II).

A375 and Hep2 tumor cells treated with PAM for 24 h, and control non-treated tumor cells, were used for preparing tumor lysates in DC cultures. Totally  $5 \times 10^6$  live tumor cells were incubated in 500 µL of 100% PAM for 24 h, and a loss of viability >90% in the PAM-treated cultures was confirmed by Trypan blue staining. Both PAM-treated and control tumor cells were then frozen at  $-80^\circ\text{C}$  for 10 min and afterward thawed at room temperature for 10 min in an ultrasonic bath, and the process was repeated at least 7 times. After that, 100 µL of complete tumor lysates were added in 2 mL of DC cultures (total 5% vol.) thus providing an equivalent of 1:1 DC: lysed tumor cells, respectively.

Direct cytotoxicity of PAM on DCs was evaluated by treating 4-day DC cultures with 12.5% or 25% of PAM, whereas control DC cultures were treated with equivalent volumes of basal RPMI medium, for the next 24 h. Apoptosis was detected by an Annexin V-FITC/PI staining kit according to manufacturer's recommendations (Thermo Fisher, Waltham, MA, USA) and analyzed on a flow cytometer (LSR II, Becton Dickinson, East Rutherford, NJ, USA). Oxidative status in the DCs treated with PAM for 24 h was assessed by staining the cells with 2.5 µM dihydrorhodamine (DHR) in PBS for 30 min at  $37^\circ\text{C}$ , followed by analysis on the flow cytometer.

### 2.5. Mixed Cell Reactions

The allostimulatory capacity of DCs (prepared as in Section 2.3) was tested by co-cultivating MACS-purified T cells ( $1 \times 10^5$ /well of 96-well U-bottom plate) labeled with CellTrace<sup>™</sup> Far Red (1 µM, Thermo Fisher, Waltham, MA, USA), with a different number of DCs ( $1 \times 10^4$ ,  $0.5 \times 10^4$ ,  $0.25 \times 10^4$  cells/well) for 5 days. To avoid transferring any stimuli

from DC cultures, the cells were washed twice in RPMI medium prior to co-cultivation with T cells. After 5-day co-cultures, the cells were washed in PBS, stained with 7AAD and then analyzed on a BD LSR II flow cytometer. CellTrace Far Red dilution was analyzed after exclusion of doublets and dead (7AAD+) cells, and the percentage of proliferated T cells (CellTrace Far Red<sup>low</sup>) was calculated in FCS Express (DeNovo Software, Pasadena, CA, USA). The capacity of DCs to induce allogeneic cytokines production by T cells was analyzed after 5-day co-cultures (1:20 DC:T cell ratio), after treating the co-cultures with PMA (20 ng/mL, Sigma, St. Louis, MO, USA), calcium ionophore (500 µg/mL, Sigma, St. Louis, MO, USA) and monensin (3 µg/mL, Sigma, St. Louis, MO, USA) for the last 4 h to stimulate cytokine accumulation in the primed T cells. Harvested cells were washed in 0.1% NaN<sub>3</sub>/PBS and stained for surface and intracellular cell markers. To detect cytokines produced in co-culture-supernatants, DC/T cell co-cultures carried out likewise, were treated with PMA and Ca Ionophore for the last 4 h, and the supernatants were collected after centrifugation at 2000 RPM for 5 min.

To evaluate the capacity of DCs to prime cytotoxic T cells, autologous T cells isolated from freshly obtained PBMC were co-cultured with A375 lysate-loaded or non-loaded DCs at a 1:40 DC:T-cell ratio for 6 days. Recombinant IL-2 (10 ng/mL) was added to these co-cultures on day 0 and day 3. After 6 days, the proliferation of autologous T cells was evaluated by staining the cells fixed in ice-cold ethanol (75%) for 2h at −20 °C and washed with PBS, with an anti-human Ki-67 antibody (Wuhan Fine Biotec Co., Wuhan, China) and secondary anti-rabbit IgG Alexa 647 (Abcam, Cambridge, UK), followed by staining with PI (1 µg/mL, Sigma, St. Louis, MO, USA) prior to the analysis of proliferation on a flow cytometer. Cytotoxic activity of the primed autologous T cells towards live A375 tumor cells was carried out by co-cultivating T cells with CellTrace Far Red-labeled live A375 cells (5 × 10<sup>5</sup> cells) at 1:2, 1:4 and 1:8 A375: T cell ratios for 4 h. After that, the cells were collected and labeled with PI prior to analysis on a flow cytometer. For all mixed cell cultures, T cells cultivated without DCs and A375 cells cultivated without T cells were used as controls.

## 2.6. Flow Cytometry

The flow cytometry analysis of DCs and T cells was performed on the flow cytometers CyFlow Cube 6 (Sysmex, Kobe, Hyogo, Japan) and LSR II (BD) by staining the cells with the following directly conjugated antibodies: anti-CD83-FITC, anti-CD86-PE, CD86-PerCPcy5.5, anti-CD40-APC, anti-CCR7-FITC, anti-IL17A-Alexa Fluor 488, anti-CD25-PerCPcy5.5, anti-CD127-PE, anti-IL10-APC, anti-HLA-DR-APCCy7 (Biolegend Inc., San Diego, CA, USA), anti-HLA-DR-PerCP (Miltenyi Biotec, Bergisch Gladbach, Germany), anti-ILT4-PE, anti-IFN $\gamma$ -FITC (R&D Systems Minneapolis, MN, USA), anti-IL-12p40/p70-PE, anti-IL-10-FITC (BioRad, Hercules, CA, USA), anti-CD4-APC, anti-CD8-PerCPcy5.5, anti-Granzyme A-PE (eBioscience, San Diego, CA, USA), anti-Foxp3-FITC, anti-IL-4-PerCP, anti-PDL1-PE (eBioscience, San Diego, CA, USA), anti-CD4-PE (Sysmex, Kobe, Hyogo, Japan), IgG1 negative control-PE, IgG1 negative control-FITC, IgG1 negative control-APC, IgG1 negative control PerCP, (Thermo Fisher, Waltham, MA, USA), IgG2 negative control APCCy7 (Millipore, Burlington, MA, USA). Surface staining with primary Abs was conducted in PBS/0.1% NaN<sub>3</sub>/0.5% FBS prior to the intracellular staining that was carried out using a flow cytometry fixation and permeabilization kit (Biolegend, San Diego, CA, USA). Signal overlap between the channels was compensated before each analysis using single labeled samples. Non-specific fluorescence was determined according to isotype control antibodies and fluorescence minus one (FMO) controls and at least 5000 cells were analyzed in each sample. Doublets were excluded according to forward scatter (FS) H/FSA, and dead cells were gated-out according to 7-aminoactinomycin D (7AAD) staining, fixable viability dye 620 (BD) staining, or low FSC properties.

## 2.7. Cytokines

TNF- $\alpha$ , IL-1 $\beta$ , IL-6, TGF- $\beta$ , IL12-p70, IL-10, IL-23 and IL-27 were measured in DC culture supernatants by a specific duo-set sandwich enzyme-linked immunosorbent assay (ELISA) (R&D Systems, Minneapolis, MN, USA) in duplicates according to manufacturer's protocol. The levels of cytokines in DC/T-cell co-cultures were determined by the LegendPlex human Th cytokine panel 13-plex (Biolegend) in duplicates, according to the manufacturer's protocol. Unknown concentrations of cytokines were calculated from standard curves generated with the manufacturer-supplied recombinant cytokines and fitting with a 4-parameter (log) dose/response curve (GraphPad Prism 8, GraphPad Software, San Diego, CA, USA).

## 2.8. Statistical Analysis

Repeated-measures one-way analysis of variance (RM-ANOVA) was performed, followed by Tukey's multiple comparison test, to analyze differences in means between the different groups of treated cells and control groups (GraphPad Prism 8). Student's T test was used to evaluate differences in levels of RONS in PAM. Data are presented as means  $\pm$  SD of the indicated number of independent experiments (different time for experiments with cell lines, different DC donors and/or DC/T cell pairs), and differences were considered significant at  $p$  values of  $\leq 0.05$ . For data presented as a heatmap, the values of each cytokine obtained in each experiment were normalized to the range 0–1, according to the following formula:

$$y = \bar{X} \left( \frac{x - \min(x)}{\max(x) - \min(x)} \right) \quad (1)$$

with  $y$ - heatmap value;  $x$ - level of cytokine in a sample in one dataset,  $(x)$ -dataset of one type of cytokine

## 3. Results and Discussion

### 3.1. Two-Electrode Plasma Jet Induces Efficient Accumulation of RONS in PAM

A two-electrode dielectric barrier discharge (DBD) atmospheric pressure plasma jet (APPJ) was used as a CAP source (Figure 1) for treating the RPMI 1640 cell culture medium. The power deposited in the effluent discharge in contact with the surface of RPMI 1640 was 1.2 W. The resistors ( $R = 1 \text{ k}\Omega$ ) in this grounded branch of the electrical circuit used for monitoring current waveforms showed stable plasma throughout the PAM generation. The distance of the APPJ to the treated liquid was kept constant at 5 mm in all experiments and treatment time was 5 min. Plasma treatment did not change the pH of the medium, according to stable phenol-red coloring and the measurements of pH. We have measured the three long-lived RONS and their concentrations in untreated RPMI 1640 and the PAM-RPMI 1640 are shown in Figure 2. In the literature,  $\text{H}_2\text{O}_2$  is the most commonly detected and characterized, followed by  $\text{NO}_2^-$ . At the end of the list is the  $\text{NO}_3^-$  radical, which is scarcely reported albeit it plays an important role in PAM-cell interactions. Their concentration mainly depends on the type of plasma device used, deposited power in the discharge, feeding gas, treatment time, and treated volume. Adding the type of the treated liquid media to this large variety of parameters that can influence the concentration of deposited RONS in the cell medium makes it very difficult to perform a direct comparison of two atmospheric plasma systems [24]. Nevertheless, the described diagnostics provide enough information to ascertain the stability of plasma and identify the most abundant species.

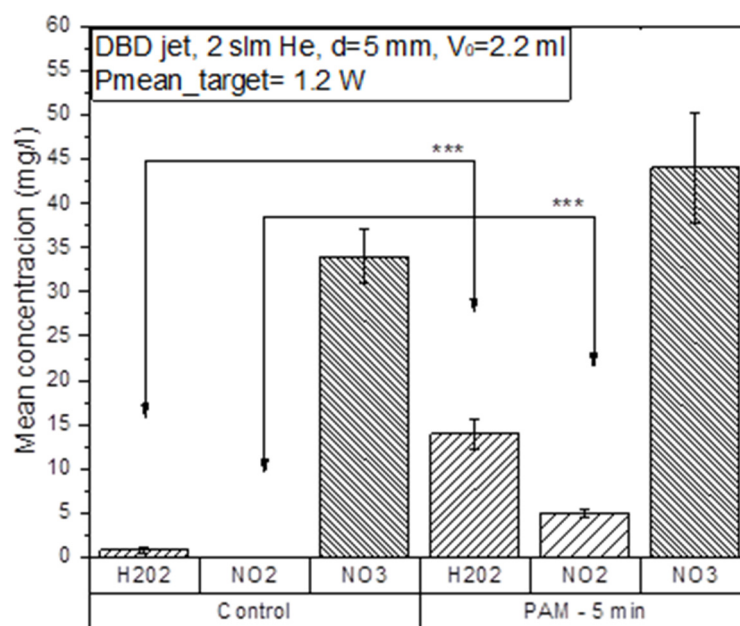


**Figure 2.** Measured concentrations of RONS in the plasma-activated medium PAM- RPMI 1640 compared to concentrations in the untreated RPMI 1640 medium. Helium flow during the treatments was kept constant at 2 slm and the power deposited in the discharge in contact with the sample was 1.2 W. The distance between the edge of the APPJ and the sample surface was 5 mm in all treatments. \*\*\*  $p < 0.005$  compared to non-treated control RPMI 1640 (0% PAM) or as indicated by line.

The measured concentration of hydrogen peroxide was 1 mg/L and of nitrate 34 mg/L, while there was no nitrite detected in the untreated RPMI 1640 medium. The largest increase in concentration was observed for hydrogen peroxide, which increased 14 times after the treatment. Hydrogen peroxide is relatively stable and has strong oxidizing properties that can cause lipid peroxidation and, among other roles, serves as a cellular messenger. In the case of PAM-RPMI 1640, the highest yield of  $H_2O_2$  was expected due to the presence of organic molecules in the cell medium (like glucose) [25]. Regardless of some reports in the literature stating that the increase in the concentration of  $H_2O_2$  is generally responsible for the decrease in the viability of cancer cells [22,26], the main reason for this is the synergistic effect with reactive nitrogen species [27]. Therefore, we monitored the concentration of nitrates and nitrites in PAM-RPMI 1640. The concentration of nitrites in PAM was 5 mg/L and the nitrate concentrations increased by 30% compared to the untreated control RPMI medium.

### 3.2. PAM Induces Immunogenic Cell Death in Tumor Cells

ICD of tumor was reported as beneficial for triggering a DC-mediated anti-tumor response [28]. Increased presence of RONS in PAM makes it a good candidate for inducing ICD in tumor cells. Therefore, we examined the dose-dependent cytotoxicity of PAM towards tumor A375 melanoma cell line and laryngeal carcinoma Hep2 cell line, as well as towards non-tumor cells, such as immortalized L929 cell line and PBMCs (Figure 3a). Results from an MTT assay suggested that even the low doses of PAM (12.5% and 25%) were cytotoxic for A375 and Hep2 cells after 24h culture, but not for L929 cells and PBMCs. Higher doses (50% and 100%) of PAM significantly reduced the metabolic activity of all cell types, but the effect was most prominent in cultures with the tumor A375 and Hep2 cells. According to the ISO standard on the cytotoxicity of medical devices, a 30% reduction in MTT is considered as non-cytotoxic [29], suggesting that the reduction of MTT in the cultures of L929 cells and PBMCs treated with 50% PAM could be considered as non-cytotoxic as well. Our results are in line with previous findings showing that induction of cell death by CAP or PAM treatment is a universal phenomenon in malignant cells [30–33]

in contrast to non-malignant cells, which are more resistant [34]. Towards tumor cells, PAM showed dose- and time-dependent cytotoxic responses in vitro. In addition, the selectivity of PAM against tumor cells is influenced by the medium to be activated and the type of tumor cell lines used [35].

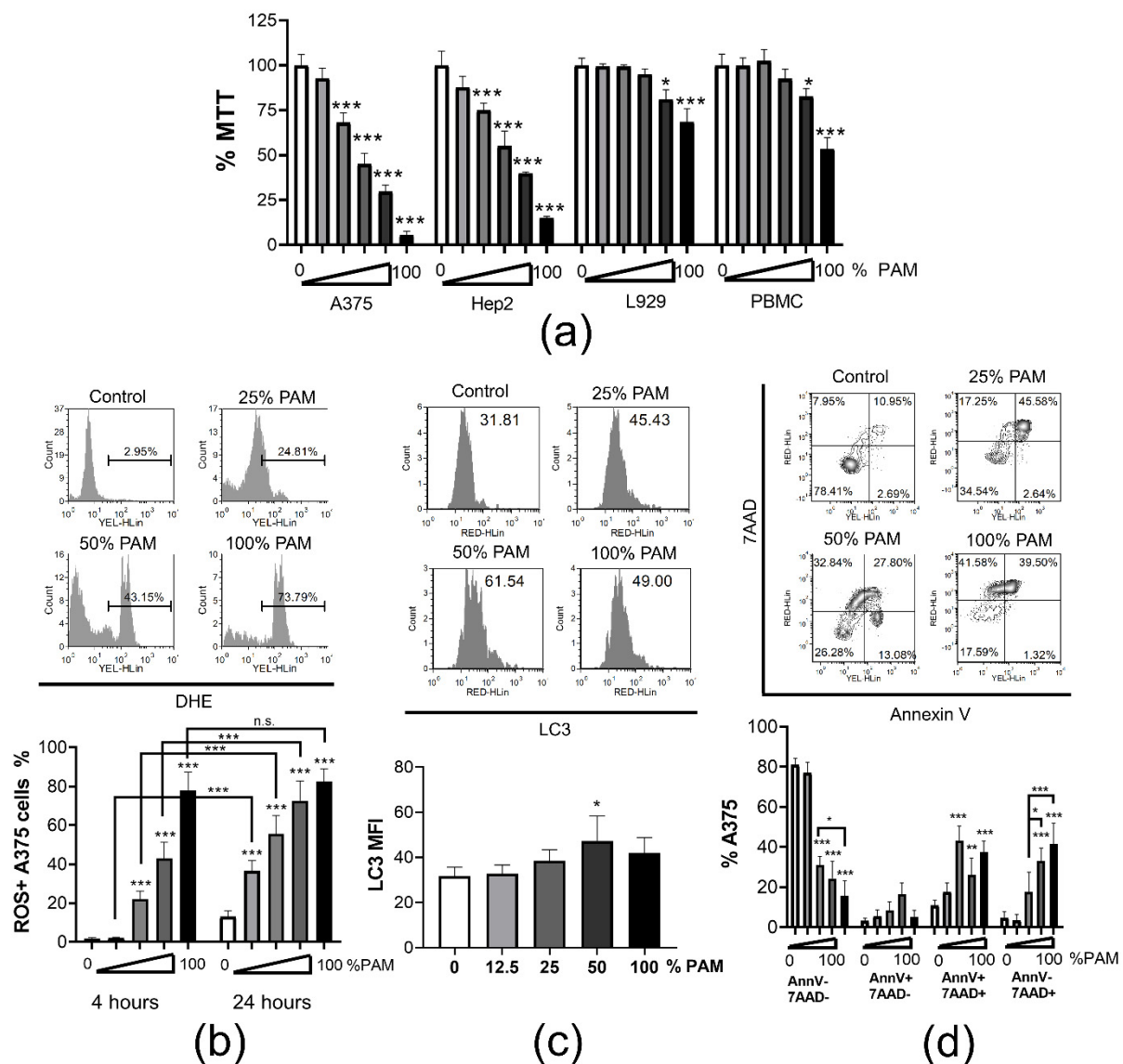


**Figure 3.** Dose dependent cytotoxicity of PAM. (a) Metabolic activity of A375, Hep2, L929, PBMC was assessed by MTT assay after 24 h treatment with serial dilutions of PAM (0% (white bars), 6%, 12.5%, 25%, 50% and 100% (black bars)) in complete RPMI medium. The results are shown as % MTT relative to the non-treated corresponding control cells 100%. Data from two independent experiments, each carried out in triplicates, are shown as the average % of MTT  $\pm$  SD. (b) A representative data on the measurement of oxidative stress by DHE in A375 cells cultivated in the presence different concentrations of PAM for 4 h is shown. The summarized data from two independent experiments, in which the oxidative stress with the different doses of PAM (0% (white bars), 12.5%, 25%, 50% and 100% (black bars)) was measured after 4 h or 24 h as indicated, is shown as mean % of ROS+ cells  $\pm$  SD. (c) A representative histograms on measurements of membranous LC3 expression in permeabilized A375 cells is shown with the indicated total mean fluorescence intensity (MFI), and the summarized data from two experiments is shown as MFI of LC3  $\pm$  SD. (d) Analysis of cell death by Annexin V/7AAD staining (AnnV–7AAD– viable; AnnV+7AAD– early apoptosis; AnnV+7AAD+ late apoptosis; AnnV–7AAD+ necrosis) in A375 cells is shown, carried out after 24 h cultures in presence of different doses of PAM (0%, 12.5%, 25%, 50%, 100%). Representative dot-plots and summarized data are shown as mean % A375 cells  $\pm$  SD of 3 independent experiments. \*  $p < 0.05$ , \*\*  $p < 0.01$ , \*\*\*  $p < 0.005$  compared to non-treated control cells (0% PAM) or as indicated by line.

High concentrations of RONS, both originating from PAM and produced by PAM-exposed cancer cells were shown responsible for cell death predominantly via induction of oxidative stress [10,36]. Considering that oxidative stress in dying cells is a hallmark of ICD [37], we analyzed oxidative stress in PAM-treated A375 cells by measuring intracellular ROS with dihydroethidium (DHE) staining (Figure 3b). PAM applied at the concentrations of 25% and higher, induced significant accumulation of ROS in A375 cells after 4 h cultures. Thereby, 100% PAM induced oxidative stress in nearly 80% of cells. After 24 h cultures, even the lower doses of PAM (12.5% PAM) induced significant accumulation of ROS in A375. These results are in line with the general mode of PAM and CAP actions in tumor cells [38]. It is known that ROS production by tumor cells treated with PAM depends on PAM-derived RONS (nitrite and H<sub>2</sub>O<sub>2</sub>) and the generation of initial singlet oxygen (<sup>1</sup>O<sub>2</sub>). This molecule is formed through the complex interaction between NO<sub>2</sub><sup>-</sup> and H<sub>2</sub>O<sub>2</sub> and the tumor cells expressing nicotinamide-adenine dinucleotide phosphate oxidase 1 (NOX1), catalase, sodium dismutase (SOD) on their surface [13]. The formation of peroxynitrite (ONOO<sup>-</sup>) plays a key role in these processes [39]. At the site of inactivated catalase, cell-generated H<sub>2</sub>O<sub>2</sub> enters the cell via aquaporins, depletes glutathione, induces the HOCl signaling pathway and promotes lipid peroxidation and cell death by apoptosis [40,41]. Non-malignant cells lack the expression of NOX1, catalase, and SOD on their surface making them resistant to cell death as long as the concentration of H<sub>2</sub>O<sub>2</sub> is below a cytotoxic threshold level [10]. An investigation showed that the cytoprotective effects of mild PAM against oxidative stress in non-malignant cells such as human skin fibroblasts are characterized by the up-regulation of HO-1 mediated by the Nrf2-ARE pathway [42].

Reactive oxygen species and RNS are the key intracellular signal transducers sustaining autophagy [43]. Autophagy is essential for the survival of cancer cells, since it provides the required energy and removes damaged organelles [44]. However, intensive and persistent activation of autophagy leads to programmed cell death [45]. Moreover, autophagy was shown critical for the induction of the ICD of tumor in a mouse model [46]. Therefore, we next measured autophagy and apoptosis in the A375 treated with PAM for 24 h by quantifying membrane-bound LC3, a key marker of autophagosome formation [47], and by annexin-V/7AAD staining, respectively. It was found that autophagy was indeed triggered in the A375 cells treated with 50% PAM, but not with higher or lower doses of PAM (Figure 3c). According to Annexin V/7AAD staining, both increased apoptosis and necrosis were observed in the A375 cells treated with 50% and 100% PAM for 24 h, whereas lower doses of PAM (25%) induced predominantly the apoptosis of these cells (Figure 3d). Apoptosis was described as a dominant mode of cell death induced by PAM. Adachi et al. [48] showed that PAM reduced the mitochondrial membrane potential, down-regulated the expression of the anti-apoptotic protein Bcl2, activated poly (ADP-ribose) polymerase-1 (PARP-1) and released apoptosis-inducing factor (AIF) from mitochondria, suggesting a caspase-independent apoptotic pathway. Aggressive tumors have a different cellular machinery that protects them from the apoptosis caused by anticancer agents, thereby making them drug resistant. Therefore, cancer therapy based on the induction of non-apoptosis has been considered as an alternative approach to treat apoptosis-resistant cancer cells, including necroptosis [48]. However, the effect of CAP and PAM on this form of cancer cell death has not been sufficiently investigated.

In addition to apoptosis and necrosis, the ICD of tumor cells is characterized by the induction of heat-shock proteins, particularly their plasma membrane localization [49], as well as the release of inflammatory mediators, such as HMBG1, IL-1 $\beta$  and others [50]. In line with this, the membrane expression of heat-shock proteins HSP60 and HSC70 on both A375 and Hep2 cells increased after 4 h treatment with high concentrations of PAM (Figure S1a,c). Moreover, significantly higher levels of IL-1 $\beta$  were detected in 24 h culture supernatants of both tumor cell lines in the presence of 50% and 100% PAM, compared to their levels in the control culture supernatants (Figure S1b,d). Considering that heat-shock proteins and IL-1 $\beta$  are strong stimulators of the immune response [50], these results suggested that PAM-treated tumor cells could strongly potentiate immune response as well.

It has been shown that PAM induced apoptotic cell death in a time-dependent manner in endometrial cancer cells. The results correlated with the G2/M-phase arrest at all PAM concentrations and the induction of intracellular ROS accumulation [51]. In addition, PAM induced autophagy as judged by increased intracellular LC3B protein expression simultaneous with a decrease in the phosphorylated mammalian target of rapamycin (mTOR) and phosphorylated AKT protein levels and a decline of autophagy-related (p62 and ATG family) proteins. The autophagy inhibitor MHY1485 rescued PAM-induced cell death by decreasing the expression of LC3B but without the influence on phosphorylation of mTOR and AKT [51]. Adhikari et al. [52] have recently shown that CAP and synimarin nanoemulsion together activate autophagy in melanoma G-361 cells by activating PI3K/mTOR and EGFR pathways, expressing autophagy-related transcription factors and genes. In contrast, a preliminary report by Ando et al. [53] showed that plasma activated infusion (PAI) solution suppressed the autophagy in melanoma and osteosarcoma cell lines by activating the mTOR pathway. The authors suggested that ROS-mediated necroptosis, but not autophagy, plays a dominant role in the cell death induced by PAI. Our results are in accordance with these, showing that the highest doses of PAM induced predominantly necrosis but not autophagy, and the potentiate induction of ICD markers, such as heat-shock proteins and IL- $\beta$ . However, all three types (autophagy, apoptosis and necrosis) of cell death are seen with 50% PAM, suggesting that further investigation of these mechanisms is necessary.

### 3.3. Tumor Lysates Prepared with PAM-Treated Cells Potentiate Maturation of Dendritic Cells

Complete tumor lysates are considered attractive and affordable sources of tumor antigens suitable for an autologous anti-tumor DC vaccine [54]. Several clinical trials used whole autologous tumor lysates prepared by multiple freeze–thaw cycles of tumor cells for DC vaccines [55,56]. Necrotic cell death by freeze-thaw enables the release of DAMPs from tumor cells such as HSP70, HSP90, HMGB1, and others [57], driving the maturation of DCs [58]. However, the finding that freeze-thaw necrotic tumor cells could inhibit toll-like receptor (TLR)-induced maturation and functions of DCs [59], opened serious doubts about the immunogenicity of thus prepared tumor lysates [60]. Different protocols for inducing immunogenic tumor lysates have been described including heat-treatment [61], hydrostatic pressure [62], electroporation [63], and others [60]. Nevertheless, it remained unclear how these protocols compare to standard freeze-thaw tumor lysates, and whether the application of PAM for the treatment of tumor cells could improve the immunogenicity of their lysates. Considering that PAM induced the ICD of A375 cells, we next investigated whether the A375 lysates prepared from A375 cells treated with 100% PAM for 24 h (PAM-A375lys) display better effects on DC maturation compared to the lysates prepared from non-treated A375 cells (A375lys). Thereby, LPS/IFN- $\gamma$  treatment was additionally used as a strong maturation stimulus potentiating the Th1 polarizing capacity of DCs, which is highly desirable in the DC anti-cancer vaccine [64,65].

Both A375 lysates increased the expression of the costimulatory CD86 molecule and reduced CD40 expression by immature (im) DC, whereas PAM-A375lys also increased the expression of HLA-DR by imDC compared to control imDC (Figure 4). Upon LPS/IFN- $\gamma$  treatment, the expression of all markers tested was up-regulated significantly. Thereby, both lysates additionally up-regulated the CD86 expression by mDC and inhibited LPS/IFN- $\gamma$ -induced up-regulation of HLA-DR and PDL1 by mDC. However, the PAM-treated A375 lysate displayed an additional stimulatory effect on the up-regulation of CD83 on mDC and reduced the LPS/IFN- $\gamma$ -induced up-regulation of ILT-4 on mDC significantly. In contrast, the control A375 lysate inhibited LPS-induced up-regulation of CD40 on mDC, unlike the PAM-treated A375 lysate.

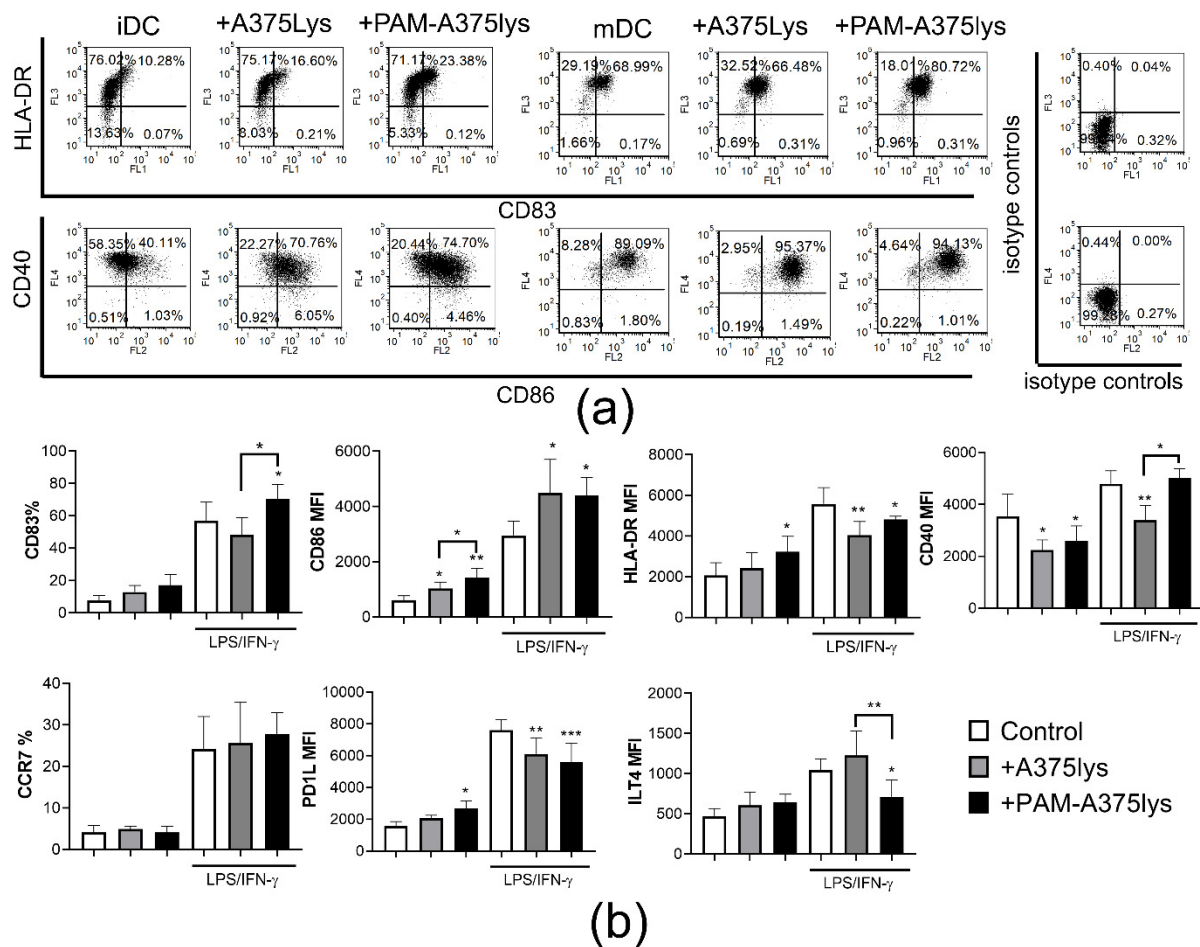


**Figure 4.** Effects of PAM-treated A375 lysates on phenotypic properties of DCs. Immature DCs differentiated for 4 days in the presence of GM-CSF/IL-4, were treated with the A375 lysate or the PAM-A375 lysate at 1:1 A375: DCs ratio, and after 4 h they were stimulated with LPS/IFN- $\gamma$  or not, for the next 16 h. (a) A representative experiment on CD83/HLA-DR and CD40/CD86 co-expression analysis is shown and, (b) the summarized data from 3 independent experiments (different DC donors) are shown for the % of cells expressing the indicated surface marker, or as mean fluorescence intensity (MFI),  $\pm$ SD. \*  $p < 0.05$ , \*\*  $p < 0.01$ , \*\*\*  $p < 0.005$  vs corresponding control DCs (white bars) or as indicated with lines (RM-ANOVA, Tukey's multiple comparison test). Statistical significance between the corresponding iDCs and mDCs was not indicated for clarity.

Miebach et al. [66] showed recently that colorectal cancer cells treated with an argon-based plasma jet increase the expression of CD80 and CD86 by monocyte-derived DCs in co-culture, unlike a neon-based plasma jet, which induced similar weak (<30%) cytotoxicity in tumor cell culture. However, the majority of CAP-treated tumor cells in the DC co-cultures were live in that study, and it remained unclear how they modulate the maturation and functions of DCs triggered by stimuli. Our study is the first report showing that DCs treated with PAM-tumor lysates display a good immunogenic phenotype, especially after the stimulation with LPS/IFN- $\gamma$ , according to their higher CD83 and lower expression of ILT-4. ILT-4 was demonstrated as an important new checkpoint molecule in tumor immunotherapy involved in the induction of regulatory T cells [67]. On the other hand, CD83 is critically involved in the maturation of DCs and their resistance to pro-tolerogenic effects of IL-10 [68].



### 3.4. Tumor Lysates Prepared from PAM-Treated Cells do Not Impair High IL-12/IL-10 Production Ratio by DCs

Besides the mature phenotype of DCs, the induction of an efficient anti-tumor response by DCs is marked by their increased IL-12 production or IL-12/IL-10 production ratio [69]. Therefore, intracellular expression of IL-12p40/p70 was analyzed in DCs after the cultures with A375 lysates (Figure 5). It was shown that the A375 lysates did not induce significant IL-12 expression in imDCs. The strongest induction of IL-12p40/p70 expression was detected after LPS/IFN- $\gamma$  treatment of PAM-A375lys-treated mDCs and control mDCs (Figure 5a), whereas mDCs treated with a control A375 lysate displayed significantly lower IL-12p40/p70 expression.

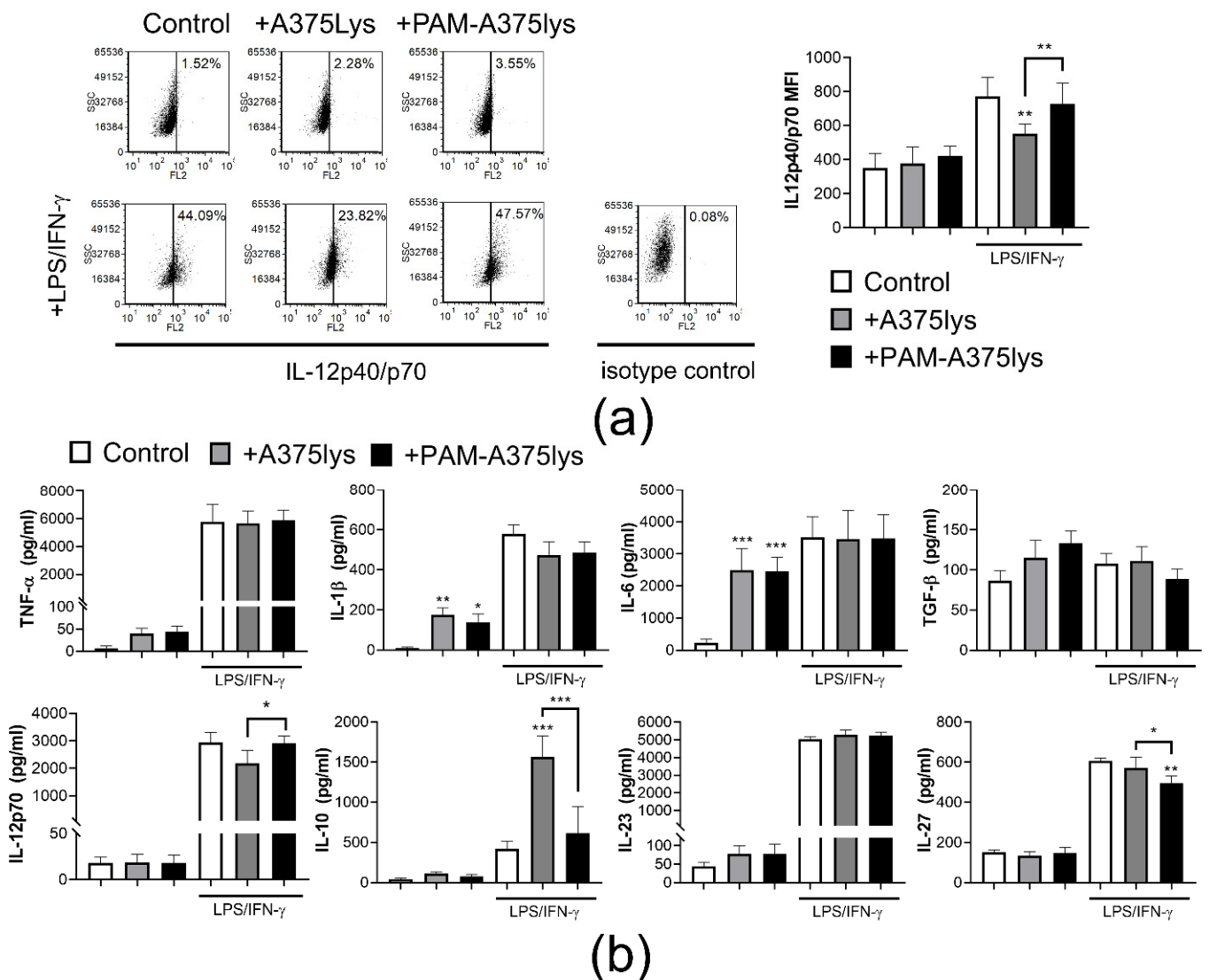


**Figure 5.** Effects of PAM-treated A375 lysates on cytokines expression by DCs. Immature DCs differentiated for 4 days in the presence of GM-CSF/IL-4, were treated with A375 lysate or PAM-treated A375 lysate at 1:1 A375: DC ratio, and after 4 h they were treated with LPS/IFN- $\gamma$  or not, for the next 16 h. (a) A representative experiment on IL-12p40/p70 expression analysis is shown, and the summarized data from 3 independent experiments (with different DC donors) are shown as mean fluorescence intensity (MFI)  $\pm$  SD. (b) The levels of indicated cytokines detected by ELISA in the cell-culture supernatants are shown as pg/mL  $\pm$  SD. \*  $p < 0.05$ , \*\*  $p < 0.01$ , \*\*\*  $p < 0.005$  vs. corresponding control DCs (white bars) or as indicated with lines (RM-ANOVA, Tukey’s multiple comparison test). Statistical significance between the corresponding iDCs and mDCs was not indicated for clarity.

A similar trend for IL-12 production was observed when protein levels were measured in cell-culture supernatants by ELISA (Figure 5b). However, it was found that control A375lys-treated mDCs produced substantially higher levels of IL-10 compared to PAM-A375lys or control mDCs, suggesting that PAM-A375lys mDCs display a significantly better IL-12/IL-10 production ratio than A375lys-treated mDCs. Previous reports also showed that freeze-thaw tumor lysates stimulate IL-10 production by mouse DCs [59], which could be a consequence of direct inhibitory effects of autocrine IL-10 on the capacity of DCs to produce IL-12 [70]. However, mouse IL-10<sup>-/-</sup> DCs treated with tumor lysates also displayed a reduced capacity for IL-12 production suggesting that this effect could be independent of IL-10 as well [59]. It remains unclear whether similar mechanisms occur in human DCs treated with tumor lysates, so this requires further investigations.

PAM-A375lys and control A375lys both increased IL-1 $\beta$  and IL-6 production by imDCs but did not modulate their production by mDCs (Figure 5b). The significance of this finding is still not clear, since a NLRP3-regulated increase in IL-1 $\beta$ , and subsequently IL-6 production was reported to promote tumor growth [71]. In contrast, Ghiringhelli et al. [72] showed that the activation of NLRP3-dependent IL-1 $\beta$  production by DCs, triggered via ATP release from dying tumor cells and activation of the P2X7 purinergic receptor, is critical for the efficient priming of IFN- $\gamma$ -producing CD8 T cells by dying tumor cells. PAM-A375lys-treated mDCs also produced significantly lower levels of IL-27 compared to both control A375lys-treated mDCs and control mDCs. IL-27 has been implicated in promoting cancer progression [73], and high IL-27 levels are associated with advanced cancer [74], most probably due to its capacity to induce regulatory T cells [75]. Therefore, the attenuating effects of PAM-A375lys on IL-27 production by DCs could be interpreted as a desirable effect for the development of a DC cancer vaccine.

To observe whether different kinds of tumor cells induce similar effects on DC maturation and IL-12/IL-10 production ratio, Hep2 tumor cells were used instead of A375 to prepare lysates after the PAM treatment. It was observed that mDCs pre-treated with PAM-Hep2lys express higher levels of CD83 and CD86, lower levels of PDL1, and display a higher IL-12/IL-10 production ratio than the control Hep2lys-treated mDCs, although Hep2lys did not stimulate IL-10 production by DCs (Figure S2a,b). PAM-Hep2lys treated mDCs also displayed higher expression of CD86 and lower expression of PD-L1 compared to control mDCs. These results suggest that the phenomenon of increasing the immunogenicity of tumor lysates by PAM is not limited to a single tumor cell line. However, additional investigations are necessary to evaluate whether this phenomenon applies to primary tumors isolated from cancer patients as well.

We also assessed whether contaminating PAM added to DC cultures along with the lysates (5% PAM) could have directly affected the maturation and the IL-12/IL-10 production ratio by DCs and found no significant effects (data not shown). The cells were also treated with 12.5% PAM, which is more than twice the amount of PAM added with the PAM-A375lys in DC cultures, as well as 25% PAM, as the highest non-toxic dose of PAM for PBMCs (Figure S3). It was found that neither concentration of PAM directly affected oxidative stress and apoptosis in DCs after 24h (Figure S3a,b), nor did it affect the maturation and IL-12 production capacity of DCs (Figure S3c,d). However, 25% of PAM reduced LPS/IFN- $\gamma$ -induced increase in IL-10 production by these cells. Unlike T and NK cells, which are more susceptible to ROS-inducing treatments [76,77], monocytes and DCs are more resistant due to their stronger anti-oxidative protection systems allowing them to secrete ROS as a part of normal immune functions [12,20,78]. However, an increased presence of exogenous ROS or their prolonged presence could induce depletion of glutathione in DCs leading to their reduced maturation and Th1 polarization capacity [79]. In this sense, 25% PAM induced attenuation of IL-10 production by DCs which could be interpreted as a beneficial effect in tumor therapy. Nevertheless, care should be taken when DCs are exposed to higher doses of PAM or for a longer period, as this could reduce the DC-mediated immune response. Cumulatively, our results suggest

that PAM-treated tumor lysates display good stable immunogenic properties on DCs, and that the effect is not merely a direct consequence of the contaminating PAM.

### *3.5. DCs Loaded with PAM-A375 Lysate Preserve Th1, Potentiate Cytotoxic CD8 T Cells and Th17 Response*

DC-mediated induction of an efficient anti-tumor response involves their increased capacity to induce Th1 and/or Th17 cells [80]. Therefore, the immunogenic properties of DCs loaded with A375 lysates were next investigated in co-cultures with allogeneic T cells to evaluate their T cell polarization capacity (Figure 6). It was found that PAM-A375lys-treated mDCs significantly increased the proportion of Th17 cells (IL-17A<sup>+</sup> CD4<sup>+</sup> T), IL17<sup>+</sup> CD8 T cells and cytotoxic CD8 (IFN- $\gamma$ <sup>+</sup> Granzyme A<sup>+</sup> CD8<sup>+</sup>) T cells compared to both control mDC and A375lys-treated mDC. According to the unaltered IL-12 production by PAM-A375lys-treated mDCs (Figure 4b), and its role [81], we also did not find altered proportions of Th1 (IFN- $\gamma$ <sup>+</sup> CD4<sup>+</sup>T cells) cells in co-culture with these DCs. In contrast, control A375lys-treated DCs reduced the proportion of Th1, Th17 and cytotoxic CD4 T cells (IFN- $\gamma$ <sup>+</sup> Granzyme A<sup>+</sup> CD4<sup>+</sup>) compared to control mDCs, probably due to their increased capacity to secrete IL-10, which is known to inhibit Th1 and Th17 polarization [82]. Moreover, PAM-A375lys-treated mDCs significantly reduced the proportion of Th2 (IL-4<sup>+</sup> CD4<sup>+</sup>) cells compared to mDCs, unlike A375lys-treated mDCs (Figure 6a,b). In general, mDCs induced lower levels of Th2 cytokines (IL-4, IL-5, IL-13) and higher levels of IL-6, Th9 (IL-9), Th1 (IFN- $\gamma$ , IL-2, TNF- $\alpha$ ) and Th17 (IL17A, IL17F, IL21, IL22) cytokines in DC/T cell co-culture supernatants, as compared to co-cultures with imDCs (Figure 6c). Thereby, PAM-A375lys-treated mDCs were the most potent in relatively lowering the Th2 and increasing the Th1 and Th17 cytokines in co-culture supernatants, confirming that PAM-treated tumor lysates potentiate beneficial anti-tumor properties in DCs. In line with this, Th2 cells demonstrated pro-tumorigenic effects in a mouse tumor model, whereas Th1 and Th17 cells displayed the opposite effects [83,84]. PAM-A375lys-treated mDCs also displayed a significantly higher capacity to stimulate proliferation of allogeneic T cells compared to A375lys-treated mDCs (Figure 6d). These results are in line with the higher levels of IL-2 detected in PAM-A375lys-DC/T co-cultures, better maturation of PAM-A375lys DCs, and their stronger IL-12 production, all of which are critical for the induction of T cell proliferation [85–87].

Analysis of the alloreactive T cell response in DC co-cultures, does not allow direct assessment of the antigen-specific T cells response. Therefore, in a pilot experiment, we additionally tested whether autologous T cells primed with A375 lysates-loaded DCs proliferate and display cytotoxic activity towards live A375 cells after 6-days of priming with DCs. Encouragingly, we observed that the PAM-A375lys-treated mDCs induced the highest proliferation of autologous T cells in co-cultures (Figure S4a). Additionally, T cells primed with PAM-A375lys-treated mDCs displayed significantly higher cytotoxic activity towards live A375 cells after 4h of co-cultures compared to T cells primed with A375lys-mDCs or control mDCs, when the same number of primed T cells was used in the co-cultures (Figure S4b) suggesting that both increased proliferation and increased cytotoxic functions are potentiated by PAM-A375lys-treated DCs.

The increased proliferation and cytotoxic activity of T cells primed with control DCs which were not treated with tumor lysates, could be attributed to the presence of other proteins during co-cultures such as FCS [88]. Therefore, additional investigations on the antigen-specific effects of DCs, especially with cells from cancer patients, are necessary to delineate the antigen-specific and direct modulatory effects of PAM-A375lys on the DCs capacity to induce proliferation and cytotoxic autologous T cells.

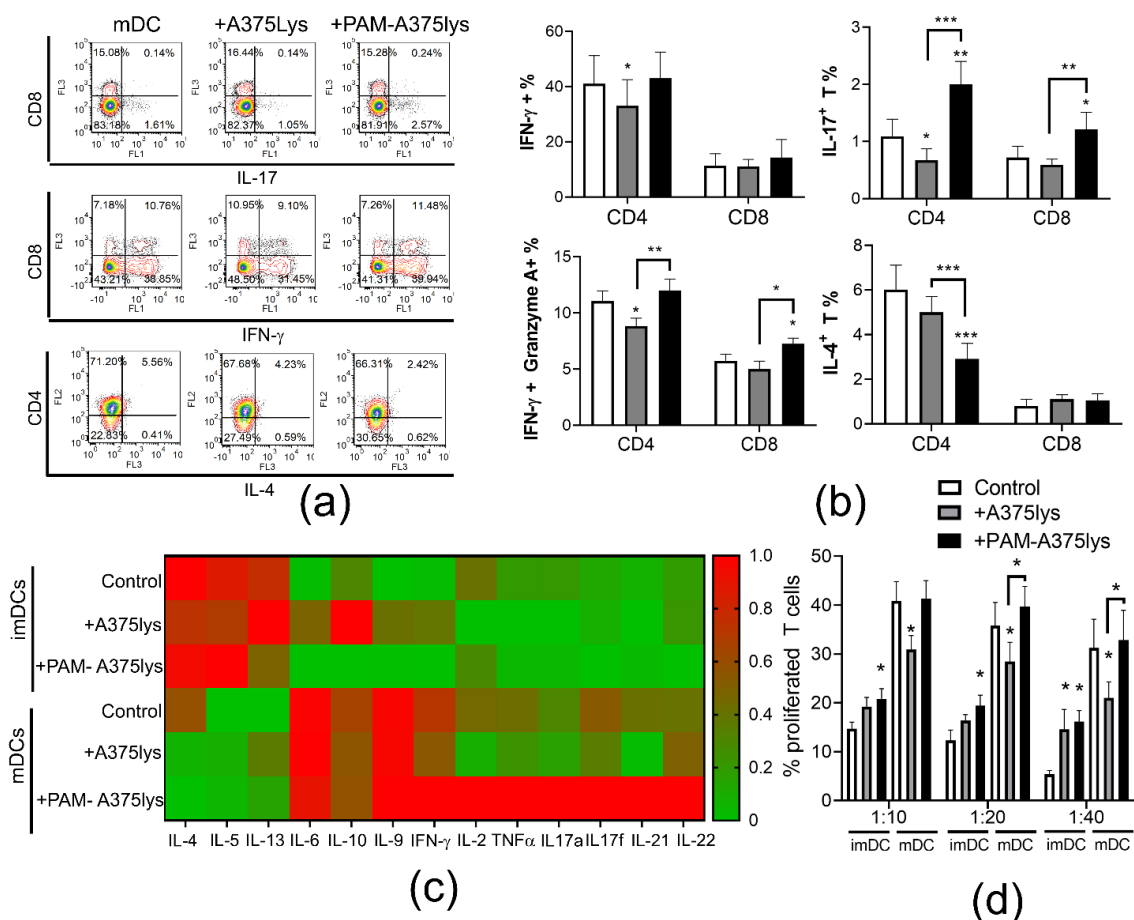


**Figure 6.** T cell polarization capacity of DCs treated with A375 lysates. (a) Immature DCs and mDCs, either treated or not with the A375 lysate (+A375lys) or the PAM-treated A375 lysate (+PAM-A375lys) were co-cultivated with MACS-purified allogeneic T cells ( $1 \times 10^5$ /well) at 1:20 (DC: T cell ratio) for 5 days, followed by the stimulation of co-cultures with PMA/Ca Ionophore/monensin for the last 3 h prior to their staining for flow cytometry. Representative dot-plots are shown on the total gated T cells that were co-cultured with the indicated mDCs and afterwards stained to CD4, CD8 and the indicated cytokines. (b) The summarized results on the % of cytokine/enzyme expressing cells normalized to 100% of T cells are shown as  $\% \pm$  SD of 3 independent experiments. (c) The levels of cytokines from DC/T cell co-cultures as in (a), stimulated for the last 3 h with PMA/ Ca ionophore, were measured with the LegendPlex Th13-plex system from the co-culture supernatants. The results are shown as a heatmap wherein each cell represent the level of cytokine normalized in each experiment to the range of 0–1, and averaged from 3 independent experiments, as described in Materials and Methods. (d) The allogeneic T cell proliferation was analyzed after 5-day co-cultures of CellTrace Far Red-labeled T cells ( $1 \times 10^5$  cell/well) and different number of DC ( $1 \times 10^4$ ,  $0.5 \times 10^4$ ,  $0.25 \times 10^4$  cells/well), providing 1:10–1:40 DC: T cell ratios. The percentage of proliferated (CellTrace Far Red<sup>low</sup>) T cells is shown as mean  $\pm$  SD of 3 independent experiments. \*  $p < 0.05$ , \*\*  $p < 0.01$ , \*\*\*  $p < 0.005$  vs. corresponding control DCs (white bars) or as indicated with lines (RM-ANOVA, Tukey's multiple comparison test). Statistical significance between the corresponding iDC and mDC was not indicated for clarity.

### 3.6. DCs Loaded with PAM-Tumor Lysate Do Not Induce Tregs

An efficient immunogenic DC vaccine ought to potentiate the Th1/Th17 response in T cells, but not regulatory T cells, which suppress immune response and display pro-tumorigenic effects [62]. In line with this, previous reports [89], including our own [23,90], have shown that regulatory IL-10-producing CD8<sup>+</sup> T cells display stronger suppressive activity than conventional FoxP3<sup>+</sup> CD4<sup>+</sup> T cells. Therefore, the presence of conventional CD4 Tregs (CD4<sup>+</sup>CD127<sup>-</sup>CD25<sup>+</sup>FoxP3<sup>+</sup>) and regulatory CD8<sup>+</sup> T cells (CD8<sup>+</sup>CD25<sup>+</sup>IL-10<sup>+</sup>IFN- $\gamma$ <sup>-</sup>) was analyzed in DC/T cell co-cultures. It was found that iDCs treated with control A375 lysates induced significant proportions of regulatory CD4 and CD8 T cells, unlike PAM-

A375lys-loaded DCs (Figure 7). Stimulation of A375lys-treated DCs with LPS/IFN- $\gamma$  did not affect the capacity of these DCs to induce CD4 Tregs, though it did lower their CD8 Treg inducing capacity. The higher capacity of A375lys-treated DCs to induce regulatory T cells is probably a consequence of their higher expression of ILT-4, IL-10, and IL-27 compared to PAM-A375lys-treated DCs. ILT-4 is critical for the induction of CD8<sup>+</sup>CD25<sup>+</sup>IL10<sup>+</sup> regulatory T cells by DCs, as we showed previously by blocking ILT-4 in the DC/T cell co-cultures [23]. IL-10 was shown to induce both regulatory CD8 and CD4 T cells [89], whereas IL-27 potentiates the functions of CD4<sup>+</sup> Tregs [91], leading to pro-tumorigenic effects in a multiple gene-deficient mouse model system [92]. Overall, these results suggest that PAM-A375lys induces desirable immunogenic properties in DCs, whereas A375 lysates prepared by the conventional freeze-thaw method could induce adverse effects in DC-vaccines via induction of pro-tumorigenic T cells subsets.

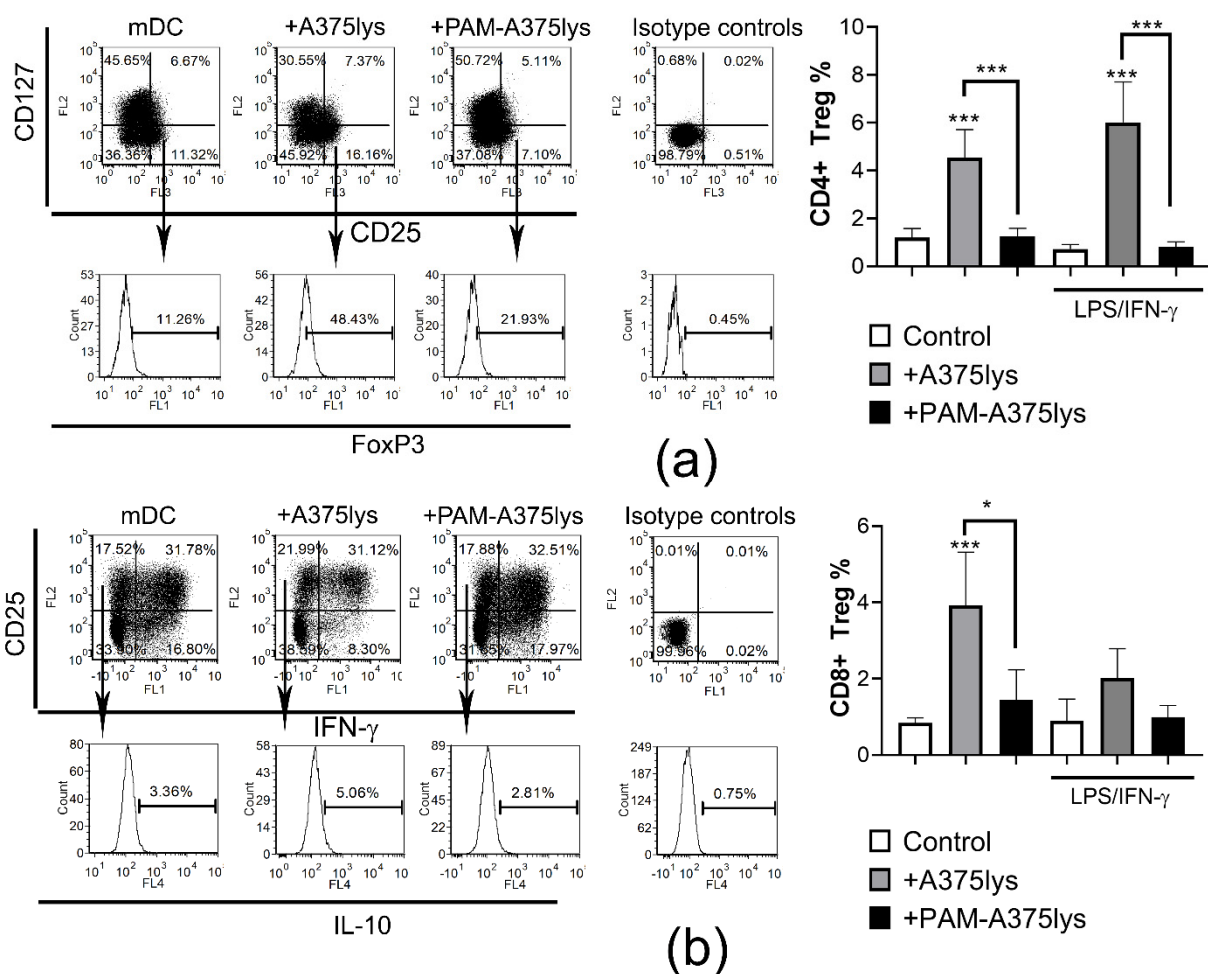


**Figure 7.** Treg induction capacity of DCs treated with A375 lysates. DCs either treated or not with the A375 lysate (+A375lys) or the PAM-treated A375 lysate (+PAM-A375lys) were co-cultivated with MACS-purified allogeneic T cells ( $1 \times 10^5$ /well) at 1:40 (DC: T cell ratio) for 5 days, in the presence of 2 ng/mL of IL-2, followed by the stimulation of the co-cultures with PMA/ Ca Ionophore/ Monensin for the last 3 h prior to their staining for flow cytometry. (a) Representative dot-plots are shown on total gated CD4<sup>+</sup> T cells after staining to CD25, CD127 and intracellular FoxP3. The summarized results on the % of CD4 Tregs are shown as %  $\pm$  SD of 3 independent experiments. (b) Representative dot-plots are shown on total gated CD8<sup>+</sup> T cells after staining to CD25, and intracellular IFN- $\gamma$  and IL-10. The summarized results on the % of CD8 Tregs are shown as %  $\pm$  SD of 3 independent experiments. \*  $p < 0.05$ , \*\*\*  $p < 0.005$  vs. corresponding control DCs (white bars) or as indicated with lines (RM-ANOVA, Tukey’s multiple comparison test). Statistical significance between the corresponding iDCs and mDCs was not indicated for clarity.

#### 4. Conclusions

A DBD atmospheric pressure plasma jet was employed as a CAP source in order to obtain PAM by treating RPMI 1640 culture medium. Three main RONS components ( $H_2O_2$ , nitrates, and nitrites) were identified in PAM. Tumor cell lines (A375 and Hep2) were more sensitive to the cytotoxic effects of PAM including the stimulation of ROS production, than a non-transformed cell line (L929 cells) and human PBMC. The type of PAM-induced ICD in A375 cells (autophagy, apoptosis, necrosis, membrane expression of heat-shock proteins, and the secretion of IL-1 $\beta$ ) depended on applied concentrations of PAM. PAM-A375 lysate potentiated the maturation of DCs by up-regulating CD83 and CD86 expression, simultaneously with a down-regulation of PDL1, and increased the IL-12/IL-10 production ratio by mature DCs, compared to the control A375 lysate without PAM treatment. Mature DCs treated with the PAM-A375 lysate preserved Th1, potentiated Th17 and down-regulated Th2 responses in co-culture with T cells. In addition, such treated DCs increased the frequency and cytotoxic activity of CD8 T cells, along with a reduction in CD8 Tregs frequency. In contrast to the DCs treated with control tumor lysate, which increased the proportion of conventional FoxP3<sup>+</sup> CD4 Tregs, the PAM-treated tumor lysate did not potentiate the Treg-inducing capacity of DCs. Cumulatively, our results suggest for the first time that priming of mature DCs with tumor cell lysates prepared by PAM-induced ICD could be explored as a new strategy for the generation of more immunogenic DC-based tumor vaccines.

**Supplementary Materials:** The following are available online at <https://www.mdpi.com/article/10.3390/cancers13071626/s1>, Figure S1: Dose dependent effects of PAM on induction of heat shock proteins and IL-1 $\beta$  secretion by tumor cell lines, Figure S2: Effects of PAM-treated Hep2 lysates on phenotype and cytokines production by DCs, Figure S3: Direct effects of PAM on oxidative stress, apoptosis, maturation, and cytokines expression by DCs, Figure S4: Proliferation and cytotoxic activity of T cells primed with DCs.

**Author Contributions:** Conceptualization, S.T., N.P., Z.L.P. and M.Č.; methodology, S.T., A.P., N.P., N.Š., M.B.; software, S.T., N.P.; formal analysis, S.T., A.P., N.P., N.Š., M.B.; investigation, S.T., A.P., N.P., N.Š., M.B.; Z.L.P., M.Č.; resources, S.T., N.P., M.Č., Z.L.P.; data curation, S.T., N.P.; writing—original draft preparation, S.T., N.P., Z.L.P., M.Č.; writing—review and editing, S.T., N.P., N.Š., Z.L.P., M.Č.; supervision, N.P., M.Č., Z.L.P.; project administration, N.P., Z.L.P., M.Č.; funding acquisition, N.P., M.Č., Z.L.P. All authors have read and agreed to the published version of the manuscript.

**Funding:** This research was funded by Ministry of Education, Science and Technological Development, grant numbers 451-03-68/2020-14/200019 and 451-03-68/2020-14/200024 and Serbian Academy of Sciences and Arts F31.

**Institutional Review Board Statement:** The study was conducted according to the guidelines of the Declaration of Helsinki and approved by the Institutional Review Board (or Ethics Committee) of Institute for the Application of Nuclear Energy, University in Belgrade (protocol code 02-765/2 from 08.11.2019.).

**Informed Consent Statement:** Informed consent was obtained from all subjects involved in the study.

**Data Availability Statement:** All data is shown in the manuscript and raw data is available from corresponding authors upon reasonable request.

**Acknowledgments:** Authors are grateful to Dragana Vučević for help during experimental procedures.

**Conflicts of Interest:** The authors declare no conflict of interest.

#### References

1. Laroussi, M.; Lu, X.; Keidar, M. Perspective: The physics, diagnostics, and applications of atmospheric pressure low temperature plasma sources used in plasma medicine. *J. Appl. Phys.* **2017**, *122*, 020901. [[CrossRef](#)]
2. Lu, X.; Naidis, G.V.; Laroussi, M.; Reuter, S.; Graves, D.B.; Ostrikov, K. Reactive species in non-equilibrium atmospheric-pressure plasmas: Generation, transport, and biological effects. *Phys. Rep.* **2016**, *630*, 1–84. [[CrossRef](#)]
3. Kong, M.G.; Kroesen, G.; Morfill, G.; Nosenko, T.; Shimizu, T.; Dijk, J.v.; Zimmermann, J.L. Plasma medicine: An introductory review. *New J. Phys.* **2009**, *11*, 115012. [[CrossRef](#)]

4. Keidar, M. A prospectus on innovations in the plasma treatment of cancer. *Phys. Plasmas* **2018**, *25*, 083504. [[CrossRef](#)]
5. Metelmann, H.-R.; Seebauer, C.; Miller, V.; Fridman, A.; Bauer, G.; Graves, D.B.; Pouvesle, J.-M.; Rutkowski, R.; Schuster, M.; Bekeschus, S.; et al. Clinical experience with cold plasma in the treatment of locally advanced head and neck cancer. *Clin. Plasma Med.* **2018**, *9*, 6–13. [[CrossRef](#)]
6. Vandamme, M.; Robert, E.; Pesnel, S.; Barbosa, E.; Dozias, S.; Sobilo, J.; Lerondel, S.; Pape, A.L.; Pouvesle, J.-M. Antitumor Effect of Plasma Treatment on U87 Glioma Xenografts: Preliminary Results. *Plasma Process. Polym.* **2010**, *7*, 264–273. [[CrossRef](#)]
7. Graves, D.B. Reactive Species from Cold Atmospheric Plasma: Implications for Cancer Therapy. *Plasma Process. Polym.* **2014**, *11*, 1120–1127. [[CrossRef](#)]
8. Furuta, R.; Kurake, N.; Ishikawa, K.; Takeda, K.; Hashizume, H.; Tanaka, H.; Kondo, H.; Sekine, M.; Hori, M. Intracellular responses to reactive oxygen and nitrogen species, and lipid peroxidation in apoptotic cells cultivated in plasma-activated medium. *Plasma Process. Polym.* **2017**, *14*, 1700123. [[CrossRef](#)]
9. Hirst, A.M.; Simms, M.S.; Mann, V.M.; Maitland, N.J.; O’Connell, D.; Frame, F.M. Low-temperature plasma treatment induces DNA damage leading to necrotic cell death in primary prostate epithelial cells. *Br. J. Cancer* **2015**, *112*, 1536–1545. [[CrossRef](#)]
10. Bauer, G. Signal amplification by tumor cells: Clue to the understanding of the antitumor effects of cold atmospheric plasma and plasma-activated medium. *IEEE Trans. Radiat. Plasma Med. Sci.* **2018**, *2*, 87–98. [[CrossRef](#)]
11. Khalili, M.; Daniels, L.; Lin, A.; Krebs, F.C.; Snook, A.E.; Bekeschus, S.; Bowne, W.B.; Miller, V. Non-Thermal Plasma-Induced Immunogenic Cell Death in Cancer: A Topical Review. *J. Phys. D Appl. Phys.* **2019**, *52*, 423001. [[CrossRef](#)] [[PubMed](#)]
12. Van Loenhout, J.; Peeters, M.; Bogaerts, A.; Smits, E.; Deben, C. Oxidative Stress-Inducing Anticancer Therapies: Taking a Closer Look at Their Immunomodulating Effects. *Antioxidants* **2020**, *9*, 1188. [[CrossRef](#)]
13. Bauer, G.; Sersenová, D.; Graves, D.B.; Machala, Z. Cold Atmospheric Plasma and Plasma-Activated Medium Trigger RONS-Based Tumor Cell Apoptosis. *Sci. Rep.* **2019**, *9*, 14210. [[CrossRef](#)]
14. Mohamed, H.; Esposito, R.A.; Kutzler, M.A.; Wigdahl, B.; Krebs, F.C.; Miller, V. Nonthermal plasma as part of a novel strategy for vaccination. *Plasma Process. Polym.* **2020**, *17*, 2000051. [[CrossRef](#)]
15. Wculek, S.K.; Cueto, F.J.; Mujal, A.M.; Melero, I.; Krummel, M.F.; Sancho, D. Dendritic cells in cancer immunology and immunotherapy. *Nat. Rev. Immunol.* **2020**, *20*, 7–24. [[CrossRef](#)] [[PubMed](#)]
16. Schlitzer, A.; McGovern, N.; Ginhoux, F. Dendritic cells and monocyte-derived cells: Two complementary and integrated functional systems. *Semin. Cell Dev. Biol.* **2015**, *41*, 9–22. [[CrossRef](#)]
17. Saxena, M.; Bhardwaj, N. Re-Emergence of Dendritic Cell Vaccines for Cancer Treatment. *Trends Cancer* **2018**, *4*, 119–137. [[CrossRef](#)]
18. Lin, A.; Truong, B.; Pappas, A.; Kirifides, L.; Oubbari, A.; Chen, S.; Lin, S.; Dobrynin, D.; Fridman, G.; Fridman, A.; et al. Uniform Nanosecond Pulsed Dielectric Barrier Discharge Plasma Enhances Anti-Tumor Effects by Induction of Immunogenic Cell Death in Tumors and Stimulation of Macrophages. *Plasma Process. Polym.* **2015**, *12*, 1392–1399. [[CrossRef](#)]
19. Crittenden, M.; Kohrt, H.; Levy, R.; Jones, J.; Camphausen, K.; Dicker, A.; Demaria, S.; Formenti, S. Current clinical trials testing combinations of immunotherapy and radiation. *Semin. Radiat. Oncol.* **2015**, *25*, 54–64. [[CrossRef](#)]
20. Bekeschus, S.; Kolata, J.; Winterbourn, C.; Kramer, A.; Turner, R.; Weltmann, K.D.; Bröker, B.; Masur, K. Hydrogen peroxide: A central player in physical plasma-induced oxidative stress in human blood cells. *Free Radic. Res.* **2014**, *48*, 542–549. [[CrossRef](#)] [[PubMed](#)]
21. Tanaka, H.; Mizuno, M.; Ishikawa, K.; Nakamura, K.; Kajiyama, H.; Kano, H.; Kikkawa, F.; Hori, M. Plasma-Activated Medium Selectively Kills Glioblastoma Brain Tumor Cells by Down-Regulating a Survival Signaling Molecule, AKT Kinase. *Plasma Med.* **2011**, *1*, 265–277. [[CrossRef](#)]
22. Yan, D.; Nourmohammadi, N.; Bian, K.; Murad, F.; Sherman, J.H.; Keidar, M. Stabilizing the cold plasma-stimulated medium by regulating medium’s composition. *Sci. Rep.* **2016**, *6*, 26016. [[CrossRef](#)]
23. Tomić, S.; Ilić, N.; Kokol, V.; Gruden-Movsesijan, A.; Mihajlović, D.; Bekić, M.; Sofronić-Milosavljević, L.; Čolić, M.; Vučević, D. Functionalization-dependent effects of cellulose nanofibrils on tolerogenic mechanisms of human dendritic cells. *Int. J. Nanomed.* **2018**, *13*, 6941–6960. [[CrossRef](#)]
24. Khlyustova, A.; Labay, C.; Machala, Z.; Ginebra, M.-P.; Canal, C. Important parameters in plasma jets for the production of RONS in liquids for plasma medicine: A brief review. *Front. Chem. Sci. Eng.* **2019**, *13*, 238–252. [[CrossRef](#)]
25. Harley, J.C.; Suchowerska, N.; McKenzie, D.R. Cancer treatment with gas plasma and with gas plasma-activated liquid: Positives, potentials and problems of clinical translation. *Biophys. Rev.* **2020**, *12*, 989–1006. [[CrossRef](#)]
26. Van Boxem, W.; Van der Paal, J.; Gorbanev, Y.; Vanuysel, S.; Smits, E.; Dewilde, S.; Bogaerts, A. Anti-cancer capacity of plasma-treated PBS: Effect of chemical composition on cancer cell cytotoxicity. *Sci. Rep.* **2017**, *7*, 16478. [[CrossRef](#)]
27. Canal, C.; Fontelo, R.; Hamouda, I.; Guillem-Marti, J.; Cvelbar, U.; Ginebra, M.-P. Plasma-induced selectivity in bone cancer cells death. *Free Radic. Biol. Med.* **2017**, *110*, 72–80. [[CrossRef](#)]
28. Pitt, J.M.; Kroemer, G.; Zitvogel, L. Immunogenic and Non-immunogenic Cell Death in the Tumor Microenvironment. *Adv. Exp. Med. Biol.* **2017**, *1036*, 65–79.
29. ISO 10993-5:2009(en). Biological Evaluation of Medical Devices—Part 5: Tests for in Vitro Cytotoxicity. Available online: <https://www.iso.org/obp/ui#iso:std:iso:10993:-5:ed-3:v1:en> (accessed on 30 January 2021).
30. Utsumi, F.; Kajiyama, H.; Nakamura, K.; Tanaka, H.; Hori, M.; Kikkawa, F. Selective cytotoxicity of indirect nonequilibrium atmospheric pressure plasma against ovarian clear-cell carcinoma. *Springerplus* **2014**, *3*, 398. [[CrossRef](#)]

31. Welz, C.; Emmert, S.; Canis, M.; Becker, S.; Baumeister, P.; Shimizu, T.; Morfill, G.E.; Harréus, U.; Zimmermann, J.L. Cold Atmospheric Plasma: A Promising Complementary Therapy for Squamous Head and Neck Cancer. *PLoS ONE* **2015**, *10*, e0141827. [[CrossRef](#)] [[PubMed](#)]
32. Xiang, L.; Xu, X.; Zhang, S.; Cai, D.; Dai, X. Cold atmospheric plasma conveys selectivity on triple negative breast cancer cells both in vitro and in vivo. *Free Radic. Biol. Med.* **2018**, *124*, 205–213. [[CrossRef](#)]
33. Saadati, F.; Mahdikia, H.; Abbaszadeh, H.-A.; Abdollahifar, M.-A.; Khoramgah, M.S.; Shokri, B. Comparison of Direct and Indirect cold atmospheric-pressure plasma methods in the B16F10 melanoma cancer cells treatment. *Sci. Rep.* **2018**, *8*, 7689. [[CrossRef](#)]
34. Jo, A.; Joh, H.M.; Chung, T.H.; Chung, J.W. Anticancer Effects of Plasma-Activated Medium Produced by a Microwave-Excited Atmospheric Pressure Argon Plasma Jet. Available online: <https://www.hindawi.com/journals/omcl/2020/4205640/> (accessed on 30 January 2021).
35. Biscop, E.; Lin, A.; Boxem, W.V.; Loenhout, J.V.; Backer, J.D.; Deben, C.; Dewilde, S.; Smits, E.; Bogaerts, A.A. Influence of Cell Type and Culture Medium on Determining Cancer Selectivity of Cold Atmospheric Plasma Treatment. *Cancers* **2019**, *11*, 1287. [[CrossRef](#)] [[PubMed](#)]
36. Graves, D.B. Oxy-nitroso shielding burst model of cold atmospheric plasma therapeutics. *Clin. Plasma Med.* **2014**, *2*, 38–49. [[CrossRef](#)]
37. Moserova, I.; Truxova, I.; Garg, A.D.; Tomala, J.; Agostinis, P.; Cartron, P.F.; Vosahlikova, S.; Kovar, M.; Spisek, R.; Fucikova, J. Caspase-2 and oxidative stress underlie the immunogenic potential of high hydrostatic pressure-induced cancer cell death. *Oncoimmunology* **2017**, *6*, e1258505. [[CrossRef](#)]
38. Turrini, E.; Laurita, R.; Stancampiano, A.; Catanzaro, E.; Calcabrini, C.; Maffei, F.; Gherardi, M.; Colombo, V.; Fimognari, C. Cold Atmospheric Plasma Induces Apoptosis and Oxidative Stress Pathway Regulation in T-Lymphoblastoid Leukemia Cells. Available online: <https://www.hindawi.com/journals/omcl/2017/4271065/> (accessed on 30 January 2021).
39. Girard, P.-M.; Arbabian, A.; Fleury, M.; Bauville, G.; Puech, V.; Dutreix, M.; Sousa, J.S. Synergistic Effect of H<sub>2</sub>O<sub>2</sub> and NO<sub>2</sub> in Cell Death Induced by Cold Atmospheric He Plasma. *Sci. Rep.* **2016**, *6*, 29098. [[CrossRef](#)]
40. Bauer, G.; Sersenová, D.; Graves, D.B.; Machala, Z. Dynamics of Singlet Oxygen-Triggered, RONS-Based Apoptosis Induction after Treatment of Tumor Cells with Cold Atmospheric Plasma or Plasma-Activated Medium. *Sci. Rep.* **2019**, *9*, 13931. [[CrossRef](#)]
41. Dai, X.; Bazaka, K.; Thompson, E.W.; Ostrikov, K. (Ken) Cold Atmospheric Plasma: A Promising Controller of Cancer Cell States. *Cancers* **2020**, *12*, 3360. [[CrossRef](#)]
42. Horiba, M.; Kamiya, T.; Hara, H.; Adachi, T. Cytoprotective effects of mild plasma-activated medium against oxidative stress in human skin fibroblasts. *Sci. Rep.* **2017**, *7*, 42208. [[CrossRef](#)]
43. Filomeni, G.; De Zio, D.; Ceconi, F. Oxidative stress and autophagy: The clash between damage and metabolic needs. *Cell Death Differ.* **2015**, *22*, 377–388. [[CrossRef](#)]
44. Bhutia, S.K.; Mukhopadhyay, S.; Sinha, N.; Das, D.N.; Panda, P.K.; Patra, S.K.; Maiti, T.K.; Mandal, M.; Dent, P.; Wang, X.-Y.; et al. Autophagy: Cancer’s friend or foe? *Adv. Cancer Res.* **2013**, *118*, 61–95. [[PubMed](#)]
45. Fulda, S. Autophagy in Cancer Therapy. *Front. Oncol.* **2017**, *7*, 128. [[CrossRef](#)]
46. Michaud, M.; Martins, I.; Sukkurwala, A.Q.; Adjemian, S.; Ma, Y.; Pellegatti, P.; Shen, S.; Kepp, O.; Scoazec, M.; Mignot, G.; et al. Autophagy-dependent anticancer immune responses induced by chemotherapeutic agents in mice. *Science* **2011**, *334*, 1573–1577. [[CrossRef](#)]
47. Klionsky, D.J.; Abdelmohsen, K.; Abe, A.; Abedin, M.J.; Abeliovich, H.; Arozena, A.A.; Adachi, H.; Adams, C.M.; Adams, P.D.; Adeli, K.; et al. Guidelines for the use and interpretation of assays for monitoring autophagy (3rd edition). *Autophagy* **2016**, *12*, 1–222. [[CrossRef](#)]
48. Adachi, T.; Tanaka, H.; Nonomura, S.; Hara, H.; Kondo, S.; Hori, M. Plasma-activated medium induces A549 cell injury via a spiral apoptotic cascade involving the mitochondrial-nuclear network. *Free Radic. Biol. Med.* **2015**, *79*, 28–44. [[CrossRef](#)]
49. Shevtsov, M.; Huile, G.; Multhoff, G. Membrane heat shock protein 70: A theranostic target for cancer therapy. *Philos. Trans. R. Soc. Lond. B Biol. Sci.* **2018**, *373*, 20160526. [[CrossRef](#)]
50. Fucikova, J.; Kepp, O.; Kasikova, L.; Petroni, G.; Yamazaki, T.; Liu, P.; Zhao, L.; Spisek, R.; Kroemer, G.; Galluzzi, L. Detection of immunogenic cell death and its relevance for cancer therapy. *Cell Death Dis.* **2020**, *11*, 1–13. [[CrossRef](#)]
51. Yoshikawa, N.; Liu, W.; Nakamura, K.; Yoshida, K.; Ikeda, Y.; Tanaka, H.; Mizuno, M.; Toyokuni, S.; Hori, M.; Kikkawa, F.; et al. Plasma-activated medium promotes autophagic cell death along with alteration of the mTOR pathway. *Sci. Rep.* **2020**, *10*, 1614. [[CrossRef](#)]
52. Adhikari, M.; Adhikari, B.; Ghimire, B.; Baboota, S.; Choi, E.H. Cold Atmospheric Plasma and Silymarin Nanoemulsion Activate Autophagy in Human Melanoma Cells. *Int. J. Mol. Sci.* **2020**, *21*, 1939. [[CrossRef](#)]
53. Ando, T.; Suzuki-Karasaki, M.; Suzuki-Karasaki, M.; Ichikawa, J.; Ochiai, T.; Yoshida, Y.; Haro, H.; Suzuki-Karasaki, Y. Synergistic anticancer effect of plasma-activated infusion and salinomycin by targeting autophagy and mitochondrial morphology. *bioRxiv* **2020**. [[CrossRef](#)]
54. González, F.E.; Gleisner, A.; Falcón-Beas, F.; Osorio, F.; López, M.N.; Salazar-Onfray, F. Tumor cell lysates as immunogenic sources for cancer vaccine design. *Hum. Vaccin Immunother.* **2014**, *10*, 3261–3269. [[CrossRef](#)] [[PubMed](#)]
55. Nakai, N.; Hartmann, G.; Kishimoto, S.; Katoh, N. Dendritic cell vaccination in human melanoma: Relationships between clinical effects and vaccine parameters. *Pigment. Cell Melanoma. Res.* **2010**, *23*, 607–619. [[CrossRef](#)]





56. Draube, A.; Klein-González, N.; Mattheus, S.; Brillant, C.; Hellmich, M.; Engert, A.; von Bergwelt-Baildon, M. Dendritic cell based tumor vaccination in prostate and renal cell cancer: A systematic review and meta-analysis. *PLoS ONE* **2011**, *6*, e18801. [[CrossRef](#)]
57. Hernández-Granados, A.J.; Franco-Molina, M.A.; Coronado-Cerda, E.E.; Zapata-Benavides, P.; Gamboa, E.M.; Ramos-Zayas, Y.; Santana-Krímskaya, S.E.; Rodríguez-Padilla, C. Immunogenic potential of three transmissible venereal tumor cell lysates to prime canine-dendritic cells for cancer immunotherapy. *Res. Vet. Sci.* **2018**, *121*, 23–30. [[CrossRef](#)] [[PubMed](#)]
58. Nace, G.; Evankovich, J.; Eid, R.; Tsung, A. Dendritic Cells and Damage-Associated Molecular Patterns: Endogenous Danger Signals Linking Innate and Adaptive Immunity. *J. Innate. Immun.* **2012**, *4*, 6–15. [[CrossRef](#)]
59. Hatfield, P.; Merrick, A.E.; West, E.; O'Donnell, D.; Selby, P.; Vile, R.; Melcher, A.A. Optimization of dendritic cell loading with tumor cell lysates for cancer immunotherapy. *J. Immunother.* **2008**, *31*, 620–632. [[CrossRef](#)] [[PubMed](#)]
60. Vandenberk, L.; Belmans, J.; Van Woensel, M.; Riva, M.; Van Gool, S.W. Exploiting the Immunogenic Potential of Cancer Cells for Improved Dendritic Cell Vaccines. *Front. Immunol.* **2016**, *6*, e663. [[CrossRef](#)]
61. Rojas-Sepúlveda, D.; Tittarelli, A.; Gleisner, M.A.; Ávalos, I.; Pereda, C.; Gallegos, I.; González, F.E.; López, M.N.; Butte, J.M.; Roa, J.C.; et al. Tumor lysate-based vaccines: On the road to immunotherapy for gallbladder cancer. *Cancer Immunol. Immunother.* **2018**, *67*, 1897–1910. [[CrossRef](#)] [[PubMed](#)]
62. Hradilova, N.; Sadilkova, L.; Palata, O.; Mysikova, D.; Mrazkova, H.; Lischke, R.; Spisek, R.; Adkins, I. Generation of dendritic cell-based vaccine using high hydrostatic pressure for non-small cell lung cancer immunotherapy. *PLoS ONE* **2017**, *12*, e0171539. [[CrossRef](#)] [[PubMed](#)]
63. Kamigaki, T.; Kaneko, T.; Naitoh, K.; Takahara, M.; Kondo, T.; Ibe, H.; Matsuda, E.; Maekawa, R.; Goto, S. Immunotherapy of autologous tumor lysate-loaded dendritic cell vaccines by a closed-flow electroporation system for solid tumors. *Anticancer Res.* **2013**, *33*, 2971–2976.
64. Tomić, S.; Janjetović, K.; Mihajlović, D.; Milenković, M.; Kravić-Stevović, T.; Marković, Z.; Todorović-Marković, B.; Spitalsky, Z.; Micusik, M.; Vučević, D.; et al. Graphene quantum dots suppress proinflammatory T cell responses via autophagy-dependent induction of tolerogenic dendritic cells. *Biomaterials* **2017**, *146*, 13–28. [[CrossRef](#)]
65. Jin, P.; Han, T.H.; Ren, J.; Saunders, S.; Wang, E.; Marincola, F.M.; Stroncek, D.F. Molecular signatures of maturing dendritic cells: Implications for testing the quality of dendritic cell therapies. *J. Transl. Med.* **2010**, *8*, 4. [[CrossRef](#)] [[PubMed](#)]
66. Miebach, L.; Freund, E.; Horn, S.; Niessner, F.; Sagwal, S.K.; von Woedtke, T.; Emmert, S.; Weltmann, K.-D.; Clemen, R.; Schmidt, A.; et al. Tumor cytotoxicity and immunogenicity of a novel V-jet neon plasma source compared to the kINPen. *Sci. Rep.* **2021**, *11*, 136. [[CrossRef](#)]
67. Gao, A.; Sun, Y.; Peng, G. ILT4 functions as a potential checkpoint molecule for tumor immunotherapy. *Biochim. Biophys. Acta (BBA) Rev. Cancer* **2018**, *1869*, 278–285. [[CrossRef](#)] [[PubMed](#)]
68. Tze, L.E.; Horikawa, K.; Domaschensz, H.; Howard, D.R.; Roots, C.M.; Rigby, R.J.; Way, D.A.; Ohmura-Hoshino, M.; Ishido, S.; Andoniou, C.E.; et al. CD83 increases MHC II and CD86 on dendritic cells by opposing IL-10-driven MARCH1-mediated ubiquitination and degradation. *J. Exp. Med.* **2011**, *208*, 149–165. [[CrossRef](#)]
69. Castiello, L.; Sabatino, M.; Ren, J.; Terabe, M.; Khuu, H.; Wood, L.V.; Berzofsky, J.A.; Stroncek, D.F. Expression of CD14, IL10, and Tolerogenic Signature in Dendritic Cells Inversely Correlate with Clinical and Immunologic Response to TARP Vaccination in Prostate Cancer Patients. *Clin. Cancer Res.* **2017**, *23*, 3352–3364. [[CrossRef](#)] [[PubMed](#)]
70. Loscher, C.E.; Draper, E.; Leavy, O.; Kelleher, D.; Mills, K.H.G.; Roche, H.M. Conjugated linoleic acid suppresses NF-kappa B activation and IL-12 production in dendritic cells through ERK-mediated IL-10 induction. *J. Immunol.* **2005**, *175*, 4990–4998. [[CrossRef](#)] [[PubMed](#)]
71. Lee, H.E.; Lee, J.Y.; Yang, G.; Kang, H.C.; Cho, Y.-Y.; Lee, H.S.; Lee, J.Y. Inhibition of NLRP3 inflammasome in tumor microenvironment leads to suppression of metastatic potential of cancer cells. *Sci. Rep.* **2019**, *9*, 12277. [[CrossRef](#)]
72. Ghiringhelli, F.; Apetoh, L.; Tesniere, A.; Aymeric, L.; Ma, Y.; Ortiz, C.; Vermaelen, K.; Panaretakis, T.; Mignot, G.; Ullrich, E.; et al. Activation of the NLRP3 inflammasome in dendritic cells induces IL-1 $\beta$ -dependent adaptive immunity against tumors. *Nat. Med.* **2009**, *15*, 1170–1178. [[CrossRef](#)]
73. Jia, H.; Dilger, P.; Bird, C.; Wadhwa, M. IL-27 Promotes Proliferation of Human Leukemic Cell Lines Through the MAPK/ERK Signaling Pathway and Suppresses Sensitivity to Chemotherapeutic Drugs. *J. Interferon. Cytokine Res.* **2016**, *36*, 302–316. [[CrossRef](#)]
74. Diakowska, D.; Lewandowski, A.; Markocka-Mączka, K.; Grabowski, K. Concentration of serum interleukin-27 increase in patients with lymph node metastatic gastroesophageal cancer. *Adv. Clin. Exp. Med.* **2013**, *22*, 683–691. [[PubMed](#)]
75. Hall, A.O.; Beiting, D.P.; Tato, C.; John, B.; Oldenhove, G.; Lombana, C.G.; Pritchard, G.H.; Silver, J.S.; Bouladoux, N.; Stumhofer, J.S.; et al. The cytokines interleukin 27 and interferon- $\gamma$  promote distinct Treg cell populations required to limit infection-induced pathology. *Immunity* **2012**, *37*, 511–523. [[CrossRef](#)] [[PubMed](#)]
76. Takahashi, A.; Hanson, M.G.V.; Norell, H.R.; Havelka, A.M.; Kono, K.; Malmberg, K.-J.; Kiessling, R.V.R. Preferential cell death of CD8+ effector memory (CCR7-CD45RA-) T cells by hydrogen peroxide-induced oxidative stress. *J. Immunol.* **2005**, *174*, 6080–6087. [[CrossRef](#)]
77. Mimura, K.; Kua, L.-F.; Shimasaki, N.; Shiraishi, K.; Nakajima, S.; Siang, L.K.; Shabbir, A.; So, J.; Yong, W.-P.; Kono, K. Upregulation of thioredoxin-1 in activated human NK cells confers increased tolerance to oxidative stress. *Cancer Immunol. Immunother.* **2017**, *66*, 605–613. [[CrossRef](#)] [[PubMed](#)]
78. Seres, T.; Knickelbein, R.G.; Warshaw, J.B.; Johnston, R.B. The phagocytosis-associated respiratory burst in human monocytes is associated with increased uptake of glutathione. *J. Immunol.* **2000**, *165*, 3333–3340. [[CrossRef](#)]

79. Kim, H.-J.; Barajas, B.; Chan, R.C.-F.; Nel, A.E. Glutathione depletion inhibits dendritic cell maturation and delayed-type hypersensitivity: Implications for systemic disease and immunosenescence. *J. Allergy Clin. Immunol.* **2007**, *119*, 1225–1233. [[CrossRef](#)]
80. Yamamoto, M.; Kamigaki, T.; Yamashita, K.; Hori, Y.; Hasegawa, H.; Kuroda, D.; Moriyama, H.; Nagata, M.; Ku, Y.; Kuroda, Y. Enhancement of anti-tumor immunity by high levels of Th1 and Th17 with a combination of dendritic cell fusion hybrids and regulatory T cell depletion in pancreatic cancer. *Oncol. Rep.* **2009**, *22*, 337–343.
81. Tsung, K.; Meko, J.B.; Peplinski, G.R.; Tsung, Y.L.; Norton, J.A. IL-12 induces T helper 1-directed antitumor response. *J. Immunol.* **1997**, *158*, 3359–3365. [[PubMed](#)]
82. Su, J.; Chen, T.; Ji, X.-Y.; Liu, C.; Yadav, P.K.; Wu, R.; Yang, P.; Liu, Z. IL-25 Downregulates Th1/Th17 Immune Response in an IL-10-Dependent Manner in Inflammatory Bowel Disease. *Inflamm. Bowel Dis.* **2013**, *19*, 720–728. [[CrossRef](#)]
83. Ziegler, A.; Heidenreich, R.; Braumüller, H.; Wollburg, H.; Weidemann, S.; Mocikat, R.; Röcken, M. EpCAM, a human tumor-associated antigen promotes Th2 development and tumor immune evasion. *Blood* **2009**, *113*, 3494–3502. [[CrossRef](#)]
84. Muranski, P.; Boni, A.; Antony, P.A.; Cassard, L.; Irvine, K.R.; Kaiser, A.; Paulos, C.M.; Palmer, D.C.; Touloukian, C.E.; Ptak, K.; et al. Tumor-specific Th17-polarized cells eradicate large established melanoma. *Blood* **2008**, *112*, 362–373. [[CrossRef](#)]
85. Soong, R.-S.; Song, L.; Trieu, J.; Lee, S.Y.; He, L.; Tsai, Y.-C.; Wu, T.-C.; Hung, C.-F. Direct T Cell Activation via CD40 Ligand Generates High Avidity CD8+ T Cells Capable of Breaking Immunological Tolerance for the Control of Tumors. *PLoS ONE* **2014**, *9*, e93162. [[CrossRef](#)] [[PubMed](#)]
86. Henry, C.J.; Ornelles, D.A.; Mitchell, L.M.; Brzoza-Lewis, K.L.; Hiltbold, E.M. IL-12 Produced by Dendritic Cells Augments CD8+ T cell Activation through the Production of the Chemokines CCL1 and CCL17. *J. Immunol.* **2008**, *181*, 8576–8584. [[CrossRef](#)] [[PubMed](#)]
87. Wuest, S.C.; Edwan, J.; Martin, J.F.; Han, S.; Perry, J.S.A.; Cartagena, C.M.; Matsuura, E.; Maric, D.; Waldmann, T.A.; Bielekova, B. A vital role for IL-2 trans-presentation in DC-mediated T cell activation in humans as revealed by daclizumab therapy. *Nat. Med.* **2011**, *17*, 604–609. [[CrossRef](#)]
88. Pullen, A.M.; Munro, A.J. “Auto-Reactive” T-Cell Hybridomas and the Role of Foetal Calf Serum. In *Immunobiology of Proteins and Peptides IV: T-Cell Recognition and Antigen Presentation*; Atassi, M.Z., Ed.; Advances in Experimental Medicine and Biology; Springer: Boston, MA, USA, 1987; pp. 253–258. ISBN 978-1-4684-5442-0.
89. Xu, Z.; Ho, S.; Chang, C.-C.; Zhang, Q.-Y.; Vasilescu, E.-R.; Vlad, G.; Suciuc-Foca, N. Molecular and Cellular Characterization of Human CD8 T Suppressor Cells. *Front. Immunol.* **2016**, *7*, 549. [[CrossRef](#)]
90. Tomić, S.; Joksimović, B.; Bekić, M.; Vasiljević, M.; Milanović, M.; Čolić, M.; Vučević, D. Prostaglandin-E2 Potentiates the Suppressive Functions of Human Mononuclear Myeloid-Derived Suppressor Cells and Increases Their Capacity to Expand IL-10-Producing Regulatory T Cell Subsets. *Front. Immunol.* **2019**, *10*, 475. [[CrossRef](#)]
91. Nguyen, Q.T.; Jang, E.; Le, H.T.; Kim, S.; Kim, D.; Dvorina, N.; Aronica, M.A.; Baldwin, W.M.; Asosingh, K.; Comhair, S.; et al. IL-27 targets Foxp3<sup>+</sup> Tregs to mediate antiinflammatory functions during experimental allergic airway inflammation. *JCI Insight* **2019**, *4*, e123216. [[CrossRef](#)]
92. Park, Y.-J.; Ryu, H.; Choi, G.; Kim, B.-S.; Hwang, E.S.; Kim, H.S.; Chung, Y. IL-27 confers a protumorigenic activity of regulatory T cells via CD39. *Proc. Natl. Acad. Sci. USA* **2019**, *116*, 3106–3111. [[CrossRef](#)] [[PubMed](#)]

Article

# Effect of Atmospheric Cold Plasma Treatments on Reduction of *Alternaria* Toxins Content in Wheat Flour

Elizabet Janić Hajnal <sup>1,\*</sup>, Milan Vukić <sup>2,3</sup> , Lato Pezo <sup>4</sup>, Dejan Orčić <sup>5</sup>, Nevena Puač <sup>6</sup>, Nikola Škoro <sup>6</sup> , Ardea Milidrag <sup>7</sup> and Dragana Šoronja Simović <sup>2</sup>

- <sup>1</sup> Research Center for Technology of Plant Based Food Products, Institute of Food Technology, University of Novi Sad, 21000 Novi Sad, Serbia
  - <sup>2</sup> Department of Carbohydrate Food Engineering, Faculty of Technology Novi Sad, University of Novi Sad, 21000 Novi Sad, Serbia; milan.vukic@tfzv.ues.rs.ba (M.V.); dragana@tf.uns.ac.rs (D.Š.S.)
  - <sup>3</sup> Department of Food Technology, Faculty of Technology Zvornik, University of East Sarajevo, 75400 Zvornik, Bosnia and Herzegovina
  - <sup>4</sup> Institute of General and Physical Chemistry, University of Belgrade, 11000 Belgrade, Serbia; latopezo@gmail.com
  - <sup>5</sup> Department of Chemistry, Biochemistry and Environmental Protection, Faculty of Sciences, University of Novi Sad, 21000 Novi Sad, Serbia; dejan.orcic@dh.uns.ac.rs
  - <sup>6</sup> Laboratory for Gaseous Electronics, Institute of Physics, University of Belgrade, 11080 Belgrade, Serbia; nevena@ipb.ac.rs (N.P.); nskoro@ipb.ac.rs (N.Š.)
  - <sup>7</sup> Chair of general physiology and biophysics, Faculty of Biology, University of Belgrade, 11000 Belgrade, Serbia; ardea304@gmail.com
- \* Correspondence: elizabet.janich@fins.uns.ac.rs; Tel.: +381-21-485-3624

Received: 26 October 2019; Accepted: 25 November 2019; Published: 3 December 2019



**Abstract:** Beside *Fusarium* toxins, *Alternaria* toxins are among the most commonly found mycotoxins in wheat and wheat products. Currently, investigations of possibilities of reduction of *Alternaria* toxins in the wheat-processing chain are limited. Therefore, the aim of this study was to explore the potency of cold atmospheric plasma treatments, as a new non-thermal approach, for reduction of alternariol (AOH), alternariol monomethyl ether (AME) and tentoxin (TEN) content in spiked white wheat flour samples. Samples were treated with plasma generated in the air during 30 s to 180 s, with an increment step of 30 s, and at four varying distances from the cold plasma source (6 mm, 21 mm, 36 mm and 51 mm). The reduction of the *Alternaria* toxins content in samples after treatment was monitored by high performance liquid chromatography coupled to tandem mass spectrometry (LC-MS/MS). The maximum reduction of the examined *Alternaria* toxins was obtained by treatment performed at 6 mm distance from the plasma source, lasting 180 s, resulting in reductions of 60.6%, 73.8% and 54.5% for AOH, AME and TEN, respectively. According to the obtained experimental results, five empirical models in the form of the second-order polynomials were developed for the prediction of AOH, AME and TEN reduction, as well as the temperature and the moisture content of the wheat flour, that gave a good fit to experimental data and were able to predict the response variables successfully. The developed second-order polynomial models showed high coefficients of determination for prediction of experimental results (between 0.918 and 0.961).

**Keywords:** wheat flour; atmospheric cold plasma; alternariol; alternariol monomethyl ether; tentoxin; LC-MS/MS; mathematical modelling

**Key Contribution:** This study represents the first report about potency of cold atmospheric plasma treatments in reduction of *Alternaria* toxins in wheat flour. The results obtained in this study indicated that exposure time of cold plasma treatment had a stronger effect than distance from the discharge on reduction of AOH, AME and TEN in wheat flour. Furthermore, longer exposure time at a shorter

distance of the cold plasma source from the sample, provided a greater degree of reduction of the examined *Alternaria* toxins.

---

## 1. Introduction

Wheat (*Triticum aestivum* L.) is one of the most important food crops, being among the ten most produced commodities [1,2]. The global quality of common wheat and wheat-based products are interrelated to various features such as protein content, protein quality, and presence of contaminants that affect the safety, generally associated with the absence of toxigenic molds and their secondary metabolites, mycotoxins [3]. Fungi of the genus *Alternaria* (about 250 species), can grow at low temperature. Frequency and ability of this genus to produce a wide range of toxins is a significant and present threat to the health of humans and animals. Due to their prevalence in various foods and cumulative effect [4], mutagenic, teratogenic and possibly carcinogenic effects of *Alternaria* toxins are possible. According to the European Food Safety Authority (EFSA), major risk factors for *Alternaria* toxin dietary exposure are cereals and cereal-based products [5]. The genus of *Alternaria* is commonly present in cereals, resulting in a high possibility of *Alternaria* toxin incidence and increased risk in affected wheat [6]. *Alternaria* toxins most frequently present on wheat include alternariol (AOH), alternariol monomethylether (AME), tenuazonic acid (TeA), tentoxin (TEN) and altertoxins (ATXs) [7]. In recent years, many studies showed that the prevalence of *Alternaria* toxins in wheat from Europe, Africa, Asia, Australia and North and South Americas should not be underestimated [8–13]. Prevention of contamination by *Alternaria* fungi is the most sensible and cost-saving approach to reducing the risks accompanied with the presence of *Alternaria* toxins. Still, this approach is not always possible with current agronomic and storage practices, when the environmental conditions favor the growth of toxigenic fungi [8].

Investigations regarding the fate of *Alternaria* toxins during wheat kernel and wheat flour processing are limited. Only a handful of studies refer to the investigation of the fate of AOH, AME and TeA during wheat cleaning, wheat milling and bread-making [14,15]. The abovementioned studies show that wheat cleaning reduces the content of AOH, AME and TeA through the removal of impurities, whereas wheat milling performs only toxin distribution into wheat flour mill streams, and the bread-making procedure only cause a reduction in AOH content. Further, the extrusion process provides possibilities for reduction of *Alternaria* toxins. In the investigation of the potential of simple pilot single screw extruder for reduction of AOH, AME and TeA in flour of whole wheat, the highest reduction of AOH (87.9%), AME (94.5%) and TeA (65.6%) was achieved when high raw material moisture ( $w = 24 \text{ g } 100 \text{ g}^{-1}$ ), high feeding rate ( $q = 25 \text{ kg h}^{-1}$ ) and medium screw speed ( $v = 390 \text{ rpm}$ ) were applied [16].

Recently, application of cold atmospheric plasma got much attention as a novel non-thermal technology for the food industry [17–19]. Some of the advantages of this technology are high efficiency with short treatment time, lack of residues, a low or positive overall impact on the quality of treated food products, and reduced costs when using ambient air as the working gas [20]. Not long ago, the research focus of the plasma treatment was on its effects on pathogenic bacteria [21,22]. Lately, much attention has been paid to studies related to plasma effects on chemical and biological compounds which showed promising results [23–25]. Degradation of mycotoxins is being studied worldwide with different types of plasma sources. Cold atmospheric plasma could possibly overcome the greatest disadvantages of classical techniques and provide a sustainable solution for mycotoxins detoxification [26–29]. Cold plasma is a weakly ionized, quasi-neutral gas with rich chemistry containing a wide variety of highly reactive species and ultraviolet radiation that are shown to be efficient in degradation of mycotoxins. The formation of reactive species in the discharge takes place through complex reaction mechanisms which depend on several factors like type of power supply, frequency, gas used, geometry of the electrode system etc. [30–32]. The choice of the most efficient plasma source is at large extent governed

also by the type of application. In order to get the desired plasma chemistry for destruction of toxins it is necessary to characterize in detail and optimize the plasma source.

Cold atmospheric plasma in air generates a favorable combination of ions, short- and long-lived reactive oxygen species (ROS) and reactive nitrogen species (RNS) that include  $\text{OH}\bullet$ ,  $\text{O}\bullet$ ,  $\text{NO}$ ,  $\text{O}_3$ ,  $\text{H}_2\text{O}_2$ ,  $\text{NO}_2$ , etc. [33–36]. By varying the plasma source geometry and type of applied voltage signal discharge can be tuned to produce ozone as one of the prevailing reactive species which degrades, to a certain degree, mycotoxins on its own [37,38]. However, in addition to ozone alone, cold plasma in air leads to the formation of radicals, ROS, RNS and ultraviolet light, culminating in greater mycotoxin degradation efficacy under shorter exposure times than ozone alone. Hence, the importance of other reactive species produced in plasma should not be overlooked [39].

With cold plasma technology, it could possibly be feasible to degrade mycotoxins effectively. Treatment would be more sustainable requiring smaller energy inputs and investment compared to classical techniques. To be applicable to treat wheat flour, cold plasma treatments need to be able to treat the bulk quantities of wheat flour. Multiple intrinsic and extrinsic parameters of wheat flour matrix, including its powdered form, possibly play a role in the effectiveness of cold plasma treatment. One of the plasma sources that can meet these criteria is surface dielectric barrier discharge (SDBD). Technology allows treating the samples at atmospheric pressure with air as the working medium, thereby reducing equipment cost and offering the great advantage of high adaptability and scaling up.

Previous studies indicate that cold atmospheric plasma is a promising technology for degrading of mycotoxins [27,28,40,41]. However, none of these studies included *Alternaria* toxins in wheat flour matrix. Thus, the aim of the present study was to investigate the effects of atmospheric SDBD cold plasma treatments on *Alternaria* toxin (AOH, AME and TEN) reduction in wheat flour. The experiments were carried out by using SDBD reactor to excite strongly oxidizing cold air plasma above the samples. To process the data obtained, the second order polynomial (SOP) models were used for mathematical modelling. Pattern recognition technique (Principal Component Analysis – PCA) was applied to the experimental data (used as descriptors) to characterize and differentiate among the observed samples. The optimum processing conditions were determined by standard score (SS) evaluation.

## 2. Results and Discussion

### 2.1. Optical Emission Spectroscopy and Electrical Characterization of Plasma Source

Species is generally identified as the main active species responsible for the effects of cold plasma, among which is degradation of chemical and biochemical compounds are atomic oxygen, ozone ( $\text{O}_3$ ), hydrogen peroxides ( $\text{H}_2\text{O}_2$ ), hydroxyl radicals ( $\bullet\text{OH}$ ), as well as peroxy nitrates and nitrogen oxides [23,24,41]. Some of the species, such as  $\bullet\text{OH}$ ,  $\text{NO}$ ,  $\text{O}$ , after excitation emit in near UV-visual range and this emission is easily recordable by the optical emission spectroscopy (OES) technique. An emission spectra of the discharge in air was recorded in a wide range of wavelengths from 270 nm to 860 nm by using the optical emission spectroscopy (OES) technique. Emission measurements were taken within the first few seconds after the plasma ignition through a quartz window inserted on one side of the plastic box. The spatial angle of the recording included the total volume of the discharge ignited at the lower side of the electrode as well as the volume directly under the electrode plate. The spectrum of the discharge (in arbitrary units) obtained in absence of flour samples is presented in Figure 1 and it gives us qualitative information regarding the chemical species present in the plasma discharge. The most intense lines recorded belong to the  $\text{N}_2$  Second Positive System band, as expected for the atmospheric air plasma. Relatively lower intensities of peaks associated with atomic oxygen (triplet at 777 nm) are due to involvement of  $\text{O}$  in creation of  $\text{O}_3$ , and quenching by  $\text{N}_2$  and  $\text{O}_2$  molecules [42]. Since the plasma operates in ambient air with certain humidity,  $\text{OH}$  radicals are produced mainly through direct  $\text{H}_2\text{O}$  dissociation. Thus, lines of the  $\text{OH}$  (A-X) band coming from excited  $\text{OH}$  radicals are also observed in the recorded spectrum with low emission intensity. Hence,

the existence of these reactive species can be confirmed by OES characterization of the SDBD unit, thus showing the application feasibility to detoxicate samples with mycotoxins in general.

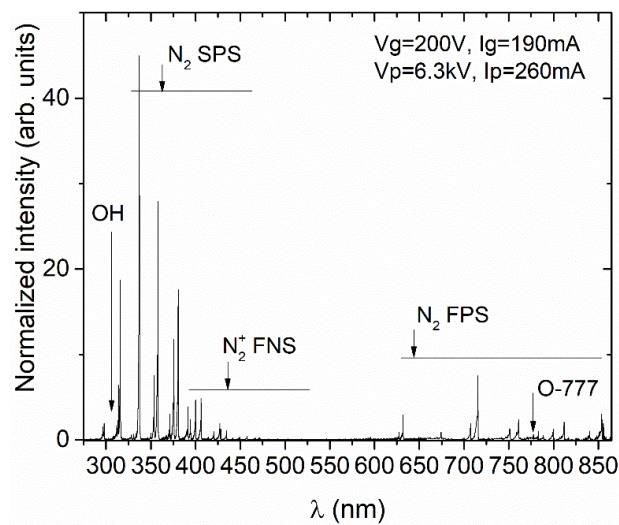


**Figure 1.** The optical emission spectra of the surface dielectric barrier discharge (SDBD) in atmospheric-pressure air.

The high-voltage (HV) given by the transformer and the current were measured at the point of electrical circuit close to the powered electrode. The dependence of root-mean-square (RMS) values of voltage and current on the variable transformer (variac) voltage are shown in Figure 2a. As expected, for an increase in the variac voltage, there is an increase in both HV and current at the electrode. The maximal RMS values for voltage and current reached with this system were 2400 V and 0.1 A, respectively.

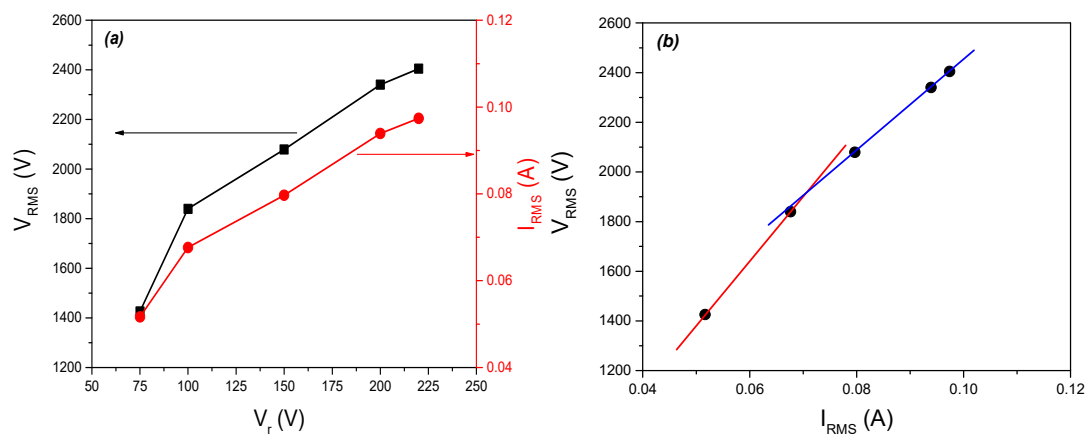


**Figure 2.** (a) Dependence of  $V_{RMS}$  and  $I_{RMS}$  values on the voltage values set by the variable transformer; (b) Voltage-current characteristics of the SDBD plasma system. Red and blue lines are guides for the eye for easier detection for impedance change.  $V_{RMS}$ —root-mean-square value of voltage;  $I_{RMS}$ —root-mean-square value of current;  $V_T$ —voltage on variable transformer.

The voltage-current (V-I) characteristics of the system is shown in Figure 2b. At lower voltages immediately after the ignition, plasma does not cover the whole surface of the electrode, but with the increase in the applied voltage, plasma spreads and covers the whole surface uniformly. Spreading of the active plasma surface causes changes in the system impedance. This can be observed as a change from red to blue line in Figure 2b. For higher voltages, the impedance is slightly lower, which indicates larger electrode surface covered by homogenous plasma. Generally, when plasma is ignited

the total impedance of the system is changed. The impedance change towards a lower value can be seen through the effective circuit of the system represented as parallel connection of two complex impedances. One impedance is due to the ignited plasma, which itself represents a complex RLC circuit, and the other one is the impedance of the electrode system. The impedance of the electrode system is due to the capacitance of the electrode system and, to some small extent, due to the resistance of the cables and connectors. Hence, in large area discharges at atmospheric pressure, the changes in the total impedance indicate the area covered by the discharge. Therefore, we have chosen 200 V as an operating voltage for the flour treatment since the plasma impedance (i.e., total impedance) is constant in this range of voltage-current parameters, since the whole electrode area is covered homogeneously. Also, we avoided the highest achieved variac value because of the danger of temperature increase, as well as the change into arcing.

## 2.2. Reduction of *Alternaria* Toxins by Atmospheric Cold Plasma Treatments

Among the most commonly found *Alternaria* toxins in wheat [7], AOH, AME, and TEN, were chosen for the focus of this study. The results obtained by the analysis of *Alternaria* toxins in treated samples suggest that there is a realistic possibility of a significant reduction of toxins by cold atmospheric plasma treatment. The experimental results are presented in Table 1. The content of toxins was reduced even after only 30 s of treatment; the reduction ranged from 2.4% to 44.6%. The reduction rate was dependent on the toxin and sample distance from the plasma. The greatest reduction for all toxins was achieved when samples were placed 6 mm from plasma discharge, with AME showing the greatest instability. Similar behaviour of other toxins is noticeable from Table 1. Thus, it can be presumed that, in addition to duration and sample distance from the electrode, structural features of toxins affect the treatment efficiency.

**Table 1.** The results of cold plasma treatments on reduction of *Alternaria* toxins content in wheat flour.

Trial	Input <i>d</i> [mm]	<i>t</i> [s]	Responses AOH (%)*	AME (%) *	TEN (%) *	T (°C)	M (%)	SS
1	6	30	21.5	44.6	30.6	29.0	14.1	0.420
2	21	30	17.0	37.0	14.4	27.0	14.1	0.327
3	36	30	8.9	32.2	13.7	25.7	14.1	0.287
4	51	30	2.4	22.3	3.6	24.0	14.1	0.200
5	6	60	29.1	61.3	37.6	33.2	13.8	0.539
6	21	60	21.8	49.7	22.7	27.9	14.1	0.418
7	36	60	12.3	40.5	16.2	26.9	14.1	0.332
8	51	60	3.0	32.9	15.4	25.9	14.1	0.275
9	6	90	32.9	61.5	38.5	37.4	13.6	0.546
10	21	90	24.2	51.4	23.2	30.0	14.0	0.430
11	36	90	12.6	41.8	22.7	28.7	14.1	0.350
12	51	90	6.3	35.2	18.5	27.5	14.0	0.306
13	6	120	33.0	65.0	48.1	41.6	13.0	0.632
14	21	120	27.5	55.9	40.7	32.0	13.8	0.534
15	36	120	16.4	48.8	39.7	30.5	14.1	0.443
16	51	120	7.7	38.2	20.7	29.1	14.0	0.319
17	6	150	35.0	69.2	50.2	45.9	12.6	0.675
18	21	150	30.5	56.4	44.1	34.1	13.8	0.544
19	36	150	16.9	49.7	40	32.2	13.9	0.458
20	51	150	9.4	47.4	29.6	30.8	13.9	0.394
21	6	180	60.7	73.8	54.5	50.0	12.3	0.800
22	21	180	47.9	62.7	48.6	36.0	13.5	0.664
23	36	180	41.1	57.3	46.4	34.0	13.5	0.627
24	51	180	28.6	52.7	31.8	32.5	13.9	0.476
Polarity			+	+	+	−	−	

*d*—distance of the cold plasma source to the sample; *t*—time range; AOH—reduction of alternariol; AME—reduction of alternariol monomethyl ether; TEN—reduction of tentoxin; T—temperature of wheat flour sample after treatment; M—moisture of wheat flour sample after treatment; SS—standard score. Polarity—negative sign is associated with “the lower the better” criteria, while positive sign is associated with “the higher the better” criteria, as explained in Section 4.10.3. \* Values are calculated (see Section 4.9).

For all treatment times, a similar reduction ratio between studied toxins is noticeable. AME was the most susceptible to cold plasma treatment, followed with TEN and AOH, respectively. There are three possible ways by which cold plasma treatment could exert such a reducing effect on *Alternaria* toxins content in wheat flour. These are heating, ultraviolet (UV) irradiation, and effects of plasma reactive species. As a non-thermal process, cold atmospheric plasma is designed to minimize heating of the samples. The temperature of SDBD treatments conducted in our experiment never exceeded 50 °C (the temperature recorded for the longest treatment period at the smallest distance of sample and plasma discharge). Thus, generally the temperature of the sample is well below the temperature required for thermal decomposition of *Alternaria* toxins. AOH and AME have melting points with decomposition at 350 °C and 267 °C, respectively, and undergo considerable reduction only after 20 min at 80 °C [43]. Hence, the contribution of heat is considered to have a negligible effect on *Alternaria* toxins degradation. The standard scores presented in Table 1 are calculated according to calculation explained in Section 4.10.3. The larger SS values are assigned to the more efficient toxins reduction (obtained by larger  $t$  and smaller  $d$  values).

As it can be observed from Figure 1, UV light was emitted due to the N<sub>2</sub> species transition in the cold plasma generation process. Still, the emission power in cold plasma generation is not significant enough to be considered as effective for the degradation of mycotoxins, or in our study, *Alternaria* toxins [43]. Thus, toxin degradation should be attributed to the effects of plasma reactive species.

As earlier demonstrated by OES measurement, when SDBD plasma is excited, ROS and RNS were generated. Since these species accumulate over time of treatment, significant contribution to toxin degradation is possible. Based on the results of other studies, the authors believe that ROS, rather than RNS have a major role in toxin degradation under SDBD treatment. Justification for this claim can be found in the study [41] that reported much lower degradation efficiency of aflatoxin when nitrogen was used as a working medium for cold plasma generation instead of air. Moreover, while Shi et al. [41] were exploring the degradation mechanism, they could not find nitrogen moieties in the degradation products of aflatoxin. Holding to these findings by analogy, the authors expect that ROS are primarily responsible for *Alternaria* toxin degradation, but do not exclude the possibility of RNS contribution. One of the major ROS generated by cold atmospheric plasma is ozone O<sub>3</sub> [44]. Ozone effects on mycotoxins degradation are known [45,46]. Several other ROS, atomic oxygen (O), the hydroxyl radical (OH•), and hydrogen peroxide (H<sub>2</sub>O<sub>2</sub>), accompany ozone in the generation of cold atmospheric plasma [26,39,44].

In addition, it was examined whether there is a correlation between process responses. The positive and highly significant correlations between AOH, AME, TEN and T can be observed in Table 2. Also, the negative, highly significant correlations between M and AOH, AME, TEN and T were obtained in Table 2.

**Table 2.** The correlation matrix of the process responses, during the cold plasma treatments on wheat flour.

Responses	AME	TEN	T	M
AOH	0.902	0.848	0.844	−0.784
AME		0.933	0.901	−0.792
TEN			0.861	−0.751
T				−0.963

AOH—reduction of alternariol; AME—reduction of alternariol monomethyl ether; TEN—reduction of tentoxin; T—temperature of wheat flour sample after treatment; M—moisture of wheat flour sample after treatment.  
\* All correlations are statistically significant at  $p < 0.01$  level.

To characterize and differentiate among the observed samples pattern recognition techniques Principal Component Analysis–PCA were applied to the experimental data (used as descriptors). The points shown in the PCA graphics, which are geometrically close to each other, indicate the similarity of patterns that represent these points. The orientation of the vector describing the variable in



factor space indicates an increasing trend of these variables, and the length of the vector is proportional to the square of the correlation values between the fitting value for the variable and the variable itself. The angles between corresponding variables indicate the degree of their correlations (small angles corresponding to high correlations). The PCA of the presented data explained that the first two components accounted for 95.47% of the total variance (88.68% and 6.79%, respectively) in the five variables system. Considering the map of the PCA performed on the data, AOH (which contributed 19.5% of total variance, based on correlations), AME (20.9%), TEN (19.7%) and T (21.2%) exhibited negative scores according to first principal component, whereas M (18.7%) showed a positive score value according to the first principal component (PC1) (Figure 3). The positive contribution to the second principal component (PC2) calculation was observed for: AME (10.9% of total variance, based on correlations), TEN (18.7%) and M (48.8%), while negative scores on the second principal component calculation was observed for T (13.3%).

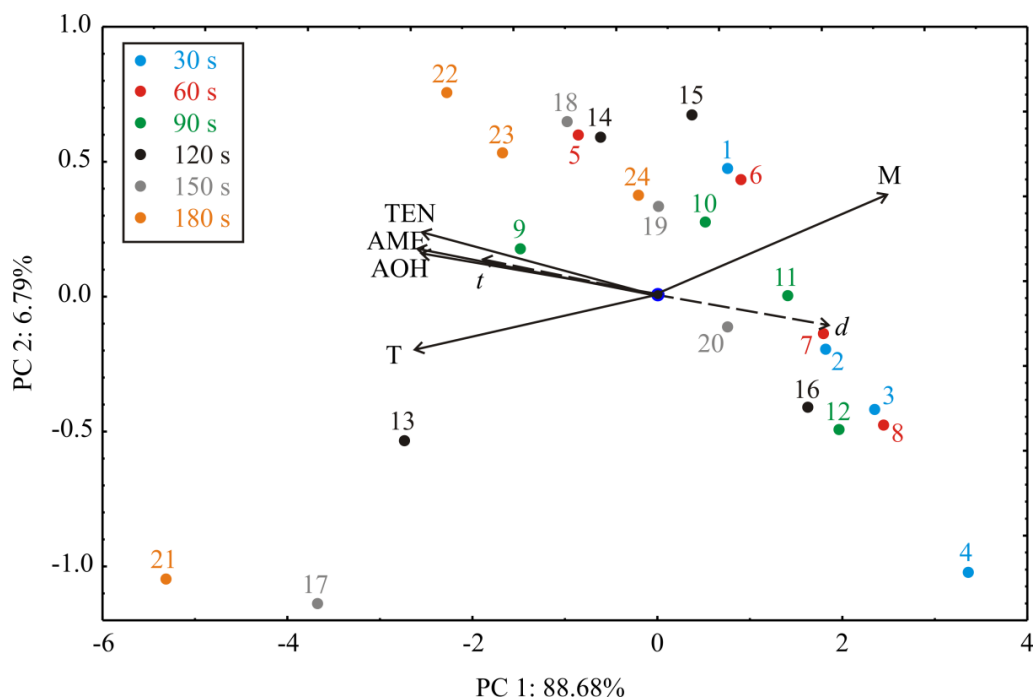


**Figure 3.** Principal Component Analysis (PCA) ordination of variables based on component correlations. *d*—distance of the cold plasma source to the sample; *t*—time range; AOH—reduction of alternariol; AME—reduction of alternariol monomethyl ether; TEN—reduction of tentoxin; T—temperature of wheat flour sample after treatment; M—moisture of wheat flour sample after treatment.

The influence of processing parameters can be observed in Figure 3. According to the PCA results, the best results in reduction of AOH, AME and TEN were observed at 6 mm plasma source distance when the temperature of wheat flour sample after treatment was higher (this conclusion coincide with the SS results (Table 1.)) compared to other treatments. The processing time vector is oriented in the same direction as the AOH, AME and TEN vectors in the PCA graph, which means that time is positively correlated to the reduction of the AOH, AME and TEN, while the treatment variable is negatively correlated to the reduction of the AOH, AME and TEN. Groups of samples with the same processing time are coded using different colors, and it is evident that better results in the reduction of the AOH, AME and TEN were gained for longer processing time (orange color). The group of samples being treated for the same processing time differs due to the distance from the plasma source (treatment); if the distance to plasma source is shorter, better results in AOH, AME and TEN reduction is gained.

Further, ANOVA was conducted for obtained Second order polynomial (SOP) models, and output variables were tested against the impact of input variables (Table 3).

**Table 3.** ANOVA calculation of the process responses, during the cold plasma treatments on wheat flour (sum of squares are presented).

Term	df	AOH	AME	TEN	T	M
$d$	1	2296.355 *	1942.272 *	1573.696 *	370.657 *	1.704 *
$d^2$	1	2.385	17.783	1.845	73.150 *	0.570 *
$t$	1	1892.277 *	1675.572 *	2626.082 *	391.053 *	1.808 *
$t^2$	1	344.607 *	21.607	6.396	0.142	0.066
$d \times t$	1	26.331	4.890	2.185	52.807 *	0.890 *
Error	18	356.801	148.727	321.540	41.188	0.451
$r^2$		0.927	0.961	0.929	0.956	0.918

$d$ —distance of the cold plasma source to the sample;  $t$ —time range; AOH—reduction of alternariol; AME—reduction of alternariol monomethyl ether; TEN—reduction of tentoxin; T—temperature of wheat flour sample after treatment; M—moisture of wheat flour sample after treatment; df—degrees of freedom;  $r^2$ —coefficient of determination. \* Statistically significant at  $p < 0.05$  level.

ANOVA analysis revealed that the linear terms of  $d$  and  $t$  considerably influenced the forming of SOP models for AOH, AME, TEN, T and M calculations, statistically significant at  $p < 0.05$  level. The quadratic term of  $t$  was influential for the AOH reduction model, while the quadratic term of  $d$  was influential for the T and M SOP models. The interchange term  $d \times t$  was influential for the SOP models of T and M prediction, statistically significant at  $p < 0.05$  level. The coefficient of determination ( $r^2$ ) for the SOP models was rather good (Table 3). According to results presented in Table 3, the higher  $r^2$  values were attributed to SOP models in which the nonlinear terms were less effective and the linear terms of  $d$  and  $t$  were more pronounced.

Since the OES measurement performed in the present study can provide only qualitative information about reactive species, it is unclear which specific reactive species play the major role in *Alternaria* toxin degradation. The most likely scenario is degradation through the synergy of all ROS since they coexist during the treatment and are interconvertible. Besides the conditions already stated, degradation depends on relative humidity, as in humid air higher concentrations of OH• and H<sub>2</sub>O<sub>2</sub> are achievable. During the samples treatment, the air was at an intermediate humidity level (40%). However, water evaporated from wheat flour samples into the surrounding air of cold plasma, which would have certainly resulted in an increase of OH• and H<sub>2</sub>O<sub>2</sub> reactive species (Table 1). Therefore, it is expected that the degradation of *Alternaria* toxins was through combined effects of the following oxidative species: OH•, H<sub>2</sub>O<sub>2</sub>, and O<sub>3</sub>.

Furthermore, the quality of the model fit was tested in Table 4. The higher  $r^2$  values, and the lower  $\chi^2$ , MBE, RMSE and MPE values show the better fit to the experimental results [47]. The residual analysis of the developed model was also performed. Skewness measures the deviation of the distribution from normal symmetry. If the skewness is clearly different from zero, then the distribution is asymmetrical, while normal distributions are perfectly symmetrical. Kurtosis measures the “peakedness” of a distribution. If the Kurtosis is clearly different than zero, then the distribution is either flatter or more peaked than normal; the Kurtosis of the normal distribution is zero. The average and the standard deviation (SD) and the variance of residuals have also been analysed and shown in Table 4.

**Table 4.** Goodness of fit for developed models of the process responses, during the cold plasma treatments on wheat flour.

Responses	$\chi^2$	RMSE	MBE	MPE	$r^2$	Skew	Kurt	Mean	StDev	Var
AOH	18.779	3.856	0.000	19.474	0.927	-0.756	-0.179	0.000	3.939	15.513
AME	7.828	2.489	0.000	4.427	0.961	0.025	-0.072	0.000	2.543	6.466
TEN	16.923	3.660	0.000	11.794	0.929	-0.038	0.681	0.000	3.739	13.980
T	2.168	1.310	0.000	3.427	0.956	-0.579	-0.210	0.000	1.338	1.791
M	0.024	0.137	0.000	0.816	0.918	0.515	-0.177	0.000	0.140	0.020

AOH—reduction of alternariol; AME—reduction of alternariol monomethyl ether; TEN—reduction of tentoxin; T—temperature of wheat flour sample after treatment; M—moisture of wheat flour sample after treatment;  $\chi^2$ —reduced chi-square; RMSE—root mean square error; MBE—mean bias error; MPE—mean percentage error;  $r^2$ —coefficient of determination; Skew—skewness; Kurt—kurtosis; Mean—mean values of residuals; StDev—standard deviation of residuals; Var—variance of residuals.

The residual analysis showed that the mean of residuals were equal to zero, and the standard deviation was between 0.140 and 3.939. These results showed a good approximation to a normal distribution around zero with a probability of 95% ( $2 \times SD$ ), which means a good generalization ability of the developed model for the range of observed experimental data.

Increasing the time of treatment increased the plasma degradation efficacy of toxins for all studied toxins in this study. Efficacy for treatment with 6 mm sample distance ranged from 21.5 %, 44.6% and 30.6% for 30 s plasma exposure to 60.7%, 73.8% and 54.5 % for AOH, AME and TEN respectively, for plasma exposure of 180 s. Observed reductions of *Alternaria* toxins can be explained with the increase of reactive species during longer treatment times. The increase in toxins degradation with time after 90 s is smaller than what one would expect based only on the first 60 s of sample exposure to cold plasma. We partly attribute this lower-than-expected increase in toxin degradation to the possibility that after the toxins are degraded in the surface layer of flour, degradation slows down due to smaller toxins availability in deeper layers. This is a specific wheat flour matrix feature, as samples were in powdered form, treatment time was probably spent on the diffusion of plasma reactive species into sample volume.

The SDBD expressed the filamentary nature of discharge across the electrode surface without directly making contact with samples placed below the electrode. This geometry certainly has an influence on the reactive species fluxes to the sample surfaces and on the effects of ROS and RNS. However, the remote production of ROS and RNS is significantly mediated by the diffusion time to the sample surface during the treatment. In all cases, degradation efficiency increases with increasing treatment time. As it can be seen from Table 1, degradation efficiency is greater for all toxins after an exposure time of 180 s at 51 mm than it is after an exposure time of 30 s and 6 mm distance from discharge. The extent of *Alternaria* toxin reduction might be dependent on the structure of mycotoxins in the first place, and then on their molecular mass. For example, AME with a molecular mass of 272.2 Da showed a greater reduction compared to AOH with a mass of 258.2 Da under the treatments studied. The reduction extent might be affected by their structure since these two mycotoxins share an identical structure with only one different group. AME is a benzochromenone that is AOH in which the hydroxy group at position 9 has been converted to the corresponding methyl ether. On the other hand, TEN is a natural cyclic tetrapeptide with molecular mass of 414.4 Da and exhibited higher reduction extent under almost all treatments studied compared to AOH. Our findings would be in accordance with the earlier results of other authors (summarized by ten Boch et al. [27]) that showed that the degradation of mycotoxins treated with atmospheric cold plasma did not correlate with a molecular mass. A hypothesis reported by other researchers suggests that mycotoxins with longer aliphatic chains are more sensitive to the influence of cold atmospheric plasma relative to mycotoxins with structures of condensed rings and aliphatic chains and mycotoxins with a compact structure of condensed aromatic rings [27]. Further, Standard Score Analysis (SS) of the five response variables was accomplished in order to find the processing variables (processing time and distance), that give

optimal values of response variables. The “higher the better” or the “lower the better” criteria have been used according to the sign in “Polarity” row in Table 1.

The standard score is the average of the five normal scores sum. Each response variable (the reduction of AOH, AME and TEN, wheat flour temperature and moisture content) has equal weight, when calculating the SS. The maximum of SS represents the optimal parameters for processing parameters, and also the optimum for response variables. SS analysis showed that the best results were obtained with treatment performed at 6 mm, during 180 s (SS was equal to 0.800, reduction of AOH was 60.6%, reduction of AME and TEN were 73.8% and 54.5%, respectively, while the obtained wheat flour temperature was 50 °C and the moisture was 12.3%). According to SS results, presented in Table 1, the satisfactory results for the observed toxins reductions were obtained at a shorter treatment distance (6 mm) and average processing time (120 and 150 s), at which the SS was 0.632 and 0.675. Using this set of process variables, relatively low reduction of AOH was performed. The different approach in optimization could be observed with average treatment distance (21 and 36 mm) and larger processing time (180 s), where gained SS reached 0.664 and 0.627. This set of variables lead to relatively low temperature of the wheat flour, but it also gained relatively lower reduction of all studied toxins.

### 2.3. Experimental Verification of the Mathematical Models

In order to test the accuracy of the developed mathematical models, the experimental verification of the model was performed. For the verification of models, the two previously untested values of distance of the cold plasma source to the sample, and the two time range values, within the tested range of values defined in Table 1, were chosen. The optimal process parameters (Trial 21 from Table 1, with  $d = 6$  mm and  $t = 180$  s) were also used in verification of the accuracy of the model. The experimental values of AOH, AME and TEN reduction were recorded, as well as the temperature and moisture of the observed material. The values of the response variables were also calculated. The results of the additional experiments and model calculated responses are presented in Table 5. According to the obtained results, only minor differences between the optimal experimental and predicted values for AOH, AME and TEN reduction, temperature and moisture content were observed, which means that the developed mathematical model could be used for prediction of the reduction of AOH, AME, TEN and also the temperature and moisture content of wheat flour.

**Table 5.** Verification of the mathematical models of the process responses, during the cold plasma treatments on wheat flour.

Verification Trial	$d$ (mm)	$t$ (s)	AOH (%) *	AME (%) *	TEN (%) *	T (°C)	M (%)
Model	40	45	8.370	32.179	12.858	24.809	14.200
Exp.	40	45	8.498	31.980	12.754	24.767	14.249
Model	15	165	43.825	65.288	49.448	40.717	13.098
Exp.	15	165	44.408	64.022	50.256	40.852	13.027
Optimal	6	180	55.708	72.484	56.482	48.106	12.409

$d$ —distance of the cold plasma source to the sample;  $t$ —time range; AOH—reduction of alternariol; AME—reduction of alternariol monomethyl ether; TEN—reduction of tentoxin; T—temperature of wheat flour sample after treatment; M—moisture of wheat flour sample after treatment. \* Values are calculated (see Section 4.9).

### 3. Conclusions

It can be seen that similar results were obtained with all statistical analyses, pointing out that for Trial 21 the best score (SS was 0.800) was gained. The highest reduction of all three *Alternaria* toxins was achieved with treatment performed at 6 mm, during 180 s. Under these treatments, a reduction of 60.6%, 73.8% and 54.5%, for AOH, AME and TEN, respectively, was achieved. The results obtained in this study indicate that cold atmospheric plasma with SDBD excitation has the great potential for reduction of *Alternaria* toxin content. It can be stated that both investigated factors (time of exposure and distance from discharge) affect degradation efficiency of *Alternaria* toxins in wheat flour matrix.

Authors attribute degradation effects to ROS of cold atmospheric plasma, and their synergies. Further, the authors do not exclude the effect of RNS completely. Thus, further research in this direction is needed. The ANOVA results revealed that the linear terms of  $d$  and  $t$  considerably influenced the forming of SOP models. The second order polynomial models showed good prediction capabilities (the coefficients of determination for the observed variables were between 0.927 and 0.961). On the basis of SOP models, the optimal treatment for toxin degradation was obtained at shorter treatment distance (6 mm) and longer time, with relatively low temperature of the wheat flour. In addition, future research should be related to the investigations of the effect of cold atmospheric plasma with SDBD excitation at optimal treatment conditions on the fate of *Alternaria* toxins by using naturally contaminated wheat milling products.

## 4. Materials and Methods

### 4.1. Material

For this study, white wheat flour was purchased at the market. The white wheat flour sample was analyzed before the spiking procedure, in order to confirm that it is a blank sample without any of the examined *Alternaria* toxins. In order to investigate the effect of atmospheric cold plasma on AOH, AME and TEN content, 10 g of white wheat flour was spiked with examined *Alternaria* toxins ( $100 \mu\text{g kg}^{-1}$  of each AOH, AME and TEN in flour).

### 4.2. Treating Spiked Samples with SDBD

The schematic of experimental set-up is shown in Figure 4. The plasma system consists of SDBD source, active cooler, translucent polypropylene box and a sample holder for a Petri dish of 100 mm diameter. The SDBD source has 9 stripe electrodes ( $\sim 1\text{mm}$  width) placed in comb-like geometry on bottom sides of 2 mm ceramic dielectric plate (length 70 mm  $\times$  width 40 mm). The distance between the stripes is 4 mm. These electrodes are placed along the plate length and connected to a high voltage (powered line from high-voltage (HV) transformer). The top of the dielectric surface is covered with a conductive layer which is connected to the ground line of the HV transformer. The plasma system was actively cooled by a cooler placed on the outside of the box cover on top of the SDBD. The electrical circuit of the plasma system consists of the SDBD source, commercial high-voltage transformer and variac regulator. The variac was powered through the standard electrical grid at the frequency of 50 Hz and it served as the regulator of HV given by the transformer. Stable plasma ignites in the surrounding air for the input voltage of 200 V given by the variac.

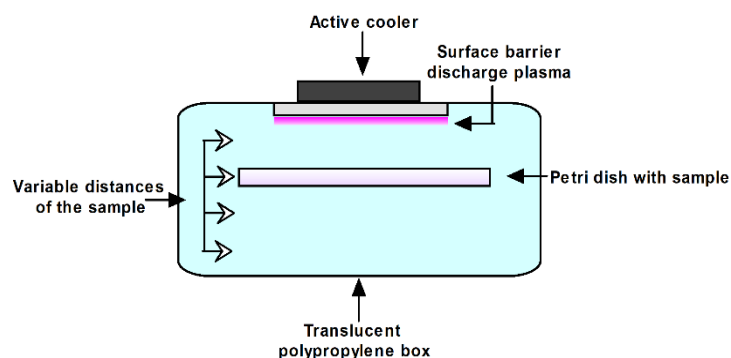


**Figure 4.** Schematic of experimental setup for SDBD treatment of *Alternaria* toxins in wheat flour.

The box was sealed to prevent leakage of the plasma species that were generated. An amount of 10 g of spike white wheat flour was placed in Petri dish and subjected to SDBD treatment. Flour samples were treated for periods of 30 s, 60 s, 90 s, 120 s, 150 s and 180 s with variable distances from the SDBD

plasma source, specifically 6 mm, 21 mm, 36 mm and 51 mm. The air in the box had a relative humidity (RH) of  $45 \pm 1\%$  at room temperature. The parameters for the experimental set-up are shown in Table 6.

**Table 6.** Parameters of the SDBD.

Parameter *	Value
Variac voltage/frequency	200 V/50 Hz
Applied RMS voltage/current	2340 V/0.094 A
Sample weight	10 g
Compartment box size (L × W × H)	195 mm × 125 mm × 65 mm
Gas temperature	≈40 °C

\* L: length, W: width, H: height.

The temperature of the plasma was measured using an infrared thermometer (Fluke 64 MAX IR Thermometer, Everett, WA, USA). After treatment, the spiked samples were removed from the box, transferred to sealed bag and stored in freezer at 4 °C until mycotoxin analysis.

#### 4.3. Optical Emission Spectroscopy

The optical emission spectroscopy (OES) of the surface barrier discharge in ambient air was captured in an empty polypropylene box, covering the near ultraviolet-visible region (270–850 nm). OES of the surface barrier discharge was acquired with a spectrometer (Shamrock 750, UK) with a detector (Andor DH734 ICCD camera, Belfast, UK) and optical fibers (Thorlabs, Newton, NJ, USA) with Ø200 µm core and collimating lens in UV and VIS range.

#### 4.4. Electrical Measurements

Electrical measurements were performed by using a high-voltage probe (Tektronix, P6015A, Beaverton, OR, USA) and current probe (Agilent N2783B) which were placed in the electrical circuit close to the powered electrode. The waveform data were collected by using digital oscilloscope (Agilent, DSOX3014A, Waldbronn, Germany). Additionally, two multimeters were used to measure the voltage and current in the part of the circuit between the variac and high-voltage transformer. The root-mean-square values of voltage and current were used to determine voltage–current characteristics of the plasma system.

#### 4.5. Moisture Content

Moisture content in white wheat flour samples before and after applied treatments was determined using IM 9500 NIR instrument with the optional Flour Module (Pertin Instruments, Hagersten, Sweden) and was expressed on the dry basis.

#### 4.6. Sample Preparation

The modified method by Siegel et al. [48], described in detail in our previous studies [8,14], was used for sample preparation.

#### 4.7. Instrumental Conditions

*Alternaria* toxins (AOH, AME and TEN) were quantified by high performance liquid chromatography coupled to tandem mass spectrometry (LC-MS/MS) using our previously published method [8] including the equipment and materials, but with some modifications. Namely, quantification of TEN (purity 99.2%) purchased from Sigma Aldrich (Seelze, Germany) was included in the method. TEN was quantified in negative ionization dynamic selected reactions monitoring mode, and was monitored at a determined retention time of  $\pm 1.5$  min. Fragmentor voltage and collision energies were optimized during infusion of the pure standard of TEN (concentration of  $5 \mu\text{g mL}^{-1}$ ), and the most

abundant fragment ions were chosen for the selected reaction monitoring. The precursor ion for TEN was  $m/z$  413.5, the fragmentor voltage for monitored product ions ( $m/z$  141 and 271) was 170 V and the collision energies were 6 V and 3 V for  $m/z$  141 and  $m/z$  271, respectively. Retention time of TEN was 5.47 min.

#### 4.8. Method Validation

The method was validated by an in-house quality control procedure following the guidelines of Commission Decision EC 657/2002 [49]. Method validation was performed in terms of matrix effects, linearity, trueness, precision, limit of detection (LOD) and limit of quantification (LOQ), by the same procedure, as were described in detail in our previous study [14].

The validation data of the analytical method for the determination of selected *Alternaria* toxins are given in Table 7. During the validation study, matrix-matched calibration (MMC) standards were used to compensate for the matrix effect, i.e., signal suppression or enhancement of the studied *Alternaria* toxins in the white wheat flour. AOH and TEN showed signal enhancement, while slight signal suppression was observed for AME.

**Table 7.** Recovery data of the employed analytical method based on solvent ( $R_A$ ) and matrix-matched ( $R_E$ ) calibration curves and matrix effect (SSE).

Analytes	Concentration Range ( $\mu\text{g kg}^{-1}$ )	Overall Method Recovery $R_A$ (%) *	Sample Preparation Recovery $R_E$ (%) **	Matrix Effect SSE (%) ***	LOD/LOQ ( $\mu\text{g kg}^{-1}$ )
AOH	2.5–100	90.4	80.4	112.5	0.75/2.5
AME	2.5–100	68.5	83.0	82.5	0.3/0.9
TEN	2.5–100	90.4	74.1	122.0	0.5/1.5

AOH—alternariol; AME—alternariol monomethyl ether; TEN—tentoxin; \* Calculated by (slope of spiked sample-prepared curve/slope of solvent calibration curve); \*\* Calculated by (slope of spiked sample-prepared curve/slope of matrix-matched calibration curve); \*\*\* Calculated by (slope of matrix-matched calibration curve/slope of solvent calibration curve).

The method exhibited good linearity, with correlation coefficients ( $r^2$ ) above 0.9924.

Trueness was evaluated through recovery studies. The overall method recoveries ( $R_A$ ) and the sample preparation recoveries ( $R_E$ ) for target analytes were calculated as were described in detail in our previous study [14]. It can be seen that the  $R_A$  and the  $R_E$  for all target analytes were above 70%, with the exception of  $R_A$  for AME.

Precision for white wheat flour, expressed as the repeatability and within-laboratory reproducibility (Table 8), gave RSD values within the range of 3.4–11.2% and 6.1–11.9%, respectively, fulfilling the criteria of  $\text{RSD} \leq 20\%$  and indicating a good precision of the developed method.

**Table 8.** Precision data of the selected *Alternaria* toxins.

Analytes	Spiking Level ( $\mu\text{g kg}^{-1}$ )	Repeatability ( $n = 6$ ) RSD (%)	Within-Laboratory Reproducibility ( $n = 3 \times 6$ ) RSDs (%)
AOH	25	11.2	11.8
	50	7.4	8.8
	100	6.0	7.7
AME	25	11.0	11.5
	50	7.0	7.2
	100	3.1	6.1
TEN	25	10.1	11.9
	50	5.3	9.8
	100	3.4	6.2

AOH—alternariol; AME—alternariol monomethyl ether; TEN—tentoxin; RSD (%)—relative standard deviation of 6 replicates at three concentration levels using the spiked white wheat flour and the matrix-matched calibration (MMC) curve; RSDs (%)—relative standard deviation of 6 replicates at three concentration levels using the spiked white wheat flour and the mmC curve, over the course of three days, using the same instrument and by the same operators.

#### 4.9. *Alternaria* Toxins Determination

*Alternaria* toxins were quantified by external matrix-matched calibration procedure in order to eliminate the effect of matrix. Matrix-matched calibration curves were constructed in the concentration range from LOD to 100  $\mu\text{g kg}^{-1}$  for AOH, AME and TEN, respectively. Linearity testing gave values of correlation coefficients ( $r^2$ ) above 0.9924 in all the investigated ranges. The obtained results were corrected for sample preparation recovery ( $R_E$ ), and were expressed on a dry matter basis. All samples were prepared and analyzed in triplicates. The reduction of AOH, AME and TEN were calculated as:

$$\text{Reduction of } Alternaria \text{ toxin (\%)} = 100 - (C_x \times 100/C_0) \quad (1)$$

where  $C_x$  is the concentration of *Alternaria* toxins (AOH, AME and TEN) in the wheat flour sample after treatment;  $C_0$  is the initial concentration of *Alternaria* toxins (AOH, AME and TEN) in spiked wheat flour sample before treatment.

#### 4.10. Statistical Analysis

The applied experimental design corresponded to a  $4 \times 6$  Latin square design with two factors (Treat. – 4 levels and Time – 6 levels). The collected data were presented using descriptive statistics tables. The analysis and mathematical modelling was performed using STATISTICA 13.3 (V13.3; StatSoft, Inc.: Tulsa, OK, USA, 2018) [50].

##### 4.10.1. SOP Models

According to general recommendations, prior to artificial neural network (ANN) modelling, five SOP models were developed. SOP models were used for the modelling, rather than first order polynomials, due to the complexity of the data, and the pronounced nonlinear dependence between variables. Furthermore, ANOVA was performed, in order to explore the effects of the input variables over the outputs, as well as to justify the later use of the ANN model by the coefficient of determination ( $r^2$ ).

The SOP model was used for estimation of the main effect of the process variables on responses. The variables used for modelling were the reduction of AOH, AME and TEN, whey temperature (Temp) and a moisture of whey (M). The SOP model was fitted to data collected from experimental measurements [51,52]:

$$Y_k = \beta_0 + \sum_{i=1}^3 \beta_i X_i + \sum_{i=1}^3 \beta_{ii} X_i^2 + \sum_{i=1}^2 \sum_{j=2}^3 \beta_{ij} X_i \cdot X_j, \quad k = 1-8 \quad (2)$$

where:  $\beta_0, \beta_i, \beta_{ii}, \beta_{ij}$ , are constant regression coefficients for intercept, linear, quadratic and product term, respectively,  $Y_k$  is the response variable, while  $X_i$  and  $X_j$  are independent variables. The significant terms in the model were found using ANOVA for each dependent variable.

##### 4.10.2. The Accuracy of the Models

The numerical verification of the developed models was tested using coefficient of determination ( $r^2$ ), reduced chi-square ( $\chi^2$ ), mean bias error (MBE), root mean square error (RMSE) and mean percentage error (MPE). These commonly used parameters can be calculated as follows [47]:

$$\chi^2 = \frac{\sum_{i=1}^N (x_{\text{exp},i} - x_{\text{pre},i})^2}{N - n} \quad (3)$$

$$\text{RMSE} = \left[ \frac{1}{N} \cdot \sum_{i=1}^N (x_{\text{pre},i} - x_{\text{exp},i})^2 \right]^{1/2} \quad (4)$$



$$MBE = \frac{1}{N} \cdot \sum_{i=1}^N (x_{pre,i} - x_{exp,i}), MPE = \frac{100}{N} \cdot \sum_{i=1}^N \left( \frac{|x_{pre,i} - x_{exp,i}|}{x_{exp,i}} \right) \quad (5)$$

where  $x_{exp,i}$  stand for the experimental values and  $x_{pre,i}$  are the predicted values by calculating from the model for these measurements. N and n are the number of observations and constants, respectively.

#### 4.10.3. Standard Score Calculation

Normal scores were calculated for each variable, and were used for complex comparison of observed samples, regarding their technological and chemical properties of the samples listed in Table 1. The ranking procedure between different samples was performed based upon the ratio of raw data and extreme values for each applied assay [53], according to these equations:

$$\bar{x}_i = 1 - \frac{\max_i x_i - x_i}{\max_i x_i - \min_i x_i}, \quad \forall i \quad (6)$$

in case of “the higher, the better” criteria, or

$$\bar{x}_i = \frac{\max_i x_i - x_i}{\max_i x_i - \min_i x_i}, \quad \forall i \quad (7)$$

in case of “the lower, the better” criteria.

where  $x_i$  represents the raw data.

**Author Contributions:** Conceptualization, E.J.H. and M.V.; validation, M.V. and E.J.H.; formal analysis, L.P. and E.J.H.; investigation, M.V., E.J.H., N.P., N.Š. and D.O.; resources, E.J.H., D.O., M.V., N.P., N.Š.; data curation, M.V. and E.J.H.; writing—original draft preparation, M.V., E.J.H. and L.P.; writing—review and editing, M.V., E.J.H., L.P., N.P., N.Š., and D.O.; supervision, E.J.H. and D.Š.S.; funding acquisition, N.P., A.M. and M.V.

**Funding:** This research was funded by the ministry of Education, Science and Technological Development, Republic of Serbia, as a part of the projects III 46001 and III41011.

**Acknowledgments:** The authors thanks Ivo Jokić from the company Jokić - invest d.o.o. from Zvornik, Bosnia and Herzegovina who funded the publication of this study.

**Conflicts of Interest:** The authors declare no conflict of interest.

## References

1. FAOSTAT. Available online: <http://fenix.fao.org/faostat/internal/en/#data/QC/> (accessed on 19 June 2019).
2. Grain Production Worldwide by Type, 2018/19|Statistic. Available online: <https://www.statista.com/statistics/263977/world-grain-production-by-type/> (accessed on 19 June 2019).
3. Doolotkeldieva, T.D. Microbiological Control of Flour-Manufacture: Dissemination of Mycotoxins Producing Fungi in Cereal Products. *Microbiol. Insights* **2010**, *3*, 1–15. [CrossRef]
4. Pinto, E.V.F.; Patriarca, A. Mycotoxigenic Fungi. *Mycotoxigenic Fungi: Methods and Protocols* **2017**, 13–32.
5. EFSA Panel on Contaminants in the Food Chain (CONTAM). Scientific opinion on the risks for animal and public health related to the presence of *Alternaria* toxins in feed and food. *EFSA J.* **2011**, *9*, 2407–2504.
6. EFSA (European Food Safety Authority); Arcella, D.; Eskola, M.; Gómez Ruiz, J.A. Scientific report on the dietary exposure assessment to *Alternaria* toxins in the European population. *EFSA J.* **2016**, *14*, 4654.
7. Walravens, J.; Mikula, H.; Rychlik, M.; Asam, S.; Ediage, E.N.; Di Mavungu, J.D.; Van Landschoot, A.; Vanhaecke, L.; De Saeger, S. Development and validation of an ultra-high-performance liquid chromatography tandem mass spectrometric method for the simultaneous determination of free and conjugated *Alternaria* toxins in cereal-based foodstuffs. *J. Chromatogr. A* **2014**, *1372*, 91–101. [CrossRef]
8. Janić Hajnal, E.; Orčić, D.; Torbica, A.; Kos, J.; Mastilović, J.; Škrinjar, M. *Alternaria* toxins in wheat from the Autonomous Province of Vojvodina, Serbia: A preliminary survey. *Food Addit. Contam. A* **2015**, *32*, 361–370.
9. Müller, M.E.H.; Korn, U. *Alternaria* mycotoxins in wheat—A 10 years survey in the Northeast of Germany. *Food Control* **2013**, *34*, 191–197. [CrossRef]

10. Xu, W.; Han, X.; Li, F.; Zhang, L. Natural Occurrence of *Alternaria* Toxins in the 2015 Wheat from Anhui Province, China. *Toxins* **2016**, *8*, 308. [[CrossRef](#)] [[PubMed](#)]
11. Juan, C.; Covarelli, L.; Beccari, G.; Colasante, V.; Mañes, J. Simultaneous analysis of twenty-six mycotoxins in durum wheat grain from Italy. *Food Control* **2016**, *62*, 322–329. [[CrossRef](#)]
12. Egbontan, A.O.; Afolabi, C.G.; Kehinde, I.A.; Enikuomelin, O.A.; Ezekiel, C.N.; Sulyok, M.; Warth, B.; Krska, R. A mini-survey of moulds and mycotoxins in locally grown and imported wheat grains in Nigeria. *Mycotoxin Res.* **2017**, *33*, 59–64. [[CrossRef](#)]
13. Scott, P.M.; Zhao, W.; Feng, S.; Lau, B.P.-Y. *Alternaria* toxins alternariol and alternariol monomethyl ether in grain foods in Canada. *Mycotoxin Res.* **2012**, *28*, 261–266. [[CrossRef](#)]
14. Janić Hajnal, E.; Mastilović, J.; Bagi, F.; Orčić, D.; Budakov, D.; Kos, J.; Savić, Z. Effect of Wheat Milling Process on the Distribution of *Alternaria* Toxins. *Toxins* **2019**, *11*, 139. [[CrossRef](#)]
15. Janić Hajnal, E.; Kos, J.; Orčić, D. Stability of *Alternaria* toxins during bread-making process. *Food Feed Res.* **2019**, *46*, 73–81. [[CrossRef](#)]
16. Janić Hajnal, E.; Čolović, R.; Pezo, L.; Orčić, D.; Vukmirović, Đ.; Mastilović, J. Possibility of *Alternaria* toxins reduction by extrusion processing of whole wheat flour. *Food Chem.* **2016**, *213*, 784–790. [[CrossRef](#)]
17. Misra, N.N. The contribution of non-thermal and advanced oxidation technologies towards dissipation of pesticide residues. *Trends Food Sci. Technol.* **2015**, *45*, 229–244. [[CrossRef](#)]
18. Vukić, M.; Vujadinović, D.; Ivanović, M.; Gojković, V.; Grujić, R. Color change of orange and carrot juice blend treated by non-thermal atmospheric plasma. *J. Food Process. Preserv.* **2018**, *42*, e13525. [[CrossRef](#)]
19. Puač, N.; Gherardi, M.; Shiratani, M. Plasma agriculture: A rapidly emerging field. *Plasma Process. Polym.* **2018**, *15*, 1700174. [[CrossRef](#)]
20. Misra, N.N.; Tiwari, B.K.; Raghavarao, K.S.M.S.; Cullen, P.J. Nonthermal Plasma Inactivation of Food-Borne Pathogens. *Food Eng. Rev.* **2011**, *3*, 159–170. [[CrossRef](#)]
21. Niemira, B.A. Cold Plasma Decontamination of Foods. *Annu. Rev. Food Sci. Technol.* **2012**, *3*, 125–142. [[CrossRef](#)]
22. Kayes, M.M.; Critzer, F.J.; Kelly-Wintenberg, K.; Roth, J.R.; Montie, T.C.; Golden, D.A. Inactivation of Foodborne Pathogens Using A One Atmosphere Uniform Glow Discharge Plasma. *Foodborne Pathog. Dis.* **2007**, *4*, 50–59. [[CrossRef](#)]
23. Sarangapani, C.; O’Toole, G.; Cullen, P.J.; Bourke, P. Atmospheric cold plasma dissipation efficiency of agrochemicals on blueberries. *Innov. Food Sci. Emerg.* **2017**, *44*, 235–241. [[CrossRef](#)]
24. Sarangapani, C.; Ziuzina, D.; Behan, P.; Boehm, D.; Gilmore, B.F.; Cullen, P.J.; Bourke, P. Degradation kinetics of cold plasma-treated antibiotics and their antimicrobial activity. *Sci. Rep.* **2019**, *9*, 3955. [[CrossRef](#)]
25. Misra, N.N.; Kaur, S.; Tiwari, B.K.; Kaur, A.; Singh, N.; Cullen, P.J. Atmospheric pressure cold plasma (ACP) treatment of wheat flour. *Food Hydrocolloids* **2015**, *44*, 115–121. [[CrossRef](#)]
26. Misra, N.N.; Yadav, B.; Roopesh, M.S.; Jo, C. Cold Plasma for Effective Fungal and Mycotoxin Control in Foods: Mechanisms, Inactivation Effects, and Applications. *Compr. Rev. Food Sci. Food Saf.* **2019**, *18*, 106–120. [[CrossRef](#)]
27. Ten Bosch, L.; Pfohl, K.; Avramidis, G.; Wieneke, S.; Viöl, W.; Karlovsky, P. Plasma-Based Degradation of Mycotoxins Produced by *Fusarium*, *Aspergillus* and *Alternaria* Species. *Toxins* **2017**, *9*, 97. [[CrossRef](#)]
28. Siciliano, I.; Spadaro, D.; Prella, A.; Vallauri, D.; Cavallero, M.; Garibaldi, A.; Gullino, M. Use of Cold Atmospheric Plasma to Detoxify Hazelnuts from Aflatoxins. *Toxins* **2016**, *8*, 125. [[CrossRef](#)]
29. Hojnik, N.; Modic, M.; Tavčar-Kalcher, G.; Babič, J.; Walsh, J.L.; Cvelbar, U. Mycotoxin Decontamination Efficacy of Atmospheric Pressure Air Plasma. *Toxins* **2019**, *11*, 219. [[CrossRef](#)]
30. Turner, M. Physics of Cold Plasma. In *Cold Plasma in Food and Agriculture*; Misra, N.N., Schlüter, O., Cullen, P.J., Eds.; Academic Press: San Diego, CA, USA, 2016; pp. 17–51.
31. Robert, E.; Barbosa, E.; Dozias, S.; Vandamme, M.; Cachoncinlle, C.; Viladrosa, R.; Pouvesle, J.M. Experimental study of a compact nanosecond plasma gun. *Plasma Process. Polym.* **2009**, *6*, 795–802. [[CrossRef](#)]
32. Maletić, D.; Puač, N.; Malović, G.; Đorđević, A.; Petrović, Z.L. The influence of electrode configuration on light emission profiles and electrical characteristics of an atmospheric-pressure plasma jet. *J. Phys. D Appl. Phys.* **2017**, *50*, 145202. [[CrossRef](#)]
33. Hasan, M.I.; Walsh, J.L. Numerical investigation of the spatiotemporal distribution of chemical species in an atmospheric surface barrier-discharge. *J. Appl. Phys.* **2016**, *119*, 203302. [[CrossRef](#)]

34. Yonemori, S.; Ono, R. Flux of OH and O radicals onto a surface by an atmospheric-pressure helium plasma jet measured by laser-induced fluorescence. *J. Phys. D Appl. Phys.* **2014**, *47*, 125401. [[CrossRef](#)]
35. Graves, D.B. The emerging role of reactive oxygen and nitrogen species in redox biology and some implications for plasma applications to medicine and biology. *J. Phys. D Appl. Phys.* **2012**, *45*, 263001. [[CrossRef](#)]
36. Pârvolescu, V.I.; Magureanu, M.; Lukes, P. *Plasma Chemistry and Catalysis in Gases and Liquids*; Wiley-VCH Verlag GmbH & Co. KGaA: Weinheim, Germany, 2012; pp. 1–401.
37. Wang, L.; Shao, H.; Luo, X.; Wang, R.; Li, Y.; Li, Y.; Luo, Y.; Chen, Z. Effect of Ozone Treatment on Deoxynivalenol and Wheat Quality. *PLoS ONE* **2016**, *11*, e0147613. [[CrossRef](#)]
38. Olszewski, P.; Li, J.F.; Liu, D.X.; Walsh, J.L. Optimizing the electrical excitation of an atmospheric pressure plasma advanced oxidation process. *J. Hazard. Mater.* **2014**, *279*, 60–66. [[CrossRef](#)]
39. Misra, N.N.; Moiseev, T.; Patil, S.; Pankaj, S.K.; Bourke, P.; Mosnier, J.P.; Keener, K.M.; Cullen, P.J. Cold Plasma in Modified Atmospheres for Post-harvest Treatment of Strawberries. *Food Bioprocess Technol.* **2014**, *7*, 3045–3054. [[CrossRef](#)]
40. Park, B.J.; Takatori, K.; Sugita-Konishi, Y.; Kim, I.-H.; Lee, M.-H.; Han, D.-W.; Chung, K.-H.; Hyun, S.O.; Park, J.-C. Degradation of mycotoxins using microwave-induced argon plasma at atmospheric pressure. *Surf. Coat. Technol.* **2007**, *201*, 5733–5737. [[CrossRef](#)]
41. Shi, H.; Iilejji, K.; Strohshine, R.L.; Keener, K.; Jensen, J.L. Reduction of Aflatoxin in Corn by High Voltage Atmospheric Cold Plasma. *Food Bioprocess Technol.* **2017**, *10*, 1042–1052. [[CrossRef](#)]
42. Walsh, J.L.; Liu, D.X.; Iza, F.; Rong, M.Z.; Kong, M.G. Contrasting characteristics of sub-microsecond pulsed atmospheric air and atmospheric pressure helium–oxygen glow discharges. *J. Phys. D Appl. Phys.* **2010**, *43*, 032001. [[CrossRef](#)]
43. Watson, D.H. *Natural Toxicants in Food*; Sheffield Academic Press: Sheffield, UK, 1998; p. 322.
44. Moiseev, T.; Misra, N.N.; Patil, S.; Cullen, P.J.; Bourke, P.; Keener, K.M.; Mosnier, J.P. Post-discharge gas composition of a large-gap DBD in humid air by UV–Vis absorption spectroscopy. *Plasma Sources Sci. Technol.* **2014**, *23*, 065033. [[CrossRef](#)]
45. Zorlugenç, B.; Zorlugenç, F.K.; Öztekin, S.; Evliya, I.B. The influence of gaseous ozone and ozonated water on microbial flora and degradation of aflatoxin B1 in dried figs. *Food Chem. Toxicol.* **2008**, *46*, 3593–3597. [[CrossRef](#)]
46. De Alencar, E.R.; Faroni, L.R.; Soares Nde, F.; da Silva, W.A.; Carvalho, M.C. Efficacy of ozone as a fungicidal and detoxifying agent of aflatoxins in peanuts. *J. Sci. Food Agric.* **2012**, *92*, 899–905. [[CrossRef](#)]
47. Arsenović, M.; Pezo, L.; Stanković, S.; Radojević, Z. Factor space differentiation of brick clays according to mineral content: Prediction of final brick product quality. *Appl. Clay Sci.* **2015**, *115*, 108–114. [[CrossRef](#)]
48. Siegel, D.; Feist, M.; Proske, M.; Koch, M.; Nehls, I. Degradation of the *Alternaria* mycotoxins alternariol, alternariol monomethyl ether, and altenuene upon bread baking. *J. Agric. Food Chem.* **2010**, *58*, 9622–9630. [[CrossRef](#)]
49. European Commission. Commission Regulation 2002/657/EC of 12 August 2002 implementing council directive 96/23/EC concerning the performance of analytical methods and the interpretation of results. *OJEC* **2002**, *221*, 8–36.
50. *STATISTICA (Data Analysis Software System)*, V13.3; StatSoft, Inc.: Tulsa, OK, USA, 2018.
51. Box, G.E.P.; Behnken, D.W. Some New Three Level Designs for the Study of Quantitative Variables. *Technometrics* **1960**, *2*, 455–475. [[CrossRef](#)]
52. Khuri, A.I.; Mukhopadhyay, S. Response surface methodology. *Wiley Interdiscip. Rev. Comput. Stat.* **2010**, *2*, 128–149. [[CrossRef](#)]
53. Brlek, T.; Pezo, L.; Voća, N.; Krička, T.; Vukmirović, Đ.; Čolović, R.; Bodroža-Solarov, M. Chemometric approach for assessing the quality of olive cake pellets. *Fuel Process. Technol.* **2013**, *116*, 250–256. [[CrossRef](#)]



PAPER

## DC discharge in low-pressure ethanol vapour

To cite this article: J Sivoš *et al* 2019 *Plasma Sources Sci. Technol.* **28** 055011

View the [article online](#) for updates and enhancements.



**IOP | ebooks™**

Bringing you innovative digital publishing with leading voices to create your essential collection of books in STEM research.

Start exploring the collection - download the first chapter of every title for free.

# DC discharge in low-pressure ethanol vapour

J Sivoš<sup>1</sup> , D Marić<sup>1</sup> , N Škoro<sup>1</sup> , G Malović<sup>1</sup>  and Z Lj Petrović<sup>1,2</sup> 

<sup>1</sup>Institute of Physics, University of Belgrade, Pregrevica 118, 11080 Belgrade, Serbia

<sup>2</sup>Serbian Academy of Sciences and Arts, Knez Mihailova 35, 11001 Belgrade, Serbia

E-mail: [sivosj@ipb.ac.rs](mailto:sivosj@ipb.ac.rs)

Received 2 November 2018, revised 25 January 2019

Accepted for publication 21 February 2019

Published 21 May 2019



CrossMark

## Abstract

In this paper, we present data from experimental studies of the DC breakdown in ethanol vapour at low pressure as well as electrical and optical measurements of DC discharge parameters from low-current to high-current regimes. A Paschen curve and the corresponding distribution of emission intensities at low-current were recorded in the range of  $pd$  (pressure  $\times$  electrode gap) from 0.10 Torr cm to 3.00 Torr cm, covering the region of Paschen minimum. Recorded axial profiles of emitted light from low-current discharge reveal that heavy particles make up a significant part in ethanol vapour breakdown in a wide range of values of  $pd$  i.e.  $E/N$ , for values  $E/N > 3$  kTd they become dominant. Also, we recorded volt–ampere characteristics at working conditions close to the minimum of the Paschen curve, together with spatial profiles of low-current discharge. In the region of transition from normal to abnormal glow, sudden changes of the regime of operation were observed.

Keywords: plasmas in liquids, electrical gas breakdown, DC discharges, alcohol vapour, volt–ampere characteristics

## 1. Introduction

Non-equilibrium plasmas are an indispensable part in the development of material processing and sputtering techniques, in microelectronics for fabrication of large-scaled integrated devices (LSI) and in the light sources industry [1]. Applications of non-equilibrium electrical discharges in organic liquids and their vapours is of interest for environmental technologies, sensor industries [2], nanotechnologies and biotechnologies [3, 4]. For instance, organic molecules (containing carbon and hydrogen atoms) play an important role in the production of graphene layers [5] and in the growth of nanotubes [6]. For a long time discharges in mixtures of gases involving alcohols have been used for elementary particle detectors [2, 7–9].

Recently, studies of discharges in ethanol (and other alcohols) began drawing attention because of their application in production of ecologically friendly sources of energy (biofuels for internal-combustion engines, PEMFC fuel cells) [10, 11], in nanoscience for fast growth of high purity carbon nanotubes (CNT's) and nanoparticles [12, 13], in the food industry, biomedicine etc. One of the main advantages of

applications of plasma operating in alcohols/alcohol vapours is the simplicity of experimental design allowing for fast emergence of new devices. However, development of applications cannot be based only on empirical technical advances in the design of devices. Key knowledge required for further advances is the understanding of discharges in liquids and their vapours and information about elementary processes taking part in the discharge [14].

One direction that research should take are measurements of elementary properties of the discharge regarding breakdown, operating regimes and discharge structure etc. Breakdown studies can reveal information on processes and their balance in discharges. Moreover, secondary electron production is an important parameter of the discharge and to obtain it, and consequently to develop realistic models of discharges, it is not sufficient to only model the Paschen curve, but also the volt–ampere (VA) characteristics of the discharge [15].

In this paper we present measurements in low pressure ethanol vapour of a Paschen curve, showing the dependence of breakdown voltages ( $V_b$ ) as a function of the product of pressure and electrode distance ( $pd$ ). Besides, we recorded

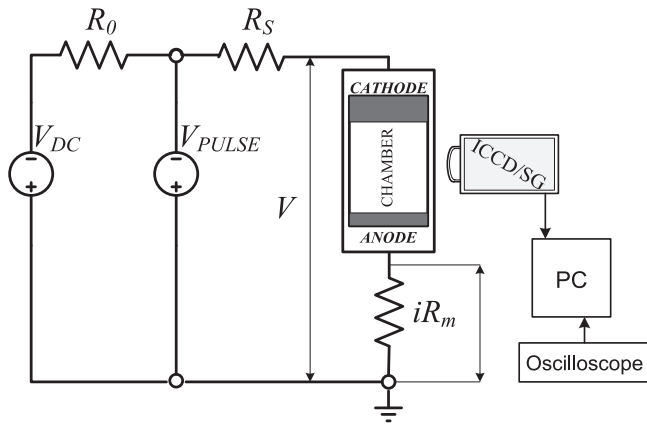


**Figure 1.** Schematic of the experimental setup and the electrical circuit used in measurements. Recordings are obtained with an ICCD camera with an objective lens and a spectrograph (SG).

VA characteristics at working conditions close to the minimum of the Paschen curve. We also noticed and performed a detailed analysis of the unusual behaviour of the discharge regime switching, observed in the abnormal glow. All measurements of electrical properties are supported with recordings of axial discharge structure by an ICCD camera. Hence, our study of low pressure discharges in ethanol vapour provides a complete set of breakdown data together with spatial profiles of low-current discharge as well as thorough investigation of electrical and optical properties of the discharge operating in a wide range of currents in the VA characteristics.

## 2. Experimental setup

Figure 1 shows a simplified schematic of the experimental setup. Discharge is initiated between two parallel-plate electrodes, placed inside a tightly fitting quartz tube. Each of electrodes is 5.4 cm in diameter. The cathode (C) is made of copper, while the anode (A) is made of quartz covered by a thin, transparent, conductive platinum film. The distance of electrodes can be adjusted and for this experiment it was set to 1.1 cm.

Construction of the discharge chamber allows side-on recordings and we used two setups to register emission coming from the discharge. In the first case, the camera was equipped with an objective lens allowing us to acquire axial discharge profiles of spectrally integrated emission in the visual range of spectra, defined by the transparency of the objective and the quantum efficiency of the ICCD photocathode. Additionally, placing band-pass optical filters that have maximum transparency at 431 nm (region of hydrocarbon CH radical emission band, the  $^2\Delta \rightarrow ^2\Pi$  transition) and at 656 nm (region of H $\alpha$  line emission, the  $n = 3$  to  $n = 2$  transition) in front of the objective lens allowed us to record the profiles of emission at quoted wavelengths. In another setup, to obtain a spectrum of emission of ethanol discharge we focused light from the discharge volume to a 100  $\mu\text{m}$  entrance slit of spectrograph ORIEL MS127i. In both cases, a

sensitive ICCD camera (Andor IStar DH720-18U-03) was used for detecting the signal. The spectrograph is equipped with a ruled grating with a wavelength range from 200 to 1200 nm and spectral resolution 0.22 nm.

In order to obtain reproducible results, it is necessary to perform preparations before every measurement. In the beginning, the system is pumped down to an initial pressure of the order of  $10^{-6}$  Torr. Before the measurements, the cathode surface is conditioned in a hydrogen discharge with a current around 30  $\mu\text{A}$  (for approximately 40 min), until the operating voltage stabilizes. Hydrogen is chosen because it is lightweight, so no cathode material is dispersed. At the same time, this treatment effectively removes chemical oxides and adsorbed layers of impurities from the cathode surface and thus produces the same surface conditions for each measurement.

Additionally, values of pressure are measured to better than 1% uncertainty. As for the gap  $d$  it is also of the order of 2% uncertainty but it is fixed for all measurements as it does not change from one pressure to another. The critical issue is the changes in the surface conditions and there we needed to ascertain the reproducibility of results. For argon, the reproducibility is excellent (better than 1% over long time periods) but for gases such as ethanol the reproducibility is not as good as there is always a possibility of deposition. Thus, we repeated cleaning cycles and checked for the reproducibility over the period of measurements. Changes in the breakdown voltage were taken as an indication that surface of the cathode has been conditioned (deposition or possibly cleaning) and we repeated cleaning that always produced results within narrow margins (to one volt). Thus, one may conclude that the uncertainty of measurements of the voltage is less than 1%, the current is accurate to several percent but bearing in mind extrapolation to the zero current uncertainty is mainly defined by the uncertainty of the voltage measurements, while uncertainties in current average out if results were obtained carefully. The experimental uncertainty is of the order of the size of the points or less.

Ethanol vapour is obtained from 95% ethanol ( $\text{C}_2\text{H}_5\text{OH}$ ) ( $M = 46.07 \text{ g mol}^{-1}$ ). The main impurity in ethanol is water, while other impurities, such as acetone, methanol, aldehydes, formic acid are present only in traces ( $<0.001\%$ ). Therefore a small percentage of water vapour is present in the discharge. Typically, molecular gas impurities produce a very large effect on the discharges in atomic gases due to lack of vibrational energy losses in the former. Another strong effect arises from the attachment to impurities that may strongly affect the gases that are not subject to attachment. However, neither of the two effects are important in the ethanol vapour and they will not affect the results strongly. We could not clean the samples any further by freezing and evacuating the liquid as the freezing of ethanol occurs at a very low temperature. The vapour is introduced into the chamber at low pressure from a container with a liquid sample, through a pressure regulatory valve at a low flow rate. Immediately after opening the valve alcohol begins to boil due to the pressure difference over its surface and the pressure of gases dissolved in the sample itself. Throughout this process alcohol becomes

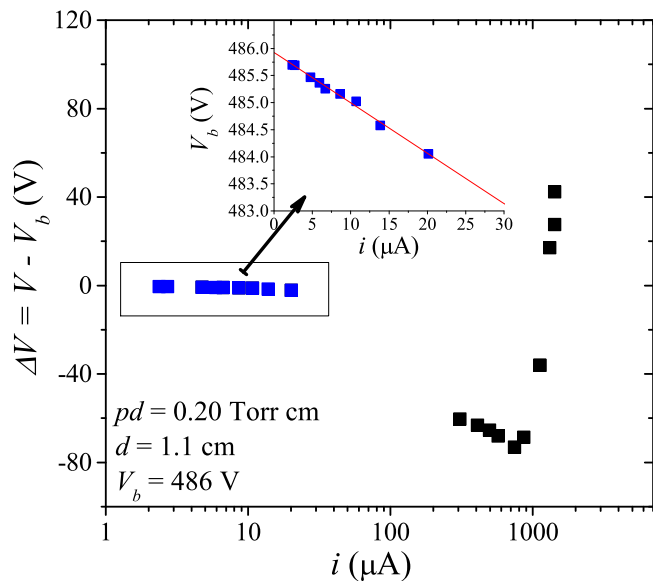


**Figure 2.** Example of VA characteristics of ethanol vapour discharge at  $pd = 0.20$  Torr cm and  $d = 1.1$  cm, with an illustration of breakdown voltage determination in the inserted graph.

devoid of dissolved volatile constituents and after few seconds the sample surface becomes still. After that, the vapour is maintained at moderate pressure ( $\sim 20$  Torr) in the chamber for periods of 1–2 h in order to saturate the electrodes and the chamber walls. The vapour pressure of ethanol, at room temperature, is around 45 Torr [16], so during the measurements operating pressure is kept well below this value to avoid the formation of liquid droplets.

The electric circuit is designed to provide operation of the discharge both at breakdown conditions (i.e. low-current limit) and at higher currents. The breakdown voltage for each  $pd$  is determined from the low-current limit of the discharge, by extrapolating the discharge voltage to zero current in the dark Townsend discharge mode [15, 17]. In figure 2 we show VA characteristics with the low-current limit enlarged and inserted in a separate graph in order to illustrate determination of the breakdown voltage. One should pay attention to the linear extrapolation with small changes of voltage from the lowest current points to the zero current limit. Usually we limit ourselves to below  $10 \mu\text{A}$  currents.

The discharge current is determined by measuring voltage drop on the resistor  $R_m$ . Recording of VA characteristics is accomplished in a pulsed regime, by imposing a short pulse of voltage in addition to running discharge at a small DC current ( $\sim 1 \mu\text{A}$ ). Pulses last long enough to allow the formation of the steady-state discharge and measurement of constant values in voltage and current signals. Pulsed mode of operation prevents the heating and conditioning of the cathode surface during the measurements, while a small DC current is also used to eliminate the breakdown delay time [18, 19]. The pulses are synchronized with the ICCD camera so electrical measurements and recording of emission can be acquired simultaneously.

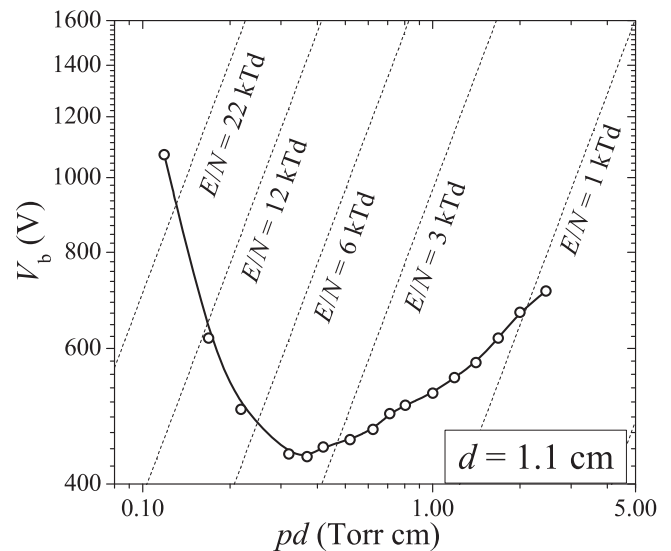


**Figure 3.** Paschen curve for discharges in ethanol vapour at  $d = 1.1$  cm, at various reduced electric field ( $E/N$ ) indicated by dashed lines [ $1 \text{ Td} = 10^{-21} \text{ Vm}^{-2}$  and  $1 \text{ Torr} = 133.32 \text{ Pa}$ ].

### 3. Results and discussion

#### 3.1. Paschen curve

The Paschen curve for the discharge in ethanol vapour at an electrode gap of 1.1 cm is shown in figure 3. Breakdown voltage dependence on  $pd$ , where  $p$  is pressure and  $d$  is electrode gap, cover a range from 0.10 Torr cm to 3.00 Torr cm.

The shape of the Paschen curve is typical for low pressure DC discharges [15]. The minimum breakdown voltage of 435 V occurs at around  $pd = 0.35$  Torr cm, which corresponds to the reduced electric field value of  $E/N = 4 \text{ kTd}$ . After breakdown, the discharge operates stably at low-currents up to  $pd = 0.70$  Torr cm, but above this value discharge ignites into oscillations. For  $pd$ s in the range between 0.70 and 3.00 Torr cm, we could not operate the discharge outside the oscillatory regime- the oscillations are the same as the oscillations annotated in the VA characteristics, and we have chosen the modes that allowed us to determine the breakdown voltage most accurately [20, 21]. There are periodic relaxation oscillations with frequencies between 250 and 800 Hz. However, above 3.00 Torr cm, it becomes difficult to control the discharge, oscillations become random and we cannot use them to establish a breakdown voltage with reasonable accuracy. Spatial profiles of emission from the discharge recorded along with breakdown data confirm that even at the highest pressures covered here, there is no evidence of transition to the streamer discharge in the range of  $pd$  covered here.

#### 3.2. Spectrally and spatially resolved measurements

Measurement of emission spectra enables identification of species existing in the discharge. In figure 4 we present optical emission spectrum for ethanol vapour discharge recorded at  $pd = 0.10$  Torr cm at low current, i.e. for the

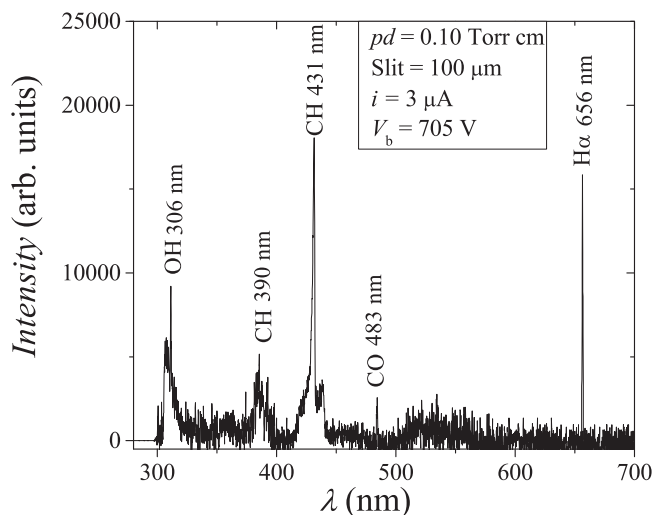


**Figure 4.** Emission spectrum of discharge in ethanol vapour at  $pd = 0.10$  Torr cm and  $d = 1.1$  cm. The width of the spectrograph slit was  $100 \mu\text{m}$ .

discharge operating in Townsend regime. Very few lines are observed because of the very small current of  $3 \mu\text{A}$ .

In the spectral range 300–700 nm, we detected OH, CO, CH, and  $H\alpha$  (Balmer series line) emission. All observed emission stems from excited species produced in dissociative excitation of the parent molecule [22–25] producing H atoms and some heavier excited dissociation fragments (OH, CO and/or  $C_xH_y$ ). As previously observed in ethanol discharges [6, 23, 25], it is possible to form CO from the molecule of ethanol either in collisions with electrons or radicals/ $H_2O$  molecules. Additionally, the spectra baseline features a broad peak at wavelengths between 500 nm and 600 nm which can be caused by  $CO_2$  continuum [26], CO band emission [27] or  $C_2$  Swan band emission [26].

Besides measurements of emission spectra we also recorded spatially resolved emission. These recordings include spatial profiles of the total emission in a visual spectral range and spatial distribution of emission in a narrow wavelength interval around the most intense lines in the visible part of the spectrum (431 nm and 656 nm). Axial emission profiles shown in figure 5 are extracted along the discharge axis from 2D images obtained for emission spectrally integrated in visual spectra and filtered by CH and  $H\alpha$  band-pass optical filters.

Profiles for different  $pd$  values between 0.10–0.60 Torr cm present how the change of  $E/N$  ( $pd$ ) influences the structure and basic processes in the discharge. Since during these recordings discharge operates at a low-current limit i.e. in the Townsend regime, where the density of space charge is insignificant so electric field between electrodes is nearly homogeneous [18], one would expect an exponential rise of emission towards the anode as electrons gain enough energy for excitation processes in electron–neutral collisions. However, presented integrated profiles (solid lines) for all  $pd$  values reveal a strong emission peak in front of the cathode. The work of Phelps and colleagues has shown that heavy-particle (fast neutral) excitation is the

dominant cause of the emission in front of the cathode [19, 28]. While CH emission singled out from the discharge (dashed lines) follows the integrated profiles in shape,  $H\alpha$  emission (dash dotted lines) exhibit dissimilar shape and a much lower emission intensity as compared to the CH emission.

At the 0.10 and 0.20 Torr cm (figures 5(a) and (b)), in the left-hand branch of the Paschen curve, predominate emission comes from the wavelength range covered by the CH filter suggesting that CH species have the most important role in heavy-particle excitations. With the increase of pressure, at  $pd = 0.60$  Torr cm (figure 5(d)), CH emission partakes less in the total emission. The peak of the total emission near the anode, that emerges at  $pd = 0.20$  Torr cm (figure 5(b)) and exceeds maximum of emission in front of the anode at  $pd = 0.60$  Torr cm at the highest values of  $pd$  (lowest  $E/N$ ) (figure 5(d)), is created due to excitation processes in electron–neutral collisions. In this case, the  $H\alpha$  emission intensity (dash dotted lines) is also much higher. The shape of  $H\alpha$  profile in the range from 0.20 Torr cm to high  $pd$  values suggest that only electron excitation plays role in the case of H atom in that range. However, at low  $pd$  (high  $E/N$ ) H atoms are also excited in collisions with heavy particles.

### 3.3. Volt–ampere characteristics

For a complete picture of ethanol vapour discharge properties, along with the breakdown and low-current recordings, it is also necessary to obtain VA characteristics. In figure 6 we show VA characteristics of ethanol vapour discharge at  $pd = 0.20$  Torr cm measured in the range of discharge currents from  $\sim 1 \mu\text{A}$  to several mA together with 2D images of typical operating regimes for low pressure DC discharges [29, 30]. These regimes are clearly distinguished [28, 29].

In the diffuse Townsend regime (up to  $20 \mu\text{A}$ ), VA characteristics shows a slightly negative slope, with a negative differential resistance of  $R_D = -84 \text{ k}\Omega$ . The negative differential resistance, jointly with the breakdown data, is important in the analysis of secondary electron yields [15, 31]. Between Townsend and normal glow regime, for currents from  $20 \mu\text{A}$  to  $300 \mu\text{A}$ , is a region of free-running oscillations characterized by a more rapidly decreasing voltage.

After this region, the discharge becomes constricted and operates in a stable regime of normal glow. With a further increment of the current, discharge becomes diffuse again and runs in an abnormal regime that is characterized by a very steep positive slope in VA characteristics for currents above  $740 \mu\text{A}$ . In 2D images recorded for all discharge regimes, i.e. at all discharge currents investigated, there is a peak of emission in front of the cathode. As for the low-current case discussed before, it has been shown that the peak of emission at the cathode in higher current regimes is a result of fast neutral excitation. These fast neutrals are mainly produced by fast ions going through charge–transfer collisions with molecules of the background gas [19, 32]. These processes are prone to occur at lower pressures since the ion energy gain has smaller dissipation in collisions. Lower pressures



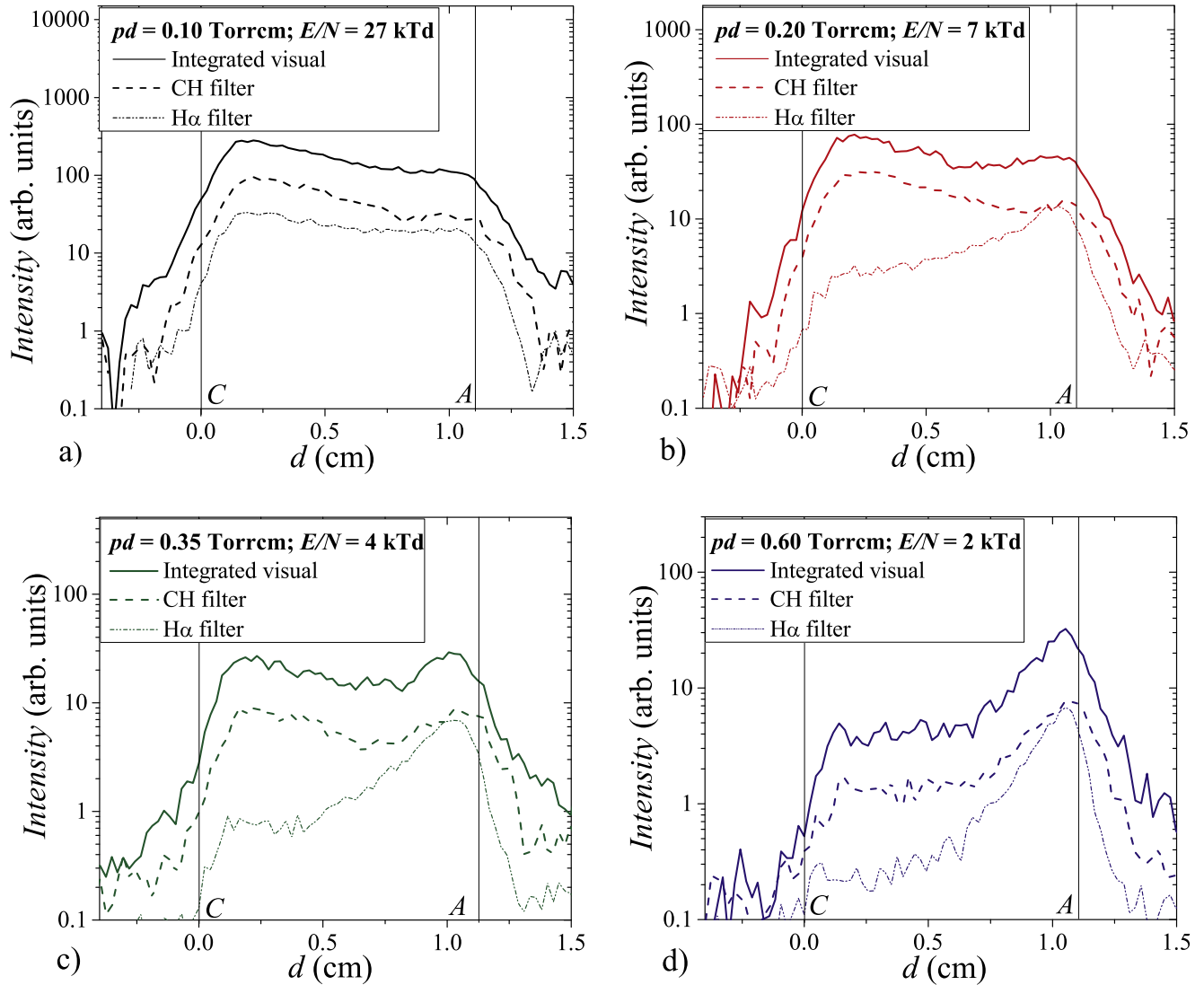


**Figure 5.** Axial profiles of emission from discharge in ethanol vapour for different values of  $pd$  (pressure  $\times$  electrode gap) and  $E/N$  (reduced electric field) at electrode gap  $d = 1.1$  cm. Filtered emission is recorded at the same intensity scale and corrected for the filter transparency. Letters C and A indicate the positions of the cathode and anode.

typically correspond to the conditions at the left-hand side of the Paschen curve, where the  $E/N$ -s are high enough, which is the case for the VA characteristics shown in figure 5. Particularly, for ethanol vapour the most probable candidates for heavy particles that participate in excitation and ionization are fast H atoms and some heavier dissociation fragments (OH, CO and CH species).

During our investigation of normal glow, sudden changes in the operating conditions (even in regime) were observed. Measurements reveal changes in the steady-state current and voltage values within a single voltage pulse. Changes in discharge operating modes have been noticed before, in the case of a normal glow in argon [17] and in the case of hollow cathode discharges [33, 34], where a sudden increase of current is followed by a decrease of operating voltage within a single pulse. However, in the present study the discharge operates at the lower current and higher voltage after the transition.

In figure 7 we show two examples of the effect where current and voltage waveforms have pronounced step-like shapes due to the mode change. The transition effect is present in the current range from around  $860 \mu\text{A}$  (beginning of positive slope of the VA characteristics) to around  $1430 \mu\text{A}$ . In the first example, at lower current shown in figure 7(a) the transition in operation mode occurs approximately 2 ms after the pulse ignition. During the transition, the discharge switches to a  $\sim 40$  V higher voltage and  $\sim 130 \mu\text{A}$  smaller current.

The transition is smooth and lasts around  $15 \mu\text{s}$ . In the second example, shown in figure 7(b), the same effect is present at a higher initial current of  $\sim 1680 \mu\text{A}$ , but the transition here happens only  $30 \mu\text{s}$  after the initial time interval of stable operation. The transition lasts around  $3 \mu\text{s}$ , and the discharge switches to  $\sim 70$  V higher voltage and  $\sim 320 \mu\text{A}$  smaller current. It appears that the transition happens earlier within the pulse for higher initial currents. At given conditions, mode change in consecutive pulses is very

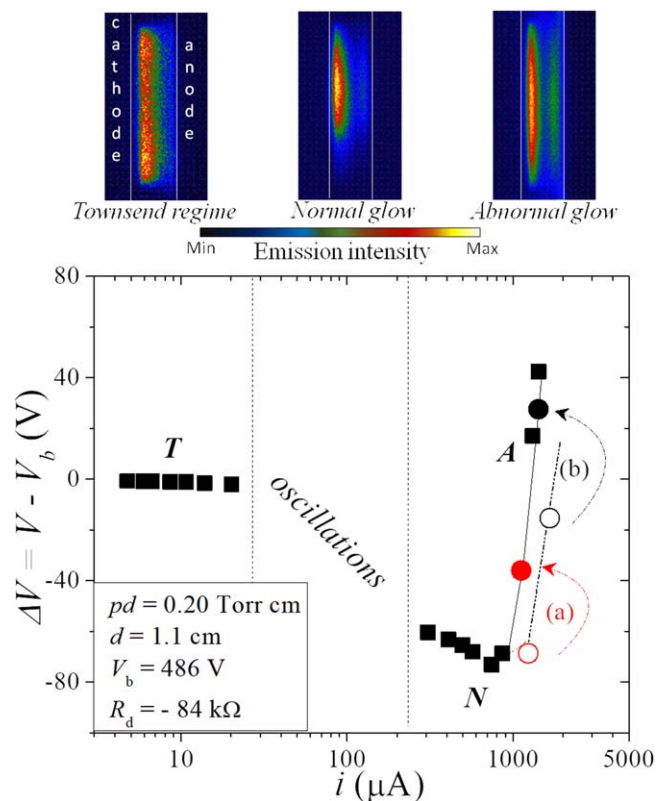


**Figure 6.** VA characteristics of ethanol vapour discharge at  $pd = 0.20$  Torr cm and  $d = 1.1$  cm. The voltage is shown as a difference between discharge ( $V$ ) and breakdown voltage ( $V_b$ ). Capital letters (T, N, A) correspond to 2D false colour images of the discharge running in different regimes. Circles and arrows indicate transitions in operating regimes shown in figure 7 (please see text for details).

reproducible, it always occurs at the same time after the beginning of the pulse. The transition is always smooth and there are no instabilities or oscillations in the voltage and current waveforms.

Together with the waveforms, recordings of light emission from the discharge are taken several times during one pulse. Figure 8 shows axial profiles of emission recorded with short exposure time ( $0.2 \mu\text{s}$ ) at time points marked in figure 7(b). Generally, in both profiles, a significant influence of heavy particles in excitation and ionization is present, judging by the peak of emission near the cathode. Although the discharge current drops after the step, the overall intensity of emission is higher. However, ratios of maximum intensities of profiles near electrodes obtained for both cases, before the step (open circles) and after the step (full circles), are the same (around 3). Moreover, from 2D images of the discharge taken before and after the transition, we estimated that in the radial direction both profiles have the same width and therefore the same effective discharge area [35]. One significant difference between profiles is in the position of emission peak that corresponds to the negative glow i.e. coincides with the edge of the cathode fall [36]. The edge of the cathode fall region shifts closer to the cathode after the transition.

This kind of behaviour is very unusual, as one would expect that the length of the cathode fall would increase with

the decrease of current [36]. The cause for such change in electric field distribution, discharge current and voltage is not clear. Bearing in mind that the timing of the effect is reproducible in consecutive pulses, we cannot attribute the effect to deposition or sputtering. Gas or electrode heating should not have a significant influence, as the discharge pulses are kept short and the discharge operates in slow flow regime to avoid those effects. Furthermore, one would expect the effect to be more significant at higher currents. From the estimates based on the complete sets of cross sections for similar gases for which such sets exist, the degree of dissociation does not affect the results. The observed behaviour is probably connected to changes in the balance of charged or excited species: ions or electronically and vibrationally excited dissociation products and adsorbed species created in discharges [22]. Thus, in some time intervals, after the pulse application, the dominant gas species produced in the discharge may be changed and consequently influence the balance of charged and excited species. In order to clarify and explain the mechanism behind the transition, additional experimental measurements and modelling should be performed.

#### 4. Conclusions

Discharges in vapours and liquids, especially organic ones, have become a very popular area of research due to a wide range of applicability [4, 14]. However, lack of relevant and complete existing data on elementary processes have become important obstacles to further understanding of these complex systems [37–41]. By measuring properties of DC breakdown, low-current and glow discharges in ethanol vapour we aim to provide information necessary for the understanding of this kind of non-equilibrium discharge.

In this paper we present data from experimental studies of the DC breakdown in ethanol vapour at low pressure as well as electrical and optical measurements of DC discharge parameters from low-current to moderately high-current regimes. A Paschen curve in ethanol vapour has a minimal breakdown voltage of 435 V at  $pd = 0.35$  Torr cm. Recorded axial profiles of emitted light from low-current discharge reveal that heavy particles make a significant contribution to ethanol vapour breakdown in a wide range of values of  $pd$  i.e.  $E/N$ . For  $E/N > 3$  kTd they become dominant. Spatially resolved emission measurements with optical filters show that most of the emission in visible spectral range originates from CH radicals and H atoms, probably mostly through dissociative excitation rather than ground state excitation [42]. Spectrally resolved measurements reveal that OH band (head at 306 nm), CH band (head at 431 nm) and H $\alpha$  line have the largest share in the emission spectrum in the range from 300 to 700 nm, while CO lines are also visible. The measured VA characteristics at  $pd = 0.20$  Torr cm has the shape typical for low pressure discharges.

Measurements in a narrow current range in the abnormal glow part of the VA characteristics reveal sudden transitions while operating in a stable discharge regime. Without any

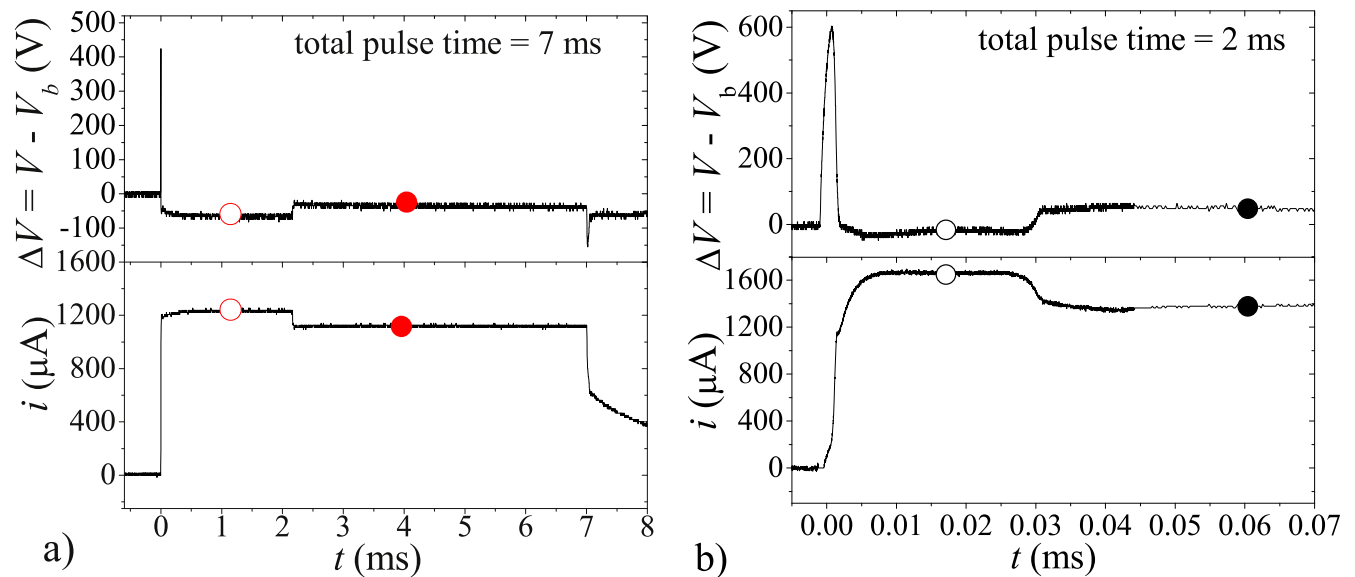


**Figure 7.** Waveforms of voltage and current obtained (a) at lower current (initially  $i_d \approx 1240 \mu\text{A}$ ) and (b) higher current (initially  $i_d \approx 1680 \mu\text{A}$ ) with the transition effect within a pulse. Voltage is presented as a difference between breakdown voltage ( $V_b = 486 \text{ V}$ ) and operating voltage. Values before and after the transition are shown as open and closed circles respectively are plotted in figure 6.

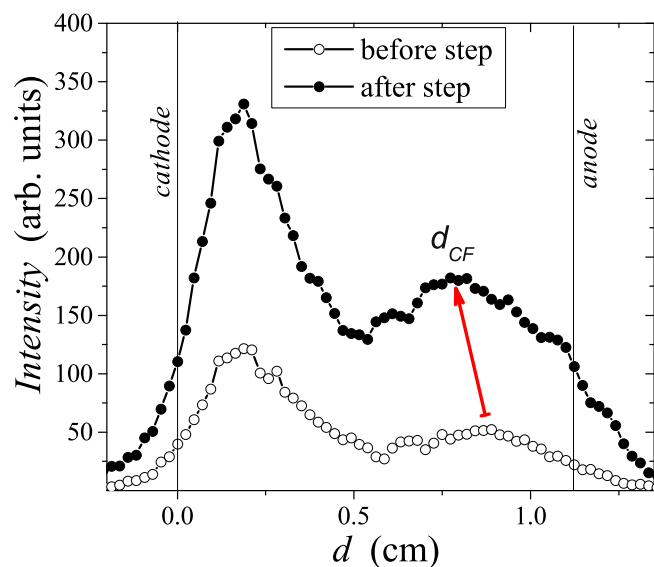


**Figure 8.** Profiles of emission taken along the axis of 2D images of the discharge recorded before (open symbols) and after (full symbols) the step at time points marked in figure 7(b). Change of the initial steady-state values of current and voltage after the step are:  $\delta i = -320 \mu\text{A}$ ,  $\delta V = 70 \text{ V}$ . Cathode fall length is indicated with  $d_{CF}$ .

instabilities or oscillations and with no significant change in the externally observed spatial structure, the discharge switches between steady-state modes of operation changing from higher to lower current and from lower to higher voltage within a single voltage pulse. The transition into a more preferable operating mode, after some time of stable operation, is probably due to changes in the balance of charged and excited species, dissociation products and adsorbed species created in the discharge. The effect is interesting from the point of view of fundamental discharge properties and from

the point of view of applications that work in pulsed or high frequency glow regime.

## Acknowledgments

The authors acknowledge support from the Serbian Ministry of Education, Science and Technological Development under project numbers OI 171037 and III 41011.

## ORCID iDs

J Sivoš <https://orcid.org/0000-0001-7872-2220>

D Marić <https://orcid.org/0000-0002-1728-5458>

N Škoro <https://orcid.org/0000-0002-0254-8008>

G Malović <https://orcid.org/0000-0003-2356-0652>

Z Lj Petrović <https://orcid.org/0000-0001-6569-9447>

## References

- [1] Adamovich I *et al* 2017 *J. Phys. D: Appl. Phys.* **50** 323001
- [2] Fonte P, Mangiarotti A, Botelho S, Goncalves J A C, Ridenti M A and Bueno C C 2010 *Nuclear Instruments Method. Phys. Res. A* **613** 40–5
- [3] Puač N, Živković S, Selaković N, Milutinović M, Boljević J, Malović G and Petrović Z L 2014 *Appl. Phys. Lett.* **104** 214106
- [4] Škoro N, Puač N, Živković S, Krstić-Milošević D, Cvelbar U, Malović G and Petrović Z L 2018 *Euro. Phys. Journal D* **72** 2
- [5] Hagino T, Kondo H, Ishikawa K, Kano H, Sekine M and Hori M 2012 *Appl. Phys. Express* **5** 035101
- [6] Suda Y, Okita A, Takayama J, Oda A, Sugawara H, Sakai Y, Oke S and Takikawa H 2009 *IEEE Transactions on Plasma Science* **37** 1150–5

- [7] Grupen C and Shwartz B 2008 *Particle Detectors* 2nd edn (New York: Cambridge University Press)
- [8] Liebson S H 1947 *Phys. Rev.* **72** 602
- [9] Elliot H 1949 *Proc. Phys. Soc. A* **62** 369
- [10] Petitpas G, Rollier J D, Darmonb A, Gonzalez-Aguilar J, Metkemeijer R and Fulcheri L 2007 *Int. J. Hydrogen Energy* **32** 2848–67
- [11] Sekine Y, Matsukata M, Kikuchi E, Kado S and Haga F 2004 *Am. Chem. Soc. Div. Fuel. Chem.* **49** 914–5
- [12] Maruyama S *et al* 2002 *Chem. Phys. Lett.* **360** 229–34
- [13] Matsushima M, Noda M, Yoshida T, Kato H, Kalita G, Kizuki T, Uchida H, Umeno M and Wakita K 2013 *J. Appl. Phys.* **113** 114304
- [14] Bruggeman P J *et al* 2016 *Plasma Sources Sci. Technol.* **25** 053002
- [15] Marić D, Savić M, Sivoš J, Škoro N, Radmilović-Radjenović M, Malović G and Petrović Z L 2014 *Eur. Phys. J. D* **68** 155
- [16] Weast R C 1970 *Handbook of Chemistry and Physics* 51st edn (Cleveland, Ohio: Chemical Rubber Co)
- [17] Petrović Z L and Phelps A V 1997 *Phys. Rev. E* **56** 5920–31
- [18] Živanov S, Živković J, Stefanović I, Vrhovac S and Petrović Z L 2000 *Eur. Phys. J. Appl. Phys.* **11** 59–69
- [19] Marić D, Hartmann P, Malović G, Donko Z and Petrović Z L 2003 *J. Phys. D: Appl. Phys.* **36** 2639–48
- [20] Marić D, Škoro N, Malović G, Graham W G and Petrović Z L 2009 *29th ICPIG (Cancun, Mexico)* 8
- [21] Kuschel T, Stefanović I, Škoro N, Marić D, Malović G, Winter J and Petrović Z L 2011 *IEEE Trans. Plasma Sci.* **39** 2692
- [22] Levko D S, Tsymbalyuk A N and Shchedrin A I 2012 *Plasma Phys. Rep.* **38** 913–21
- [23] Yanguas-Gil A, Hueso J L, Cotrino J, Caballero A and González-Elipse A R 2004 *Appl. Phys. Lett.* **85** 4004
- [24] Reyes P G, Gómez A, Martínez H, Flores O, Torres C and Vergara J 2016 *IEEE Trans. Plasma Sci.* **44** 2995–3000
- [25] Donohue D E, Schiavone J A and Freund R S 1977 *J. Chem. Phys.* **67** 769
- [26] Gaydon A 2012 *The Spectroscopy of Flames* (Netherlands: Springer)
- [27] Poncin-Epaillard F and Aouinti M 2002 *Plasmas and Polymers* **7** 1–17
- [28] Petrović Z L, Jelenković B M and Phelps A V 1992 *Phys. Rev. Lett.* **68** 325
- [29] Marić D, Malović G and Petrović Z L 2009 *Plasma Sources Sci. Technol.* **18** 034009
- [30] Raizer Y P 1991 *Gas Discharge Physics* (Berlin: Springer)
- [31] Phelps A V, Pitchford L C, Pedoussat C and Donkó Z 1999 *Plasma Sources Sci. Technol.* **8** B1–2
- [32] Petrović Z L and Stojanović V 1998 *J. Vacuum Sci. Technol. A* **16** 329–36
- [33] Marić D, Škoro N, Malović G, Petrović Z L, Mihailov V and Djulgerova R 2009 *J. Phys.: Conf. Ser.* **162** 012007
- [34] Li S, Ouyang J T and He F 2010 *Chinese Phys. Lett.* **27** 065201
- [35] Škoro N, Marić D and Petrović Z L 2008 *IEEE Trans. Plasma Sci.* **36** 994–5
- [36] Marić D, Kutasi K, Malović G, Donko Z and Petrović Z L 2002 *Eur. Phys. J. D* **21** 73
- [37] Stojanović V, Raspopović Z, Jovanović J, Nikitović Ž, Marić D and Petrović Z L 2017 *Eur. Phys. Journal D* **71** 283
- [38] Stojanović V, Raspopović Z, Marić D and Petrović Z L 2015 *Eur. Phys. J. D* **69** 63
- [39] Petrović Z L, Marić D, Savić M, Marjanović S, Dujko S and Malović G 2017 *Plasma Process Polym.* **14** 1600124
- [40] Puač M, Marić D, Radmilović-Radjenović M, Šuvakov M and Petrović Z L 2018 *Plasma Sources Sci. Technol.* **27** 075013
- [41] Petrović Z L, Simonović I, Marjanović S, Bošnjaković D, Marić D, Malović G and Dujko S 2017 *Plasma Phys. Control. Fusion* **59** 014026
- [42] Tennyson J *et al* 2017 *Plasma Sources Sci. Technol.* **26** 055014

FULL PAPER

# Activity of catalase enzyme in *Paulownia tomentosa* seeds during the process of germination after treatments with low pressure plasma and plasma activated water

Nevena Puač<sup>1</sup>  | Nikola Škoro<sup>1</sup> | Kosta Spasić<sup>1</sup> | Suzana Živković<sup>2</sup> |  
Milica Milutinović<sup>2</sup> | Gordana Malović<sup>1</sup> | Zoran Lj. Petrović<sup>1,3</sup>

<sup>1</sup> Institute of Physics, University of Belgrade, Pregrevica 118, 11080 Belgrade, Serbia

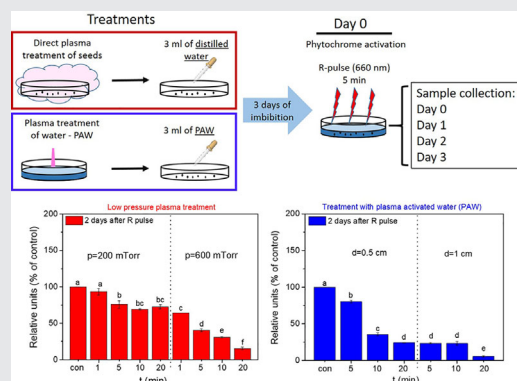
<sup>2</sup> Institute for Biological Research “Siniša Stanković”, University of Belgrade, Bulevar despota Stefana 142, 11060 Belgrade, Serbia

<sup>3</sup> Serbian Academy of Sciences and Arts, Knez Mihailova 35, 11000 Belgrade, Serbia

## Correspondence

Institute of Physics, University of Belgrade, Pregrevica 118, 11080 Belgrade, Serbia.  
Email: nevena@ipb.ac.rs

In this work we present results of two significantly different types of plasma treatment on *Paulownia tomentosa* Steud. seeds. In the first type, seeds were directly treated in low-pressure plasma and then imbibed with distilled water. In the second type, an atmospheric pressure plasma was used for obtaining plasma activated water (PAW) which is then used for imbibition of seeds. The CAT activity and protein content is evaluated during 4 d following the imbibition process, i.e., immediately after the phytochrome activation and in the 3 subsequent days. Comparison of results of treated seeds to the control group allows to correlate the enzyme activity and protein content during the initial stages of germination with plasma treatment types and treatment conditions.



## KEYWORDS

catalase, non-equilibrium plasma, plasma activated water, seed germination

## 1 | INTRODUCTION

Non-equilibrium plasmas for decades played an important role in treatments of various types of materials in order to modify roughness, hydrophobicity, produce coatings, polymerization, nanostructuring, increase the active area for absorbed dyes on textile surface, etc.<sup>[1–6]</sup> The choice which plasma system will be used is determined mainly by the type of the sample and the effect that plasma needs to achieve.

Another very important point in favor of plasmas is that they are environmentally friendly and, in most cases, cost efficient solutions that can supplement or replace in total classical treatments. Lately, the driving force for development of plasma sources, especially those that operate at atmospheric pressure, is the expansion of biomedical applications of plasmas. Low temperature plasmas so far have been successfully used for sterilization, wound healing, blood coagulation, cancer treatment, increasing of differentiation,

and proliferation of normal and human stem cells, stomatology, dermatology, and treatment/production of biocompatible materials.<sup>[7–14]</sup> Applications of these devices is accompanied by their detailed characterization by various diagnostic techniques<sup>[5,15,16]</sup> as well as comprehensive modeling that describe plasma behavior and chemistry, especially chemistry of reactive oxygen and nitrogen species (RONS) production that have key importance in biomedical applications.<sup>[4,17–24]</sup>

In recent times, new and fast developing field of low temperature plasma applications is plasma agriculture (application of plasmas for different aspects of agriculture and food industry). It was shown that both low pressure and atmospheric pressure plasmas can be successfully used in stimulation of seed growth, increase of germination percentage and decontamination, breaking of dormancy or increase in the length of seed sprout.<sup>[25–34]</sup> Plasma treatment of seeds became one of the starting points in opening of a wide area of applications of plasmas in agriculture and related biotechnologies. Nowadays, this list is much wider including treatments of seeds, soil, usage of plasma activated water, etc.<sup>[35–41]</sup>

In direct plasma treatments, i.e. where seeds are in direct contact with plasma or afterglow, the surface of seeds undergoes a variety of changes. During the plasma treatment, depending on the plasma conditions, the surface is activated so other functional groups can be attached (-COOH, -COH, -COO, -NH<sub>2</sub>, -OH, -NO, etc.). Also, during the treatment seed surface is etched and, at the same time, decontaminated from various types of microbes. As a result the surface contact angle is reduced and seeds' surface changes from hydrophobic to hydrophilic.<sup>[42,43]</sup> The main species responsible for this type of changes are neutrals and ions of nitrogen and oxygen, especially O(<sup>3</sup>P), O<sub>2</sub>(<sup>1</sup>Δ<sub>g</sub>), O<sub>3</sub>, NO, N, O(<sup>1</sup>D) and O<sub>2</sub><sup>-</sup> ion, which is signaling molecule in most of the cell processes. Lately, as an alternative to the direct plasma treatment of seeds and plants, application of water treated by plasma, the plasma activated water (PAW), gives similar results in the increase of germination percentage, decontamination of both seeds and plants and faster growth.<sup>[44–46]</sup> The reason for these enhancement lies in the fact that in comparison to regular water PAW contains large amounts of chemically active species produced in plasma and at the plasma-liquid interface. These species are transferred from the interface volume to the liquid bulk and are able to trigger desired responses in biological samples. Some of the most important species appearing in the liquid bulk of PAW that are involved in triggering cell mechanisms are OH, O, NO, H, H<sub>2</sub>O<sub>2</sub>, NO<sub>2</sub><sup>-</sup>, O<sub>2</sub><sup>-</sup>, NO<sub>3</sub><sup>-</sup>, OH<sup>-</sup>.<sup>[47–50]</sup> In this paper, we want to compare the effects of these two significantly different types of treatments on the seeds of model plant *P. tomentosa* Steud. To accomplish this we have used a low pressure radio-frequency (RF) plasma system for direct treatment of seeds and an atmospheric pressure plasma jet (APPJ)<sup>[51]</sup> for treatment of distilled water in order to obtain PAW which is then used for

imbibition of the seeds. In addition to being a model plant *P. tomentosa* is a viable agricultural product often used in medical supplements and as addition to alcoholic drinks.

Seeds of *P. tomentosa* are positively photoblastic and their germination is phytochrome-controlled. The light requirement for maximum germination may vary from brief exposure to several hours of red light, depending on seed maturation conditions.<sup>[52]</sup> A large number of RONS are continuously produced during seed and plant development, from embryogenesis to germination.<sup>[53]</sup> However, cells have evolved protective mechanisms in order to control free radical-induced cellular damage.<sup>[54]</sup>

Process of *P. tomentosa* seeds germination consists of three phases: imbibition, the phase of phytochrome activity and the phase of radicle protrusion and elongation. The optimum imbibition time is 3 d. Previous findings showed that a 5 min illumination with red light (660 nm) is sufficient for the phytochrome activation, the phase that lasts from 48 to 72 h. The processes following, including radicle protrusion, require several days after which germination is completed.<sup>[52,55,56]</sup>

In the experiments that will be presented in this paper we have investigated the early phase of germination, preferentially immediately after the light treatment and up to 3 d after the phytochrome activation, through CAT enzyme protein content and activity. Catalase (CAT, EC 1.11.1.6) is a tetrameric protein found in all aerobic organisms that catalyzes the dismutation of H<sub>2</sub>O<sub>2</sub> into water and oxygen.<sup>[57]</sup> CAT represents one of the several cellular antioxidant defenses that play an important role in scavenging reactive oxygen species (ROS).<sup>[58]</sup> It was shown that, particularly in oily seeds, CAT is very important in the early germination events because it removes H<sub>2</sub>O<sub>2</sub> produced during β-oxidation of the fatty acids.<sup>[59]</sup>

Increased generation of ROS seems to be a common feature of the early germination phase, which is the critical step of the process, since it involves activation of a regulatory system controlled by intrinsic (i.e., dormancy) and extrinsic (i.e., environmental conditions, such as temperature, oxygen, and water availability) factors.<sup>[53]</sup>

Plasma treatment has been found to promote seedling growth, increase proline concentration as well as activities of superoxide dismutase (SOD) and peroxidase (POD) in wheat seedlings under drought stress.<sup>[60]</sup> Similar observations have been made for oilseed rape seedlings, confirming that SOD and CAT activities were significantly increased after cold plasma treatment. Jiang et al.<sup>[61]</sup> reported that cold plasma treatment increases activities of POD, phenylalanine ammonia lyase (PAL), and polyphenol oxidase (PPO) of tomato under disease stress.<sup>[62]</sup> In spite of these studies of antioxidant enzymes activity in plasma treated seedlings and plants, evaluation of cold plasma effect on seeds during germination has not been investigated. Having in mind that plasma treatment of seed induces a significant increase in germination, it is of particular interest to study the effect of plasma on seeds.

Hydrogen peroxide is widely generated in plants and mediates various physiological and biochemical processes. As a signaling molecule, it can activate proteins/genes related to plant growth and development. Accumulation of hydrogen peroxide can reinforce cell walls through lignification. CAT activity is essential for the removal of the potentially toxic hydrogen peroxide produced under various stress conditions and then for the avoidance of oxidative-stress-related damage.<sup>[63]</sup> CAT is also important in fine-tuning the cellular  $H_2O_2$  and then in modulating the related signaling pathways.<sup>[64,65]</sup>

In order to investigate the correlation between the plasma effects and CAT activity and protein content during the initial stages of germination process we performed direct treatment of *P. tomentosa* seeds in an asymmetrical capacitively coupled plasma (CCP) reactor under two different pressures and several treatment times. Apart from direct plasma treatment of seeds, an indirect treatment method was used where we treated distilled water by using APPJ in order to obtain PAW. After the treatment, PAW was used for imbibition of *P. tomentosa* seeds. In both cases, the CAT activity and protein content was evaluated during 4 d following the imbibition process, i.e., immediately after the phytochrome activation and in the 3 subsequent days.

## 2 | EXPERIMENTAL SECTION

### 2.1 | Low pressure plasma treatments

Low pressure treatments of seeds were performed in the cylindrically shaped capacitively coupled plasma (CCP) reactor with a powered electrode centrally positioned along the axis (see Figure 1). This asymmetrical system has ability to produce large volume of homogeneous plasma performing mild treatments of many seeds at the same time. Until now it was successfully used for different types of textile treatments<sup>[66,67]</sup> and in treatments of seeds and commercial grains for disinfection and to increase the germination percentage.<sup>[26,27,68]</sup> It was previously characterized in more detail and also the PIC model was used to estimate the main parameters of plasma treatments.

Main goal in construction of this RF plasma system was to achieve homogeneous plasma in large volume with the low energy of ions that bombard the grounded electrode that serves as sample holder. This was achieved by using large surface ratio between the powered and grounded electrode ( $A_{pow}/A_{gnd} = 700$ ). The results obtained from the PIC simulation show us that the energy of ions impinging the grounded electrode and the samples are around 1–2 eV. The samples are positioned on the grounded electrode and due to their small size we can say that they are positioned in the plasma sheath. The estimation of the sheath thickness obtained from the PIC simulation is around 2 cm at the

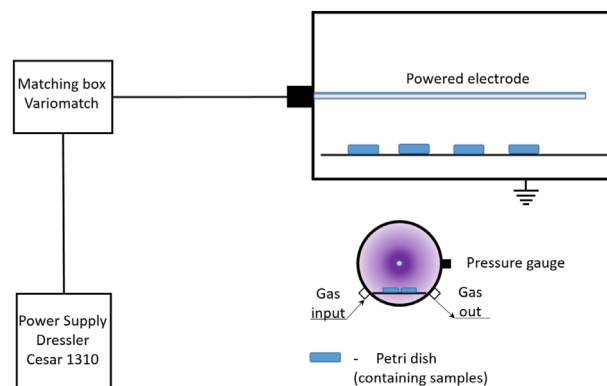


**FIGURE 1** Schematics of the experimental set-up

grounded electrode. At the same time the electrical field at this electrode does not exceeds 75 V/cm. The averaged concentration of oxygen ions given by PIC analysis is  $\sim 10^{15} \text{ m}^{-3}$ .<sup>[69,70]</sup> The concentration of neutral oxygen atoms obtained by using catalytic probe in the same chamber geometry, but larger in scale, is of the order of  $10^{19} \text{ m}^{-3}$ . It was shown that the concentration of ions coincides with the results obtained by PIC simulation ( $\sim 10^{15} \text{ m}^{-3}$ ). Mass spectrometry measurement revealed that the main ions in the discharge are  $O^-$ ,  $O_2^-$ ,  $O_2^+$ , and  $O^+$ . But the most important is the presence of the atomic and molecular oxygen metastables, especially  $O_2(^1\Delta_g)$ . As with other species that concentration of excited and metastable increases with the increase of working pressure.<sup>[71]</sup>

The length and diameter of the chamber are 46 and 37.5 cm, respectively. Chamber wall, which serves as the grounded electrode, is made of stainless steel while the powered electrode is made of aluminum. The powered electrode is axially placed, with length of 40 cm and diameter of 1.4 cm. The electrode is powered by RF signal at 13.56 MHz through automatically adjusting matching network. The power during the treatments was kept constant at 100 W given by RF power supply (Dressler Cesar 1310).

The platform for holding samples is positioned 13 cm below powered electrode. Since it is connected to the chamber wall it is also electrically grounded. A door mounted on one side of the cylindrical chamber provides an easy access and allows positioning of samples on the holder.

During all treatments flow of the gas was controlled by a flow controller connected to the gas inlet of the chamber while the exhaust line was connected to the mechanical pump. Here we need to emphasize that only mechanical pump was used. Therefore, the baseline pressure that could be reached was 20 mTorr which implies that certain amount of impurities (air, in particular) were present. Pressure in the chamber was measured by a capacitive gauge attached to one of the chamber ports.

Treatments were performed in oxygen at pressures of 200 and 600 mTorr which, with a constant pumping speed,

corresponded to gas flows of 80 and 435 sccm. For each pressure four different treatment times were engaged: 1, 5, 10, and 20 min. During the treatments four Petri dishes (6 cm in diameter), each containing 100 seeds, were positioned on the platform inside the chamber. After the end of the treatment, the seeds were immediately taken out of the chamber and transferred to other sterile Petri dishes. The imbibition of the treated seeds was performed by using 3 ml of distilled water.

## 2.2 | Atmospheric pressure plasma treatments – Plasma Activated Water

We have used a standard atmospheric pressure plasma jet (APPJ)<sup>[51,72,73]</sup> for treatments of distilled water (see Figure 2). After the treatments, the obtained plasma activated water (PAW) was used for imbibing the *P. tomentosa* seeds. The design of the APPJ used in the experiments is simple and it consists of a glass tube with the electrode made of copper tape wrapped around the tube 5 mm from its end. The outer and inner diameters of the glass tube were 6 and 4 mm, respectively. The electrode was connected to a high voltage sinusoidal signal of 50 kHz that allows plasma to ignite immediately after the signal is turned on. The high voltage signal is obtained by home-made power supply system consisting of a function generator (PeakTech DDS Function Generator 4025), a home-made amplifier, and a high-voltage transformer.

To allow operation of plasma in glow regime,<sup>[16,74]</sup> He gas was flown through the tube with the rate of four slm. For treatments of water, the jet was positioned vertically with a glass Petri dish underneath. At the bottom of the dish we placed copper tape that was connected to the ground through a 100 k $\Omega$  resistance. This electrical circuit permits monitoring of the discharge current going to the ground by measuring the voltage drop on the resistor. At the same time, high-voltage probe connected to the powered electrode measures voltage supplied to the

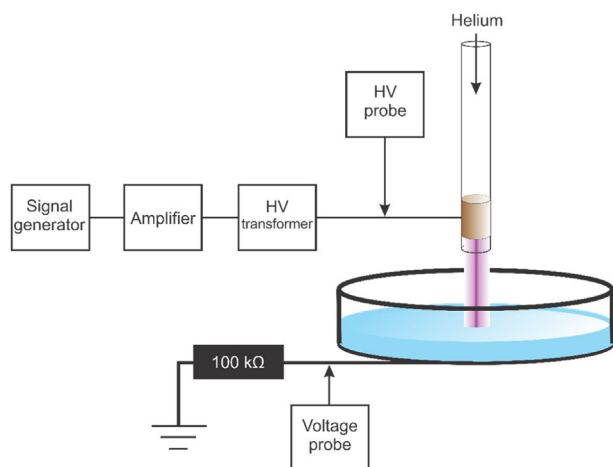


**FIGURE 2** Experimental set-up for treatment of distilled water

plasma jet. To produce plasma activated water we placed 12 ml of distilled water into the Petri dish (6 cm in diameter). The distances between the end of the glass tube of the jet and the water surface used in treatments were 0.5 and 1 cm. For both distances the applied voltage was kept constant at 6 kV<sub>Peak-to-Peak</sub> and measured current was 6 mA<sub>Peak-to-Peak</sub> for 0.5 cm distance and 4 mA<sub>Peak-to-Peak</sub> for the distance of 1 cm. The water volume after treatments was checked and found to be the same as the initial. Treatment times were 5, 10, and 20 min.

In order to characterize PAW we have measured pH and dissolved oxygen content immediately after the treatment. Dissolved oxygen content analysis measures the amount of gaseous oxygen (O<sub>2</sub>) dissolved in an aqueous solution. For the pH measurements we have used Hanna Instruments HI1131B pH electrode with HI5522 controller and for the percentage of dissolved oxygen in water Hanna Instruments DO electrode HI764080 powered by HI2004 unit.

## 2.3 | Plant material and seed treatment

Seeds of the empress tree (*P. tomentosa* Steud.) were collected during 2015 in the Garden of the Institute for Biological Research “Siniša Stanković,” University of Belgrade, and stored at room temperature until use. Batches of 100 seeds (plasma pre-treated or not) or 200 seeds (PAW treated or not) were placed in Petri dishes (6 cm in diameter) and imbibed with 3 ml of distilled water or plasma treated water, respectively. Germination was performed at 25 ± 2 °C, in darkness. Seeds were induced to germinate with a 5 min red light pulse (660 nm, Philips TL 20/15 fluorescent tubes with 3 mm plastic Röhms & Haas filters, No. 501; fluence rate 3.54 μmol m<sup>-2</sup> s<sup>-1</sup>) applied after 3 d of imbibition.<sup>[52]</sup> Seed samples were taken subsequently during next 4 d, in 24 h intervals, weighted and stored at -70 °C until further analysis. A weak green safelight was used for manipulations in the dark. All experiments were repeated twice, with 3–5 replicates each. The schematics of the procedure for the sample collection is given in Figure 3.

## 2.4 | Protein extraction

*P. tomentosa* seeds (about 0.025 g FW) were grounded in liquid nitrogen with a mortar and pestle and homogenized in 1 ml of potassium phosphate buffer (100 mM, pH 7.5) containing 2 mM PMSF, 0.5 mM EDTA, 0.5% Triton X-100, and 2% (w/v) polyvinylpyrrolidone (PVPP). The homogenates were centrifuged at 14000×g for 20 min, at +4 °C. The supernatant was used for assays. Protein content in seed extracts was determined according to Bradford<sup>[75]</sup> using bovine serum albumin as a standard.



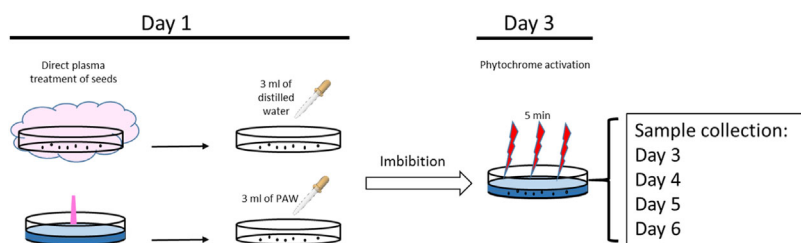


**FIGURE 3** The experimental procedure for collecting the samples for enzyme analysis

## 2.5 | Native polyacrylamide gel electrophoresis and enzyme activity staining

Proteins were separated on the 10% non-denaturing polyacrylamide gel. Electrophoresis was performed at +4 °C for 2.5 h, at constant current of 120 V using Mini-Protein II system (Bio-Rad, Richmond, CA). Equal amounts of proteins (30 µg) were loaded on gels. Gels were stained for CAT activity according to Woodbury et al.<sup>[76]</sup>

## 2.6 | SDS-PAGE and immunoblotting

Samples for sodium dodecyl sulfate polyacrylamide gel electrophoresis (SDS-PAGE) were dissolved in the equal volume of Laemmli buffer.<sup>[77]</sup> Separation of proteins was performed at room temperature using Mini-Protein II system (Bio-Rad, Richmond, CA) for 50 min at 200 V. Equal amounts of proteins (15 µg) were loaded on 10% SDS polyacrylamide gels. For detecting molecular weight of separated proteins, colored molecular weight markers 10–260 kDa (Spectra™ Multicolor Broad Range Protein Ladder, Fermentas GmbH, Germany) were used. After separation, proteins were transferred electrophoretically (60 V for 1.5 h, at 4 °C) onto PVDF membranes (Bio-Rad, SAD) using Mini Trans-Blot Module (Bio-Rad, SAD). Membranes were blocked overnight at 4 °C in a solution of 10% (w/v) non-fat dry milk (NFDM; Nestle, USA) and probed with anti-catalase antibody (1:1000, AS09501; Agrisera Antibodies, Sweden), and goat HRP conjugated anti-rabbit IgG secondary antibody (1:20000, Ao545, Sigma Aldrich, St. Louis, USA). Secondary antibodies were visualized using an enhanced chemiluminescence detection system (ECL) and densitometrically quantified using ImageJ 1.32j software (W. Rasband, National Institute of Health, USA).

## 2.7 | Statistical analysis

Densitometry was performed on scanned gel and immunoblot images using the ImageJ gel analysis tool.<sup>[78]</sup> Statistical analysis was performed using Stagraphics software, version 4.2 (StatPoint, Inc. 1982–2006, USA). Differences among different treatments were tested using standard analysis of variance

(ANOVA). The means were separated using Fisher's Least Significant Difference (LSD) post hoc test for  $p \leq 0.05$ . Treatments denoted by the same letter are not significantly different ( $p \leq 0.05$ ).

## 3 | RESULTS AND DISCUSSION

### 3.1 | Low pressure plasma treatments

It was previously shown that asymmetrical CCP system described above can be successfully used in treatments of *P. tomentosa* seeds in order to increase percentage of germination. However, the effect of plasma on germination is affected by plasma parameters like electric field, power, time, pressure, and type of gas used in treatments.

It is well documented that electric field can positively influence germination.<sup>[79,80]</sup> On the other hand, detrimental effect can appear if seeds are exposed to electric field for a very long time or if the field is very strong.<sup>[79]</sup> In our case electric field (75 V cm<sup>-1</sup>) influencing the samples is quite low comparing to the electric fields (up to several kV cm<sup>-1</sup>) used in literature. We believe that influence of electric field is not significant and main effect is obtained through bombardment of the seed surface by reactive chemical species created in the plasma and accelerated by the electric field in the sheath.

Regarding the plasma power, it was shown that higher powers can induce damage to the seeds due to increased thermal effects and destruction of seed wall by particle bombardment. Therefore, for our chamber it was found that optimal treatment times are up to 10 min for power of 100 W.<sup>[26,27,66]</sup> Concerning the pressure, its changes affect densities and energies of particles present in plasma (the most important are reactive species such are O<sup>-</sup>, O<sub>2</sub><sup>-</sup>, O<sub>2</sub><sup>+</sup>, O<sup>+</sup>, and O<sub>2</sub>(<sup>1</sup>Δ<sub>g</sub>)). At lower pressures, densities of particles produced in plasma are lower, but they have higher energies due to fewer number of collisions, i.e., longer mean free paths.<sup>[4]</sup> Energies of ions are directly influenced by the pressure through the balance of energy gained from the field and dissipated in collisions. Fast neutral particles can be affected indirectly as those may be created by the charge exchange collisions with ions.<sup>[81]</sup>

In our case, we performed treatment at two pressures which are not far apart: 200 and 600 mTorr. Thus, the main difference between two pressures would be in higher particle densities (neutrals, radicals, and ions) that reach surface of treated seeds at 600 mTorr in comparison to the case of 200 mTorr. Taking into account all this, a set of plasma parameters close to the optimal for germination has been chosen in order to investigate the response of the CAT enzyme to the plasma treatments.

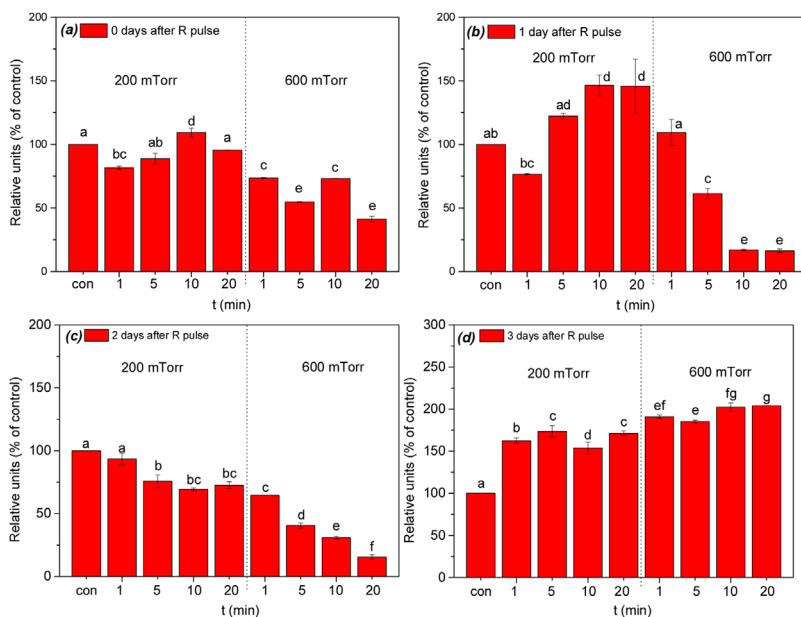


**FIGURE 4** Catalase activity in plasma treated *P. tomentosa* seeds measured immediately (a), 1 d (b), 2 d (c), or 3 d after R light pulse (d). Results for different treatment times (t) and two pressures are shown. The band volume was recorded by using densitometric analysis. Data were normalized using control signal. Values are means obtained from three independent experiments shown with standard error. Treatments denoted by the same letter are not significantly different ( $p \leq 0.05$ ) according to the Fisher's LSD test

As for the effect of the pressure on the seeds and their germination, the selected seeds do not have a hydrophobic protective seed coat so oxidization of the protective layer to allow water to penetrate the seed is not an issue. It has been postulated<sup>[26,27]</sup> that a deposition of different active molecules and radicals may promote germination and growth of these seeds mainly through their signaling functions in the cell. Thus the explanation of the effect must be sought in plasma chemistry leading to production of active species. Understanding, control, and optimization of the effects of plasmas depends on being able to connect the plasma chemical processes to the processes inside the cells of the seed. The effect of plasma should be small enough to promote the germination and not too large to have detrimental effect on the living cells.

We have measured both CAT protein content and CAT enzyme activity at the beginning of the germination process (immediately after activation of phytochrome) and in 3 subsequent days. The activity of CAT for samples treated for different times is shown in Figure 4. Relative intensity for each experimental band was calculated by normalizing the experimental absolute intensity to the corresponding control absolute intensity. One should bear in mind that the control group follows the entire process as other seeds with the exception of plasma treatment (see Figure 3). In other words, control groups have passed imbibition (3 d) then they were initiated by the R pulse and then subsequently taken for analysis in 4 subsequent days. Standard behavior of CAT enzyme activity in control samples of

*P. tomentosa* is observed and it increases after R light pulse. CAT is only one of the relevant enzymes that is responsible in early stages of germination and later on peroxidase becomes even more important. Both of these enzymes together with the related radicals play their part in a complex mechanism of germination that is being triggered by plasma. Thus, one cannot easily correlate activity of one enzyme to the efficiency of germination. While effects of plasma are similar and in the same direction as those reported earlier<sup>[26,27]</sup> results will strongly depend on the season, duration of storage, and other parameters. Thus we have to find optimal conditions for each batch. In addition we have improved performance of our plasma source in the meantime.

When comparing the effects of pressures on the enzyme activity measured immediately after the activation of the phytochrome (day 0), the samples treated in plasma at 600 mTorr of oxygen exhibit a higher reduction in CAT activity if compared to 200 mTorr treatments (see Figure 4(a)). On the contrary, for the treatment at 200 mTorr changes in the activity are small, seeds treated for 1 min show slightly

lower activity, while the others show either similar (5 and 20 min) or slightly higher (10 min) CAT activity. Similar trends can be observed in the samples collected on day 1 (see Figure 4(b)) with a much larger increase of the activity at 200 mTorr. The treatments with higher pressure (600 mTorr) and longer treatment times (10 and 20 min) induce four times lower CAT activity compared to the untreated sample. At the same time for pressure of 200 mTorr we can see increase in the CAT activity as the treatment time increases. Two days after the R pulse the enzyme activity declines more or less linearly with increment of pressure and treatment time (see Figure 4(c)). Thus, CAT activity in seeds after 20 min treatment at 600 mTorr was nearly four times lower in comparison with control samples. However, 3 d after the R pulse the activity of CAT increased for both treatments, exhibiting 1.5–2 fold higher values in comparison with CAT activity measured in control samples (Figure 4(d)). *P. tomentosa* seeds are positively photoblastic, meaning that their germination is stimulated by light. After the imbibition (rapid initial water uptake) seeds were induced to germinate by red light pulse, and entered the next-plateau phase.<sup>[82]</sup> Plateau phase involves the reactivation of metabolism, including the resumption of cellular respiration, the biogenesis of mitochondria, DNA repair, the translation and/or degradation of stored mRNAs, the transcription and translation of new mRNAs, and the activation of antioxidant enzymes at the appropriate time.<sup>[83,84,85]</sup> Therefore, sequential expression of antioxidant enzymes has been considered to

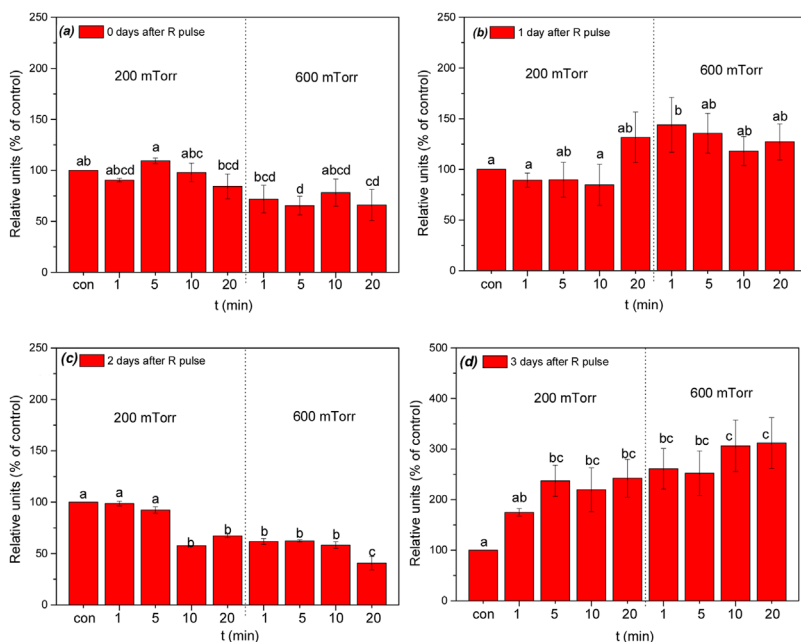


**FIGURE 5** Immunoblot analysis of catalase in *P. tomentosa* seeds, measured immediately (a), 1 d (b), 2 d (c), or 3 d after R light pulse (d). Results for different treatment times (t) and two pressures are shown. The band volume was recorded by using densitometric analysis. Data were normalized using control signal. Values are means obtained from three independent experiments shown with standard error. Treatments denoted by the same letter are not significantly different ( $p \leq 0.05$ ) according to the Fisher's LSD test

be of particular importance for the completion of germination.<sup>[86,87]</sup> It is possible that a renewal of antioxidant system may be initiated with the repair of cell membranes and organelle development, which are required for complete germination and growth demands by the seedlings.<sup>[88]</sup> Increased CAT activity could be an indication of the cellular evaluated ROS, since the amount of CAT present in aerobic cells is directly proportional to the oxidative state of the cells.<sup>[89]</sup> Measurement of CAT activity may be a parameter to determine seed viability and germination as observed by Baily et al.<sup>[90]</sup>

With few exceptions, radicle extension through the structures surrounding the embryo is the event that terminates germination and marks the commencement of the seedling growth.<sup>[91]</sup> The time for this event to be completed varies from several hours to many weeks, depending on the plant species and the germination conditions. The present study shows a significant increase in the enzyme activity 3 d after R pulse (see Figure 4(d)), which can be associated with metabolic switch occurring in seeds between germination and subsequent post-germination phase. Apart from CAT, it was shown previously that another antioxidant enzyme peroxidase (POD) also has very important role in germination. In *P. tomentosa* seeds activity of POD is very low before the process of radicle protrusion begins, i.e., the activity is increased during later phases of germination. On the other hand, in germinated seeds and seedlings, POD activity

increases significantly.<sup>[92]</sup> Final result of seed germination process (measured as percent of germinated seeds) will be reflection of overall metabolic activity in seeds and young seedlings, including antioxidant enzymes activity (e.g., CAT, but also the activity of other enzymes).

Immunoblot analysis showed that only one isoform of 50 kDa is detected in all the samples and in Figure 5 we present the results of CAT protein content obtained for the same set of parameters as CAT activity. Germination process immediately and 1 d after the R light pulse resulted in an increase in CAT protein content, but with slight difference in comparison to the control seeds (Figure 5(a, b)).

Significant reduction in CAT content was observed 2 d after the phytochrome activation (see Figure 5(c)). Here we can observe a reduction in CAT protein content for longer treatment times at 200 mTorr and for all treatment times at 600 mTorr. Similar behavior was observed in the CAT activity (Figure 1(c)). It should be noted that enzyme content was by far the highest in treated seeds 3 d after the activation of phytochrome (about 2.5 fold greater than control samples) and remained more or less constant regardless of experimental

conditions used in this study. Enhanced CAT protein content is in accordance with the increment in enzyme activity in germinating seeds showed in Figure 4(d). It must be remembered that immunoblot analysis gives indications about the synthesis of CAT subunits and does not necessarily reflect the enzyme activity.<sup>[93]</sup> This may explain why the slight apparent decrease or increase in protein content (Figure 5) was not correlated with the changes of CAT activity in the same batch of *P. tomentosa* seeds (Figure 4).

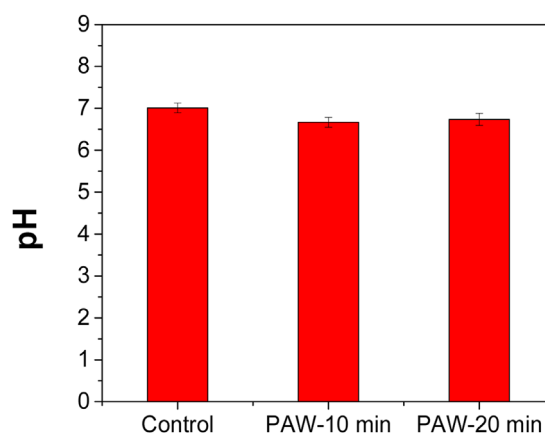


**FIGURE 6** pH values of plasma treated water for two different treatment times. Distance from the edge of the glass tube of the plasma jet and water surface was 1 cm

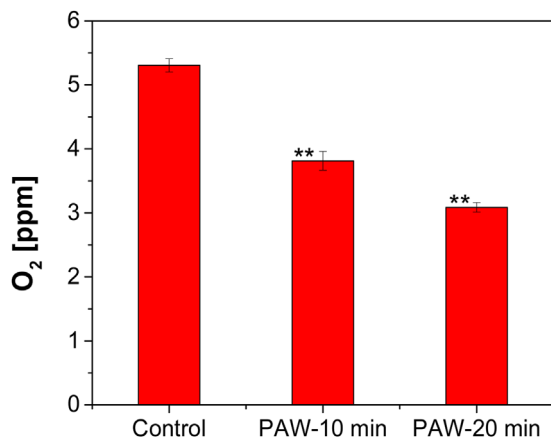


**FIGURE 7** Dissolved oxygen content in treated water in the control sample and after the treatments. Distance from the edge of the glass tube of the plasma jet and water surface was 1 cm

### 3.2 | Atmospheric pressure plasma treatment of distilled water - PAW

Unlike the case of low pressure treatments where seeds were in direct contact with plasma, when it comes to APP treatments the seeds are only indirectly influenced by plasma through the imbibition with plasma activated water. CAT activity and protein content are more affected when plasma is

further away from the liquid for all durations. While this may be counter intuitive it could be the result of the liquid interrupting the plasma at closer proximities or it may result from the greater obstruction to the gas flow including more likely turbulence for smaller proximity. During the water treatment reactive species produced in the plasma are transported to the gas-liquid interface from where they can penetrate and/or induce chemical reactions and creation of new species in the bulk liquid.<sup>[47,94]</sup> Some of these species, like H<sub>2</sub>O<sub>2</sub>, O<sub>2</sub><sup>-</sup>, NO<sub>2</sub><sup>-</sup>, NO<sub>3</sub><sup>-</sup>, have direct influence on processes in biological systems so changes in their concentration should affect enzyme activity. Before using PAW for imbibition of seeds, we have measured pH of treated water and amount of dissolved oxygen (DO) after plasma treatments. Measurements of pH were performed as described in experimental section and the results are presented in Figure 6.

In Figure 6 we can see that plasma does not change significantly the pH value of treated water. In other words, we kept plasma treatment within the limits of only small variations of pH value in order to avoid detrimental effect due to a significantly changed pH factor. Its value is slightly decreased, from pH<sub>Ctrl</sub> = 7 to pH<sub>treat</sub> = 6.7, after the treatments (regardless of treatment time). Gregory D. et al. showed that process of germination and seedling growth of *P. tomentosa* seeds is influenced if the pH values of the environment are below pH = 5.<sup>[95]</sup> If the pH values are in the range 6–7, the germination process and development of the seedling is not influenced. Similarly, the CAT activity in plants is pH-dependent.<sup>[96]</sup> Arabaci and Usluoglu showed that the CAT activity is significantly influenced if the pH value drops below 4.<sup>[97]</sup> Therefore, taking into account measured pH, our PAW used for imbibition of *P. tomentosa* seeds should have negligible influence on the enzyme activity and germination of seeds due to the change in pH.

Another parameter that was measured was oxygen content in the water before and after the treatment. The results are shown in Figure 7. We can see that plasma treatment reduces the oxygen content in water. The reduction of the oxygen content can be assigned to the presence of the helium flow.<sup>[98]</sup> The presence of He flow above the water surface reduces the partial pressure of O<sub>2</sub> and therefore reducing the solubility of oxygen in the water. The He flow used in the experiment is sufficient to create sparging effect and cause decrease of oxygen content.<sup>[99]</sup> With an increase of the treatment times at distance of 1 cm oxygen content is reduced by 40%. Similar result is observed at

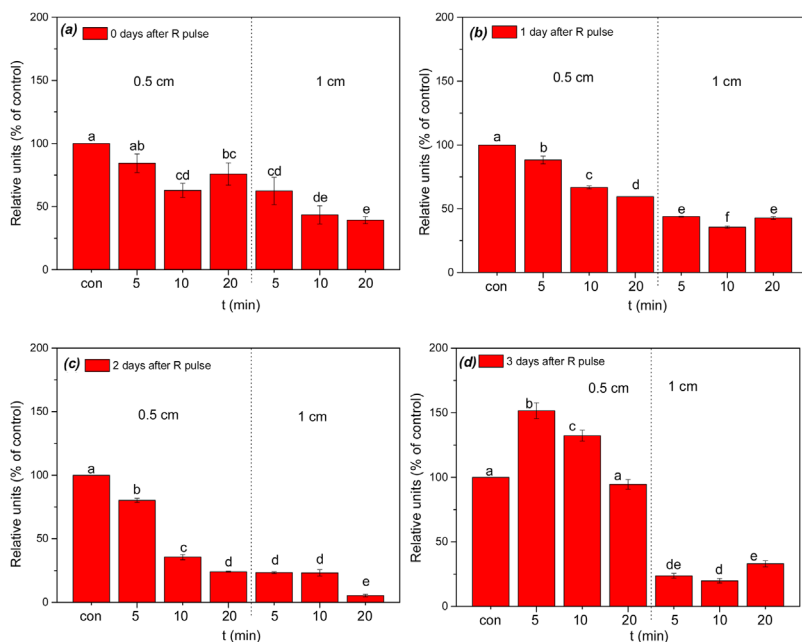


**FIGURE 8** Catalase activity of *P. tomentosa* seeds germinated in plasma treated water, measured immediately (a), 1 d (b), 2 d (c), or 3 d after R light pulse (d). Results for different treatment times (t) to obtain PAW and two distances are shown. The band volume was recorded by using densitometric analysis. Data were normalized using control signal. Values are means obtained from three independent experiments shown with standard error. The values with the same letter indicate statistically homogenous groups ( $p \leq 0.05$ ), as per Fisher's LSD test

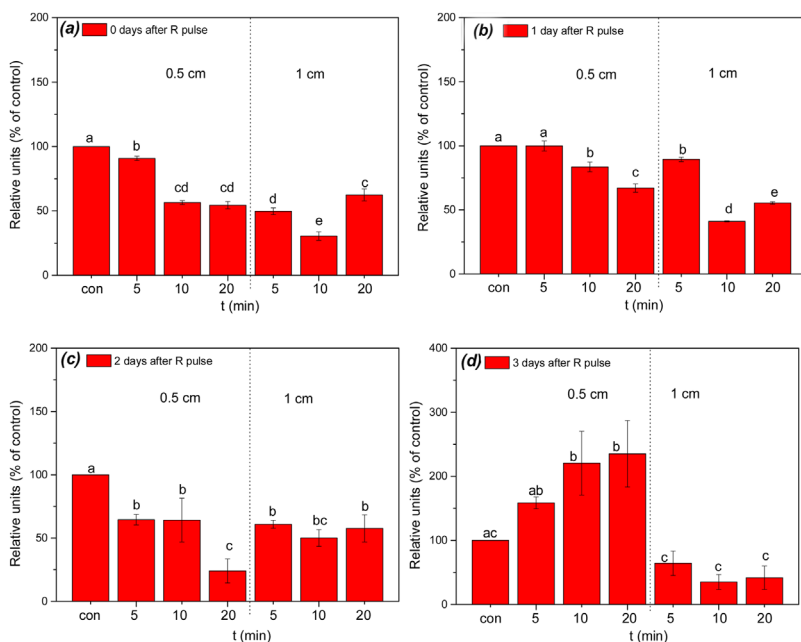


**FIGURE 9** Immunoblot analysis of catalase in *P. tomentosa* seeds germinated in plasma treated water, measured immediately (a), 1 d (b), 2 d (c), or 3 d after R light pulse (d). Results for different treatment times (t) to obtain PAW and two distances are shown. The band volume was recorded by using densitometric analysis. Data were normalized using control signal. Values are means obtained from three independent experiments shown with standard error. Treatments denoted by the same letter are not significantly different ( $p \leq 0.05$ ) according to the Fisher's LSD test

both distances. One has to bear in mind that oxygen content cannot be directly correlated with CAT activity due to the complexity of mechanisms involved.

Nevertheless, the seed germination is particularly sensitive to oxygen deficiency. The oxygen requirement for seeds typically varies depending on the species and their dormancy status.<sup>[100]</sup> During early phase of imbibition, seeds consume oxygen at slower rates, but at a much higher rate during radicle protrusion and hypocotyl growth. For example, Rajashekar and Baek show that oxygen limitation during imbibition can produce adverse effects which may last during early seedling growth and development. On the other hand, adding of the hydrogen peroxide reversed the effect of hypoxia resulting in normal hypocotyl elongation and stem growth.<sup>[101]</sup>

CAT enzyme activity obtained after the imbibition with PAW is shown in Figure 8. The samples were collected and the CAT activity is measured in the same manner as in the case of low pressure plasma treatments. As in the low-pressure case, the data were normalized to signal of the control group of the corresponding day. We can see that CAT activity in samples that were imbibed with PAW is lower than in the untreated samples immediately after the phytochrome activation and in 2 subsequent days (see Figure 8(a–c)). Also, the activity does not change significantly between day 0 and day 1 (see Figure 8(a, b)). In both cases it is decreased

maximally 2.5–3 times if compared with control samples. At day 2 we have even more reduction in CAT activity, going up to 10 times lower than untreated samples (see Figure 8(c)). In all cases, the reduction in the activity is higher for PAW treated with 1 cm distance between the plasma jet tube and water surface than for the case of 0.5 cm distance. The decrease in CAT activity within 3 d after R light pulse (Figure 8(d)) can be to some extent correlated to the decreased level of dissolved oxygen.

Significant increase in CAT activity occurred 3 d after the R light pulse at 0.5 cm treatment (Figure 8(d)), and it appears that this increment corresponds to the initial phase of post germination process, designated as phase of radicle protrusion and elongation, as already mentioned above.

Most likely CAT reserves are broken down during early stages of germination and de novo synthesis is occurring along with the radicle protrusion. It should be noted that ROS produced in PAW, especially hydrogen peroxide, could mitigate the adverse effects of hypoxia, both during imbibition and germination, as it can generate free oxygen and water by CAT and other catalysts including many transition metal ions present in the seeds.<sup>[102]</sup> When density of radicals increases it is likely that it would stimulate a greater production of CAT. If that production is insufficient to keep up with radicals, then depletion may occur. In addition, several radicals and other active species may participate in the kinetics of a particular enzyme. Active species produced in PAW, such as nitrate ( $\text{NO}_3^-$ ) and nitrite ( $\text{NO}_2^-$ ) ions most likely deposit on the seed surface, having an influence on seed germination as well as on the CAT activity. The same is true for hydrogen peroxide ( $\text{H}_2\text{O}_2$ ). Although it could be expected that  $\text{H}_2\text{O}_2$  concentration increases with treatment time, which would result in higher CAT activity, Figure 8 shows the opposite results (lower CAT values for longer treatment time of PAW), particularly for 0.5 cm treatment. Most likely higher content of ROS produced in the case of 0.5 cm treatment contributes to the higher levels of active species that could impair the enzyme activity. Precise regulation of  $\text{H}_2\text{O}_2$  accumulation by cell antioxidant machinery is crucial to achieve a balance between oxidative signaling that promotes germination and oxidative damage that prevents or delays germination. According to “oxidative window” hypothesis proposed by Bailly et al.,<sup>[103]</sup> both lower and higher levels of ROS impair seed germination, and it is only possible within a critical range of concentrations.

One subunit of 50 kDa was present in *P. tomentosa* seeds in all treatments (Figure 9). The intensity of the band

corresponding to the CAT subunit appeared to decrease significantly for both treatment distances in comparison to the control sample, up to 3rd day after the R light pulse. A sharp decline in CAT protein content (1.5–2 fold) was noticed immediately after the R light pulse, for longer exposure treatments at 0.5 cm distance (10 and 20 min) and for all treatments at 1 cm distance between the jet and water surface, respectively (Figure 9(a)). CAT content in PAW treated seeds showed similar pattern on the 1st and 2nd day after the phytochrome activation (Figure 9(b, c)). Subsequent germination process (3 d after R pulse) resulted in an increase in CAT protein content in seeds after the 0.5 cm distance PAW treatment, but after the 1 cm PAW treatment it showed no significant difference compared to control seeds (Figure 9(d)).

One should bear in mind that different levels of enzymatic activity are not exclusively dependent on enzyme synthesis, but on various other factors as well. Thus, in future studies it would be advisable to take into account the differences between the effect of plasma treatment on germination and subsequent post-germination process of *P. tomentosa* seeds, suggesting that CAT activity at these stages may be subject to post-translational regulation.

## 4 | CONCLUSION

In this paper we have presented results of CAT enzyme activity and protein content obtained during the second phase of germination of *P. tomentosa* seeds (phase of phytochrome activity). Two significantly different types of plasma treatments were used. In the first type, the seeds were in direct contact with plasma and, in the second, atmospheric pressure plasma was used for obtaining PAW which is then applied to the seeds. In the former case, for direct plasma treatments, we have used low pressure RF discharge that was previously shown to be a good solution for increasing germination percentage of *P. tomentosa* seeds.<sup>[26,27]</sup> In the latter case, an APPJ was used in order to obtain PAW and immediately after the plasma treatment of water pH and dissolved oxygen content were measured. In our case the pH does not change significantly and stays in the range 6.5–7. Therefore, the processes related to germination and protrusion of radicle are not influenced by change in pH. On the other hand, the percentage of dissolved oxygen in the PAW is decreased to up to 40% compared to untreated water. This can influence the germination process in negative way by reducing the germination percentage, radicle protrusion, and slow early seedling growth and development. However, PAW contains H<sub>2</sub>O<sub>2</sub> produced during plasma treatments which could substitute for O<sub>2</sub> deficiency and activate CAT genes for synthesis of new proteins.

We have observed standard behavior of CAT enzyme activity in control samples of *P. tomentosa* seeds. In these

samples the CAT enzyme activity increases in the first 3 d after R light pulse. However, both plasma treatments used in this study, low-pressure plasma seed treatment and PAW, cause decrease in CAT activity/protein content in seeds compared to the control samples in time period up to 2 d after R light pulse. For low-pressure direct treatments decayed levels of CAT activity and protein content are correlated to the treatment times and pressures with the biggest change for 600 mTorr and longest treatment time. In the case of indirect PAW treatment we observed similar behavior at the longest distance and for the longest treatment time of PAW.

Differences in CAT activity/content noticed 3 d after the inductive light pulse strongly suggest that approximately 48 h after the R pulse *P. tomentosa* seeds enter the 3rd phase of germination process-phase of radicle protrusion and elongation, i.e., germination *sensu stricto* is terminated and post germination processes take place.<sup>[52]</sup> Moreover, discrete differences on the level of CAT content could be distinguished between the treatments used in this study.

## ACKNOWLEDGMENT

This research has been supported by the Ministry of Education, Science, and Technological Development, Republic of Serbia, under projects III41011 and ON171037.

## REFERENCES

- [1] P. Favia, G. Cicala, A. Milella, F. Palumbo, P. Rossini, R. d'Agostino, *Surf. Coat. Tech.* **2003**, *169*, 609.
- [2] D. Mihailovic, Z. Saponjic, R. Molina, N. Puac, P. Jovancic, J. Nedeljkovic, M. Radetic, *ACS Appl. Mater. Interfaces.* **2010**, *2*, 1700.
- [3] S. Vizireanu, S. D. Stoica, C. Luculescu, L. C. Nistor, B. Mitu, G. Dinescu, *Plasma Sources Sci. Technol.* **2010**, *19*, 034016.
- [4] T. Makabe, Z. L. Petrovic, *Plasma Electronics: Applications in Microelectronic Device Fabrication*. CRC Press, Boca Raton, Florida, USA **2014**.
- [5] J. Vasiljević, M. Gorjanc, B. Tomšič, B. Orel, I. Jerman, M. Mozetič, A. Vesel, B. Simončič, *Cellulose* **2013**, *20*, 277.
- [6] D. Kontziampasis, G. Boulousis, A. Smyrnakis, K. Ellinas, A. Tserepi, E. Gogolides, *Microel. Eng.* **2014**, *121*, 33.
- [7] D. Dobrynin, G. Fridman, G. Friedman, A. Fridman, *New J. Phys.* **2009**, *11*, 115020.
- [8] M. Gherardi, E. Turrini, R. Laurita, E. De Gianni, L. Ferruzzi, A. Liguori, A. Stancampiano, V. Colombo, C. Fimognari, *Plasma Process. Polym.* **2015**, *12*, 1354.
- [9] E. Sardella, R. Gristina, G. S. Senesi, R. d'Agostino, P. Favia, *Plasma Processes Polym.* **2004**, *1*, 63.
- [10] M. Vandamme, E. Robert, S. Lerondel, V. Sarron, D. Ries, S. Dozias, J. Sobilo, D. Gosset, C. Kieda, B. Legrain, J. M. Pouvesle, *Int. J. Cancer* **2012**, *130*, 2185.
- [11] R. Matthes, C. Bender, R. Schlüter, I. Koban, R. Bussiahn, S. Reuter, J. Lademann, K. D. Weltmann, A. Kramer, *PLoS ONE* **2013**, *8*, 70462.

- [12] Z. Machala, K. Hensel, Y. Akishev, *Plasma for Bio-Decontamination, BT Medicine and Food Security*. Springer Science & Business Media, Demanovska Dolina, Slovakia **2011**.
- [13] S. Lazović, N. Puač, M. Miletić, D. Pavlica, M. Jovanović, D. Bugarški, S. Mojsilović, D. Maletić, G. Malović, P. Milenković, Z. Petrović, *New J. Phys.* **2010**, *12*, 083037.
- [14] H. Tanaka, M. Mizuno, F. Kikkawa, M. Hori, *Plasma Med.* **2016**, *6*, 101.
- [15] S. Große-Kreul, S. Hübner, S. Schneider, D. Ellerweg, A. Von Keudell, S. Matejčík, J. Benedikt, *PSST* **2015**, *24*, 044008.
- [16] M. Gherardi, N. Puač, D. Marić, A. Stancampiano, G. Malović, V. Colombo, Z. L. Petrović, *Plasma Sources Sci. Technol.* **2015**, *24*, 064004.
- [17] A. Bogaerts, Z. Donko, K. Kutasi, G. Bano, N. Pinhao, M. Pinheiro, *Spectrochim. Acta B.* **2000**, *55*, 1465.
- [18] K. Kutasi, B. Saoudi, C. D. Pintassilgo, J. Loureiro, M. Moisan, *Plasma Process. Polym.* **2008**, *5*, 840.
- [19] M. J. Kushner, *J. Phys. D* **2005**, *38*, 1633.
- [20] M. S. Benilov, G. V. Naidis, *IEEE Trans. Plasma Sci.* **2003**, *4*, 488.
- [21] N. Škoro, N. Puač, S. Lazović, U. Cvelbar, G. Kokkoris, E. Gogolides, *J. Phys. D* **2013**, *46*, 475206.
- [22] Z. L. Petrović, S. Dujko, D. Marić, G. Malović, Ž. Nikitović, O. Šašić, J. Jovanović, V. Stojanović, M. Radmilovic-Radenovic, *J. Phys. D* **2009**, *42*, 194002.
- [23] R. D. White, R. E. Robson, S. Dujko, P. Nicoletopoulos, B. Li, *J. Phys. D* **2009**, *42*, 194001.
- [24] M. Savic, M. Radmilovic-Radjenovic, M. Suvakov, S. Marjanovic, D. Maric, Z. L. Petrovic, *IEEE Trans. Plasma Sci.* **2011**, *39*, 2556.
- [25] B. Šerá, V. Straňák, M. Šerý, M. Tichý, P. Špatenka, *Plasma Sci. Technol.* **2008**, *10*, 506.
- [26] S. Živković, N. Puač, Z. Giba, D. Grubišić, Z. Lj. Petrović, *Seed Sci. Technol.* **2004**, *32*, 693.
- [27] N. Puač, Z. Lj. Petrović, S. Živković, Z. Giba, D. Grubišić, A. R. Đorđević, *Plasma Processes and Polymers*, Weinheim, Germany **2005**, Ch. 15.
- [28] E. Bormashenko, R. Grynyov, Y. Bormashenko, E. Drori, *Sci. Rep.* **2012**, *2*, 3.
- [29] L. K. Randeniya, G. J. J. B. de Groot, *Plasma Process. Polym.* **2015**, *12*, 608.
- [30] B. Šerá, P. Špatenka, M. Šerý, N. Vrchotová, I. Hrušková, *IEEE Trans. Plasma Sci.* **2010**, *38*, 2963.
- [31] Z. Zhou, Y. Huang, S. Yang, W. Chen, *Agricultural Sciences* **2011**, *2*, 23.
- [32] B. Peethambaran, J. Han, K. Kermalli, J. Jiaying, G. Fridman, R. Balsamo, A. Fridman, V. Miller, *Plasma Medicine* **2015**, *5*, 87.
- [33] L. Sivachandiran, A. Khacef, *RSC Adv.* **2016**, *7*, 1822.
- [34] S. Ikawa, A. Tani, Y. Nakashima, K. Kitano, *J. Phys. D.* **2016**, *49*, 425401.
- [35] M. Hijosa-Valsero, R. Molina, H. Schikora, M. Müller, J. M. Bayona, *J. Hazard. Mater.* **2013**, *262*, 664.
- [36] V. I. Parvulescu, M. Magureanu, P. Lukes, *Plasma Chemistry and Catalysis in Gases and Liquids*. John Wiley & Sons, Weinheim, Germany **2012**.
- [37] N. Hayashi, A. Nakahigashi, M. Goto, S. Kitazaki, K. Koga, M. Shiratani, *Jpn. J. Appl. Phys.* **2011**, *50*, 08JF04.
- [38] G. Kamgang-Youbi, J. M. Herry, T. Meylheuc, J. L. Brisset, M. N. Bellon-Fontaine, A. Doubla, M. Naitali, *Lett. Appl. Microbiol.* **2009**, *48*, 13.
- [39] M. J. Traylor, M. J. Pavlovich, S. Karim, P. Hait, Y. Sakiyama, D. S. Clark, D. B. Graves, *J. Phys. D.* **2011**, *44*, 472001.
- [40] L. Sivachandiran, A. Khacef, *RSC Adv.* **2017**, *7*, 1822.
- [41] H. D. Stryczewska, K. Ebihara, M. Takayama, Y. Gyoutoku, M. Tachibana, *Plasma Process. Polym.* **2005**, *2*, 238.
- [42] L. Ling, J. Jiafeng, L. Jiangang, S. Minchong, H. Xin, S. Hanliang, D. Yuanhua, *Sci. Rep.* **2014**, *4*, 1.
- [43] L. K. Randeniya, G. J. J. N. de Groot, *Plasma Process. Polym.* **2015**, *12*, 608.
- [44] R. Ma, G. Wang, Y. Tian, K. Wang, J. Zhang, J. Fang, *J. Hazard. Mater.* **2015**, *300*, 643.
- [45] A. Bertaccini, A. Canel, V. Colombo, N. Contaldo, M. Gherardi, L. Laurita, A. Stancampiano, Y. Zambon, Presented at 6th ICPM, Bratislava, Slovakia, September, **2016**.
- [46] A. Bertaccini, E. Biondi, V. Colombo, M. Gherardi, L. Laurita, C. Lucchese, S. Perez, A. Stancampiano, Presented at 6th ICPM, Bratislava, Slovakia, September, **2016**.
- [47] P. J. Bruggeman, M. J. Kushner, B. R. Locke, J. G. E. Gardeniers, W. G. Graham, D. B. Graves, R. C. H. M. Hofman-Caris, D. Maric, J. P. Reid, E. Ceriani, D. Fernandez, Rivas, J. E. Foster, S. C. Garrick, Y. Gorbanev, S. Hamaguchi, F. Iza, H. Jablonowski, E. Klimova, J. Kolb, F. Krcma, P. Lukes, Z. Machala, I. Marinov, D. Mariotti, S. Mededovic, Thagard, D. Minakata, E. C. Neyts, J. Pawlat, Z. L. Petrovic, R. Pflieger, S. Reuter, D. C. Schram, S. Schröter, M. Shiraiwa, B. Tarabová, P. A. Tsai, J. R. R. Verlet, T. von Woedtke, K. R. Wilson, K. Yasui and, G. Zvereva, *Plasma Sources Sci. Technol.* **2016**, *25*, 53002.
- [48] M. M. Hefny, C. Pattyn, P. Lukes and, J. Benedikt, *J. Phys. D. Appl. Phys.* **2016**, *49*, 404002.
- [49] S. Samukawa, M. Hori, S. Rauf, K. Tachibana, P. Bruggeman, G. Kroesen, J. C. Whitehead, A. B. Murphy, A. F. Gutsol, S. Starikovskaia, U. Kortshagen, J. P. Boeuf, T. J. Sommerer, M. J. Kushner, U. Czarnetzki and, N. Mason, *J. Phys. D. Appl. Phys.* **2012**, *45*, 253001.
- [50] I. Adamovich, S. D. Baalrud, A. Bogaerts, P. J. Bruggeman, M. Cappelli, V. Colombo, U. Czarnetzki, U. Ebert, J. G. Eden, P. Favia, D. B. Graves, S. Hamaguchi, G. Hieftje, M. Hori, I. D. Kaganovich, U. Kortshagen, M. J. Kushner, N. J. Mason, S. Mazouffre, S. M. Thagard, H. R. Metelmann, A. Mizuno, E. Moreau, A. B. Murphy, B. A. Niemira, G. S. Oehrlein, Z. L. Petrovic, L. C. Pitchford, Y. K. Pu, S. Rauf, O. Sakai, S. Samukawa, S. Starikovskaia, J. Tennyson, K. Terashima, M. M. Turner, M. C. M. v. d. Sanden, A. Vardelle, *J. Physics D: Appl. Phys.* **2017**, *50*, 323001.
- [51] N. Puač, D. Maletić, S. Lazović, G. Malović, A. Đorđević, Z. L. Petrović, *Appl. Phys. Lett.* **2012**, *101*, 024103.
- [52] D. Grubišić, M. Nešković, R. Konjević, *Plant Sci.* **1985**, *39*, 13.
- [53] C. Bailly, H. El-Maarouf-Bouteau, F. Corbineau, *C. R. Biol.* **2008**, *331*, 806.
- [54] L. Rajjou, I. Debeaujon, *C. R. Biol.* **2008**, *331*, 796.
- [55] D. Grubišić, R. Konjević, *Planta* **1990**, *181*, 239.
- [56] D. Grubišić, Z. Giba, and, R. Konjević, *Photochem. Photobiol.* **1992**, *56*, 629.
- [57] J. G. Scandalios, L. Guan, A. N. Polidoros, *Cold Spring Harbor Monograph Series* **1997**, *34*, 343.
- [58] W. F. Beyer, Jr, I. Fridovich, *Oxygen Radicals in Biology and Medicine*, Springer, Boston, MA, USA **1988**, Ch. 49, p. 651.
- [59] J. D. Bewley, M. Black, *Seeds*, Springer, Boston, MA, USA **1994**, Ch. 1.
- [60] HU Ming-jing, *J. Shanxi Agricultural Sci.* **2010**, *11*, 9.
- [61] L. Ling, L. Jiangang, S. Minchong, Z. Chunlei, D. Yuanhua, *Sci. Rep.* **2015**, *5*, 13033.

- [62] J. Jiang, Y. Lu, J. Li, L. Li, X. He, H. Shao, Y. Dong, *PLoS ONE* **2014**, *9*, e97753.
- [63] H. Willekens, D. Inzé, M. Van Montagu, W. Van Camp, *Mol. Breeding* **1995**, *1*, 207.
- [64] R. Mittler, *Trends Plant Sci.* **2002**, *7*, 405.
- [65] S. O. Neill, K. S. Gould, P. A. Kilmartin, K. A. Mitchell, K. R. Markham, *Funct. Plant Biol.* **2002**, *29*, 1437.
- [66] M. Gorenšek, M. Gorjanc, V. Bukošek, J. Kovač, Z. Petrović, N. Puač, *Text. Res. J.* **2010**, *80*, 1633.
- [67] D. Mihailović, Z. Šaponjić, R. Molina, N. Puač, P. Jovančić, J. Nedeljković, M. Radetić, *ACS Appl. Mater. Interfaces* **2010**, *2*, 1700.
- [68] I. Filatova, V. Azharonok, V. Lushkevich, A. Zhukovsky, K. Spasić, S. Živković, N. Puač, S. Lazović, G. Malović, Z. Lj. Petrović, Presented at 31st ICPIG, Granada, Spain, July, **2013**.
- [69] N. Puač, Z. Raspopović, Z. Lj. Petrović, Presented at 22nd SPIG, Tara, Serbia, August, **2004**.
- [70] N. Puač, Z. Lj. Petrović, M. Radetić, A. Djordjević, *Mater. Sci. Forum* **2005**, *494*, 291.
- [71] K. Spasić, N. Škoro, N. Puač, G. Malović, Z. Lj. Petrović, Presented at ICOPS, Antalya, Turkey, May, **2015**.
- [72] D. Maletić, N. Puač, N. Selaković, S. Lazović, G. Malović, A. Đorđević, Z. Lj. Petrović, *Plasma Sources Sci. Technol.* **2015**, *24*, 025006.
- [73] D. Maletić, N. Puač, G. Malović, A. Đorđević, Z. L. Petrović, *J. Phys. D: App Phys.* **2017**, *50*, 145202.
- [74] J. Benedikt, S. Hofmann, N. Knake, H. Boettner, R. Reuter, A. von Keudell, V. Schulz-von der Gathen, *Eur. Phys. J. D.* **2010**, *60*, 539.
- [75] M. M. Bradford, *Anal. Biochem.* **1976**, *72*, 248.
- [76] W. Woodbury, A. K. Spencer, M. A. Stahmann, *Anal. Biochem.* **1971**, *44*, 301.
- [77] U. K. Laemmli, *Nature* **1970**, *227*, 680.
- [78] M. D. Abramoff, P. J. Magelhaes, S. J. Ram, *Biophoton. Int.* **2004**, *11*, 36.
- [79] J. D. Moon, H. S. Chung, *J. Electrostat.* **2000**, *48*, 103.
- [80] S. Lynikiene, A. Pozeliene, G. Rutkauskas, *Int. Agrophys.* **2006**, *20*, 195.
- [81] D. Marić, P. Hartmann, G. Malović, Z. Donkó, Z. Lj. Petrović, *J. Phys. D: Appl. Phys.* **2003**, *36*, 2639.
- [82] Z. Giba, D. Grubišić, R. Konjević, in *Nitric Oxide Signaling in Higher Plants*, J. R. Magalhaes, R. P. Singh, L. P. Pasos, (Eds.), Studium Press, LLC, Houston, USA **2004**.
- [83] Ł. Wojtyła, K. Lechowska, S. Kubala, M. Garnczarska, *Front. Plant Sci.* **2016**, *7*, 66.
- [84] H. Nonogaki, G. W. Bassel, J. D. Bewley, *Plant Sci.* **2010**, *179*, 574.
- [85] J. D. Bewley, K. J. Bradford, H. W. Hilhorst, H. Nonogaki, *Seeds*. Springer, New York, USA **2013**.
- [86] C. Bailly, A. Benamar, F. Corbineau, D. Côme, *Seed Sci. Res.* **2000**, *10*, 35.
- [87] J. Bogdanović, K. Radotić, A. Mitrović, *Biologia Plantarum* **2008**, *52*, 396.
- [88] K. Chen, R. Arora, *Plant Sci.* **2011**, *180*, 212.
- [89] K. Apel, H. Hirt, *Annu. Rev. Plant Biol.* **2004**, *55*, 373.
- [90] C. Bailly, A. Benamar, F. Corbineau, D. Come, *Physiol. Plant.* **1998**, *104*, 646.
- [91] J. D. Bewley, *The plant cell* **1997**, *9*, 7, 1055.
- [92] B. Živković, *Master Thesis*, University of Belgrade, Serbia, September, **2006**.
- [93] C. Bailly, J. Leymarie, A. Lehner, S. Rousseau, D. Côme, F. Corbineau, *J. Exp. Bot.* **2004**, *55*, 475.
- [94] S. A. Norberg, W. Tian, E. Johnsen, M. J. Kushner, *J. Phys. D: Appl. Phys.* **2014**, *47*, 475203.
- [95] G. D. Turner, R. R. Lau, D. R. Young, *J. Appl. Ecology* **1988**, *25*, 561.
- [96] B. Chance, *J. Biol. Chem.* **1952**, *194*, 471.
- [97] G. Arabaci, A. Usluoglu, *J. Chem.* **2012**, *2013*, 686185.
- [98] O. Jun-Seok, E. J. Szili, S. Ito, S.-H. Hong, N. Gaur, H. Furuta, R. D. Short and, A. Hatta, *Plasma Med.* **2015**, *5*, 125.
- [99] O. S. Degenhardt, B. Waters, A. Rebelo-Cameirao, A. Meyer, H. Brunner, N. P. Toltl, *Dissolution Technol.* **2004**, *11*, 6.
- [100] V. B. Cardwell, *American Society of Agronomy and the Crop Science Society of America.* **1984**, 53–92.
- [101] C. B. Rajashekar, K.-H. Baek, *Am. J. Plant Sci.* **2015**, *2014*, 3572.
- [102] B. Halliwell, J. M. Gutteridge, *Free Radicals in Biology and Medicine*. Oxford University Press, NY, USA **1999**.
- [103] C. Bailly, H. El-Maarouf-Bouteau, F. Corbineau, *C. R. Biol.* **2008**, *331*, 806.

**How to cite this article:** Puač N, Škoro N, Spasić K, et al. Activity of catalase enzyme in *Paulownia tomentosa* seeds during the process of germination after treatments with low pressure plasma and plasma activated water. *Plasma Process Polym.* 2018;15:e1700082.  
<https://doi.org/10.1002/ppap.201700082>





# Direct and Indirect Treatment of Organic Dye (Acid Blue 25) Solutions by Using Cold Atmospheric Plasma Jet

Amit Kumar<sup>1,2\*</sup>, Nikola Škoro<sup>1</sup>, Wolfgang Gernjak<sup>3,4</sup>, Dragan Povrenović<sup>5</sup> and Nevena Puač<sup>1\*</sup>

<sup>1</sup>Institute of Physics, University of Belgrade, Belgrade, Serbia, <sup>2</sup>Faculty of Sciences, Universitat de Girona, Girona, Spain, <sup>3</sup>Catalan Institute for Water Research (ICRA), Girona, Spain, <sup>4</sup>Catalan Institution for Research and Advanced Studies (ICREA), Barcelona, Spain, <sup>5</sup>Faculty of Technology and Metallurgy, University of Belgrade, Belgrade, Serbia

## OPEN ACCESS

### Edited by:

Pankaj Attri,  
Kyushu University, Japan

### Reviewed by:

Dheerawan Boonyawan,  
Chiang Mai University, Thailand  
Udit Narayan Pal,  
Central Electronics Engineering  
Research Institute (CSIR), India  
Tae Hun Chung,  
Dong-A University, South Korea

### \*Correspondence:

Amit Kumar  
amit@ipb.ac.rs  
Nevena Puač  
nevena@ipb.ac.rs

### Specialty section:

This article was submitted to  
Plasma Physics,  
a section of the journal  
Frontiers in Physics

**Received:** 14 December 2021

**Accepted:** 24 January 2022

**Published:** 15 February 2022

### Citation:

Kumar A, Škoro N, Gernjak W,  
Povrenović D and Puač N (2022) Direct  
and Indirect Treatment of Organic Dye  
(Acid Blue 25) Solutions by Using Cold  
Atmospheric Plasma Jet.  
Front. Phys. 10:835635.  
doi: 10.3389/fphy.2022.835635

In this work, the direct and indirect removal of Acid Blue 25 (AB25) from water by using cold atmospheric pressure plasma jet (APPJ) has been demonstrated. APPJ with a pin electrode type configuration operating with argon as a working gas was used as a plasma source for treatments. In this configuration, argon plasma was formed in the contact with surrounding air over the liquid surface. The plasma was driven by using a high voltage radio frequency (RF) power supply. The system was characterized by the measurement of electrical characteristics and by employing optical emission spectroscopy (OES). The electrical characterization gave information about the voltages and currents, i.e., working points of the discharge, as well as power deposition to the sample. OES recorded the emission spectra and confirmed several existing reactive species in the gas phase of the plasma system. During the direct treatment, AB25-containing solution was directly exposed to APPJ. The direct treatment was performed by modifying various experimental parameters, such as initial AB25 concentrations, treatment times, and input powers. In the indirect treatment, AB25 was treated by using plasma activated water (PAW). The characterization of PAW was performed and various plasma-induced long-lived species, such as nitrate ( $\text{NO}_3^-$ ), nitrite ( $\text{NO}_2^-$ ) and hydrogen peroxide ( $\text{H}_2\text{O}_2$ ) have been quantified using colorimetric techniques. Besides, blank experiments have been conducted with main constituents in PAW, where AB25 was treated individually by  $\text{NO}_3^-$ ,  $\text{NO}_2^-$ , and  $\text{H}_2\text{O}_2$  and with a mixture of these three species. As expected, with the direct treatment almost complete removal of AB25 was achieved. The measurements also provided an insight into the kinetics of the degradation of AB25. In the indirect treatment, PAW removed a significant amount of AB25 within 17 days. In the blank experiments,  $\text{H}_2\text{O}_2$  containing solutions created a favourable influence on removal of AB25 from liquid.

**Keywords:** atmospheric pressure plasma jet, acid blue 25, plasma treatment, plasma diagnostics, plasma-activated water

## INTRODUCTION

Organic dyes are the major group of toxic pollutants that have been constantly detected in the environment [1–3] with the textile industries as the main source of dyes in the water bodies [4, 5]. It has been estimated that 200 thousand tons of different dyes are discharged every year into the environment during their application process [6]. Therefore, around 17–20% of industrial wastewater originates only from the textile industries [7, 8]. From an environmental point of view, dye effluents can lead to adverse effects on aquatic life, plant life as well as on public health [6, 9–11]. However, it has been reported that many organic dyes are extremely difficult to degrade by conventional wastewater treatment plants due to their stable chemical structures (e.g., aromatic rings) [12–14].

Many advanced oxidation processes (AOPs), with various approaches including  $\text{H}_2\text{O}_2/\text{Fenton}$ ,  $\text{UV}/\text{TiO}_2$ ,  $\text{O}_3/\text{H}_2\text{O}_2$ ,  $\text{UV}/\text{H}_2\text{O}_2$ ,  $\text{UV}/\text{O}_3$ , ozonation have been studied for the treatment of organic dyes from wastewater [15–17]. AOPs are known to generate hydroxyl radical (HO), which is well known as a powerful oxidant with an oxidation potential of around 2.86 V [12, 17, 18]. HO can react and degrade almost all the non-biodegradable stable organic compounds *via* abstraction of hydrogen bond, electrophilic addition and electron transfer reactions [10, 18, 19]. Many authors have reported that the reactivity of non-selective HO towards most of the organic substrates in the range of  $10^6$ – $10^{10} \text{ M}^{-1}\text{s}^{-1}$ , which of course depends on the nature of the target pollutants [10, 17, 18, 20, 21].

In recent years, cold atmospheric plasma (also known as non-thermal or non-equilibrium plasma) has gained attention and proven to be an alternative tool for the oxidation of organic contaminants from water due to the abundant production of reactive species without addition of chemicals and increment of ambient temperature [22–26]. Cold atmospheric plasma is an electrically conductive gas and multi-component system of high-energy electrons, and reactive species, negative and positive ions, neutrals, metastables with thermal energies, and photons of different wavelengths [27–31]. It has been frequently tested for variety of applications, including agriculture [32], destruction of toxic gases [33], food preservations [34], medicines [27], surface modification [35], etc.

Although plasma can be formed inside a liquid, plasma formed in the gas phase above the liquid target require lower operating voltages. Plasma in contact with liquid has been demonstrated by many researchers to be suitable for the successful treatment of various organic pollutants, such as organic dyes [25, 36, 37], pharmaceuticals [21, 38], pesticides [39, 40], and so on. Plasma interacts with liquid leading to the formation of several reactive oxygen (ROS) and nitrogen species (RNS): HO, O,  $\text{H}_2\text{O}_2$ , NO, ONOOH,  $\text{O}_3$ , etc., that proved to be highly effective in the elimination of a high range of organic pollutants from water [13, 19, 26, 41–43].

Various APPJ with different reactor configurations were used and reported as promising plasma sources for the treatment of dye-containing polluted waters [11, 14, 22, 44, 45].

Generally, in the direct treatment process, where the solution is directly exposed to the plasma formed in the gaseous phase, several factors such as high energetic electrons, short and long-

lived ROS and RNS, UV emission, electric field, all originating from the active plasma volume, can play a significant role in the degradation of organic dyes [24–26, 41]. However, in case of PAW application i.e. indirect treatment only long-lived ROS and RNS that remained in the water after plasma treatment can be responsible for the degradation [42, 46–50].

AB25 dye is widely used for dyeing wool, silk, polyamide, leather and mixed fabric [51, 52]. AB25 has an anthraquinone structure with three fused aromatic rings, which makes the molecule resistant to oxidation by conventional wastewater treatment [13, 53, 54]. Anthraquinone dyes together with azo dyes are the most commonly used in the textile industries [55].

In the present study, AB25 dye was selected as a model anthraquinone compound. The removal of AB25 was carried out with direct exposure to APPJ and by using the PAW—indirect treatment. To the best of our knowledge, we could not find a similar report in the literature. The electrical characterization of the plasma system was performed and power deposition to the sample was determined. OES was carried out to study existing short-lived reactive species in the plasma. In indirect AB25 treatments, quantification of long-lived reactive species in PAW was performed. Then, AB25 treatment results with PAW and with chemicals were compared.

## MATERIALS AND METHODS

### Characteristics of AB25

AB25 (product number: 210684; purity: 45%; chemical formula:  $\text{C}_{20}\text{H}_{13}\text{N}_2\text{NaO}_5\text{S}$ ; chemical class: anthraquinone; classification: anionic; maximum absorbance: 602 nm) was purchased from Sigma Aldrich. A stock dye-containing solution with a concentration of 50 mg/L was prepared by dissolving an adequate amount of analytical grade of AB25 in distilled water. The lower concentration was achieved by the addition of distilled water into the stock solution.

### Plasma System

The schematic diagram of the experimental setup is given in **Figure 1**. APPJ consists of glass and ceramic tubes and a stainless steel electrode (powered electrode). The powered electrode is a 1 mm diameter stainless steel wire with a sharpened edge placed inside a ceramic tube, both axially positioned. The outer and inner diameters of the glass tube are 6 and 4 mm, respectively. The inner powered electrode is connected to the high voltage (HV) source. The sample vessel was grounded with a copper tape placed at the bottom side *via* a 1 k $\Omega$  resistor. A commercial high voltage RF power supply (T&C Power Conversion AG0201HV) provided a sine signal at the frequency of 330 kHz. Argon (5.0 purity) was used as a feed gas with a flow rate of 1 slm (standard liters per minute) and the flow rate was controlled through a mass flow meter (OMEGA, FMA5800/5500). We have chosen argon as a feed gas because it reduces the breakdown voltage of the discharge. The discharge is ignited in the mixture of argon with air. For discharge in air we would need tens of kV of applied voltage and our power supply was a limiting factor. The distance between the tip of the powered electrode and the surface of the liquid sample placed underneath was 10 mm. In all experiments, the sample volume was 5 ml.

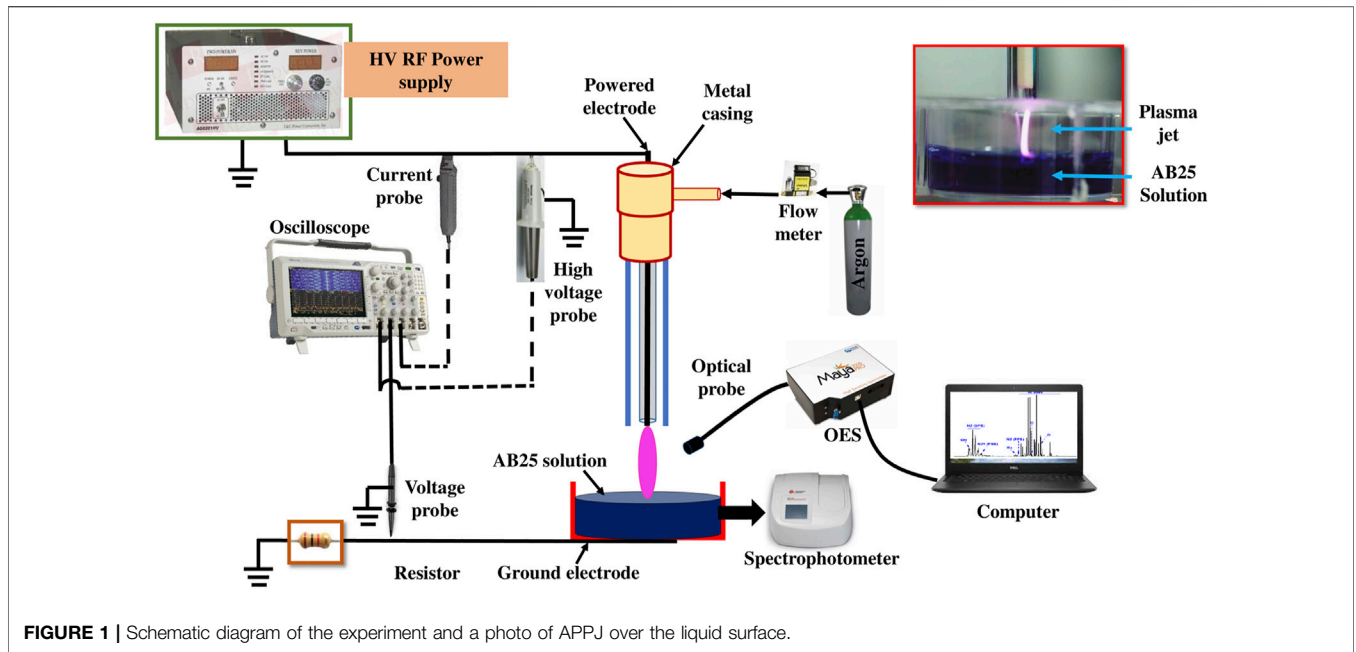


FIGURE 1 | Schematic diagram of the experiment and a photo of APPJ over the liquid surface.

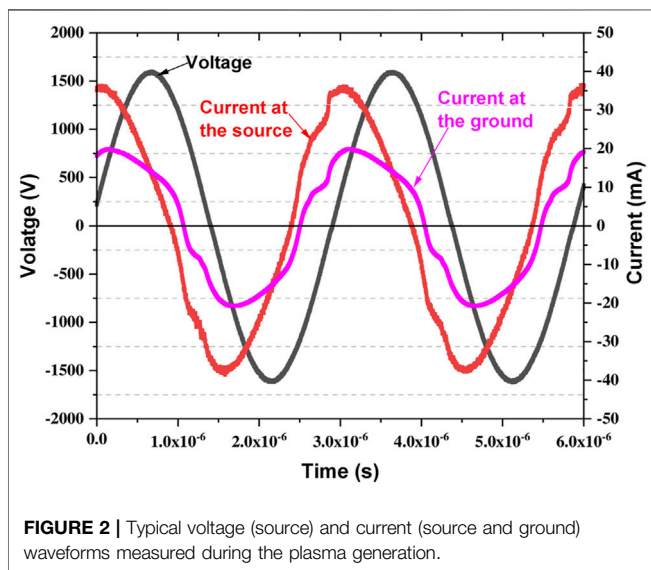


FIGURE 2 | Typical voltage (source) and current (source and ground) waveforms measured during the plasma generation.

The voltage at the powered electrode was determined by a high voltage probe (Tektronix 6015A). The current at the powered electrode was measured with a current probe (Agilent N2783B). The voltage drop across the 1 kΩ resistor used to establish the current in the grounded part was recorded using a voltage probe (Agilent 10073C). The time variable voltage and current signals were monitored by using an oscilloscope (Tektronix MDO3024). Simultaneously, the data from the oscilloscope was transferred to a laptop for further analysis. The power delivered from the power supply to the plasma source and the power in the grounded line, i.e., the power deposited from the plasma passing through the sample, were calculated.

An example of the recorded voltage and current waveform during the direct treatment of AB25 is displayed in Figure 2.

The mean power at the source is determined by averaging the instantaneous power (product of measured voltage and current) over a time interval of 6 periods.

$$P_{mean} = \frac{1}{nT} \int_{T_1}^{T_2} v(t) \times i_s(t) \times dt \quad (1)$$

Where,  $P_{mean}$ : mean power at the source;  $v(t)$ : voltage signal at the source;  $i_s(t)$ : current at the source:  $nT = T_2 - T_1$ .

The mean power at the ground (in contact with the sample) was similarly determined.

$$P_{mean} = \frac{1}{nT} \int_{T_1}^{T_2} v(t) \times i_g(t) \times dt \quad (2)$$

With  $i_g(t)$ : current at the ground:

$$i_g(t) = v_R(t)/R \quad (3)$$

Where  $P_{mean}$ : mean power at the sample;  $v_R(t)$ : voltage drop at the resistor; resistance  $R = 1 \text{ k}\Omega$ .

### Optical Emission Spectroscopy

OES spectra of excited species in the plasma system were captured by using Maya2000 Pro-UV-NIR (Ocean Insight-High Sensitive Spectrometer) and an optical fiber (M114L02). The fiber diameter (core) and length were 600 μm and 2 m, respectively. The position of the fiber enabled the recording of the emission from the whole volume of the plasma jet. The emission was recorded in the range of 200–1,100 nm with the exposure time of 10 ms. The background spectra (without plasma) was subtracted

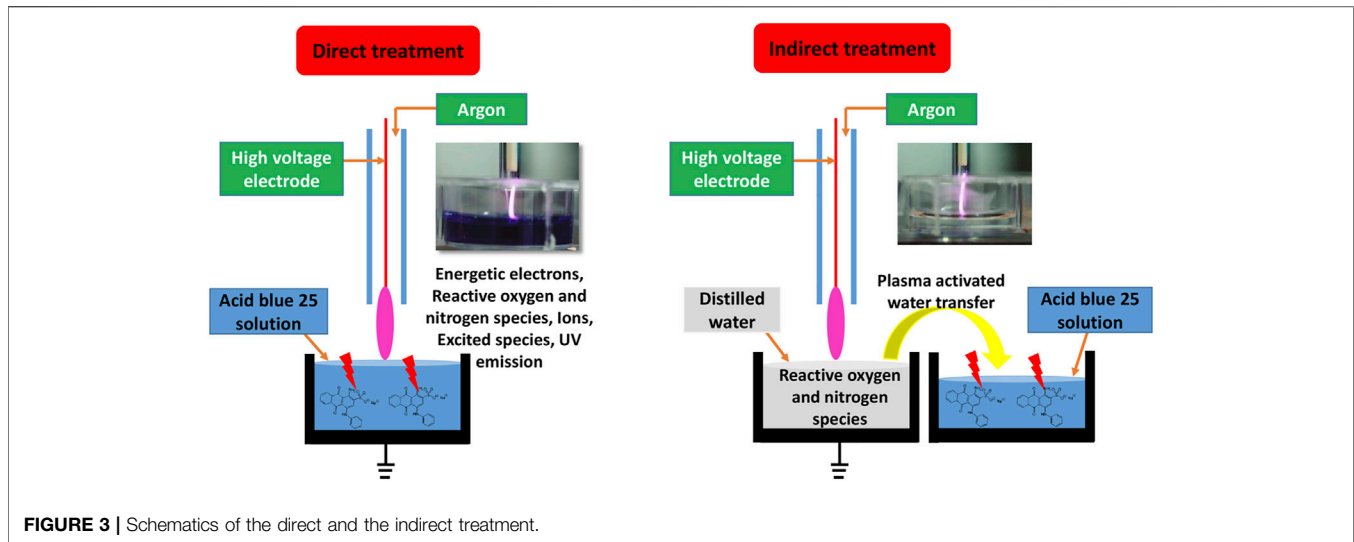


FIGURE 3 | Schematics of the direct and the indirect treatment.

from the plasma emission spectra. The spectral intensity was corrected for the optical system efficiency.

### Direct and Indirect Plasma Treatment

During the direct treatment, AB25-containing solution was directly exposed to APPJ and the solution was characterized immediately after the treatment. In the indirect treatment, AB25 was treated by mixing with plasma-activated water (PAW). The PAW was generated by exposing distilled water to APPJ for 10 min. After PAW was added into AB25 solution, we monitored and analysed the solution for several days to understand the role of long-lived reactive species in PAW on AB25 degradation. Schematics of both processes are illustrated in **Figure 3**.

### Solution Analysis

A spectrophotometer (Beckman Coulter DU 720 UV/Visible) with a 5 ml cuvette was used for the investigation of AB25 dye degradation. The maximum intensity of the AB25 absorbance occurs in the visible region at 602 nm and this wavelength was used to detect the degradation of the dye by direct plasma or PAW [56]. It is expected that during degradation of the AB25 through the chemical oxidation process the color donating chemical moiety will be influenced thus eliminating the molecule's capacity to absorb light in the visual region.

AB25 removal efficiency was determined by using **Eq. 4**:

$$\text{Removal (\%)} = \frac{C_o - C \times d}{C_o} \times 100 \quad (4)$$

Whereas  $C_o$  (mg/L) is the initial dye concentration,  $C$  (mg/L) is the final dye concentration after the treatment and  $d$  is the evaporation coefficient.

The energy yield ( $Y$ ), defined by the removal of AB25 per unit power deposition to the sample that was determined by **Eq. 5**

$$Y \left( \frac{\text{mg}}{\text{kWh}} \right) = \frac{C_o \left( \frac{\text{mg}}{\text{L}} \right) \times V_o \text{ (L)} \times \frac{1}{100} \times \text{Removal (\%)} }{P_{\text{mean at the sample}} \text{ (kW)} \times t \text{ (h)}} \quad (5)$$

Where  $V_o$  indicates the initial volume of solution (in liters),  $P_{\text{mean}}$  is power deposition at the sample (in kW) and  $t$  is the treatment time (in h).

The energy yield at 50% removal was calculated by the following **Eq. 6**

$$Y_{50} \left( \frac{\text{mg}}{\text{kWh}} \right) = \frac{C_o \left( \frac{\text{mg}}{\text{L}} \right) \times V_o \text{ (L)} \times \frac{1}{100} \times \text{Removal (50\%)} }{P \text{ (kW)} \times t_{50} \text{ (h)}} \quad (6)$$

The determination of long-lived ROS and RNS in the PAW was performed. After the plasma activation, the PAW was immediately characterized, and the concentrations of  $\text{NO}_3^-$ ,  $\text{NO}_2^-$  and  $\text{H}_2\text{O}_2$  are determined by using a UV/Visible spectrophotometer. In order to determine the concentration of  $\text{H}_2\text{O}_2$ , titanium oxysulfate ( $\text{TiOSO}_4$ ) reagent was added to the PAW.  $\text{H}_2\text{O}_2$  in the PAW reacted with  $\text{TiOSO}_4$  giving a yellow colour and the absorbance was recorded at 407 nm.  $\text{NO}_3^-/\text{NO}_2^-$  were measured by using Griess assay kits (Nitrate test—1.09713.0002, Nitrite test—1.14776.0002, Merck).  $\text{NO}_3^-$  was measured with the use of sulphuric acid ( $\text{H}_2\text{SO}_4$ ) and nitrate reagent. However,  $\text{NO}_2^-$  was determined by using  $\text{H}_2\text{SO}_4$  and nitrite reagent. The absorbance of the formed complexes were recorded at 357 and 525 nm for  $\text{NO}_3^-$  and  $\text{NO}_2^-$ , respectively.

In all treatment processes, the solution conductivity and pH are measured by a conductivity (HANNA-HI76312) and a pH (HANNA-HI1330) meter, respectively. The pH meter measures the concentration of hydrogen ions ( $\text{H}^+$ ). Hence, the concentration of  $\text{H}^+$  ions based on the measured pH of treated and untreated solutions was determined and discussed in *Direct Plasma Treatment of AB25*.

## RESULTS AND DISCUSSION

### Characterization of Plasma

#### Electrical Characterization of Plasma

Volt-ampere (V-A) characteristics of the pin-APPJ system were investigated and power deposition was calculated for different

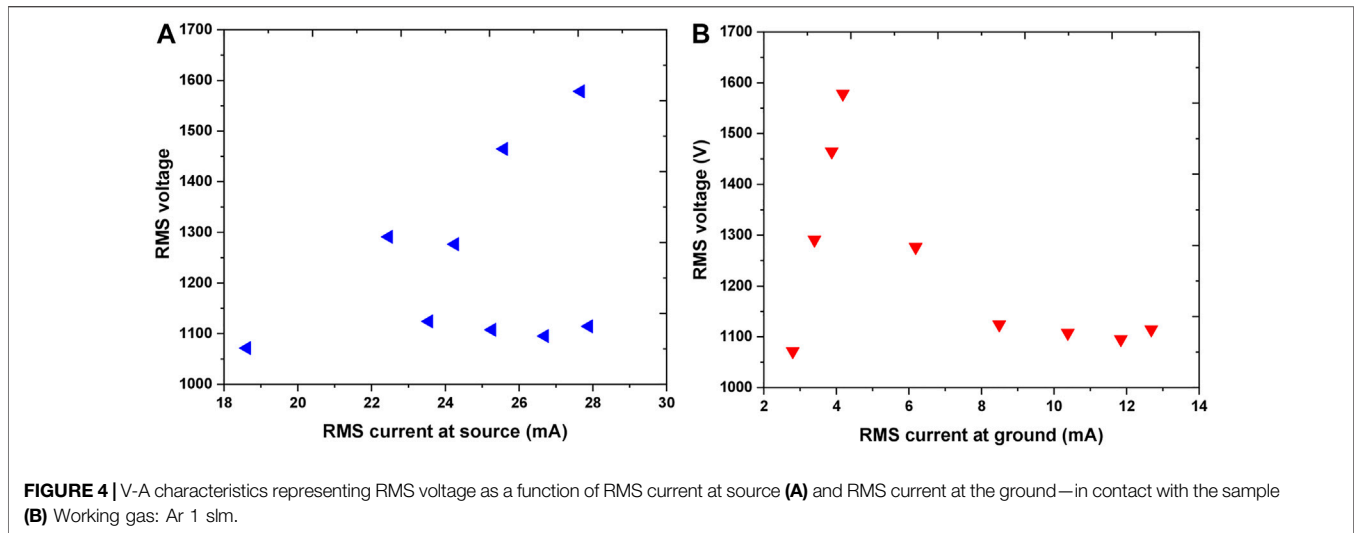


**FIGURE 4** | V-A characteristics representing RMS voltage as a function of RMS current at source **(A)** and RMS current at the ground—in contact with the sample **(B)** Working gas: Ar 1 slm.

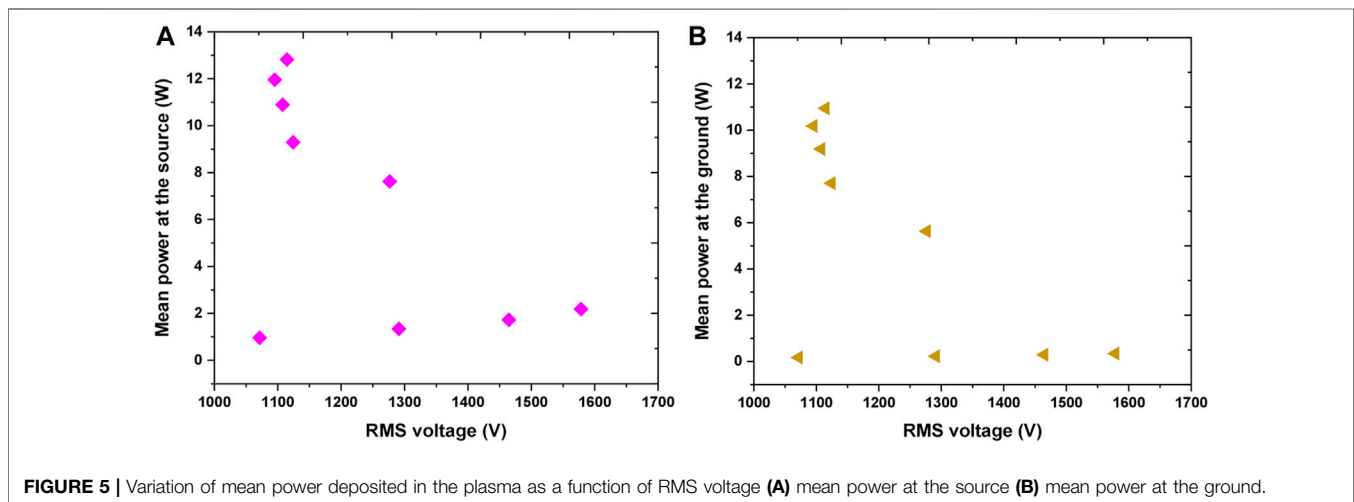


**FIGURE 5** | Variation of mean power deposited in the plasma as a function of RMS voltage **(A)** mean power at the source **(B)** mean power at the ground.

input conditions. The characterization was done in the identical conditions as in treatments, with the AB25 aqueous sample as a grounded target and Ar flow of 1 slm.

The results of electrical characterization are given in **Figures 4, 5**. **Figure 4A** represents the V-A at the jet, while **Figure 4B** shows the V-A of the plasma in contact with the sample. In both plots, RMS (root mean square) values of the voltage and appropriate current are presented. The linear part of the dependence represents the conditions when plasma is not ignited. At around  $1.6 \text{ kV}_{\text{RMS}}$  voltage the plasma was ignited resulting in a considerable reduction in voltage. One needs to keep in mind that here we did not measure the breakdown voltage but the operating voltage. With a further increase of power given by the RF power supply after plasma ignition, operating voltage did not change significantly and remained at about  $1.1 \text{ kV}_{\text{RMS}}$ . However, after ignition, the values of  $I_{\text{RMS}}$  at ground, i.e., in the plasma, raise more than 50%. In comparison to the  $I_{\text{RMS}}$  in the source,  $I_{\text{RMS}}$  in the part of the circuit that includes the sample were observed to be more than two fold lower.

The most important parameter for plasma treatments is power deposited into the plasma system. The variation in the power deposition at the source and sample are illustrated in **Figures 5A,B**, respectively. For the lowest powers applied, when the plasma was not ignited, it was observed that there was a small power deposition of 1–2 W at the source even though the system is mainly capacitive. This is due to the small resistive impedance of the electrical connections and components. When the applied voltage increased above  $1.6 \text{ kV}_{\text{RMS}}$  the breakdown occurs and with the inception of plasma the power deposition is increased. We can see that the increase of the power deposited in the system occurred while the voltage stayed almost constant or slightly decreasing indicating that the power increment is significantly due to the higher current in the source and through the ground i.e., in contact with the sample. Of particular importance was to calculate the power at the ground, i.e., deposited in the part of the electrical circuit in contact with the sample. It can be observed in **Figure 5B** that when the plasma was ignited the power delivered to the sample was in the range of about 5–11 W.

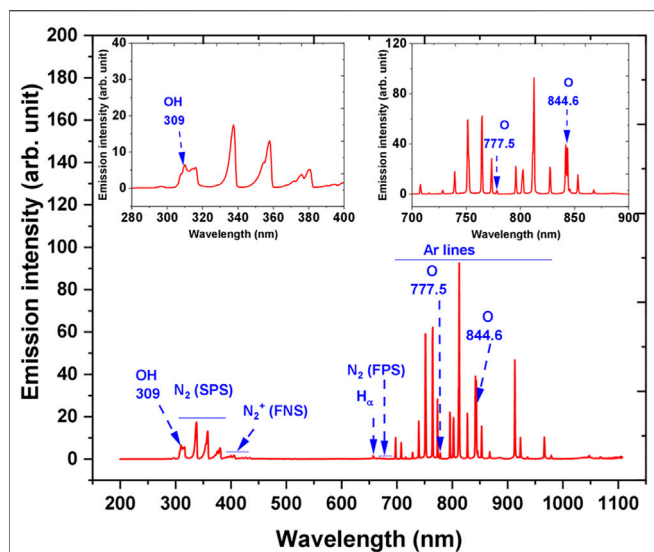


**FIGURE 6** | The emission spectrum of Ar—APPJ in contact with ambient air and over a liquid surface. During the diagnostics, AB25 was placed under APPJ,  $V_0 = 5$  ml, Ar 1 slm,  $P_{\text{mean}}$  at the sample 11 W. Inset plots show parts of the spectrum zoomed.

### Optical Characterization of Plasma

OES was used for the detection of excited species in argon plasma in the air interacting with the liquid. A typical OES spectrum during AB25 treatment in the range of 200–1,100 nm can be seen in **Figure 6**. Excited species such as hydroxyl radical (HO), atomic hydrogen (H), atomic oxygen (O), atomic argon, nitrogen second positive system (SPS), nitrogen first positive system (FPS) and nitrogen first negative system (FNS) were observed.

A-X band of HO and  $H_\alpha$  line were detected with maximum emission of at 309 and 656.2 nm, respectively. In the discharge HO emission could have originated due to dissociative excitation of water molecules in collisions of electron or argon metastables [57–59]. The main source of water molecules in the gaseous phase or discharge region mostly comes from the evaporation of the target sample due to the effect of purging caused by gas flow or could be *via* local heating caused by the impact of heavy ions in APPJ [57, 60]. Since the plasma was ignited in the mixture of argon with the surrounding air, excited argon lines, molecular nitrogen bands and atomic oxygen lines were present. The emission of O lines were at 777.5 and 844.6 nm, excited molecular nitrogen SPS between 300 and 405.8 nm with intensive band-head at 337.7 nm. For the molecular ions, the nitrogen molecular FNS between 391.4 and 428 nm and a weak intensity of FPS are also present. Excited argon lines were observed in the spectral region between 696.5 and 965.7 nm and the strongest emission occurred at 773.5 and 811.5 nm, respectively. The formation of O and molecular nitrogen can be attributed to the reactions of energetic electrons or argon metastables with ambient air [57]. Many authors have reported that HO and O radicals are considered as one of the main short-lived ROS in the plasma discharge, and they can directly react with organic pollutants which lead to degradation [14, 19, 24, 61].

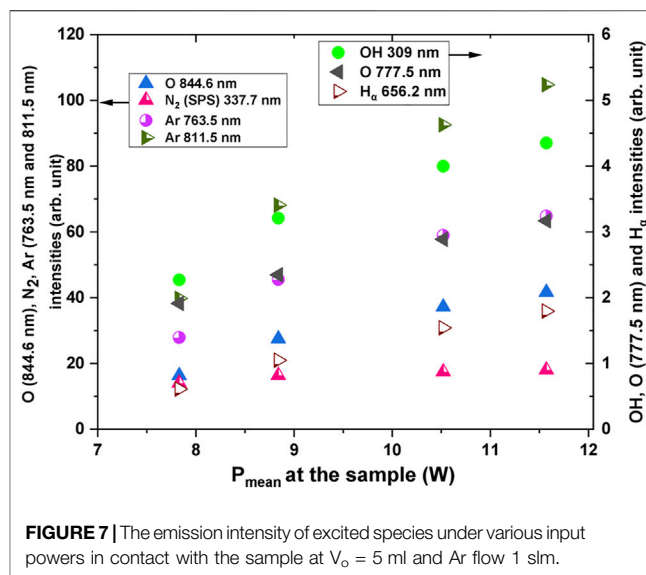
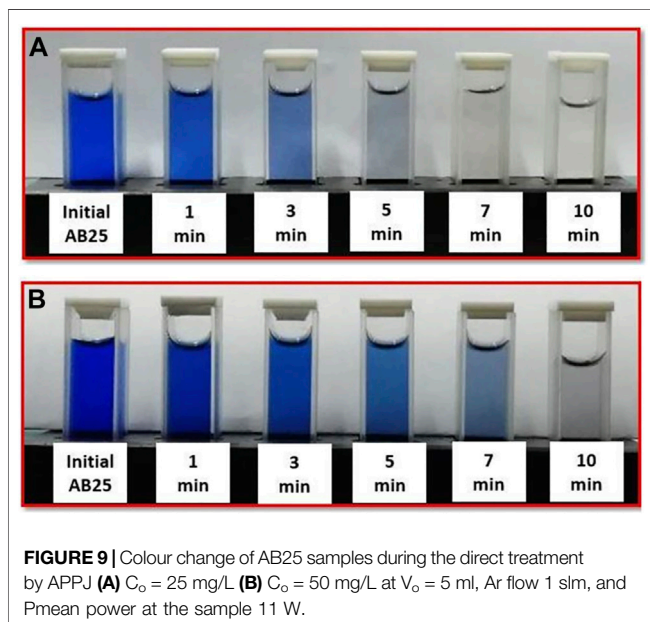
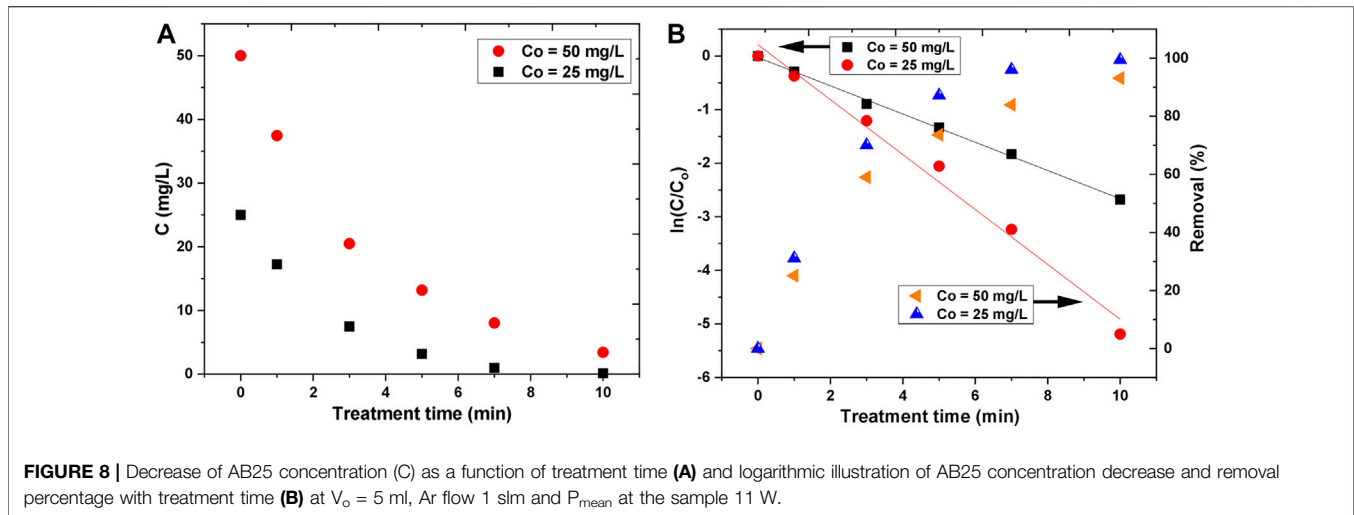


**FIGURE 7** | The emission intensity of excited species under various input powers in contact with the sample at  $V_0 = 5$  ml and Ar flow 1 slm.

Emission intensities are determined with various input powers. **Figure 7** illustrates that the emission intensities of HO, H, nitrogen SPS, excited argon as a function of deposited power to the sample (ground). It can be observed that the spectral emission intensity of the species increases almost linearly with the increase in deposited power. The largest change in the intensity occurred with species such as O (844.6 nm), nitrogen SPS and excited argon, whereas the intensity of HO, H, and O (777.5 nm) only slightly increases with input powers. The observed influence of input power correlates with results presented by other researchers [57]. Changes in emission intensities with power are related to higher energy delivered to the plasma. Higher power probably could lead to an increase in the electron temperature as well as electron density which influences the emission intensity of excited species [62]. From the viewpoint of treatments, higher intensities and concentrations of reactive species are the essential factors in order to degrade organic pollutants [11, 44]. The OES is a simple and, more important, non-intrusive diagnostic technique that can give information about the excited atomic, molecular and ion species. Its simplicity makes it readily available and the obtained results can be easily interpreted. However, they do not give the whole picture about the plasma chemistry (especially in the gas phase). This can be done by using the Fourier transform infrared (FTIR) spectroscopy, which was not readily available in our case. In the literature, FTIR analysis was carried out to analyze long-lived reactive species in the gas phase. For example, in the study of [11], FTIR analysis was performed to characterize the plasma-liquid interaction, where a plasma jet was formed over the liquid surface in ambient air. It was found that FTIR confirmed the presence of various reactive species (e.g.,  $O_3$ ,  $NO_2$ ,  $HNO_3$ ,  $HNO_2$ , etc.) during plasma-liquid interaction in ambient air. [63] have demonstrated the effect of a water surface on the production of reactive species and FTIR spectroscopy was applied to identify  $O_3$  and  $NO_2$  in the far-field of the cold atmospheric plasma jet. [64] investigated the synthesis of nanoparticles in liquid with cold atmospheric plasma and they have used FTIR for surface characterization of the  $TiO_2$ . Another diagnostic technique that



can give information about plasma chemistry (both radicals, atoms, molecules, and ions) is mass spectrometry at atmospheric pressure. We have performed characterization of various plasma sources that operate at atmospheric pressure by using HIDDEN HPR60 and obtained mass spectra of neutral radicals (atoms/molecules) and ions (results are presented here) [65–68].

## Direct Plasma Treatment of AB25

In the direct treatment process, the effect of various experimental parameters, including initial concentration of AB25, treatment time and power deposition on the degradation of dye was investigated.

### Effect of Initial AB25 Concentration

In the laboratory-scale experiments, two initial concentrations of AB25 were used. The degradation of dye in the solutions as a function of treatment time is given in **Figure 8A**. With the

**TABLE 1 |** Degradation rate constants and half-life at two different AB25 concentrations in the sample.

AB25 concentration (mg/L)	First-order rate constant $k$ ( $\text{min}^{-1}$ )	$R^2$	$t_{1/2}$ (min)
25	0.512	0.98	1.35
50	0.263	0.99	2.63

\* $R^2$ : Regression coefficient.

increase of treatment time, the concentration of AB25 was decreased exponentially. In both cases, the degradation was significantly more pronounced in the first 5 min. The removal efficiency values were about 87% for 25 mg/L and 73% for 50 mg/L within 5 min. In case of lower initial concentration, the destruction of AB25 for the longest treatment time (10 min) was about 100%, whereas for the two times greater initial concentration the obtained removal efficiency was around 93%. It can be expected that for a longer time the higher initial concentration of AB25 would be completely removed.

Visually, the change in the coloring of the sample can be observed in **Figure 9**. For lower AB25 concentration and within 10 min of treatment time, dye almost disappeared. On the other hand, for the higher concentration, the solution was not completely colorless.

The kinetic study was performed in order to understand the degradation rate of AB25. It was found that the degradation of AB25 for both initial concentrations followed the first-order kinetics during investigated treatment duration (**Figure 8B**) with good regression coefficient values ( $R^2 \geq 0.98$ ).

First-order kinetics is defined by the following **Eq. 7**, where  $k$  is rate constant and  $t$  is treatment time.

$$\frac{C}{C_o} = e^{-kt} \quad (7)$$

The half-life ( $t_{1/2}$ ) AB25 decomposition time was determined by the given **Eq. 8** and shown in **Table 1**.

$$t_{1/2} = \frac{0.693}{k} \quad (8)$$

It can be inferred from **Table 1** that the lower initial concentration of AB25 promotes the higher degradation rate constant. The half-life time for 25 mg/L was almost 2 times lower than 50 mg/L, which attributed to a faster degradation rate for the lower AB25 initial concentration. The higher concentration of AB25 means a higher number of dye molecules in the solution, whereas the formation of plasma species remains almost the same. Moreover, at the higher concentration, intermediate products may become more relevant and not all introduced plasma species continue reacting with the original AB25 molecules (competition with intermediates). Yet, concerning that equation for first-order kinetics (7) precisely fits the data, the effect involving intermediate products is not pronounced. Almost a similar behavior was reported in the previous research on the degradation of AB25, where DC glow discharge was formed in ambient air over the liquid surface [9].

Ghodbane et al. [9] have studied the degradation of AB25 with direct exposure to glow discharge, whereas plasma-treated samples were characterized by using HPLC and HPLC-MS. They have reported that the key reactive species such as high energy electrons, O<sub>3</sub>, and HO can attack at various positions of AB25 molecules and lead to the formation of low molecular weight residues. For example, initially, the reactive species can attack various chemical bonds in the AB25 molecule, including amino, sulfonic and vinylsulfonyl since they are located far from anthraquinone rings (stable), and then various bonds in naphthaquinone rings can be eliminated. It was found that low molecular weight products such as pyrocatechol, 3,6-diamino-4-methylphthalic acid, benzene, and 2,5-dimethylphenol appeared due to oxidation of AB25. [69] have investigated the degradation of AB25 with AOPs (e.g., UV-H<sub>2</sub>O<sub>2</sub> and UV-TiO<sub>2</sub>), and they reported the possible degradation pathways for AB25. It was mentioned that degradation can be initiated by attacking at C-N bond to separate the aromatic ring and then hydroxylation in the secondary amine position. In further steps, splitting of quinone ring leading to the formation of 2-amino-4-(2-carboxybenzoyl)-5-hydroxybenzenesulfonate, after that it further oxidizes to phthalic acid and then turns into formic and oxalic acids. Finally, ending up with complete mineralization of the dye. In the study of [70] corona discharge was used for degradation of AB25. Authors reported degradation pathways of AB25, whereas O<sub>3</sub> and H<sub>2</sub>O<sub>2</sub> were the major reactive species that are responsible for degradation. The products such as CO<sub>2</sub>, H<sub>2</sub>O, SO<sub>4</sub><sup>2-</sup>, NO<sub>3</sub><sup>-</sup> were found by the end of treatment.

The energy yield was calculated and it depended on the removal percentage of AB25 for both initial concentrations. The energy yield was higher at the beginning of the treatment (shorter treatment times) due to a faster degradation rate. However, for fixed removal percentage the difference in the energy yield was not significant for both initial AB25 concentrations. In this case, the energy yield was about 259 mg/kWh for 50 mg/L and 252 mg/kWh for 25 mg/L at 50% removal, respectively.

The pH and the conductivity of the treated solutions were also measured. The results are presented in **Figure 10**. For both initial concentrations, the pH changed in the same way and it drastically dropped with the treatment time. After 10 min of treatment time, the final pH was about 2.5. The decrease in the pH can be attributed to the formation of acidic molecules (e.g., HNO<sub>3</sub> and HNO<sub>2</sub>) and the higher concentration of hydrogen ions (H<sup>+</sup>) inside the solution [11, 71–73]. Based on measured pH, the concentration of H<sup>+</sup> ions was determined by **Eq. 9** [74]. The concentration of H<sup>+</sup> ions with treatment time is plotted in **Figure 10A**, where it increased linearly with treatment time.

$$[H^+] = 10^{-pH} \quad (9)$$

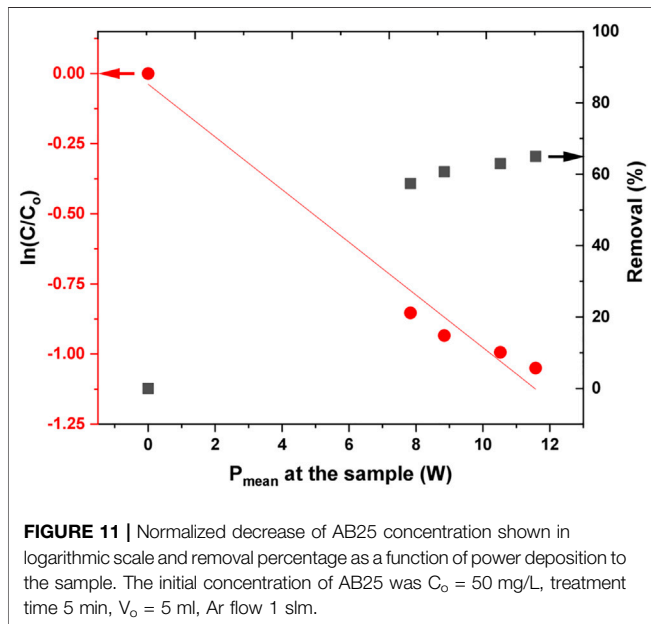
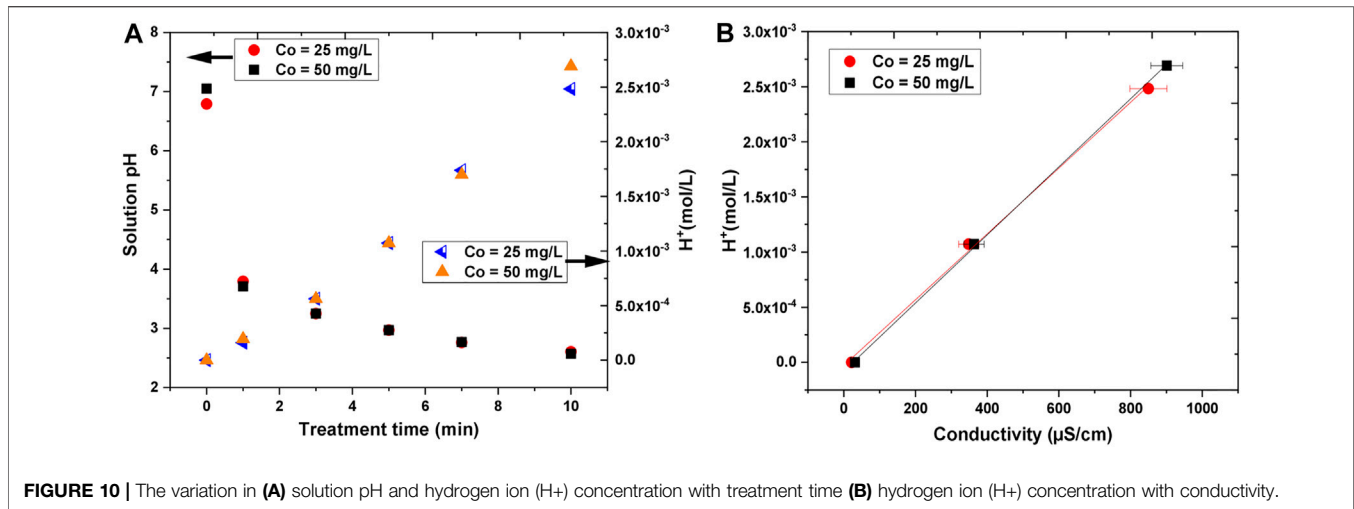
It was observed that the conductivity of the treated solutions increased with the increase in treatment time. The initial conductivity, which was quite small (21–31 μS/cm), was enhanced up to about 850–900 μS/cm after 10 min of treatment. The conductivity was somewhat higher for the higher initial concentration of AB25, but the difference was not significant. The electrical conductivity is determined by the Kohlrausch law taking into account the concentration and nature of ions inside solution, whereby H<sup>+</sup> ions can contribute strongly because of the Grotthus proton-hopping mechanism leading to an exceptionally high limiting molar ionic conductivity (349.8 S cm<sup>2</sup>/mol). **Figure 10B** shows that the H<sup>+</sup> ions concentration measured against conductivity has a linear dependence.

### Effect of Input Power on AB25 Degradation

The influence of deposited power on AB25 degradation was also investigated. The experiment was carried at the initial AB25 concentration of 50 mg/L and treatment time of 5 min. In **Figure 11**, the effect of the deposited power into the discharge on the change in AB25 concentration and removal percentage is shown. As expected, the higher degradation of AB25 was accomplished when there was more power transferred to the sample. At higher input power, more energy can be delivered to the plasma to support the formation of more reactive species. It was evident from OES result (**Figure 7**), where emission intensities of reactive species increased with input powers. Therefore, the presence of more reactive species in the gas phase can lead to the degradation of AB25. The observed effect was illustrated in various papers, showing that input power played a beneficial role in the degradation of various organic dyes [75, 76].

The kinetic curves for the removal of AB25 as a function of deposited power are shown in **Figure 11**. In the first-order reaction (**Eq. 7**), the time was replaced by input power to determine what is more cost-efficient: to increase the power or to use a longer treatment time. The value of the rate constant revealed that increasing the input power shows slower degradation compared to increasing the treatment time. A modified first-order and half-life equation is described by a given equation.





$$\frac{C}{C_o} = e^{-k'P} \quad (10)$$

It takes about 7 W of input power to decompose 50% of AB25 (Table 2), calculated by Eq. 11.

$$P'_{1/2} = \frac{0.693}{k'} \quad (11)$$

Since the treatment was carried out at different input powers, the energy yield was also determined based on the amount of power consumed to remove 50% of AB25 at a fixed treatment time of 5 min and AB25 concentration of 50 mg/L. The calculated energy yield was about 203 mg/kWh. Comparing to Table 1 for 50% proves that removal varying the power at fixed treatment time was not cost-effective. It is more effective to use lower power and longer treatment times.

### Indirect Plasma Treatment of AB25

In the indirect treatment, AB25 was treated with PAW and, as control experiments, with solutions containing: (a)  $H_2O_2$  (b)  $NO_3^-$ , (c)  $NO_2^-$  and (d)  $H_2O_2 + NO_3^- + NO_2^-$ .

The control experiments were commenced taking into account that PAW is a cocktail of various long-lived stable species (e.g.,  $H_2O_2$ ,  $NO_3^-$ ,  $NO_2^-$ ,  $ONOOH$ ,  $O_3$ , etc.) [27, 48]. In this study, the PAW has been generated by exposure of distilled water for 10 min to APPJ argon plasma, with deposited power delivered to the sample of about 11 W and with Ar flow of 1 slm. After the generation of PAW, concentrations of several identified species were measured and the measured values are:  $H_2O_2$ —255 mg/L,  $NO_3^-$ —222 mg/L,  $NO_2^-$ —0.06 mg/L. After the activation, it was observed that the pH dropped from about 6.5 to 2.62 and conductivity increased from around 12 to 708.4  $\mu S/cm$ , respectively. Many authors have worked on the generation and characterization of PAW, where they quantified various long-lived ROS and RNS [14, 57, 77, 78].

It was evident from OES spectra, that  $HO\cdot$ ,  $O\cdot$ ,  $H\cdot$  and nitrogen species were formed in the plasma discharge. These species could contribute to produce varieties of oxygen and nitrogen-based species in the gaseous phase as well as at the gas-liquid interface. The generated species could transfer into the liquid phase and be converted to long-lived species, such as  $H_2O_2$ ,  $NO_3^-$ , and  $NO_2^-$ . The comprehensive overview of the origination of ROS and RNS during plasma and liquid interactions has been investigated by several authors [19, 24, 41, 79].

$H_2O_2$  is the key active ROS formed in the PAW [14, 42], with an oxidation potential of 1.77 V [24]. The formation of  $H_2O_2$  can be attributed mainly due to the recombination reactions of  $HO$  radicals, generated during plasma and liquid interactions [9]. The most dominant and straightforward reaction pathways in the gaseous phase which contribute to the production of  $H_2O_2$  are described by Eqs 12, 13 [14, 25, 48, 57, 79].

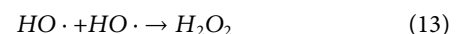
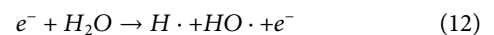
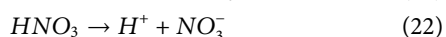
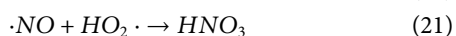
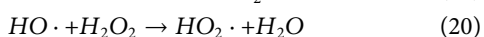
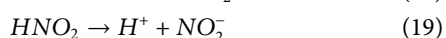
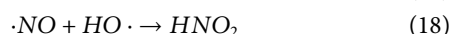
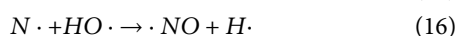
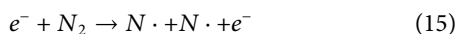


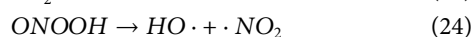
**TABLE 2** | Degradation rate constant and half-life at different power in plasma.

AB25 concentration (mg/L)	Treatment time (min)	First-order rate constant $k'$ ( $W^{-1}$ )	$R^2$	$P_{1/2}$ (W)
50	5	0.093	0.97	7.38

The formation of  $NO_2^-$  and  $NO_3^-$  in the PAW can be generated due to the dissociation of acids such as  $HNO_2$  and  $HNO_3$  [42, 79]. Both acids can be formed from the reaction of  $N_2$  and  $O_2$  in the gaseous phase as well as at the gas and liquid interface.  $NO_2^-$  and  $NO_3^-$  inside the liquid can be formed through the following possible reaction pathways [42, 79].



The presence of long-lived species, including  $H_2O_2$ ,  $NO_2^-$  and  $H^+$  in the liquid with a lower pH can produce peroxyxynitrous acid (ONOOH), which is a powerful oxidizing agent with an oxidation potential of 2.0 V [46]. ONOOH can also be decomposed and it is possible to generate HO *via* the following reaction mechanism [48, 79].



After creation, PAW was immediately mixed with AB25-containing solution. Based on the quantified concentration of species that were produced in PAW, four different solutions, namely (I)  $H_2O_2$ , (II)  $NO_3^-$ , (III)  $NO_2^-$  and (IV)  $H_2O_2 + NO_3^- + NO_2^-$ , were prepared and mixed with AB25-containing solution as control experiments. The PAW and AB25 containing solution, as well as, solutions (I)–(IV) and AB25 containing solution have then been followed and periodically characterized for 17 days to check the influence of long-lived reactive species on the degradation of AB25. The initial pH of each solution were measured and the measured values are: pH of PAW + AB25—2.97,  $H_2O_2$  + AB25—4.22,  $NO_3^-$  + AB25—6,  $NO_2^-$  + AB25—6, and  $H_2O_2 + NO_3^- + NO_2^-$  + AB25—4.55.

The effect of PAW and chemicals on the degradation of AB25 is shown in **Figure 12**. There was no degradation observed immediately after the PAW or solutions (I)–(IV) were mixed with AB25 containing solution (at 0 days). Degradation was noticed after a couple of days of experiment. The solutions containing individual chemicals (II)— $NO_3^-$  or (III)— $NO_2^-$  did not play any significant role up to 17 days (almost negligible). In case of solution (I)— $H_2O_2$  the degradation of the AB25 became significant after 8 days ending at close to the 50%.

The mixture of all three chemicals solution (IV) gave slightly better results in the first days after the solution (IV) was added to the AB25 solution, but on day 17 the removal percentage was similar as in case of only solution (I)— $H_2O_2$ . The degradation of AB25 was more pronounced with a combination of all three chemicals in the first 10 days, whereas almost the same influence occurred with both cases in between 14 and 17 days. Such influence could attribute to the formation of other reactive species in the solution with the presence of  $H_2O_2 + NO_3^- + NO_2^-$ , which might be responsible for the faster degradation in the first 10 days. The best degradation rate was obtained when AB25 solution was mixed with PAW with the maximal removal percentage of about 71% within 17 days. The PAW seems to have a significant influence on the depletion of AB25 compared to the solution with chemicals. Such difference can be explained by the probability of the formation of other reactive species in PAW, which supported and contributed to faster degradation. In the study by Cadorin et al. [46] and Moussa et al. [47], it was reported that the presence of ONOOH in the plasma-activated solution favored the degradation of organic dye (methyl orange).

To examine the effect of low pH on AB25 removal, an additional experiment with a control sample was performed, where hydrochloric acid (HCl) was added into AB25 solution to maintain a low pH of 3.04. It was observed that the concentration of AB25 almost remained the same within

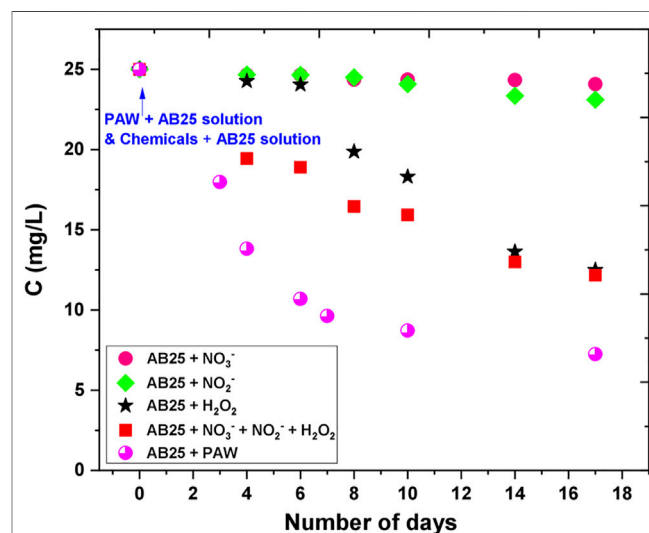
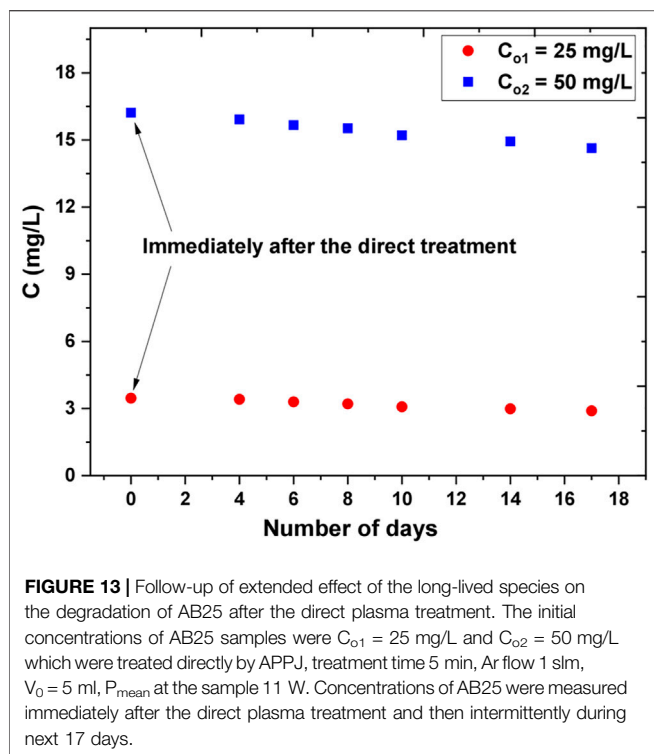


**FIGURE 12** | Effect of PAW and artificial RONS solutions on the degradation of AB25. The initial concentration of AB25 was 25 mg/L. The concentration of AB25 was intermittently measured during 17 days.



17 days. Hence, only in acidic conditions, there was no significant acid-catalyzed hydrolysis of AB25.

To allow comparison to the long-term effects of the indirect treatment, direct treatment experiments were carried out with two different initial AB25 concentrations and the plasma-treated solutions were kept and analyzed for 17 days as in the indirect case (e.g., with PAW and reagents). The objective was to investigate the effect of formed long-lived ROS and RNS on the degradation of AB25 after direct exposure to APPJ. After 5 min of treatment, the concentration of AB25 decreased from 50 mg/L to about 16 mg/L and 25 mg/L to about 3 mg/L, respectively. Here, AB25 solution was not directly treated for a longer duration because of evidence from the direct treatment indicating that higher treatment time favored almost complete degradation. Therefore, the treatment time was kept short so that the effect of long-lived reactive species on the degradation of residual AB25 after the direct treatment could be studied.

As shown in **Figure 13**, it was observed that there was minor decay of AB25 concentration after the analysis of the plasma-treated sample for several days. Since  $H_2O_2$  was the important long-lived ROS in the indirect treatment process (**Figure 12**) we can assume that insufficient amount of  $H_2O_2$  remained after the direct exposure of AB25 solution to APPJ due to its role in degradation processes. This revealed that dominant  $HO\cdot$  was consumed immediately after it was formed and consequently reacted with dye molecules.

## CONCLUSION

The treatment of AB25 with direct APPJ exposure, with PAW, and with solution of mixed chemicals have been studied. A pin-type APPJ was studied as a potentially efficient tool to remove AB25 from water. The plasma characteristics of pin type-APPJ including electrical characterization with calculations of mean power deposited to the discharge were presented. OES shows the emission spectra of the discharge with various reactive species (e.g., HO, O, H etc.). The plasma was ignited in a mixture of argon with the surrounding air, hence there was a significant presence of argon lines, the nitrogen molecule and ion bands. In the emission spectrum, HO as well as O radicals, were the most important detected short-lived species, since they could attack AB25 molecules and contribute to degradation. It was also noticed that the emission intensities of these species increase with the input power. The increase of the emission intensity of reactive oxygen species such as HO and O (844.6 nm) was more pronounced with input power, whereas O (777.5 nm) emission intensity increased only slightly.

In the direct treatment process, the removal rate of AB25 was increased by decreasing the initial AB25 concentration. The removal efficiency was about 87% with a lower concentration of 25 mg/L and 73% with a higher concentration of 50 mg/L within 5 min of treatment and power deposition of 11 W. Almost complete removal was obtained with a treatment time of 10 min and at AB25 concentration of 25 mg/L and power deposition of 11 W. For both initial concentrations, the degradation rates followed the first-order kinetics. An explanation for a continued first-order degradation could be that the bulk of the AB25 degradation happens through a species that reacts selectively with AB25 and that it is present in a pseudo-steady-state concentration. It was observed that the degradation is enhanced with the increase of the input power and this was supported with OES results. On the other hand, the increase in power does not lead to such a significant increase in the degradation rate as compared with the increase in treatment time.

The indirect treatments of AB25 with PAW and with solutions containing main PAW chemicals and their mixture were performed and compared during 17 days monitoring period. It was observed that the degradation was higher with PAW and with the mixture of  $H_2O_2 + NO_3^- + NO_2^-$ . Within 17 days, the highest removal efficiency was found to reach about 71% when AB25 solution was mixed with PAW. However, individual reagents such as  $NO_3^-$  and  $NO_2^-$  did not contribute any major role to the degradation. AB25 solution was also kept at low pH without any reagents, the results confirm that acidic condition does not influence degradation.

Apart from indirect treatment experiments, samples after the direct treatment by APPJ were kept and characterized for 17 days to facilitate comparison. It was noticed that there was no significant difference in the concentration of AB25, which indicated that there might be unavailability of enough long-lived ROS in the solution (e.g.,  $H_2O_2$ ).

Considering all experimental results, it can be concluded that removal of AB25 from water can be accomplished in a direct treatment with APPJ, indirect treatment with PAW, as well as

adding H<sub>2</sub>O<sub>2</sub>, and mixture H<sub>2</sub>O<sub>2</sub> + NO<sub>3</sub><sup>-</sup> + NO<sub>2</sub><sup>-</sup>. The depletion of AB25 was faster after the direct treatment with APPJ and slower for indirect treatment with PAW and with added chemicals.

## DATA AVAILABILITY STATEMENT

The original contributions presented in the study are included in the article/supplementary material, further inquiries can be directed to the corresponding authors.

## AUTHOR CONTRIBUTIONS

Conceptualization AK, NP, WG, NS; writing—original draft preparation AK, review and editing AK, NS, NP, WG; supervision NP, WG, DP; project administration NP, WG. All authors have read and agreed to the published version of the manuscript.

## REFERENCES

- Bayomie OS, Kandeel H, Shoeib T, Yang H, Youssef N, El-Sayed MMH. Novel Approach for Effective Removal of Methylene Blue Dye from Water Using Fava Bean Peel Waste. *Sci Rep* (2020) 10:1–10. doi:10.1038/s41598-020-64727-5
- Tiwari M, Shukla SP, Mohan D. Toxicity of Disperse Dyes and its Removal from Wastewater Using Various Adsorbents: A Review. *Res J Environ Toxicol* (2017) 11:72–89. doi:10.3923/rjet.2017.72.89
- Fernández C, Larrechi MS, Callao MP. An Analytical Overview of Processes for Removing Organic Dyes from Wastewater Effluents. *Trac Trends Anal Chem* (2010) 29:1202–11. doi:10.1016/j.trac.2010.07.011
- Islam M, Mostafa M. Textile Dyeing Effluents and Environment Concerns - A Review. *J Environ Sci Nat Resour* (2019) 11:131–44. doi:10.3329/jesnr.v11i1-2.43380
- Mia R, Selim M, Shamim AM, Chowdhury M, Sultana S, Armin M, et al. Review on Various Types of Pollution Problem in Textile Dyeing & Printing Industries of Bangladesh and Recommendation for Mitigation. *J Text Eng* (2019) 5:220–6. doi:10.15406/jteft.2019.05.0205
- Drumond Chequer FM, de Oliveira GAR, Anastacio Ferraz ER, Carvalho J, Boldrin Zanoni MV, de Oliveir DP. Textile Dyes: Dyeing Process and Environmental Impact. *Eco-Friendly Text Dye Finish* (2013) 6:151–17. doi:10.5772/53659
- Wong S, Ghafar NA, Ngadi N, Razmi FA, Inuwa IM, Mat R, et al. Effective Removal of Anionic Textile Dyes Using Adsorbent Synthesized from Coffee Waste. *Sci Rep* (2020) 10:1–13. doi:10.1038/s41598-020-60021-6
- Kant R. Textile Dyeing Industry an Environmental Hazard. *Nat Sci* (2012) 04:22–6. doi:10.4236/ns.2012.41004
- Ghodbane H, Nikiforov AY, Hamdaoui O, Surmont P, Lynen F, Willems G, et al. Non-Thermal Plasma Degradation of Anthraquinonic Dye in Water: Oxidation Pathways and Effect of Natural Matrices. *J Adv Oxid Technol* (2014) 17:372–84. doi:10.1515/jaots-2014-0223
- Mitrović J, Radović-Vučić M, Kostić M, Velinov N, Najdanović S, Bojić D, et al. The Effect of Anions on Decolorization of Textile Azo Dye Reactive Orange 16 with UV/H<sub>2</sub>O<sub>2</sub> Process. *Adv Technol* (2019) 8:33–40. doi:10.5937/savteh1901033m
- Naz MY, Shukrullah S, Rehman SU, Khan Y, Al-Arainy AA, Meer R. Optical Characterization of Non-thermal Plasma Jet Energy Carriers for Effective Catalytic Processing of Industrial Wastewaters. *Sci Rep* (2021) 11:1–13. doi:10.1038/s41598-021-82019-4
- Guivarch E, Trevin S, Lahitte C, Oturan MA. Degradation of Azo Dyes in Water by Electro-Fenton Process. *Environ Chem Lett* (2003) 1:38–44. doi:10.1007/s10311-002-0017-0

## FUNDING

This work was carried out under NOWELTIES project. NOWELTIES received funding from the European Union's Horizon 2020 research and innovation programme under the Marie Skłodowska-Curie grant agreement No. 812880. NS and NP are funded by the Ministry of Education, Science and Technological Development, grant number 451-03-68/2020-14/200024.

## ACKNOWLEDGMENTS

This article is based upon work from COST Action PLAGRI—CA19110, supported by the COST (European Cooperation in Science and Technology), www.cost.eu. AK is grateful to Ms. Andjelija Petrovic and Ms. Olivera Jovanovic for useful instructions and help regarding plasma diagnostics and protocols for liquid samples.

- Merouani DR, Abdelmalek F, Taleb F, Martel M, Semmoud A, Addou A. Plasma Treatment by Gliding Arc Discharge of Dyes/dye Mixtures in the Presence of Inorganic Salts. *Arabian J Chem* (2015) 8:155–63. doi:10.1016/j.arabj.2011.01.034
- Attri P, Yusupov M, Park JH, Lingamdinne LP, Koduru JR, Shiratani M, et al. Mechanism and Comparison of Needle-Type Non-Thermal Direct and Indirect Atmospheric Pressure Plasma Jets on the Degradation of Dyes. *Sci Rep* (2016) 6:1–14. doi:10.1038/srep34419
- Ruppert G, Bauer R, Heisler G. UV-O<sub>3</sub>, UV-H<sub>2</sub>O<sub>2</sub>, UV-TiO<sub>2</sub> and the Photo-Fenton Reaction - Comparison of Advanced Oxidation Processes for Wastewater Treatment. *Chemosphere* (1994) 28:1447–54. doi:10.1016/0045-6535(94)90239-9
- Abhilasha J, Ashma A, Marazban K. A Greener Approach for the Degradation of Dye Methylene Blue by Organic Additive Catalysed Photo-Fenton Process. *J Chil Chem Soc* (2016) 61:3043–8. doi:10.4067/S0717-97072016000300007
- Papić S, Koprivanac N, Božić AL, Vujević D, Dragičević SK, Kušić H, et al. Advanced Oxidation Processes in Azo Dye Wastewater Treatment. *Water Environ Res* (2006) 78:572–9. doi:10.2175/106143006x101665
- Cuerda-Correa EM, Alexandre-Franco MF, Fernández-González C. Advanced Oxidation Processes for the Removal of Antibiotics from Water. An Overview. *Water* (2019) 12:102. doi:10.3390/w12010102
- Mouele ESM, Tijani JO, Fatoba OO, Petrik LF. Degradation of Organic Pollutants and Microorganisms from Wastewater Using Different Dielectric Barrier Discharge Configurations-A Critical Review. *Environ Sci Pollut Res* (2015) 22:18345–62. doi:10.1007/s11356-015-5386-6
- Hama Aziz KH, Miessner H, Mueller S, Kalass D, Moeller D, Khorshid I, et al. Degradation of Pharmaceutical Diclofenac and Ibuprofen in Aqueous Solution, a Direct Comparison of Ozonation, Photocatalysis, and Non-Thermal Plasma. *Chem Eng J* (2017) 313:1033–41. doi:10.1016/j.cej.2016.10.137
- Lesage O, Falk L, Tatoulian M, Mantovani D, Ognier S. Treatment of 4-Chlorobenzoic Acid by Plasma-Based Advanced Oxidation Processes. *Chem Eng Process Process Intensification* (2013) 72:82–9. doi:10.1016/j.ccep.2013.06.008
- Abdel-Fattah E. Atmospheric Pressure Helium Plasma Jet and its Applications to Methylene Blue Degradation. *J Electrostatics* (2019) 101:103360. doi:10.1016/j.elstat.2019.103360
- Hijosa-Valsero M, Molina R, Monrás A, Müller M, Bayona JM. Decontamination of Waterborne Chemical Pollutants by Using Atmospheric Pressure Nonthermal Plasma: A Review. *Environ Technol Rev* (2014) 3:71–91. doi:10.1080/21622515.2014.990935
- Jiang B, Zheng J, Qiu S, Wu M, Zhang Q, Yan Z, et al. Review on Electrical Discharge Plasma Technology for Wastewater Remediation. *Chem Eng J* (2014) 236:348–68. doi:10.1016/j.cej.2013.09.090

25. Sarangapani C, Dixit Y, Milosavljevic V, Bourke P, Sullivan C, Cullen PJ. Optimization of Atmospheric Air Plasma for Degradation of Organic Dyes in Wastewater. *Water Sci Technol* (2017) 75:207–19. doi:10.2166/wst.2016.471
26. Škoro N, Puač N, Živković S, Krstić-Milošević D, Cvelbar U, Malović G, et al. Destruction of Chemical Warfare Surrogates Using a Portable Atmospheric Pressure Plasma Jet. *Eur Phys J D* (2018) 72:1–8. doi:10.1140/epjd/e2017-80329-9
27. Tomić S, Petrović A, Puač N, Škoro N, Bekić M, Petrović ZL, et al. Plasma-Activated Medium Potentiates the Immunogenicity of Tumor Cell Lysates for Dendritic Cell-Based Cancer Vaccines. *Cancers* (2021) 13:1626–13. doi:10.3390/cancers13071626
28. Fridman A. *Plasma Chemistry*. 1st ed. Cambridge: Cambridge University Press (2008). doi:10.1017/CBO9780511546075
29. Bruggeman P, Brandenburg R. Atmospheric Pressure Discharge Filaments and Microplasmas: Physics, Chemistry and Diagnostics. *J Phys D: Appl Phys* (2013) 46:464001. doi:10.1088/0022-3727/46/46/464001
30. Chen FF. *Introduction to Plasma Physics and Controlled Fusion*. 3rd ed. Cham: Springer International Publishing (2016). doi:10.1007/978-3-319-22309-4
31. Jaiswal AK, Ananthanarasimhan J, Shivapuji AM, Dasappa S, Rao L. Experimental Investigation of a Non-catalytic Cold Plasma Water-Gas Shift Reaction. *J Phys D: Appl Phys* (2020) 53:465205. doi:10.1088/1361-6463/aba92d
32. Puač N, Gherardi M, Shiratani M. Plasma Agriculture: A Rapidly Emerging Field. *Plasma Process Polym* (2018) 15:1700174. doi:10.1002/ppap.201700174
33. Dobsław C, Glocker B. Plasma Technology and its Relevance in Waste Air and Waste Gas Treatment. *Sustainability* (2020) 12:8981–39. doi:10.3390/sul12218981
34. López M, Calvo T, Prieto M, Múgica-Vidal R, Muro-Fraguas I, Alba-Eliás F, et al. A Review on Non-Thermal Atmospheric Plasma for Food Preservation: Mode of Action, Determinants of Effectiveness, and Applications. *Front Microbiol* (2019) 10:622. doi:10.3389/fmicb.2019.00622
35. Bornholdt S, Wolter M, Kersten H. Characterization of an Atmospheric Pressure Plasma Jet for Surface Modification and Thin Film Deposition. *Eur Phys J D* (2010) 60:653–60. doi:10.1140/epjd/e2010-00245-x
36. Sun B, Aye NN, Gao Z, Lv D, Zhu X, Sato M. Characteristics of Gas-Liquid Pulsed Discharge Plasma Reactor and Dye Decoloration Efficiency. *J Environ Sci* (2012) 24:840–5. doi:10.1016/S1001-0742(11)60837-1
37. Tichonovas M, Krugly E, Racys V, Hippler R, Kauneliene V, Stasiulaitiene I, et al. Degradation of Various Textile Dyes as Wastewater Pollutants under Dielectric Barrier Discharge Plasma Treatment. *Chem Eng J* (2013) 229:9–19. doi:10.1016/j.cej.2013.05.095
38. Magureanu M, Piroi D, Mandache NB, David V, Medvedovici A, Bradu C, et al. Degradation of Antibiotics in Water by Non-Thermal Plasma Treatment. *Water Res* (2011) 45:3407–16. doi:10.1016/j.watres.2011.03.057
39. Sarangapani C, Misra NN, Milosavljevic V, Bourke P, O'Regan F, Cullen PJ. Pesticide Degradation in Water Using Atmospheric Air Cold Plasma. *J Water Process Eng* (2016) 9:225–32. doi:10.1016/j.jwpe.2016.01.003
40. Vanraes P, Ghodbane H, Davister D, Wardenier N, Nikiforov A, Verheust YP, et al. Removal of Several Pesticides in a Falling Water Film DBD Reactor with Activated Carbon Textile: Energy Efficiency. *Water Res* (2017) 116:1–12. doi:10.1016/j.watres.2017.03.004
41. Locke BR, Sato M, Sunka P, Hoffmann MR, Chang J-S. Electrohydraulic Discharge and Nonthermal Plasma for Water Treatment. *Ind Eng Chem Res* (2006) 45:882–905. doi:10.1021/ie050981u
42. Bradu C, Kutasi K, Magureanu M, Puač N, Živković S. Reactive Nitrogen Species in Plasma-Activated Water: Generation, Chemistry and Application in Agriculture. *J Phys D: Appl Phys* (2020) 53:223001. doi:10.1088/1361-6463/ab795a
43. Kumar A, Škoro N, Gernjak W, Puač N. Cold Atmospheric Plasma Technology for Removal of Organic Micropollutants from Wastewater-A Review. *Eur Phys J D* (2021) 75:1–26. doi:10.1140/epjd/s10053-021-00283-5
44. Jaiswal S, Aguirre EM. Comparison of Atmospheric Pressure Argon Producing O(1S) and Helium Plasma Jet on Methylene Blue Degradation. *AIP Adv* (2021) 11:045311. doi:10.1063/5.0046948
45. Shutov DA, Bogdanov PV, Pleskunov PL. Destruction of Organic Dyes in Aqueous Solution by Low-Temperature Plasma Jet Treatment. *High Energy Chem* (2016) 50:77–81. doi:10.1134/S0018143915050124
46. Cadorn BM, Tralli VD, Ceriani E, Benetoli LOd. B, Marotta E, Ceretta C, et al. Treatment of Methyl orange by Nitrogen Non-thermal Plasma in a corona Reactor: The Role of Reactive Nitrogen Species. *J Hazard Mater* (2015) 300:754–64. doi:10.1016/j.jhazmat.2015.08.009
47. Moussa D, Doubla A, Kamgang-Youbi G, Brisset J-L. Postdischarge Long Life Reactive Intermediates Involved in the Plasma Chemical Degradation of an Azoic Dye. *IEEE Trans Plasma Sci* (2007) 35:444–53. doi:10.1109/TPS.2007.892578
48. Zhou R, Zhou R, Prasad K, Fang Z, Speight R, Bazaka K, et al. Cold Atmospheric Plasma Activated Water as a Prospective Disinfectant: The Crucial Role of Peroxynitrite. *Green Chem* (2018) 20:5276–84. doi:10.1039/c8gc02800a
49. Liu ZC, Liu DX, Chen C, Li D, Yang AJ, Rong MZ, et al. Physicochemical Processes in the Indirect Interaction between Surface Air Plasma and Deionized Water. *J Phys D: Appl Phys* (2015) 48:495201. doi:10.1088/0022-3727/48/49/495201
50. Piskarev IM, Ivanova IP. Comparison of Chemistry Induced by Direct and Indirect Plasma Treatment of Water to the Effect of UV Radiation. *Plasma Chem Plasma Process* (2021) 41:447–75. doi:10.1007/s11090-020-10127-6
51. Ghodbane H, Hamdaoui O. Decolorization of Antraquinonic Dye, C.I. Acid Blue 25, in Aqueous Solution by Direct UV Irradiation, UV/H<sub>2</sub>O<sub>2</sub> and UV/Fe(II) Processes. *Chem Eng J* (2010) 160:226–31. doi:10.1016/j.cej.2010.03.049
52. Kooh MRR, Dahri MK, Lim L, Hoon LL. Removal of Acid Blue 25 from Aqueous Solution by Using Common Salts and Seawater to Induce the Salting Out Effect. *Sci Bruneiana* (2018) 16:5–11. doi:10.46537/scibru.v16i2.61
53. Routoula E, Patwardhan SV. Degradation of Anthraquinone Dyes from Effluents: A Review Focusing on Enzymatic Dye Degradation with Industrial Potential. *Environ Sci Technol* (2020) 54:647–64. doi:10.1021/acs.est.9b03737
54. Fanchiang J-M, Tseng D-H. Degradation of Anthraquinone Dye C.I. Reactive Blue 19 in Aqueous Solution by Ozonation. *Chemosphere* (2009) 77:214–21. doi:10.1016/j.chemosphere.2009.07.038
55. Lihong H-H, Wangtao Y-T, Wang Y, Wangxia H-X, Sunkai K-K, Lumei Z-M. Bacterial Degradation of Anthraquinone Dyes. *J Zhejiang Univ Sci B* (2019) 20:528–40. doi:10.1631/jzus.B1900165
56. Ghodbane H, Hamdaoui O, Vandamme J, Van Durme J, Vanraes P, Leys C, et al. Degradation of AB25 Dye in Liquid Medium by Atmospheric Pressure Non-Thermal Plasma and Plasma Combination with Photocatalyst TiO<sub>2</sub>. *Open Chem* (2014) 13:325–31. doi:10.1515/chem-2015-0040
57. Ghimire B, Szili EJ, Patenall BL, Lamichhane P, Gaur N, Robson AJ, et al. Enhancement of Hydrogen Peroxide Production from an Atmospheric Pressure Argon Plasma Jet and Implications to the Antibacterial Activity of Plasma Activated Water. *Plasma Sourc Sci. Technol.* (2021) 30:035009. doi:10.1088/1361-6595/abe0c9
58. Barkhordari A, Ganjovi A, Mirzaei I, Falahat A, Rostami Ravari MN. A Pulsed Plasma Jet with the Various Ar/N<sub>2</sub> Mixtures. *J Theor Appl Phys* (2017) 11:301–12. doi:10.1007/s40094-017-0271-y
59. Sremački I, Jurov A, Modic M, Cvelbar U, Wang L, Leys C, et al. On Diagnostics of Annular-Shape Radio-Frequency Plasma Jet Operating in Argon in Atmospheric Conditions. *Plasma Sourc Sci. Technol.* (2020) 29:035027. doi:10.1088/1361-6595/ab71f7
60. Liu J, He B, Chen Q, Li J, Xiong Q, Yue G, et al. Direct Synthesis of Hydrogen Peroxide from Plasma-Water Interactions. *Sci Rep* (2016) 6:1–7. doi:10.1038/srep38454
61. Schiorlin M, Paradisi C, Brandenburg R, Schmidt M, Marotta E, Giardina A, et al. Pollutant Degradation in Gas Streams by Means of Non-Thermal Plasmas. In: *Current Air Quality Issues*. InTechOpen (2015). doi:10.5772/60049
62. Sornskandanuphap J, Suanpoot P, Hong YJ, Ghimire B, Cho G, Uhm HS, et al. Electron Temperature and Density of Non-Thermal Atmospheric Pressure Argon Plasma Jet by Convective Wave Packet Model. *J Korean Phys Soc* (2017) 70:979–89. doi:10.3938/jkps.70.979
63. Hansen L, Schmidt-Bleker A, Bansemer R, Kersten H, Weltmann K-D, Reuter S. Influence of a Liquid Surface on the NO<sub>x</sub> Production of a Cold Atmospheric Pressure Plasma Jet. *J Phys D: Appl Phys* (2018) 51:474002. doi:10.1088/1361-6463/aa66f0

64. Liu Y, Sun D, Askari S, Patel J, Macias-Montero M, Mitra S, et al. Enhanced Dispersion of TiO<sub>2</sub> Nanoparticles in a TiO<sub>2</sub>/PEDOT:PSS Hybrid Nanocomposite via Plasma-Liquid Interactions. *Sci Rep* (2015) 5:1–11. doi:10.1038/srep15765
65. Stancampiano A, Selaković N, Gherardi M, Puač N, Petrović ZL, Colombo V. Characterisation of a Multijet Plasma Device by Means of Mass Spectrometric Detection and iCCD Imaging. *J Phys D: Appl Phys* (2018) 51:484004. doi:10.1088/1361-6463/aae2f2
66. Maletić D, Puač N, Lazović S, Malović G, Gans T, Schulz-Von Der Gathen V, et al. Detection of Atomic Oxygen and Nitrogen Created in a Radio-Frequency-Driven Micro-scale Atmospheric Pressure Plasma Jet Using Mass Spectrometry. *Plasma Phys Control Fusion* (2012) 54:124046. doi:10.1088/0741-3335/54/12/124046
67. Malović G, Puač N, Lazović S, Petrović Z. Mass Analysis of an Atmospheric Pressure Plasma Needle Discharge. *Plasma Sourc Sci. Technol.* (2010) 19: 034014. doi:10.1088/0963-0252/19/3/034014
68. Selaković N. *Mass Spectrometry of Plasma Jet and Application of Electrical Discharges Operating at Atmospheric Pressure in Biomedicine*. PhD Thesis. Beograd: University of Belgrade (2021).
69. Azerrad SP, Kurzbaum E. Chemical Decolorization of Textile Wastewater via Advanced Oxidation Processes: Case Study of Key Parameters with Acid Blue 25. *Water Air Soil Pollut* (2021) 232:1–14. doi:10.1007/s11270-021-04997-5
70. El-Tayeb A, El-Dein AZ, Elnaggar AY, Hussein EE. Influence of Temperature in Degradation of Organic Pollution Using corona Discharge Plasma. *Sustainability* (2021) 13:12971. doi:10.3390/su132312971
71. Vlad I-E, Anghel SD. Time Stability of Water Activated by Different On-Liquid Atmospheric Pressure Plasmas. *J Electrostatics* (2017) 87:284–92. doi:10.1016/j.elstat.2017.06.002
72. Adhikari B, Adhikari M, Ghimire B, Park G, Choi EH. Cold Atmospheric Plasma-Activated Water Irrigation Induces Defense Hormone and Gene Expression in Tomato Seedlings. *Sci Rep* (2019) 9:1–15. doi:10.1038/s41598-019-52646-z
73. Thirumdas R, Kothakota A, Annapure U, Siliveru K, Blundell R, Gatt R, et al. Plasma Activated Water (PAW): Chemistry, Physico-Chemical Properties, Applications in Food and Agriculture. *Trends Food Sci Technol* (2018) 77: 21–31. doi:10.1016/j.tifs.2018.05.007
74. Paetzold P. *Introduction to Chemistry*. Aachen: De Gruyter (2009). doi:10.1515/9783110211351
75. Li J, Zhou Z, Wang H, Li G, Wu Y. Research on Decoloration of Dye Wastewater by Combination of Pulsed Discharge Plasma and TiO<sub>2</sub> Nanoparticles. *Desalination* (2007) 212:123–8. doi:10.1016/j.desal.2006.10.006
76. Tang Q, Jiang W, Zhang Y, Wei W, Lim TM. Degradation of Azo Dye Acid Red 88 by Gas Phase Dielectric Barrier Discharges. *Plasma Chem Plasma Process* (2009) 29:291–305. doi:10.1007/s11090-009-9181-3
77. Jin YS, Cho C, Kim D, Sohn CH, Ha C-S, Han S-T. Mass Production of Plasma Activated Water by an Atmospheric Pressure Plasma. *Jpn J Appl Phys* (2020) 59:SHHF05. doi:10.35848/1347-4065/ab7e13
78. Pawlat J, Terebun P, Kwiatkowski M, Tarabová B, Kovačová Z, Kučerová K, et al. Evaluation of Oxidative Species in Gaseous and Liquid Phase Generated by Mini-Gliding Arc Discharge. *Plasma Chem Plasma Process* (2019) 39: 627–42. doi:10.1007/s11090-019-09974-9
79. Mai-Prochnow A, Zhou R, Zhang T, Ostrikov K, Mugunthan S, Rice SA, et al. Interactions of Plasma-Activated Water with Biofilms: Inactivation, Dispersal Effects and Mechanisms of Action. *npj Biofilms Microbiomes* (2021) 7:1–12. doi:10.1038/s41522-020-00180-6

**Conflict of Interest:** The authors declare that the research was conducted in the absence of any commercial or financial relationships that could be construed as a potential conflict of interest.

**Publisher's Note:** All claims expressed in this article are solely those of the authors and do not necessarily represent those of their affiliated organizations, or those of the publisher, the editors and the reviewers. Any product that may be evaluated in this article, or claim that may be made by its manufacturer, is not guaranteed or endorsed by the publisher.

Copyright © 2022 Kumar, Škoro, Gernjak, Povrenović and Puač. This is an open-access article distributed under the terms of the Creative Commons Attribution License (CC BY). The use, distribution or reproduction in other forums is permitted, provided the original author(s) and the copyright owner(s) are credited and that the original publication in this journal is cited, in accordance with accepted academic practice. No use, distribution or reproduction is permitted which does not comply with these terms.

## Article

# Use of Natural Clinoptilolite in the Preparation of an Efficient Adsorbent for Ciprofloxacin Removal from Aqueous Media

Barbara Kalebić<sup>1</sup>, Jelena Pavlović<sup>2</sup>, Jelena Dikić<sup>2</sup> , Aleksander Rečnik<sup>3</sup>, Sašo Gyergyek<sup>3</sup> , Nikola Škoro<sup>4</sup>   
and Nevenka Rajić<sup>1,\*</sup>

<sup>1</sup> Faculty of Technology and Metallurgy, University of Belgrade, 11120 Belgrade, Serbia; bkalebic@tmf.bg.ac.rs

<sup>2</sup> Innovation Centre of Faculty of Technology and Metallurgy, University of Belgrade, 11120 Belgrade, Serbia; jelena.pavlovic@tmf.bg.ac.rs (J.P.); jdikic@tmf.bg.ac.rs (J.D.)

<sup>3</sup> Jožef Stefan Institute, 1000 Ljubljana, Slovenia; aleksander.recnik@ijs.si (A.R.); saso.gyergyek@ijs.si (S.G.)

<sup>4</sup> Institute of Physics, University of Belgrade, 11080 Belgrade, Serbia; nskoro@ipb.ac.rs

\* Correspondence: nena@tmf.bg.ac.rs

**Abstract:** The adsorption of the antibiotic ciprofloxacin (CIP) from an aqueous solution by natural zeolite, the calcium-rich clinoptilolite (CLI), and magnetite-coated CLI (MAG-CLI) was investigated. Both CLI and MAG-CLI showed a high adsorption affinity towards CIP at 283, 288 and 293 K at a pH of 5. Adsorption kinetics studied for the initial concentrations of 15–75 mg CIP dm<sup>-3</sup> follow Lagergren's pseudo-second order equation and the adsorption is best represented by the Langmuir model. The adsorption mechanism involves strong electrostatic interactions between negatively charged aluminosilicate lattice and the cationic form of CIP accompanied by an ion-exchange reaction. Magnetite coverage (approx. 12 wt.%) induces magnetism, which can facilitate the separation process. The coverage does not influence the adsorption activity of CLI. The leaching test showed that the MAG coating protects the adsorbent from CIP leaching. This is ascribed to interactions between the CIP carboxyl groups and magnetite nano-particles. Antibacterial tests showed strong antibacterial activity of the ciprofloxacin-containing adsorbents towards pathogenic *E. coli* and *S. aureus*.

**Keywords:** natural zeolite; magnetite; ciprofloxacin; adsorption; disinfection



**Citation:** Kalebić, B.; Pavlović, J.; Dikić, J.; Rečnik, A.; Gyergyek, S.; Škoro, N.; Rajić, N. Use of Natural Clinoptilolite in the Preparation of an Efficient Adsorbent for Ciprofloxacin Removal from Aqueous Media. *Minerals* **2021**, *11*, 518. <https://doi.org/10.3390/min11050518>

Academic Editor: Francisco Franco

Received: 5 April 2021

Accepted: 5 May 2021

Published: 14 May 2021

**Publisher's Note:** MDPI stays neutral with regard to jurisdictional claims in published maps and institutional affiliations.



**Copyright:** © 2021 by the authors. Licensee MDPI, Basel, Switzerland. This article is an open access article distributed under the terms and conditions of the Creative Commons Attribution (CC BY) license (<https://creativecommons.org/licenses/by/4.0/>).

## 1. Introduction

In the last few decades, the use of antibiotics has constantly increased in both human and veterinary medicine. Although some countries have established monitoring systems in order to restrict inappropriate use of antibiotics, water pollution by antibiotics is generally poorly regulated. Different types of antibiotics can be found in both surface waters and in drinking water [1]. Due to their structural complexity, antibiotic molecules are usually very stable, exhibiting a long-lived persistence in the environment and therefore pose a risk to the environment and to human health [2]. They are toxic towards algae and other aquatic organisms and their excessive use leads to bacterial resistance [3,4].

Ciprofloxacin (CIP) is one of the most widely applied fluoroquinolone-type antibiotics for treatment of human and animal bacterial infections because it shows excellent activity against both Gram-positive and Gram-negative bacteria. Its extensive use leads to the presence of fluoroquinolone in waters in a wide range of concentrations. Thus, the CIP concentration in wastewater effluents varies from ng to mg dm<sup>-3</sup>. An extremely high concentration of up to 50 mg dm<sup>-3</sup> can be found near drug manufacturing plants [5].

The CIP molecule (Figure 1) has two ionizable groups, amine and carboxyl, with pK<sub>a</sub> = 5.90 ± 0.15 and 8.89 ± 0.11, respectively. Depending on the pH value, CIP can exist as a cation, zwitterion or anion [6,7].

The removal of CIP from wastewater by conventional wastewater treatments, including oxidation [8], ozonation [9], as well as several photocatalytic [10] and biological treatments [11,12], is usually complex, energy-inefficient, and incomplete [13].

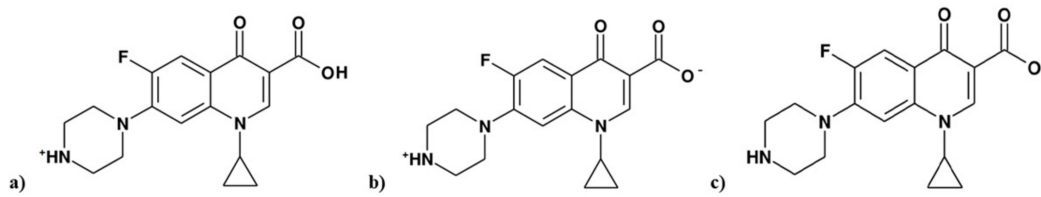


**Figure 1.** The molecular structures of CIP depending on pH: (a) cationic form (in the range 3–6); (b) zwitterionic form (in the range 6–9); and (c) anionic form (in the range 9–12).

Adsorption is generally regarded as a simple method for the removal of different types of pollutants due to its relatively simple design, easy operation and cost effectiveness. Since the operating cost of a treatment based on the adsorption process is greatly dependent on the cost of the adsorbent material and its recyclability, a variety of low-cost adsorbents have been explored, showing adsorption to be superior in comparison to other methods [14–18]. Thus, carbon-based materials [19–22], clay minerals [23], nano-sized metal oxides [5,24], waste biomaterials [25], biochar [26], coal fly ash [27], as well as different zeolites [28–30] have been studied as adsorbents for the removal of antibiotics from wastewater. Removal efficiency of CIP on different adsorbents are listed in Table 1.

**Table 1.** Removal efficiency of ciprofloxacin on different types of adsorbent.

Adsorbent	Experimental Conditions	CIP Removal Efficiency, %	Recyclability	Ref.
Nano-sized magnetite	$C_0 = 33 \text{ mg dm}^{-3}$ Adsorbent dose = $10 \text{ g dm}^{-3}$ pH = 5.97 $t = 24 \text{ h}$	80	* n.r.	[5]
Graphene hydrogel	$C_0 = 50 \text{ mg dm}^{-3}$ $T = 25 \text{ }^\circ\text{C}$ $t \approx 36 \text{ h}$	75	n.r.	[19]
Carbon from date palm leaflets	$C_0 = 100 \text{ mg dm}^{-3}$ Adsorbent dose = $2 \text{ g dm}^{-3}$ pH = 6 $T = 45 \text{ }^\circ\text{C}$ $t = 48 \text{ h}$	56	n.r.	[22]
Halloysite nanotubes	$C_0 = 30 \text{ mg dm}^{-3}$ Adsorbent dose = $1.7 \text{ g dm}^{-3}$ pH = 5–6 $T = 20 \text{ }^\circ\text{C}$ $t = 90 \text{ min}$	95	95% after five cycles	[23]
$\gamma\text{-Al}_2\text{O}_3$ nanoparticles	$C_0 = 20 \text{ mg dm}^{-3}$ Adsorbent dose = $0.775 \text{ g dm}^{-3}$ pH = 7.5 $t = 46.25 \text{ min}$	53	n.r.	[24]
Biomaterials from banyan aerial roots	$C_0 = 60 \text{ mg dm}^{-3}$ Adsorbent dose = $1.2 \text{ g dm}^{-3}$ pH = 8 $T = 25 \text{ }^\circ\text{C}$ $t = 48 \text{ h}$	97	n.r.	[25]
Biochar-montmorillonite	$C_0 = 25 \text{ mg dm}^{-3}$ Adsorbent dose = $1 \text{ g dm}^{-3}$ pH = 5–6 $t = 400 \text{ min}$	86	n.r.	[26]



Table 1. Cont.

Adsorbent	Experimental Conditions	CIP Removal Efficiency, %	Recyclability	Ref.
Coal fly ash	$C_0 = 160 \text{ mg dm}^{-3}$ Adsorbent dose = $40 \text{ g dm}^{-3}$ $T = 40 \text{ }^\circ\text{C}$ $t = 100 \text{ min}$	39	n.r.	[27]
Clinoptilolite	$C_0 = 5 \text{ mg dm}^{-3}$ Adsorbent dose = $2 \text{ g dm}^{-3}$ $\text{pH} = 6$ $T = 25 \text{ }^\circ\text{C}$	99	n.r.	[29]
Synthesized zeolites (A, X, Y)	$C_0 = 150 \text{ mg dm}^{-3}$ Adsorbent dose = $0.5 \text{ g dm}^{-3}$ $\text{pH} = 3$ $T = 20 \text{ }^\circ\text{C}$ $t = 24 \text{ h}$	27–61.4	n.r.	[30]
Commercial zeolites (A, X, Y)	$C_0 = 150 \text{ mg dm}^{-3}$ Adsorbent dose = $0.5 \text{ g dm}^{-3}$ $\text{pH} = 3$ $T = 20 \text{ }^\circ\text{C}$ $t = 24 \text{ h}$	34–87	n.r.	[30]

\* n.r.—not reported.

It should be noted that the data shown in Table 1 are difficult to compare because they are obtained under different experimental conditions. Moreover, for most adsorbents CIP adsorption is an irreversible process.

Natural zeolites have been extensively studied because of their unique ion-exchange, molecular sieving, and adsorption properties. Their worldwide abundance recommends them as available, low-cost materials [31]. Clinoptilolite (CLI) is the most abundant natural zeolite. Its three-dimensional structure consists of two interconnected micropore channels occupied by exchangeable cations and water molecules. CLI can efficiently remove different pollutants from wastewaters, including inorganic toxic ions such as heavy metal cations [32,33], anions [34,35] as well as various organic species such as pesticides, dyes, or pharmaceuticals [36]. The removal efficacy of CLI can be ascribed to its unique structural features as well as to its propensity to be modified without structural changes. Impregnation of CLI with oxide nanoparticles or with biopolymers leads to an increase of its specific surface and adsorption performance [37–43].

Generally, the literature data on the adsorption of organic pollutants by zeolites are relatively scarce which can be ascribed to the fact that most zeolites are hydrophilic. Hydrophobicity of zeolites increases by the increase of the Si/Al ratio. However, it should be noted that CLI has been the most studied natural zeolite adsorbent not only for inorganic but also for organic pollutants [6]. Its adsorptive effectiveness towards specific pollutants varies because the Si/Al molar ratio and elemental composition of CLI from different regions differ. Among synthetic zeolites, the zeolite Y was reported to be an efficient antibiotic adsorbent [44]. However, the adsorption was found to be irreversible, so the reuse of the spent adsorbent is questionable.

The aim of this research was to study: (1) the adsorptive efficacy of natural clinoptilolite (CLI) for CIP removal at different temperatures and for different initial CIP concentrations, (2) adsorption kinetics and mechanisms, (3) impregnation of CLI with magnetite nanoparticles (MAG-CLI) to allow a facile adsorbent separation, and (4) antibacterial activity of the CIP-containing CLI.

CLI was used for the CIP removal because an extensive study conducted in the last decade showed that clinoptilolite-rich tuffs from Serbia can be perspective adsorbents for the removal of various toxic species [32,33].

## 2. Materials and Methods

### 2.1. Materials

The clinoptilolite-rich zeolitic tuff obtained from the Serbian deposit in Slanci (near the capital city of Belgrade) was used as a starting material. Rietveld analysis [45] showed that CLI was the major mineral phase (>80 wt.%), with quartz (<7.5 wt.%) and feldspar (<13 wt.%) the major satellite phases. The cation exchange capacity (CEC), measured by standard procedure [46], was 162.2 mmol M<sup>+</sup>/100 g.

Prior to the experiments, the sample was sieved, washed with deionized water to remove impurities, and then dried in an oven at 105 °C overnight to a constant mass. The particle size used in the experiments was in the range of 0.063–0.125 mm since previous studies showed the best adsorptive performance was in particles in that size range [32,33].

All chemicals used were of analytical grade. All the experiments were carried out under controlled conditions. The experiments were performed in a thermostated bath where the temperature was maintained constant to within  $\pm 0.1$  °C; the CLI samples were weighed to a four-digit accuracy, and the solution concentrations were determined with a four-digit accuracy. In all experiments, deionized water was used.

### 2.2. Preparation of Magnetite

The magnetite nanoparticles were synthesized per the literature procedure [5,47]. Briefly, FeCl<sub>3</sub>·6H<sub>2</sub>O and FeCl<sub>2</sub>·4H<sub>2</sub>O were dissolved in degassed distilled water under N<sub>2</sub> in a molar ratio of 2:1. A solution of ammonia was then added dropwise to the prepared Fe(II) and Fe(III) solution, increasing the pH to 10. A black solid that precipitated was magnetically separated and washed with distilled water until a negative reaction to chloride ions.

### 2.3. Preparation of Magnetite-Coated Clinoptilolite (MAG-CLI)

Conversion of CLI to MAG-CLI was carried out following a slightly modified method as described by Mohseni-Bandpi [48]. Briefly, 10 g of CLI were suspended in 120 cm<sup>3</sup> of deionized water and stirred under the N<sub>2</sub> atmosphere at 350 rpm for about 10 min. Then, a solution, which contained FeCl<sub>3</sub>·6H<sub>2</sub>O and FeSO<sub>4</sub>·7H<sub>2</sub>O in a molar ratio of 2:1, was added to the CLI suspension under stirring. The pH of the suspension was adjusted to pH ~10 by the dropwise addition of a water solution of NH<sub>4</sub>OH (25 wt.%), followed by a vigorous stirring in a water bath at ~80 °C under N<sub>2</sub> for 1 h. The resulting black precipitate was separated from the suspension by centrifugation and washed several times with deionized water until a negative reaction to chloride ions. Finally, the obtained MAG-CLI was left to dry at 80 °C overnight until constant mass.

### 2.4. Characterization

#### 2.4.1. Powder X-ray Diffraction Analysis (PXRD)

Analysis of the mineral phases present in the samples was done via the powder X-ray diffraction method (PXRD). PXRD patterns were obtained using a Rigaku SmartLab powder diffractometer (Rigaku, Tokyo, Japan), with CuK $\alpha$  ( $\lambda = 1.54178$  Å) radiation at 40 kV and 30 mA and Bragg-Brentano focusing geometry. The samples were scanned in the  $2\theta$  range from 5° to 65°, with 0.01° step and a scan rate of 5° min<sup>-1</sup>.

#### 2.4.2. Energy Dispersive X-ray Spectroscopy (EDS)

Elemental compositions of CLI and MAG-CLI were obtained by a Carl Zeiss Supra<sup>TM</sup> 3VP (Zeiss, Jena, Germany) field-emission gun scanning electron microscope (FEG-SEM) equipped with an EDS detector (Oxford Analysis) with the INCA Energy system for quantification of elements. Before analysis, the samples were coated with gold.

#### 2.4.3. Thermal Analysis

Thermal behavior was examined by simultaneous thermogravimetric (TGA) and differential thermal analysis (DTA) using a SDT Q-600 instrument (TA Instruments, New

Castle, DE, USA). The samples were heated in standard alumina sample cups (90  $\mu\text{L}$ ) from room temperature to 800  $^{\circ}\text{C}$  at a heating rate of 10  $^{\circ}\text{C min}^{-1}$  under synthetic air with a flow rate of 100  $\text{cm}^3 \text{min}^{-1}$ .

#### 2.4.4. Textural Properties

The specific surface area and porosity characteristics were determined by the  $\text{N}_2$  adsorption at  $-196^{\circ}\text{C}$  using a Micromeritics ASAP 2020 instrument (Micromeritics, Norcross, GA, USA). Prior to the measurements, the samples were degassed in a vacuum at 423 K for 10 h. The specific surface area of samples was calculated using the Brunauer-Emmett-Teller (BET) method from the linear part of the  $\text{N}_2$  adsorption isotherm. The total pore volume ( $V_{\text{tot}}$ ) was determined from the desorption isotherm at  $p/p_0 = 0.998$ , and the volume of mesopores was calculated by the Barrett-Joyner-Halenda (BJH) method from the desorption isotherms. The average maximum pore diameter ( $D_{\text{max}}$ ) was determined from the BJH desorption analysis.

#### 2.4.5. TEM Analysis

TEM analysis was carried out at 200 kV using a transmission electron microscope (JEM-2100, JEOL Ltd., Tokyo, Japan) equipped with an ultra-high-resolution objective lens pole piece with a point-to-point resolution of 0.19 nm. The samples were crushed in an agate mortar, dispersed in absolute ethanol, and a fine fraction of the suspension was deposited on Cu holey carbon-coated grids. To determine the average size of magnetite particles, their diameters were measured from the obtained TEM images. Due to the relatively small size of the magnetite nanoparticles, the selected area electron diffraction (SAED) was performed over multiple nanocrystals to obtain the characteristic diffraction rings with the structure-specific  $d$ -values.

#### 2.4.6. FTIR Analysis

The Fourier transform infrared spectroscopy (FTIR) analysis was performed using a Digilab FTS-80 interferometer (Bio-Rad, Cambridge, MA, USA). The spectra were recorded in the range of 400 to 4000  $\text{cm}^{-1}$ , at a resolution of 4  $\text{cm}^{-1}$  and 100 scans.

#### 2.4.7. Zeta Potential Measurement

The zeta potentials were measured using a Zetasizer Nano ZS90 (Malvern Instruments Ltd., Malvern, UK) according to the method described by Gulicovski [49]. Briefly, the sample (0.1 g) was suspended in 50  $\text{cm}^3$  of deionized water and left at room temperature overnight. The pH value of the suspension was then adjusted in the range of 2–12 using 0.1  $\text{mol dm}^{-3}$  HCl or NaOH. Before measurement, the suspensions were ultrasonically treated for 20 s. The pH values were measured using a Mettler Toledo (Columbus, OH, USA) digital pH meter.

#### 2.4.8. Magnetic Measurements

Magnetic properties were measured using a vibrating sample magnetometer LakeShore 7400 Series VSM (LakeShore, Westerville, OH, USA) at the room temperature and with an applied magnetic field strength of 1.53 T.

### 2.5. CIP Adsorption Experiments

CIP adsorption experiments were performed at 283, 288 and 293 K by the batch method using 0.2 g of CLI or MAG-CLI in 50  $\text{cm}^3$  of the chosen CIP concentration (15, 25, 50 or 75  $\text{mg dm}^{-3}$ ). The adsorption experiments were carried out at a pH of 5, which previous studies showed had the best CIP removal efficacy (vide infra). The pH adjustment was performed using HCl or NaOH solutions (0.1  $\text{mol dm}^{-3}$ ). The suspensions were left shaking (100 rpm) in a thermostated water bath (Memmert, WBE 22) at the chosen temperature for 5 to 60 min. The solid was separated by centrifugation and then filtered through a 0.22  $\mu\text{m}$  nylon filter. The CIP concentration was measured in the filtrate by

standard procedure using a UV-Vis spectrometer, Perkin Elmer Lambda 365 (Perkin Elmer Inc., Waltham, MA, USA) at 278 nm [50]. The amount of the adsorbed CIP per unit of the adsorbent after time  $t$  ( $q_t$ ) was calculated using the following formula:

$$q_e = (C_0 - C_e) \cdot V / m \quad (1)$$

### 2.6. Leaching Test

Zero point two grams of the spent CLI or MAG-CLI, containing about 21 mg CIP per gram of the adsorbent (CLI or MAG-CLI), were suspended in 50 cm<sup>3</sup> of 0.1 mol dm<sup>-3</sup> NaCl and left for 24 h in a thermostated water bath at 25 °C. After filtration, the CIP content in the filtrate was determined by UV-Vis. The desorbed amount of CIP was calculated as the ratio of the CIP amount in the solution and on the adsorbent.

The concentration of exchangeable cations (K<sup>+</sup>, Mg<sup>2+</sup> and Ca<sup>2+</sup>) in filtrates after the CIP adsorption was measured using an atomic absorption spectrophotometer, Varian SpectrAA 55B (SpectraLab Inc., Markham, ON, Canada).

### 2.7. Antibacterial Activity Test

The antibacterial activity of CIP and of the spent adsorbents (CLI-CIP and MAG-CLI-CIP) was tested towards the Gram-negative bacterium *Escherichia coli* strain DSM 498 and the Gram-positive bacterium *Staphylococcus aureus* strain ATCC 25923. Bacteria were pre-grown on a nutrient agar (NA, Torlak, Serbia) for 16 h at 37 ± 0.1 °C to obtain cultures in the log phase of growth. Prior to the experiments, the samples were sterilized by UV light for 30 min.

The disk diffusion method was used for a qualitative assessment of antibacterial activity. The biomass of each bacterial strain was separately suspended in a sterile physiological solution to achieve the bacterial concentration of about 10<sup>9</sup> CFU cm<sup>-3</sup> (colony forming units) and then inoculated onto NA with a sterile swab. Antibacterial activity was tested as follows: 0.01 cm<sup>3</sup> of suspensions containing 5, 10 or 20 mg of CIP, CLI-CIP, or MAG-CLI-CIP per cm<sup>3</sup> in a sterile phosphate buffer solution (pH = 7.02) was dropped onto the bacteria inoculated NA and the plates were incubated for 24 h at 37 °C. The results were reported as the presence or absence of the inhibition zone.

## 3. Results and Discussion

### 3.1. Powder X-ray Diffraction (PXRD)

The PXRD pattern (Figure 2) showed that CLI was the main mineral phase, displaying diffractions at  $2\theta = 9.79^\circ, 11.16^\circ, 13.06^\circ, 16.89^\circ, 19.00^\circ, 22.31^\circ, 25.01^\circ, 25.98^\circ, 29.90^\circ, 31.84^\circ$  and  $32.68^\circ$  [51]. Diffractions at  $2\theta = 26.6^\circ$  and  $27.1^\circ$  corresponded to quartz and feldspar, respectively [38,51]. The PXRD pattern of MAG-CLI showed that the modification of CLI to MAG-CLI did not significantly affect the CLI crystallinity. New diffraction peaks that appeared in the pattern of MAG-CLI at  $2\theta = 35.64^\circ, 43.23^\circ$  and  $62.96^\circ$  suggest the presence of magnetite Fe<sub>3</sub>O<sub>4</sub> [52,53]. According to the EDS analysis (vide infra), the content of magnetite is 12.2 wt.%.

### 3.2. Energy Dispersive X-ray Spectroscopy (EDS)

The average chemical compositions of CLI and MAG-CLI obtained by the EDS analysis are listed in Table 2. It is evident that the zeolite phase consisted of the calcium-rich clinoptilolite with a Si/Al molar ratio of 5.03. The Si/Al molar ratio increased to 6.12 during modification to MAG-CLI, suggesting a partial dealumination. Moreover, the content of exchangeable cations (Ca and K) decreased in MAG-CLI, whereas the content of Fe increased. Since the content increase of Fe is significantly higher than the content decrease of exchangeable cations, it can be concluded that the modification of CLI to MAG-CLI proceeds not only through an ion exchange but also through precipitation of the Fe species on the CLI surface.

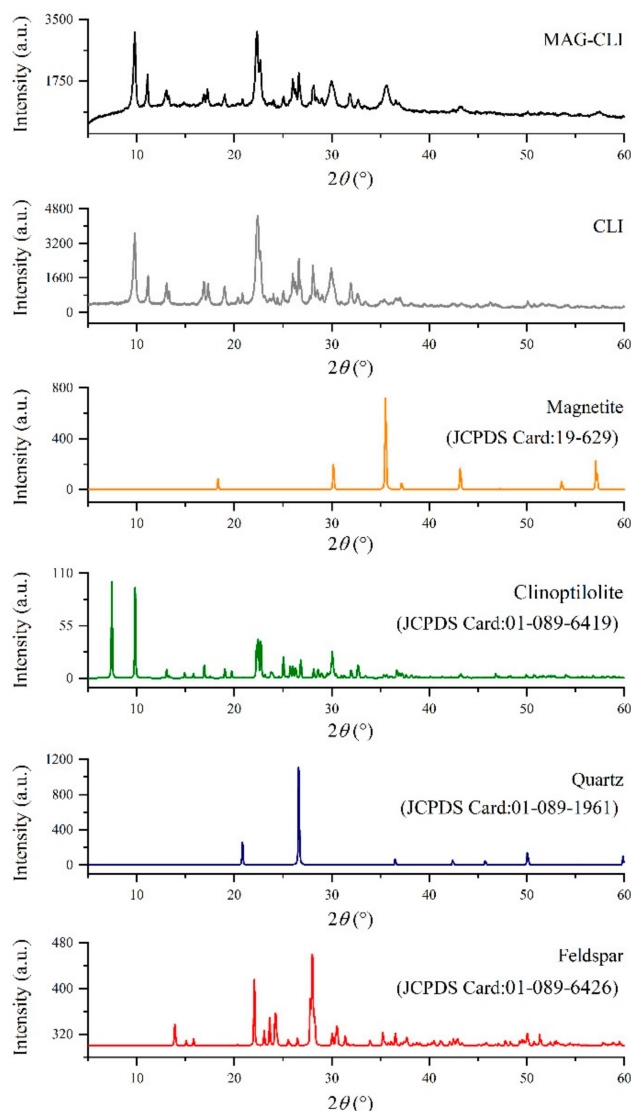


**Figure 2.** PXRD patterns of CLI and MAG-CLI.

**Table 2.** The average chemical composition of the CLI phase of CLI and MAG-CLI obtained by EDS analysis.

Sample	Si	Al	O	K	Ca	Fe	Si/Al
	at.%						
CLI	18.35	3.65	75.97	0.44	1.20	0.40	5.03
MAG-CLI	18.39	3.01	72.15	0.27	0.18	5.63	6.12

### 3.3. Thermogravimetric Analysis (TGA)

The thermograms of CLI and MAG-CLI (Figure 3) show that the TG curves of both samples display similar continual weight loss up to 300 °C. At higher temperatures, the weight loss of MAG-CLI differed from that of CLI. CLI lost weight continuously up to 800 °C, whereas the weight loss of MAG-CLI took place in two stages (300–500 °C and 500–800 °C). The total weight losses were similar (wt. %: 14.2—CLI and 13.1—MAG-CLI). The weight losses are accompanied by the following DTG events: (a) weak DTG maxima at 58, 160 and 600 °C on the DTG curve of CLI, suggesting a release of water molecules from different crystallographic sites in the aluminosilicate lattice, and (b) a strong maximum at 470 °C on the DTG curve of MAG-CLI, indicating a conversion of magnetite to maghemite ( $\gamma$ -Fe<sub>2</sub>O<sub>3</sub>) [54].

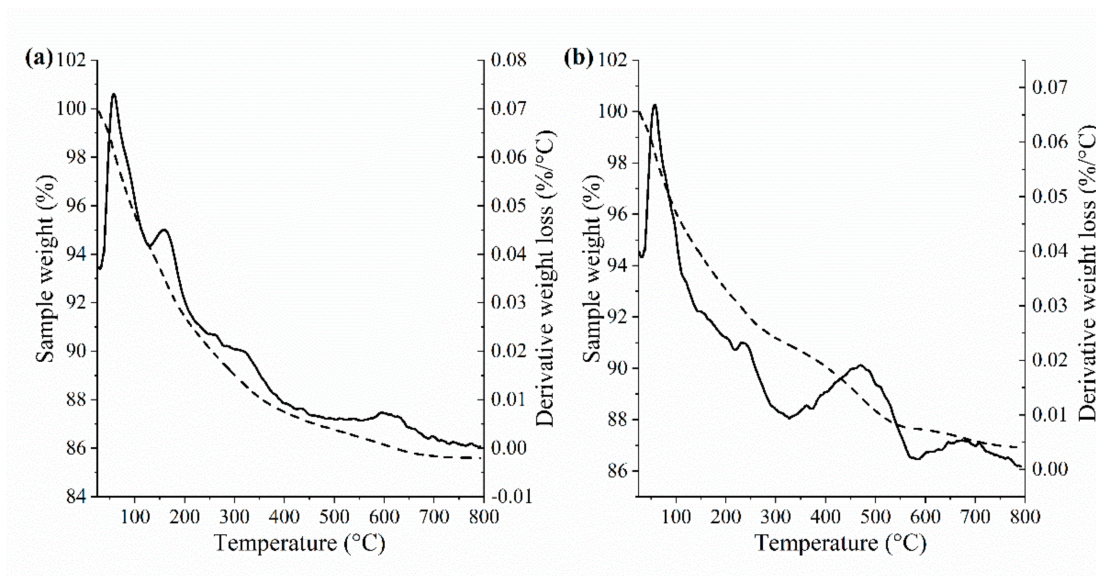


**Figure 3.** TG (dash) and DTG (solid) curves of CLI (a) and MAG-CLI (b).

### 3.4. TEM Analysis

Figure 4 gives the TEM image of MAG-CLI. For comparison, the image of pure magnetite (MAG) is given in Figure 4a. The magnetite particles are in the range of 5–30 nm, with few particles exceeding 100 nm. The selected area electron diffraction (SAED) pattern displays rings typical for the spinel (magnetite) structure, with the most intense ring of the {311} reflections in randomly oriented nanocrystals. MAG shows characteristic octahedral morphology with many crystals connected by the {111} spinel-twin law that forms through self-assembly [55]. On the TEM image of MAG-CLI (Figure 4b) an abundant coverage of the CLI plates by rounded magnetite nanocrystals with highly degraded morphology is evident. The SAED pattern shows interrupted ring patterns that are indicative of nanocrystal ordering. The intensity peaks with a six-fold symmetry, which can be seen for the {111} and {311} magnetite reflections [56,57].

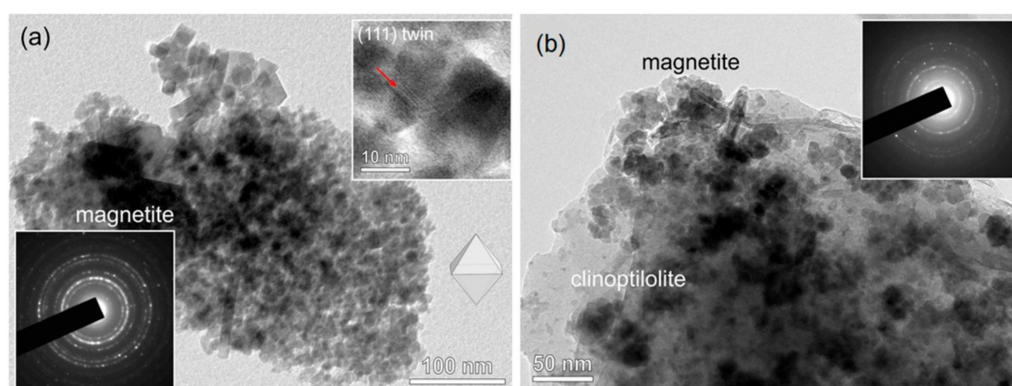


**Figure 4.** TEM image with SAED pattern of pure MAG (a) and MAG-CLI (b) samples.

### 3.5. FTIR Analysis

Figure 5 shows the FTIR spectra of the synthesized samples. The MAG spectrum displays characteristic vibration bands of the Fe–O stretching at about  $570\text{ cm}^{-1}$  [47]. The bands overlap with the vibration of the (Al, Si) $\text{O}_4$  tetrahedral units of the aluminosilicate lattice [58]. On the spectra of CLI and MAG-CLI, the stretching vibrations of the OH groups of water molecules ( $1590\text{--}1670$  and  $3400\text{--}3700\text{ cm}^{-1}$ ) and of the (Al, Si) $\text{O}_4$  tetrahedral units ( $1050\text{--}1250\text{ cm}^{-1}$ ) are evident, confirming that the modification of CLI into MAG-CLI did not influence the zeolite aluminosilicate lattice.

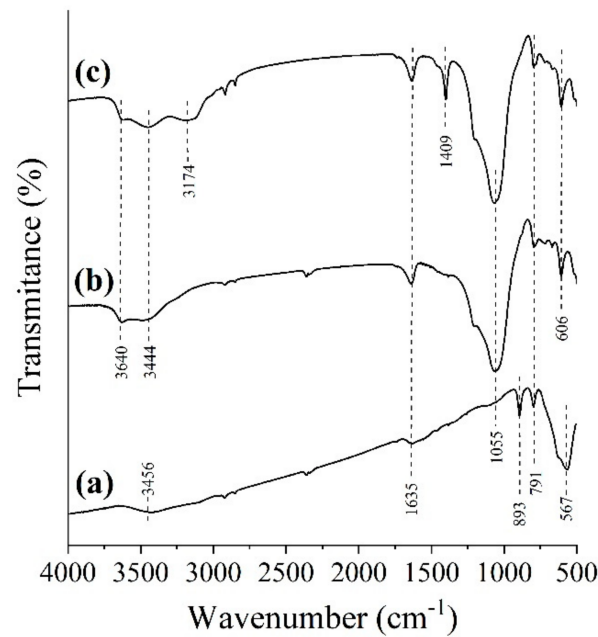


**Figure 5.** FTIR spectra of MAG (a), CLI (b) and MAG-CLI (c).

### 3.6. Zeta Potential Measurements

The graphs of the zeta potential as a function of pH (Figure 6) show that the zeta potential of CLI changed by the modification to MAG-CLI, although both CLI and MAG-CLI have a negatively charged surface in a wide pH range from 2 to 12. For MAG-CLI, the point of zero charge (PZC) was at a pH of ~2, which is in accordance with the literature data [59]. The effect of pH on the CIP removal efficiency is presented in Figure 7. The removal efficiency decreased in alkaline media, which is in accord with the fact that both CIP and the surfaces of CLI and MAG-CLI are negatively charged. In acidic media, the CIP is positively charged ( $CIP^+$ ) and the attractive forces between  $CIP^+$  and CLI/MAG-CLI favor adsorption. The highest removal efficiency is at pH = 5.

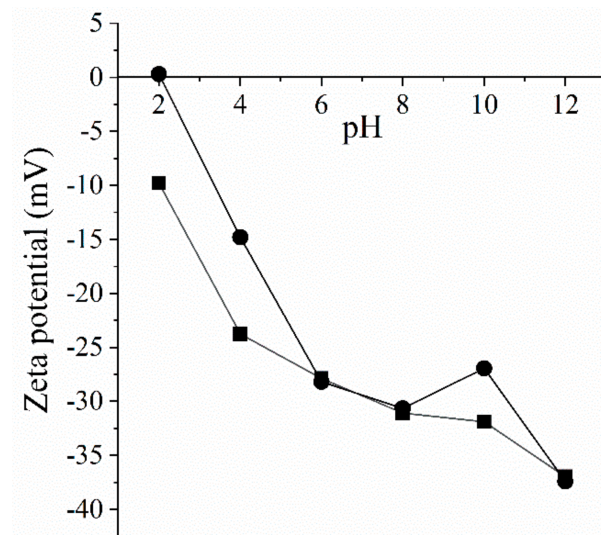


**Figure 6.** Zeta potential measurements as a function of pH for CLI (square) and MAG-CLI (circle).

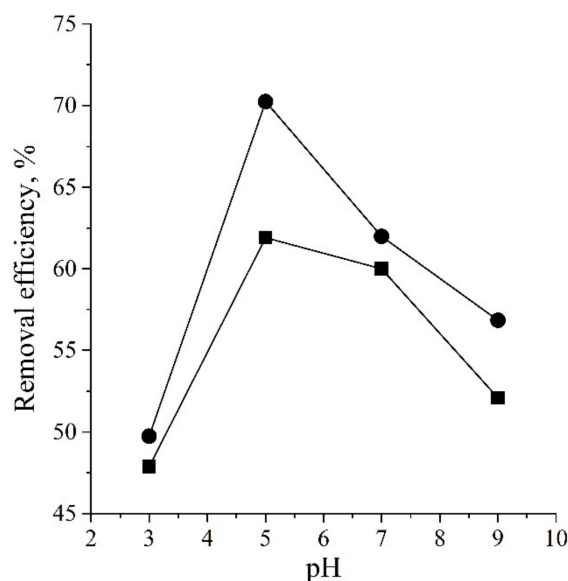


**Figure 7.** The influence of pH in the CIP adsorption on CLI (squares) and MAG-CLI (circles);  $C_0 = 50 \text{ mg dm}^{-3}$ , adsorption time = 60 min, adsorbent dose =  $4 \text{ g dm}^{-3}$  and  $T = 293 \text{ K}$ .

Similar results were found for metal oxides, clays, and a graphene oxide composite [5,24,60,61].

### 3.7. Textural Analysis

Table 3 presents the textural parameters of CLI and MAG-CLI, which show that textural properties changed during conversion. The specific surface area ( $S_{\text{BET}}$ ) of MAG-CLI is two times larger than that of CLI and so is the total pore volume ( $V_{\text{tot}}$ ). The pore size diameter ( $D_{\text{max}}$ ) of MAG-CLI is smaller than in CLI, which could be explained by two phenomena: (1) the formation of a second layer at the CLI surface consisting of magnetite nanoparticles [39,40], and (2) a partial blockage of the CLI pore system caused by the formation of MAG particles.

**Table 3.** Textural properties of CLI and MAG-CLI.

Sample	$S_{\text{BET}}$ ( $\text{m}^2 \text{ g}^{-1}$ )	$V_{\text{tot}}$ ( $\text{cm}^3 \text{ g}^{-1}$ )	$D_{\text{max}}$ (nm)
CLI	23.57	0.0988	16.26
MAG-CLI	45.17	0.1531	3.50

$S_{\text{BET}}$ —specific surface area,  $\text{m}^2 \text{ g}^{-1}$ ;  $V_{\text{tot}}$ —total pore volume,  $\text{cm}^3 \text{ g}^{-1}$ ;  $D_{\text{max}}$ —average maximum pore diameter, nm.

### 3.8. Magnetic Measurements

The magnetic properties of MAG-CLI were also studied and compared with those of MAG. The magnetization curves are presented in Figure 8a. Both MAG and MAG-CLI showed similar magnetic behavior with the saturation magnetization values of  $49.57$  and  $8.93 \text{ emu g}^{-1}$  within magnetic field lower than  $1.5 \text{ T}$ , respectively. The lower saturation magnetization value of MAG-CLI is the result of MAG precipitation on the CLI surface. However, this value indicates that MAG-CLI possesses magnetic properties since CLI itself does not exhibit magnetism (not shown). Furthermore, the magnetization loops showed an absence of hysteresis, which is a characteristic of the superparamagnetic behavior of some nanoparticles [53]. It is worth noting that MAG-CLI retains magnetic properties after the CIP adsorption (Figure 8b), suggesting that the magnetic separation of the spent MAG-CLI from water media is possible.



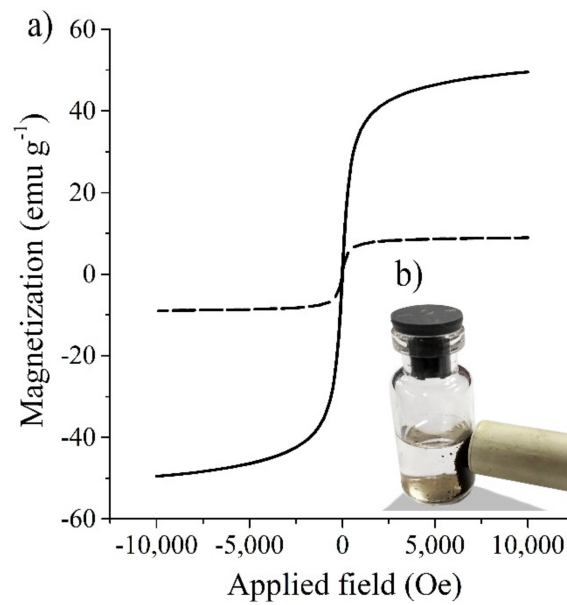


**Figure 8.** The (a) magnetization curve of MAG (solid) and MAG-CLI (dash), and (b) magnetic separation of the spent MAG-CLI from suspension.

### 3.9. Adsorption Isotherm Study

Adsorption of CIP on both CLI and MAG-CLI was studied at 283, 288 and 293 K for the initial CIP concentrations of 15, 25, 50 and 75 mg dm<sup>-3</sup> and at a pH of 5. The solid to liquid ratio was 1:250, which the experiments had shown to be optimal (Figure 9).

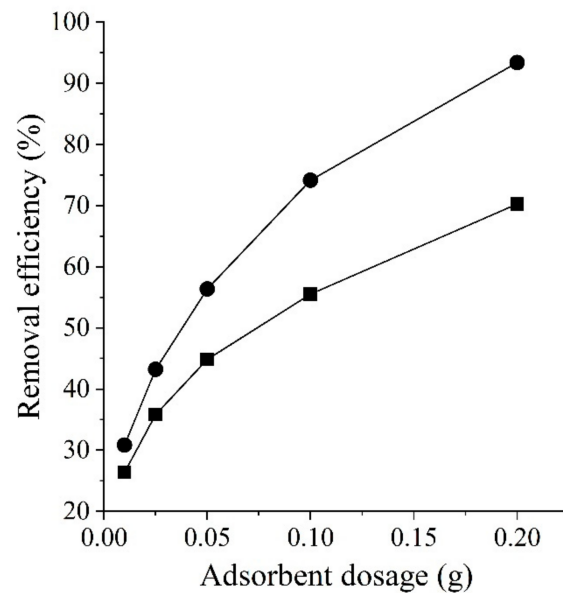


**Figure 9.** CIP removal as a function of CLI (square) and MAG-CLI (circle) dose ( $C_0 = 50$  mg dm<sup>-3</sup>, adsorption time = 60 min,  $T = 298$  K and pH = 5).

The adsorption capacity of both CLI and MAG-CLI increased with the initial CIP concentration at all studied temperatures (Figure 10). At 293 K, the adsorption of CIP onto CLI increased from 4.39 mg CIP g<sup>-1</sup> (for  $C_0 = 15$  mg CIP dm<sup>-3</sup>) to 12.52 mg CIP g<sup>-1</sup> (for  $C_0 = 75$  mg CIP dm<sup>-3</sup>). Similar increases were observed for MAG-CLI: 4.26 mg CIP g<sup>-1</sup> (for  $C_0 = 15$  mg CIP dm<sup>-3</sup>) to 12.59 mg CIP g<sup>-1</sup> (for  $C_0 = 75$  mg CIP dm<sup>-3</sup>), suggesting that the MAG cover did not influence the CIP adsorption.

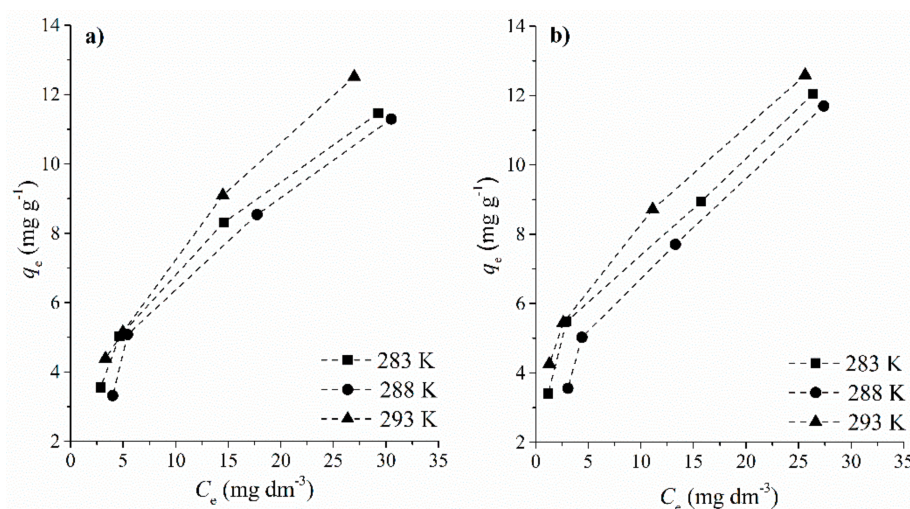


**Figure 10.** The adsorption isotherms for CIP on CLI (a) and MAG-CLI (b);  $q_e$  is the amount of the adsorbed CIP (mg per 1 g of CLI or MAG-CLI) and  $C_e$  is the CIP solution concentration at equilibrium.

The adsorption equilibrium data given in Figure 10 were analyzed by widely applied empirical adsorption isotherm models [17,62]. Among the two-parameter models, only the Langmuir and Freundlich isotherm models gave acceptable fits.

The Langmuir model [63] is represented as:

$$q_e = (q_{\max} \cdot b_L \cdot C_e) / (1 + b_L \cdot C_e) \quad (2)$$

where  $C_e$  is the equilibrium concentration of CIP ( $\text{mg dm}^{-3}$ ),  $q_e$  is the equilibrium concentration of the adsorbed CIP ( $\text{mg g}^{-1}$ ), while  $q_{\max}$  ( $\text{mg g}^{-1}$ ) and  $b_L$  ( $\text{dm}^3 \text{mg}^{-1}$ ) are Langmuir constants ( $q_{\max}$  corresponding to the maximum achievable uptake by the system, and  $b_L$  is related to the affinity between CIP and CLI or MAG-CLI).

The Freundlich isotherm model is described with the following equation:

$$q_e = K_f \cdot C_e^{1/n} \quad (3)$$

where  $C_e$  is the equilibrium concentration of CIP ( $\text{mg dm}^{-3}$ ),  $q_e$  is the equilibrium concentration of the adsorbed CIP ( $\text{mg g}^{-1}$ ),  $K_f$  is the Freundlich isotherm constant ( $\text{mg g}^{-1}$ ) and  $n$  is a parameter related to the adsorption intensity.

The results are listed in Table 4. As can be seen from the obtained values of the linear regression correlation coefficients ( $R^2$ ), the Langmuir model gave a slightly better description for the CIP adsorption on both CLI and MAG-CLI. The maximum calculated capacities were  $17.30 \text{ mg CIP g}^{-1}$  (at 293 K) and  $15.86 \text{ mg CIP g}^{-1}$  (at 288 K) for CLI and MAG-CLI, respectively. Considering the assumptions of the Langmuir model [63], it could be concluded that one active site at the surface of MAG-CLI is occupied by only one CIP species and that the CIP removal from the water solution proceeds as a monolayer adsorption. Furthermore, the Langmuir separation factor  $R_L$  (results not shown) was in the range of 0–1, indicating that the adsorption is a favorable process.

#### Adsorption Mechanism

The obtained results indicate a strong affinity of both CLI and MAG-CLI towards CIP, which could be explained by electrostatic interactions between the positively charged CIP and negatively charged CLI and MAG-CLI surface. Moreover, the measurements of concentration of exchangeable cations in the filtrate after the CIP adsorption (Table 5) showed that  $\text{K}^+$ ,  $\text{Mg}^{2+}$ , and  $\text{Ca}^{2+}$  are present in the filtrate, suggesting that ion exchange reactions occur during adsorption. Since dimensions of the CIP molecule ( $1.35 \times 0.3 \times 0.74 \text{ nm}$ ) [64] exceed the size of the pore openings in the CIP lattice (0.4 nm), the ion exchange likely

takes place only at the surface of the adsorbent. Ion exchange was also proposed as the main adsorption mechanism for the CIP adsorption by montmorillonite [30].

**Table 4.** The parameters obtained by the adsorption isotherm Equations (2) and (3) for the adsorption of CIP on CLI and MAG-CLI;  $R^2$  is the correlation coefficient.

CLI						
T, K	Langmuir Isotherm			Freundlich Isotherm		
	$q_{max}, \text{mg g}^{-1}$	$b_L, \text{dm}^3 \text{mg}^{-1}$	$R^2$	$K_f, \text{mg g}^{-1} (\text{dm}^3 \text{mg}^{-1})^{1/n}$	$n$	$R^2$
283	14.96	0.1028	0.9944	2.24	2.05	0.9924
288	16.31	0.0697	0.9877	1.73	1.80	0.9804
293	17.30	0.0893	0.9909	2.34	1.97	0.9993
MAG-CLI						
T, K	Langmuir Isotherm			Freundlich Isotherm		
	$q_{max}, \text{mg g}^{-1}$	$b_L, \text{dm}^3 \text{mg}^{-1}$	$R^2$	$K_f, \text{mg g}^{-1} (\text{dm}^3 \text{mg}^{-1})^{1/n}$	$n$	$R^2$
283	13.27	0.2235	0.9834	3.34	2.62	0.9831
288	15.86	0.0914	0.9827	2.16	1.97	0.9809
293	14.25	0.2263	0.9870	3.85	2.81	0.9981

$q_{max}$ —maximum adsorption capacity,  $\text{mg g}^{-1}$ ;  $b_L$ —Langmuir constant,  $\text{dm}^3 \text{mg}^{-1}$ ;  $K_f$ —Freundlich constant,  $\text{mg g}^{-1} (\text{dm}^3 \text{mg}^{-1})^{1/n}$ ;  $n$ —adsorption intensity.

**Table 5.** The concentration of exchangeable cations in filtrates after the CIP adsorption on CLI and MAG-CLI.

Sample	Cations		
	$\text{K}^+$	$\text{Mg}^{2+}$	$\text{Ca}^{2+}$
	$\text{mg dm}^{-3}$		
CLI	0.9325	1.2513	4.2280
MAG-CLI	0.6796	0.3823	2.1890

### 3.10. Kinetic Analysis

The CIP adsorption dependence on time was investigated at 283, 288 and 293 K for solutions with  $C_0 = 15, 25, 50$  and  $75 \text{ mg CIP dm}^{-3}$ . Figures 11 and 12 show the CIP uptake from water solution for CLI and MAG-CLI, respectively.

For both CLI and MAG-CLI, the CIP uptake increases rather sharply in the first 10 min, as is evident for all studied temperatures and initial concentrations. Later, the adsorption occurs more slowly. More than 80% of the maximum adsorption capacity was achieved within the first 10 min, indicating fast adsorption kinetics.

The data from Figures 11 and 12 were analyzed using two reaction-based kinetic models and a diffusion-based model. The first model is given by the Lagergren’s first-order rate equation [63]:

$$dq_t/dt = k_1 (q_e - q_t) \tag{4}$$

where  $q_e$  ( $\text{mg g}^{-1}$ ) is the adsorption capacity at equilibrium and  $k_1$  ( $\text{min}^{-1}$ ) is the first-order kinetic rate constant. By integrating the Equation (4) using the boundary conditions  $t = 0$  to  $t = t$  as well as  $q_t = 0$  ( $t = 0$ ) and  $q_t = q_e$  ( $t = t$ ), the following expression is obtained:

$$\log(q_e - q_t) = \log q_e - (k_1/2.303) t \tag{5}$$

The plot of  $\log(q_e - q_t)$  vs.  $t$  is a straight line if the experimental data follow this kinetic model.

The second reaction-based model that was applied is described by the pseudo-second order rate equation [65]:

$$dq_t/dt = k_2 (q_e - q_t)^2 \tag{6}$$

Here  $k_2$  ( $\text{g mg}^{-1} \text{min}^{-1}$ ) is the rate constant of the pseudo-second order adsorption. Integration between the same limits as above gives the following expression:

$$t/q_t = 1/(k_2 q_e^2) + (1/q_e) t \quad (7)$$

The plot of  $t/q_t$  vs.  $t$  is a straight line if the experimental data conform to this kinetic model and the values of  $q_e$  and  $k_2$  are obtained from the slope and intercept of the plot, respectively.

The influence of diffusion in the CIP adsorption was analyzed by the Weber–Morris mass transfer model [28,58]. The following equation defined this model:

$$q_t = K_{id} t^{1/2} + I \quad (8)$$

where  $K_{id}$  ( $\text{mg g}^{-1} \text{min}^{-1/2}$ ) is the intra-particle diffusion rate constant and  $I$  ( $\text{mg g}^{-1}$ ) is the parameter related to the thickness of the boundary layer.

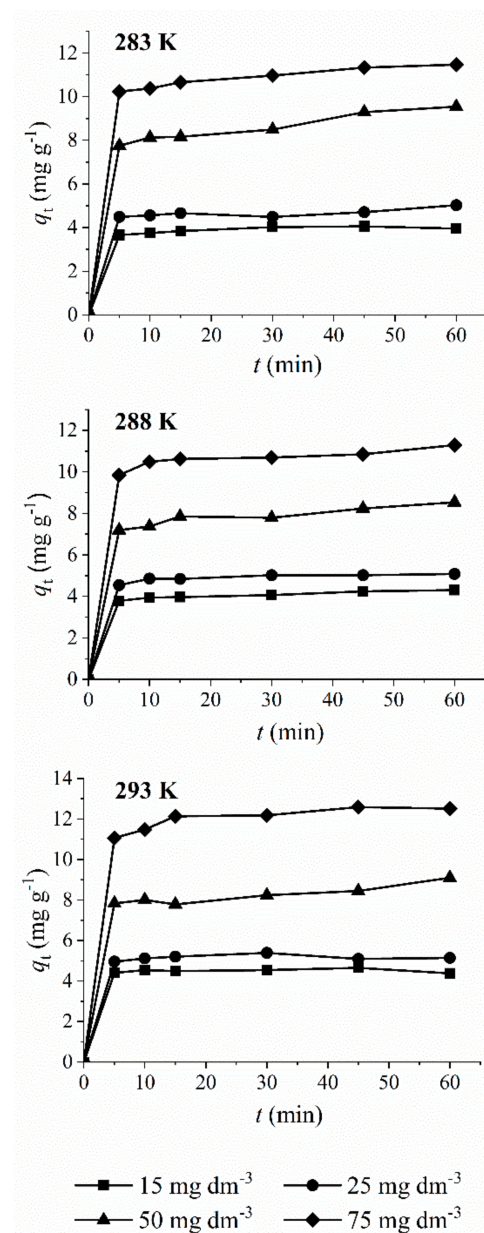


**Figure 11.** Adsorption kinetics for CIP on CLI for different temperatures;  $q_t$  is the amount of the adsorbed CIP ( $\text{mg}$  per  $1 \text{ g}$  of CLI) after time  $t$ .

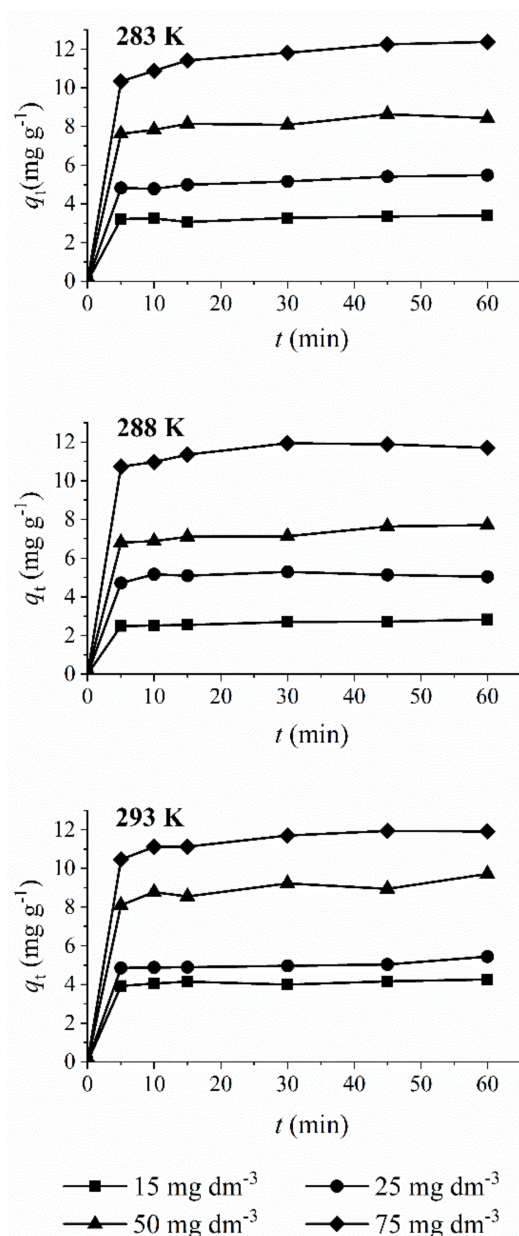


**Figure 12.** Adsorption kinetics for CIP on MAG-CLI for different temperatures;  $q_t$  is the amount of the adsorbed antibiotic ( $\text{mg}$  per  $1 \text{ g}$  of MAG-CLI) after time  $t$ .

Application of the two reaction-based kinetic models on the experimental data showed that Lagergren's first-order model gives a poor agreement (the results are not shown since the  $R^2$  was lower than 0.80). The pseudo-second order model gives the best fit as judged by the  $R^2$  values (Table 6). This suggests that chemisorption occurs during the CIP adsorption. In addition, the maximum calculated capacities obtained for the highest studied concentration,  $13.27 \text{ mg CIP g}^{-1}$  (at 293 K) and  $13.00 \text{ mg CIP g}^{-1}$  (at 283 K) for CLI and MAG-CLI, respectively, correspond to the experimentally obtained values. The Lagergren's pseudo-second order rate constant ( $k_2$ ) was in the range of  $0.0346\text{--}0.4011 \text{ g mg}^{-1} \text{ min}^{-1}$  for both CLI and MAG-CLI. The  $k_2$  values changed rather irregularly with temperature for all initial CIP concentrations. A similar phenomenon was reported for the CIP adsorption on clay minerals and on  $\gamma\text{-Al}_2\text{O}_3$  [23,24], indicating complexity of the CIP adsorption mechanism.

**Table 6.** Rate constant for the two studied kinetic models for the adsorption of CIP on CLI and MAG-CLI ( $R^2$  is the correlation coefficient of the linear regression).

CLI							
$C_0$ , mg CIP dm <sup>-3</sup>	$T$ , K	Weber-Morris Model Parameters			Lagergren's Pseudo-Second-Order Rate Parameters		
		$K_{id}$ , mg g <sup>-1</sup> min <sup>-1/2</sup>	$I$ , mg g <sup>-1</sup>	$R^2$	$k_2$ , g mg <sup>-1</sup> min <sup>-1</sup>	$q_e$ , mg g <sup>-1</sup>	$R^2$
15	283	0.0729	3.54	0.9301	0.3393	4.09	0.9999
	288	0.0768	3.66	0.9638	0.2490	4.28	0.9998
	293	0.0599	4.29	0.9221	0.2275	4.82	0.9996
25	283	0.0592	4.35	0.7707	0.1896	4.90	0.9988
	288	0.0820	4.50	0.8933	0.2900	5.13	0.9999
	293	0.0377	4.99	0.5450	0.4011	5.24	0.9995
50	283	0.3033	7.15	0.9436	0.0436	9.78	0.9983
	288	0.1946	6.93	0.9386	0.0703	8.63	0.9991
	293	0.1632	7.44	0.8792	0.0714	8.94	0.9989
75	283	0.1442	10.26	0.7653	0.0868	11.58	0.9997
	288	0.1822	9.77	0.7612	0.0886	11.28	0.9991
	293	0.3307	10.46	0.9285	0.0443	13.27	0.9982
MAG-CLI							
$C_0$ , mg CIP dm <sup>-3</sup>	$T$ , K	Weber-Morris Model Parameters			Lagergren's Pseudo-Second-Order Rate Parameters		
		$K_{id}$ , mg g <sup>-1</sup> min <sup>-1/2</sup>	$I$ , mg g <sup>-1</sup>	$R^2$	$k_2$ , g mg <sup>-1</sup> min <sup>-1</sup>	$q_e$ , mg g <sup>-1</sup>	$R^2$
15	283	0.0390	3.07	0.7268	0.3133	3.43	0.9997
	288	0.0877	2.24	0.9268	0.1361	3.03	0.9964
	293	0.0434	3.88	0.7702	0.3242	4.26	0.9995
25	283	0.1337	4.46	0.9771	0.1159	5.59	0.9996
	288	0.0399	4.88	0.4335	0.1185	5.08	0.9996
	293	0.0885	4.59	0.8507	0.1257	5.41	0.9980
50	283	0.1972	7.29	0.9393	0.1359	8.60	0.9995
	288	0.1708	6.38	0.9613	0.0861	7.84	0.9993
	293	0.1060	8.21	0.5944	0.0673	8.85	0.9994
75	283	0.3857	9.59	0.7299	0.0346	13.00	0.9930
	288	0.2409	10.12	0.8105	0.0859	12.00	0.9994
	293	0.3047	9.96	0.9832	0.0558	12.46	0.9997

$K_{id}$ —intra-particle diffusion rate constant, mg g<sup>-1</sup> min<sup>-1/2</sup>;  $I$ —parameter related to the thickness of the boundary layer, mg g<sup>-1</sup>;  $k_2$ —pseudo-second-order rate constant, g mg<sup>-1</sup> min<sup>-1</sup>;  $q_e$ —adsorption capacity, mg g<sup>-1</sup>.

Table 6 shows that the analysis of the adsorption data by the Weber-Morris mass transfer model gave parameter  $I$  values that were higher than one, suggesting that the intra-particle diffusion is not the rate-limiting step [32,65].

### 3.11. Leaching Test

Leaching of the adsorbed CIP from the spent adsorbents was studied by treating the spent adsorbents in NaCl solution over 24 h. It was found that 20.6% of the CIP is released from CLI (containing 20.2 mg CIP g<sup>-1</sup>) and 4.40% from MAG-CLI (with 22.1 mg CIP g<sup>-1</sup>). This suggests the following: (1) magnetite coverage prevents leaching of CIP from the adsorbent, and (2) the CIP adsorption is an irreversible process. The protection of the magnetite coverage could be explained by an interaction of the CIP carboxylic groups with magnetite particles. Namely, adsorptive ability of nano-magnetite was ascribed to the formation of an inner-sphere complex between CIP and magnetite, mediated by carboxylic acid groups [5]. Moreover, the fact that only 20% of the adsorbed CIP can be replaced by Na<sup>+</sup> ions from CLI suggests a strong interaction of CIP and the clinoptilolite surface.

### 3.12. Regeneration of the Adsorbent

The unsuccessful removal of adsorbed CIP by ion exchange confirms that the adsorption is irreversible. A similar result was also reported for the CIP adsorption onto zeolite A, Y and X [44]. Adsorbent reusability is a very important issue for the operational cost of wastewater treatment based on the adsorption process. With this in mind, we explored a low-temperature atmospheric pressure plasma treatment for the recovery of the spent adsorbent. Plasma treatment is an effective method for the surface modification of various materials including zeolites. Plasma treatments of zeolites were found to increase the removal efficiency of organic species from water after a short treatment time [66,67]. This effect is attributed to an interaction between the reactive species produced in plasma and the zeolite surface [68].

A surface dielectric barrier discharge (SDBD) source with a segmented electrode operating in air was used for plasma treatment of the spent MAG-CLI. Plasma was generated using a 50 Hz sine wave high-voltage signal ( $V(\text{amplitude}) = 12.5 \text{ kV}$ ) within the  $d = 2 \text{ mm}$  gap between the upper (powered) and lower (grounded) electrode which also served as a sample holder. The duration of the treatment was  $t = 20 \text{ min}$ . The preliminary results of four regeneration cycles are shown in Figure 13.

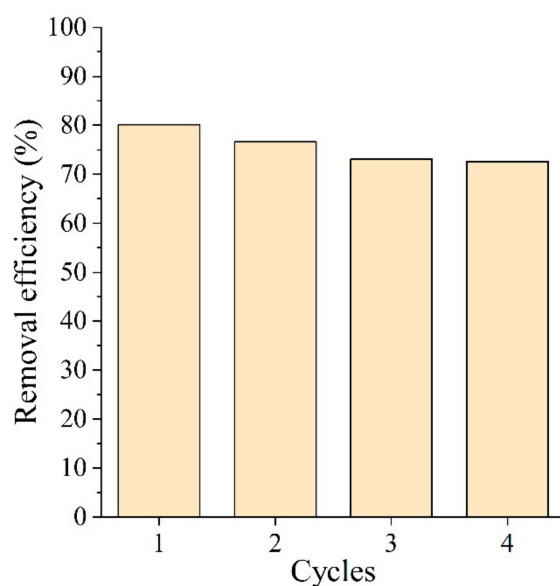


**Figure 13.** CIP removal efficiency on the MAG-CLI during four adsorption and plasma regeneration cycles ( $C_0 = 50 \text{ mg dm}^{-3}$ , adsorption time = 60 min,  $T = 298 \text{ K}$  and  $\text{pH} = 5$ ).

The results indicate that almost 80% of the adsorbent capacity can be recovered by the plasma treatment (Figure 13). This suggests that such a method is suitable for adsorbent recycling. Further investigation into the optimization of the plasma operational parameters is in progress and will be published.

### 3.13. Antibacterial Test

In order to make the management of the spent adsorbents cost-effective, antibacterial activity of the CIP-containing CLI and MAG-CLI was tested.

Previously published results showed that clinoptilolite itself does not exhibit antibacterial activity towards tested bacteria strains [69]. Figure 14 shows that CIP has a strong antibacterial effect towards both *E. coli* and *S. aureus*, which is in accordance with the literature data [70,71]. Moreover, according to the inhibition zone, it is evident that both CLI-CIP and MAG-CLI-CIP exhibit a strong antibacterial effect. The effect of the CIP, as well as that of the spent adsorbents, is stronger towards *E. coli* than towards *S. aureus*. This can be explained by differences in structure and composition of the cell wall of Gram-negative and Gram-positive bacteria [72,73]. It is important to note that the CIP concentration used in this assessment was 100 times higher than that on CLI-CIP and MAG-CLI-CIP. This suggests that the CIP immobilized on CLI could be used in water disinfection.

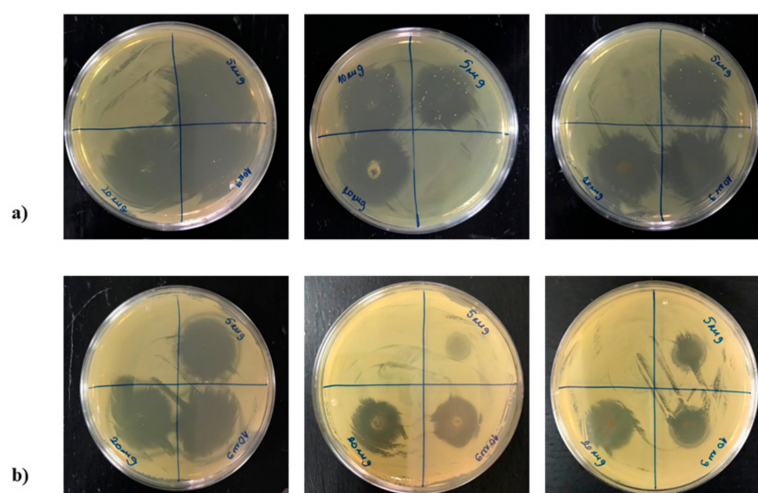


**Figure 14.** Antibacterial activity of CIP, CLI-CIP and MAG-CLI-CIP towards *E. coli* (a) and *S. aureus* (b). Initial number of bacteria ( $t_0$ ): *E. coli* =  $1.4 \cdot 10^9$ ; *S. aureus* =  $1.2 \cdot 10^9$  CFU cm<sup>-3</sup>.

## 4. Conclusions

From the obtained results, the following can be concluded:

- Calcium-rich natural clinoptilolite shows a high adsorptive activity towards antibiotic ciprofloxacin;
- Clinoptilolite strongly adsorbs ciprofloxacin at a pH of 5 via electrostatic interactions and ion exchange reaction occurring between the ciprofloxacin cations and clinoptilolite;
- The adsorption proceeds quickly following the Lagergren's pseudo-second order rate equation. More than 80% of the maximum adsorption capacity was achieved within the first 10 min for the temperature range of 283 to 293 K;
- Impregnation of clinoptilolite by nano-magnetite particles does not influence the adsorption ability and capacity of clinoptilolite, but brings magnetism to the clinoptilolite-based adsorbent which allows for the easy removal of the spent adsorbent by magnetic separation;
- Magnetite coverage protects the spent adsorbent from the CIP leaching through an interaction of the carboxylic groups of the adsorbed CIP and magnetite particles;
- Preliminary studies indicate that atmospheric pressure plasma could be an efficient method for the regeneration of spent adsorbent;



- Ciprofloxacin-containing clinoptilolite shows strong antibacterial activity towards pathogens (*E. coli* and *S. aureus*), suggesting its possible use in a tertiary stage of water treatment.

**Author Contributions:** Conceptualization, N.R.; methodology, B.K., J.P. and N.R.; validation, N.R.; formal analysis, B.K., J.P., A.R. and S.G.; investigation, B.K., J.D. and N.Š.; resources, N.R.; data curation, B.K.; writing—original draft preparation, B.K.; writing—review and editing, J.P., J.D., N.Š. and N.R.; visualization, N.R.; supervision, N.R.; project administration, N.R.; funding acquisition, N.R. All authors have read and agreed to the published version of the manuscript.

**Funding:** This research was funded by the European Union’s Horizon 2020 research and innovation program under the Marie Skłodowska-Curie grant agreement, MSCA-ITN-2018, [grant number 812880], and the Ministry of Education, Science and Technological Development of the Republic of Serbia, [grant numbers 451-03-68/2020-14/200287, 451-03-68/2020-14/200135].

**Data Availability Statement:** All data is shown in the manuscript and raw data is available from corresponding authors upon a request.

**Conflicts of Interest:** The authors declare no conflict of interest. The funders had no role in the design of the study, in the collection, analyses, or interpretation of data, in the writing of the manuscript, or in the decision to publish the results.

## References

1. Kraemer, S.A.; Ramachandran, A.; Perron, G.G. Antibiotic pollution in the environment: From microbial ecology to public policy. *Microorganisms* **2019**, *7*, 180. [[CrossRef](#)] [[PubMed](#)]
2. Verlicchi, P.; Al Aukidy, M.; Zambello, E. Occurrence of pharmaceutical compounds in urban wastewater: Removal, mass load and environmental risk after a secondary treatment—A review. *Sci. Total Environ.* **2012**, *429*, 123–155. [[CrossRef](#)] [[PubMed](#)]
3. Frade, V.M.F.; Dias, M.; Teixeira, A.C.S.C.; Palma, M.S.A. Environmental contamination by fluoroquinolones. *Braz. J. Pharm. Sci.* **2014**, *50*, 41–54. [[CrossRef](#)]
4. Johnson, A.C.; Keller, V.; Dumont, E.; Sumpter, J.P. Assessing the concentrations and risks of toxicity from the antibiotics ciprofloxacin, sulfamethoxazole, trimethoprim and erythromycin in European rivers. *Sci. Total Environ.* **2015**, *511*, 747–755. [[CrossRef](#)]
5. Rakshit, S.; Sarkar, D.; Elzinga, E.J.; Punamiya, P.; Datta, R. Mechanisms of ciprofloxacin removal by nano-sized magnetite. *J. Hazard. Mater.* **2013**, *246–247*, 221–226. [[CrossRef](#)]
6. Genç, N.; Dogan, E.C. Adsorption kinetics of the antibiotic ciprofloxacin on bentonite, activated carbon, zeolite, and pumice. *Desalin. Water Treat.* **2013**, *53*, 1–9. [[CrossRef](#)]
7. Carabineiro, S.A.C.; Thavorn-Amornsri, T.; Pereira, M.F.R.; Serp, P.; Figueiredo, J.L. Comparison between activated carbon, carbon xerogel and carbon nanotubes for the adsorption of the antibiotic ciprofloxacin. *Catal. Today* **2012**, *186*, 29–34. [[CrossRef](#)]
8. Cuerda-Correa, E.M.; Alexandre-Franco, M.F.; Fernández-González, C. Advanced oxidation processes for the removal of antibiotic from water. An overview. *Water* **2020**, *12*, 102. [[CrossRef](#)]
9. De Witte, B.; Van Langenhove, H.; Demeestere, K.; Saerens, K.; De Wispelaere, P.; Dewilf, J. Ciprofloxacin ozonation in hospital wastewater treatment plant effluent: Effect of pH and H<sub>2</sub>O<sub>2</sub>. *Chemosphere* **2010**, *78*, 1142–1147. [[CrossRef](#)]
10. Li, W.; Guo, C.; Su, B.; Xu, J. Photodegradation of four fluoroquinolone compounds by titanium dioxide under simulated solar light irradiation. *J. Chem. Technol. Biotechnol.* **2011**, *87*, 643–650. [[CrossRef](#)]
11. Li, B.; Zhang, T. Biodegradation and adsorption of antibiotics in the activated sludge process. *Environ. Sci. Technol.* **2010**, *44*, 3468–3473. [[CrossRef](#)]
12. Dorival-García, N.; Zafra-Gómez, A.; Navalón, A.; González, J.; Vílchez, J.L. Removal of quinolone antibiotics from wastewater by sorption and biological degradation in laboratory-scale membrane bioreactors. *Sci. Total Environ.* **2013**, *442*, 317–328. [[CrossRef](#)]
13. Jia, A.; Wan, Y.; Xiao, Y.; Hu, J. Occurrence and fate of quinolone and fluoroquinolone antibiotics in a municipal sewage treatment plant. *Water Res.* **2012**, *46*, 387–394. [[CrossRef](#)]
14. Lin, C.-C.; Lee, C.-Y. Adsorption of ciprofloxacin in water using Fe<sub>3</sub>O<sub>4</sub> nanoparticles formed at low temperature and high reactant concentrations in a rotating packed bed with co-precipitation. *Mater. Chem. Phys.* **2020**, *240*, 122049. [[CrossRef](#)]
15. Attia, T.M.S.; Hu, X.L.; Qiang, Y.D. Synthesized magnetic nanoparticles coated zeolite for the adsorption of pharmaceutical compounds from aqueous solution using batch and column studies. *Chemosphere* **2013**, *93*, 2076–2085. [[CrossRef](#)]
16. Hsini, A.; Esseki, A.; Aarab, N.; Laabd, M.; Addi, A.A.; Lakhmiri, R.; Albourine, A. Elaboration of novel polyaniline@Almond shell biocomposite for effective removal of hexavalent chromium ions and Orange G dye from aqueous solutions. *Environ. Sci. Pollut. Res.* **2020**, *27*, 15245–15258. [[CrossRef](#)]

17. Hsini, A.; Naciri, Y.; Benafqir, M.; Ajmal, Z.; Aarab, N.; Laabd, M.; Navío, J.A.; Puga, F.; Boukherroub, R.; Bakiz, B.; et al. Facile synthesis and characterization of a novel 1,2,4,5-benzene tetracarboxylic acid doped polyaniline@zinc phosphate nanocomposite for highly efficient removal of hazardous hexavalent chromium ions from water. *J. Colloid Interface Sci.* **2021**, *585*, 560–573. [[CrossRef](#)]
18. Hsini, A.; Naciri, Y.; Laabd, M.; El Ouardi, M.; Ajmal, Z.; Lakhmiri, R.; Boukherroub, R.; Albourine, A. Synthesis and characterization of arginine-doped polyaniline/walnut shell hybrid composite with superior clean-up ability for chromium (VI) from aqueous media: Equilibrium, reusability and process optimization. *J. Mol. Liq.* **2020**, *316*, 113832. [[CrossRef](#)]
19. Ma, J.; Yang, M.; Yu, F.; Zheng, J. Water-enhanced removal of ciprofloxacin from water by porous graphene hydrogel. *Sci. Rep.* **2015**, *5*, 13578. [[CrossRef](#)]
20. Sun, Y.; Yang, Y.; Yang, M.; Yu, F.; Ma, J. Response surface methodological evaluation and optimization for adsorption removal of ciprofloxacin onto graphene hydrogel. *J. Mol. Liq.* **2019**, *284*, 124–130. [[CrossRef](#)]
21. Nogueira, J.; António, M.; Mikhalev, S.M.; Fateixa, S.; Trindade, T.; Daniel-da-Silva, L.A. Porous carrageenan-derived carbon for efficient ciprofloxacin removal from water. *J. Nanomater.* **2018**, *8*, 1004. [[CrossRef](#)]
22. El-Shafey, E.-S.I.; Al-Lawati, H.; Al-Sumari, A.S. Ciprofloxacin adsorption from aqueous solution onto chemically prepared carbon from date palm leaflets. *J. Environ. Sci.* **2012**, *24*, 1579–1586. [[CrossRef](#)]
23. Cheng, R.; Li, H.; Liu, Z.; Du, C. Halloysite nanotubes as an effective and recyclable adsorbent for removal of low-concentration antibiotics ciprofloxacin. *Minerals* **2018**, *8*, 387. [[CrossRef](#)]
24. Najafpoor, A.A.; Sani, O.N.; Alidadi, H.; Yazdani, M.; Fezabady, A.A.N.; Taghavi, M. Optimization of ciprofloxacin adsorption from synthetic wastewater using  $\gamma$ -Al<sub>2</sub>O<sub>3</sub> nanoparticles: An experimental design based on response surface methodology. *Colloids Interface Sci. Commun.* **2019**, *33*, 100212. [[CrossRef](#)]
25. Fan, H.; Ma, Y.; Wan, J.; Wang, Y.; Li, Z.; Chen, Y. Adsorption properties and mechanisms of novel biomaterials from banyan aerial roots via simple modification for ciprofloxacin removal. *Sci. Total Environ.* **2020**, *708*, 134630. [[CrossRef](#)]
26. Ashiq, A.; Sarkar, B.; Adassooriya, N.; Walpita, J.; Rajapaksha, A.U.; Ok, Y.S.; Vithanage, M. Sorption process of municipal solid waste biochar-montmorillonite composite for ciprofloxacin removal in aqueous media. *Chemosphere* **2019**, *236*, 124384. [[CrossRef](#)]
27. Zhang, C.-L.; Qiao, G.-L.; Zhao, F.; Wang, Y. Thermodynamic and kinetic parameters of ciprofloxacin adsorption onto modified coal fly ash from aqueous solution. *J. Mol. Liq.* **2011**, *163*, 53–56. [[CrossRef](#)]
28. Wang, S.; Peng, Y. Natural zeolites as effective adsorbents in water and wastewater treatment. *Chem. Eng. J.* **2010**, *156*, 11–24. [[CrossRef](#)]
29. Ngeno, E.C.; Shikuku, V.O.; Orata, F.; Baraza, L.D.; Kimosop, S.J. Caffeine and ciprofloxacin adsorption from water onto clinoptilolite: Linear isotherms, kinetics, thermodynamic and mechanistic studies. *S. Afr. J. Chem.* **2019**, *72*, 139–142. [[CrossRef](#)]
30. Zide, D.; Fatoki, O.; Oputu, O.; Opeolu, B.; Nelana, S.; Olatunji, O. Zeolite ‘adsorption’ capacities in aqueous acidic media; The role of acid choice and quantification method on ciprofloxacin removal. *Microporous Mesoporous Mater.* **2018**, *255*, 226–241. [[CrossRef](#)]
31. Wang, C.-J.; Li, Z.; Jiang, W.-T.; Jean, J.-S.; Liu, C.-C. Cation exchange interaction between antibiotic ciprofloxacin and montmorillonite. *J. Hazard. Mater.* **2010**, *183*, 309–314. [[CrossRef](#)]
32. Rajić, N.; Stojaković, D.; Jovanović, M.; Zabukovec Logar, N.; Mazaj, M.; Kaučič, V. Removal of nickel(II) ions from aqueous solutions using the natural clinoptilolite and preparation of nano-NiO on the exhausted clinoptilolite. *Appl. Surf. Sci.* **2010**, *257*, 1524–1532. [[CrossRef](#)]
33. Stojaković, D.; Milenković, J.; Daneu, N.; Rajić, N. A study of the removal of copper ions from aqueous solution using clinoptilolite from Serbia. *Clay Clay Miner.* **2012**, *59*, 277–285. [[CrossRef](#)]
34. Pavlović, J.B.; Milenković, J.K.; Rajić, N.Z. Modification of natural clinoptilolite for nitrate removal from aqueous media. *J. Serb. Chem. Soc.* **2014**, *79*, 1309–1322. [[CrossRef](#)]
35. Jevtić, S.; Arčon, I.; Rečnik, A.; Babić, B.; Mazaj, M.; Pavlović, J.; Matijašević, D.; Nikšić, M.; Rajić, N. The iron(III)-modified natural zeolitic tuff as an adsorbent and carrier for selenium oxyanions. *Microporous Mesoporous Mater.* **2014**, *197*, 92–100. [[CrossRef](#)]
36. Muir, B.; Wołowicz, M.; Bajda, T.; Nowak, P.; Czupryński, P. The removal of organic compounds by natural and synthetic surface-functionalized zeolites: A mini-review. *Mineralogia* **2017**, *48*, 145–156. [[CrossRef](#)]
37. Ambrozova, P.; Kynicky, J.; Urubek, T.; Nguyen, V.D. Synthesis and modification of clinoptilolite. *Molecules* **2017**, *22*, 1107. [[CrossRef](#)]
38. Rajic, N.; Stojakovic, D.; Daneu, N.; Recnik, A. The formation of oxide nanoparticles on the surface of natural clinoptilolite. *J. Phys. Chem. Solids* **2011**, *72*, 800–803. [[CrossRef](#)]
39. Ahribesh, A.A.; Lazarević, S.; Janković-Častvan, I.; Jokić, B.; Spasojević, V.; Radetić, T.; Janačković, D.; Petrović, R. Influence of the synthesis parameters on the properties of the sepiolite-based magnetic adsorbents. *Powder Technol.* **2017**, *305*, 260–269. [[CrossRef](#)]
40. Javanbakht, V.; Ghoreishi, S.M.; Habibi, N.; Javanbakht, M. A novel magnetic chitosan/clinoptilolite/magnetite nanocomposite for highly efficient removal of Pb(II) ions from aqueous solution. *Powder Technol.* **2016**, *302*, 372–383. [[CrossRef](#)]
41. Savić, A.B.; Čokeša, D.; Lazarević, S.; Jokić, B.; Janačković, D.; Petrović, R.; Živković, L.S. Tailoring of magnetic powder properties for enhanced phosphate removal: Effect of PEG addition in the synthesis process. *Powder Technol.* **2016**, *301*, 511–519. [[CrossRef](#)]
42. Arora, M.; Eddy, N.K.; Mumford, K.A.; Baba, Y.; Perera, J.M.; Stevens, G.W. Surface modification of natural zeolite by chitosan and its use for nitrate removal in cold regions. *Cold. Reg. Sci. Technol.* **2010**, *62*, 92–97. [[CrossRef](#)]

43. Kragović, M.; Pašalić, S.; Marković, M.; Petrović, M.; Nedeljković, B.; Momčilović, M.; Stojmenović, M. Natural and modified zeolite–alginate composites. Application for removal of heavy metal cations from contaminated water solutions. *Minerals* **2017**, *8*, 11. [[CrossRef](#)]
44. Braschi, I.; Blasioli, S.; Gigli, L.; Gessa, C.E.; Alberti, A.; Martucci, A. Removal of sulfonamide antibiotics from water: Evidence of adsorption into an organophilic zeolite Y by its structural modifications. *J. Hazard. Mater.* **2010**, *178*, 218–225. [[CrossRef](#)] [[PubMed](#)]
45. Coelho, A. *TOPAS Academic 4.1*; Coelho Software: Brisbane, Australia, 2007.
46. Ming, D.W.; Dixon, J.B. Quantitative determination of clinoptilolite in soils by a cation-exchange capacity method. *Clay Clay Miner.* **1987**, *35*, 463–468. [[CrossRef](#)]
47. Khalil, M.I. Co-precipitation in aqueous solution synthesis of magnetite nanoparticles using iron(III) salts as precursors. *Arab. J. Chem.* **2015**, *8*, 279–284. [[CrossRef](#)]
48. Mohseni-Bandpi, A.; Al-Musawi, T.J.; Ghahramani, E.; Zarrabi, M.; Mohebi, S.; Vahed, S.A. Improvement of zeolite adsorption capacity for cephalexin by coating with magnetic Fe<sub>3</sub>O<sub>4</sub> nanoparticles. *J. Mol. Liq.* **2016**, *218*, 615–624. [[CrossRef](#)]
49. Gulicovski, J.J.; Čerović, L.S.; Milonjić, S.K. Point of zero charge and isoelectric point of alumina. *Mater. Manuf. Process.* **2008**, *23*, 615–619. [[CrossRef](#)]
50. Naveed, S.; Waheed, N. Simple UV spectrophotometric assay of ciprofloxacin. *MJPMS* **2014**, *3*, 10–13.
51. Hawash, H.B.I.; Chmielewska, E.; Netriová, Z.; Majzlan, J.; Pálková, H.; Sokolík, R. Innovative comparable study for application of iron oxyhydroxide and manganese dioxide modified clinoptilolite in removal of Zn(II) from aqueous medium. *J. Environ. Chem. Eng.* **2018**, *6*, 6489–6503. [[CrossRef](#)]
52. Rajput, S.; Pittman, C.U., Jr.; Mohan, D. Magnetic magnetite (Fe<sub>3</sub>O<sub>4</sub>) nanoparticles synthesis and applications for lead (Pb<sup>2+</sup>) and chromium (Cr<sup>6+</sup>) removal from water. *J. Colloid Interface Sci.* **2016**, *468*, 334–346. [[CrossRef](#)] [[PubMed](#)]
53. Kouli, M.-E.; Banis, G.; Tsarabaris, P.; Ferraro, A.; Hristoforou, E. A study on magnetic removal of sodium, calcium and potassium ions from seawater using magnetite/c clinoptilolite–Na composite nanoparticles. *J. Magn. Magn. Mater.* **2018**, *465*, 692–699. [[CrossRef](#)]
54. Attia, T.M.S.; Hu, X.L.; Yin, D.Q. Synthesised magnetic nanoparticles coated zeolite (MNCZ) for the removal of arsenic (As) from aqueous solution. *J. Exp. Nanosci.* **2014**, *9*, 551–560. [[CrossRef](#)]
55. Rečnik, A.; Nyirő-Kósa, I.; Dódon, I.; Pósfai, M. Growth defects and epitaxy in Fe<sub>3</sub>O<sub>4</sub> and γ-Fe<sub>2</sub>O<sub>3</sub> nanocrystals. *Cryst. Eng. Comm.* **2013**, *15*, 7539–7547. [[CrossRef](#)]
56. Nyirő-Kósa, I.; Rečnik, A.; Pósfai, M. Novel methods for the synthesis of magnetite nanoparticles with special morphologies and textured assemblages. *J. Nanopart. Res.* **2012**, *14*, 1150–1159. [[CrossRef](#)]
57. Jordan, V.; Javornik, U.; Plavec, J.; Podgornik, A.; Rečnik, A. Self-assembly of multilevel branched rutile-type TiO<sub>2</sub> structures via oriented lateral and twin attachment. *Sci. Rep.* **2016**, *6*, 24216. [[CrossRef](#)]
58. Lin, H.; Liu, Q.-L.; Dong, Y.-B.; He, Y.-H.; Wang, L. Physicochemical properties and mechanism study of clinoptilolite modified by NaOH. *Microporous Mesoporous Mater.* **2015**, *218*, 174–179. [[CrossRef](#)]
59. Cotton, A. Dissolution kinetics of clinoptilolite and heulandite in alkaline conditions. *Biosci. Horiz.* **2008**, *1*, 38–43. [[CrossRef](#)]
60. Duan, W.; Wang, N.; Xiao, W.; Zhao, Y.; Zheng, Y. Ciprofloxacin adsorption onto different micro-structured tourmaline, halloysite and biotite. *J. Mol. Liq.* **2018**, *269*, 874–881. [[CrossRef](#)]
61. Wang, F.; Yang, B.; Wang, H.; Song, Q.; Tan, F.; Cao, Y. Removal of ciprofloxacin from aqueous solution by a magnetic chitosan grafted graphene oxide composite. *J. Mol. Liq.* **2016**, *222*, 188–194. [[CrossRef](#)]
62. Ullah, S.; Azmi, B.M.; Ali, A.M.; Al-Sehemi, A.G.; Gonfa, G.; Mukhtar, A.; Abdal Kareem, F.A.; Ayoub, M.; Saqib, S.; Binti Mellon, N. Synthesis and characterization of mesoporous MOF UMCM-1 for CO<sub>2</sub>/CH<sub>4</sub> adsorption; an experimental, isotherm modeling and thermodynamic study. *Microporous Mesoporous Mat.* **2020**, *294*, 1387–1811. [[CrossRef](#)]
63. Langmuir, I. The adsorption of gases on plane surfaces of glass, mica, and platinum. *J. Am. Chem. Soc.* **1918**, *40*, 1361–1403. [[CrossRef](#)]
64. Ma, S.; Si, Y.; Wang, F.; Su, L.; Xia, C.; Yao, J.; Chen, H.; Liu, X. Interaction processes of ciprofloxacin with graphene oxide and reduce graphene oxide in the presence of montmorillonite in simulated gastrointestinal fluids. *Sci. Rep.* **2017**, *7*, 2588.
65. Weber, W.J., Jr.; Morris, J.C. Advances in Water Pollution Research: Removal of biologically resistant pollutants from waste waters by adsorption. In *Proceedings of the International Conference on Water Pollution Symposium*; Pergamon Press: London, UK, 1962.
66. Mirzaei, H.; Almasian, M.R.; Mousavian, S.M.A.; Kalal, H.S. Plasma modification of a natural zeolite to improve its adsorption capacity of strontium ions from water samples. *Int. J. Environ. Sci. Technol.* **2019**, *16*, 6157–6166. [[CrossRef](#)]
67. Garcia, J.J.M.; Nuñez, J.A.P.; Salapare, H.S.; Vasquez, M.R., Jr. Adsorption of diclofenac sodium in aqueous solution using plasma-activated natural zeolites. *Results Phys.* **2019**, *15*, 102629. [[CrossRef](#)]
68. Kogelschatz, U. Dielectric-barrier discharges: Their history, discharge physics, and industrial applications. *Plasma Chem. Plasma Proc.* **2003**, *23*, 1–46. [[CrossRef](#)]
69. Hrenovic, J.; Milenkovic, J.; Ivankovic, T.; Rajic, N. Antibacterial activity of heavy metal-loaded natural zeolite. *J. Hazard. Mater.* **2012**, *201–202*, 260–264. [[CrossRef](#)]
70. Simões, M.; Rocha, S.; Coimbra, M.; Vieira, M. Enhancement of *Escherichia coli* and *Staphylococcus aureus* antibiotic susceptibility using sesquiterpenoids. *J. Med. Chem.* **2008**, *4*, 616–623. [[CrossRef](#)]

71. Chalkley, L.J.; Koornhof, H.J. Antimicrobial activity of ciprofloxacin against *Pseudomonas aeruginosa*, *Escherichia coli*, and *Staphylococcus aureus* determined by the killing curve method: Antibiotic comparisons and synergistic interactions. *Antimicrob. Agents Chemother.* **1985**, *28*, 331–342. [[CrossRef](#)]
72. Berlanga, M.; Montero, M.T.; Hernández-Borrell, J.; Viñas, M. Influence of the cell wall on ciprofloxacin susceptibility in selected wild-type Gram-negative and Gram-positive bacteria. *Int. J. Antimicrob. Agents* **2004**, *23*, 627–630. [[CrossRef](#)]
73. Mohsen, E.; El-Borady, O.M.; Mohamed, M.B.; Fahim, I.S. Synthesis and characterization of ciprofloxacin loaded silver nanoparticles and investigation of their antibacterial effect. *J. Radiat. Res. Appl.* **2020**, *13*, 416–425. [[CrossRef](#)]

PAPER

# A comparison of power measurement techniques and electrical characterization of an atmospheric pressure plasma jet

To cite this article: Olivera JOVANOVI *et al* 2022 *Plasma Sci. Technol.* **24** 105404

View the [article online](#) for updates and enhancements.

You may also like

- [Using Mathematica software to graph Lissajous figures](#)  
Deyvid W da M Pastana and Manuel E Rodrigues
- [Establishing an equivalent circuit for a quasihomogeneous discharge atmospheric-pressure plasma jet with a breakdown-voltage-controlled breaker and power supply circuit](#)  
Shih-Sen Huang, Hsing-Che Tsai, Jerry Chang *et al.*
- [Effect of insulating oil covering electrodes on the characteristics of a dielectric barrier discharge](#)  
Trung Nguyen TRAN, Bounyang OANTHAVINSAK, Shinichiro KADO *et al.*





## Analysis Solutions for your Plasma Research

- Knowledge,
- Experience,
- Expertise

Click to view our product catalogue

Contact Hiden Analytical for further details:

[www.HidenAnalytical.com](http://www.HidenAnalytical.com)  
[info@hiden.co.uk](mailto:info@hiden.co.uk)



Surface Science

- ▶ Surface Analysis
- ▶ SIMS
- ▶ 3D depth Profiling
- ▶ Nanometre depth resolution



Plasma Diagnostics

- ▶ Plasma characterisation
- ▶ Customised systems to suit plasma Configuration
- ▶ Mass and energy analysis of plasma ions
- ▶ Characterisation of neutrals and radicals

# A comparison of power measurement techniques and electrical characterization of an atmospheric pressure plasma jet

Olivera JOVANOVIĆ\* , Nevena PUAČ  and Nikola ŠKORO 

Institute of Physics, University of Belgrade, Pregrevica 118, Belgrade 11080, Serbia

E-mail: [olivera@ipb.ac.rs](mailto:olivera@ipb.ac.rs)

Received 8 February 2022, revised 27 April 2022

Accepted for publication 27 May 2022

Published 27 July 2022



CrossMark

## Abstract

In the last two decades a growing interest has been shown in the investigation of atmospheric pressure plasma jets (APPJs) that operate in contact with liquid samples. In order to form a complete picture about such experimental systems, it is necessary to perform detailed diagnostics of plasma jets, as one step that will enable the adjustment of system properties for applications in different areas. In this work, we conducted a detailed electrical characterisation of a plasma system configuration used for water treatment. A helium plasma jet, with a pin electrode powered by a continuous sine wave at a frequency of 330 kHz, formed a streamer that was in contact with a distilled water sample. An electrical circuit allowed the monitoring of electrical signals supplied to the jet and also to the plasma itself. An electrical characterisation together with power consumption measurements was obtained by using two different methods. The first method was based on the direct measurements of voltage and current signals, while in the second method we used ‘Lissajous figures’. We compared these two methods when used for discharge power estimation and addressed their advantages and limitations. The results showed that both of these methods could be used to successfully determine power consumed by a discharge in contact with water, but only when taking into account power dissipation without plasma.

Keywords: APPJ, electrical characterization, discharge power, Lissajous figure

(Some figures may appear in colour only in the online journal)

## 1. Introduction

Over the past decades, non-equilibrium atmospheric pressure plasmas have been extensively investigated, because they represent a powerful tool in various applications. In the treatment of thermally sensitive and unstable materials, especially in biomedicine, the key asset is plasma operating at room temperature [1–4]. Besides biomedical applications, these plasmas are also used in agriculture and water treatment technologies [5–10]. Nevertheless, in all cases, the potential of cold plasma has been used to create specific particles and form a chemically active medium without additional chemical reagents.

APPJs are sources of non-equilibrium plasmas that can be made in various geometries and electrode arrangements.

They usually consist of a dielectric tube, a powered electrode, that can be additionally isolated, and a grounded electrode. Depending on the geometry of the electrodes, operation frequency, power source and working gas, different types and modes of discharge can be generated. In all configurations, the discharge is created when the gas at atmospheric pressure is exposed to a strong electric field. These plasmas are called non-equilibrium, owing to the different temperatures, i.e. energies, of the particles [11].

In the case of APPJs, the realized discharge can be a classical streamer or a more diffuse discharge. Discharges generated by dielectric barrier discharge (DBD) devices can be spatially homogeneous and diffuse [11, 12] while those discharges generated by plasma jets are usually streamers or streamer-like discharges. The streamer discharge occurs after the streamer breakdown. The formed electrical field

\* Author to whom any correspondence should be addressed.

accelerates the charged particles providing energy to the plasma. The presence of an electric field causes the ionization in the gas gap and the formation of space charges at the head of the ionization wave. The field amplification owing to the space charge in the head leads to self-extending streamer discharge. Thus, after inception, the streamer propagation and properties depend on the system configuration, gaseous surrounding and the target. The energy of the fast-progressing streamer is mostly dissipated into the excitation of the working gas [13, 14]. In case of APPJs this is demonstrated through the propagation of PAPS (Pulsed Atmospheric pressure Plasma Streamer) or, so called, 'plasma bullets' [15–17]. Streamers are also present in other types of plasma sources. When the discharge current is not limited they precede other types of discharge, such as sparks and lightning [18].

In several publications it has been investigated how the configuration of a plasma jet system influences the properties of plasma. It has been shown that the efficiency of the power transfer process from the power supply to the plasma system determines the mode of the discharge [14, 19, 20]. For example, a comparison of two discharge regimes produced by different excitation sources (direct current (DC)-pulsed and sine-wave alternating current (AC)) in the same single electrode plasma jet was reported. It was found that the excitation source determines discharge current, the length of plasma plume and plasma temperature [21]. The grounded electrode, due to its capacitive nature, can additionally lead to the energy loss influencing behavior of the plasma bullet. But at the same time it can increase the local electric field that will result in lower voltages needed to sustain plasma [14]. Control of these plasma properties is essential when comes to plasma treatments.

Many studies have shown that an interaction coupling between plasma and the target exists in atmospheric pressure plasma systems. Target properties influence the discharge morphology and affect the creation of turbulence in the gas flow [22, 23]. In the presence of the liquid target, plasma heating leads to evaporation and changes in the composition of the surrounding atmosphere, modifying the physico-chemical properties of both the gas and liquid phases [24]. Studies of the influence of treatment conditions on water properties have shown that small changes in the distance and volume of liquid lead to changes in the concentrations of deposited reactive species [25, 26]. Therefore, an additional complexity is introduced in the plasma system with a liquid target. Exposure of aqueous samples to non-thermal plasma leads to changes in water properties, creating an acidic environment under certain treatment conditions, changing conductivity and redox potential, and creating reactive oxygen and nitrogen species (RONS) [27, 28]. Creating plasma-activated liquid with specific, predetermined properties and a certain content of reactive species provides huge potential for application, but at the same time, is an extremely demanding task. Depending on the plasma jet configuration, the type of discharge and the energy released in the plasma, different reactions will occur in the gas phase (plasma) and the liquid [29]. One step towards a better understanding of the entangled relationship between the characteristics of the plasma source, the discharge properties, and treated sample characteristics, is

to carry out detailed diagnostics of the plasma jet. An important part of that includes the investigation of the electrical parameters, such as the efficiency of the input power transfer to the source, power dissipation, and impedance of the whole system.

In this study, we assessed in detail the electrical characteristics of the He plasma jet operating against a water target. The jet was supplied by a continuous sine high-voltage signal at the frequency of 330 kHz. The electrical discharge is generated in the gas phase above the liquid by applying the voltage at the pin electrode of the jet with distilled water serving as grounded electrode. The main idea of the research was to perform a proper determination of the dissipated powers and evaluate the typically used methods in plasma systems applied for water treatments. To estimate the powers dissipated in the system, we employed two standard methods. In the first method, the power is calculated directly from the product of the measured time-varying current and voltage signals ( $V-I$ ). The second method is based on measuring the voltage across a capacitor connected in a series with the grounded sample ( $Q-V$ ).

These two methods,  $V-I$  and  $Q-V$ , as we named them here, are some of the most widely used power determination procedures. They have been extensively implemented in numerous plane geometry DBD configurations and several plasma jet systems, including conventional plasma jet configurations supplied with both AC [30] and DC voltages [9, 31], driven by either a pulsed high-voltage signal [32] or continuous sinusoidal signal [33]. Furthermore, the input power and the discharge power have been estimated for diverse plasma jet arrangements such as hollow electrode APPJ [14, 34], kINPen [33], single-electrode jet [35] and DBD jet [36], etc.

In recent years, a number of researchers have investigated cold plasma sources that interact with the targets of certain characteristics for a particular application. Plasma jet treatments are most commonly performed in secondary electrode configurations with a grounded or floating electrode. The two methods investigated in this work were used for power dissipation measurement in various plasma jet configurations for the treatment of biological materials and the inactivation of bacteria [37, 38], biomedical applications that include *in vitro* and *in vivo* treatments [39] and producing of plasma activated (tap) water [40].

The research to date has tended to compare the differences between several measurement techniques for power determination only in the field of DBD plasma reactors [41–44]. However, as the  $Q-V$  method is mostly used with different DBD source configurations, there are few comprehensive analyses and comparisons of the two methods for pin-to-plate plasma jets [33, 35] operating with pulsed excitation. Although previous studies have investigated pin-to-plate configurations of a plasma jet, there has been no study that we are aware of, which has dealt with plasma jets interacting with liquid targets and driven by a continuous sine wave. Therefore, the aim of this work was to assess the power consumption (at the target) of a high-frequency pin type plasma jet by using both  $V-I$  and  $Q-V$  methods and to compare the obtained results.

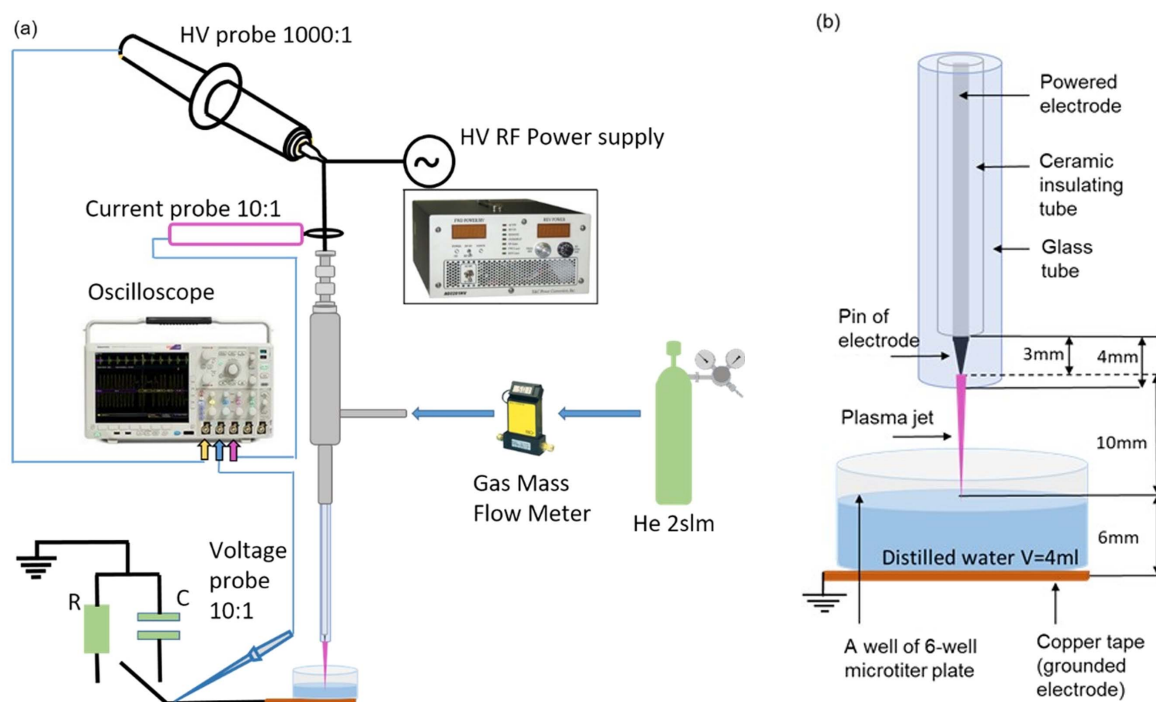


**Figure 1.** Schematic representation of the experimental setup (a) and enlarged view of the powered electrode and target placed below the tip of the electrode (b).

## 2. Experimental setup and methods

### 2.1. Plasma jet system

Figure 1 presents a schematic diagram of an experimental setup. The plasma source used in this experiment was a plasma jet designed to operate as a pin-electrode configuration at atmospheric pressure. It consisted of a cylindrical metal body (diameter 22 mm) and glass tube, whose inner and outer diameters are 4 mm and 6 mm, respectively. A powered electrode was made of stainless steel wire with a diameter of 1 mm. It was covered with a ceramic insulating tube and placed along the glass tube axis. The sharpened tip of the wire protruded 3 mm from the ceramic insulation into the glass tube (see figure 1(b)). The powered electrode was connected to the high-voltage (HV) signal by a BNC connector positioned at the top of the metallic jet body. The second electrode was the target—a distilled water sample placed in a well of 6-well microtiter plate. The initial conductivity of water was  $1.5 \mu\text{S cm}^{-1}$  (Hanna Instruments, HI76312 electrode, HI5521 controller). The plate was positioned below the tip of the powered electrode (see figure 1(b)). The volume of water sample in the well was 4 ml. The distance between the liquid surface and the wire tip was 10 mm in all measurements. The copper tape was attached at the outer bottom side of the well and grounded. The experimental setup, together with the positioning of the grounding tape, is a typical system which is used for the plasma treatment of liquid samples. The setup on one side allows for the measurement of electrical signals while, on the other side, treated liquid is in contact only with the clean vessel, so the chemical reactions are governed solely by the plasma-liquid interaction. Treatment of a liquid in

contact with a copper tape showed that it produced additional chemical reactions and specific species in the liquid after the treatment [25]. Comparison between a setup where copper tape is inside the liquid sample or outside has been investigated for a similar system [29] showing rather small differences in the signals recorded in the grounded line. Also, working with the sine wave high voltage signal at high frequencies allows the use of different materials as a vessel for the samples.

The plasma in the experiments was generated and controlled by using a commercial HV high-frequency power supply (T&C Power Conversion AG 0201HV-OS 140 W–500 kHz with continuous sinusoidal signal with a frequency of 330 kHz). The power supply allows control of an output power (not output voltage or current) and measures the power forwarded from the device to the plasma system as well as the reflected power. The reflected power in all experiments was below 2 W. Due to several elements in the electrical circuit, there is a difference between the power measured at the source and the power delivered to the plasma. Since the power delivered to a discharge is a crucial parameter in the electrical diagnostics of a plasma jet, this indicates a need to measure current and voltage waveforms at the plasma jet itself. To monitor the instantaneously applied voltage waveforms at the power electrode we have used an HV probe (P6015A TEKTRONIX). The current waveforms were measured by using a current probe (Agilent N2783B) connected to the main line of the plasma jet (see figure 1(a)). To avoid an offset in the signal, the current probe was regularly demagnetized.

In the part of the electrical circuit containing the water sample we used two different approaches to measure the



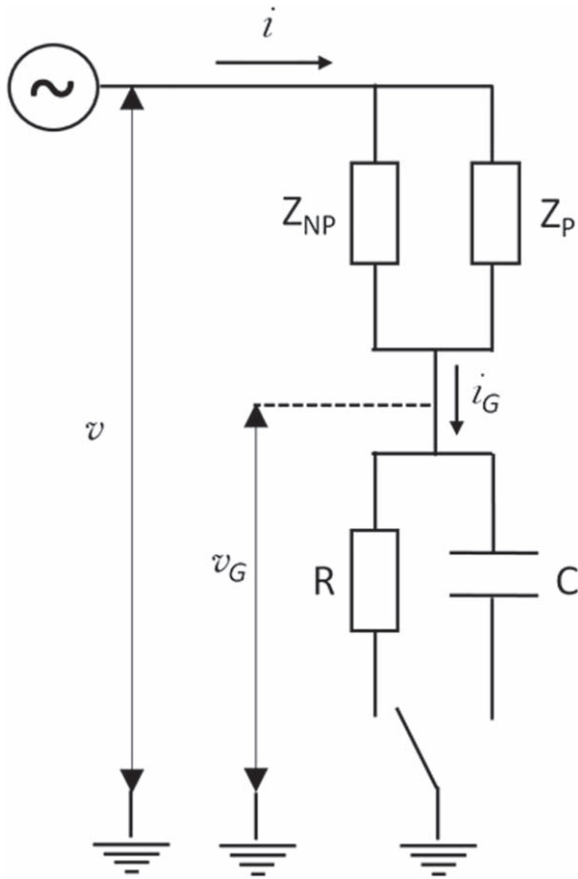


**Figure 2.** The electrical circuit of the plasma jet system:  $v$ —applied alternating voltage at the powered electrode,  $v_G$ —voltage in the ground line,  $i$ —current in the plasma jet main line,  $i_G$ —current through the grounded line,  $R = 1 \text{ k}\Omega$ ,  $C = 0.8 \text{ nF}$  and  $10.3 \text{ nF}$ ,  $Z_{NP}$ —impedance of the plasma jet system configuration without plasma,  $Z_P$ —impedance of plasma.

voltage and current waveforms. When utilizing the  $V$ - $I$  method, the resistor of  $1 \text{ k}\Omega$  resistance was connected in a series to the ground line of the electrical circuit (see schematic in figure 2). For the  $Q$ - $V$  method (Lissajous figures) a capacitor was connected in series to the ground line of the electrical circuit (see schematic in figure 2). For these purposes, the capacitors had capacities of  $0.8 \text{ nF}$  and  $10.3 \text{ nF}$ . In both cases, the voltage drop across the elements placed in the ground line ( $v_G$ ) was measured by using a voltage probe (Agilent N2863B). The resistivity and capacitance of the voltage probe are appropriate so it minimally perturbs the electrical circuit and influences the measurements. We used the Tektronix MDO3024 oscilloscope to record all waveforms.

In all experiments He was used as a working gas with a fixed flow rate of  $2 \text{ slm}$  adjusted by a mass flow controller (Omega FMA5400/5500). The open-end geometry of the plasma jet enables the mixing of the He with the surrounding air. When the plasma is ignited, the filamentary type discharge operates in the gas mixture around the tip of the powered electrode. With the increase of the input power, the generated streamer propagates through the gap and, for most operating parameters, it was touching the liquid sample.

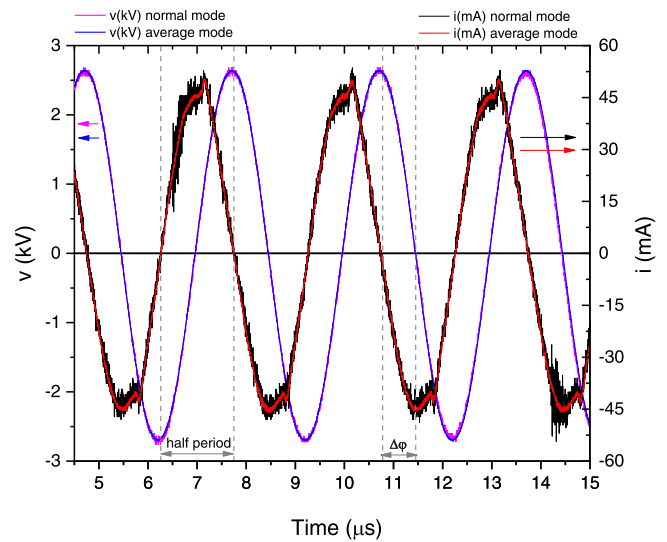


**Figure 3.** Voltage and current waveforms obtained at the electrode in normal mode and average mode (16 cycles averaged). The waveforms were measured for applied peak-to-peak voltage of  $5.5 \text{ kV}$ ,  $f = 330 \text{ kHz}$ , and He flow of  $2 \text{ slm}$ . The electrical circuit configuration was with the resistor  $R = 1 \text{ k}\Omega$  in the grounded line. The half period of applied voltage ( $T/2 = \pi/f$ ) and phase difference ( $\Delta\varphi$ ) are noted in the plot.

## 2.2. The root mean square (RMS) values and $V$ - $I$ method

The electrical circuit (schematic in figure 2) allows the monitoring of voltage and current instantaneous signals through the plasma jet main line and in the ground line. The waveforms of applied voltage  $v$  and current  $i$  through the plasma jet main line are plotted in figure 3.

These signals were captured by the oscilloscope in normal acquisition mode and also by averaging 16 acquired waveforms. The signals obtained in average mode closely follow the shape of the signals recorded in normal mode but without the noise which is visible mostly at the current waveform.

The acquired time-dependent values of voltage and current through the plasma jet main line,  $v(t)$  and  $i(t)$ , and voltage drop across a resistor in the ground line  $v_G(t)$  were used for electrical characterisation and power calculations. The root mean square values of the voltage and current were calculated in the following way:

$$V_{\text{RMS}} = \sqrt{\frac{1}{nT} \int_0^{nT} v^2(t) dt} \quad (1)$$

$$I_{\text{RMS}} = \sqrt{\frac{1}{nT} \int_0^{nT} i^2(t) dt} \quad (2a)$$

$$I_{G\_RMS} = \sqrt{\frac{1}{nT} \int_0^{nT} i_G^2 dt}, \quad (2b)$$

where  $T$  is a period of the given signal and  $n$  is the number of periods,  $i_G(t) = v_G(t)/R$  and  $R$  is the electrical resistance of the resistor in the grounded line.

In the  $V$ - $I$  method, first the time-dependent powers delivered to the plasma jet and consumed by plasma were calculated as the product of voltage  $v(t)$  multiplied by the

appropriate current,  $i(t)$  or  $i_G(t)$ . The average powers are then obtained as:

$$P_{\text{mean}} = \frac{1}{nT} \int_0^{nT} v(t) \cdot i(t) dt \quad (3a)$$

$$P_{\text{mean}_G} = \frac{1}{nT} \int_0^{nT} v(t) \cdot i_G(t) dt. \quad (3b)$$

In all calculations, as input data we used the waveform values obtained in averaging mode. Comparison between two sets of data (obtained in normal and averaging mode) showed differences in calculated values of less than 1%, which is below the experimental error. The phase differences ( $\Delta\varphi$ ) (see figure 3) between high voltage and other obtained signals were calculated in the following way:  $\Delta\varphi = (\Delta t/T) \times 360^\circ$ , where  $\Delta t$  is the time period between points where both signals had zero values.

### 2.3. Q-V method

Another method commonly used for the electrical characterization and measurement of power consumed by plasma is based on a charge-voltage plot or Lissajous figure. For these measurements, the capacitor was inserted in series with the plasma jet and grounded line, so that the same electrical charges formed in the discharge flow through the grounded target and the capacitor. By measuring the capacitor voltage, knowing the capacitance and assuming purely capacitive properties, the charge flow through the capacitor can be obtained. In the Lissajous figure, the area enclosed by the curve is equal to the energy dissipated per one period of applied voltage:

$$E = C \oint v(t) dv_G = \oint v(t) \frac{dQ}{dt} dt = \frac{P_{\text{mean}_G}}{f}, \quad (4)$$

where  $C$  and  $v_G(t)$  are capacity and voltage across the additional capacitor (figure 2),  $v(t)$  is the applied high-voltage signal,  $f = 1/T$  is the corresponding frequency, and  $P_{\text{mean}_G}$  is the average power consumed by the plasma [43, 45, 46]. In this work, the closed area of a Lissajous figure was obtained by the Polygon area function in the Origin software (Origin Lab Corporation, Northampton, MA, USA). A different approach to calculate the area inside the Lissajous figure can be found in [47].

To ensure that the influence of the capacitor on the whole system is minimal, the capacitance was chosen to be large compared to the equivalent capacitance of the plasma jet, gas gap, and target. This difference is at least one order of magnitude. The second important property is the type of capacitor selected. It has been suggested that ceramic capacitors are preferred, owing to their relatively low parasitic losses and accuracy in measurement of charge [48]. An additional advantage is that they are not polarized and may be safely connected to an AC source.

## 3. Results and discussion

### 3.1. Instantaneous voltage and current

Before the onset of the plasma jet electrical measurements, the power supply has been set to operate at the frequency of

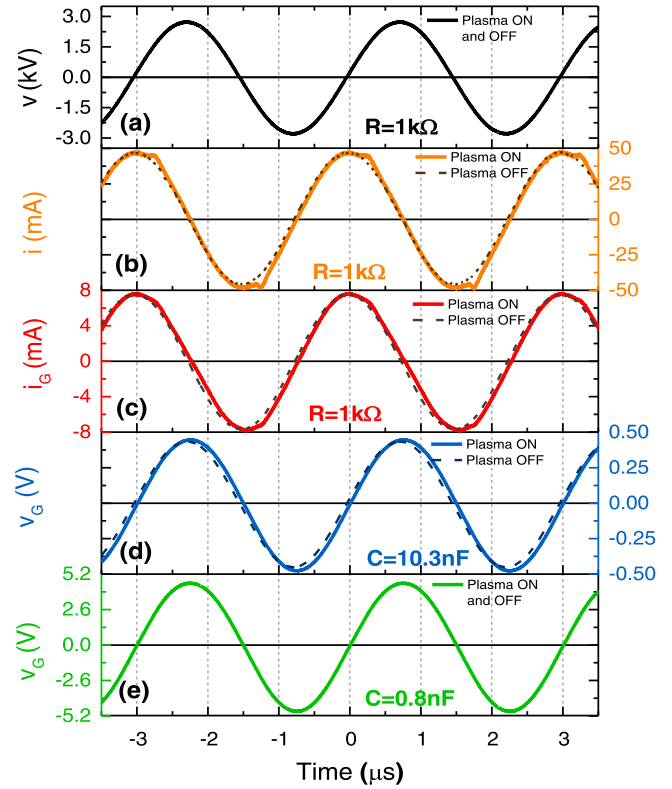


**Figure 4.** Voltage and current waveforms were measured for an applied peak-to-peak voltage of 5.5 kV and frequency of 330 kHz. The dashed lines represent cases when the plasma was OFF, while full lines represent the Plasma ON regime. In plots (a) and (e) Plasma ON and Plasma OFF signals overlap. (a)  $v$ —applied voltage at the electrode. (b) and (c) electrical circuit configuration with the resistor  $R = 1 \text{ k}\Omega$ ,  $i$ —current in the plasma jet main line,  $i_G$ —current through the grounded line. (d) and (e) electrical circuit configurations with capacitors:  $v_G$ —voltage across the 10.3 nF (blue line) and 0.8 nF (green line) capacitor.

330 kHz with the lowest reflected power. The voltage and current signals were monitored for three different configurations of the ground line. In figure 4 we show the waveforms for particular applied voltages. The measurement was performed without feed gas (Plasma OFF) and with the He flow of 2 slm (Plasma ON).

The waveforms when the plasma was on are plotted by a full line, while the dashed line shows the case without plasma (achieved without He flow). All presented signals were recorded with the applied peak-to-peak voltage of 5.5 kV. The waveforms in figures 4(a)–(c) are acquired in electrical circuit configuration with the resistor and represent the averaged value of 16 acquired waveforms. The signals in figures 4(d) and (e) were obtained in electrical circuit configurations with capacitors by averaging 512 waveforms. Identical waveforms were obtained for the applied voltages  $v(t)$  (figure 4(a)) and currents  $i(t)$  (figure 4(b)) in configurations when two capacitors were inserted in the grounded branch of the circuit. Therefore, for simplicity, only one set of  $v(t)$  and  $i(t)$  signals are presented.

The high voltage signal applied to the plasma jet in the configuration with resistance  $R$  in the grounded branch of the circuit is shown in figure 4(a). It has a regular sinusoidal

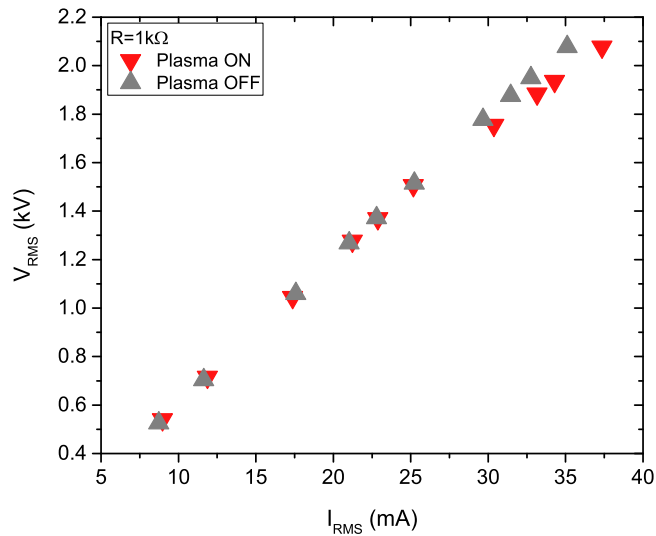


**Figure 5.**  $V$ - $A$  characteristics obtained at the plasma jet in the presence (Plasma ON) and absence (Plasma OFF) of plasma for the configuration with  $R = 1 \text{ k}\Omega$  in the grounded line. The  $V$ - $A$  characteristics obtained when  $C = 0.8 \text{ nF}$  and  $C = 10.3 \text{ nF}$  were used in the electrical circuit are the same and not presented here to retain the clarity of the figure.

shape, regardless of whether the plasma is ignited or not. Figure 4(b) shows the current  $i(t)$  obtained by the current probe and flowing through the main line to the plasma jet. When there is no helium flow, the obtained current signal is sinusoidal, since the applied voltage is lower than the breakdown voltage in air. When the plasma is ignited, the current waveform is deformed from the sine wave and it has two peaks, one per each positive and negative half period of the imposed voltage. The appearance of the peak in the current waveform is connected to the streamer type of the discharge. The observed deformation in the current waveform when discharge occurs has been found previously in other atmospheric plasma jet systems [15, 49–51]. It was the result of discrete propagation of the discharge outside the gas tube in a form of PAPS. In general, changes in the shape of the current signal occur because the current in the plasma jet main line is superimposed on the displacement current. The displacement (capacitive) current can be measured directly when the tube is not filled with feed gas and there is no plasma.

The waveform of the current through the ground line  $i_G(t)$  is presented in figure 4(c). This is the discharge current that passes through the liquid target and a resistor connected in series to the ground. The difference between the waveform shape in the absence and presence of the plasma exists, but it is less noticeable than that in the case of current  $i(t)$ . Related to the phase difference, the plasma off current waveforms  $i(t)$  and  $i_G(t)$  in figures 4(b) and (c) lead to the high voltage waveform by  $85^\circ$  and  $88^\circ$ , respectively. This points to a system that is mainly capacitive (for pure capacitance the phase difference is  $90^\circ$ ) with small deviation from  $90^\circ$  due to the inherent resistivity of the components of the electrical circuit and the plasma source. Deflection from a  $90^\circ$  phase difference means that we observe dissipation of the power even when the plasma is not ignited. After the ignition of the

plasma these phase differences remain almost the same, indicating that deposited power in plasma is small, in the order of a few watts. Voltages across two different capacitors are presented in figure 4(d) for  $C = 10.3 \text{ nF}$  and in figure 4(e) for  $C = 0.8 \text{ nF}$ . The voltages across the  $0.8 \text{ nF}$  capacitor are in phase with the applied voltage independently of the plasma being ignited or not, while in the case of  $10.3 \text{ nF}$  capacitor a small difference in voltage signals is visible.

### 3.2. Volt-ampere characteristics of the plasma jet

The volt-ampere  $V$ - $A$  characteristics of the plasma jet with distilled water as the liquid target are presented in figures 5 and 6. By using the recorded waveforms for each selected operation point, the  $V$ - $A$  characteristics were plotted as a function of the RMS current through the plasma jet main line (figure 5) and the RMS current through the target and ground line (figure 6).

Both characteristics were recorded for the applied peak-to-peak voltages from 1.5 to 6 kV. The points were obtained by increasing the output power of the power supply. All measurements were performed in triplicate and observed differences in the obtained values were not more than 7%. For all measurements as a target we used distilled water of the same initial conductivity, because it was noticed that the conductivity of the liquid sample affects the power consumption [52, 53].

The  $V$ - $A$  characteristic obtained at the plasma jet (figure 5) was recorded when the resistor was inserted in ground line of the electrical circuit. The characteristics that were the same within the error margins were obtained in the other two configurations of the electrical circuit (with capacitors  $C = 0.8 \text{ nF}$  and  $C = 10.3 \text{ nF}$ ) and are not shown to keep the graph in figure 5 clear.

Increasing the power delivered to the plasma jet without plasma (triangles) results in a linear increase of both voltage RMS ( $V_{\text{RMS}}$ ) and current RMS ( $I_{\text{RMS}}$ ). With the gas flow, the discharge becomes visible at a  $V_{\text{RMS}}$  of 0.5 kV and it first appears as a small bright point at the tip of the powered electrode. At a  $V_{\text{RMS}}$  of 1.3 kV, a plasma filament forms and extends 2 mm from the electrode tip. The filament elongates with an increase of the input power. The discharge crosses the entire gap between the powered electrode and target, and streamer touches the water surface at a  $V_{\text{RMS}}$  of 1.75 kV. As can be seen in figure 5, for currents above 30 mA and voltage above 1.75 kV the  $V$ - $A$  characteristic measured with plasma on (inverted triangles) changes slope and it differs from the  $V$ - $A$  characteristics obtained without plasma (triangles). A further increase in the output power of the HV source (applied voltage  $V_{\text{RMS}} > 1.75 \text{ kV}$ ) leads to a more intense light emission from the plasma and to a change of colour. The streamer also begins to move on the liquid surface. For the highest applied voltages, it is observable that several short and thin filaments are adjoined in a streamer.

The  $V$ - $A$  characteristics of the discharge plotted against the current in the grounded line  $I_{G,\text{RMS}}$ , shown in figure 6, were measured in the configurations with the resistor  $R = 1 \text{ k}\Omega$  (figure 6(a)) and capacitor  $C = 10.3 \text{ nF}$  (figure 6(b)). The

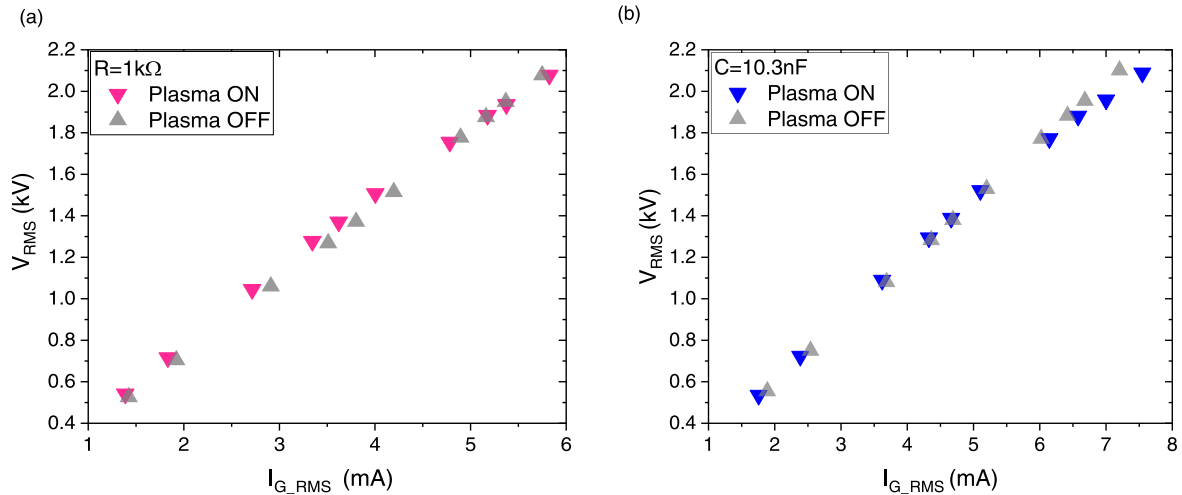


**Figure 6.**  $V$ - $A$  characteristics obtained for the current through the ground line  $I_{G\_RMS}$  in the presence (Plasma ON) and absence (Plasma OFF) of plasma for the configuration with (a)  $R = 1 \text{ k}\Omega$  and (b)  $C = 10.3 \text{ nF}$  in the grounded line. The  $V$ - $A$  characteristic obtained when  $C = 0.8 \text{ nF}$  was used in the electrical circuit is identical to the characteristic in (a). For better clarity in the figure it is not presented here.

pink and blue triangles show the results for measurement when the plasma is ignited, while the grey inverted triangles show results without plasma (without working gas flow).

The  $V$ - $A$  characteristics presented in figure 6(a) shows linear dependence and there is no significant difference between the characteristics when plasma is ignited or not. When the capacitor  $C = 0.8 \text{ nF}$  was inserted into the electrical circuit, the obtained  $V$ - $A$  characteristic is similar to the characteristics presented in figure 6(a). However, the  $V$ - $A$  characteristic obtained with capacitor  $C = 10.3 \text{ nF}$  (figure 6(b)) has a lower slope and departs from linear dependence at higher currents. The impedances of the capacitors used can explain the observed difference. It can be assumed that the capacitor impedance is equal to the capacitive reactance  $X_c = \frac{1}{2\pi fC}$ , i.e. that resistance losses are negligible. Thus, the values of  $597 \Omega$  and  $46 \Omega$  are obtained for  $C = 0.8 \text{ nF}$  and  $C = 10.3 \text{ nF}$ , respectively. Comparing these results with the resistance of  $1 \text{ k}\Omega$ , it is clear that the impedance of the  $0.8 \text{ nF}$  capacitor is closer to  $1 \text{ k}\Omega$  while the impedance of the  $10.3 \text{ nF}$  capacitor differs by one and a half orders of magnitude from that value.

### 3.3. Impedance of the plasma jet

In order to determine the impedance of the system, we have used a linear fitting of the plotted  $V$ - $A$  characteristics obtained at the plasma jet. The total impedance of the plasma jet system  $\hat{Z}$  was obtained as the line slope of the calculated linear fit. It was calculated for both regimes, in the absence (Plasma OFF) and presence (Plasma ON) of plasma, and for three different components in the ground line of the electrical circuit. The equivalent circuit presented in figure 2 is a very simple one and serves only for the estimation of the impedance of the used geometry (Plasma OFF) and of the discharge. These rough estimations of the jet system and plasma impedances are important when developing and/or choosing the appropriate power supply system. They present a load that will influence the work of the power supply, its output and

optimal operating frequency. The plasma, which is a highly non-linear system, will in most cases reduce the optimal operation frequency ('frequency pulling') of the power supply [54]. This means that the output voltage can be reduced due to the exiting resonant state with the power supply transformer.

During the Plasma OFF regime, the complex impedance  $\hat{Z}$  can be considered as a series connection of the impedance  $\hat{Z}_{NP}$  and the impedance of the measuring element in the grounded line of the circuit, the resistor or capacitor (see figure 2):

$$\hat{Z} = \hat{Z}_{NP} + \hat{Z}_{R,C}, \quad (5)$$

where all impedances are in the complex form,  $|\hat{Z}_R| = R$ , and  $|\hat{Z}_C| = X_c = \frac{1}{2\pi fC}$ , assuming that the contribution of the equivalent series resistance of the capacitor can be neglected.  $\hat{Z}_{NP}$  represents the equivalent impedance of the plasma jet system configuration without plasma, including the capacitance of the plasma jet configuration, target impedance, stray capacitance and parasitic resistance of the cables and connections.

When the plasma is ignited (Plasma ON regime), the plasma impedance is represented by  $\hat{Z}_p$  in parallel with the impedance  $\hat{Z}_{NP}$  (figure 2). Plasma impedance is a complex system and it is beyond the scope of this work to estimate each of the components. After the plasma inception, the impedance  $\hat{Z}$  is given by:

$$\hat{Z} = \frac{1}{\hat{Z}_{NP}} + \frac{1}{\hat{Z}_p} + \hat{Z}_{R,C}. \quad (6)$$

Table 1 shows the total impedances of the plasma jet system  $|\hat{Z}|$  obtained in the presence and absence of plasma. The impedances  $|\hat{Z}|$  obtained with three different configurations are in agreement with each other, with the difference smaller than 3%. This is expected since the differences in the configurations were in the grounded line part. After the plasma is ignited, the total impedance is reduced by 10%.

**Table 1.** The total impedance of the plasma jet  $|\hat{Z}|$  in Plasma ON and Plasma OFF states for three different measuring elements in the ground line.

Element in the ground line	$ \hat{Z} $ (k $\Omega$ )	
	Plasma ON	Plasma OFF
$R = 1.0$ k $\Omega$	54.2	59.0
$C = 0.8$ nF	54.3	59.8
$C = 10.3$ nF	55.6	58.4

### 3.4. Mean powers dissipated into the system

In this part, we present and discuss two measured powers: the mean power delivered to the plasma jet -  $P_{\text{mean}}$  and the mean power consumed by the plasma  $P_{\text{mean,G}}$ , i.e., the power measured in the grounded line originating from the plasma and through the target. Additionally, a comparison of the results obtained using two standard methods, by integrating the current and voltage product ( $V$ - $I$ ) and by the Lissajous figure method ( $Q$ - $V$ ) is presented.

The mean power delivered to the plasma jet  $P_{\text{mean}}$  was determined in all experiments, regardless of which measurement element was inserted in the grounded line. The powers  $P_{\text{mean}}$  consumed with ignited plasma (red squares in plots) and without plasma i.e. feed gas (empty squares) were calculated by using equation (3) and is presented in figures 7 and 8.

Determination of the power  $P_{\text{mean}}$  without plasma has significance for determining the mean power delivered only to the plasma, since parasitic resistance in the system is included in the power dissipation measured when the plasma is ignited. Therefore, to obtain the values delivered to the plasma itself ( $P_{\text{mean(NET)}}$ ), the input power measured without He flow (Plasma OFF) was subtracted from the input power when the plasma was on (Plasma ON) for the same applied voltage value:

$$P_{\text{mean(NET)}} = P_{\text{mean(Plasma ON)}} - P_{\text{mean(Plasma OFF)}}. \quad (7)$$

The minimal uncertainty of both methods in our experiments was estimated to be 0.2 W for voltages below 1.5 kV given by power supply. In this range  $P_{\text{mean(NET)}}$  is within this margin. It is found that the power  $P_{\text{mean(Plasma OFF)}}$  increases nearly linearly with the applied voltage. Fitting a linear function to the obtained data points permits the determination of power losses for any applied voltage or current in the measured range. Comparing the dependences of  $P_{\text{mean}}$  on applied voltage  $V_{\text{RMS}}$  and on the current through the plasma jet  $I_{\text{RMS}}$  (see figure 8), it is clear that using either voltage or current as an independent parameter leads to the same power dependence.

The obtained  $P_{\text{mean(NET)}}$  as function of  $V_{\text{RMS}}$  is presented in the plot in figures 7 and 8 (star symbol). Figure 7 shows the power  $P_{\text{mean}}$  obtained in the configuration with capacitor  $C = 0.8$  nF, while figure 8 shows results measured in the arrangement with a resistor  $R$ . This power was found to be up to 6 W for the  $V_{\text{RMS}}$  range between 0.5 and 2 kV. In both figures 7 and 8, there is a jump in values  $P_{\text{mean(NET)}}$  with the applied voltage above 1.5 kV (or  $I_{\text{RMS}}$  above 25 mA). This is the situation when the streamer reached and

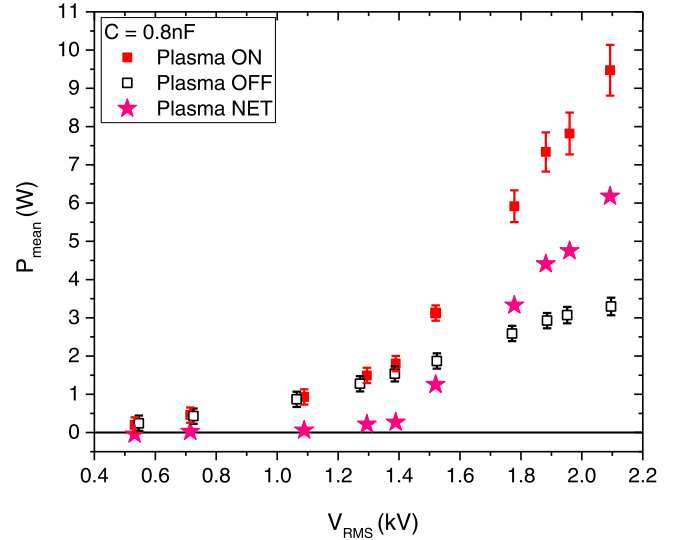


**Figure 7.** Mean power delivered to plasma jet  $P_{\text{mean}}$  in the presence (ON) and absence (OFF) of plasma as a function of applied voltage  $V_{\text{RMS}}$  for a configuration with  $C = 0.8$  nF in the grounded line. The power delivered only to plasma ( $P_{\text{mean(NET)}}$  points) is acquired by subtracting the values.

connected to the liquid target surface. By switching to that regime, the power  $P_{\text{mean}}$  jumps to higher values and continues to increase with increasing applied voltage.

In the case of the measurement of power consumption by plasma,  $P_{\text{mean,G}}$ , we used two different methods ( $V$ - $I$  and  $Q$ - $V$ ). With the serial resistor in the ground line ( $V$ - $I$  method), the power  $P_{\text{mean,G}}$  was calculated by using equations (3) and (7). When a capacitor was connected in series with the grounded target, the  $Q$ - $V$  method was employed. Figure 9 shows the dependence of the charge on the measurement capacitor on the applied peak-to-peak voltage for capacitor  $C = 0.8$  nF. Lissajous curves and the calculated deposited powers for three different input voltages of 5 kV, 5.5 kV, and 5.9 kV are presented.

The powers were calculated by using equation (4). Since both the applied voltage and the charge oscillate with the same frequency, a  $Q$ - $V$  plot will form an ellipsoid Lissajous figure. The elliptical shape of the  $Q$ - $V$  diagrams is obtained when a continuous plasma current flows during a full period of the high voltage signal [21, 48].

From the data in figure 9, it was apparent that the Lissajous loop retained the same shape and changed the slope (the line connecting points of minimum and maximum voltage) as the voltage changed. The centre of the ellipse coincided with the coordinate system point of origin. Comparing the results for two different capacitors, it was found that the power measured using the 10 nF capacitor was slightly higher than the power estimated with 0.8 nF capacitor for the same applied voltage. The difference was around 23%, and it can be due to capacitor properties or plasma adjustment to different circuit elements [33].

Charge-voltage plots for states with and without plasma at the same applied voltage for 0.8 nF and 10.3 nF monitor capacitors are presented in figures 10(a) and (b), respectively. Our measurements show that the obtained Lissajous figure in

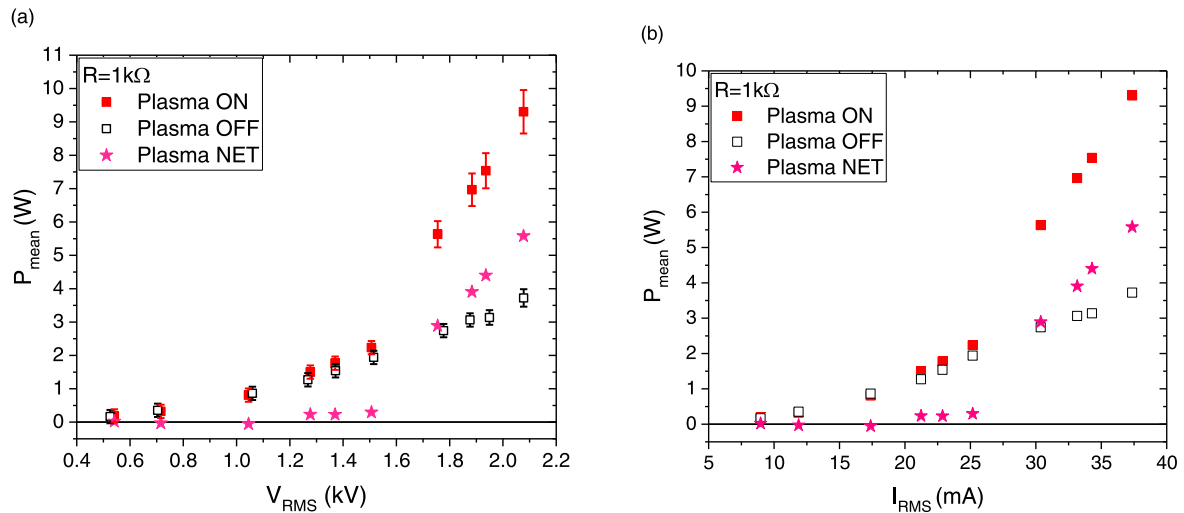


**Figure 8.** Mean power delivered to plasma jet  $P_{\text{mean}}$  in the presence (ON) and absence (OFF) of plasma for a configuration with  $R = 1 \text{ k}\Omega$  in the grounded line.  $P_{\text{mean(NET)}}$  points are acquired by subtracting the values. (a)  $P_{\text{mean}}$  dependence on the applied voltage  $V_{\text{RMS}}$ , (b)  $P_{\text{mean}}$  dependence on the current through plasma jet main line  $I_{\text{RMS}}$ .

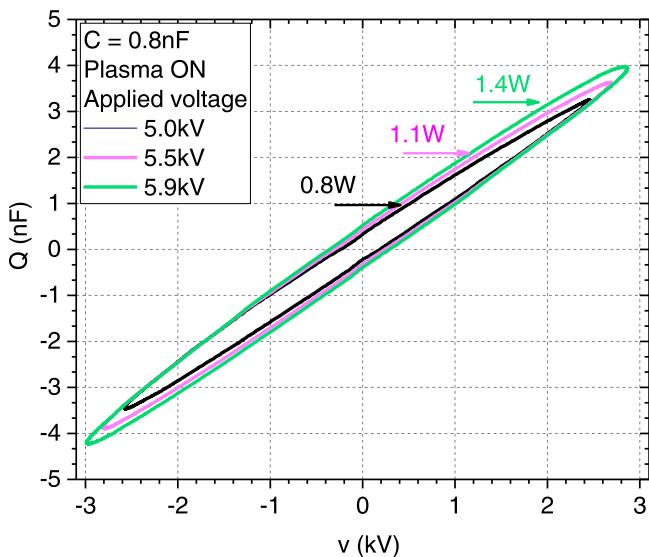


**Figure 9.** Charge-voltage plot (Lissajous figure) and consumed power  $P_{\text{mean\_G}}$  in the presence of plasma for three different applied peak-to-peak voltages (5 kV, 5.5 kV, 5.9 kV) and a signal frequency of 330 kHz. A capacitor of 0.8 nF was used for measurement.

the absence of plasma had a nonzero area, i.e. it was a very elongated ellipse. Usually, the curves obtained without plasma ignition in the  $Q$ - $V$  diagram are considered to be a straight line, as it was assumed in the other studies with different plasma sources employed [42, 44]. The existence of the elongated ellipse when plasma is not ignited may be the result of technical issues such as defective wire connections or uncompensated probes [48]. In our case, these contingencies were checked and excluded. So, this power dissipation in the Plasma OFF regime manifested the resistive losses present in the system, i.e. that a certain power was consumed in this part of the circuit even without plasma. This was observed also with Plasma OFF power values measured

at the plasma jet (figures 7 and 8). Comparing the plots in figure 10, it can be seen that the power losses measured with 10.3 nF capacitor are one order of magnitude less than those in the case of 0.8 nF capacitor. In the case of high excitation signal frequency, the parasitic properties of the capacitor can have a significant value, thus influencing the total impedance of the capacitor in the circuit [33, 41, 55]. This, in turn, influences the determination of power, particularly in the Plasma OFF case.

The  $Q$ - $V$  plot in the absence of plasma has a shape of an elongated ellipse, with the sharp turning point at maximum input voltage, meaning that the charge and supplied voltage are in phase reaching the peak value at the same time. When the plasma is turned on, a Lissajous curve gains rounded endpoints indicating additional resistive losses in the system. However, the waveforms of voltage across the capacitor  $v_G(t)$  and high voltage  $v(t)$  remain in the phase for Plasma ON. Therefore, it can be assumed that the ignition of plasma does not lead to an increase in the impedance of an element of the plasma jet system, which can change the phase between voltage signals. This analysis suggests that the power obtained with Plasma ON contains the total power consumed in the system. Thus, the determination of the mean power consumed only by plasma,  $P_{\text{mean\_G}}(\text{NET})$ , has to follow a similar procedure used for the  $V$ - $I$  method in equation (7): the power calculated from the Plasma OFF Lissajous figure should be subtracted from the power determined from the Plasma ON Lissajous figure for the same applied peak-to-peak voltage.

In order to evaluate the two methods for the determination of the dissipated power, the dependence of the mean power consumed by plasma  $P_{\text{mean\_G}}(\text{NET})$  on  $V_{\text{RMS}}$  was plotted in figure 11 with values obtained with three different electrical elements in the grounded line.

The power  $P_{\text{mean\_G}}(\text{NET})$  ranges from 0 to 1.7 W for  $V_{\text{RMS}}$  between 0.5 and 2 kV. Compared to the results calculated for the power  $P_{\text{mean}}$ , we observed that less than 30% of  $P_{\text{mean}}$  is consumed by the plasma and forwarded through the

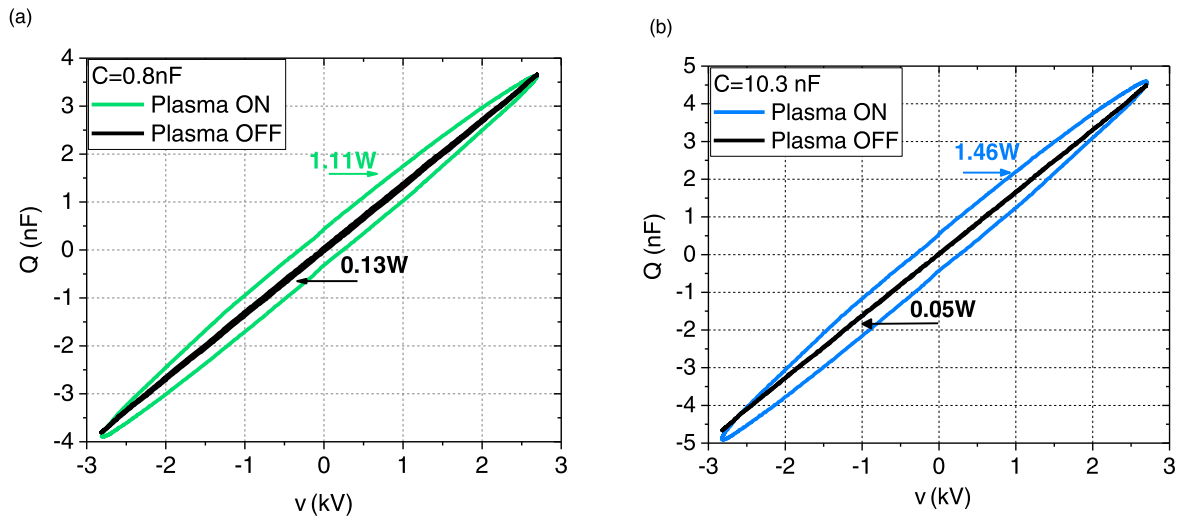


**Figure 10.** Charge-voltage plot (Lissajous figure) and consumed power  $P_{\text{mean}_G}$  for the applied peak-to-peak voltage of 5.5 kV and a signal frequency of 330 kHz. Data in (a) green and (b) blue represent state with plasma and data in black (a) and (b) represent state without plasma (without He flow). Capacitors of (a) 0.8 nF and (b) 10.3 nF were used for measurements.

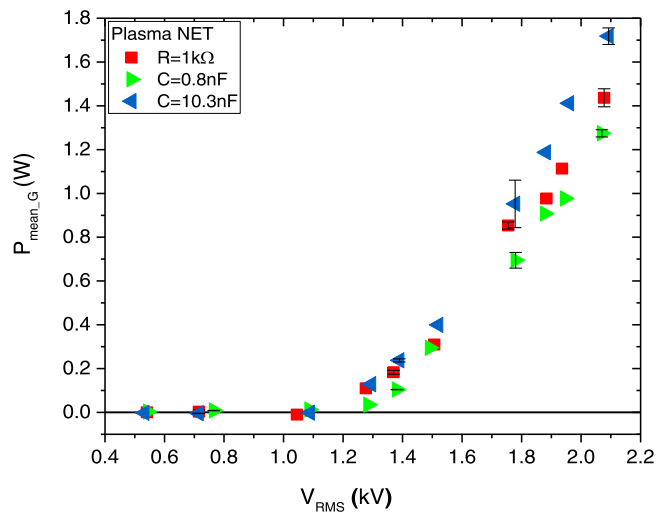


**Figure 11.** Mean power consumed by plasma  $P_{\text{mean}_G}$  (NET) for three different measuring elements in the grounded line.

grounded line. It can be seen in figure 11 that the power dependence on  $V_{\text{RMS}}$  calculated by the Lissajous figure (triangles) is in excellent agreement with those values obtained by the  $V$ - $I$  method (squares). The error bars were estimated as standard errors from three different measurements. In the  $V_{\text{RMS}}$  range from 0.5 to 1.1 kV, the calculated difference between powers measured in the presence and absence of plasma is close to zero. However, the plasma could be observed with the naked eye as a small bright region at the tip of the electrode, even in this range of applied voltages. Therefore, these power values were lower than the sensitivity of the methods.

### 3.5. Difficulties in measurements of power

The most common problems in the power measurement are unwanted losses in the circuit that affect repeatability of the measurements. The losses in the plasma jet system occur due

to the connections of the circuit elements, their quality i.e. characteristics, cables and also measuring equipment (especially when approaching the high frequency range). In the ground line of the electrical circuit, we noticed that any change in connections, such as the change of cables, connectors or a grounding technique, will affect the measured values. To minimize the power losses and ensure reproducible results, the cables of appropriate length, connection and quality should be selected before measurement.

Several cautions need to be noted regarding the use of the  $Q$ - $V$  method. The most common difficulties to pay attention to are: the selection of the appropriate type of capacitor, the use of proper cables for grounding the capacitor and the appearance of nodes or discontinuities in the curve.

First, the selection of an appropriate capacitor is considered as the most important part of the successful application of this method. It was found that different types of capacitors with the same capacitance yield different results. The use of film capacitors has been found to lead to non-physical results. When using a 10 nF metalized polyester (PET) capacitor, we measured more dissipated power when the plasma was OFF than when the discharge was ignited. In some cases when a PET capacitor was used, we observed a self-intersecting loop in the part of the figure where the charge and voltage change sign. The appearance of node points in the curve indicates different oscillation frequencies of the two signals—the applied voltage and capacitor voltage. These findings suggest that PET capacitors should not be used in the  $Q$ - $V$  technique for power determination, at least not with high-frequency signals.

The capacitor size should be chosen with respect to the plasma jet system capacitance, i.e. a capacitor should be selected that can store all of the charge that has passed through the discharge during one half-cycle of the applied voltage. This can be fulfilled if the capacitor size is at least one order of magnitude higher than the plasma source capacitance. In this work, the capacitance size was selected to be

three orders of magnitude greater than the plasma jet system capacitance.

As already mentioned, the connections in the grounded branch of the circuit greatly influence the repeatability of measurements. Small changes in the position of the cable between the grounded electrode and the monitor capacitor could cause changes in the inclination and width of the  $Q$ - $V$  elliptic loop. A suitable cable which does not influence the characteristics of the Lissajous curve should be selected for the measurement.

Finally, despite its type and capacitance, every capacitor gives open loops. The  $Q$ - $V$  plot is discontinuous because the curve after one period of applied voltage does not return to the starting point. That is, the charge and voltage values are different in points  $t = 0$  and  $t = T$ . This feature of the Lissajous figure has already been observed for DBD plasma reactors [41, 56]. Despite this, the integration of the figure area is still possible, although there is a gap in the curve. This issue can be diminished when using a high-resolution oscilloscope that provides waveforms with a large number of points.

The main challenge with the use of the  $V$ - $I$  method is resistor selection. It should be large enough to limit the discharge current. This is especially important in the case of low resistivity targets (conductive targets). An uncontrolled increase in discharge current can lead to a change in the type of discharge and then to heating and evaporation of the liquid target. However, the measurement resistor must be small enough to measure the voltage across the resistor with a voltage probe. Moreover, there are certain problems with using the  $V$ - $I$  method when a pulsed power source is used in the experiment. In that case, when calculating the power, it is necessary to perform integration over the entire pulse duration period. Integration over one part of the period of the input signal which is shorter than the pulse duration, gives an inaccurate result for the power deposition, as it could include only the positive or negative part of the waveform oscillation. This would lead to an underestimation or overestimation of the measured power.

#### 4. Conclusion

In this paper, we presented the results of electrical diagnostics of the He plasma jet powered by continuous sine HV signal and operating in contact with a liquid sample. The main goals were to use data from systematically performed measurements of the electrical parameters of such a system for the determination and comparison of the mean power consumed by plasma  $P_{\text{mean}_G}$  obtained by using two different methods -  $V$ - $I$  and  $Q$ - $V$ . It must be emphasized that the displacement current can be significant, especially in the case of atmospheric pressure plasma sources, and it needs to be taken into account. Since it is mainly a result of the capacitive characteristics of the plasma systems, it does not influence the mean power deposited to (consumed by) the plasma. This is evoked by the fact that the plasma jets in the configuration with the pin electrode are employed in different applications in contact with the liquid target, but without thorough

investigation of the power measurement techniques, especially for the case of a continuous wave power supply.

For that purpose, voltage and current waveforms were monitored and  $V$ - $A$  characteristics of the plasma jet and the discharge were established. The phase difference between the current and voltage signal showed mainly the capacitive nature of the system, regardless of the plasma presence in the system. As the obtained  $V$ - $A$  characteristics were linear, the data were used to determine the impedance of the whole system from the linear fitting of the plot. The impedance was almost the same regardless of the ground circuit configurations.

The mean power delivered to the plasma jet was determined by using the  $V$ - $I$  method and found to be up to 6 W for a  $V_{\text{RMS}}$  range between 0.5 kV and 2 kV. It was shown that plotting the power values using either voltage or current as an independent parameter results in the same power dependence.

The mean power consumed by the plasma was determined by using two different methods. In both case when the capacitor was inserted in the ground line of the electrical circuit, an elliptical shape of the Lissajous figure was obtained. However, the measured power observed with two different capacitors differs by 23%, suggesting a slightly different adjustment of the plasma operating point due to the system conditions. Also, it shows that the properties of the capacitor should not be neglected when calculating the power delivered to the plasma, as the capacitor should not be considered as an ideal element of the circuit. Nevertheless, this study has found that the discharge power dependence on  $V_{\text{RMS}}$  calculated by the  $V$ - $I$  method is consistent with those observed by the Lissajous figure ( $Q$ - $V$  method).

Nevertheless, proper utilization of the power measurement method is necessary if one performs an optimization of the energy efficiency of the plasma system. The mean power delivered to plasma calculated by both methods ranges from 0 to 1.7 W for a  $V_{\text{RMS}}$  range between 0.5 kV and 2 kV. Therefore, this means that less than 30% of the power delivered to the plasma jet is consumed by the plasma.

#### Acknowledgments

This research has been supported by MESTD Republic of Serbia (No. 451-03-68/2020-14/200024).

#### ORCID iDs

Olivera JOVANOVIĆ  <https://orcid.org/0000-0003-2633-1580>

Nevena PUAČ  <https://orcid.org/0000-0003-1142-8494>

Nikola ŠKORO  <https://orcid.org/0000-0002-0254-8008>

#### References

- [1] Laroussi M, Lu X and Keidar M 2017 *J. Appl. Phys.* **122** 020901
- [2] Khlyustova A et al 2019 *Front. Chem. Sci. Eng.* **13** 238



- [3] Bauer G et al 2019 *Sci Rep.* **9** 14210
- [4] Tomić S et al 2021 *Cancers* **13** 1626
- [5] Puač N, Gherardi M and Shiratani M 2018 *Plasma Process. Polym.* **15** 1700174
- [6] Graves D B et al 2019 *Plasma Chem. Plasma Process.* **39** 1
- [7] Magureanu M et al 2021 *J. Hazard. Mater.* **417** 125481
- [8] Foster J E 2017 *Phys. Plasmas* **24** 055501
- [9] Škoro N et al 2018 *Eur. Phys. J. D* **72** 2
- [10] Janić Hajnal E et al 2019 *Toxins* **11** 704
- [11] Bruggeman P J, Iza F and Brandenburg R 2017 *Plasma Sources Sci. Technol.* **26** 123002
- [12] Brandenburg R 2017 *Plasma Sources Sci. Technol.* **26** 053001
- [13] Reuter S, Von Woedtke T and Weltmann K D 2018 *J. Phys. D: Appl. Phys.* **51** 233001
- [14] Sobota A, Guaitella O and Rousseau A 2014 *Plasma Sources Sci. Technol.* **23** 025016
- [15] Puač N et al 2012 *Appl. Phys. Lett.* **101** 024103
- [16] Winter J, Brandenburg R and Weltmann K D 2015 *Plasma Sources Sci. Technol.* **24** 064001
- [17] Robert E et al 2012 *Plasma Sources Sci. Technol.* **21** 034017
- [18] Nijdam S, Teunissen J and Ebert U 2020 *Plasma Sources Sci. Technol.* **29** 103001
- [19] Walsh J L et al 2010 *J. Phys. D: Appl. Phys.* **43** 075201
- [20] Lu P et al 2017 *Appl. Phys. Lett.* **110** 264102
- [21] Xiong Q et al 2010 *Phys. Plasmas* **17** 043506
- [22] Simoncelli E et al 2019 *Plasma* **2** 369
- [23] Sobota A et al 2019 *Plasma Sources Sci. Technol.* **28** 045003
- [24] Judée F et al 2019 *J. Phys. D: Appl. Phys.* **52** 245201
- [25] Kutasi K et al 2019 *Plasma Sources Sci. Technol.* **28** 095010
- [26] Kovačević V V et al 2018 *J. Phys. D: Appl. Phys.* **51** 065202
- [27] Bruggeman P and Brandenburg R 2013 *J. Phys. D: Appl. Phys.* **46** 464001
- [28] Machala Z et al 2019 *J. Phys. D: Appl. Phys.* **52** 034002
- [29] Ng S W et al 2021 *J. Appl. Phys.* **129** 123303
- [30] Kostov K G et al 2014 *Appl. Surf. Sci.* **314** 367
- [31] Ghimire B et al 2018 *Appl. Phys. Lett.* **113** 194101
- [32] Deng X L et al 2013 *J. Appl. Phys.* **113** 023305
- [33] Gerling T et al 2017 *Eur. Phys. J. Appl. Phys.* **78** 10801
- [34] Takeda K et al 2019 *J. Phys. D: Appl. Phys.* **52** 165202
- [35] Prysiashnyi V, Ricci A H C and Kostov K G 2016 *Braz. J. Phys.* **46** 496
- [36] Maletić D et al 2017 *J. Phys. D: Appl. Phys.* **50** 145202
- [37] Hensel K et al 2015 *Biointerphases* **10** 029515
- [38] Van Gils C A J et al 2013 *J. Phys. D: Appl. Phys.* **46** 175203
- [39] Stancampiano A et al 2020 *IEEE Trans. Radiat. Plasma Med. Sci.* **4** 335
- [40] Laurita R et al 2021 *Plasma Process. Polym.* **18** 2000206
- [41] Ashpis D E, Laun M C and Griebeler E L 2017 *AIAA J.* **55** 2254
- [42] Biganzoli I et al 2014 *J. Phys. Conf. Ser.* **550** 012039
- [43] Hořub M 2012 *Int. J. Appl. Electromagn. Mech.* **39** 81
- [44] Pipa A V et al 2012 *Rev. Sci. Instrum.* **83** 075111
- [45] Lu X P et al 2019 *Nonequilibrium Atmospheric Pressure Plasma Jets: Fundamentals, Diagnostics, and Medical Applications* (Boca Raton: CRC Press)
- [46] Weltmann K D et al 2010 *Pure Appl. Chem.* **82** 1223
- [47] Nguyen T T et al 2019 *Plasma Res. Express* **1** 015009
- [48] Peeters F and Butterworth T 2019 Electrical diagnostics of dielectric barrier discharges *Atmospheric Pressure Plasma—from Diagnostics to Applications* (London: Intech Open) p 8
- [49] Maletić D et al 2015 *Plasma Sources Sci. Technol.* **24** 025006
- [50] Chang Z S et al 2018 *Sci Rep.* **8** 7599
- [51] Li J et al 2021 *Commun. Phys.* **4** 64
- [52] Darny T et al 2017 *Plasma Sources Sci. Technol.* **26** 045008
- [53] Klarenaar B L M et al 2018 *Plasma Sources Sci. Technol.* **27** 085004
- [54] Law V J and Anghel S D 2012 *J. Phys. D: Appl. Phys.* **45** 075202
- [55] Wang R X et al 2021 *IEEE Trans. Plasma Sci.* **49** 2210
- [56] Jiang H et al 2013 *IEEE Trans. Dielectr. Electr. Insul.* **20** 1101



# Helium atmospheric pressure plasma jet parameters and their influence on bacteria deactivation in a medium

Andrea Jurov<sup>1,2,a</sup>, Nikola Škoro<sup>3</sup>, Kosta Spasić<sup>3</sup>, Martina Modić<sup>1</sup>, Nataša Hojnik<sup>1</sup>, Danijela Vujošević<sup>4</sup>, Milena Đurović<sup>4</sup>, Zoran Lj. Petrović<sup>5,6</sup>, and Uroš Cvelbar<sup>1,2</sup>

<sup>1</sup> Jozef Stefan Institute, Jamova 39, 1000 Ljubljana, Slovenia

<sup>2</sup> Jozef Stefan International Postgraduate School, Jamova 39, 1000 Ljubljana, Slovenia

<sup>3</sup> Institute of Physics, University of Belgrade, Pregrevica 118, Belgrade 11080, Serbia

<sup>4</sup> Center for Medical Microbiology, Institute of Public Health Montenegro, Dzona Dzeksona bb, 81000 Podgorica, Montenegro

<sup>5</sup> Serbian Academy of Sciences and Arts, Knez Mihajlova 35, Belgrade 11001, Serbia

<sup>6</sup> School of Engineering, Ulster University, York St., Belfast BT15 1ED, UK

Received 22 November 2021 / Accepted 25 January 2022

© The Author(s), under exclusive licence to EDP Sciences, SIF and Springer-Verlag GmbH Germany, part of Springer Nature 2022

**Abstract.** Atmospheric pressure plasmas are becoming relevant in local microbial deactivation and other combined effects of plasmas on living organisms. For this reason, our research was focussed on optimisation of atmospheric pressure plasma jet (APPJ) parameters to complete the deactivation of different bacteria strains in a medium. Different helium APPJ treatments with different discharge parameters were used, such as input voltages and gas flows. To better understand plasma properties behind complete bacteria deactivation at optimised discharge parameters, optical and electrical plasma jet diagnostics were performed, including electrical characterisation of the plasma source, optical emission spectroscopy of the plasma plume and intensified charged coupled device imaging of the discharge behaviour for every set of plasma parameters. Then, the resulting plasma liquid chemistry was assessed to establish the connections between reactive species generated in the gaseous and liquid phases. The most efficient deactivation was found for higher discharge powers and gas flow rates, and that was linked to higher densities of reactive oxygen and nitrogen species, especially hydrogen peroxide and medium solvated charges.

## 1 Introduction

It is well known that some microorganisms, such as bacteria, fungi and viruses, act as pathogens and induce various diseases. Moreover, microorganisms can cause food spoilage and damage to materials such as corrosion of plumbing systems. For these reasons, several conventional sterilisation techniques which lead to complete microbial deactivation or removal have been developed, including heating, filtration, chemical liquid agents and radiation. However, a disadvantage of these sterilisation techniques is that they can be used only on thermally resistant and chemically inert substrates, as those techniques can influence substrate properties [1].

In recent years, non-thermal atmospheric pressure plasmas have been proposed as an alternative to conventional sterilisation techniques. Most frequently reported is sterilisation with atmospheric pressure plasma jets (APPJs) due to their low operating temperatures and cost-effective operation [2–5]. APPJs are suitable for selective treatment of specific substrates as they contain more known inactivation agents without

the downsides of conventional sterilisation techniques. Research suggests that reactive oxygen species play the biggest role in bacteria inactivation, but UV radiation, electric field, other reactive species and charged particles also contribute to the process [5–8]. In this way, APPJs represent one of the most promising discharge candidates for different biological applications, including complete deactivation of bacteria [9–12].

This research tested the efficiency of a constructed APPJ on four different bacteria: *Escherichia coli*, *Staphylococcus aureus*, *Bacillus subtilis*, and *Bacillus stearothermophilus*. *B. stearothermophilus* and *B. subtilis* are spore-forming bacteria and the most commonly recognised and widely used biological indicators for monitoring the effectiveness of sterilisation processes. Spores are dormant bacterial structures, highly resistant to disinfectants and sterilising agents. Spore-forming bacteria are commonly found in processed foods and dairy products [13–15]. These bacteria were tested in order to see how an APPJ affects spore-forming bacteria. Additionally, *E. coli* and *S. aureus*, the most common pathogens in humans and widespread in nature (in hospitals and working and living surroundings), were selected. They are commonly found

<sup>a</sup> e-mail: [andrea.jurov@ijs.si](mailto:andrea.jurov@ijs.si) (corresponding author)

in different environments, contaminating various items, medical tools and food, and can cause hospital infections and food poisoning, as well as medically severe and sometimes fatal infections [16–19]. Moreover, these bacterial strains are known to possibly be multidrug-resistant [20, 21]. In addition, these bacteria tend to form biofilms where bacteria are well protected from the outside agents. It has been shown that plasmas may sterilize even the biofilms as well as planktonic samples [22].

There have been many reports on atmospheric pressure plasma-induced bacteria deactivation and decontamination [23–27]. However, there is a knowledge gap in optimising plasma parameters so that complete bacteria deactivation in a medium can be achieved in the shortest (optimal) times. Therefore, this research focuses on finding the most efficient parameters of a non-thermal helium APPJ as one of the most frequently used sources for deactivating bacteria. For this purpose, various combinations of input DC power unit voltages and gas flows were tested. Appropriate diagnostics were done both on plasma source and discharge, and on medium bacteria were suspended in.

## 2 Experimental setup

### 2.1 Preparation of bacteria samples

The deactivation effect of an APPJ, operated with helium as a working gas, was investigated on four different types of bacteria: *B. stearothermophilus* (ATCC No. 7953), *B. subtilis* (ATCC No. 6633), *S. aureus* (ATCC No. 25923) and *E. coli* (ATCC No. 25922). Bacterial cultures were grown overnight on Columbia (COS) agar plates (bioMérieux SA, Marcy l’Etoile, France) at 55 °C for *B. stearothermophilus* and 37 °C for *B. subtilis*, *S. aureus* and *E. coli*. Bacteria were picked up with a loop and resuspended in sterile saline to obtain 0.5 McF ( $1.5 \times 10^8$  CFU/ml) initial bacterial suspension. The concentration was constant in all experiments. 100  $\mu$ l of these initial 0.5 McF bacterial suspensions was evenly transferred to a 96-well plate with a flat bottom. Bacterial suspensions were exposed to the He APPJ at a constant distance for different exposure times. The samples were treated each time in triplicates.

To determine viable counts and evaluate plasma treatment effects, the Miles and Misra viable count

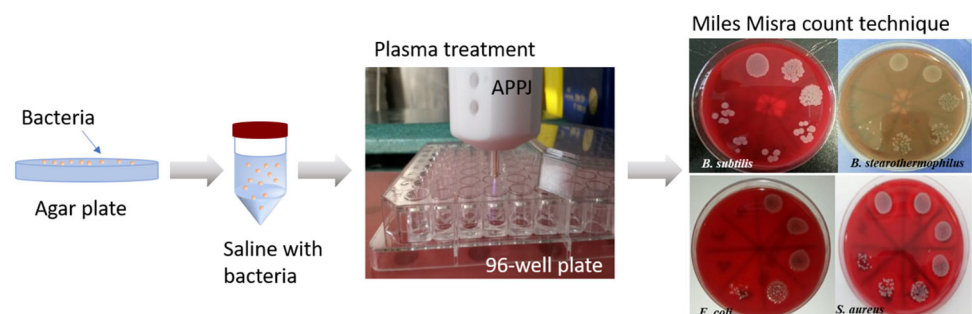
technique on COS blood agar plate (bioMérieux SA, Marcy l’Etoile, France) was used. A 20  $\mu$ l properly diluted plasma-treated bacterial suspension, as well as a positive (untreated bacterial suspension) and negative control (sterile saline), was placed onto the blood agar plate. This procedure is depicted in Fig. 1. Measurements of the reactive species and pH were also conducted. Reactive species concentrations of  $\text{NO}_2^-$  and  $\text{H}_2\text{O}_2$  were measured by a spectrophotometer (UV VIS Lambda 25) via colorimetric assays in sterile saline. The pH measurements were performed by a pH-meter (Sentron<sup>®</sup>) also in saline.

### 2.2 APPJ system

Bacteria-containing medium was treated by APPJ source which is designed to be handheld and highly portable, schematic of which is shown in Fig. 2. The portability of the device was facilitated by a small-size custom-made power source which is placed inside a 20  $\times$  12  $\times$  6 cm plastic box including connectors and switches. It was connected to a commercial DC power supply Voltcraft SPS12-12 W-A. The power source output signal amplitude was varied by changing the DC input signal voltage, at discrete voltages 3, 4.5, 6, 9 and 12 V. Based on the DC input voltage, the output signal at 16 kHz was supplied to the jet enabling plasma operation at several high voltages from 1200 to 3500 V (RMS values). The jet had a copper wire, which serves as needle-type powered electrode that was placed inside the glass tube with inner diameter of 2 mm and outer diameter of 4 mm. The tube itself is held by 125 mm long and 26 mm wide Teflon housing, from which it protrudes 8 mm on the one side. On the other side, the tube was connected to gas inlet and Bronkhorst Mass-View MV-194 flow controller. For these treatments, we used He as a working gas at various fixed flows (0.5, 1, 1.5 and 2 slm).

Optical characterisation comprised optical emission spectrometry and plasma imaging by using an intensified charged coupled device (ICCD) camera. Optical emission spectroscopy was performed with an Andor Shamrock 500i spectrometer equipped with iXon Ultra 897 as a detector. An optical fibre was used to receive the emission from the plasma plume and direct it to the entrance slit of the spectrometer. The fibre was positioned at a distance of 5 cm from the jet tube

**Fig. 1** Schematic representation of the experimental protocol procedure



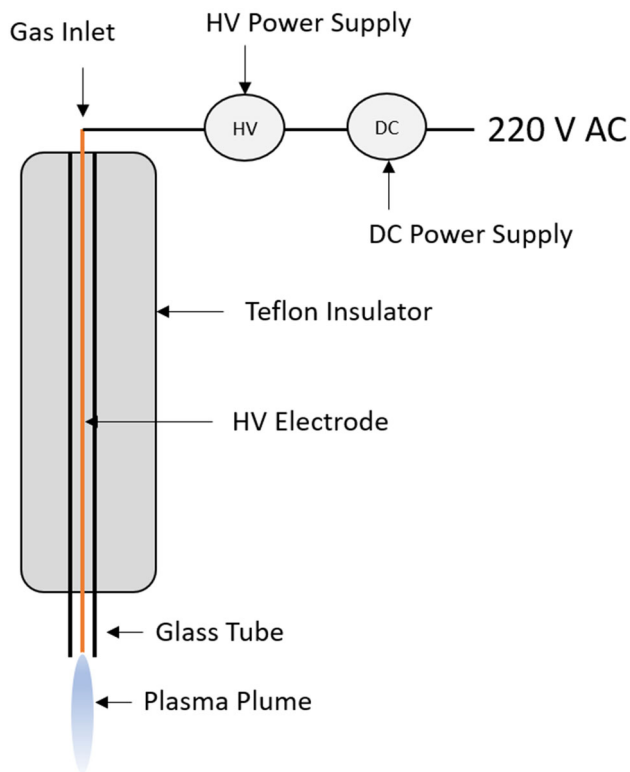


**Fig. 2** Schematic representation of an APPJ used in this research

axis to gather the light coming from the whole channel volume. Recording of the spectra was performed for exposure times of 100 ms and with averaging of 10 spectrum acquisitions. Thus, obtained results represent space- and time-averaged emission from the plasma. Plasma imaging was performed with an Andor iStar ICCD camera DH334T-18U-03 equipped with a photographic objective. Images were taken in single-shot mode with an exposure time of 20 ms. Furthermore, electrical characterisation was performed by measuring the average power given to the jet. Voltage and current on the powered electrode were measured before the APPJ with an oscilloscope (Rigol DS1102E), high voltage probe (Rigol RP1018H) and current monitor (Pearson 8590C).

Estimation of saline solution evaporation during treatments was performed to evaluate changes in the treatment conditions throughout the experiments. For the longest treatment times, the highest DC supply voltages and He flow of 2 slm, the evaporated solution volume from the 96-well plate was not more than 50  $\mu$ l. This change in volume caused a maximum liquid level reduction of 1.2 mm, thus increasing the distance between the plasma jet and the liquid surface. However, these changes did not drastically influence plasma properties, and these maximum values were reached only for the longest treatment times and plasma powers. For most treatment conditions, volume changes fell within the experimental error of transferring the liquid volume into the plate.

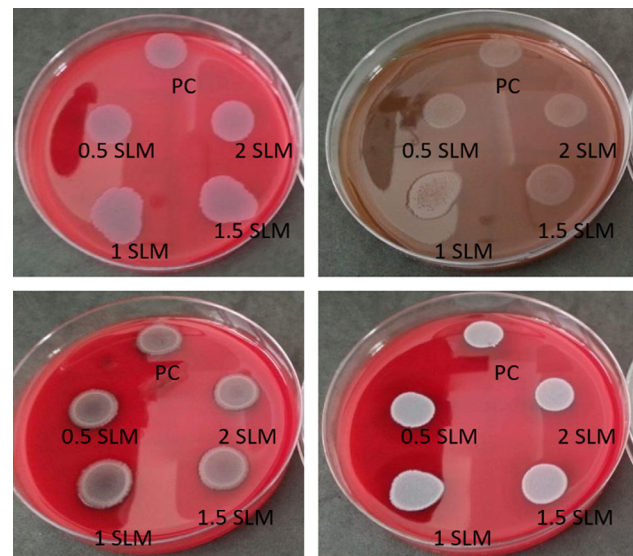


**Fig. 3** Effect of gas flow-only (no plasma) treatment of bacteria **a** *B. subtilis*, **b** *B. stearothermophilus*, **c** *E. coli* and **d** *S. aureus* exposed to 0.5, 1, 1.5 and 2 slm compared to the positive control (PC) by Miles and Misra plate counting

## 3 Results and discussion

### 3.1 Bacteria deactivation

At first, bacterial suspension control samples were exposed only to helium gas flow with rates of 0.5, 1, 1.5 and 2 slm, without plasma and with no voltage applied, for the same duration as required for deactivation using the plasma. The obtained results exhibit no difference in bacteria viability (Fig. 3) compared to the untreated samples (positive control; PC), which confirms that helium alone is insufficient for bacteria deactivation. The effects of the APPJ were then further tested for all bacteria and analysed with a quantitative and informative approach, which involved dynamical studies of bacterial growth after treatments. Typically, survival curves were determined as the numbers of colony-forming units (CFUs; surviving culturable bacteria as a function of plasma treatment time). However, to limit the presentation, only complete bacteria deactivation, achieving sterility of the medium, is shown in Fig. 4.

Furthermore, Fig. 4 presents the time needed for complete deactivation of *E. coli*, *S. aureus*, *B. stearothermophilus* and *B. subtilis* within a medium, exposed to a He APPJ generated with different DC input powers and gas flows. If there are no data shown for a specific set of parameters (usually 3 V and 0.5 slm), the bacteria were not completely deactivated within the maximum treatment time of 240 s used in experiments. In most cases, it was found that *E. coli* was deactivated faster than other bacteria, proving to be a less plasma-resistant strain. In this case,

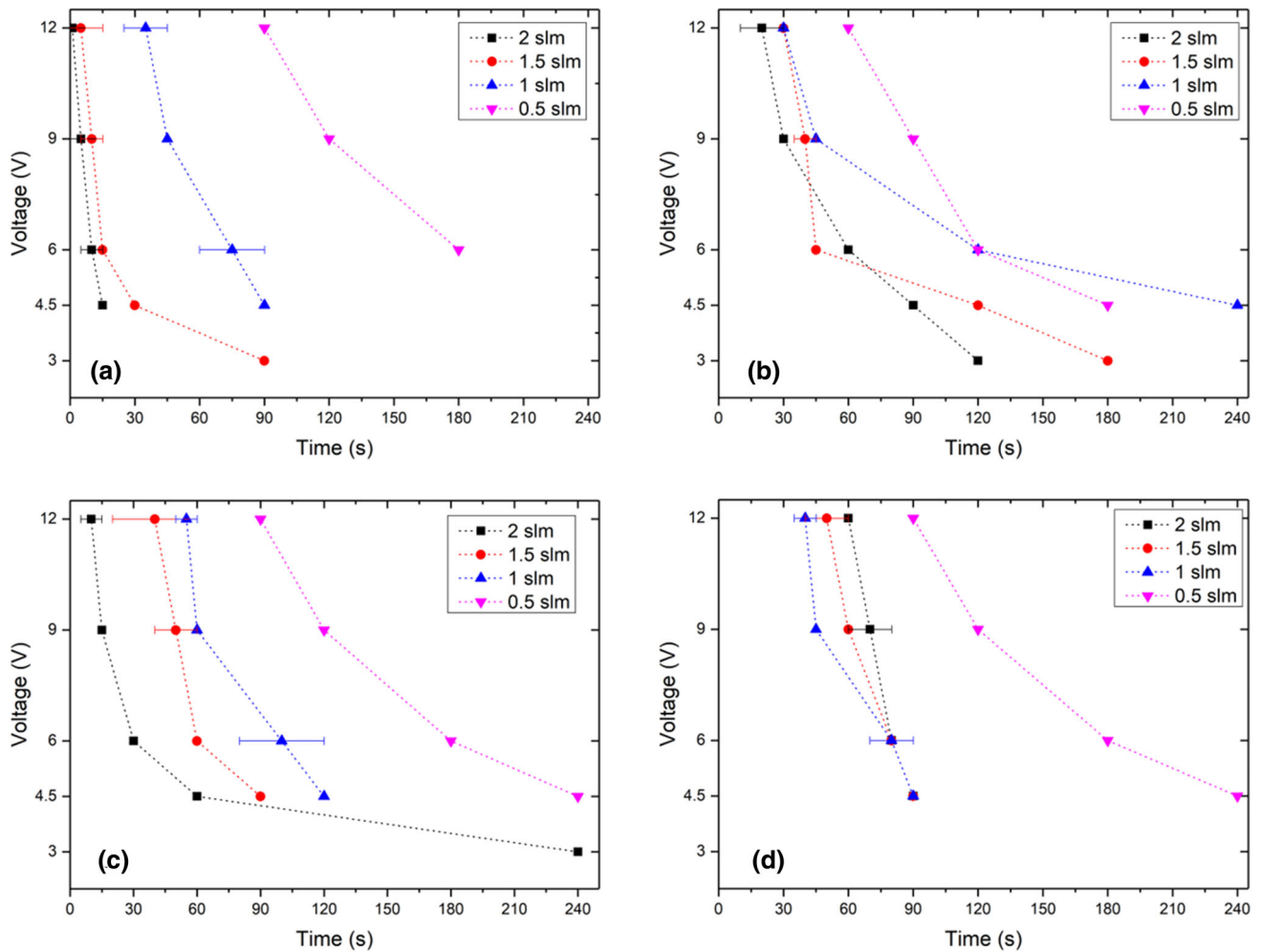


**Fig. 4** Points of complete bacteria deactivation (the point at which the initial CFU/ml concentration drops to zero) **a** *E. coli*, **b** *S. aureus*, **c** *B. subtilis* and **d** *B. stearothermophilus* exposed to He APPJ generated with powers of 3, 6, 9 and 12 V, and flow rates of 0.5, 1, 1.5 and 2 slm

the highest treatment time was 180 s for deactivation under the lowest gas flow of 0.5 slm, which typically did not prove very efficient. *B. stearothermophilus* strains proved the most resistant to plasma treatments. Surprisingly, the lowest flow rate deactivation curves for 0.5 slm are very similar for all types of bacterial strains, except a small deviation with *E. coli*. This indicates that the APPJ generated at these conditions and its consequent reactive oxygen and nitrogen species (RONS) chemistry within the medium are similar (although, moving to higher flow rates, the chemistries and deactivations changed significantly). The trend follows the same patterns, where 0.5 slm is the least, and 2 slm is the most efficient, which are plasma properties connected to its subsequent interaction. The exception to this general rule is *B. stearothermophilus*, the most thermally stable and resistant strain, which seems to deviate from the rule. In this case, the most efficient chemistry for deactivation is at 1 slm. Chemical analyses of the medium chemistry elucidate the reasons for this behaviour in the following paragraphs.

From the perspective of the DC input voltage parameter used for jet discharge, the general rule is: the higher the energy input into discharge, the faster the deactivation of bacterial strains. However, it seems there is a minimum level at which the jets are efficient. It was found that an input DC voltage of 3 V was not sufficient to deactivate most bacteria strains even for the highest gas flow and treatment times because the plasma plume was the shortest and was not in direct contact with the substrate. If deactivation of the bacteria strain was achieved, then the treatment time was significantly prolonged. Therefore, the results indicate that He APPJ is most efficient at bacteria strain deactivation with higher applied power and higher gas flows, considering marked limits in discharge parameters and experimental constraints. We do not reach conditions where additional heating would produce thermal necrosis (40 °C) in the covered range of powers. While increasing efficiency with power is expected as for the flow, one could expect that beyond some point, further increasing of the flow may reduce efficiency by affecting the chain of

plasma chemical events needed to produce the radicals that cause sterilization.

### 3.2 Chemical analysis of reactive species of saline medium treated by APPJ

To explain the obtained results for bacterial deactivation in a medium, the initiated medium chemistry was investigated, determining RONS species, especially  $\text{H}_2\text{O}_2$  and  $\text{NO}_2^-$  concentrations of the APPJ treated saline solution. Immediately after treatments, we performed measurements of pH changes. These parameters are known to influence the viability of bacterial strains significantly, as marked by numerous reports [28–31].

*pH measurements* were made under the same conditions as for reactive species measurement. The influence of different He plasma parameters (different gas flow rates of 0.5, 1, 1.5 and 2 slm and different input DC powers of 3, 4.5, 6, 9 and 12 V) on pH value was systematically measured. A pH value decrease was observed during the plasma treatment for most cases (Fig. 5). These decreasing trends featured an initial drop and then a steady decrease. An exception was 1 slm, which had an increasing pH trend for input DC voltage of 3 V. This could be explained by the fact that the plasma jet did not touch the surface of the liquid, and in this case, the chemistry of the medium was different than in other cases.

Reactive species concentrations of  $\text{NO}_2^-$  and  $\text{H}_2\text{O}_2$  were determined after plasma treatment of saline; 50  $\mu\text{l}$  of sterile saline was placed in the 96-well plate with a flat bottom. The distance between the bottom of the well and the APPJ orifice was 15 mm, as for the treatment of bacteria, and was kept constant during the treatment. The results are presented in Fig. 6, and the results are obtained with only the parameters yielding the most efficient plasma treatment—input voltage of 12 V and a flow rate of 2 slm. An expected, steady increase of  $\text{H}_2\text{O}_2$  concentrations was observed for increasing treatment time. In contrast, the concentration of  $\text{NO}_2^-$  increased until 30 s, where it reached its maximum value and then started decreasing. The concentration dropped to zero after 120 s. This could be explained through decreasing of the pH value during the treatment.  $\text{NO}_2^-$  is very sensitive to low pH values, which is the cause of its decomposition or transformation into other compounds [32].

### 3.3 Diagnostics of the plasma source

In order to analyse properties of the plasma used for treatments, we performed diagnostic experiments at the same conditions as when treating media with bacterial strains. Due to safety, a saline medium was used without bacteria for these measurements.

*Power measurements* were made via electrical characterisation, where the average power ( $P_{\text{avg}}$ ) input into

the jet was measured. This was calculated over 30 periods of current and input voltage as:

$$P_{\text{avg}} = \frac{1}{30T} * \int_{t_1}^{t_2} P(t) dt,$$

where  $T$  is oscillation period, and  $P(t)$  is instantaneous power in every moment  $t$  calculated as  $I(t) * V(t)$  from the beginning  $t_1$  and end  $t_2$  of 30 periods. The measurements were performed on the electrode before the plasma jet coming out of the tube and at two gas flow rates of 1 and 2 slm. The calculated values present an average power that the power source gives to the plasma jet (Fig. 7 left axis) and represents the ‘real’ power input into plasma. In order to link electrode voltage and power and to facilitate comparison to the other experimental data, we calculated  $V_{\text{RMS}}$  values as a function of input DC voltage (Fig. 7 right axis). The RMS values were calculated for 30 periods assessing several  $V(t)$  signals at the same DC voltage in order to estimate differences. The measurements were performed on the electrode at two gas flow rates of 1 and 2 slm. It was observed that the power was not influenced by the gas flow rate but was instead dependent on the DC input voltage and provided powers in the range of 0.1–1.5 W. The power that is transferred from plasma to the treated samples is somewhat lower than calculated power since part is always lost.

*Optical emission spectroscopy* was used as a plasma diagnostic tool. A typical spectrum of He discharge of an APPJ at gas flow rate of 2 slm where a jet was positioned above the saline solution target is presented in Fig. 8. The spectrum was recorded in a wide range of wavelengths, between 300 and 800 nm. The characteristic spectrum of excited species has already been assessed for this kind of plasma jet [33–35]. The most intense lines came from the molecular OH (A–X) band, atomic lines of He and O, and molecular bands of  $\text{N}_2$ ; the second positive system (SPS) and the first positive system as well as from the nitrogen ion—the first negative system (FNS) [36, 37]. Excited He atoms were produced from the ground state neutrals in the working gas used in the system. At the same time, OH and  $\text{N}_2$  bands and atomic O lines and H $\alpha$  line were present since the experiments were conducted in an ambient air (with some humidity) and in contact with the saline solution. Neutral species from the surrounding air were mixed with the helium flow and therefore participated in gas phase reactions induced by plasma [38, 39]. In contrast to the case where solid NaCl was treated [40], the spectrum obtained with saline solution did not show any additional lines from Na (or Cl). This suggests that these species were not excited in the gas phase above the water for the plasma source to excite them.

Additional analysis regarding line intensity was performed on specific atomic and molecular lines for different DC input voltages used in the experiment (3, 4.5, 6, 9 and 12 V) at two gas flows (1 and 2 slm). The intensities at different discharge parameters with two emission lines from  $\text{N}_2$  SPS (337.1 nm and 315.9 nm), head

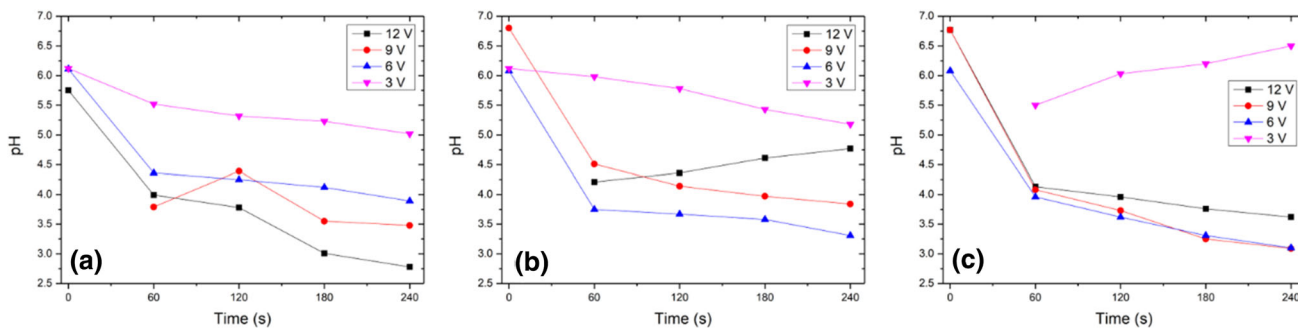


Fig. 5 pH values of He APPJ treated saline for gas flow of a 2 slm, b 1.5 slm and c 1 slm

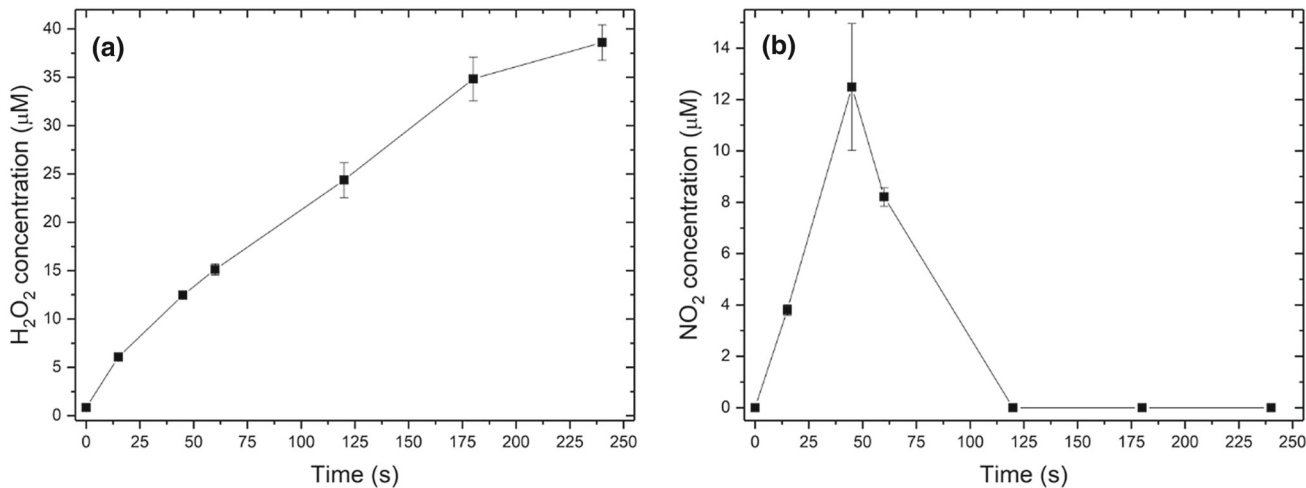


Fig. 6 Concentration of reactive species: a H<sub>2</sub>O<sub>2</sub> and b NO<sub>2</sub><sup>-</sup> with respect to treatment time

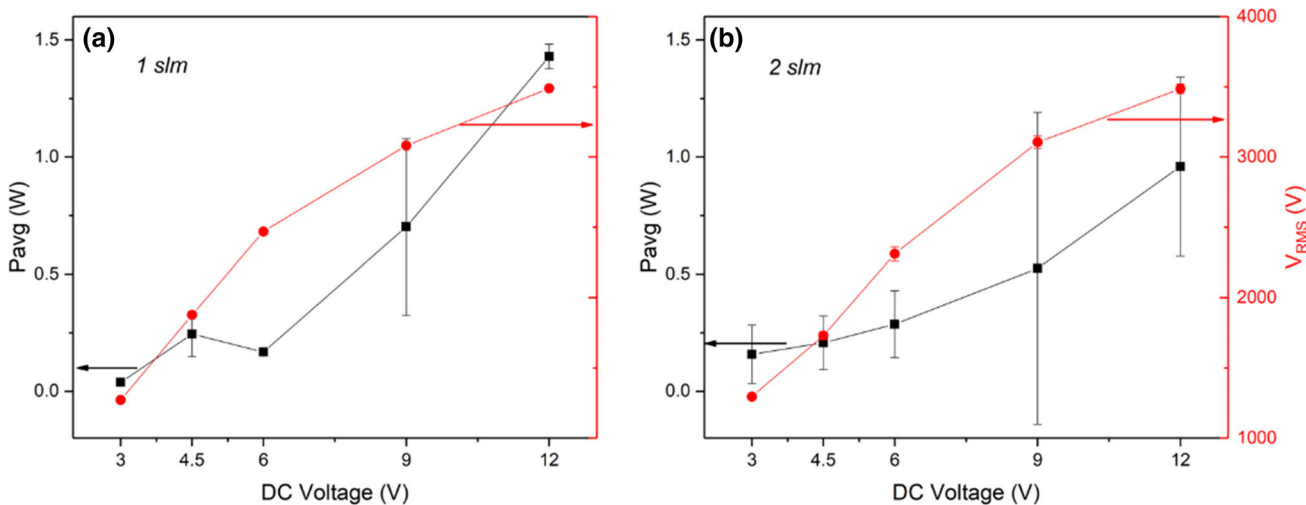
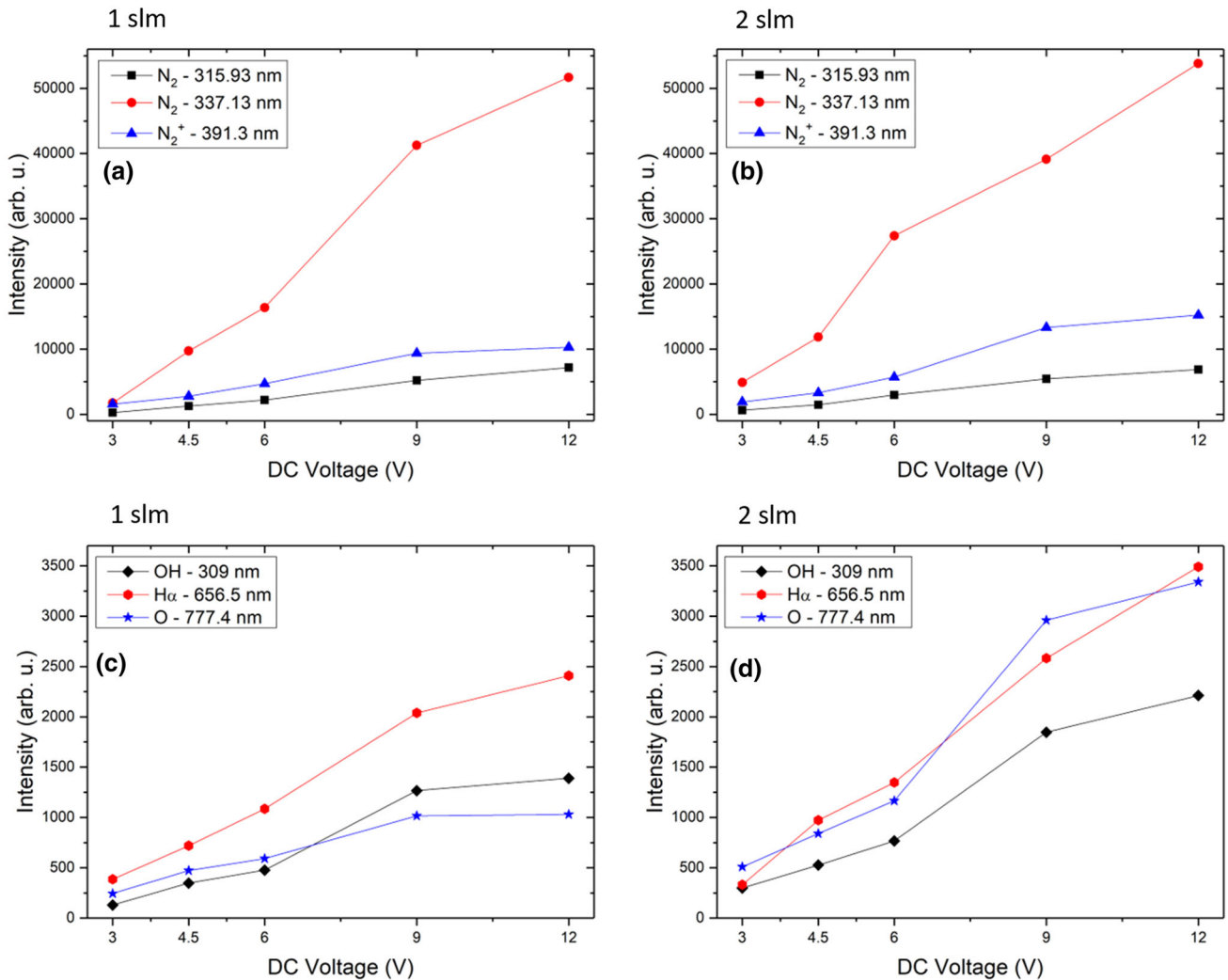
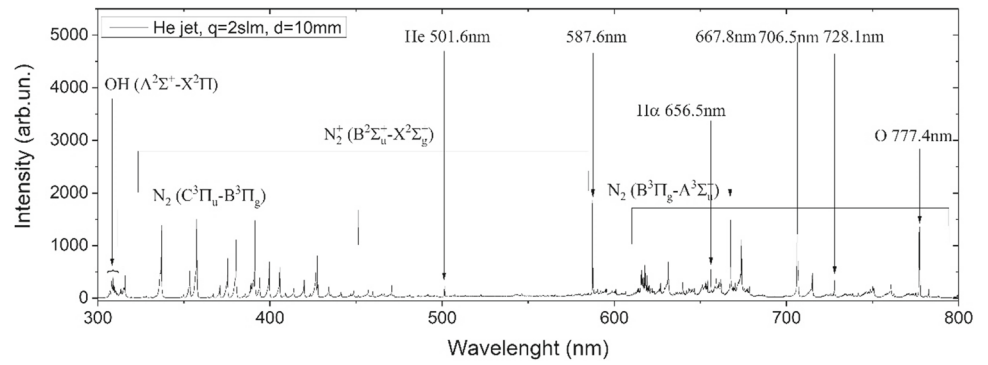


Fig. 7 Average input power to the plasma jet for He gas flows of a 1 slm and b 2 slm

**Fig. 8** Optical emission spectroscopy of the He APPJ with a characteristic spectrum generated during the treatments above the liquid medium



**Fig. 9** Optical emission spectroscopy: intensities of certain atomic and molecular lines of nitrogen (a for 1 slm and b for 2 slm), and hydrogen, oxygen and hydroxyl c for 1 slm and d for 2 slm)



line from FNS  $N_2^+$  (391.3 nm), the strongest molecular OH line (309 nm),  $H\alpha$  (656.6 nm) and O atom line (777.4 nm) are presented in Fig. 8, while He line (706.5 nm) intensities are depicted in Fig. 9. All line intensities are normalised to the same recording conditions and corrected for spectral efficiency of the system, thus allowing direct intensity comparison between different lines. The position of the jet and the distance to the bottom of the 96-well plate were the same as for the treatments of bacteria. There was an increase in intensities for all observed lines when the source power (DC voltage) was increased. The increase of He flow had a minor influence on line intensities, resulting in a somewhat higher line intensity. In all cases, there was a stronger or weaker ‘jump’ between the emission intensities recorded for 6 V and 9 V. This change in peak values occurred due to the change in plasma regime since, as observed with the naked eye, the plasma channel did not connect to the surface of the saline until the 9 V were reached [41]. Therefore, the intensities recorded for voltages below 9 V can be regarded as free-standing jet cases, while for the voltages of 9 V and 12 V, plasma plume was in contact with the liquid surface.

The highest line intensities belong to the mainline of  $N_2$  SPS, and these intensities have pronounced increments between 6 and 9 V input voltage (Fig. 9a and b). The second strongest line of the same band has a much lower increase in intensity. However, excitation of both of the excited levels in  $N_2$  probably happened through electron collisions with the ground state or excited  $N_2$  molecules [35, 42]. The increasing line intensity tendency is in accordance with the dependence observed with similar jet configurations [34]. The intensity of the strongest of FNS  $N_2^+$  lines at 391.3 nm also increased with DC voltage, yet much less than the 337.1 nm line (Fig. 9a and b). This line comes from the excited state of  $N_2^+$  ions that were efficiently produced in the Penning ionisation process, involving He metastables [43] and the direct electron impact ionisation process [42]. Consequently, an increase in He flow made the emission of the 391.3 nm line rise. On the other hand, lines from the OH band and  $H\alpha$  came from dissociation of water vapour molecules in plasma [35, 44]. In this jet configuration, the amount of water vapour present in the surrounding air was sufficient to produce several excited species of OH and H visible in the emission spectrum. An increase in the He flow and discharge voltage resulted in the increase of OH emission intensity (Fig. 9c and d), which has been observed before [34, 45]. The atomic O (777.4 nm) line exhibited similar behaviour. Production of both OH and O species is important when it comes to the treatment of bacteria.

The intensity trend of the He line at 706.5 nm was similar to that of other spectral lines and is presented in Fig. 10. As expected, line intensity was observed to increase when we increase either working gas flow or DC input voltage. This He line is the most intense compared to other lines observed in the spectrum (Fig. 10). The result is due to amount of He and its mixture with air present in the plasma plume.

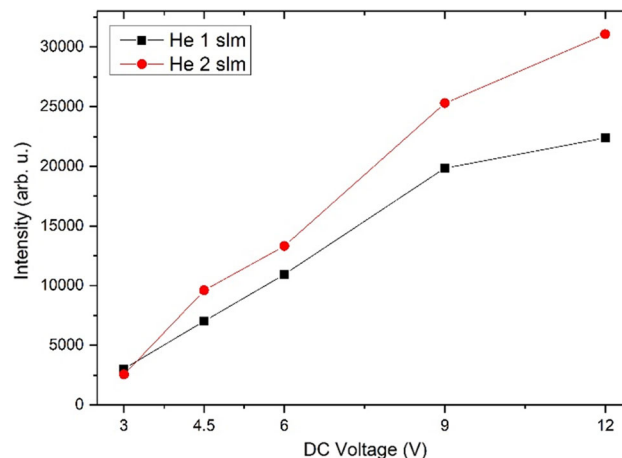
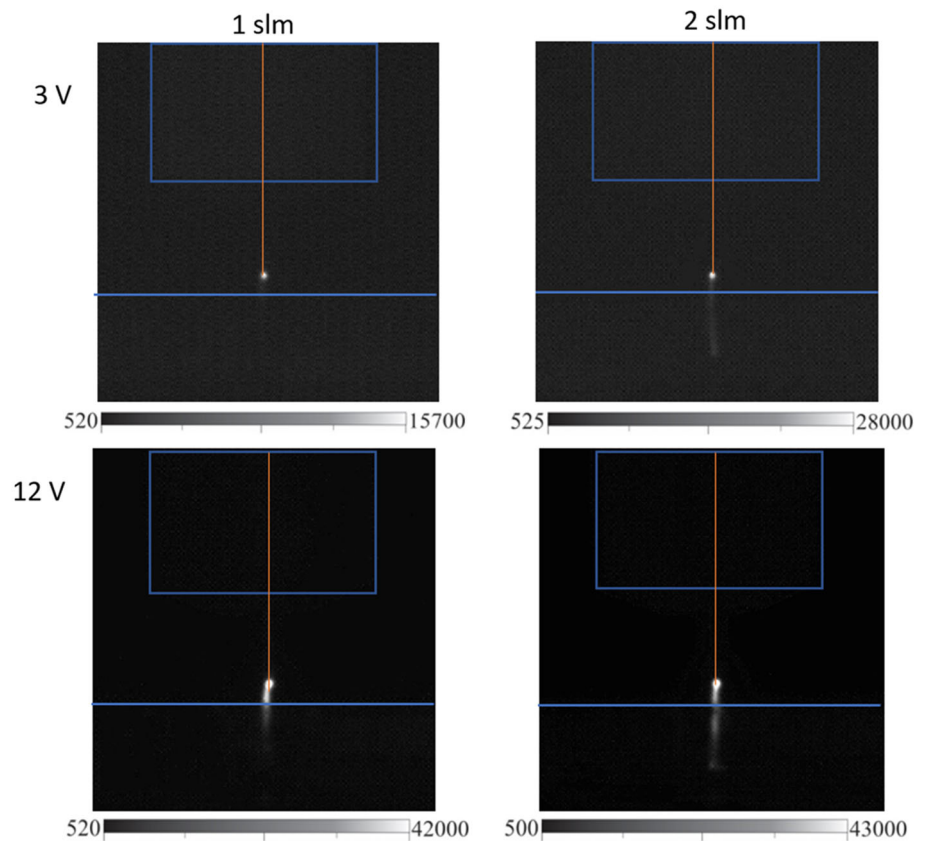


**Fig. 10** He 706.5 nm line intensities for different gas flow and voltages

Observing all line intensities analyzed here, one can conclude that within the range of voltages varied in the experiment, there is a steady increase of the line intensity with increase in applied voltage. This reflects a fact that for all lines, i.e. processes related to specific emission, concentration of excited species continuously rises with voltage increment, without any abrupt changes. Hence, we can say that both voltage and flow changes applied here do not influence plasma chemistry but only concentration of species involved in the processes.

*Discharge imaging* can provide information about the way plasma plume forms and how it propagates between electrode and bacteria-containing medium. Additionally, a relative abundance of active species can be roughly assessed through emission intensity as brighter intensity corresponds to more emitting particles. For this, ICCD imaging was employed with time-averaged images of the streamer structure obtained for all He flows and DC input powers. Typical results are presented in Fig. 11 for 1 slm and 2 slm, at only the lowest (3 V) and highest (12 V) DC voltages used in the experiments. Similar to optical emission measurements, the jet position and its distance to the liquid surface in the 96-well plate were the same as for bacteria treatments. For all conditions, a ball-shaped bright plasma was visible on the tip of the pin electrode with a plasma plume extending towards the target. For the lowest DC voltage employed, a weak plasma channel existed only for the 2 slm flow of He. Obviously, for  $V_{DC} = 3$  V and 1 slm of He, the field attained at the electrode with these power supply conditions was not enough to achieve sufficient ionisation in the whole volume between the jet and sample surface. At the highest power, i.e. DC voltage of 12 V, a streamer-like plasma channel with strong emission bridged the distance from the electrode tip to the liquid surface. After processing all images recorded by subtracting the background intensity level, it was determined that in all applied conditions, except for 3 V at 1 slm, the plasma plume reached the liquid surface, meaning that streamer length in this range of conditions did not depend on either voltage or helium flow.

**Fig. 11** Images of the discharge structure at different flows and DC voltages from the power supply. A thin vertical line represents a pin electrode protruding from the body of the jet (rectangle shape). The horizontal line in the lower part of the images signifies the upper edge of the 96-well plate



This indicates that the medium chemistry of bacteria deactivation depends on streamer forming behaviour, which almost doubles the procedure's efficacy.

## 4 Conclusion

To optimise bacteria deactivation in media and obtain sterilisation with plasmas, a parameter study involving a large number of experiments using different plasma conditions was performed. It included monitoring the viability of different bacteria strains with respect to several plasma diagnostics measurements. This research clearly shows non-thermal helium APPJs' ability to deactivate four standard strains of bacteria used in such experiments. The deactivation effects of the plasma jet were significant and dependant on the bacterial strain, exposure time and plasma configuration (gas flow rate and input DC power unit voltage). The obtained results are expected and indicate that *E. coli* is deactivated faster than other strains. Generally, all bacterial strains—*E. coli*, *S. aureus*, *B. stearothermophilus* and *B. subtilis*—follow the same deactivation trends. The only discrepancy is in the optimal parameters for deactivation of *B. stearothermophilus*, where optimal deactivation is reached at lower flow rate levels. This might be because of the bacterial strain's properties and its response to the changing environment by

interacting plasma. The interaction of plasma and bacteria suspension (saline) was twofold—it changed the concentration of reactive species and pH in the solution with bacteria. This RONS species (He, O, N, H, photons) generated in the gas phase and high-energy electrons and ions were interacting with the liquid. As a result of the combined action of produced reactive species and chemical reactions, which also influenced the pH in the liquid phase, increased bacteria deactivation efficacy. Combining all the chemically initiated processes managed to sterilise given bacterial strains in a medium in fairly short treatment times, maximum efficacy was observed at high flow rates and DC input powers. More power transferred into the plasma shortens the deactivation process. Increasing the flow rate from 0.5 to 2 slm also shortens the inactivation process as reactive species concentration in the gas phase rises.

**Acknowledgements** This work was carried out within projects NATO SPS, and Slovenian Research Agency grant J4-1770. This article is also based upon work from COST Action PLAGRI—CA19110, supported by COST (European Cooperation in Science and Technology), [www.cost.eu](http://www.cost.eu). K. S. acknowledges also partial funding from bilateral project Serbia-Slovenia from MESTD of Republic of Serbia. We thank Dr. Nevena Puac for useful advices related to electrical characterization.

## Author contributions

UC and ZLP conceived and planned the experiments. NH, MM, DV and MĐ performed plasma treatment of bacteria and liquid chemistry analyses along with the interpretation of those results. NŠ, KS and AJ performed plasma diagnostics and electrical characterization along with interpretation of those results. AJ wrote the original draft, and all co-authors helped with manuscript revision.

**Data availability statement** This manuscript has no associated data or the data will not be deposited. [Authors' comment: Data available on request from the authors - The data that support the findings of this study are available from the corresponding author, A. J., upon reasonable request.]

## References

- Z. Dai, J. Ronholm, Y. Tian, B. Sethi, X. Cao, Sterilization techniques for biodegradable scaffolds in tissue engineering applications. *J. Tissue Eng.* **7**, 204173141664881 (2016). <https://doi.org/10.1177/2041731416648810>
- J. Ehlbeck et al., Low temperature atmospheric pressure plasma sources for microbial decontamination. *J. Phys. D Appl. Phys.* (2011). <https://doi.org/10.1088/0022-3727/44/1/013002>
- R. Ben Gadri et al., Sterilization and plasma processing of room temperature surfaces with a one atmosphere uniform glow discharge plasma (OAUGDP). *Surf. Coat. Technol.* **131**(1–3), 528–541 (2000). [https://doi.org/10.1016/S0257-8972\(00\)00803-3](https://doi.org/10.1016/S0257-8972(00)00803-3)
- P.M. Schneider, New technologies and trends in sterilization and disinfection. *Am. J. Infect. Control* **41**(5 SUPPL.), S81–S86 (2013). <https://doi.org/10.1016/j.ajic.2012.12.007>
- A. Sakudo, Y. Yagyu, T. Onodera, Disinfection and sterilization using plasma technology: fundamentals and future perspectives for biological applications. *Int. J. Mol. Sci.* (2019). <https://doi.org/10.3390/ijms20205216>
- M. Laroussi, Nonthermal decontamination of biological media by atmospheric-pressure plasmas: review, analysis, and prospects. *IEEE Trans. Plasma Sci.* **30**(4I), 1409–1415 (2002). <https://doi.org/10.1109/TPS.2002.804220>
- X. Liao et al., Bacterial spore inactivation induced by cold plasma. *Crit. Rev. Food Sci. Nutr.* **59**(16), 2562–2572 (2019). <https://doi.org/10.1080/10408398.2018.1460797>
- H. Halfmann, B. Denis, N. Bibinov, J. Wunderlich, P. Awakowicz, Identification of the most efficient VUV/UV radiation for plasma based inactivation of *Bacillus atrophaeus* spores. *J. Phys. D Appl. Phys.* **40**(19), 5907–5911 (2007). <https://doi.org/10.1088/0022-3727/40/19/019>
- S. Hofmann, Atmospheric pressure plasma jets - characterisation and interaction with human cells and bacteria, no. december. (2013)
- M. Keidar, E. Robert, Preface to special topic: plasmas for medical applications. *Phys. Plasmas* **22**(12), 121901 (2015). <https://doi.org/10.1063/1.4933406>
- M. Keidar, D. Yan, I.I. Beilis, B. Trink, J.H. Sherman, Plasmas for treating cancer: opportunities for adaptive and self-adaptive approaches. *Trends Biotechnol.* **36**(6), 586–593 (2018). <https://doi.org/10.1016/j.tibtech.2017.06.013>
- S. Schneider et al., The role of VUV radiation in the inactivation of bacteria with an atmospheric pressure plasma jet. *Plasma Process. Polym.* **9**(6), 561–568 (2012). <https://doi.org/10.1002/ppap.201100102>
- N. Gopal, C. Hill, P.R. Ross, T.P. Beresford, M.A. Fenelon, P.D. Cotter, The prevalence and control of *Bacillus* and related spore-forming bacteria in the dairy industry. *Front. Microbiol.* (2015). <https://doi.org/10.3389/fmicb.2015.01418>
- S. André, T. Vallaëys, S. Planchon, Spore-forming bacteria responsible for food spoilage. *Res. Microbiol.* **168**(4), 379–387 (2017). <https://doi.org/10.1016/j.resmic.2016.10.003>
- S. Caulier, C. Nannan, A. Gillis, F. Licciardi, C. Braggard, J. Mahillon, Overview of the antimicrobial compounds produced by members of the *Bacillus subtilis* group. *Front. Microbiol.* (2019). <https://doi.org/10.3389/fmicb.2019.00302>
- J. Vila et al., *Escherichia coli*: an old friend with new tidings. *FEMS Microbiol. Rev.* **40**(4), 437–463 (2016). <https://doi.org/10.1093/femsre/fuw005>
- J. Jang, H.-G. Hur, M.J. Sadowsky, M.N. Byappanahalli, T. Yan, S. Ishii, Environmental *Escherichia coli*: ecology and public health implications—a review. *J. Appl. Microbiol.* **123**(3), 570–581 (2017). <https://doi.org/10.1111/jam.13468>
- T.J. Foster, J.A. Geoghegan, *Staphylococcus aureus*, in *Molecular Medical Microbiology*. (Elsevier, Amsterdam, 2015), pp. 655–674
- S.Y.C. Tong, J.S. Davis, E. Eichenberger, T.L. Holland, V.G. Fowler, *Staphylococcus aureus* Infections: epidemiology, pathophysiology, clinical manifestations, and management. *Clin. Microbiol. Rev.* **28**(3), 603–661 (2015). <https://doi.org/10.1128/CMR.00134-14>
- S. Basak, P. Singh, M. Rajurkar, Multidrug resistant and extensively drug resistant bacteria: a study. *J. Pathog.* **2016**, 1–5 (2016). <https://doi.org/10.1155/2016/4065603>
- L. Poirel et al., Antimicrobial resistance in *Escherichia coli*. *Microbiol. Spectr.* (2018). <https://doi.org/10.1128/microbiolspec.ARBA-0026-2017>
- M. Miletić et al., Inhibition of methicillin resistant *Staphylococcus aureus* by a plasma needle. *Open Phys.* (2014). <https://doi.org/10.2478/s11534-014-0437-z>
- A.H. Asghar, O.B. Ahmed, A.R. Galaly, Inactivation of *E. Coli* using atmospheric pressure plasma jet with dry and wet argon discharges. *Membranes* (Basel) **11**(1), 1–20 (2021). <https://doi.org/10.3390/membranes11010046>
- A. Moldgy, G. Nayak, H.A. Aboubakr, S.M. Goyal, P.J. Bruggeman, Inactivation of virus and bacteria using cold atmospheric pressure air plasmas and the role of reactive nitrogen species. *J. Phys. D Appl. Phys.* **53**(43), 434004 (2020). <https://doi.org/10.1088/1361-6463/aba066>

25. J.-W. Lackmann, J.E. Bandow, Inactivation of microbes and macromolecules by atmospheric-pressure plasma jets. *Appl. Microbiol. Biotechnol.* **98**(14), 6205–6213 (2014). <https://doi.org/10.1007/s00253-014-5781-9>
26. C.A.J. van Gils, S. Hofmann, B.K.H.L. Boekema, R. Brandenburg, P.J. Bruggeman, Mechanisms of bacterial inactivation in the liquid phase induced by a remote RF cold atmospheric pressure plasma jet. *J. Phys. D Appl. Phys.* **46**(17), 175203 (2013). <https://doi.org/10.1088/0022-3727/46/17/175203>
27. F. Saadati, H. Mahdikia, H.A. Abbaszadeh, M.A. Abdollahifar, M.S. Khorangah, B. Shokri, Comparison of Direct and Indirect cold atmospheric-pressure plasma methods in the B16F10 melanoma cancer cells treatment. *Sci. Rep.* **8**(1), 1–15 (2018). <https://doi.org/10.1038/s41598-018-25990-9>
28. S. Ikawa, K. Kitano, S. Hamaguchi, Effects of pH on bacterial inactivation in aqueous solutions due to low-temperature atmospheric pressure plasma application. *Plasma Process. Polym.* **7**(1), 33–42 (2010). <https://doi.org/10.1002/ppap.200900090>
29. S.M. Hosseini, B. Hosseinzadeh Samani, S. Rostami, Z. Lorigooini, Design and characterisation of jet cold atmospheric pressure plasma and its effect on *Escherichia coli* colour, pH, and bioactive compounds of sour cherry juice. *Int. J. Food Sci. Technol.* **56**(10), 4883–4892 (2021). <https://doi.org/10.1111/ijfs.15220>
30. V.S.S.K. Kondeti et al., Long-lived and short-lived reactive species produced by a cold atmospheric pressure plasma jet for the inactivation of *Pseudomonas aeruginosa* and *Staphylococcus aureus*. *Free Radic. Biol. Med.* **124**, 275–287 (2018). <https://doi.org/10.1016/j.freeradbiomed.2018.05.083>
31. A.L.V. Cubas et al., Effect of chemical species generated by different geometries of air and argon non-thermal plasma reactors on bacteria inactivation in water. *Sep. Purif. Technol.* **222**, 68–74 (2019). <https://doi.org/10.1016/j.seppur.2019.03.057>
32. P. Lukes, M. Clupek, V. Babicky, B. Pongrac, M. Simek, Bulk-phase chemistry induced by nanosecond discharge plasma in water. In: 2017 IEEE 19th International Conference on Dielectric Liquids (ICDL), (2017), pp. 1–3. <https://doi.org/10.1109/ICDL.2017.8124702>
33. Y.S. Seo, A.A.H. Mohamed, K.C. Woo, H.W. Lee, J.K. Lee, K.T. Kim, Comparative studies of atmospheric pressure plasma characteristics between He and Ar working gases for sterilization. *IEEE Trans. Plasma Sci.* **38**(10 PART 2), 2954–2962 (2010). <https://doi.org/10.1109/TPS.2010.2058870>
34. E. Ilik, T. Akan, Optical properties of the atmospheric pressure helium plasma jet generated by alternative current (a.c.) power supply. *Phys. Plasmas* (2016). <https://doi.org/10.1063/1.4948718>
35. A.N. Korbut, V.A. Kelman, Y.V. Zhmenyak, M.S. Klenovskii, Emission properties of an atmospheric-pressure helium plasma jet generated by a barrier discharge. *Opt. Spectrosc. (English Transl. Opt. i Spektrosk.)* **116**(6), 919–925 (2014). <https://doi.org/10.1134/S0030400X14040146>
36. J.J. Camacho, J.M.L. Poyato, L. Díaz, M. Santos, Optical emission studies of nitrogen plasma generated by IR CO2 laser pulses. *J. Phys. B At. Mol. Opt. Phys.* **40**(24), 4573–4590 (2007). <https://doi.org/10.1088/0953-4075/40/24/003>
37. S.J. Strickler, The identification of molecular spectra (Pearse, R. W. B.; Gaydon, A. G.). *J. Chem. Educ.* **41**(5), A398 (1964). <https://doi.org/10.1021/ed041pA398>
38. T. Darny, J.M. Pouvesle, J. Fontane, L. Joly, S. Dozias, E. Robert, Plasma action on helium flow in cold atmospheric pressure plasma jet experiments. *Plasma Sources Sci. Technol.* (2017). <https://doi.org/10.1088/1361-6595/aa8877>
39. M. Foletto, V. Puech, J. Fontane, L. Joly, L.C. Pitchford, Evidence of the influence of plasma jets on a helium flow into open air. *IEEE Trans. Plasma Sci.* **42**(10), 2436–2437 (2014). <https://doi.org/10.1109/TPS.2014.2331393>
40. R. Zaplotnik, M. Bišćan, Z. Kregar, U. Cvelbar, M. Mozetič, S. Milošević, Influence of a sample surface on single electrode atmospheric plasma jet parameters. *Spectrochim. Acta Part B At. Spectrosc.* **103–104**, 124–130 (2015). <https://doi.org/10.1016/j.sab.2014.12.004>
41. P.J. Bruggeman et al., Plasma-liquid interactions: a review and roadmap. *Plasma Sources Sci. Technol.* (2016). <https://doi.org/10.1088/0963-0252/25/5/053002>
42. Q. Xiong et al., Temporal and spatial resolved optical emission behaviors of a cold atmospheric pressure plasma jet. *J. Appl. Phys.* (2009). <https://doi.org/10.1063/1.3239512>
43. G. Nersisyan, T. Morrow, W.G. Graham, Measurements of helium metastable density in an atmospheric pressure glow discharge. *Appl. Phys. Lett.* **85**(9), 1487–1489 (2004). <https://doi.org/10.1063/1.1784514>
44. G.V. Naidis, Production of active species in cold helium-air plasma jets. *Plasma Sources Sci. Technol.* (2014). <https://doi.org/10.1088/0963-0252/23/6/065014>
45. R. Ono, Optical diagnostics of reactive species in atmospheric-pressure nonthermal plasma. *J. Phys. D Appl. Phys.* (2016). <https://doi.org/10.1088/0022-3727/49/8/083001>



# Cold atmospheric plasma technology for removal of organic micropollutants from wastewater—a review

Amit Kumar<sup>1,2,a</sup> , Nikola Škoro<sup>1</sup> , Wolfgang Gernjak<sup>3,4</sup>, and Nevena Puač<sup>1,b</sup> 

<sup>1</sup> Institute of Physics, University of Belgrade, Pregrevica 118, 11080 Belgrade, Serbia

<sup>2</sup> Universitat de Girona, 17003 Girona, Spain

<sup>3</sup> Catalan Institute for Water Research (ICRA), 17003 Girona, Spain

<sup>4</sup> Catalan Institution for Research and Advanced Studies (ICREA), 08010 Barcelona, Spain

Received 17 February 2021 / Accepted 1 October 2021

© The Author(s) 2021

**Abstract.** Water bodies are being contaminated daily due to industrial, agricultural and domestic effluents. In the last decades, harmful organic micropollutants (OMPs) have been detected in surface and groundwater at low concentrations due to the discharge of untreated effluent in natural water bodies. As a consequence, aquatic life and public health are endangered. Unfortunately, traditional water treatment methods are ineffective in the degradation of most OMPs. In recent years, advanced oxidation processes (AOPs) techniques have received extensive attention for the mineralization of OMPs in water in order to avoid serious environmental problems. Cold atmospheric plasma discharge-based AOPs have been proven a promising technology for the degradation of non-biodegradable organic substances like OMPs. This paper reviews a wide range of cold atmospheric plasma sources with their reactor configurations used for the degradation of OMPs (such as organic dyes, pharmaceuticals, and pesticides) in wastewater. The role of plasma and treatment parameters (e.g. input power, voltage, working gas, treatment time, OMPs concentrations, etc.) on the oxidation of various OMPs are discussed. Furthermore, the degradation kinetics, intermediates compounds formed by plasma, and the synergetic effect of plasma in combination with a catalyst are also reported in this review.

## 1 Introduction

Clean water is necessary to the ecosystem, to sustain life as well as social and economic development [1, 2]. However, as the population is growing, the anthropogenic effect on the surrounding environment is increasing every day [3, 4]. Nowadays, the wastewater generated from sources such as industry, agriculture, houses, and so on contains considerable amounts of organic micropollutants (OMPs) and thus causes many problems related to the environment and health [3, 5–7]. According to several investigations, various OMPs such as pharmaceuticals, pesticides, organic dyes have been frequently detected in the wastewater, surface water, and even in drinking water (see Fig. 1) [5, 8–10].

Examples of frequently observed OMPs are listed in Table 1.

Many wastewater effluents contain a high level of contaminants due to a considerable number of OMPs being non-biodegradable. Thus, the degradation of OMPs in water became a major challenge [5, 10]. Typical characteristics of wastewater from textile, pharmaceutical, and pesticide industries are presented in Table 2. According to the data, the higher ratio of COD to BOD

that appear in all three cases indicates that wastewater had an extremely high level of refractory organic substances. This kind of wastewater must be treated before releasing in nature in order to prevent harm to living beings and the environment.

The degradation of most OMPs in conventional wastewater treatment plants (e.g. using biological processes) is inefficient because of their complex and stable molecular structures. As a consequence, OMPs unaffected by the treatment are returned to the natural waters [7, 29, 30]. Recently, for the removal of OMPs from wastewater several advanced oxidation processes (AOPs) have been developed including  $\text{H}_2\text{O}_2$  - Fenton, UV/TiO<sub>2</sub>, O<sub>3</sub>/H<sub>2</sub>O<sub>2</sub>, UV/H<sub>2</sub>O<sub>2</sub>, UV/H<sub>2</sub>O<sub>2</sub>/O<sub>3</sub>, and Ultrasound [31–34]. These AOPs are based on the generation of unstable strong oxidants like hydroxyl free radicals (HO·). The HO· is extremely reactive due to unpaired electron and it can destroy a broad range of non-biodegradable organic compounds that are unaltered by conventional methods. The possibilities of chemical pathways for HO· production in different AOPs are given in Table 3.

Cold plasmas are non-equilibrium non-thermal plasmas due to the difference in the temperature between electrons (Te) and other plasma species and the fact that in active plasma volume overall gas temperature (Tg) is close to ambient [35–40]. In these plasmas,

<sup>a</sup> e-mail: amit@ipb.ac.rs (corresponding author)

<sup>b</sup> e-mail: nevena@ipb.ac.rs

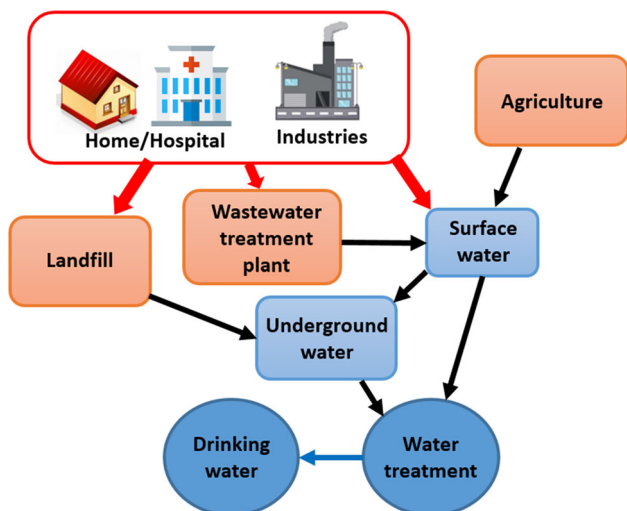


Fig. 1 Source of OMPs and their flow in the environment

Table 1 List of some commonly observed OMPs in water bodies

Class of OMPs	Sub-categories	Ref.
Dyes	Azo	[11]
	Anthraquinone	[12]
	Sulfur	[13]
	Nitro	[14]
	Triarylmethane	[14]
Pharmaceuticals	Antibiotics	[15]
	Hormones	[16]
	Anticonvulsants	[17]
	NSAIDs	[18]
	Antihypertensives	[19]
	Antidepressants	[20]
Pesticides	Herbicides	[21]
	Fungicides	[22]
	Insecticides	[23]
	Rodenticides	[24]
	Bactericides	[25]

highly energetic electrons play a key role in triggering chemical reactions and governing plasma chemistry via processes of excitation, ionization, dissociation, etc. [36,38,41–44]. On the other hand, in the thermal plasma system, Te and Tg are similar so these systems can be considered to be in local thermodynamic equilibrium. Comparison of both types of plasma-based on electron temperature, electron density and gas temperature is presented in Table 4. The range of plasma properties depends on the type of plasma source, discharge, power signal, working gas, and much more. In terms of energy consumption, the cold plasma system requires lower energy to generate reactive species than thermal plasma system [38,45–48].

For decades non-equilibrium plasmas operating at low pressures have been used in various applications due to their rich chemistry [35,37,50–53]. Thus, cold atmospheric plasmas technologies have been considered a viable alternative to low-pressure plasma mainly due to the numerous applications that include samples that cannot undergo a vacuum [36,38,54–65]. However, ignition and sustaining of cold atmospheric pressure plasmas are more challenging due to the considerably higher breakdown voltage and set of parameters usually falling in the unfavorable region of Paschen’s curve [43,63,66–68]. These issues have been overcome by using noble gasses as feeding gas, electrode geometry, operation frequency, type of power supply, etc. The cold atmospheric

Table 2 Characteristics of some examples of industrial wastewaters

Physico-chemical parameters					
	COD	BOD	pH	TSS	References
Textile	3300 – 3500	2100 – 2300	8.2–9.6	350 – 410	[26]
Pharmaceuticals	4000 – 6000	300 – 1500	6.5–8.0	600–700	[27]
Pesticides	6000 – 7000	2000 – 3000	12–14	250–300	[28]

All values are in mg/L except pH, COD - Chemical oxygen demand, BOD - Chemical oxygen demand, TSS - Total suspended solids

Table 3 HO· generation mechanism by various AOPs

Processes	Reactions
H <sub>2</sub> O <sub>2</sub> – Fenton	H <sub>2</sub> O <sub>2</sub> + Fe <sup>2+</sup> → Fe <sup>3+</sup> + HO· + OH <sup>-</sup>
UV/TiO <sub>2</sub>	TiO <sub>2</sub> + hν → e <sup>-</sup> + h <sup>+</sup> h <sup>+</sup> + H <sub>2</sub> O → H <sup>+</sup> + HO·
O <sub>3</sub> /H <sub>2</sub> O <sub>2</sub>	2O <sub>3</sub> + H <sub>2</sub> O <sub>2</sub> → 2 HO· + 3O <sub>2</sub>
UV/H <sub>2</sub> O <sub>2</sub>	H <sub>2</sub> O <sub>2</sub> + UV → 2 HO·
UV/H <sub>2</sub> O <sub>2</sub> /O <sub>3</sub>	2O <sub>3</sub> + UV + H <sub>2</sub> O <sub>2</sub> → 2HO· + 3O <sub>2</sub>
Ultrasound/UV/O <sub>3</sub>	Ultrasound + UV + O <sub>3</sub> → HO·

**Table 4** Characteristics of non-thermal plasma and thermal plasma

	Non-thermal plasmas	Thermal plasmas	Reference
Plasma state	$T_e \gg T_g$	$T_e \approx T_g$	[41, 49]
Electron temperature	1–10 eV	$\sim 1$ eV	
Electron density	Lower electron density ( $< 10^{19} \text{ m}^{-3}$ )	High electron density ( $< 10^{21}$ – $10^{26} \text{ m}^{-3}$ )	
Gas temperature	300–1000 K	10000 K	
Discharge type	Corona, Glow, Streamer	Arc plasma	

$T_e$ —electron temperature,  $T_g$  - gas temperature  
 1eV  $\approx$  10000 K

pressure plasmas are fulfilling the major requirements, which is the production of highly reactive species at low gas temperature and this characteristic of cold atmospheric pressure plasmas is the main reason for their beneficial effect in wastewater treatment sectors [69–72].

Apart from other approaches for the realization of AOPs, nowadays, cold plasma-based oxidation techniques have gained a lot of interest. It is shown that this type of plasma can be used to degrade a variety of toxic OMPs in water such as pharmaceuticals, organic dyes, pesticides [30, 73–76]. Cold plasma is responsible for the formation of many reactive oxygen species (e.g.  $\text{HO}\cdot$ ,  $\text{O}\cdot$ ,  $\text{HO}_2\cdot$ ,  $\text{O}_3$ ,  $\text{H}_2\text{O}_2$ , etc.), as well as ultraviolet light (UV), electric field, and sometimes shockwaves [10, 42, 58, 77–80]. Plasma generated reactive species have high oxidation potential and they can react and eliminate many stable OMPs at low temperature, at atmospheric pressure, and without using any kind of hazardous chemicals. For example, plasma generated oxidants  $\text{HO}\cdot$ ,  $\text{O}\cdot$ ,  $\text{O}_3$ , and  $\text{H}_2\text{O}_2$  have oxidation potentials of 2.86 V, 2.42 V, 2.07 V and 1.78 V, respectively. These oxidation potentials are all higher than chlorine (1.36 V) [77, 81], which is sometimes used as a bleaching agent to reduce colour in industrial effluents [82]. Moreover, the treatment of polluted water by using chlorine is not an eco-friendly process [83, 84]. The cold plasma grants abundant formation of highly reactive species without adding chemical agents. Plasma treatments will not add to a secondary pollution and during the processing creates less toxic transformation intermediates that are biodegradable [85, 86]. We can consider plasma decontamination processes as an eco-friendly technology. But one needs to be aware that some of the species may persist in the treated water and might be harmful to some aquatic life [87–89]. Moreover, the cold plasma system can be used alone or in a combination of conventional wastewater treatment techniques [72, 90].

In the last decade, many authors have studied the use of cold plasmas in applications for wastewater treatment. A few reviews have been carried out where authors discussed previously obtained results based on the treatment of various compounds dissolved in water (e.g. dyes, phenol, pharmaceuticals, surfactants, pesticides, personal care products, etc.) by plasma technology. In the review of Magureanu et al. [10], the overview of published data between 1996 and 2013 on the treat-

ment of various pharmaceuticals by plasma is discussed. In this publication, they assess various reactor configurations and experimental parameters and related their influence to the performance of the plasma system. It was observed that the plasma generation in the gaseous phase over thin water film by DBD or corona was frequently performed for the removal of pharmaceuticals. In 2014, Hijosa-Valsero et al. [30] reviewed different plasma reactors and their operating conditions used for the degradation of various organic compounds, such as volatile organic carbon, phenols, dyes, pharmaceuticals, personal care products, and surfactants. According to their review, they stated that generation of plasma at the gas-liquid interface was more efficient for degradation as well as for the energy yield than the case when plasma was generated in the liquid phase. In 2010, the removal of various classes of dyes by utilizing plasma is reviewed by Malik, [71]. In his review, the various plasma reactors were discussed and compared including the energy efficiency. It was found that the formation of pulsed corona discharge in fine droplets and over thin water film was the most effective approach among those analyzed. In 2006 and 2014, Jiang et al. [69] and Locke, [91] reviewed the use of cold plasma reactors with varied of reactor configurations for the degradation of phenol and phenolic compounds. They showed that cold plasma can effectively degrade range of phenolic compounds. Another investigation on the combined effect of heterogeneous catalysts and cold plasmas for the removal and mineralization of organic pollutants from water is summarized in the critical review of Russo et al. [92]. They concluded that catalysts played a significant role to enhance the performance of the plasma systems. A recent review by Barjasteh et al. [93] illustrated the overview of cold plasma for water treatment with a focus on the inactivation of bacteria and degradation of some of the organic compounds.

In recent years, a continuation of work on the treatment of dyes, pharmaceuticals and pesticides by plasma has been presented in many publications. However, it was noticed that there were limited review studies performed on papers published in the last 5 to 6 years. In this article, we tried to make an up-to-date review of recent investigations that have not obtained attention, as well as on research papers that were published in the last almost 10 years. All gathered data in this review can be used for easier selection of the most suitable plasma source for degradation of three different

types of OMPs (pesticides, pharmaceuticals and dyes). We have tried to discuss the implementation of plasma sources with various operational parameters and their effects on the degradation efficiency of OMPs. Where possible we have tried to take into account the energy efficiency of the above mentioned plasma sources.

This article presents a literature review on the degradation of various OMPs such as pharmaceuticals, organic dyes, and pesticides in wastewater under the cold atmospheric plasma treatments with a special focus on plasma sources, reactor configuration as well as some operating parameters that influence the degradation of specific OMPs. After general information about different kinds of plasma sources employed for OMP treatment, the paper describes specific approaches used for the degradation of organic dyes, pharmaceuticals and pesticides. For each pollutant type, we performed an excessive literature survey to obtain published information on various sources in terms of design, working conditions and plasma properties as well as treatment parameters and removal efficiency. We put through a comparison of different sources based on specific plasma and sample parameters and make conclusions for each pollutant type regarding plasma application.

## 2 Removal of organic micropollutants by using cold atmospheric plasmas

For several years, cold plasma discharges have been extensively used for the elimination of organic pollutants from water [72,94–97]. Many different plasma sources, e.g. corona, dielectric barrier discharge (DBD), atmospheric pressure plasma jet (APPJ), gliding arcs, and others have been investigated for wastewater treatment. They operate with various power supply signals (continuous wave at the wide range of frequencies – Hz to kHz, pulsed voltage signals, etc.), electrode geometries such as a needle to plate, pin to ring, pin to pin and many other, as well as a variety of working gases and their mixtures (e.g. air, oxygen, argon, etc.) and have been extensively tested for the removal of different OMPs.

Generally, cold atmospheric plasma setups used for liquid treatments can be divided into three categories: discharge above the liquid surface, discharge in bubbles, and direct discharge inside the liquid, and have been investigated by many researchers to study plasma–liquid interface phenomenon. Schematics of typical arrangements are shown in Fig. 2 but in all three categories, there are many electrode geometries used to produce plasma in particular experiments [42,79].

The setups where plasma is formed above the liquid surface and in bubbles are commonly used for wastewater treatment whereas direct discharge inside the liquid is not frequently employed. In the case of a discharge above the liquid surface, plasma species are formed in the gas phase near the liquid surface and then transferred inside the liquid sample where they trigger degra-

dition of OMPs in water [45,76]. In the case of bubbles in the liquid, plasma is again formed in the gaseous phase inside the bubble and reactive species originate from separate plasma sites and enter the sample. So, in general, the mechanism behind these two approaches is very similar. The formation of plasma species above liquid has been studied and it is strongly dependent on the plasma source, electrode geometries, working gas, reduced electric field [38,72,98]. The next phase in plasma treatment, the interaction of plasma with liquid is an overly complex phenomenon with many processes occurring simultaneously: ionization, excitation and dissociation in the gaseous phase, heterogeneous mass transfer, chemical reactions in bulk liquid, evaporation, electrolysis, and so on [42,98,99].

When the cold plasma is introduced over a liquid surface in presence of surrounding air, the interaction environment can be divided into three parts—plasma in the gas-phase, plasma-liquid interface, and the bulk liquid phase, as schematically shown in Fig. 3 [98]. Reactive species generated in the gas phase can diffuse into the liquid or trigger chemical reactions within the liquid in order to produce secondary species. These reactive oxygen and nitrogen species were formed in the gaseous, interface, and liquid phase either in plasma with an addition of a noble gas (e.g. argon) or only in the plasma formed in surrounding air over the liquid surface [63,98]. In the case of discharge above the liquid surface, the degradation rate of OMPs inside water depends on the formation of reactive species near the interface as well diffusion/penetration of reactive species from gas to the bulk phase [76,100].

Apart from this approach, plasma can be ignited inside the liquid with or without using an external gas source. The generation of plasma inside liquid water with the bubbling of gases for the removal of OMPs has been investigated by many researchers [73,101,102]. Formation of the discharge in bubbles could improve the interfacial areas between plasma generated reactive species and OMPs and consequently increase the elimination rate of pollutants. Additionally, mass transfer from the gaseous environment to the bulk phase can also enhance through external gas bubbling. The most frequently used plasma sources for the generation of discharge inside bubbles are different corona geometries and DBD [45,73,103,104], whereas, for initiation of a discharge directly inside liquid without the introduction of feed gases, electrode configuration creating corona discharge has been employed [105].

### 2.1 Removal of organic dyes

One large group of organic micropollutants are dyes that are commercially used in textile industries. Statistically, around 20 % of industrial water pollution is caused by the discharging of dye effluents [106]. It is one of the biggest contributors to the water pollution. Consequently, some dyes are responsible for the catastrophic damage to aquatic ecological systems ascribed to their stability in nature [107,108]. Besides, recent



studies have been illustrated that some dyes are carcinogenic [107,109]. Some of the dyes are difficult to decompose by conventional water treatment methods [110–112]. For almost 20 years wide research has been carried out on the degradation of organic dyes in solution by cold plasma [77,94,113]. In plasma-based degradation of organic dyes in solution, there are several plasma sources such as corona, DBD, gliding arc, APPJ that have been evaluated with different reactor configurations, continuous and pulsed voltage signals, input powers, working gases, etc. Generally speaking, cold plasma-based advanced oxidation methods show great potential in mineralization of organic dyes into  $\text{CO}_2$  and  $\text{H}_2\text{O}$  or decomposition to the less hazardous intermediates [86,90].

Results of the different studies on the cold plasma-based degradation of organic dyes are given in Table 5 as a result of a survey of the literature published in the last 18 years. For selected target compounds we listed characteristics of plasma sources and operating parameters used for the decontamination as well as parameters related to the treatment, as they were stated in the reference. In cases where one publication contained several pollutants treated under the same conditions, we grouped the results.

Corona discharge with various reactor configurations has been introduced by many researchers for the treatment of organic dyes. In the case of corona discharge, mostly the plasmas were formed in the gas phase over the solution and inside bubbles. Magureanu et al. [74] evaluated the elimination of methylene blue from aqueous solution by using a pulsed high voltage corona discharge with multi-hollow needle electrodes (6 array of needles). The needle electrodes were situated at the bottom of the reactor and a grounded electrode was placed about 5 cm above the tip of the needles. Both electrodes were located inside the liquid and discharge takes place in bubbles inside dye solution. The paper presented results obtained when different feed gases (air, argon, and oxygen) were bubbled in the solution through the needles. The multi-needle electrodes promote a large volume of plasma which leads to enhance the interaction between reactive species and dye solution. It was observed that at the same external power input degradation of methylene blue was enhanced in the particular order of feed gases: air < argon < oxygen. They have explained that more efficient degradation in oxygen and argon in comparison to air plasmas was due to fact that energy delivered to plasma in these gases is used to generate more reactive species, whereas, in air, some

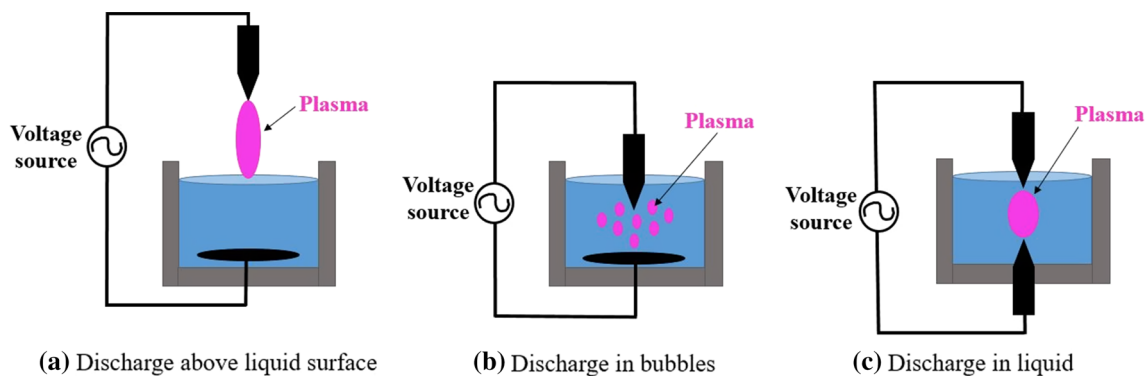


**Fig. 2** Schematics of experimental setups used in studies of liquid treatments with cold plasma

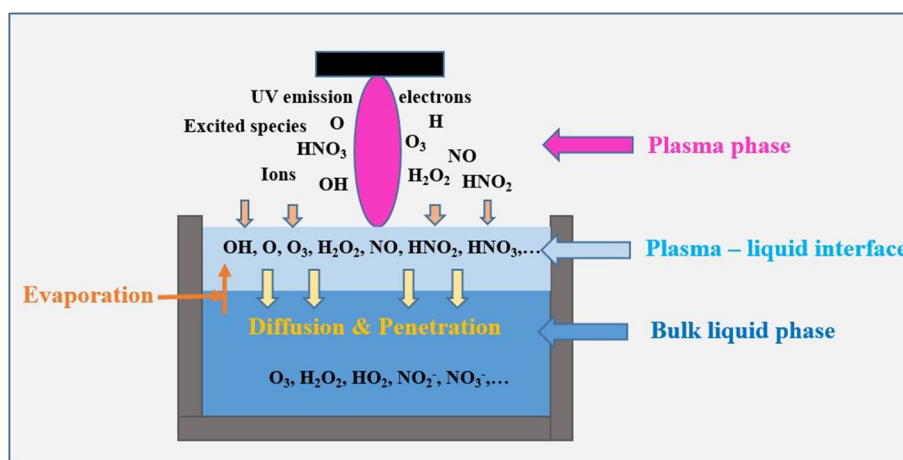


**Fig. 3** Schematic representation of plasma-generated short and long-lived species in the gas phase, at the plasma-liquid interface, and bulk liquid

**Table 5** Literature overview of different types of plasma systems used for organic dye removal

Target compounds	Characteristics of plasma devices			T (min)	C <sub>0</sub> (mg/L)	V <sub>0</sub> (ml)	η (%)	References
	Plasma source	Mode of discharge	Signal type					
Methylene Blue	Corona	Discharge in bubbles	Pulsed	Voltage: 17 kV, 20 pulse repetition rate: 72 Hz, gas: O <sub>2</sub> -800 sccm, power: 10 W	150	100	90	[74]
Acid Orange 7	Corona	Discharge in bubbles	Pulsed	Voltage: 27 kV, 45 repetitive frequency: 70 Hz, gas: air - 1.4 m <sup>3</sup> /h,	20	600	83	[114]
Reactive Brilliant Blue	Corona + TiO <sub>2</sub> Corona	Discharge above liquid surface	DC	Voltage: 14 kV, gas: air-2 L/min, discharge gap/electrode gap: 0.5	100	1000	98 ~ 91	[86]
Methylene Blue	Corona	Discharge in bubbles	Pulsed/DC	Voltage: 4 kV, gas: O <sub>2</sub> -10 ml/min, power: 4 W	13.25	20	~ 100	[94]
Acid Orange 142	Corona	Discharge above liquid surface	DC	Voltage: 12.5 kV, gas: atmosphere air	20	100	~ 90	[90]
Rhodamine B, Methyl Orange, Chicago Sky Blue, Crystal Violet	Corona DBD	Discharge in liquid	Pulsed	Voltage: 20 kV, frequency: 25 Hz	10 (each)	300	~ 77, 70, 91	[105]
Indigo Carmine	DBD	Post-discharge	Pulsed	Voltage: 12 kV, 1 frequency: 20 kHz, pulse width: ~ 50 ns, gas: O <sub>2</sub> -700 ml/min, power: 5 W	4.08	250	100	[115]
Indigo Carmine	DBD	Discharge in bubbles	Pulsed	Voltage: 4kV, pulse 3.2 frequency: 5 kHz, pulsed width: 750 ns, gas: mixture of Ar & O <sub>2</sub> -250 sccm	50	200	99	[101]
Methyl Red	DBD	Discharge above liquid surface & post discharge	Pulsed	Voltage: 11 kV, 10 pulse repetition rate: 76 Hz, gas: O <sub>2</sub> -600 ml/min, power: 1 W	50	200	93	[109]

Table 5 continued

Target compounds	Characteristics of plasma devices			T(min)	C <sub>o</sub> (mg/L)	V <sub>o</sub> (ml)	η(%)	References
	Plasma source	Mode of discharge	Signal type					
Methylene Blue	DBD	Discharge in bubbles	AC	Voltage: 6–8 kV, 30 current: 30–50 mA, frequency: 9.7 kHz, gas: air - 1.5 L/min, power: 8.6 W	100	100	~ 98	[45]
Methylene Blue	Point-to-plate	Discharge above liquid surface and in bubbles	AC	Voltage: 2.57 kV, 60 current: 27.7 mA, frequency: 60 Hz, Gas: N <sub>2</sub> - 0.1 L/min, power: 59.2 W	20	100	~ 100	[113]
Acid Red 88	DBD	Post discharge	AC	Voltage: 20 kV, gas: 4, 5 air-7 L/min, power: 60 W	25, 50	500	92, 91	[108]
Methylene Methyl Congo Red	Blue, Indirect-APPJ Orange,	Discharge above liquid surface	AC	Voltage: 20 kV, gas: 1 O <sub>2</sub> -7 L/min, power: 60 W	25		95	
Methylene Methyl Congo Red	Blue, Direct-APPJ Orange,	Discharge above liquid surface	AC	Voltage 0.7 kV, 20 current 3 mA, frequency: 16 kHz, gas: Ar-3 slm, power: 0.2 W	200		71, 81, 76	[116]
Methylene Methyl Congo Red	Blue, Direct-APPJ Orange,	Discharge above liquid surface	AC	Voltage: 1.2 kV: 20 current: 5 mA, frequency: 16 kHz, gas: Ar-3 slm, power: 0.4 W		200	87, 92, 84 95, 97, 86	
Orange I, Violet, Black T	Crystal Gliding arc	Discharge above liquid surface	liq-uid	Voltage: 10 kV, gas: 30, 60, 60 air-900 L/h	52.54, 53.03	83.23	97, 99, 90 95, 89, 88.4	[117]

Table 5 continued

Target compounds	Characteristics of plasma devices			T(min)	C <sub>o</sub> (mg/L)	V <sub>o</sub> (ml)	η(%)	References
	Plasma source	Mode of discharge	Signal type					
Acid Blue 25	Glow discharge	Discharge above liquid surface	DC	Voltage: 15 kV, current: 0–100 mA, gas: Ar–I slm	60	20	500	78 [107]
	Glow discharge +TiO <sub>2</sub>				60	20		90
Methyl Orange	Gas discharge circuitary airtight configuration-ion	Discharge above liquid surface & post discharge	Pulsed	Voltage: 46 kV, pulses: 80 per second, gas: O <sub>2</sub> –0.08 m <sup>3</sup> /h, power: 5.67 W	20	60	400	92 [118]
Methyl Orange	Multi-needle configuration-ion	Discharge above liquid surface	Pulsed	Voltage: 22 kV, frequency: 50 Hz, gas: O <sub>2</sub>	15	10	450	~ 90 [119]

T – Treatment time

C<sub>o</sub> – Initial concentrationV<sub>o</sub> – Volume

η – Removal efficiency

part of the energy is consumed for the dissociation of nitrogen molecules. On the other hand, they reported that the degradation of methylene blue depended on initial dye concentration and volume of the solution, i.e. higher dye concentration degraded more rapidly in smaller volumes. Li et al. [114] investigated the degradation of Acid Orange 7 dye in a pulsed discharge reactor with a needle-to-plate electrode configuration and with air bubbling into the reaction system in the presence of  $\text{TiO}_2$ . They observed more decoloration efficiency of dye by adding  $\text{TiO}_2$  particles into the reactor, which attributed to photocatalysis in the presence of the ultraviolet light produced in the pulsed plasma system. They also found that the decoloration efficiency of dye was improved by increasing the input power. Jingyu et al. [86] studied reactive brilliant blue dye removal with a point-to-plane DC corona discharge reactor using air as a working gas while the discharge was ignited over the liquid surface. In this case, 72 stainless-steel pin electrodes were powered and stainless-steel plate immersed in dye solution served as a grounded electrode. The idea behind the multi-pin electrodes is to enable the large plasma volume on the liquid surface by physically increasing the number of reaction points. The authors evaluated the effect of the ratio of the discharge gap and the adjacent point distance between two electrodes on decoloration efficiency. The main degradation by-products that were traced were 2,5-dinitrobenzoic acid, 1,2-diacetylene, and 3-nitrobenzoic acid.

Malik et al. [94] have designed a pulsed corona discharge reactor with needle-plate type electrodes for the decolorization of methylene blue and they studied the influence of oxygen and ozone bubbling on the dye decomposition. The removal efficiency was much higher when a combination of oxygen and ozone was bubbled in compared to plasma in pure oxygen and without bubbling of any gases. The presence of additional oxygen and ozone enhances the production of chemically reactive species in water, which leads to a higher degradation of the dye. They also suggested that the removal efficiency of dye was higher in distilled water than in tap water, probably due to the interaction of plasma generated species with impurities in tap water. Recently, Fahmy et al. [90] used a DC corona discharge to eliminate Acid Orange 142 from the water where the plasma was generated in atmospheric air at the surface of the sample in a small discharge gap. It was found that the degradation rate was increased by either increasing the applied voltage or decreasing the discharge gap. Higher applied voltage influenced generation of more energetic electrons and metastables due to the stronger electric field, which led to the formation of more reactive oxygen species. In the study of Sugiarto et al. [105], pulsed streamer corona discharge with a ring-to-cylinder electrode geometry system was used to remove dyes including rhodamine B, methyl orange, and Chicago sky blue from water and plasma was ignited inside the solution. The sample was recirculated inside the plasma reactor. At the given power input, the degradation rate of dyes depended on the initial pH of the solution and the best degradation observed in the acidic medium was

caused by faster reactivity of hydroxyl radicals with dye molecules at lower pH. Degradation of dyes was higher with the addition of hydrogen peroxide into the solution, as a consequence of the dissociation of hydrogen peroxide by ultraviolet light from the plasma. Additionally, they concluded that the pulsed streamer corona discharge reactor with two rings was more efficient than one ring because it provided larger contact area between the plasma streamer and the solution.

DBD has also been used extensively for the degradation of various types of organic dyes. DBD plasma formed between two electrodes, however, at least one electrode covered with a dielectric material, such as glass, quartz and so on. For most of the cases, the post-discharge and discharge in bubbles type of configurations have been widely reported in the papers for the removal of organic dyes. Rahimpour et al. [115] performed an investigation on the removal of crystal violet dye from a liquid via a post-discharge pulsed DBD reactor, using oxygen as a working gas. In the analysis, oxygen was supplied into the DBD reactor and the effluent gas was bubbled through the solution to enhance the mass transfer of reactive oxygen species into the solution which in turn resulted in higher degradation of the dye. The addition of argon in the working gas at the fixed input power, lead to a higher degradation of dye in comparison to pure oxygen case. This effect is due to the formation of more ozone molecules caused by higher dissociation of oxygen molecules in the presence of argon metastables and energetic electrons in the plasma system. The degradation kinetics of crystal violet was found to follow the first-order reaction. A complete elimination of total organic carbon (TOC) was obtained after the plasma treatment, which revealed the full mineralization of treated solution from unwanted organic carbon. In the study of Muradia [101], a parallel plate DBD plasma system was used for the decolorization of indigo carmine. The powered (upper) electrode was a metal plate with punched holes and covered with mica sheets with porous grounded electrode made of graphite. The system was inside the solution and the working gas (Ar,  $\text{N}_2$ , He) was bubbled through the grounded electrode. It has been found that, at the fixed source voltage, the addition of oxygen in the mixture greatly improved the decolorization rate of dye in comparison to the pure argon case.

The degradation of methyl red in an aqueous solution was performed with a pulsed DBD in the coaxial configuration by Piroi et al. [109] where oxygen was used as working gas. They proposed such a configuration to enhance the contact between plasma generated species and the dye, while the solution was recirculated from the reservoir to the DBD reactor in the form of a thin layer of water flowing on the surface of the inner electrode of the reactor. Additionally, the effluents from the DBD reactor were bubbled through a reservoir containing the solution, promoting the interaction between ozone and dye molecules and faster degradation of dye. Since oxygen was used as working gas, ozone was generated due to oxygen discharge in the DBD reactor, and it was the main oxidizer in the

effluent gas. In this paper author also observed that degradation kinetics followed the first-order and that faster degradation of the dye occurred with lower initial dye concentration. Besides, they also found several by-products after the treatment, some of them are identified: 2-ethoxy-2 methylpropane, 2-tert-butoxyethanol, 3-methoxy-3methyl-1-butanol. Recently, an air DBD reactor with a glass bead packed bed and microporous diffuser plate was developed by Wu et al. [45] for the treatment of wastewater containing methylene blue. The plasma was formed in the glass bead packed bed and the species were transferred into the dye solution via a microporous diffuser plate. The role of the microporous diffuser plate inside the DBD reactor was to enhance the mixing between propagating plasma species and the solution. Additionally, plasma species were generated in micropores on the diffuser plate and they interacted with dye molecules. The authors suggested that the packing beads in the plasma zone played a significant role to produce more reactive species in the reactor as they enable the formation of strong electric fields in the cavities. The degradation was higher for the lower initial concentration of dye. On the other hand, it was found that the influence of initial pH and conductivity of the solution on the dye degradation was small. They proposed a possible degradation mechanism involving energetic electrons, ozone, and hydroxyl radicals responsible for the formation of intermediate compounds and their subsequent elimination after the treatment.

Benetoli et al. [113] evaluated the removal of methylene blue from water by using a point-to-plate type plasma reactor configuration. Corona discharge was generated in nitrogen over the liquid surface. Nitrogen was bubbled in the solution from the bottom of the reactor. The initial temperature of the solution was particularly important for the removal, and it has been found that the removal efficiency improved when the temperature was increased. Several long-lived nitrogen-based species were traced inside the solution and they found zeroth-order degradation kinetics of methylene blue for higher initial concentration, whereas first-order for the lower initial concentration. In the study of Tang et al. [108], a post-discharge of a DBD reactor was used for the removal of Acid Red 88 from aqueous solutions, with air containing 100 % relative humidity and oxygen were supplied as the working gas. The gas effluents containing reactive species from the DBD plasma were injected through the bottom of the solution reservoir through an annular porous diffuser device. The degradation of Acid Red 88 was faster when pure oxygen was introduced into the DBD reactor than in the case of a mixture with air with 100 % relative humidity, which implied that higher ozone generation was obtained with pure oxygen. The degradation process was fitted with the pseudo-first-order kinetics model and depended on the input power, initial dye concentration, gas flow rate, and initial pH value of the solution.

Apart from corona and DBD systems, a few studies have also been carried by authors for the treatment of organic dyes by sources such as APPJ, gliding arc,

glow discharge. With these kinds of sources, generally, plasma occurred in the gas phase over the liquid surface. Attri et al. [116] compared two needle-type atmospheric pressure plasma jets (called indirect and direct APPJ) for the degradation of congo red, methyl orange, and methylene blue dyes and argon was used as a plasma gas for both reactors. The indirect APPJ was made with a hollow inner needle electrode and the grounded ring-type electrode (copper tape) that was placed outside the glass tube surface, whereas in the case of direct APPJ, the copper tape as a grounded electrode was positioned on the outer side of the bottom of the vessel. The degradation of all three dyes was higher when direct APPJ was introduced to the sample in comparison to the indirect jet. However, the sample volumes were not reported. According to the optical characterization of both sources, they identified higher intensity of excited argon species in direct APPJ, which contributed to the formation of a higher density of reactive species due to collisions between excited argon species and water molecules. The authors suggested that the hydroxyl radicals were the main oxidative species produced in plasma that was responsible for the degradation of dyes.

Decomposition of Orange I, Crystal Violet, and Eriochrome Black T dyes in the aqueous solutions under the action of gliding arc discharge was studied by Abdelmalek et al. [117]. The plasma was created between two diverging electrodes when humid air was supplied. It was found that the degradation of all three dyes followed first-order kinetics. On the other hand, they also reported that the mineralization of dyes decreased with a decrease in the plasma exposure time. Ghodbane et al. [107] evaluated a DC glow discharge reactor with a combination of photocatalyst ( $\text{TiO}_2$ ) to remove Acid Blue 25 dye from the liquid medium. Argon was used as a feed gas and plasma was generated near the liquid surface in a closed reactor chamber with the absence of air. At the same treatment time, the presence of photocatalyst enhanced the destruction of Acid Blue 25. They reported faster degradation in strongly acidic conditions. Jiang et al. [118] designed a pulsed-discharge with the needles-to-plate electrodes operating in an airtight reactor system with plasma treated sample circulation. They treated methyl orange as the target compound using oxygen as a working gas that was introduced from the bottom of the reactor into the discharge zone through the liquid sample. The needles, i.e. powered electrodes were located vertically above the dye solution while the grounded electrode was placed inside the solution. The plasma was generated between the needle electrodes and the liquid surface. The plasma-treated solution was injected into the reservoir containing the dye to enhance degradation. They obtained better degradation for lower initial concentrations and low volume of the compound. In the study of Sun et al. [119], multi-needle jet (with 24 needle electrodes) produced pulsed plasma that was used to treat aqueous solution containing methyl orange dye using different working gases (oxygen, air, argon, and nitrogen). A plate disc placed inside dye solution served as

a grounded electrode and the plasma was formed in the gaseous phase, between needle electrodes and the dye solution. Decoloration rate was achieved in the following order of working gases, from higher to lower: oxygen > air > argon > nitrogen. Moreover, it was reported that a smaller discharge gap was more effective in terms of degradation caused by the enhancement of the electric field in the gap, which leads to the formation of a large number of reactive species.

## 2.2 Removal of pharmaceuticals

The daily intensive consumption of pharmaceuticals has resulted in the increment of water pollution [97]. Many pharmaceuticals have been identified in the environment in both low and high concentrations [120]. It has been found that several pharmaceuticals released in the environment cause risk on both aquatic species as well as human health [97]. The greatest source of pharmaceuticals in the environment are effluents from wastewater treatment and drug manufacturing plants [121, 122]. However, traditional wastewater treatment plants are not designed for the reduction of certain pharmaceuticals [123]. Therefore, cold plasma-based advanced oxidation processes have been investigated extensively to remove various non-biodegradable pharmaceutical compounds [10, 96, 124].

Various cold plasma devices have been successfully applied by many researchers for the degradation of pharmaceuticals, as summarized in Table 6. We listed references based on different pharmaceutical contaminants or groups of contaminants together with plasma sources and treatment parameters used for their decomposition.

In the study of He et al. [73], a combination of corona discharge with a needle-type electrode and a TiO<sub>2</sub> catalyst was demonstrated for decomposition of tetracycline antibiotic in an aqueous solution with plasma generated in the liquid when air was bubbled. The powered electrode was situated at the top of the reactor and the tip was immersed in the solution, whereas grounded electrode was attached within the solution. In this case, the plasma was driven by a high voltage AC power signal. It has been found that high input power and low initial concentration of antibiotics were beneficial for faster degradation, while TiO<sub>2</sub> catalyst also played a significant role in the degradation. According to the proposed degradation mechanism of tetracycline, they observed that several processes such as hydroxylation, deamination, oxidation, and opening of the aromatic ring were responsible for degradation. To increase the contact surface between plasma reactive species and solution, a plasma reactor with wetted-wall and pulsed high-voltage source was investigated by Rong and Sun [125] for the degradation of sulfadiazine. On the other hand, the authors explained that at higher pH (strong alkaline solution) lower degradation was due to the scavenging effect since hydroxyl radicals reacted with carbonate ions. They also investigated addition of hydrogen and hydroxyl radical scavengers and showed that

this played a significant role in degradation. Hydrogen radical scavengers improved the degradation rate and hydroxyl radical scavengers inhibited the degradation. Moreover, several intermediates are identified before the almost complete mineralization of sulfadiazine.

Dobrin et al. [126] assessed a pulsed corona discharge reactor with 15 copper wires as electrodes and used oxygen to produce plasma at the water surface to remove drug diclofenac. The formation of long-lived reactive species such as hydrogen peroxide measured in the water and ozone was determined in the gas phase, where the concentration of hydrogen peroxide in the solution and ozone in the gas phase was dependent on the plasma treatment time. Complete removal of diclofenac and several carboxylic acids by-products (e.g. formic, acetic, oxalic, malonic, maleic, and succinic) was reported. A different type of corona discharge reactors operating with benchtop batch and benchtop flow-through systems were evaluated by Krause et al. [127] for removing carbamazepine, clofibric acid, and iopromide from an aqueous solution. In the case of benchtop batch configuration, pulsed corona discharge occurred in the air on the liquid surface, whereas in the system with the sample flow corona discharge was generated also in argon-air mixture over a thin water film. In both cases, the grounded electrode coated with catalyst was submerged inside the solution. The concentration of all target compounds decreased with an increase of the plasma treatment time. Several types of submerged electrodes (e.g. boron-doped diamond, iridium oxide, titanium, and iron) serving as a catalyst have been tested. Faster degradation of carbamazepine in the presence of a boron-doped diamond electrode has been observed in comparison to other submerged electrodes.

In order to enhance contact of an effective plasma area with the liquid, Banaschik et al. [128] used a pulsed corona discharge reactor with a coaxial geometry to eliminate seven pharmaceutical compounds (carbamazepine, diatrizoate, diazepam, diclofenac, ibuprofen, 17 $\alpha$ -ethinylestradiol, trimethoprim) from water. The corona discharge was directly generated in the liquid by a wire-type electrode inserted in the center of the tube. The sample was continuously recirculated with about 80 % of the total sample volume processed in the plasma reactor at the time. The complete degradation of diclofenac and ethinylestradiol was noticed. They discussed that the solution pH and concentration of long-lived nitrogen species inside the bulk liquid were not varying significantly because the liquid was not in the contact with any kind of air discharge. They suggested that the short-time high-voltage pulses with fast-rising time lead to the efficient transfer of energy to electrons, whereas longer voltage pulses are prone to thermal losses. They proposed degradation pathways for phenol and found that the hydroxyl radicals were responsible for the primary degradation of phenol. Singh et al. [129] employed a pulsed corona discharge with multiple needles to remove various pharmaceuticals such as diclofenac, carbamazepine, and ciprofloxacin from water. Similarly, the plasma was created in ambient air

**Table 6** Comparison of selected results on the degradation of the pharmaceuticals by different plasma systems

Target compounds	Characteristics of plasma devices	Mode of discharge	Signal type	Operating conditions	T (min)	C <sub>0</sub> (mg/L)	V <sub>0</sub> (ml)	η (%)	References
Tetracycline	Corona	Discharge in bubbles	AC	Gas: air-0.06 m <sup>3</sup> /h, power: 36 W	24	50	250	61.9	[73]
Sulfadiazine	Corona + TiO <sub>2</sub>	Gas-liquid interface discharge	Pulsed	Gas: atmospheric air, power: 100 W	30	10	100	~100	[125]
Diclofenac	Corona	Discharge above liquid surface	Pulsed	Voltage: 20 kV, pulse frequency: 22 Hz, gas: O <sub>2</sub> -1 L/min, power: ~24 W	15	50	55	100	[126]
Carbamazepine, Clofibrac Acid, Iopromide	Corona	Discharge above liquid surface	AC	Voltage: 25-35 kV, frequency: 30 kHz, power: 500 W, gas: air	30	23.6, 21.5, 79.1	200	98, 100, 99	[127]
Diclofenac, Ethinylestradiol, Carbamazepine, Ibuprofen, Trimethoprim, Diazepam, Diatrizoate	Corona	Discharge in liquid	Pulsed	Voltage: 80 kV, repetition rate: 20 Hz, pulses duration 270-300 ns	~60	0.5	300	45-99	[128]
Diclofenac, Carbamazepine and Ciprofloxacin	Corona	Discharge above liquid surface	Pulsed	Voltage: 25 kV, frequency: 30 Hz, gas: ambient air, power: 101.5 W	4 - 8	1	50	~100	[129]



Table 6 continued

Target compounds	Characteristics of plasma devices		T (min)	C <sub>o</sub> (mg/L)	V <sub>o</sub> (ml)	η (%)	References
	Plasma source	Mode of discharge					
Tetracycline	DBD	Gas-liquid interface discharge	30	50	500	92.3	[130]
Paracetamol	DBD	Discharge above liquid surface	60	25	40	81	[131]
Nitrobenzene	DBD	Post discharge	60	20		75	[132]
Pentoxifyline	DBD	Discharge above water film & post discharge	60	100	200	92	[133]
Amoxicillin, Oxacillin, Ampicillin	DBD	Discharge above water film & post discharge	10, 30, 20	100	200	> 90	[122]
Ampicillin	DBD	Discharge above liquid surface	3	6988	1	100	[134]
Enalapril	DBD	Discharge above water film & post discharge	20	50	300	90	[135]
17β-Estradiol	DBD	Discharge above liquid surface	30	0.1	500	100	[136]

Table 6 continued

Target compounds	Characteristics of plasma devices				T(min)	C <sub>o</sub> (mg/L)	V <sub>o</sub> (ml)	η(%)	References
	Plasma source	Mode of discharge	Signal type	Operating conditions					
Cyanide	DBD	Discharge over thin water film	Pulsed	Voltage: 12 kV, , repetition frequency: 94 kHz, power: 24 W, gas: He-500 sccm	3	1	175	99	[137]
Telmisartan	APPJ	Discharge above liquid surface	AC	Voltage: 33 kV, frequency: 30 kHz, gas: Ar-9000 sccm	20			63	[138]
Verapamil	Gliding arc	Discharge above liquid surface		Power: 750 W, frequency: 50 Hz, gas: air-0.86 m <sup>3</sup> /h	80	2.45-24.45	25	37-97	[124]
Oxytetracycline	Pin-to-water electrode	Discharge above liquid surface	AC	Voltage: 3 kV, current: 3 mA, frequency: 5 kHz, gas: ambient air	90	50	50	< 100	[96]
Doxycycline Hyclate	Water-electrode discharge	Discharge in bubbles	AC	Voltage: 3 kV, current: 3 mA, frequency: 5 kHz, gas: air-1 L/min	~ 20	50	50	~ 100	

over the solution surface. They conducted a series of studies on the influence of various parameters like voltage, frequency, initial pH, etc. on the degradation efficiency. They claimed that the degradation was faster in acidic conditions and revealed that more reactive oxygen species were formed for lower pH conditions. The degradation kinetics followed the first-order, and the oxidation rate decreased with an increase in initial concentration.

Recently, Hao et al. [130] used a pulsed coaxial DBD for the degradation of tetracycline in an aqueous solution. The screw-type electrode was connected to a high voltage signal and the aqueous solution was falling over it. The plasma was formed over water film while the air was introduced as a working gas. They reported that the screw-type electrode produced a strong local electric field at the tip, which resulted in a higher plasma intensity. They obtained a higher first-order oxidation rate constants with lower initial concentration of the pollutant compound and higher voltage of the pulsed signal, respectively. Additionally, several intermediates were identified. Baloul et al. [131] studied paracetamol removal by using a DBD plasma with a multiple needle-to-plate reactor configuration and different working gases (air, argon, and nitrogen) with plasmas generated between the tip of the electrodes and the liquid surface. The authors found that higher removal of paracetamol in air plasma. They noticed two types of discharge regimes, spark and streamer. It was observed that the formation of hydroxyl radicals in the spark regime was higher than in the streamer regime because the spark regime supported more evaporation and dissociation of water.

Nawaz et al. [132] investigated the degradation of nitrobenzene in water by utilizing a parallel-plate type DBD reactor with various working gases including oxygen, air, and nitrogen. In this configuration, the reactive species were formed in the DBD system and propagated into a reservoir containing nitrobenzene, so plasma effluent was reacting with the target molecules. They also tested the addition of hydrogen peroxide,  $\text{Fe}^{2+}$  ions and methanol in the solution. Hydrogen peroxide and  $\text{Fe}^{2+}$  ions played a significant role in enhancing degradation, whereas methanol greatly decreased the degradation rate due to its scavenging effect. The degradation process followed first-order kinetic models. In terms of application, nitrobenzene is used to make analgesic acetaminophen or paracetamol. Furthermore, Magureanu et al. [133] studied the decomposition of pentoxifylline by using a pulsed coaxial DBD reactor with oxygen used as the working gas. The sample solution was introduced over the surface of the inner electrode using several holes from the top of the DBD reactor whereas the discharge occurred in the gaseous phase above the thin water film. The solution and gas effluent containing ozone was transferred into a reservoir at the bottom of the plasma reactor, where the post-discharge reaction occurred. The degradation was observed at the plasma-liquid interface as well as in the solution reservoir by bubbling of the gas effluent. Higher pulse frequency and lower initial concentration

of pentoxifylline were noticed to be advantageous for higher degradation. Several by-products were identified before the almost complete degradation was achieved. The same pulsed coaxial DBD plasma reactor with the same conditions was used by Magureanu et al. [122] to remove antibiotics amoxicillin, oxacillin, and ampicillin from an aqueous solution. The researchers observed that amoxicillin was decomposed for the shortest treatment time, whereas oxacillin and ampicillin required longer times. In another study, Magureanu et al. [135] investigated the degradation mechanism of the enalapril compound by using the same plasma reactor. They suggested that processes such as hydrolysis, oxidation, and intra-molecular dehydration were responsible for the breakdown of enalapril. Higher mineralization was obtained at a longer plasma treatment time.

In the study of Smith et al. [134], plasma was generated in ambient air over the liquid surface by using a nanosecond pulsed DBD source with a floating electrode for the treatment of high concentrations of antibiotic ampicillin. The degradation rate was higher with increase in plasma treatment time. According to the results of the characterization of treated solutions, they claimed the complete degradation of ampicillin was achieved. Gao et al. [136] assessed pulsed DBD with a slightly different electrode configuration, where the plasma was formed in ambient air in between the ceramic crucible wall (dielectric) and the surface of the solution, that was used for the treatment of 17 $\beta$ -Estradiol. A high-voltage wire type electrode was submerged in a ceramic crucible containing water, while another electrode was placed in the aqueous solution of pollutant. The experimental results showed degradation was dependent on the initial amount of pollutants, applied peak voltage, pH, and type of water samples. On the other hand, with different water samples, the level of degradation was observed in the following descending order: ultrapure water, tap water, landfill leachate. The authors hypothesized that the lowest degradation of 17 $\beta$ -Estradiol with landfill leachate could be due to higher conductivity and existing impurities (e.g. organic and inorganic). They reported that higher conductivity caused formation of a weaker electric field and less reactive species in the solution which consequently had a negative influence on degradation. Hijosa-Valsero et al. [137] compared two DBD plasma reactors - conventional batch and coaxial thin falling water film for the removal of cyanide from aqueous solution with helium as a working gas in both plasma reactors. In a conventional batch-type reactor, plasma was formed directly underneath the Petri dish containing solution, while, in the other reactor, plasma was generated over the thin falling water film. It was found that a thin falling water film reactor had better performance in comparison to a conventional batch type caused by the large surface of aqueous solution exposed to the plasma. The degradation of cyanide in both types of DBD reactors followed the first-order kinetics. In medicine, the compound cyanide can be found in anti-hypertensive, sodium nitroprusside.

Recently, Vasu et al. [138] used an APPJ with rod and ring-type electrode configuration for the decomposition of telmisartan, where the plasma occurred in argon gas over the liquid surface. However, a complete comparison with the other results could not be accomplished since the initial concentration and sample volume were not reported. Authors observed solution pH decreased and conductivity enhanced with an increase in treatment time and applied voltage. The degradation of telmisartan was observed as pseudo-first-order kinetics with applied voltage. Krishna et al. [124] evaluated the removal of Verapamil hydrochloride from water under the action of gliding arc plasma in air where the discharge was created between two divergent electrodes above the solution. The first-order degradation was obtained and a higher removal rate constant was noticed when the initial concentration of the target compound was lower. These researchers proposed a degradation mechanism with high energy electrons, ozone, and hydroxyl radicals playing dominant roles in the degradation. In a recent article, El Shaer et al. [96] compared two plasma reactors with different configurations - single pin-to-water electrode with plasma above air-water interface and a configuration with water as an electrode with plasma below the interface. The degradation of two antibiotics in water: oxytetracycline hydrochloride and doxycycline hyclate was examined. In the pin-to-water electrode configuration, a wire-type powered electrode formed plasma in air over the liquid surface. In the case of water-electrode configuration, the powered electrode was a hollow needle inserted in a glass tube that was located at the bottom of the vessel. The discharge occurred in the liquid phase when the air was bubbled through the needle. In both cases, grounded electrode was the copper plate placed along the vessel wall and submerged inside the liquid. They concluded that faster degradation was observed when the plasma generated inside the water sample than over the water surface.

### 2.3 Removal of pesticides

Pesticides are nowadays commonly used to protect crops, vegetables and fruits from pathogens [103]. Most of the pesticides discharged into water bodies come from the agricultural industries and through runoff from the agricultural soils [139]. A variety of pesticides (herbicides, insecticides, fungicides, etc.) have been observed in surface and ground waters. Even a low concentration (range of ng/L to  $\mu$  g/L) of pesticides in water can have negative effects on the environment and thus on public health [102,140]. Unfortunately, many pesticides are non-biodegradable while for certain pesticides conventional treatment methods are inefficient for degradation due to their chemical structure complexity [141]. Therefore, to eliminate the potential risks related to pesticides, it is necessary to treat wastewater containing pesticides before releasing them to the natural water recipient.

The oxidation of organic pesticides in water based on low-temperature plasma treatments has been employed by many authors in order to tackle this issue and it was found that plasma processing can successfully eliminate pesticides from water without formation of the secondary toxic by-products [142]. A number of research papers have been published on plasma sources for the degradation of pesticides in water and a comparison of selected data is presented in Table 7.

Singh et al. [142] have designed a multiple needle-to-plane pulsed corona discharge reactor for the treatment of an aqueous solution containing carbofuran, where the plasma was formed in ambient air (without any external feed gas) over the liquid surface. The tungsten needle high voltage electrodes were attached to the circular plate and located above the solution, whereas the ground electrode was fixed in the solution. The streamer propagation occurs due to the high intensity of local electric field over the tip of the needle electrodes. They studied the effect of several experimental parameters on the degradation of carbofuran, including applied pulsed voltage, pulsing frequency, initial carbofuran concentration, initial pH and dependence of the process on radical scavengers. It was observed that higher pulsing frequency and applied pulsed voltage favored faster degradation, suggesting that more reactive species were produced and transferred to the solution. On the other side, addition of radical scavengers ( $\text{HCO}_3^-$ ,  $\text{CO}_3^{2-}$  and humic acid) diminished the degradation by quenching the hydroxyl radicals. The degradation followed the first-order kinetics model, and the oxidation rate was higher for the lower initial concentration of carbofuran. Moreover, they identified seven intermediates compounds before complete mineralization. Bradu et al. [143] used a slightly different type of pulsed corona discharge reactor for the degradation of 2,4-dichlorophenoxyacetic acid herbicide in water, where oxygen plasma was formed in between a multi-wire array (consisting of 20 copper electrodes) and the liquid surface. The solution was circulated from the reservoir to the plasma reactor while the plasma effluent that consisted mainly of oxygen and ozone was bubbled inside the solution from the bottom of the reservoir to induce post-discharge reactions. The concentration of ozone was measured in the plasma effluent and separately the same amount of ozone was introduced inside the reservoir using a solution for ozonation. They observed faster degradation when the plasma was generated at the gas-liquid interface and with the plasma effluent bubbled inside the solution in comparison to the ozonation alone. Additionally, when 2,4-dichlorophenoxyacetic was treated directly by plasma without bubbling of effluent slower degradation was noticed than for both cases. In the study of Mededovic and Locke [144], a pulsed corona discharge with a combination of  $\text{FeSO}_4 \cdot 7\text{H}_2\text{O}$  electrolyte was employed for the degradation of atrazine in water. The plasma was formed in between point-to-plane electrode inside the liquid. They claimed the addition of  $\text{FeSO}_4 \cdot 7\text{H}_2\text{O}$  leads to complete removal of the target compound caused by Fenton reaction between ferrous ions and plasma

**Table 7** Overview of plasma systems described in the literature for the degradation of the pesticides

Target compounds	Characteristics of plasma devices			Operating conditions	T (min)	C <sub>o</sub> (mg/L)	V <sub>o</sub> (ml)	η (%)	References
	Plasma source	Mode of discharge	Signal type						
2,4-dichlorophenoxyacetic acid	Corona discharge + Ozonation	Discharge above liquid surface + Post discharge	DC/Pulsed	Voltage: 18 kV, Pulse repetition rate: 25 Hz, plasma gas: O <sub>2</sub> -0.3 L/min, power: 11 W	30	25	330	~ 100	[143]
Atrazine	Corona + Fenton	Discharge in liquid	DC/Pulsed	Voltage: 45 kV, pulse frequency: 60 Hz, pulse width: 1 μs	10	5	400	100	[144]
Atrazine	DBD	Discharge above liquid surface	DC/Pulsed	Voltage: 23 kV, frequency: 300 Hz, pulse duration: 400 ns, gas-air 0.5 SLM, power: 1.7 W	45	0.03	100	61	[145]
Dichlorvos, Malathion, Endosulfan	DBD + Nanofiber membrane	Discharge above liquid surface	DC/Pulsed	Voltage: 80 kV, frequency: 50 Hz, gas: atmospheric air	8	2	20	78.98, 69.62, 57.71	[139]
Atrazine	DBD	Discharge above liquid surface	AC	Voltage: 20 kV, frequency: 100 kHz, gas: Helium-5 L/min, power: 30 W	5	5	4	93	[146]
Chlorfenvinphos						5		94	

Table 7 continued

Target compounds	Characteristics of plasma devices			Operating conditions	T(min)	C <sub>o</sub> (mg/L)	V <sub>o</sub> (ml)	η(%)	References
	Plasma source	Mode of discharge	Signal type						
Dichlorvos	DBD	Discharge above liquid surface	AC	Voltage: 0–250 V, frequency: 5–35 kHz, current: 0–1.2 A, gas: air, power: 85 W	6	60	40	~ 100	[147]
Dimethoate	DBD	Discharge above liquid surface	AC	Voltage: 80 V, current: 1–2.5 A, power: 200 W	6	10	40	~ 100	[148]
Nitenpyram					180	100	~ 83		
Acetamiprid	DBD	Discharge above liquid surface	AC	Voltage: 250 V, current: 0–4 A, power: 170 W	200	50		~ 83	[149]
Alachlor	DBD	Discharge in bubbles	AC	Voltage: 8 kV, frequency: 50 kHz, gas: O <sub>2</sub> –1 L/min, power: 40 W	30	1	500	~ 100	[103]
	DBD + Ozonation	Discharge in bubbles and post-discharge			15			~ 100	

generated hydrogen peroxide. The authors compared processes with a high voltage electrode made of platinum and nickel-chromium and observed that degradation was amplified with a platinum type electrode.

Vanraes et al. [145] evaluated the DBD plasma-induced degradation of atrazine in the presence of adsorption nanofiber polyamide membranes. The plasma was generated in dry air above a thick water film which was introduced on the membrane. It was found that degradation was increased with addition of the nanofiber polyamide membrane in comparison to the plasma alone. The main influence of the membrane was to expose the pollutants absorbed on the membrane to the plasma. They identified deethylatrazine and ammelide as by-products in the degradation process. Sarangapani et al. [139] investigated the degradation of three pesticides dichlorvos, malathion, and endosulfan in water in a sealed DBD plasma reactor with two circular plate-type electrodes configuration. The solution containing pesticides was placed in a petriplate in between two electrodes, whereas the plasma was formed in the ambient air above the solution. At fixed applied voltage and treatment time, decomposition rates of pesticides were in the following order: dichlorvos, malathion, endosulfan. The degradation of pesticides was fitted by the first-order kinetics and the rate constant increased with applied voltage. Also, they reported the generation of acidic species in the solution including nitric acid and nitrous acid. Hijosa-Valsero et al. [146] compared the degradation of atrazine, chlorfenvinphos, 2,4-dibromophenol and lindane in the aqueous solutions in a batch type DBD system and in a coaxial thin falling water film reactor with noble gas helium as a working gas in both types of reactors. In the case of the DBD batch reactor, a solution containing a petri dish was placed in two Pyrex glass containers (served as dielectric barriers). When high voltage was applied to the electrode the discharge takes place in gas in contact with the sample. In a coaxial thin-film DBD reactor, a copper mesh type of electrode was used as a high voltage electrode and it was wrapped over the glass vessel (served as a dielectric barrier). A stainless steel tube acted as a grounded electrode was situated at the vessel's axial center. The solution was introduced from the top and wetted surface was formed on the tube. The discharge occurs in helium over the thin falling film. The degradation followed the first-order kinetics for both reactors and the degradation rate of all pollutants was faster in the batch type DBD reactor. Reddy et al. [102] studied the degradation of pesticide endosulfan in an aqueous solution in a combination of a DBD plasma and a cerium oxide catalyst. The plasma occurred inside the solution when air as a working gas was bubbled through the sample. They claimed that the addition of catalyst showed better degradation performance than plasma alone and the enhancement of degradation of endosulfan in the aqueous solution was attributed to the catalyst-induced decomposition of ozone into atomic oxygen species. They reported fitting of the first-order degradation kinetics on both treatment conditions (plasma – catalyst and plasma alone).

Hu et al. [147] demonstrated the degradation of dichlorvos and dimethoate in wastewater by utilizing DBD plasma formed in the air over the solution. It was found that the reduction of the discharge gap had a significant positive effect on degradation due to formation of a stronger electric field and hence higher concentrations of reactive species. On the other hand, the addition of hydroxyl radical scavenger (tertbutyl alcohol) had an adverse effect on the degradation of both pesticides, demonstrating that hydroxyl radicals were the main species responsible for degradation. The degradation kinetics of both compounds were a combination of the zeroth and first-order. An unusual DBD plasma reactor has been evaluated by Li et al. [148] for the treatment of a solution containing nitenpyram, where the plasma was created in ambient air above the sample. The reactor consists of a radial-flow sedimentation tank, with a high-voltage electrode situated on top of the tank above the quartz glass while the ground electrode was a wire inserted in the center of the tank, inside the liquid. The solution was recirculated continuously during plasma treatments. They studied a series of parameters that influence the degradation, including initial pH, the addition of catalysts ( $\text{FeSO}_4$ ,  $\text{Fe}_2(\text{SO}_4)_3$  and  $\text{MnO}_2$ ), solution conductivity, plasma power, and so on. The degradation rate was improved by the addition of the catalysts. Apart from this, higher pH, lower conductivity and higher power supplied to plasma favored faster degradation process. Li et al. [149] used the same DBD plasma reactor configuration for the decomposition of acetamiprid in wastewater. They tested the effect of a radical scavenger ( $\text{Na}_2\text{B}_4\text{O}_7$ ) on the degradation and showed that it was inhibited by the addition of  $\text{Na}_2\text{B}_4\text{O}_7$ . Recently, Wardenier et al. [103] used a pulsed DBD plasma reactor coupled with activated carbon and ozonator for the elimination of pesticide alachlor. The experiments were performed in two different modes of operation of the sample flow, batch recirculation and single-pass. The oxygen was used as a working gas. They concluded that faster removal of alachlor was achieved during the plasma-ozonation in the batch recirculation type reactor configuration.

### 3 Discussion

A broad range of cold plasma systems with different reactor configurations and operational parameters have been employed and evaluated for the removal of OMPs. In general, the majority of analyzed studies use gas-phase plasma established above liquid samples in air or air mixtures with other working gases. Volumes of samples processed in the experiments range from 1 ml to 1000 ml. Types of plasma sources present in the literature and used in the decontamination processes of the pesticides, pharmaceuticals and dyes are corona, APPJs, DBDs, etc. [73, 74, 97, 116, 122, 143]. Of course, this list is much longer, but we tried to limit the types of plasma sources that will be discussed to the ones most commonly used. The corona discharges usually

have pin pin-to-pin, pin-to-plate or multi-pin configurations and are powered predominantly with pulsed signals [94, 113, 142]. They can operate in the gas phase where the powered electrode is above the treated solution or in liquid phase. In liquid phase powered electrode is inside the treated solution and the plasma is formed inside the bubbles or directly in liquid. The pin electrode configuration is needed in order to obtain the high electric field to ignite the discharge [71, 72, 91]. The drawback associated with single pin electrode type configuration is the generation of lower plasma volume. To enlarge the reaction zone multi-pin electrodes were studied that can lead to the treatment of larger quantity of contaminated water in a shorter period of time.

Similar issues can be found when using the APPJs for decontamination of water. The APPJs have plasma confined in the small volumes and only adding more APPJs will lead to the treatments of larger volumes of contaminated water. Geometry of the APPJs will also influence the efficiency of the treatments. With pin-APPJ (powered electrode is pin type) lower applied powers will be needed for sustaining the discharge (larger electric field at the tip) if compared with the DBD type of APPJ (electrodes wrapped around the glass tube). Another way how to improve the plasma treatment, especially in the case of pin type plasma systems, is to increase the plasma-solution interaction volume through geometries that involve discharges over the falling film [125, 130, 146] or recirculation of the treated solution [105, 128]. With DBDs that have parallel electrode system this issue is addressed to some extent. In this case the plasma-liquid interaction surface is larger, but again, if the volume of the treated solution is significant this can hinder the final outcome. In this case the recirculation of the treated solution or treatment of large area of thin layer of solution will increase the transfer of the reactive species from the plasma to the bulk of the solution and increase the efficiency.

Pulsed DC corona and DBD plasma over the thin water film are considered most efficient in the degradation of OMPs [71, 109, 125, 127, 130] with the efficiencies going to 100%. Higher mass transfer of reaction species from gas to bulk phase with molecular diffusion along with the plasma discharge leads to faster degradation of OMPs [69, 150, 151]. The thin water film offers a larger surface to volume ratio than other configurations. The bigger plasma-solution contact surface means higher residence time, hence, more interaction of reactive species with the solution for oxidation reaction [152, 153]. Another way to increase the contact surface is the pulsed corona discharge with a wetted-wall type reactor and coaxial geometry [125, 128]. It was observed that plasma reactors with continuously mixed solutions have better performance [109, 143, 154].

In most cases present in the literature, during the treatments discharges are in contact with water or operating in water. Apart from the configurations where short- and long-lived reactive species created in the plasma are in direct contact with the contaminated solution, there are also examples where only long-lived

species created in plasma are responsible for the degradation of pollutants [30, 108, 115, 118]. In these cases the short-lived radicals, ions and UV emission are not involved in the processes of degradation. For example, Rahimpour et al. [115] used DBD reactor for the treatment of crystal violet dye, where oxygen was used as a feed gas, and the plasma effluents (e.g. ozone) were bubbled in the solution column. In another study by Jiang et al. [118], plasma discharge occurred in the bubble in the liquid solution, where oxygen was used as a feed gas. In this case, the plasma effluent along with treated methyl orange solution passed through the tube and finally bubbled in the reservoir (outside of the plasma reactor). The post-discharge configuration was more favorable than other operation methods for dye treatment. It provides a large interfacial area that leads to an increase in mass transfer between the gas phase and the liquid phase.

Cold atmospheric plasmas are generated by using various feed gases, but mostly by using noble gases (e.g. argon and helium) with the combination of pure molecular gases and/or air (e.g. oxygen and nitrogen) [72, 119]. Argon and helium have lower breakdown voltage potential characteristics at atmospheric pressure. Therefore, due to the addition of argon and helium with other working gases, the lower voltage can effectively ignite and produce stable plasma discharge and to improve the formation of reactive species. Since they are usually sustained in air the nitrogen-based species are formed and transferred to the solution that can lead to lower pH value of the solution and increased electrical conductivity [113]. From several experimental studies, it has been found that the presence of pure oxygen in the feed promotes faster OMPs degradation due to the production of the greater amounts of short and long-living reactive oxygen species [71, 74, 155]. The negative side of using the noble gases (especially helium) is their price and need for a more complex system for decontamination. One of the solution is to use the cheaper working gas (for example Ar) and to recirculate it within the system [30, 156].

We can see that direct comparison of the different types of plasma devices is not straightforward. Too many parameters are influencing the efficiency of the decontamination and it does not depend only on the type of the plasma device used. Of course, with increase of the power deposited to the discharge one can achieve higher decontamination efficiency regardless of the device type [101, 108]. Corona discharges have the advantage of not using the additional working gas (APPJs and DBD plasma systems mostly use them). But the corona pin type discharges are usually low volume discharges. As we mentioned above that is a setback that can be overcome. Similarly with the APPJs if one uses recirculation of the working gas (for example Ar) the efficiency is obtained and the overall price is still manageable. All of these issues need to be addressed in order to be able to upscale the plasma systems in order to use them in large installations. Unfortunately, there is no definite conclusion which type of plasma device is the most efficient one especially when we take



into account the type of the pollutant that needs to be decontaminated.

The same experimental conditions different compounds show different treatment results, which revealed that each target compound behaves differently when they come in contact with the plasma [10,30,117,157]. The authors reported that the same plasma device cannot degrade various OMPs to the same extent, therefore different compounds demand different plasma conditions for degradation. Attri et al. [116] have noticed different degradation results at the same experimental condition during the treatment with three organic dyes (methylene blue, methyl orange and congo red dyes) by using argon APPJ. A study conducted by Banaschik et al. [128], where 7 different pharmaceuticals (carbamazepine, diatrizoate, diazepam, diclofenac, ibuprofen, 17 $\alpha$ -ethinylestradiol, trimethoprim) were treated by pulsed corona discharge, while plasma occurs directly in aqueous solution. It was found that diclofenac and ethinylestradiol were almost completely degraded, whereas other compounds were not destroyed completely at the same plasma conditions. It was claimed that reactivity between compound and ozone was significantly slow. In the case of pesticides, almost the same dissimilarity is obtained between different pollutants while treatment with the same plasma conditions [139]. Degradation depends on the nature of compounds (e.g. functional group, molecular structure, etc.). Some persistent organic compounds are not very responsive to all plasma-generated reactive species ( $H_2O_2$ ,  $O_3$ , etc) due to their chemical stability [30,69,128]. Some pollutants are hydrophobic and they accumulate at the surface which leads to an increase in their concentration compared to average bulk concentration [91,157]. In this case proper mixing is required in order to transfer the reactive species into the bulk liquid and to avoid the consumption of reactive species by pollutants at the surface. In such cases, plasma reactor with a configuration where reactive species generated over large surfaces (e.g. thin falling film with continuous recirculation) could be more efficient for degradation [125,127].

The presence of impurities in the water sample can diminish the interaction of plasma-produced reactive species and target molecules in the liquid. For example, higher degradation of OMPs were observed in pure water than tap water and other water samples with impurities [94,136]. This effect is due to the interaction between plasma generated chemically active species with minerals and some organic substances present in tap water. Lower solution pH (acidic conditions) and lower electrical conductivity of the sample seem to enhance the decomposition of most pollutants due to the faster reactivity of reactive oxygen species in such a liquid environment [105,148]. However, a decreased pH is often not desirable in environmental applications. The effect of increased solution temperature was shown to have a positive influence on the degradation [113] due to the faster reactivity of plasma-generated reactive species.

When it comes to chemical kinetics and decomposition rates, general degradation of OMPs in most of

the experiments followed the first-order kinetic model with different applied voltage, plasma power, initial pollutant concentration [90,108,129,147]. Additionally, a few zero-order degradation kinetics have also been present in the case of the treatment of dichlorvos and dimethoate by DBD plasma where the air plasma was formed over the solution [147]. The first-order rate kinetics indicates that the degradation of OMPs is directly proportional to the initial concentration of OMPs. On the other hand, the zero-order kinetics means that the degradation of OMPs is independent of the initial concentration of OMPs. Generally, zero-order kinetics occurs where all reactive species react with OMPs, especially at a higher initial concentration.

Degradation pathways were analyzed by many authors using various tools such as liquid or gas chromatography coupled to mass spectrometry (LC-MS, GC-MS) and nuclear magnetic resonance spectroscopy (NMR) enabling identification of typically several transformations products [45,134,142]. Generally, such studies show similar degradation patterns obtained with plasma treatment in comparison to the other oxidative water treatment processes. Unlike other oxidation processes, the study of transformation by-products provided also evidence for reductive pathway occurrence in plasma treatments, which is an uncommon and potentially useful feature of plasma-driven degradation processes [142]. For example, reductive processes can contribute to the degradation of perfluorinated compounds, a group of compounds of major environmental and human health concern [158].

A synergetic combination of heterogeneous catalysts and plasma reactors has been proposed as another innovative approach and recommended for efficient OMPs degradation [114,148]. In all synergetic experimental setups, adding the catalyst had a beneficial effect on the efficiency of the decomposition process. The most commonly used catalyst with a combination of plasma reactors are  $TiO_2$  nanoparticles, and these systems showed better performances than systems with plasma only. The increased decomposition with the addition of  $TiO_2$  catalyst in the solution is ascribed to the formation of hydroxyl radicals due to photocatalytic reactions on the surface of  $TiO_2$  in the presence of plasma generated ultraviolet radiation. Therefore, the degradation of OMPs can be significantly improved by the addition of  $TiO_2$ . On the other hand, there are a few drawbacks associated with catalyst implementation. For example, if the catalysts are added in the form of a slurry then the separation step must be needed to remove them from the treated water for safety concerns.

The energy yield is an important, but complex factor in cold plasma-based wastewater treatment and it depends on several factors (applied power, geometry of the plasma device, plasma volume/surface, working gas that is used etc.). The energy yield is mostly expressed in milligrams or grams/kilowatt-hour (mg or g/kWh) and represents the energy (kWh) needed to effectively eliminate the amount of (mg or g) of OMPs from water [118]. Unfortunately, not all the papers published on the plasma decontamination have reported the energy

yields or data necessary to calculate this value. Generally, various authors suggest that a higher energy yields were obtained with pulsed corona and pulsed DBD plasma when discharge takes place in oxygen at the gas-liquid interface [30, 71, 115, 118, 122, 143]. Based on the covered literature and available data, the energy yields for cold plasma-based wastewater treatment systems are in the range of 1 mg/kWh – 12.24 g/kWh for organic dyes, 0.13 mg/ kWh – 105 g/kWh for pharmaceuticals and 1.22 mg/kWh – 5.1 g/kWh for pesticides.

## 4 Conclusions

Cold plasma technology-based AOPs is a fast emerging field of research aiming to eliminate a wide variety of non-biodegradable OMPs from water. In this article, we reviewed various types of cold atmospheric plasma devices with different operating parameters employed for the degradation of different OMPs (organic dyes, pharmaceuticals, and pesticides) in wastewater. It was found that many parameters can influence degradation, including plasma source, reactor configuration, plasma gas, type of discharge, target compound, and so on. Since many different experimental setups are exploiting a variety of plasma sources, for proper comparison one needs to involve plasma, sample and treatment characteristics.

Overall, it is evident from previous investigations that the cold atmospheric plasma systems showed the potential and innovative route for an effective degradation and complete mineralization of OMPs which cannot successfully be removed by conventional treatment methods. A specifically distinctive feature of plasma chemistry is that simultaneously oxidative and reductive contaminant transformation processes can occur. Therefore, treatment with cold plasma could be an attractive, valuable, and versatile tool for future applications of OMPs removal from wastewater.

However, the authors would like to highlight that there was a lack of information in the majority of papers related to experimental parameters, such as the exact amount of power consumption in order to generate the plasma, sample volume, initial solution pH, solution conductivity, solution temperature, etc. These parameters can have a significant effect on the degradation of OMPs. Specifically, they are needed to assess thoroughly decontamination process performance beyond simple criteria such as the degree of removal achieved. Widely accepted parameter suitable for comparing between different wastewater treatment methods, the energy efficiency, in the case of plasma treatment is not only the function of plasma sources and reactor configurations but it is also dependent on the electrical property of the sample. This entanglement hinders the straight-forward calculation of the parameter and therefore energy efficiency of the plasma sources could not be discussed in this paper. Apart from this, there are several other factors influencing the efficiency of the plasma process, including types of pollutants,

chemical structure, concentration, initial pH, the ability of the water matrix to scavenge reactive species, mode of discharge, working gases, applied voltage characteristics, etc. We hence would like to conclude that for the field of wastewater treatment with plasma to further evolve and allow for objective comparisons, a more methodological approach to the characterization of experimental systems should be developed.

**Acknowledgements** This work was carried out within project NOWELTIES. NOWELTIES received funding from the European Union's Horizon 2020 research and innovation programme under the Marie Skłodowska-Curie grant agreement No. 812880. N.S. and N.P. are funded by Ministry of Education, Science and Technological Development, grant number 451-03-68/2020-14/200024. This article is based upon work from COST Action PLAGRI - CA19110, supported by COST (European Cooperation in Science and Technology), [www.cost.eu](http://www.cost.eu).

## Author contributions

Conceptualization N.P., W.G., N.S.; literature survey A.K.; writing—original draft preparation, review and editing A.K., N.S., N.P., W.G.; supervision, N.P., W.G.; project administration, N.P., W.G.. All authors have read and agreed to the published version of the manuscript.

**Data Availability Statement** This manuscript has associated data in a data repository [Authors comment: The data that support the findings of this study are available from the corresponding author upon reasonable request.]

**Open Access** This article is licensed under a Creative Commons Attribution 4.0 International License, which permits use, sharing, adaptation, distribution and reproduction in any medium or format, as long as you give appropriate credit to the original author(s) and the source, provide a link to the Creative Commons licence, and indicate if changes were made. The images or other third party material in this article are included in the article's Creative Commons licence, unless indicated otherwise in a credit line to the material. If material is not included in the article's Creative Commons licence and your intended use is not permitted by statutory regulation or exceeds the permitted use, you will need to obtain permission directly from the copyright holder. To view a copy of this licence, visit <http://creativecommons.org/licenses/by/4.0/>.

## References

1. S. Khalifa, M. Bidaisee, Sch. J. Appl. Sci. Res. **1**, 17 (2018)
2. F. Mugagga, B.B. Nabaasa, Int. Soil Water Conserv. Res. **4**, 215 (2016)
3. S. Naidoo, A. Olaniran, Int. J. Environ. Res. Public Health **11**, 249 (2013)

4. A. Jelić, M. Gros, M. Petrović, A. Ginebreda, D. Barceló, *Emerg. Prior. Pollut. Rivers*. **19**, 1 (2012)
5. Y. Luo, W. Guo, H.H. Ngo, L.D. Nghiem, F.I. Hai, J. Zhang, S. Liang, X.C. Wang, *Sci. Total Environ.* **473–474**, 619 (2014)
6. L. Sbardella, I. Velo-Gala, J. Comas, I. Rodríguez-Roda Layret, A. Fenu, and W. Gernjak, *J. Hazard. Mater.* **380**, 120869 (2019)
7. L. Rizzo, S. Malato, D. Antakyali, V. G. Beretsou, M. B. Dolić, W. Gernjak, E. Heath, I. Ivancev-Tumbas, P. Karaolia, A. R. Lado Ribeiro, G. Mascolo, C. S. Mc Ardell, H. Schaar, A. M. T. Silva, D. Fatta-Kassinou, *Sci. Total Environ.* **655**, 986 (2019)
8. V. Katheresan, J. Kansedo, S.Y. Lau, *J. Environ. Chem. Eng.* **6**, 4676 (2018)
9. N. Pathak, V.H. Tran, A. Merenda, M.A.H. Jahir, S. Phuntsho, H. Shon, *Appl. Sci.* **10**, 2969 (2020)
10. M. Magureanu, N.B. Mandache, V.I. Parvulescu, *Water Res.* **81**, 124 (2015)
11. E. Forgacs, T. Cserhádi, G. Oros, *Environ. Int.* **30**, 953 (2004)
12. E. Routoula, S.V. Patwardhan, *Environ. Sci. Technol.* **54**, 647 (2020)
13. T.A. Nguyen, R.-S. Juang, *Chem. Eng. J.* **219**, 109 (2013)
14. S. Benkhaya, S. Mrabet, A. El Harfi, *Inorg. Chem. Commun.* **115**, 107891 (2020)
15. N. Wardenier, Non-Equilibrium plasma in contact with water as advanced oxidation process for decomposition of micropollutants, Masters dissertation, Ghent University, 2016
16. P. Schröder, B. Helmreich, B. Škrbić, M. Carballa, M. Papa, C. Pastore, Z. Emre, A. Oehmen, A. Langenhoff, M. Molinos, J. Dvarioniene, C. Huber, K.P. Tsagarakis, E. Martinez-Lopez, S.M. Pagano, C. Vogel-sang, G. Mascolo, *Environ. Sci. Pollut. Res.* **23**, 12835 (2016)
17. C.S. Leal, D.P. Mesquita, A.L. Amaral, A.M. Amaral, E.C. Ferreira, *Crit. Rev. Environ. Sci. Technol.* **50**, 698 (2020)
18. M.J. Ahmed, *J. Environ. Manage.* **190**, 274 (2017)
19. A. Bayer, R. Asner, W. Schüssler, W. Kopf, K. Weiß, M. Sengl, M. Letzel, *Environ. Sci. Pollut. Res.* **21**, 10830 (2014)
20. A. Lajeunesse, S.A. Smyth, K. Barclay, S. Sauvé, C. Gagnon, *Water Res.* **46**, 5600 (2012)
21. H. He, Y. Liu, S. You, J. Liu, H. Xiao, Z. Tu, *Int. J. Environ. Res. Public Health* **16**, 5129 (2019)
22. N. Stamatis, D. Hela, I. Konstantinou, *J. Hazard. Mater.* **175**, 829 (2010)
23. T. Ahmad, M. Rafatullah, A. Ghazali, O. Sulaiman, R. Hashim, A. Ahmad, *J. Environ. Sci. Heal. Part C* **28**, 231 (2010)
24. J. Regnery, P. Parrhysius, R.S. Schulz, C. Möhlenkamp, G. Buchmeier, G. Reifferscheid, M. Brinke, *Water Res.* **167**, 115090 (2019)
25. W.-Q. Han, L.-J. Wang, X.-Y. Sun, J.-S. Li, *J. Hazard. Mater.* **151**, 306 (2008)
26. R. Katal, H. Zare, S.O. Rastegar, P. Mavaddat, G.N. Darzi, *Environ. Eng. Manag. J.* **13**, 43 (2014)
27. W. Zheng, X. Li, Z. Hao, D. Wang, Q. Yang, G. Zeng, *Water Sci. Technol.* **62**, 15 (2010)
28. N. Misra, R. Satyanarayan, S. Potle, *Int. J. Chem. Phys. Sci.* **2**, 39–51 (2013)
29. E.M. Cuerda-Correa, M.F. Alexandre-Franco, C. Fernández-González, *Water* **12**, 102 (2019)
30. M. Hijosa-Valsero, R. Molina, A. Monràs, M. Müller, J.M. Bayona, *Environ. Technol. Rev.* **3**, 71 (2014)
31. P.R. Gogate, A.B. Pandit, *Adv. Environ. Res.* **8**, 553 (2004)
32. P.R. Gogate, A.B. Pandit, *Adv. Environ. Res.* **8**, 501 (2004)
33. O. Legrini, E. Oliveros, A.M. Braun, *Chem. Rev.* **93**, 671 (1993)
34. A.S. Stasinakis, *Glob. NEST J.* **10**, 376 (2008)
35. Z. L. Makabe, T., & Petrovic, *Plasma electronics: applications in microelectronic device fabrication* (Vol. 26), (CRC Press, 2014)
36. F.F. Chen, *Introduction to plasma physics and controlled fusion*, 3rd edn. (Springer, Cham, 2016)
37. M.A. Lieberman, A.J. Lichtenberg, *Principles of plasma discharges and materials processing*, 2nd edn. (Wiley, Hoboken, NJ, USA, 2005)
38. A. Fridman, *Plasma chemistry*, 1st edn. (Cambridge University Press, Cambridge, 2008)
39. P. Bruggeman, R. Brandenburg, *J. Phys. D. Appl. Phys.* **46**, 464001 (2013)
40. A. Schutze, J.Y. Jeong, S.E. Babayan, J. Park, G.S. Selwyn, R.F. Hicks, *IEEE Trans. Plasma Sci.* **26**, 1685 (1998)
41. C. Tendero, C. Tixier, P. Tristant, J. Desmaison, P. Leprince, *Spectrochim. Acta Part B. At. Spectrosc.* **61**, 2 (2006)
42. J.E. Foster, *Phys. Plasmas* **24**, 055501 (2017)
43. P.J. Bruggeman, F. Iza, R. Brandenburg, *Plasma Sour. Sci. Technol.* **26**, 123002 (2017)
44. J. Ananthanarasimhan, R. Lakshminarayana, M.S. Anand, S. Dasappa, *Plasma Sources Sci. Technol.* **28**, 085012 (2019)
45. L. Wu, Q. Xie, Y. Lv, Z. Wu, X. Liang, M. Lu, Y. Nie, *Water* **11**, 1815 (2019)
46. S. Gopi, A. Sarma, A. Patel, G. Ravi, *Instrum. Sci. Technol.* **41**, 651 (2013)
47. F. Rezaei, P. Vanraes, A. Nikiforov, R. Morent, N. De Geyter, *Mater. (Basel)*. **12**, 2751 (2019)
48. A.K. Jaiswal, J. Ananthanarasimhan, A.M. Shivapuji, S. Dasappa, L. Rao, *J. Phys. D. Appl. Phys.* **53**, 465205 (2020)
49. A.M. Ali, M.A.A. Hassan, B.I. Abdulkarim, *IOSR. J. Environ. Sci.* **10**, 63 (2016)
50. P. Favia, G. Cicala, A. Milella, F. Palumbo, P. Rossini, R. D-Agostino, *Surf. Coatings Technol.* **169–170**, 609 (2003)
51. E.E. Kunhardt, *IEEE Trans. Plasma Sci.* **28**, 189 (2000)
52. J.R. Roth, *Industrial plasma engineering*, 1st edn. (CRC Press, Florida, 1995)
53. M. Gorenšek, M. Gorjanc, V. Bukošek, J. Kovač, Z. Petrović, N. Puač, *Text. Res. J.* **80**, 1633 (2010)
54. D. Mance, R. Wiese, T. Kewitz, H. Kersten, *Eur. Phys. J. D* **72**, 98 (2018)
55. S. Živković, N. Puač, Z. Giba, D. Grubišić, Z.L. Petrović, *Seed Sci. Technol.* **32**, 693 (2004)
56. J. Heinlin, G. Morfill, M. Landthaler, W. Stolz, G. Isbary, J.L. Zimmermann, T. Shimizu, S. Karrer,

- J.D.D.G.J. Der Dtsch, Dermatologischen Gesellschaft **8**, 968 (2010)
57. D. Mariotti, T. Belmonte, J. Benedikt, T. Velusamy, G. Jain, V. Švrček, *Plasma Process. Polym.* **13**, 70 (2016)
  58. N. Puač, M. Gherardi, M. Shiratani, *Plasma Process. Polym.* **15**, 1700174 (2018)
  59. N. Puač, Z.L. Petrović, G. Malović, A. Dordević, S. Živković, Z. Giba, D. Grubišić, *J. Phys. D. Appl. Phys.* **39**, 3514 (2006)
  60. J. Winter, R. Brandenburg, K.-D. Weltmann, *Plasma Sour. Sci. Technol.* **24**, 064001 (2015)
  61. J. Peran & S. Ercegović Ražić, *Text. Res. J.* **90**, 1174 (2020)
  62. A. Zille, F.R. Oliveira, A.P. Souto, *Plasma Process. Polym.* **12**, 98 (2015)
  63. C. Bradu, K. Kutasi, M. Magureanu, N. Puač, S. Živković, *J. Phys. D. Appl. Phys.* **53**, 223001 (2020)
  64. T. von Woedtke, S. Reuter, K. Masur, K.-D. Weltmann, *Phys. Rep.* **530**, 291 (2013)
  65. M.G. Kong, G. Kroesen, G. Morfill, T. Nosenko, T. Shimizu, J. van Dijk, J.L. Zimmermann, *New J. Phys.* **11**, 115012 (2009)
  66. V.I. Parvulescu, M. Magureanu, P. Lukes, *Plasma chemistry and catalysis in gases and liquids*, 1st edn. (Wiley, New York, 2012)
  67. N. Škoro, D. Marić, G. Malović, W.G. Graham, Z.L. Petrović, *Phys. Rev. E* **84**, 055401 (2011)
  68. L. Bárdos, H. Baránková, *Thin Solid Films* **518**, 6705 (2010)
  69. B. Jiang, J. Zheng, S. Qiu, M. Wu, Q. Zhang, Z. Yan, Q. Xue, *Chem. Eng. J.* **236**, 348 (2014)
  70. J. Zhang, J. Chen, X. Li, *J. Water Resour. Prot.* **01**, 99 (2009)
  71. M.A. Malik, *Plasma Chem. Plasma Process.* **30**, 21 (2010)
  72. P. Vanraes, A. Y. Nikiforov, and C. Leys, in *Plasma Sci. Technol. - Prog. Phys. States Chem. React.* (InTech, 2016)
  73. D. He, Y. Sun, L. Xin, J. Feng, *Chem. Eng. J.* **258**, 18 (2014)
  74. M. Magureanu, D. Piroi, F. Gherendi, N.B. Mandache, V. Parvulescu, *Plasma Chem. Plasma Process.* **28**, 677 (2008)
  75. N. Škoro, N. Puač, S. Živković, D. Krstić-Milošević, U. Cvelbar, G. Malović, Z.L. Petrović, *Eur. Phys. J. D* **72**, 2 (2018)
  76. P. Lukes, E. Dolezalova, I. Sisrova, M. Clupek, *Plasma Sources Sci. Technol.* **23**, 015019 (2014)
  77. R. Zhou, T. Zhang, R. Zhou, A. Mai-Prochnow, S.B. Ponraj, Z. Fang, H. Masood, J. Kananagh, D. McClure, D. Alam, K. Ostrikov, P.J. Cullen, *Sci. Total Environ.* **750**, 142295 (2021)
  78. N. Puač, M. Miletić, M. Mojović, A. Popović-Bijelić, D. Vuković, B. Miličić, D. Maletić, S. Lazović, G. Malović, Z.L. Petrović, *Open Chem.* **13**, 332 (2014)
  79. P. Bruggeman, C. Leys, *J. Phys. D. Appl. Phys.* **42**, 053001 (2009)
  80. J. Du, Z. Liu, C. Bai, L. Li, Y. Zhao, L. Wang, J. Pan, *Eur. Phys. J. D* **72**, 179 (2018)
  81. A. Capodaglio, *Appl. Sci.* **9**, 4562 (2019)
  82. J. Foster, B.S. Sommers, S.N. Gucker, I.M. Blankson, G. Adamovsky, *IEEE Trans. Plasma Sci.* **40**, 1311 (2012)
  83. D. Ghernaout, N. Elboughdiri, *OALib* **07**, 1 (2020)
  84. S. M, in *Proc. MOL2NET 2018, International Conference on Multidisciplinary Science*. 4th Ed. (MDPI, Basel, Switzerland, 2018), p. 5502
  85. Y. Cui, J. Cheng, Q. Chen, Z. Yin, *I.O.P. Conf. Ser. Earth Environ. Sci.* **208**(2018)
  86. J. Ren, T. Wang, G. Qu, D. Liang, S. Hu, *Plasma Sci. Technol.* **17**, 1053 (2015)
  87. C. Sarangapani, D. Ziuzina, P. Behan, D. Boehm, B.F. Gilmore, P.J. Cullen, P. Bourke, *Sci. Rep.* **9**, 1 (2019)
  88. M. Markovi, M. Jovi, D. Stankovi, V. Kova, G. Rogli, G. Gojgi, D. Manojlovi, *Sci. Total Environ.* **505**, 1148 (2015)
  89. J. Yu, Y. Cui, H. Zhang, Y. Liu, G. Oinuma, *Chemosphere* **234**, 471 (2019)
  90. A. Fahmy, A. El-Zomrawy, A. M. Saeed, A. Z Sayed, M. A Ezz El-Arab, H. Shehata, and J. Friedrich, *Plasma Res. Express* **2**, 015009 (2020)
  91. B.R. Locke, M. Sato, P. Sunka, M.R. Hoffmann, J.S. Chang, *Ind. Eng. Chem. Res.* **45**, 882 (2006)
  92. M. Russo, G. Iervolino, V. Vaiano, V. Palma, *Catalysts* **10**, 1 (2020)
  93. A. Barjasteh, Z. Dehghani, P. Lamichhane, N. Kaushik, E.H. Choi, N.K. Kaushik, *Appl. Sci.* **11**, 3372 (2021)
  94. M. A. Malik, Ubaid-Ur-Rehman, A. Ghaffar, and K. Ahmed, *Plasma Sour. Sci. Technol.* **11**, 236 (2002)
  95. E. Marotta, E. Ceriani, V. Shapoval, M. Schiorlin, C. Ceretta, M. Rea, C. Paradisi, *Eur. Phys. J. Appl. Phys.* **55**, 13811 (2011)
  96. M. El Shaer, M. Eldaly, G. Heikal, Y. Sharaf, H. Diab, M. Mobasher, A. Rousseau, *Plasma Chem. Plasma Process.* **40**, 971 (2020)
  97. K. H. Hama Aziz, H. Miessner, S. Mueller, D. Kalass, D. Moeller, I. Khorshid, and M. A. M. Rashid, *Chem. Eng. J.* **313**, 1033 (2017)
  98. P. J. Bruggeman, M. J. Kushner, B. R. Locke, J. G. E. Gardeniers, W. G. Graham, D. B. Graves, R. C. H. M. Hofman-Caris, D. Maric, J. P. Reid, E. Ceriani, D. Fernandez Rivas, J. E. Foster, S. C. Garrick, Y. Gorbanev, S. Hamaguchi, F. Iza, H. Jablonowski, E. Klimova, J. Kolb, F. Krcma, P. Lukes, Z. Machala, I. Marinov, D. Mariotti, S. Mededovic Thagard, D. Minakata, E. C. Neyts, J. Pawlat, Z. L. Petrovic, R. Pflieger, S. Reuter, D. C. Schram, S. Schröter, M. Shiraiwa, B. Tarabová, P. A. Tsai, J. R. R. Verlet, T. von Woedtke, K. R. Wilson, K. Yasui, and G. Zvereva, *Plasma Sources Sci. Technol.* **25**, 053002 (2016)
  99. L. Lin, S.A. Starostin, S. Li, V. Hessel, *Phys. Sci. Rev.* **3**, 1 (2018)
  100. Y. Gorbanev, A. Privat-Maldonado, A. Bogaerts, *Anal. Chem.* **90**, 13151 (2018)
  101. S. Muradia, Study of low-voltage pulsed plasma discharges inside water using a bubble-generating porous ceramic electrode for wastewater treatment, Doctoral dissertation, Shizuoka University, 2013
  102. P. Manoj Kumar Reddy, S. Mahammadunnisa, and C. Subrahmanyam, *Chem. Eng. J.* **238**, 157 (2014)
  103. N. Wardenier, Y. Gorbanev, I. Van Moer, A. Nikiforov, S.W.H. Van Hulle, P. Surmont, F. Lynen, C. Leys, A. Bogaerts, P. Vanraes, *Water Res.* **161**, 549 (2019)
  104. F. Tampieri, A. Giardina, F.J. Bosi, A. Pavanello, E. Marotta, B. Zaniol, G. Neretti, C. Paradisi, *Plasma Process. Polym.* **15**, 1700207 (2018)

105. A.T. Sugiarto, T. Ohshima, M. Sato, *Thin Solid Films* **407**, 174 (2002)
106. R. Kant, *Nat. Sci.* **04**, 22 (2012)
107. H. Ghodbane, A.Y. Nikiforov, O. Hamdaoui, P. Surmont, F. Lynen, G. Willems, C. Leys, *J. Adv. Oxid. Technol.* **17**, 372 (2014)
108. Q. Tang, W. Jiang, Y. Zhang, W. Wei, T.M. Lim, *Plasma Chem. Plasma Process.* **29**, 291 (2009)
109. D. Piroi, M. Magureanu, N. B. Mandache, and V. I. Parvulescu, in *19th International Symposium of Plasma Chemistry* (2009), pp. 1–4
110. G. Farabegoli, L. Pletrelli, E. Rolle, A. Sabene, *Water Sci. Technol. Water Supply.* **4**, 65 (2004)
111. I. M. C. Gonçalves\*, A. Gomes, R. Brás, M. I. A. Ferra, M. T. P. Amorim, and R. S. Porter, *J. Soc. Dye. Colour.* **116**, 393 (2000)
112. T. Shindhal, P. Rakholiya, S. Varjani, A. Pandey, H.H. Ngo, W. Guo, H.Y. Ng, M.J. Taherzadeh, *Bioeng* **12**, 70 (2021)
113. L. O. B. de Benetoli, B. M. Cadorin, C. Da S. Postiglione, I. G. De Souzaa, and N. A. Debacher, *J. Braz. Chem. Soc.* **22**, 1669 (2011)
114. J. Li, Z. Zhou, H. Wang, G. Li, Y. Wu, *Desalin* **212**, 123 (2007)
115. M. Rahimpour, H. Taghvaei, S. Zafarnak, M.R. Rahimpour, S. Raeissi, *J. Environ. Chem. Eng.* **7**, 103220 (2019)
116. P. Attri, M. Yusupov, J.H. Park, L.P. Lingamdinne, J.R. Koduru, M. Shiratani, E.H. Choi, A. Bogaerts, *Sci. Rep.* **6**, 1 (2016)
117. F. Abdelmalek, M.R. Ghezzer, M. Belhadj, A. Addou, J.L. Brisset, *Ind. Eng. Chem. Res.* **45**, 23 (2006)
118. B. Jiang, J. Zheng, Q. Liu, M. Wu, *Chem. Eng. J.* **204–205**, 32 (2012)
119. B. Sun, N.N. Aye, Z. Gao, D. Lv, X. Zhu, M. Sato, *J. Environ. Sci.* **24**, 840 (2012)
120. I. Panorel, S. Preis, I. Kornev, H. Hatakka, M. Louhi-Kultanen, *Environ. Technol. (United Kingdom)* **34**, 923 (2013)
121. D.G.J. Larsson, C. de Pedro, N. Paxeus, *J. Hazard. Mater.* **148**, 751 (2007)
122. M. Magureanu, D. Piroi, N.B. Mandache, V. David, A. Medvedovici, C. Bradu, V.I. Parvulescu, *Water Res.* **45**, 3407 (2011)
123. X. Hao, M. Zhou, Q. Xin, L. Lei, *Chemosphere* **66**, 2185 (2007)
124. S. Krishna, A. Maslani, T. Izdebski, M. Horakova, S. Klementova, P. Spatenka, *Chemosphere* **152**, 47 (2016)
125. S. Rong, Y. Sun, *J. Chem. Technol. Biotechnol.* **89**, 1351 (2014)
126. D. Dobrin, C. Bradu, M. Magureanu, N.B. Mandache, V.I. Parvulescu, *Chem. Eng. J.* **234**, 389 (2013)
127. H. Krause, B. Schweiger, J. Schuhmacher, S. Scholl, U. Steinfeld, *Chemosphere* **75**, 163 (2009)
128. R. Banaschik, P. Lukes, H. Jablonowski, M.U. Hammer, K.D. Weltmann, J.F. Kolb, *Water Res.* **84**, 127 (2015)
129. R.K. Singh, L. Philip, S. Ramanujam, *Water Res.* **121**, 20 (2017)
130. C. Hao, Z. Yan, K. Liu, J. Qiu, *IEEE Trans. Plasma Sci.* **48**, 471 (2020)
131. Y. Baloul, D. Hong, S. Chuon, O. Aubry, *Int. J. Plasma Environ. Sci. Technol.* **10**, 102 (2016)
132. M.I. Nawaz, C. Yi, P.J. Asilevi, T. Geng, M. Aleem, A.M. Zafar, A. Azeem, H. Wang, *Water.* **11**, 842 (2019)
133. M. Magureanu, D. Piroi, N.B. Mandache, V. David, A. Medvedovici, V.I. Parvulescu, *Water Res.* **44**, 3445 (2010)
134. J. Smith, I. Adams, H.-F. Ji, *Plasma* **1**, 1 (2017)
135. M. Magureanu, D. Dobrin, N.B. Mandache, C. Bradu, A. Medvedovici, V.I. Parvulescu, *Plasma Process. Polym.* **10**, 459 (2013)
136. L. Gao, L. Sun, S. Wan, Z. Yu, M. Li, *Chem. Eng. J.* **228**, 790 (2013)
137. M. Hijosa-Valsero, R. Molina, H. Schikora, M. Müller, J.M. Bayona, *Water Res.* **47**, 1701 (2013)
138. V. Vasu, D. Raji, A. Pandiyaraj, K.N. Padmanabhan, P.V.A. Kandhavelu, *Front. Adv. Mater. Res.* **1**, 46 (2019)
139. C. Sarangapani, N.N. Misra, V. Milosavljevic, P. Bourke, F. O-Regan, P.J. Cullen, *J. Water Process Eng.* **9**, 225 (2016)
140. A. Székács, M. Mörtl, B. Darvas, *J. Chem.* **2015**, 15 (2015)
141. C. Vanraes, P. Ghodbane, H. Davister, D. Wardenier, N. Nikiforov, A. Verheust, Y.P. Van Hulle, S.W.H. Hamdaoui, O. Vandamme, J. Durme, J.V. Surmont, P. Lynen, F. Leys, *Water Res.* **116**, 1 (2017)
142. R.K. Singh, L. Philip, S. Ramanujam, *Ind. Eng. Chem. Res.* **55**, 7201 (2016)
143. C. Bradu, M. Magureanu, V.I. Parvulescu, *J. Hazard. Mater.* **336**, 52 (2017)
144. S. Mededovic, B.R. Locke, *Ind. Eng. Chem. Res.* **46**, 2702 (2007)
145. P. Vanraes, G. Willems, N. Daels, S.W.H. Van Hulle, K. De Clerck, P. Surmont, F. Lynen, J. Vandamme, J. Van Durme, A. Nikiforov, C. Leys, *Water Res.* **72**, 361 (2015)
146. M. Hijosa-Valsero, R. Molina, H. Schikora, M. Müller, J.M. Bayona, *J. Hazard. Mater.* **262**, 664 (2013)
147. Y. Hu, Y. Bai, H. Yu, C. Zhang, J. Chen, *Bull. Environ. Contam. Toxicol.* **91**, 314 (2013)
148. S.P. Li, Y.Y. Jiang, X.H. Cao, Y.W. Dong, M. Dong, J. Xu, *Environ. Technol. (United Kingdom)* **34**, 1609 (2013)
149. S. Li, X. Ma, Y. Jiang, X. Cao, *Ecotoxicol. Environ. Saf.* **106**, 146 (2014)
150. V.V. Kovačević, B.P. Dojčinović, M. Jović, G.M. Roglić, B.M. Obradović, M.M. Kuraica, *J. Phys. D. Appl. Phys.* **50**, 155205 (2017)
151. S. Mohades, A.M. Lietz, J. Kruszelnicki, M.J. Kushner, *Plasma Process. Polym.* **17**, 1900179 (2020)
152. L. Patinglag, D. Sawtell, A. Iles, L.M. Melling, K.J. Shaw, *Plasma Chem. Plasma Process.* **39**, 561 (2019)
153. O. Lesage, T. Roques-Carmes, J.-M. Commenge, X. Duten, M. Tatouliau, S. Cavadias, D. Mantovani, S. Ognier, *Ind. Eng. Chem. Res.* **53**, 10387 (2014)
154. Z. Kozakova, E.J. Klimova, B.M. Obradovic, B.P. Dojcinovic, F. Krcma, M.M. Kuraica, Z. Olejnickova, R. Sykora, M. Vavrova, *Plasma Process. Polym.* **15**, 1700178 (2018)
155. B.R. Locke, K.-Y. Shih, *Plasma Sources Sci. Technol.* **20**, 034006 (2011)
156. S. Jaiswal, E.M. Aguirre, *AIP Adv.* **11**, 045311 (2021)

157. S.M. Thagard, G.R. Stratton, F. Dai, C.L. Bellona, T.M. Holsen, D.G. Bohl, E. Paek, E.R.V. Dickenson, *J. Phys. D. Appl. Phys.* **50**, 014003 (2017)
158. R.K. Singh, S. Fernando, S.F. Baygi, N. Multari, S.M. Thagard, T.M. Holsen, *Environ. Sci. Technol.* **53**, 2731 (2019)

# EPJ D



Recognized by European Physical Society

Atomic, Molecular,  
Optical and Plasma  
Physics

Eur. Phys. J. D (2018) 72: 2

DOI: [10.1140/epjd/e2017-80329-9](https://doi.org/10.1140/epjd/e2017-80329-9)

## **Destruction of chemical warfare surrogates using a portable atmospheric pressure plasma jet**

Nikola Škoro, Nevena Puač, Suzana Živković, Dijana Krstić-Milošević, Uroš Cvelbar, Gordana Malović, and Zoran Lj. Petrović



# Destruction of chemical warfare surrogates using a portable atmospheric pressure plasma jet<sup>\*</sup>

Nikola Škoro<sup>1,a</sup>, Nevena Puač<sup>1</sup>, Suzana Živković<sup>2</sup>, Dijana Krstić-Milošević<sup>2</sup>, Uroš Cvelbar<sup>3</sup>, Gordana Malović<sup>1</sup>, and Zoran Lj. Petrović<sup>1,4</sup>

<sup>1</sup> Institute of Physics Belgrade, University of Belgrade, Pregrevica 118, 11080 Belgrade, Serbia

<sup>2</sup> Institute for Biological Research “Siniša Stanković”, University of Belgrade, Bul. despota Stefana 142, 11060 Belgrade, Serbia

<sup>3</sup> Jožef Stefan Institute, Jamova cesta 39, Ljubljana 1000, Slovenia

<sup>4</sup> Serbian Academy of Sciences and Arts, Knez Mihailova 35, 11000 Belgrade, Serbia

Received 10 May 2017 / Received in final form 31 October 2017

Published online 16 January 2018 – © EDP Sciences, Società Italiana di Fisica, Springer-Verlag 2018

**Abstract.** Today’s reality is connected with mitigation of threats from the new chemical and biological warfare agents. A novel investigation of cold plasmas in contact with liquids presented in this paper demonstrated that the chemically reactive environment produced by atmospheric pressure plasma jet (APPJ) is potentially capable of rapid destruction of chemical warfare agents in a broad spectrum. The decontamination of three different chemical warfare agent surrogates dissolved in liquid is investigated by using an easily transportable APPJ. The jet is powered by a kHz signal source connected to a low-voltage DC source and with He as working gas. The detailed investigation of electrical properties is performed for various plasmas at different distances from the sample. The measurements of plasma properties *in situ* are supported by the optical spectrometry measurements, whereas the high performance liquid chromatography measurements before and after the treatment of aqueous solutions of Malathion, Fenitrothion and Dimethyl Methylphosphonate. These solutions are used to evaluate destruction and its efficiency for specific neural agent simulants. The particular removal rates are found to be from 56% up to 96% during 10 min treatment. The data obtained provide basis to evaluate APPJ’s efficiency at different operating conditions. The presented results are promising and could be improved with different operating conditions and optimization of the decontamination process.

## 1 Introduction

The omnipresent threat from the chemical and biological warfare agents have been emphasized in calamitous events of the last decade. In comparison to other weapons of mass destruction, the Chemical Warfare (CW) agents are probably one of the most vicious weapons created by mankind given that they are inexpensive and relatively easy to produce, but may result in mass casualties even by using a small agent quantities. Within the efforts to counter this threats, several physical and chemical methods have been developed [1] and successfully employed in CW incidents.

The chemical neutralization methods, depending on the type of the agent, are principally based on hydrolysis and oxidative processes, whereas in a few cases nucleophilic substitution reactions are also employed [1]. However, CW agents present in dilute solutions can undergo an efficient hydrolysis only in the alkaline surroundings, thus an

efficient source of OH radicals is necessary for successful decontamination process. In case of oxidative processes, the crucial limitation for detoxification is presence of sufficient oxidant species with this condition depending on type of the agent and solvent used in particular situation. Nevertheless, several types of chemical decontaminants proved to be efficient source of both species needed for efficient destruction of CW agents [1].

However, chemical methods involve the use of large amounts of chemically hazardous solutions that are dangerous to the environment and require proper storage as well as disposal [1,2]. Moreover, these solutions are not adequate for treatment of sensitive surfaces and demand safety installations in facilities for their application. Recently, the raise of novel emerging technologies such as photocatalytic methods and non-equilibrium plasmas is seen as a new promising route to safe decontamination of CW agents [2–4]. One of these technologies is atmospheric pressure plasma based processing, which has proved its usage versatility in many large-scale and industrial applications [5,6]. Atmospheric pressure plasma jets (APPJ) demonstrated to be technically simple, but efficient sources of cold atmospheric pressure plasmas

<sup>\*</sup> Contribution to the Topical Issue “Physics of Ionized Gases (SPIG 2016)”, edited by Goran Poparic, Bratislav Obradovic, Dragana Maric and Aleksandar Milosavljevic.

<sup>a</sup> e-mail: [nskoro@ipb.ac.rs](mailto:nskoro@ipb.ac.rs)



suitable for various kinds of biological and medical applications. There are numerous reports confirming the efficiency of plasma jets in sterilization and cleaning, i.e. their effect on organic materials and microorganisms [7–11]. Latest direction of research, featuring plasma-liquid systems with APPJ, has revealed that chemically reactive environment produced by this type of plasma source is capable of rapid destruction of a broad spectrum of microorganisms, poisonous chemicals and medical drugs [12–16]. Along with these applications, we aim to investigate a possibility of destruction of CW agent surrogates dissolved in liquids by using an APPJ.

So far, several studies investigated decontamination of CW agents (or its surrogates) by using different types of plasma sources [2,17–19]. However, in these studies treatment target is a coupon spiked with a toxic substance, i.e. treatment is performed over very thin film of the substance. In a lifelike situation of a CW incident, the contaminated environment surfaces are covered with the film of an agent but the main contaminating activity is through an aerosol. Thus, an efficient decontamination of CW agents dissolved in a liquid phase would mean that agents in a form of aerosol will be destroyed with an even higher efficiency.

The simple decontamination setup for investigation of our proof-of-concept is based on frequently used APPJ with He as working gas and its interaction with the liquid sample surface. The jet operating in the air generates high-energy electrons, reactive oxygen and nitrogen species, OH radicals,  $H_2O_2$  and ultraviolet radiation which is then transferred to the liquid through an interface layer [20,21]. The idea is that the reactive oxygen or nitrogen species produced inside the plasma jet and in the interfacial layer then subsequently react with organic molecules and oxidize them [22], which might lead to neutralization of CW agents. This hypothesis is then tested in this paper on 3 models of CW surrogates and the efficiency of decontamination source is evaluated.

## 2 Experimental setup and measurement methods

Plasma source used in this investigation was atmospheric pressure plasma jet (APPJ) with needle-type electrode. The experimental setup used for treatments of CW surrogates is presented in Figure 1. The plasma jet Teflon housing (width 26 mm, length 125 mm) contains a glass tube of 2 mm inner diameter and 4 mm outer diameter connected to the gas inlet through a flow regulator. The tube end protrudes shorter side of the housing by 8 mm. For all experiments, the helium (5.0 purity) was used as the feed gas and kept at the constant flow rate of 2slm. The copper wire was placed axially inside the tube acted as a needle-type powered electrode. The electrode was connected through a BNC connector on top of the housing to the kHz signal provided by a custom made power source. The source itself was packed inside a plastic box 20 cm × 12 cm × 6 cm with connection plugs and a switch. It was powered by a low-voltage DC supply providing at the output several kilovolts signal. Output voltage range

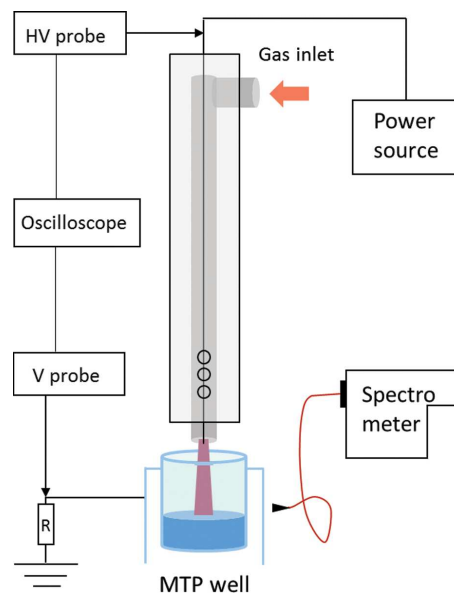


**Fig. 1.** Experimental setup for treatment of liquid samples by APPJ.

of the source was dependent on the DC voltage. In experiments an 8 V DC power supply with maximum current of 400 mA was used.

Described APPJ can be used as a hand-held device due to the small size. This feature, along with a compact power supply and ability to be powered by low-voltage DC source makes this system highly portable and in perspective enables the opportunity to be employed as a personal protection device.

Samples for treatments were placed in a 24-well microtiter plate underneath the jet. The distance between the end of the jet tube and the liquid surface was fixed at 15 mm for all sample treatments. In all cases volume of the sample placed into the plate well was 1 mL, occupying approximately one half of the well volume.

In order to allow the complete electrical characterization, the copper tape was fixed to the outer side of the well bottom and connected to the ground in a series with a 100 k $\Omega$  resistor. In this way, by measuring voltage drop at this resistor, the discharge current was monitored on the oscilloscope. At the same time, the high-voltage probe connected to the needle electrode connector was displaying driving voltage from the power supply.

In addition to electrical measurements, the optical emission spectrometry during sample treatments was performed. The axis of lens, 5 mm in diameter and 3 mm focal length, was placed at the liquid-gas interface level. It was positioned side on, at the distance of 3 cm from the central axes of the jet tube. The lens was collecting and forwarding discharge emission through an optical fiber connected to the entrance of Andor Shamrock 750, 750 mm focal length Czerny-Turner spectrograph, equipped with an ICCD camera (Andor iStar 734i) as a detector.

Aqueous solutions of three chemical compounds, the surrogates of CW agents, were used in experiments. As simulant for nerve agent VX we used the organophosphate Malathion (92% purity, Sigma-Aldrich), as simulant for

**Table 1.** Details of HPLC measurement methods used for CW agent simulants.

Mobile phase A	Water with 1% phosphoric acid			
Mobile phase B	Acetonitrile			
Column temperature	25 °C			
Sample injection volume	10 $\mu$ L			
	A%	B%	Flow rate	Peak detection
Malathion	40	60	1 mL/min	210 nm
DMMP	50	50	0.5 mL/min	210 nm
Fenitrothion	30	70	0.4 mL/min	210 nm

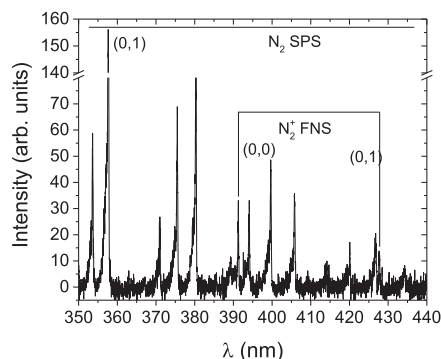


**Fig. 2.** Intensity normalized optical emission from the plasma region directly above the liquid surface for DMMP – CW surrogate at 2slm of He flow and 15mm distance between the jet and liquid surface. Second positive system (SPS) and first negative system (FNS) bands of  $N_2$  and  $N_2^+$  are observed.

GD – Fenitrothion (97% purity, Sigma–Aldrich) [23], while Dimethyl Methylphosphonate (DMMP) was applied as a GB agent – Sarine surrogate [23]. The solutions in water were prepared just before treatments, whereas the liquid chromatography measurements were conducted after the end of plasma treatment. No excessive heating of the whole sample during treatments was noticed although evaporation of the sample was observed. Additionally, during experiments in a microtiter plate well, the control sample was placed in another well in the vicinity of the experiment, and was exposed to the same room environment (without gas flow above). This way we accounted also for evaporation of the sample placed in the open air. After the treatment, the volume of both samples was carefully determined before proceeding to the liquid chromatography measurements.

Chromatographic analysis of samples was performed on a Agilent HPLC system, model 1100 with DAD, using Hypersil BDS-C18 (5  $\mu$ m), 125 mm  $\times$  2 mm I.D. column (Phenomenex, USA). The samples were filtered through a 0.2  $\mu$ m cellulose filters (Agilent technologies, Santa Clara, CA, USA) prior to analysis. Acetonitrile (ACN) and 1% (v/v) solution of ortho-phosphoric acid in water were used as mobile phases. Isocratic elution was performed with details given in Table 1.

Solvents for analysis (ACN and ortho-phosphoric acid) were HPLC grade, obtained from Fisher Scientific (Loughborough, UK). Ultrapure water was generated by deionization (Millipore, Billerica, USA). UV detection of the signal was set at 210nm for all three chemicals [24]. HP

ChemStation Chromatographic Software (Palo Alto, CA, USA) was employed for data collection.

### 3 Results and discussion

Plasma treatments of CW agent surrogates by APPJ were conducted for different duration times for all three organophosphate compounds. In order to characterize treatment conditions for every treatment, the optical emissions from the discharges were recorded. In addition, the measurements of voltage and current waveforms for different distances between sample and the jet were also performed.

#### 3.1 Optical emission spectra and electrical characterization of the plasma jet

Optical emission measurements were performed by collecting the light coming from the interface region between the liquid sample and plasma during treatments for all three CW agent simulants. Since the level of this interface was within the well, approximately at half of the well depth, the plastic well wall prevented transmission of any light below 350 nm. Moreover, at shorter distances most of the plasma was not accessible for optical emission recording due to the microtiter plate covering most of the volume of the plasma while for distances beyond 21 mm plasma does not reach the liquid. Thus, discharge emission was measured in the wavelength range from 350 nm to 750 nm only at 15 mm distance between the jet and liquid surface – the position used for treatment of CW agent surrogates.

The spectra obtained during treatments of all three chemicals were identical, indicating that the emitting particles were only those from the mixture of surrounding air and He excited in plasma. However, in the recorded spectra above 440 nm the only line visible was He line at 706.5 nm. In Figure 2 the limited part of the spectrum of DMMP in the range from 350 nm to 440 nm with identified nitrogen molecule lines is presented. The largest number and the strongest lines in this spectral range come from the second positive system (SPS) of  $N_2$ . Apart from this emission, the two lines of  $N_2^+$  ionic first negative system (FNS) were also visible.

The observation of both molecular and ionic lines of  $N_2$  is known for similar types of APPJs operating in He/air mixture [25–28]. Usually, the  $N_2^+$  FNS (0,0) line intensity (at 391 nm) is similar or even of stronger than

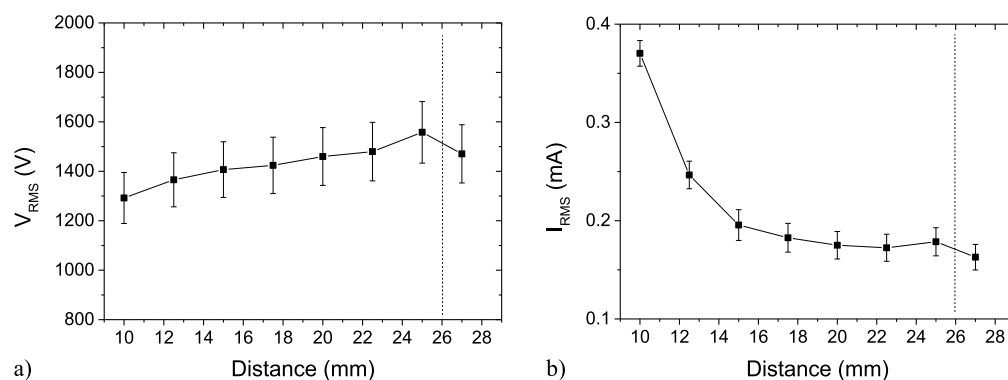


**Fig. 3.** Values of driving voltage (a) and discharge current (b) for different distances between the jet and liquid sample surface.

the strongest  $N_2$  SPS (0, 0) line at 337 nm (not shown in Fig. 1). Nevertheless, in presented case the 391 nm  $N_2^+$  line is considerably weaker than the one of the usually lower intensity  $N_2$  SPS lines (358 nm) that correspond to (0, 1) transition. Changes in radiative intensities of lines of the plasma jet operating in air or in He/air mixture were observed before, and it was exposed that they depend on the distance of the light collection region from the jet tube end [29–31]. On the other hand, it has also been confirmed that properties of the dielectric target affect intensities of atomic and molecular emission lines and the structure of plasma effluent [32–34]. Since in our case the emission is recorded just above the liquid, away from the jet tube, almost certainly both the decrease of excited species concentration along the effluent and the proximity of the liquid target affect the reduction of intensities of the  $N_2^+$  lines.

Electrical measurements showed that with the jet position the voltage and current RMS values change. This is observed in Figure 3, where the distance between the jet tube end and the liquid sample surface correlation is plotted. The RMS values are calculated from the waveforms of the driving voltage and the voltage drop measured over the resistor in grounded line. At the shortest distance of 10 mm end of the jet tube is positioned at the brim level of the well. For distance above 26 mm it appears from visual observation that plasma plume is not touching surface of the liquid (indicated with dashed line in Fig. 3).

Voltage RMS values have a steady rise from 1300 V up to around 1550 V with the distance increase, as observed in Figure 3a. At the largest distance, when visually plasma plume is not connected to the liquid surface, the voltage decreases. Current RMS values in Figure 3b are significantly reduced with the distance from 10 mm to 15 mm and then they stay almost constant at longer distances. Again, similar to  $V_{RMS}$ , there is a small drop in the current when plasma is visually detached from the liquid surface. As it has been shown before, the behavior of the plasma in plasma jet systems is influenced by the gas flow, geometrical features of the jet tube, geometry of the electrode system and dielectric properties of the target [35–38]. As distance between the tip of the plasma jet tube and the substrate increases two critical changes will occur. Radial losses will increase with the distance thereby making the measured current smaller and also the abundance of air

in the plasma will increase thereby increasing the losses of electrons and reduction of conductivity. Other possible mechanisms could affect the actual selfsustaining field at the tip of the developing streamer and overall distribution of the field but those are much more difficult to predict. Nevertheless in all scenarios an increase of the gap would lead to reduction of the current (provided that the available voltage is limited).

### 3.2 Decontamination of CW surrogates

In order to investigate effectiveness of plasma treatments on degradation of CW surrogates dissolved in water, the high performance liquid chromatography (HPLC) analysis were performed in the samples before and after the treatments. Quantification in HPLC analysis is based on calibration and calculation procedure that uses area or height of a peak of measured compound to determine its concentration. However, the peaks of CW surrogate degradation products were not identified nor quantified in this study, thus only comparison between the peak areas of the non-treated and treated samples was performed. Nevertheless, using this data we could calculate the decontamination efficiency and subsequently the removal rate as decontamination efficiency in 10 min treatment. The decontamination efficiency is defined as  $(C_0 - C)/C_0$ , where  $C_0$  is quantity of an agent surrogate in untreated sample and  $C$  is the residue quantity of the substance. Measurements of control and treated samples obtained in repeated treatments returned almost identical results suggesting stability and repeatability of the plasma treatment.

The HPLC results for 0.1% solution of Malathion ( $C_{10}H_{19}O_6PS_2$ ) in water treated for 10 min and 20 min are presented in Figure 4. In Figure 4a, the chromatograms of the control sample (black line) and treated samples (red and green) with two significant peaks are labeled in the plot. All chromatograms are normalized to the final sample volume because of evaporation of the solvent. The initial volume of the samples are reduced for 25% and 30% after 10 min and 20 min of treatment, respectively. The peak labeled as Peak 1 corresponds to Malathion while the one labeled as Peak 2 corresponds to its main degradation product Malaoxon [17,39]. According to manufacturer's

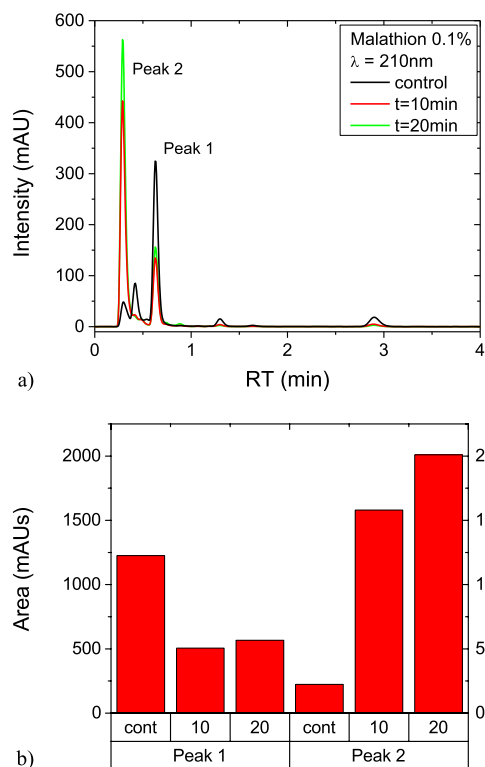


**Fig. 4.** (a) Chromatogram of control and treated samples of Malathion. (b) Comparison of designated peak areas calculated for control and treated samples. Boxes below bars indicate processing time in minutes.

specification, other peaks that are visible in the control sample chromatogram belong to impurities.

The calculated areas of the identified peaks from different samples are compared in Figure 4b. The treated samples exhibit significant decrease in the concentration of the parent molecule. The area of Peak 1 is reduced for both treatment durations with reduction of around 5 times for treatment of 10 min. Simultaneously, Peak 2 area of the decomposition product is increased for about 2 and 4 times after treatments of 10 min and 20 min, respectively. Taking into account the reduction of Peak 1 area, removal rate of Malathion after 10 min is 76%.

Peak 1 area of the sample treated for 20 min does not show any further decrease as compared to the area after 10 min (Fig. 4b). The lack of further reduction at later times can be attributed to the quenching of the radicals responsible for the destruction due to the higher concentrations of product molecules present in the solution. It has been reported in the literature that the destruction rate of the parent molecule can be decreased with an increase of the treatment time which can be attributed to the quenching of the radicals responsible for the destruction [40,41].

The Peak 2 (Fig. 4b) that represents the decomposition product exists also in the non-treated, control sample. This suggests that Malathion is decomposing in the aqueous solution also unrelated to the plasma treatment. Measurements of the control sample left at room temperature conducted right after making the solution,

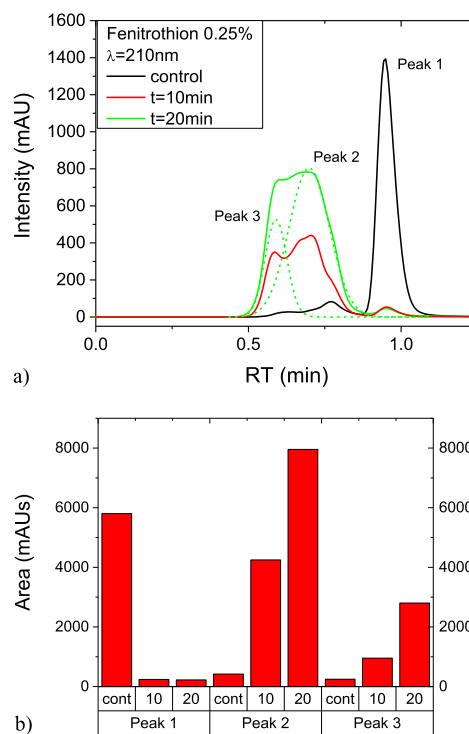


**Fig. 5.** (a) Chromatogram of control and treated samples of Fenitrothion. (b) Comparison of designated peak areas calculated from control and treated samples. Boxes below bars indicate processing time in minutes.

and after 15 and 30 days of preparation showed that in latter measurements Peak 1 area, corresponding to Malathion, is the same as in the initial measurement. Therefore, the decomposition process which is not induced by plasma occurs immediately after dissolving Malathion in water and then stabilizes, leaving the rest of the parent substance unchanged.

The HPLC measured data for 0.25% solution of Fenitrothion ( $C_9H_{12}NO_5PS$ ) in water is presented in Figure 5. After the treatment of 10 min and 20 min the samples have reduced its volumes for 30% and 50%, respectively, in comparison to the control sample. The volume-normalized chromatograms of the control (black line) sample and samples treated for 10 min and 20 min (red and green) with three significant peaks labeled in the plot is shown in Figure 5a. Similar to the Malathion sample, the Peak 1 corresponds to the parent molecule, i.e. Fenitrothion, while Peak 2 and Peak 3 belong to its main degradation products [42]. Unlike for the Malathion, where peaks in all chromatograms are separate, in treated Fenitrothion samples peaks of degradation products overlap. However, by changing the measurement method parameters with the existing HPLC setup it was not possible to improve separation of the peaks. Therefore, in order to compare peak areas, two Gauss-shaped peaks were deconvoluted from the envelope signal of overlapping peaks which appeared in the retention time (RT) range between 0.4 min and 0.9 min for all chromatograms. This example deconvolution is presented in Figure 5a for 20 min treated sample (dashed lines).

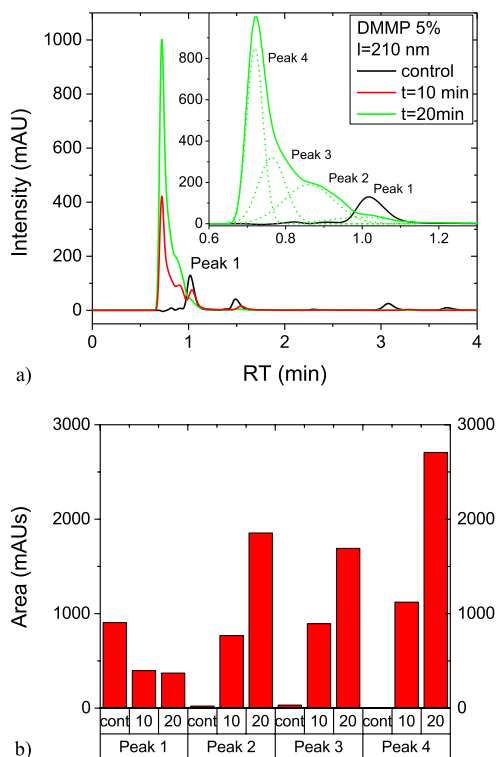


**Fig. 6.** (a) Chromatogram of control and treated samples of Dimethyl Methylphosphonate (DMMP). (b) Comparison of designated peak areas calculated from control and treated samples. Boxes below bars indicate processing time in minutes.

Comparison of identified peak areas from different chromatograms is exposed in Figure 5b. After treatment of 10 min, the Peak 1 (parent molecule) almost vanishes with the area from almost 6000 mAU trimmed down to around 200 mAU (30 times reduction). Additional 10 min of treatment causes only minor continuation of agent simulant destruction. Taking into account the reduction of area of Peak 1, the removal rate of Fenitrothion after treatment of 10 min is 96%. However, both peaks of the decomposition products (Peak 2 and Peak 3) exhibit increase with longer treatment time, displaying that parent molecule and maybe some of the decomposition products continuously degrade during treatment.

The measurements of non-treated and treated samples of 5% aqueous solution of DMMP ( $C_3H_9O_3P$ ) by HPLC device are revealed in Figure 6. Counter to the previous CW agent surrogates, volumes of the treated samples are only slightly changed – reduction up to 10% of the initial volume. The chromatograms normalized to the post-treatment sample volume of the control (black line) sample and samples treated for 10 min and 20 min (red and green) are plotted in Figure 6a with major peaks labeled. Since the chromatogram of DMMP control sample extends until 4 min of RT, the inset zooms in the range from the starting point up to RT = 1.3 min, i.e. immediately after detection of the parent molecule peak (Peak 1). All decomposition products (Peak 2–Peak 4) appear in the time before the parent molecule peak. In this case as well, the peaks of decomposition products overlap, so deconvolution

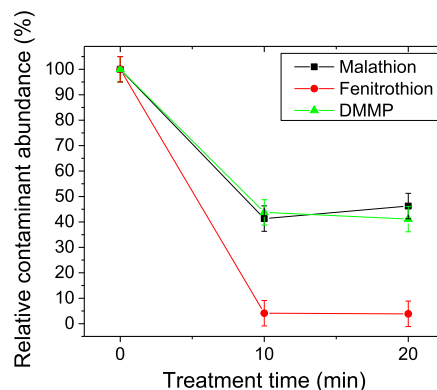


**Fig. 7.** Relative abundance of the target compound (contaminant) as a function of the treatment time. The distance between the plasma jet and liquid target was 15 mm and helium flow was 2 slm for all three contaminants.

of the measured signal by using Gauss-type functions is performed. Following our assumption of 3 major decomposition products [43–45], 4 peaks (including the one of parent molecule) are fitted in the RT range from 0.64 min to 1.13 min. The fitted functions to the chromatogram of 20 min treatment (dashed lines) with decomposition product peaks designated by Peak 2–Peak 4 are presented in the inset of Figure 6a.

Areas of all identified peaks obtained from chromatograms are exposed in Figure 6b. Practically, the only peak detected in the control sample is the parent molecule Peak 1 with the reduction of the peak area of 2.3 times after 10 min of treatment which results in removal rate of 56%. After 20 min of treatment, the area is reduced 2.4 times compared to the control sample. Nevertheless, peak areas of the decomposition products, which appear after 10 min treatment, are significantly higher at the end of the 20 min treatment time, for Peak 2 and Peak 4 – 2.4 times higher while Peak 3 is 2 times higher. Therefore, the destruction process obviously persists in the extended time treatments, but further quantitative analysis of decomposition products is necessary for better understanding of destruction mechanisms.

In Figure 7 we show the reduction of the abundance for all three contaminants. We can see that plasma treatment has the highest efficiency in the case of Fenitrothion (reduction almost by 100%) while reduction for Malathion and DMMP are of the order of 60%. Concerning the treatment times, there is no significant difference in contaminant abundance between the 10 min and 20 min treatments.

## 4 Conclusions

In this paper, a possibility of application of APPJ for decontamination of CW agent surrogates dissolved in water is examined. This approach takes into account the fact that most of the CW agents are spread in form of aerosols or liquids, therefore the destruction of the liquid phase CW is the most important for a successful implementation of decontamination. Recently, the presented

models demonstrated that the efficiency of the plasma liquid interactions is higher, when the liquid is in the form of droplets [46,47]. That being said, carrying out plasma decontamination in liquid is the most difficult case to perform. Nevertheless, these results also show promise for treatment of droplets and aerosol decontamination that is more difficult to quantify and thus we focused on liquid samples. Before investigation of the decontamination efficiency in liquid samples, the systematic investigation of the electric characteristics of APPJ while treating a liquid sample at different conditions, i.e. distances between the jet and liquid surface was performed. The measurements of voltage RMS values displayed only minor increase with the increasing distance, while the current RMS values drop sharply as the distance increase to 15 mm and then stay almost constant at longer gaps. Changes in voltage and current are correlated with changes in air/He mixture due to different position between the jet and the microtiter plate. As the first step in the study of the efficiency of decontamination, we examined here the destruction of agents at fixed position of 15 mm above the liquid surface.

Optical emission spectroscopy of the plasma-liquid interaction volume was also performed. However, the comparison of measured optical emission spectra during treatments of all three agent simulants in the wavelength range from 350 nm to 750 nm showed no differences, meaning that observable emission comes only from particles in air/He mixture excited in plasma. Accordingly, the most abundant lines belong to nitrogen molecule species which emit below 440 nm and one He line at 706.5 nm.

HPLC analysis of liquid samples before and after the treatment confirmed that significant and efficient degradation of all CW surrogates could be achieved. The destruction of the parent substance is detected on the basis of its peak area reduction and the appearance of new peaks in chromatograms of treated samples. The removal rates of toxic chemicals after 10 min of treatment ranged from 56% in case of DMMP (GB agent surrogate), to 76% for Malathion (VX agent) and even 96% for Fenitrothion (GD agent). Efficient destruction of simulant chemicals exhibits a promise that this kind of cold plasma treatments could be successful for removal of the real CW agents from surfaces and aerosols by personalized tools.

However, for now the open questions are whether the remaining decomposition products are still harmful and whether these byproducts could be fragmented further by plasma treatment. For instance, in case of Malathion, the main product of destruction is Malaoxon that is also highly toxic. Nevertheless, the precise determination of mass spectra of treated samples would enable identification and characterizations of the decomposition products of CW agent surrogates as well as their toxicity level. All this data would be valuable for evaluation of APPJ's efficiency at different operating conditions and further optimization of the decontamination process. Recent advances in understanding of the physics and chemistry of the breakdown in liquids [20,21] open new possibilities to optimize removal of contaminants even as dangerous as CW agents. In general these techniques may be employed for removal of a broad spectrum of contaminants from water supplies.

This work is supported by NATO Science for Peace Multi-Year Project SPS 984555, "Atmospheric pressure plasma jet for neutralization of CBW (chemical biological weapons)", COST TD1208 and projects ON171037 and III41011 of MESTD, Serbia.

## Author contribution statement

U.C. and Z.Lj.P. conceived the idea and supervised the project. U.C. designed the device, N.Š., N.P. and S.Ž. performed the experiments and measurements and analyzed the data. D.K.M. supervised and assisted with HPLC measurements, G.M. helped supervise the project. N.Š., N.P. and S.Ž. wrote the manuscript and U.C. and Z.Lj.P. contributed to the final version of the manuscript.

## References

1. Y.C. Yang, J.A. Baker, J. Richard Ward, Chem. Rev. **92**, 1729 (1992)
2. H.W. Herrmann, I. Henins, J. Park, G.S. Selwyn, Phys. Plasmas **6**, 2284 (1999)
3. T. Hirakawa, N. Mera, T. Sano, N. Negishi, K. Takeuchi, J. Pharm. Soc. Jpn. **129**, 71 (2009)
4. C. Bisio, F. Carniato, C. Palumbo, S.L. Safronyuk, M.F. Starodub, A.M. Katsev, L. Marchese, M. Guidotti, Catal. Today **277**, 192 (2016)
5. A. Fridman, A. Chirokov, A. Gutsol, J. Phys. D: Appl. Phys. **38**, R1 (2005)
6. C. Tendero, C. Tixier, P. Tristant, J. Desmaison, P. Leprince, Spectrochim. Acta B **61**, 2 (2006)
7. N. Puač, M. Miletić, M. Mojović, A. Popović-Bijelić, D. Vuković, B. Miličić, D. Maletić, S. Lazović, G. Malović, Z.Lj. Petrović, Open Chem. **13**, 332 (2015)
8. J.L. Zimmermann, T. Shimizu, H.U. Schmidt, Y.F. Li, G.E. Morfill, G. Isbary, New J. Phys. **14**, 073037 (2012)
9. G. Fridman, G. Friedman, A. Gutsol, A.B. Shekhter, V.N. Vasilets, A. Fridman, Plasma Proc. Polym. **5**, 503 (2008)
10. U. Cvelbar, M. Mozetic, N. Hauptman, M. Klanjek-Gunde, J. Appl. Phys. **106**, 103303 (2009)
11. M. Moisan, J. Barbeau, S. Moreau, J. Pelletier, M. Tabrizian, L.H. Yahia, Int. J. Pharm. **226**, 1 (2001)
12. T. Vukusic, M. Shi, Z. Herceg, S. Rogers, P. Estifae, S.M. Thagard, Innov. Food Sci. Emerg. Technol. **38**, 407 (2016)
13. M. Magureanu, N.B. Mandache, V.I. Parvulescu, Water Res. **81**, 124 (2015)
14. E.J. Klimova, F. Krcma, L. Jonisova, Eur. Phys. J. Appl. Phys. **75**, 24709 (2016)
15. S. Krishna, E. Ceriani, E. Marotta, A. Giardina, P. Špatenka, C. Paradisi, Chem. Eng. J. **292**, 35 (2016)
16. J.E. Foster, Phys. Plasmas **24**, 055501 (2017)
17. Z. Wen-Chao, W. Bai-Rong, X. Hai-Ling, P. Yi-Kang, Plasma Chem. Plasma Process. **30**, 381 (2010)
18. Z. Li, Y. Li, P. Cao, H. Zhao, Plasma Sci. Technol. **15**, 696 (2013)
19. H.W. Herrmann, G.S. Selwyn, I. Henins, J. Park, M. Jeffery, J.M. Williams, IEEE Trans. Plasma Sci. **30**, 1460 (2002)
20. P.J. Bruggeman, M.J. Kushner, B.R. Locke, J.G.E. Gardeniers, W.G. Graham, D.B. Graves, R.C.H.M. Hofman-Caris, D. Maric, J.P. Reid, E. Ceriani, D. Fernandez Rivas, J.E. Foster, S.C. Garrick, Y. Gorbanev,

- S. Hamaguchi, F. Iza, H. Jablonowski, E. Klimova, J. Kolb, F. Krcma, P. Lukes, Z. Machala, I. Marinov, D. Mariotti, S. Mededovic Thagard, D. Minakata, E.C. Neyts, J. Pawlat, Z.Lj. Petrovic, R. Pflieger, S. Reuter, D.C. Schram, S. Schroeter, M. Shiraiwa, B. Tarabová, P.A. Tsai, J.R.R. Verlet, T. von Woedtke, K.R. Wilson, K. Yasui, G. Zvereva, *Plasma Sources Sci. Technol.* **25**, 053002 (2016)
21. I. Adamovich, S. Baalrud, A. Bogaerts, P.J. Bruggeman, M. Cappelli, V. Colombo, U. Czarnetzki, U. Ebert, J.G. Eden, P. Favia, D.B. Graves, S. Hamaguchi, G. Hieftje, M. Hori, I.D. Kaganovich, U. Kortshagen, M.J. Kushner, N.J. Mason, S. Mazouffre, S. Mededovic Thagard, H.-R. Metelmann, A. Mizuno, E. Moreau, A.B. Murphy, B.A. Niemira, G.S. Oehrlein, Z.Lj. Petrovic, L.C. Pitchford, Y.-K. Pu, S. Rauf, O. Sakai, S. Samukawa, S. Starikovskaia, J. Tennyson, K. Terashima, M.M. Turner, M.C.M. van de Sanden, A. Vardelle, *J. Phys. D: Appl. Phys.* **50**, 323001 (2017)
22. M.M. Hefny, C. Pattyn, P. Lukes, J. Benedikt, *J. Phys. D: Appl. Phys.* **49**, 404002 (2016)
23. S.L. Bartelt-Hunt, D.R.U. Knappe, M.A. Barlaz, *Environ. Sci. Technol.* **38**, 112 (2008)
24. R.T. Rewick, M.L. Schumacher, D.L. Haynes, *Appl. Spectrosc.* **40**, 152 (1986)
25. E. Nwankire, V.J. Law, A. Nindrayog, B. Twomey, K. Niemi, V. Milosavljević, W.G. Graham, D.P. Dowling, *Plasma Chem. Plasma Process.* **30**, 537 (2010)
26. J. Benedikt, S. Hofmann, N. Knake, H. Boettner, R. Reuter, A. von Keudell, V. Schulz-von der Gathen, *Eur. Phys. J. D* **60**, 539 (2010)
27. Y.S. Seo, A.-A.H. Mohamed, K.C. Woo, H.W. Lee, J.K. Lee, K.T. Kim, *IEEE Trans. Plasma Sci.* **38**, 2954 (2010)
28. R. Brandenburg, J. Ehlbeck, M. Stieber, T. von Woedtke, J. Zeymer, O. Schlueter, K.-D. Weltmann, *Contrib. Plasma Phys.* **47**, 72 (2007)
29. A.N. Korbut, V.A. Kelman, Yu.V. Zhmenyak, M.S. Klenovskii, *Opt. Spectrosc.* **116**, 919 (2014)
30. E. Ilik, T. Akan, *Phys. Plasmas* **23**, 053501 (2016)
31. G.V. Naidis, *Plasma Sources Sci. Technol.* **23**, 065014 (2014)
32. A.V. Nastuta, V. Pohoata, I. Topala, *J. Appl. Phys.* **113**, 183302 (2013)
33. S. Hofmann, K. van Gils, S. van der Linden, S. Iseni, P. Bruggeman, *Eur. Phys. J. D* **68**, 56 (2014)
34. X. Damany, S. Pasquiersa, N. Blin-Simiand, G. Bauville, B. Bournonville, M. Fleury, P. Jeanney, J.S. Sousa, *Eur. Phys. J. Appl. Phys.* **75**, 24713 (2016)
35. N. Puač, D. Maletić, S. Lazović, G. Malović, A. Đorđević, Z.Lj. Petrović, *Appl. Phys. Lett.* **101**, 024103 (2012)
36. D. Maletić, N. Puač, N. Selaković, S. Lazović, G. Malović, A. Đorđević, Z.Lj. Petrović, *Plasma Sources Sci. Technol.* **24**, 025006 (2015)
37. E. Robert, V. Sarron, T. Darny, D. Ries, S. Dozias, J. Fontane, L. Joly, J.-M. Pouvesle, *Plasma Sources Sci. Technol.* **23**, 012003 (2014)
38. S. Hofmann, K. van Gils, S. van der Linden, S. Iseni, P. Bruggeman, *Eur. Phys. J. D* **68**, 56 (2014)
39. A.W. Abu-Qare, M.B. Abou-Donia, *J. Pharm. Biomed. Anal.* **26**, 291 (2001)
40. B. Jiang, J. Zheng, S. Qiu, M. Wu, Q. Zhang, Z. Yan, Q. Xue, *Chem. Eng. J.* **236**, 348 (2014)
41. M. Hijosa-Valsero, R. Molina, A. Monràs, M. Müller, J.M. Bayona, *Environ. Technol. Rev.* **3**, 71 (2014)
42. P. Kuklenyik, Ph.D. thesis, Georgia State University, 2009
43. H. Ando, Y. Miyata, in *Drugs and poisons in humans*, edited by O. Suzuki, K. Watanabe (Springer-Verlag, Berlin, Heidelberg, New York, 2005)
44. S.C. Cho, H.S. Uhm, Y.C. Hong, Y.G. Park, J.S. Park, *J. Appl. Phys.* **103**, 123303 (2008)
45. T.Z. Tzou, S.W. Weller, *J. Catal.* **146**, 370 (1994)
46. J. Kruszelnicki, A.M. Lietz, M.J. Kushner, in *Proceedings of Intern. Conf. on Plasmas with Liquids-ICPL 2017, Prague*, edited by P. Lukes, K. Kolacek (IPP CAS, Prague, 2017), p. 371
47. W. Tian, A.M. Lietz, M.J. Kushner, *Plasma Sources Sci. Technol.* **25**, 055020 (2016)

# PLASMA MEDICINE: THE GREAT PROSPECTS WHEN PHYSICS MEETS MEDICINE

■ J.M. Sadowska<sup>1</sup>, N. Skoro<sup>2</sup>, R. Laurita<sup>3</sup>, S. Bekeschus<sup>4</sup>, A. Przekora-Kuśmierz<sup>5</sup>, A. Lin<sup>6</sup>, S. Laurencin<sup>7</sup>, S. Sério<sup>8</sup>, S. Cousty<sup>7</sup>, C. Canal<sup>9</sup> – DOI: <https://doi.org/10.1051/eprn/2022303>

■ <sup>1</sup>Royal College of Surgeons in Ireland University of Medicine and Health Sciences, Dublin, Ireland

■ <sup>2</sup>Institute of Physics, University of Belgrade, Belgrade, Serbia

■ <sup>3</sup>Department of Industrial Engineering, Alma Mater Studiorum-Università di Bologna, Italy

■ <sup>4</sup>ZIK *plasmatis*, Leibniz Institute for Plasma Science and Technology (INP), Germany

■ <sup>5</sup>Unit of Tissue Engineering and Regenerative Medicine, Medical University of Lublin, Poland

■ <sup>6</sup>Plasma Lab for Applications in Sustainable and Medicine-Antwerp, University Antwerp, Belgium

■ <sup>7</sup>Toulouse Health Faculty, CHU Toulouse, Paul Sabatier University, France.

■ <sup>8</sup>Laboratory of Instrumentation, Biomedical Engineering and Radiation Physics (LIBPhys-UNL), Department of Physics, NOVA School of Science and Technology, NOVA University Lisbon, 2829-516 Caparica, Portugal.

■ <sup>9</sup>Research Center for Biomedical Engineering, Universitat Politècnica de Catalunya, Spain.



The research has demonstrated the antimicrobial properties of plasma urging the incorporation of cold atmospheric plasma (CAP) decontamination in current clinical therapies with the aim to improve the benefits on the patients and on society.

Plasma medicine is an innovative and interdisciplinary field of science which has experienced an immense international upswing in the last years. It has emerged two decades ago as a commingling of plasma technology with physics, chemistry, engineering and life science. The final aim of plasma medicine research is to introduce CAPs into clinical medicine and bioengineering fields for human and veterinary therapeutic applications [1].

## What is plasma and how it works?

Gas discharge plasma is an ionized gas, composed of free electrons, ions, radicals, excited atoms and molecules, neutral molecules, electromagnetic fields and UV-Vis radiation with no net electrical charge [1] (Figure 1). The features of CAP, according to their non-equilibrium

character, include the extremely high concentration of chemically reactive species and a bulk temperature close to the room temperature, which makes it an ideal tool for applications in many fields including agriculture, environment, manufacturing and most of all, medicine. The reactive species, derived from oxygen and nitrogen (RONS - *i.e.* O, <sup>1</sup>O<sub>2</sub>, O<sub>3</sub>, ·OH, ·O<sub>2</sub>H, ·O<sup>2-</sup>, ·O<sup>3-</sup>, ·NO, ·NO<sub>2</sub>) are particularly relevant for the medical field as they can diffuse from the gas phase to a solution/biological medium, generating less reactive and longer-lived secondary species, which offer a myriad of potential biological applications [1].

Hence, this has led to the development of two approaches with regards to the putative application methods of plasmas (Figure 2):

i) a direct CAP treatment of the biological target



(e.g. microbes, eukaryotic cells healthy or diseased and pathological tissue), which exhibits the synergetic effects derived of all the above-mentioned plasma components on cells.

ii) an indirect CAP treatment consisting on the treatment of biocompatible and biologically relevant liquids (plasma treated liquids - PTLs), which allows for minimally invasive therapy in the target site. The PTLs-based therapy mainly delivers the RONS, which have been reported to be one of the major players controlling biological processes [2,3].

### Plasma-generated RONS and their biological relevance

Part of the action of CAP can be explained thanks to advances in redox biology, which can be used as the scientific basis to explain the biological effects related to CAP-generated RONS [3]. Briefly, the two general molecular mechanisms of the RONS to highlight are (i) alterations of the intracellular redox state and (ii) oxidative modification of proteins involved in multiple signalling pathways. According to this, CAP treatment can affect all physiological processes in the human or animal body, where RONS play an important role, such as regulation of blood coagulation, vascular contraction, nerve impulse transmission, angiogenesis, inflammation, and immune system response. In addition, at the cellular level, CAP-derived RONS can alter molecular signalling pathways in both prokaryotic (e.g. bacteria) and eukaryotic cells (e.g. cancer cells) related to cell-to-cell adhesion, synthesis of growth factors, cell differentiation, division, migration, and apoptosis [3]. The important biological role of RONS in prokaryotic and eukaryotic cells has led to two main capabilities of CAPs targeting both type of organisms with corresponding therapeutical applications.

#### Plasma medicine:

##### CAPs effects on prokaryotic cells

The antimicrobial properties of CAPs have been investigated for over the last two decades, anchoring the concept of plasma decontamination in this field of science. The main medical application of plasma has been focused on the sterilization of surfaces, materials and devices such as prostheses or implants [4]. Nevertheless, the increasingly growing development of atmospheric pressure plasma has promoted the exploration of novel potential applications, especially on living tissues targeting different pathogens such as bacteria, viruses, yeasts and fungi [5].

The ever-growing incidence of bacteria with resistance to most antibiotics and the emergence of new unknown pathogens whose transmission is most probably airborne (i.e. SARS-CoV-2) has necessitated novel solutions to overcome the handicaps of the available treatments. In this regard, recent research has proved the effectiveness

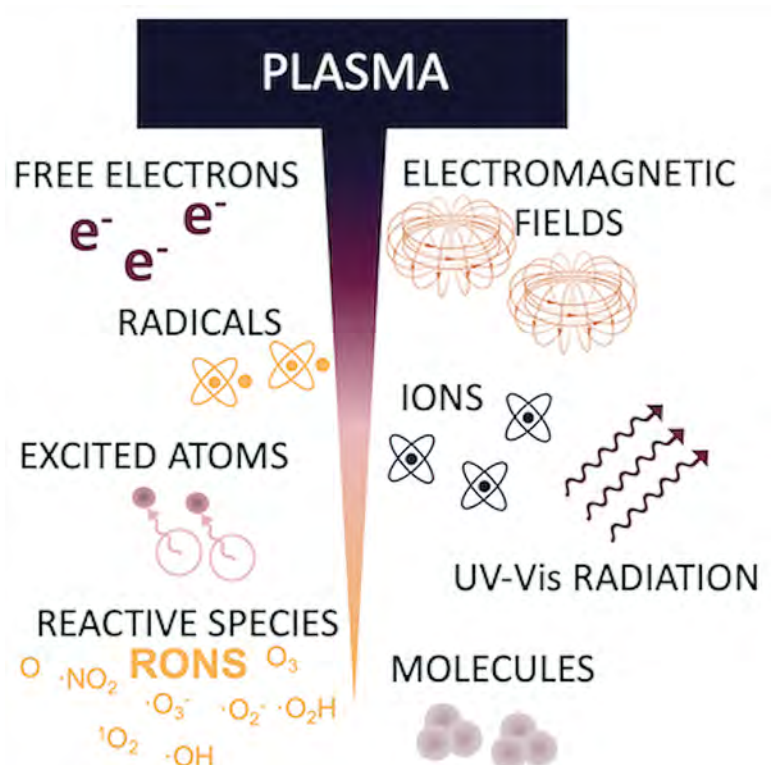
of CAP for inactivation of biofilms and overcoming their acquired resistance to antibiotics [6]. From another point of view, a fundamental finding in this area has been the discovery that under specific conditions, CAP can kill or inactivate harmful microorganisms infecting skin, without causing damage to patient's tissue, thereby facilitating the acceleration of wound healing and treatment of pathogen-based skin diseases [7]. Moreover, CAP has proved to be very effective against bio non-cellular infection-transmitting agents that are resistant to more conventional techniques, like the prions, which are held responsible for neurodegenerative diseases such as transmissible spongiform encephalopathy or Alzheimer's disease, respectively [8]. The research has demonstrated the antimicrobial properties of plasma medicine urging the incorporation of CAP decontamination in current clinical therapies with the aim to improve the welfare on patients and on society.

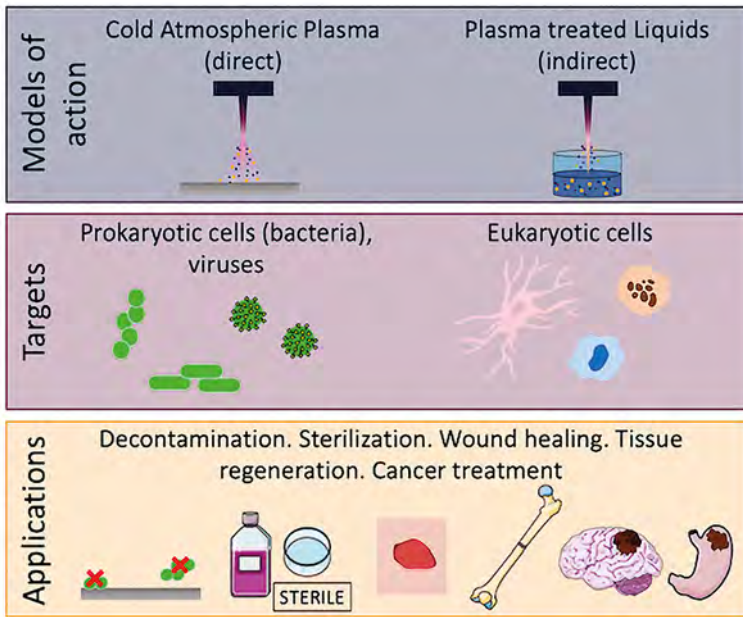
#### Plasma medicine:

##### CAPs effects on eukaryotic cells

The recent advances in plasma medicine have shown that CAPs can exhibit the effects on eukaryotic cells and living tissues in the human and animal body evidencing the versatility of plasma treatment. Specifically, it has been demonstrated that the controlled exposure of mammalian cells to different conditions of CAP can lead either to stimulation or inhibition of cellular functions, such as cell proliferation, tissue regeneration, cell detachment, apoptosis, and necrosis [9]. This has opened the door to new therapeutical applications such as tissue

▼ FIG. 1: Plasma components include free electrons, ions, radicals, excited atoms and molecules, neutral molecules, electromagnetic fields and UV-Vis radiation with no overall electrical charge.



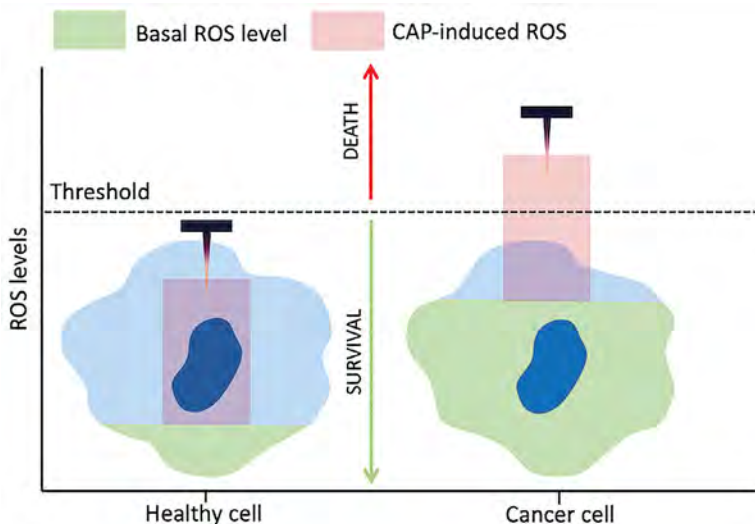


▲ FIG. 2: Models of action, targets and applications of cold atmospheric plasmas (CAPs).

● ● ● regeneration and wound healing (e.g. diabetic leg healing, ulcers, burns, etc.), with potential implications in the cosmetics field (e.g. skin regeneration, scar treatment, etc.), as well as cancer therapy (e.g. melanoma, glioblastoma, colon cancer, etc.).

For instance, different atmospheric pressure plasma jets, which have been recently commercialized, have demonstrated their effectiveness at supporting the healing of non-infected acute wounds (kINPen, PlasmDERM, SteriPlas, Plason, PlasmaCare) [10]. To date, these plasma sources have also been applied in the treatment of long-lasting chronic and infected wounds, particularly in cases where conventional treatment have failed, with evidence *in vitro* and *in vivo* with studies in animals, that have led to the initiation of the first clinical trials. In diabetic patients with chronic leg and venous ulcers, plasma-treated patients experienced accelerated wound healing [5]. These results suggest that wound healing may

▼ FIG. 3: Treatment with CAP delivers exogenous ROS bringing the metabolically more active cancer cells over the survival/death threshold.



be accelerated due to the simultaneous stimulation of tissue regeneration and angiogenesis. The results observed in such studies enable this vision of CAP technology on its way to becoming a clinical routine for wound healing and skin treatment. This regenerative potential of CAP on skin is currently being explored in the anti-aging and skin-wellness industry. This capacity of plasmas to stimulate tissue regeneration and repair can also be exploited for other tissues [11], opening new avenues that deserve further exploration.

Recent advances in plasma medicine have been exploiting the potential use of CAP in cancer therapies. Cancer is a leading cause of death worldwide and despite the enormous amount of research and rapid developments seen during the past decade, cancer treatment is still challenging. In this sense, one key aspect which is attracting increased attention is the ability of CAPs to selectively kill cancer cells without damaging the surrounding tissues, thus offering a less aggressive solution compared to common anticancer therapies (*i.e.* chemotherapy and radiotherapy). The anticancer effects of CAP have been, at least in part, related to the RONS generated by plasmas, which are important mediators in stem cell biology. In fact, high levels of RONS have long been suggested to be detrimental to cellular health, and adding high amounts of exogenous RONS can induce cell cycle arrest, while higher doses lead to the induction of apoptotic and/or necrotic cell death (Figure 3). In this context, cancer cells are metabolically more active than healthy cells, thereby generating higher amount of intrinsic RONS. For this reason, delivering plasma with low exogenous RONS, triggers cancer cells to surpass the toxicity threshold and activate apoptosis without affecting normal cells of the surrounding healthy tissue. Interestingly, many studies demonstrated that indirect treatment using PTLs exert very similar effects compared to direct CAP treatment what could be particularly favorable in the treatments of areas harder to reach and an injection of PTLs may be a suitable alternative [12].

### Quo Vadis, plasma medicine?

Merging physics, chemistry, and engineering with medical science gave rise to plasma medicine, which aims to develop novel and innovative technologies to improve the quality of life of patients and their families. The recent advancements in the field have demonstrated the great versatility of CAP systems and their ability to induce, mainly through RONS delivery, specific biological responses in pathogens (bacteria, viruses, yeasts and fungi), cells (healthy and cancellous), and living tissues. This has opened the door to a myriad of applications on the edge of tissue engineering and regenerative medicine such as eradication of biofilms, wound-healing, treatment of neurodegenerative diseases or cancer therapy. Nevertheless,

there is still much to be done including the rigorous in vivo evaluation of plasma treatments or unravelling the specific molecular mechanisms that are involved on the intra- or inter-cellular level of on living cells and tissues treated with plasmas. Thus, the research community must keep exploring the CAP-tivating versatility, feasibility and therapeutic potential of plasma medicine.

The recently initiated COST Action CA20114 PlasTHER “Therapeutical Applications of Cold Plasmas” ([www.plas-ther.eu](http://www.plas-ther.eu)) is dealing with all the aforementioned challenges, with the help of a big network of experts in different areas and hopes to bring significant advances to the field forward in the coming years. ■

### Acknowledgements

This article/publication is based upon work from COST Action Action CA20114 PlasTHER “Therapeutical Applications of Cold Plasmas”, supported by COST (European Cooperation in Science and Technology).

### References

- [1] M. Laroussi, *Plasma Process. Polym* **11**(12), 1138 (2014)
- [2] P. J. Bruggeman *et al.*, *Plasma Sources Sci. Technol.* **25**(5), 53002 (2016)
- [3] T. Von Woedtke *et al.*, *In Vivo* **33**(4), 1011 (2019).
- [4] M. Laroussi, *Plasma Process. Polym.* **2**(5), 391 (2005).
- [5] T. Bernhardt *et al.*, *Oxid. Med. Cell. Longev.* **2019**, 10 (2019).
- [6] T. T. Gupta *et al.*, *Appl. Sci.* **9**(17), (2019).
- [7] B. Haertel *et al.*, *Biomol. Ther.* **22**(6), 477 (2014).
- [8] H. C. Baxter *et al.*, *J. Gen. Virol.* **86**(8), 2393 (2005).
- [9] F. Virard *et al.*, *PLoS One* **10**(8), 1 (2015).
- [10] S. Vandersee *et al.*, *Laser Phys. Lett.* **11**(11), 115701 (2014).
- [11] P. Eisenhauer *et al.*, *J. Tissue Eng. Regen. Med.* **10**(9), 772 (2016).
- [12] J. Tornin *et al.*, *Nat. Protocols* **16**, 2826 (2021).



The Authors, from left to right:  
 Joanna M. Sadowska, Nikola Skoro,  
 Romolo Laurita, Sander Bekešchus,  
 Agata Przekora-Kuśmierz, Abraham  
 Lin, Sara Laurencin, Susana Sério,  
 Sarah Cousty, Cristina Canal

# quantum approved.



## Laser Rack Systems

Quantum Technology meets Industry Standards

Our lasers do not need an optical table! The T-RACK is the perfect home for TOPTICA's high-end tunable diode lasers and frequency combs in a modular 19" form factor. Pick yours!

- Tunable Diode Laser Systems
- Frequency Comb Systems
- Wavelength Meters
- Locking Electronics
- 330 .. 1770 nm



**9<sup>th</sup> Central European Symposium on  
Plasma Chemistry (CESPC-9)**  
joint with  
**COST Action CA19110 Plasma Applications for  
Smart and Sustainable Agriculture (PIAgri)**

---

Vysoké Tatry, Slovakia  
September 4–9, 2022

# **BOOK OF ABSTRACTS**

including general information and program



Edited by Karol HENSEL, Richard CIMERMAN, Aleksandra LAVRIKOVA,  
Mário JANDA, and Zdenko MACHALA

## Wednesday, September 7

8 <sup>30</sup>	I-9	<b>Petr Lukeš</b> Chemistry induced by atmospheric plasma in aqueous liquids	<u>Chair: E. Marotta</u>
9 <sup>05</sup>	O-22	<b>Nikola Škoro</b> Correlation between properties of plasma treated liquids with characteristics of atmospheric pressure ...	
9 <sup>25</sup>	O-23	<b>Michael Schmidt</b> Non-thermal plasma for generation of antimicrobial aerosol	
9 <sup>45</sup>	O-24	<b>Ana Sainz García</b> Forest material treatment by PAW	
10 <sup>05</sup>		Coffee break ☕	
10 <sup>30</sup>	I-10	<b>Bogdana Mitu</b> Plasma driven synthesis of NPs and their immobilization	<u>Chair: M. Mozetič</u>
11 <sup>05</sup>	O-25	<b>Ionut Topala</b> Revision of 3.4 um band destruction rates under ion beam irradiation of hydrogenated amorphous ...	
11 <sup>25</sup>	O-26	<b>Kerstin Sgonina</b> Selective study of ion-substrate interactions using the VUV-photoionization chamber	
11 <sup>45</sup>		Lunch	
13 <sup>00</sup>		Excursion	
19 <sup>30</sup>		Gala Dinner	

O-10	<b>Kostyantyn Korytchenko</b> - Optical and electrical investigation of plasma generated by high-energy self-stabilized spark ignition system	41
O-11	<b>Zlata Kelar Tučeková</b> - Optimization of plasma-activated media generation for decontamination of thermally sensitive materials	42
O-12	<b>Robin Menthéour</b> - Synergic antibacterial effect of pulsed electric field and plasma activated water	43
O-13	<b>Josef Khun</b> - Comparison of non-thermal plasma produced by cometary and point-to-ring discharges for portable devices usable in biomedical applications	44
O-14	<b>Marley Becerra</b> - Investigation of CO <sub>2</sub> decomposition in pulsed warm arc plasma by optical emission spectroscopy	45
O-15	<b>Richard Cimerman</b> - Nonthermal plasma regeneration of deactivated catalysts after plasma-catalytic removal of toluene and naphthalene	46
O-16	<b>Thomas Vazquez</b> - Indoor air decontamination by cold atmospheric plasma and photocatalysis	47
O-17	<b>Miran Mozetič</b> - Hydrophilization of fluorinated polymers	48
O-18	<b>Matteo Gherardi</b> - Control strategies for aerosol-assisted atmospheric pressure plasma deposition of fluorinated silane thin films	49
O-19	<b>Slavomír Sihelník</b> - Dry cleaning and activation of flexible glass using nonthermal plasma before PEDOT:PSS coating	50
O-20	<b>Senne Van Alphen</b> - Modelling study of CO <sub>2</sub> conversion enhancement in microwave plasmas using a quenching nozzle	51
O-21	<b>Eduardo Morais</b> - CH <sub>4</sub> coupling in nanosecond pulsed plasma discharges: 0D modelling to unravel the effect of pressure and temperature on product selectivity	52
O-22	<b>Nikola Škoro</b> - Correlation between properties of plasma treated liquids with characteristics of atmospheric pressure plasma devices	53
O-23	<b>Michael Schmidt</b> - Non-thermal plasma for generation of antimicrobial aerosol	54
O-24	<b>Ana Sainz García</b> - Forest material treatment by PAW	55
O-25	<b>Ionut Topala</b> - Revision of 3.4 μm band destruction rates under ion beam irradiation of hydrogenated amorphous carbon as interstellar dust analogues	56
O-26	<b>Kerstin Sgonina</b> - Selective study of ion-substrate interactions using the VUV-photoionization chamber	57

## Poster Presentations

ID	Presenter – Presentation Title	Page
P-1	<b>Fernando Alba-Elías</b> - Biocidal effect of i-PAW	58
P-2	<b>Jan Čech</b> - CaviPlasma: A large-throughput technology for plasma treatment of contaminated water using peroxide chemistry	59
P-3	<b>Ludmila Čechová</b> - Evaluation of the effect of plasma activated water on plants contaminated with heavy metals using laser-induced breakdown spectroscopy	60
P-4	<b>Richard Cimerman</b> - Multi-hollow surface dielectric barrier discharge: Variations of gaseous products under conditions of various air flow rates and relative humidities	61
P-5	<b>Sandra Ďurčányová</b> - Preparation of protective hydrophobic layers on aluminum using plasma polymerization at atmospheric pressure	62

## Correlation between properties of plasma treated liquids with characteristics of atmospheric pressure plasma devices

**N. Škoro, O. Jovanović, A. Kumar, A. Petrović, N. Puač**

Institute of Physics, University of Belgrade, Belgrade, Serbia

e-mail: nskoro@ipb.ac.rs

Non-equilibrium plasma at atmospheric pressure that operate in contact with liquids has proven to induce various chemical reactions in liquids. The most important chemically reactive species formed in the gas discharge above the liquid target are reactive oxygen and nitrogen species (RONS), electrons, UV radiation etc [1]. In complex interactions these species penetrate and/or react with liquid-phase molecules producing short and long-lived species in the target. Thus, adjusting of the plasma chemistry in the gas phase results in different outcomes of the liquid treatment which supports employment of the plasma treatments for different applications [2,3]. With respect to the purpose of the plasma treatment, it can be used for creation of new species, i.e. for liquid activation and creation of plasma activated water (PAW) and plasma activated medium (PAM), or for destruction of dissolved pollutant molecules – for decontamination processes. In this work we will present both kind of plasma treatments featuring comparison of properties of the treated liquids depending on different plasma setups, operating parameters etc. Treatments of pure and contaminated water (with organic dye AB25) were performed by using pin-type of plasma sources operating with He and Ar. These jets were operated with continuous sine signal at the frequency around 350 kHz. The setups were designed to enable precise determination of power delivered to the plasma and the sample. We investigated the influence of the working gas as well as sample volume to the RONS concentration in the activated water. For PAW treatments, we observed much higher production of H<sub>2</sub>O<sub>2</sub> in case of Ar plasma than in He. We tested variation in the efficiency of the plasma decontamination by adding multi-pin source and for conditions of recirculation of the contaminated sample. The effective treatment surface parameter proved to be significant for regulation of the decontamination efficiency. With respect to the treatments of the cell media, we used a dielectric barrier discharge (DBD) jet configuration that operated with continuous signal at around 80 kHz. We studied the influence of the input power on production of RONS in the PAW and PAM. It was shown also that important operating parameter for this kind of plasma jet was gas feed gas humidity. Understanding and optimizing the production of RONS in the plasma system is important due to their roles in major biological processes, thus fine tuning of the produced species is of great importance.

*This work was supported by NOWELTIES project - EU H2020 MSCA ITN No. 812880 and by Ministry of Education, Science and Technological Development of Republic of Serbia grant number 451-03-68/2022-14/200024.*

### References

- [1] P. Vanraes, A. Bogaerts, *Appl. Phys. Rev.* **5**, 031103 (2018).
- [2] N. Kumar Kaushika, B. Ghimirea, Y. Lia, M. Adhikaria, M. Veeranaa, N. Kaushika, N. Jhaa, B. Adhikari, S.-J. Lee, K. Masur, T. von Woedtke, K.-D. Weltmann, E. H. Choi, *Biol. Chem.* **400**, 39 (2019).
- [3] A. Kumar, N. Škoro, W. Gernjak, N. Puač, *Eur. Phys. J. D*, **75** (11), 1 (2021).



# GEC 2022

75th Annual Gaseous Electronics Conference



# ICRP-11

11th International Conference on Reactive Plasmas

## PROGRAM BOOK

Date : October 3-7, 2022

Sendai International Center Conference Building

Joint Conference in Sendai, Japan

Supported by  
American Physical Society  
Co-sponsored by  
The Japan Society of Applied Physics



Photo courtesy of Miyagi Prefecture Tourism Promotion Division



**IR4 Plasma Liquid Interaction III**Chair: Naoki Shirai (*Hokkaido University*)

- IR4.00001  
1:30PM - 2:00PM  
**Generating enhanced chemical reactions inside highly charged microscale droplets for remote delivery of reactive radicals and high purity nanomaterials**  
**Invited Speaker** Paul Maguire
- IR4.00002  
2:00PM - 2:15PM  
**Analyses of chemical reactions in plasma generated within humid oxygen bubbles with highly concentrated ozone**  
Nozomi Takeuchi, Ryota Kazama, Taichi Watanabe, Shungo Zen
- IR4.00003  
2:15PM - 2:30PM  
**Measurement of Radicals Generated by Plasma in Contact with Dilute Sulfuric Acid by Using Electron Spin Resonance (ESR) Method**  
Kosuke Tachibana, Nao Murata, Kaede Saito, Seiji Kanazawa, Katsuyuki Takahashi, Junko Hieda, Nozomi Takeuchi, Oi Lun Li
- IR4.00004  
2:30PM - 2:45PM  
**Creation of reaction species by an atmospheric pressure plasma jet when treating liquids**  
Nikola Skoro, Olivera Jovanović, Anđelija Petrović, Gordana Malović, Nevena Puac
- IR4.00005  
2:45PM - 3:00PM  
**Numerical simulation of chemical reactions in PBS-like solution exposed to atmospheric-pressure plasmas**  
Enggar Alfianto, Kazumasa Ikuse, Zoltan Donko, Satoshi Hamaguchi
- IR4.00006  
3:00PM - 3:15PM  
**Experimental study of the plasma chemistry in atmospheric pressure plasma contacts with dilute sulfuric acid**  
Siqi Deng, Nozomi Takeuchi, Junko Hieda, Katsuyuki Takahashi, Kosuke Tachibana, Oi Lun Li
- IR4.00007  
3:15PM - 3:30PM  
**Polymerization of EDOT on H<sub>2</sub>O by DBD treatment**  
Tomohiro Okamoto, Tatsuru Shirafuji, Jun-Seok Oh

**DR5 Optical Diagnostics**Chair: Holger Kersten (*Kiel University, Germany*)

- DR5.00001  
4:00PM - 4:15PM  
**Coupled Electrical and Optical Characterization of Electrostatic Discharges**  
Claudia A Schrama, Sarah Hinnegan, Jonathan Barolak, Daniel Adams, Alex Wilhelm, Charles G Durfee
- DR5.00002  
4:15PM - 4:30PM  
**Locally-resolved temperature and electron number density measurements in the VKI inductively-coupled plasma wind tunnel**  
Andrea Fagnani, Diana Luis, Damien Le Quang, Alan Viladegut, Bernd Helber, Olivier Chazot
- DR5.00003  
4:30PM - 5:00PM  
**Optical Emission Spectroscopy Measurement for Plasma Parameter Identification — from Kinetic Modeling to Data Science**  
**Invited Speaker** Hiroshi Akatsuka

## Bulletin of the American Physical Society

### 75th Annual Gaseous Electronics Conference

Monday–Friday, October 3–7, 2022; Sendai International Center, Sendai, Japan

The session times in this program are intended for Japan Standard Time zone in Tokyo, Japan (GMT+9)

#### Session IR4: Plasma Liquid Interaction III

1:30 PM–3:30 PM, Thursday, October 6, 2022  
Sendai International Center Room: Sakura 2

Chair: Naoki Shirai, Hokkaido University

#### **Abstract: IR4.00004 : Creation of reaction species by an atmospheric pressure plasma jet when treating liquids\***

2:30 PM–2:45 PM

← Abstract →

#### **Presenter:**

Nikola Skoro  
(Institute of Physics, University of Belgrade, Pregrevica 118, 11080 Belgrade, Serbia)

#### **Authors:**

Nikola Skoro  
(Institute of Physics, University of Belgrade, Pregrevica 118, 11080 Belgrade, Serbia)

Olivera Jovanović  
(Institute of Physics, University of Belgrade, Pregrevica 118, 11080 Belgrade, Serbia)

Anđelija Petrović  
(Institute of Physics, University of Belgrade, Pregrevica 118, 11080 Belgrade, Serbia)

Gordana Malović  
(Institute of Physics, University of Belgrade, Pregrevica 118, 11080 Belgrade, Serbia)

Nevena Puac  
(Institute of Physics, University of Belgrade, Pregrevica 118, 11080 Belgrade, Serbia)

Versatility of effects induced in liquids after plasma treatments has facilitated development of various applications in the fields of medicine, biology, water treatment etc. Plasma treated liquids (PTL) may contain different long-lived chemical species, but their occurrence and concentrations depend on the plasma system used. Some of the fundamental and significant reactions have been specified, but due to complexity of the chemistry in both plasma and liquid and their interaction, obtaining a wider prospect is still remote. To investigate interaction between atmospheric pressure plasma and a liquid target, in this study we associated results of spectrally resolved imaging and optical emission spectroscopy with quantification of reactive oxygen and nitrogen species (RONS) formed in the treated sample. For creation of the plasma above the sample we used a plasma jet operating in kHz regime with He/Ar as working gases. Relation between plasma and liquid properties has been established for wide range of different plasma parameters and several liquid targets. Obtained results provided relation between creation of RONS in the gas phase and in PTL.

\*This research was supported by the Science Fund of the Republic of Serbia, grant No. 3114/2021 - Project APPerTAin-BIOM and the MESTD of the Republic of Serbia grant No. 451-03-68/2022-14/200024.

This site uses cookies. To find out more, read our [Privacy Policy](#).

I Agree



# SAPP XXIV

24<sup>th</sup> Symposium on Application of Plasma Processes  
and  
13<sup>th</sup> EU-Japan Joint Symposium on Plasma  
Processing

Book of Contributed Papers

Štrbské Pleso, Slovakia  
27 Jan - 1 Feb, 2023

Edited by J. Országh, B. Stachová, D. Mészáros, P. Papp, Š. Matejčík



Book of Contributed Papers: 24<sup>th</sup> Symposium on Application of Plasma Processes and 13<sup>th</sup> EU-Japan Joint Symposium on Plasma Processing, Štrbské Pleso, Slovakia, 27 January – 1 February 2023.

Symposium organised by Department of Experimental Physics, Faculty of Mathematics, Physics and Informatics, Comenius University in Bratislava and Society for Plasma Research and Applications in hotel SOREA TRIGAN\*\*\*.

Editors: J. Országh, B. Stachová, D. Mészáros, P. Papp, Š. Matejčík

Publisher: Society for Plasma Research and Applications, Bratislava, Slovakia

Issued: January 2023, Bratislava, first issue

ISBN: 978-80-972179-3-8

URL: <https://neon.dpp.fmph.uniba.sk/sapp/>

## Local Organizers

---

### Department of Experimental Physics

Faculty of Mathematics, Physics and Informatics

Comenius University in Bratislava

Mlynská dolina F2

842 48 Bratislava, Slovakia

URL: <http://www.fmph.uniba.sk/>

Tel.: +421 2 602 95 686

Fax: +421 2 654 29 980



### Society for plasma research and applications

Faculty of Mathematics, Physics and Informatics

Comenius University Bratislava

Mlynská dolina F2

842 48 Bratislava, Slovakia

E-mail: [spvap@neon.dpp.fmph.uniba.sk](mailto:spvap@neon.dpp.fmph.uniba.sk)

Tel.: +421 2 602 95 686



## Local Organizing Committee

---

Štefan Matejčík (chair)

František Krčma

Peter Papp

Juraj Országh

Ladislav Moravský

Veronika Medvecká

# Table of Contents

## INVITED LECTURES

<b>IL-1</b>	Kinga Kutasi	EFFICIENT DEPOSITION AND TRAPPING OF REACTIVE SPECIES IN LIQUIDS AND HYDROGELS	11
<b>IL-2</b>	Erik Képeš	SPATIOTEMPORAL SPECTROSCOPIC CHARACTERIZATION OF ASYMMETRIC LASER-INDUCED PLASMAS	14
<b>IL-3</b>	Jaroslav Kočišek	DNA ORIGAMI NANOSTRUCTURES FOR STUDIES OF RADIATION DAMAGE	16
<b>IL-4</b>	Jean-Michel Pouvesle	PLASMA JET INTERACTIONS WITH TARGETS: PHYSICS AND APPLICATIONS	17
<b>IL-5</b>	Nikola Škoro	DEVELOPMENTS OF PLASMA ACTIVATED LIQUIDS FOR AGRICULTURAL AND WATER TREATMENT APPLICATIONS	18
<b>IL-6</b>	Pankaj Attri	CONTRIBUTION OF NON-THERMAL PLASMA IN AGRICULTURE: FOCUS ON PRE-HARVEST TREATMENT	19
<b>IL-7</b>	Jozef Breka	TECHNOLOGICAL 3D PLASMA SOURCES SCALING AND COMPUTATION	20
<b>IL-8</b>	Zdenko Machala	TRANSPORT OF COLD PLASMA REACTIVE SPECIES INTO WATER AND BIO-RELEVANT EFFECTS OF PLASMA-ACTIVATED WATER	21
<b>IL-9</b>	Anna Zahoranová	COLD ATMOSPHERIC PRESSURE PLASMA TECHNOLOGY FOR ECOLOGICAL AGRICULTURE	22
<b>IL-10</b>	Mehrnoush Narimisa	DIAGNOSTICS AND CHARACTERIZATION OF A NOVEL MULTIPURPOSE RF ATMOSPHERIC PRESSURE PLASMA JET FOR MATERIAL PROCESSING	28
<b>IL-11</b>	Vahideh Ilbeigi	DETECTION OF PLANT HORMONES BY ION MOBILITY SPECTROMETRY	33
<b>IL-12</b>	Marián Lehotský	PLASMA ASSISTED POLYMER BIOFUNCTIONALIZATION	36
<b>IL-13</b>	Judith Golda	DIAGNOSTIC CHALLENGES IN ATMOSPHERIC PRESSURE PLASMAS FOR PLASMA CATALYSIS	38
<b>IL-14</b>	Ján Žabka	LABORATORY VERSION OF THE ORBITRAP MASS ANALYZER WITH SEVERAL TYPES OF ION SOURCES HANKA – SPACE INSTRUMENT	39
<b>IL-15</b>	Kanako Sekimoto	FUNDAMENTAL PROCESSES OF ATMOSPHERIC PRESSURE DARK-CURRENT DISCHARGE IONIZATION	40
<b>IL-16</b>	Manabu Tanaka	DEVELOPMENT OF THERMAL PLASMA SOURCES WITH DIODE-RECTIFICATION AND THEIR APPLICATIONS TO NANOMATERIAL FABRICATION	42

# DEVELOPMENTS OF PLASMA ACTIVATED LIQUIDS FOR AGRICULTURAL AND WATER TREATMENT APPLICATIONS

Nikola Škoro<sup>1</sup>, Olivera Jovanović<sup>1</sup>, Amit Kumar<sup>1</sup>, Andjelija Petrović<sup>1</sup> and Nevena Puač<sup>1</sup>

<sup>1</sup>*Institute of Physics, University of Belgrade, Pregrevica 118, 11080 Belgrade, Serbia*  
E-mail: nskoro@ipb.ac.rs

In recent years many applications of cold atmospheric plasmas (CAP) are focused on treatment of liquid samples. CAP induces rich chemistry in active plasma volume creating short and long lived reactive species that penetrate and/or react with molecules in the liquid-phase producing short and long-lived species [1]. From the application point of view, the plasma treatment could be used for liquid activation and creation of plasma activated water (PAW) and plasma activated medium (PAM), or for destruction of dissolved pollutant molecules – for decontamination processes. For the latter case, plasma can be used as a chemically free advanced oxidation process (AOP) that can efficiently remove various organic micropollutants (OMP) from water. The major area of interest for PAW and plasma decontamination lie within the field of plasma agriculture [2]. Apart this field, liquid activation has a high potential in plasma medicine. For all these applications, clear knowledge of the entangled connection between plasma properties, plasma chemistry and interaction with the liquid target is necessary in order to tune the plasma for different outcomes of the liquid treatment [3,4]. In this work we will present several kinds of plasma treatments featuring investigation of both plasma and treated liquid properties and their dependence on the plasma jet type, operating parameters etc. Results of treatments of pure and contaminated water (with organic contaminant) were performed by using high-frequency pin-type atmospheric pressure plasma jet operating with He and Ar. For PAW creation, we demonstrated how the plasma operating in different regimes with He as working gas yield different concentrations of reactive nitrogen and oxygen species. Moreover, we investigated the influence of the working gas as well as sample volume to the RONS concentration in the activated water. We observed much higher production of H<sub>2</sub>O<sub>2</sub> in case of Ar plasma than in He. For treatments of the cell media used in plasma medicine applications, we used a dielectric barrier discharge (DBD) jet configuration that operated at 80 kHz. We showed that the power deposited to the plasma in contact with target was the key parameter for monitoring the production of RONS in the PAW and PAM. Thus precise power determination is crucial for fine tuning of the produced species.

Acknowledgement: This work was supported by MSTDI Republic of Serbia grant number 451-03-68/2022-14/200024, NOWELTIES project - EU H2020 MSCA ITN No. 812880 and the Science Fund of the Republic of Serbia, grant No. 3114/2021 - Project APPerTain-BIOM.

## References

- [1] Vanraes P and Bogaerts A 2018 *Appl. Phys. Rev.* **5** 031103.
- [2] Puač N, Gherardi M and Shiratani M 2017 *Plasma Process Polym.* e1700174.
- [3] Tomic S, Petrovic A, Puac N, Škoro N, Bekic M, Petrovic Z Lj and Colic M 2021 *Cancers* **13** 1626.
- [4] Kumar A, Škoro N, Gernjak W, Jovanović O, Petrović A, Živković S, Cuervo Lumbaqué E, José Farré M and Puač N 2023 *Sci. Total Env.* **864** 161194.

**icpm<sup>9</sup>**   
From June 27<sup>th</sup> to July 1<sup>st</sup> 2022, Utrecht, The Netherlands  
**9<sup>th</sup> international conference on plasma medicine**



# Book of Abstracts

Editors: Gerrit Kroesen, Romolo Laurita,  
Ana Sobota, Matteo Gherardi



Oral Contributions		
O1 D1A1*	Sander Bekeschus -Medical gas plasma augments bladder cancer cell toxicity and immunogenicity in preclinical models and patient-derived tumor tissues	25
O2 D1A1*	Francesco Tampieri -Biocompatible Composite Hydrogels for Storage and Delivery of Plasma-Generated Reactive Species	26
O3 D1A1*	Lukes Petr -Chemistry and cytotoxic properties of amino acids modified by He/O <sub>2</sub> plasma in saline solutions	27
O4 D1A1*	Andjelija Petrovic -Optimization of a DBD plasma jet in contact with liquids for application in biomedicine	28
O5 D1A1*	Parisa Shali -Plasma directly generated in liquids as an innovative method to treat cancer	29
O1 D1A2*	Zdenko Machala -Cold plasma/photocatalysis decontamination of FFP2 respirators and indoor air contaminants	30
O2 D1A2*	Pasquale Isabelli -Cold Plasma Systems to reduce airborne transmission of Hospital Acquired Infectious & COVID-19	31
O3 D1A2*	Gabriele Neretti -Sterilization of disposable devices performed by indirect plasma treatment	32
O4 D1A2*	Fernando Alba-Elías -Atmospheric Pressure Cold Plasma for Mask Disinfection	33
O1 D1B1	Ita Junkar -Gaseous plasma treatment of vascular stents - a powerful tool for new generation vascular stents	34
O2 D1B1	Eline Biscop -Elucidating Non-Thermal Plasma-induced Cell Death Mechanisms for Direct and Indirect Treatment Condition	35
O3 D1B1	Vandana Miller -Plasma immunomodulation: secondary and tertiary effects	36
O4 D1B1	Johanna Striesow -Formation of lipid peroxidation products by gas plasmas - translation from the liposome model to human platelets	37
O5 D1B1	Kai Masur -Plasma modulation of human progenitor cells	38
O6 D1B1	Li Lin -The Physical Effects of Plasma Medicine on Cells: Radio Frequency Stimulated Intercellular and Intracellular Mechanical Waves	39
O7 D1B1	Sybillle Hasse -Investigations on microbiome and proteome in chronic wound exudates under plasma and standard wound treatment	40
O8 D1B1	Osvaldo Daniel Cortázar -Healing of torpid ulcers treated with atmospheric cold air plasma jet: preliminary results	41
O9 D1B1	Augusto Stancampiano -In-vivo safety assessment for fractioned and continuous direct plasma treatments	42
O1 D1B2*	Susana Sérgio -Interaction of a Cold Atmospheric Argon Plasma Jet Device with Human Skin Cells	43
O2 D1B2*	Benjamin Harris -Tailoring reactive oxygen species production in pulsed He+H <sub>2</sub> O plasmas through Pulse Repetition Rate	44
O3 D1B2*	František Krčma -Diagnostics of Dielectric Barrier Discharge Based Plasma Pen for Skin Treatment	45
O4 D1B2*	Katayoon Hadian Rasnani -Electrical and optical investigation of the long term operation of an endoscopic plasma devic	46
O5 D1B2*	Shinya Kumagai -Analysis of cell irradiated with non-thermal atmospheric pressure plasma for effective gene transfer	47

## Optimization of a DBD plasma jet in contact with liquids for application in biomedicine

Andelija Petrović<sup>1</sup>, Nikola Škoro<sup>1</sup>, Nevena Puač<sup>1</sup> and Zoran Lj. Petrović<sup>2,3</sup>

<sup>1</sup>Institute of Physics, University of Belgrade, Pregrevica 118, 11080 Belgrade, Serbia

<sup>2</sup>Serbian Academy for Sciences and Arts, Belgrade, Serbia

<sup>3</sup>School of Engineering, Ulster University, Jordanstown, Co. Antrim, United Kingdom

E-mail: andjelija@ipb.ac.rs

The interaction of atmospheric pressure plasmas (APPs) with liquids has gained increasing attention due to the importance of biological effects induced by plasmas as well as plasma activated liquids (PAL) [1]. PAL may be prepared by treating water or different aqueous solutions, including cell culture media. The interaction of gas-phase reactive oxygen and nitrogen species (RONS) with aqueous organics produces other long-lived RONS, such as hydrogen peroxide (H<sub>2</sub>O<sub>2</sub>), nitrates, nitrites [2]. For example, due to existence of long-lived RONS, PAL has been shown to be effective in death induction of cancer cells while the normal cells were found to be less sensitive [3-4]. The “treatment dose” depends on the type of plasma source, the time of exposure of the liquid to the plasma, as well as the period for which the cells or tissue is allowed to remain in contact with PAL.

The interaction between plasma and liquids, particularly RONS production, has been the subject of intense research since it is of a great relevance for plasma biomedical applications to establish precise control over these reactive species in order to achieve the desired biological response. The relation between plasma and target has been demonstrated to be mutual, potentially affecting both the target and the plasma characteristics.

In this study, we performed detailed diagnostics and optimization of the dielectric barrier discharge (DBD) type of the APP jet system in order to improve the understanding of the plasma chemistry and the means for its tailoring in medium treatment applications. This is made by electrical characterization since the power deposited to the discharge is a crucial parameter, then plasma imaging (to reveal spatial plasma structure), and optical emission spectroscopy (OES) to detect excited and metastable species. We tried to identify plasma parameters that can be used as reliable markers for plasma efficiency and are relevant for the consistent description of effects on treated liquids - RPMI 1640 cell culture medium and distilled water. We also investigated physicochemical properties of PAL - measurement of temperature, dissolved O<sub>2</sub>, conductivity, pH, and concentrations of long lived reactive species H<sub>2</sub>O<sub>2</sub>, NO<sub>2</sub><sup>-</sup> and NO<sub>3</sub><sup>-</sup>. All measurements were related to effectiveness of plasma activated water in the healing of diabetic wounds and the application of plasma activated medium for cell treatment in order to produce tumor lysates for tumor vaccine.

This research is funded by Ministry of Education, Science and Technological Development, grant number 451-03-9/2021-14/200024.

### References

- [1] M. Laroussi, X. Lu and M. Keidar, *J. Appl. Phys.*, 122, 020901(2017)
- [2] Bruggeman P and Leys C *J. Phys. D. Appl. Phys.* 42 2009 53001
- [3] S. Tomić, A. Petrović, N. Puač, N. Škoro, M. Bekić, Z.Lj. Petrović, M. Čolić, *Cancers* 13 2021
- [4] Kaushik, N., Ghimire, B., Li, Y., Adhikari, M., Veerana, M., Kaushik, N., Jha, N., Adhikari, B., Lee, S., Masur, K., von Woedtke, T., Weltmann, K. & Choi, E. *Biological Chemistry*, 400(1), 39-62 2019.

**icpm<sup>9</sup>**   
From June 27<sup>th</sup> to July 1<sup>st</sup> 2022, Utrecht, The Netherlands  
**9<sup>th</sup> international conference on plasma medicine**



# Book of Abstracts

Editors: Gerrit Kroesen, Romolo Laurita,  
Ana Sobota, Matteo Gherardi

O6 D2B2	Jordanne-Amee Maybin -Cold atmospheric pressure plasma as a method to improve efficacy of antibiotics against biofilm-forming <i>Pseudomonas aeruginosa</i>	71
O1 D3A1*	Augusto Stancampiano -Cold plasma and Electrochemotherapy: in vivo combined treatment	72
O2 D3A1*	Thierry DUFOUR -Cold plasma endoscopy applied to cholangiocarcinoma: therapeutic study & feasibility study on porcine anatomical models	73
O3 D3A1*	Maja Miletić -Does cold plasma pretreatment of beta-tricalcium phosphate together with periodontal ligament stem cells enhance bone regeneration in vivo?	74
O4 D3A1*	Sander Bekeschus -Repeated exposure of the oral mucosa over 12 months with cold plasma is not carcinogenic in mice	75
O5 D3A1*	Kai Masur -Standardization in Plasma Medicine: From DIN Spec to IEC standards	76
O6 D3A1*	Albert Espona-Noguera -Dual action of RONS/Biomolecule-loaded Hydrogels: Killing Cancer Cells and Enhancing Stem Cells Viability	77
O7 D3A1*	Abraham Lin -Investigating Non-Thermal Plasma-Resistant Molecular Pathways through Development and Interrogation of a Resistant Melanoma Cell Line	78
O1 D3B1	Nicholas L Sponzel -Atmospheric Plasma Generated Nitrate Production and Optimization in a Water-sealed DBD Bubbler	79
O2 D3B1	Duncan Trosan -Characterization and Optimization of Complex Surface Dielectric Barrier Discharges for the Purpose of Food Decontamination	80
O3 D3B1	Hemaditya Malla -Identifying Important Reactive Oxygen-Nitrogen Species in Sub-nanosecond Pulsed Discharges using Zero-dimensional Simulations	81
O4 D3B1	Vasyl Shvalya -Plasma-made optical sensors for ppb level mycotoxins diagnostics	82
O5 D3B1	Alexandra Waskow -Understanding the molecular mechanisms of non-thermal plasma treatments on <i>Arabidopsis thaliana</i> seeds	83
O6 D3B1	Sonal Chaple -The effects of Cold Plasma treatment on physicochemical and rheological modification of hydrocolloids	84
O7 D3B1	Anna Dzimitrowicz -Continuous flow plasma brush as an effective tool for degradation of drugs from liquid disposals	85
O1 D4A1	Robin Mentheour -Antibacterial combination of cold plasma-activated water and pulsed electric fields	86
O2 D4A1	Anna Machková -Comparing the biocidal properties of non-thermal plasma sources with controlled treatment parameters by reference protocol	87
O3 D4A1	Min Xie -Growth phase, short-living RONS and acidity govern cold atmospheric plasma (CAP) antibacterial membrane activity in suspension	88
O4 D4A1	Courti Ibtissam -Impact of Bacterial Growth Phase on Liquid Decontamination Efficiency Using Atmospheric Pressure Plasma	89
O5 D4A1	Soukaina Barroug -Optimizing Plasma Functionalized Liquids for Control of Microbiological Risks Associated with Poultry Processing Chain	90
O6 D4A1	Maxime Sahun -Rapid viral inactivation by cold atmospheric plasma offering great opportunities to decontaminate materials in hospital environments	91
O7 D4A1	Florin Bilea -The influence of chemical and physical parameters on plasma driven antibiotic degradation	92

## Does cold plasma pretreatment of beta-tricalcium phosphate together with periodontal ligament stem cells enhance bone regeneration *in vivo*?

Maja Miletić<sup>1</sup>, Nevena Puač<sup>2</sup>, Nikola Škoro<sup>2</sup>, Božidar Brković<sup>1</sup>, Miroslav Andrić<sup>1</sup>, Bogumir Prokić<sup>3</sup>, Vesna Danilović<sup>1</sup>, Sanja Milutinović-Smiljanić<sup>1</sup>, Olivera Mitrović-Ajtić<sup>4</sup>, Slavko Mojsilović<sup>4</sup>

<sup>1</sup>School of Dental Medicine, University of Belgrade, Dr Subotića 8, 11000 Belgrade, Serbia

<sup>2</sup>Institute of Physics, University of Belgrade, Pregrevica 118, 11080 Belgrade, Serbia

<sup>3</sup>Faculty of Veterinary Medicine, University of Belgrade, Bulevar oslobođenja 18, 11000 Belgrade, Serbia

<sup>4</sup>Institute for Medical Research, University of Belgrade, Dr Subotića 4, POB 102, 11129 Belgrade, Serbia

E-mail: [maja.miletic@stomf.bg.ac.rs](mailto:maja.miletic@stomf.bg.ac.rs)

Bone regeneration is a complex physiological process of bone formation that is involved in continuous remodeling throughout life and in reparation after trauma. However, there are specific conditions, especially in oral and maxillofacial surgery, as well as in the case of large bone defects caused by various pathological changes, which require a large amount of bone regeneration that exceeds the normal potential for self-healing. A new strategy in the field of regenerative bone tissue medicine involves the combination of artificial bone substitutes (hydroxyapatite, calcium phosphate) and progenitor cells (mesenchymal stem cells (MSCs), mature bone cells) [1]. MSCs can be isolated from a variety of tissues including bone marrow, adipose, and dental tissues. These cells can differentiate into different specialized cell types and have other desirable features that make them ideal candidates for use in regenerative medicine and tissue engineering. It was shown that MSCs in combination with calcium phosphate-based biomaterials induce bone regeneration [2]. Physicochemical properties of biomaterials such as chemical composition, hydrophilicity, surface energy, and topography are key factors that control the behavior of cells on the surface of the materials. Previously it was shown that all these properties can be very easily modified by treatment with cold atmospheric plasma (CAP)[3].

In this study, we examined if CAP-pretreated beta-tricalcium phosphate ( $\beta$ -TCP) scaffolds alone, or in combination with periodontal ligament stem cells (PDLSCs), increases the regeneration of critical size bone defects *in vivo*. The PDLSC were isolated from the human periodontal ligament of normal impacted third molars, characterized and cultivated until the experiment.  $\beta$ -TCP was treated with CAP by using atmospheric pressure dielectric barrier discharge prior to the implantation. With rabbits under general anesthesia, four bone defects were made and filled with treated/non-treated  $\beta$ -TCP with or without PDLSCs. After two and four weeks of healing, animals were sacrificed and samples were taken for histological, histomorphometric, and immunohistochemical analysis.

This work was supported by MESTD of Republic of Serbia, Grants no. 451-03-9/2021-14/200129, 451-03-9/2021-14/200024, 451-03-9/2021-14/200015.

### References

- [1] C. Gao, S. Peng, P. Feng et al. *Bone Res*, 5, 17059 (2017).
- [2] W. Chen, J. Liu, N. Manuchehrabadi, MD. Weir, Z. Zhu, and HH. Xu, *Biomaterials*, 34, 9917-25 (2013).
- [3] SC. Cheuk, FL. Wei, L. PeiYing, W. Yi-Fan, H. Haw-Ming, T. Nai-Chia, P. Yu-Hwa, S. Eisner, and C. Wei-Jen, *Scientific Reports*, 11, 9234 (2021).

**icpm<sup>9</sup>**   
From June 27<sup>th</sup> to July 1<sup>st</sup> 2022, Utrecht, The Netherlands  
**9<sup>th</sup> international conference on plasma medicine**



# Book of Abstracts

Editors: Gerrit Kroesen, Romolo Laurita,  
Ana Sobota, Matteo Gherardi

Plenary talks		Page
P1*	Cristina Canal - Lessons learnt in plasma-treated liquid therapies for bone cancer: opportunities for plasma medicine	2
P2	Peter Bruggeman -Plasma Regulated Biology: A Pathway Towards Defining a 'Dose' in Plasma-Medicine	3
P3	Katharina Stapelmann -Plasma and Plasma-Liquid Chemistry in the Presence of Organic Matter	4
P4	Yuzuru Ikehara -Understanding and uses the plasma effects as what interacts with the biomolecules having the electric charge	5
P5	Julia Bandow -Plasma-driven biocatalysis: challenges and opportunities	6
Invited talks		
I1 D1A1*	Hiromasa Tanaka -Molecular mechanisms of cell death by plasma-activated solutions in glioblastoma cells	8
I2 D1A1*	Valeria Veronico -The active role of the liquid in the formation of long-lived RONS in Plasma Treated Water Solutions	9
I1 D1A2*	Stephan Reuter -Plasma Tailoring for Pathogen Inactivation	10
I1 D1B2*	James Walsh -Influence of external factors on plasma jet dynamics	11
I1 D2B1	Konstantin Kostov -Development of Remote Atmospheric Plasma Jets for Biomedical Applications	12
I1 D2A1*	Yury Gorbanev -Cold plasma interacting with liquids: Non-equilibrium all the way	13
I2 D2B1	Mário Janda -The role of HNO <sub>2</sub> in the generation of plasma activated water by transient spark discharge	14
I1 D3A1*	Evelien Smits -The tumor immunologist's point of view on preclinical and clinical studies in the context of plasma oncology	15
I1 D3B1	Nevena Puac -Plasma treatment of seeds and plant cells: role of reactive oxygen and nitrogen species in formation of plantlets and embryos in non-permissive conditions	16
I1 D4B1	Ramona Clemen -Gas Plasma Technology Augments Ovalbumin Immunogenicity and OT-II T Cell Activation Conferring Tumor Protection in Mice	17
I1 D4A1	Suresh Joshi -Plasma-Based Solution for Bacterial Inactivation: A Novel Approach	18
I1 D4A2	Steffen Emmert -Clinical Plasma Medicine: From Routine Application in Wound Healing to New Applications in Dermatology	19
I2 D4B1	Hiroaki Kajiyama -The aqueous plasma therapy for ovarian cancer ~Aiming for controlling disseminated peritoneal metastasis	20
I1 D4B2	Kyriakos Sklias -The role of short- and long-lived reactive species on the anti-cancer action of plasma-activated liquids: in-vitro and in-vivo applications	21
I1 D5A	Lea Miebach -Conductivity augments ROS and RNS delivery and tumor toxicity of an argon plasma jet	22
I1 D5B	Andrew Gibson -Control of plasma-chemical processes in atmospheric pressure plasmas for life science-related applications	23
<b>* 1st Annual Meeting of COST Action PlasTHER CA20114</b>		

## Plasma treatment of seeds and plant cells: role of reactive oxygen and nitrogen species in formation of plantlets and embryos in non-permissive conditions

Nevena Puač<sup>1</sup>, Suzana Živković<sup>2</sup>, Milica Milutinović<sup>2</sup>, Olivera Jovanović<sup>1</sup>, Anđelija Petrović<sup>1</sup>, Gordana Malović<sup>1</sup> and Nikola Škoro<sup>1</sup>

<sup>1</sup>Institute of Physics, National Institute of the Republic of Serbia, University of Belgrade, Pregrevica 118, 11080 Belgrade, Serbia

<sup>2</sup>Institute for Biological Research “Siniša Stanković”, National Institute of the Republic of Serbia, University of Belgrade, Bulevar despota Stefana 142, 11060 Belgrade, Serbia

E-mail: [nevena@ipb.ac.rs](mailto:nevena@ipb.ac.rs)

The population growth together with constant climate changes represent a serious challenge for humankind. Additionally, the usage of the pesticides have created adverse effect on environment, which in return impact even more agricultural production. In order to comply with the demands and to adapt to the new conditions the farmers need to change or upgrade existing practices by employing new technologies. As being a promising tools in application in medicine, non-thermal (cold) plasmas (NTPs) are seen as a green alternative to conventional fertilizers in agriculture to improve yields, increase size and robustness of plants and to reduce (or eliminate) the need for pesticides [1, 2].

NTPs have rich chemistry of Reactive Oxygen and Nitrogen Species (RONS) that are formed in gas phase and, in case of water treatment, in gas/liquid interface in liquid [2, 3]. We can use NTPs in direct treatments of seeds or plant cells where samples are in contact with plasma gas phase chemistry or indirectly when treated water is applied to the biological samples. In both cases RONS (short or long-living) are responsible for triggering various mechanisms and effects in plant cells. To better understand the reasons for triggered mechanisms and outcomes (better germination percentage and speed, breakout of dormancy, creation of embryos etc.) it is important to characterize the plasma chemistry both in gas and liquid phase. We have used several atmospheric pressure plasma systems in treatments of seeds and plant cells in order to investigate the mechanisms responsible for better germination in seeds, enzyme response and formation of somatic embryos in non-permissive conditions. The mechanisms investigated were linked with the chemistry of RONS created in gas phase and/or deposited in liquid phase. Thus, we were able to acquire the data that can be used in optimization of plasma treatment processes.

This work was supported by Ministry of Education, Science and Technological Development of Republic of Serbia, grant numbers 451-03-9/2021-14/200007 and 451-03-9/2021-14/200024.

### References

- [1] N. Puač, M. Gherardi and M. Shiratani, *Plasma Process Polym.*, e1700174 (2017).
- [2] I. Adamovich et al., *J. Phys. D. Appl. Phys.*, 50, 323001 (2017).
- [3] Petr Lukes, Bruce R. Locke, and Jean-Louis Brisset, “Aqueous-Phase Chemistry of Electrical Discharge Plasma in Water and in Gas–Liquid Environments”, *Plasma chemistry and catalysis in gases and liquids*, Wiley-VCH Verlag GmbH&Co. (2012).



**icpm<sup>9</sup>**   
From June 27<sup>th</sup> to July 1<sup>st</sup> 2022, Utrecht, The Netherlands  
**9<sup>th</sup> international conference on plasma medicine**



# Book of Abstracts

Editors: Gerrit Kroesen, Romolo Laurita,  
Ana Sobota, Matteo Gherardi

P2.6*	Aur�lie Marches: Cold atmospheric helium plasma activates migration but not proliferation of human keratinocytes	162
P2.7	Rita Agus: Investigation of plasma activated water inactivation mechanisms of Escherichia coli through single-cell microfluidic experiments	163
P2.8	Filippo Capelli: Plasma assisted decontamination of food packaging material	164
P2.9	Karol Hensel: Effects of cold plasma generated by transient spark discharge on proteins and amino acids in water solutions	165
P2.10	Carmen Kirner: Viability of commercially available non-thermal atmospheric pressure plasma (APP) sources for decontamination of polypropylene surfaces	166
P2.11	Erika Muratov: Analysis of biofilm inactivation mechanisms under cold plasma treatment	167
P2.12	Inna Orel: Gram-negative and gram-positive bacteria disinfection by cold atmospheric plasma using an in vitro agar plate model of a chronic wound	168
P2.13	Jovana Petkovic: Are bubbles efficient in the production of plasma-treated water?	169
P2.14	Roopesh Mohandas Syamaladevi: Inactivation mechanisms of Listeria monocytogenes during in-package atmospheric cold plasma treatment and post-treatment storage	170
P2.15	Krist�na Trebulov�: Impact of cold plasma treatment on the yeast candida glabrata	171
P2.16*	Slavom�r P�sztor: Chemical Analysis of Four Types of Plasma Activated Liquid Stored at Different Temperatures and Neutrophils Treated by PAL	172
P2.17	Behnaz Bagheri: Molecular dynamics study of effect of oxidation induced by plasma on properties of lipid bilayers	173
P2.18	Fred Krebs: Immunomodulatory effects of non-thermal plasma in a model of latent HIV-1 infection: Implications for an immunotherapy effective against HIV-1 infection	174
P2.19	Jaroslav Kristof: Rat Intestine Cells Absorption of Fluorescein Isothiocyanate–Dextran Induced by Microplasma Treatment	175
P2.20	Angela Maldonado: Cold atmospheric plasma does not affect stellate cells phenotype in pancreatic tissues in ovo	176
P2.21	Jose Moreno Martinez: Application of cytogenetic marker for the quantification of radio-induced damage produced by a pulsed x-ray plasma focus devices	177
P2.22	Aled Morton: Cold atmospheric plasma for the treatment of intracellularly infected osteoblasts and osteoclasts	178
P2.23	Kae Nakamura: Immunostimulatory Effect of Plasma-Activated Solutions in the Intraperitoneal Environment of Ovarian Cancer	179
P2.24	Yokoyama Ryo: Study on Control of Macromolecular Drug Transfer to Epithelial Cells Using Non-Invasive Microplasma	180
P2.25	Ilva Noa Stellingwerf: Cancer cell metabolism and cold atmospheric plasma treatment	181
P2.26	Shu Xiao: Nanosecond Pulses Delivered by Plasma Streamer Channels Modulate Cell Response in Space (in-vitro Study)	182
P2.27*	Nikola Skoro: Cold Atmospheric Plasma treatment of dentin substrate for adhesive dental procedures	183
P2.28	Mohamed Boudifa: On the effect of atmospheric plasma jet on 3D printing of hydrogels for tissue engineering	184

## Cold Atmospheric Plasma treatment of dentin substrate for adhesive dental procedures

T. Lainović<sup>1</sup>, N. Škoro<sup>2</sup>, A. Krmpot<sup>2</sup>, M. Rabasović<sup>2</sup>, N. Selaković<sup>2</sup>, E. Novta<sup>1</sup>, L. Blažić<sup>1,3</sup> and N. Puač<sup>2</sup>

<sup>1</sup>Faculty of Medicine, School of Dental Medicine, University of Novi Sad, Novi Sad, Serbia

<sup>2</sup>Institute of Physics, University of Belgrade, Belgrade, Serbia

<sup>3</sup>Dental Clinic of Vojvodina, Novi Sad, Serbia

E-mail: [nskoro@ipb.ac.rs](mailto:nskoro@ipb.ac.rs)

Advances in materials science were primarily responsible for enabling the development of adhesive dentistry, which today is the state-of-art of minimally invasive dental approaches. In recent years, in addition to the development of materials, there is a research trend for a better understanding of the biological substrate, dentin, and its modifications [1], in order to improve the quality and durability of adhesively bonded restorations.

This study aimed to microscopically analyze the morphology of dentin-adhesive interface, after previous treatment of dentin substrate by the Cold Atmospheric Plasma (CAP). First-class dental cavities were prepared in human teeth, extracted according to medical indications. The underlying hard-dental tissue, dentin, was exposed for the adhesive-bonding procedures. Two standard adhesive protocols were applied to the samples: 1. etch-and-rinse (ER) and 2. self-etch (SE) technique. Samples in both of these experimental groups were modified by using the CAP treatment of dentin before adhesive placement. The plasma used for treatments was produced by a RF plasma needle, with 1 slm of He as a feeding gas and tip-to-surface distance of 2 mm. The power deposited to plasma was determined by using derivative probes for each treatment and it was between 1 W and 2 W.

Following listed preparation, the samples were examined using Nonlinear Laser Scanning Microscopy (NLSM) [2]. The surface free energy was calculated by measuring the contact angles on the dentinal substrate in experimental and control groups.

The CAP treatment prepared the dentinal substrate in a way that significantly changed the interaction with adhesives, by increasing its surface energy and wetting properties. As NLSM measurements showed, the hybrid layer created between collagen fibers and adhesive was denser, wider and resin-tags were significantly longer entering much deeper into the dentinal substrate. It seems that the flow of adhesive placed at the treated samples was greatly facilitated by the CAP dentinal modification.

It remains to be examined how plasma activation of dentin subsequently interact with the adhesive and enables such a deep penetration. Moreover, as an important step towards application, it is important to determine the exact clinical situations in which the CAP treatment would be useful and in which it should be limited or restrictively controlled. Thus, further research will be focused on process optimization.

### Acknowledgment

Supported by the Ministry of Education, Science and Technological Development of Republic of Serbia (No. NIO 200114 and No. 451-03-68/2021-14/200024), Project HEMMAGINERO, No. 6066079 from Program PROMIS, Science Fund of the Republic of Serbia.

### References

[1] J.N. Stašić, N. Selaković, N. Puač, M. Miletić, G. Malović, Z.Lj. Petrović, D.N. Veljović and V. Miletić, *Clin Oral Invest*, 23, 1383 (2019).

[2] T. Lainović, J. Margueritat, Q. Martinet, X. Dagany, L. Blažić, D. Pantelić, M.D. Rabasović, A.J. Krmpot and T. Dehoux, *Acta Biomater*, 105, 214, (2020).

**icpm<sup>9</sup>**   
From June 27<sup>th</sup> to July 1<sup>st</sup> 2022, Utrecht, The Netherlands  
**9<sup>th</sup> international conference on plasma medicine**



# Book of Abstracts

Editors: Gerrit Kroesen, Romolo Laurita,  
Ana Sobota, Matteo Gherardi

O1 D2A1*	Utku Kürşat Ercan -Determination of Antimicrobial Strength of Cold Atmospheric Plasma Activated Water by Colorimetric and Electrochemical Methods	48
O2 D2A1*	Romolo Laurita -On the use of cold atmospheric pressure plasmas and plasma activated water for food processing	49
O3 D2A1*	Ana Megía -Plasma Activated Water (PAW) Against Virus and Multidrug Resistant Bacteria: characterization and in vitro experiments	50
O4 D2A1*	Olivera Jovanović -Plasma pin-jet for treatment of water: production of reactive species in distilled and tap water	51
O5 D2A1*	Jean-Michel Pouvesle -The, so-called blob, slime mold Physarum polycephalum as a new model for biological applications of atmospheric pressure non-thermal plasmas	52
O6 D2A1*	Aleksandra Lavrikova -Bacteria inactivation pathways induced by cold atmospheric plasma	53
O7 D2A1*	Nishtha Gaur -Methods to enhance the anti-microbial effects of an argon plasma jet	54
O1 D2A2*	Allan Pavy -Remodeling of cholangiocarcinoma microenvironment by cold atmospheric plasma through in vitro approach	55
O2 D2A2*	Matteo Gherardi -Control strategies for atmospheric pressure PECVD	56
O3 D2A2*	Beatrice Olayiwola -Deposition of Antibiotic Layers onto Implant Surfaces using Low Temperature Plasma	57
O4 D2A2*	Metka Benčina -Plasma treated nanostructured TiO <sub>2</sub> surface for vascular stents applications	58
O5 D2A2*	Hamed Mahdikia -MENs Surface Modification for Drug Delivery Applications Using Low-Pressure Plasma	59
O6 D2A2*	Fernando Alba-Elías-Anti-friction coatings on medical needles using atmospheric-pressure plasma-polymerization	60
O1 D2B1	Eun Ha Choi -Calculation of O <sub>3</sub> and O density containing humidity generated from nonthermal atmospheric plasma	61
O2 D2B1	Julien Bissonnette-Dulude -Coupling of microfluidic devices with reference cold plasma jet	62
O3 D2B1	Sebastian Burhenn -Impact of humidity on the OH distribution in the effluent of the COST-jet measured by laser induced fluorescence	63
O4 D2B1	Andra-Cristina Bostanaru-Mycobactericidal Efficacy of Non-Thermal Plasma Activated Water	64
O5 D2B1	Paul Maguire -Electron and hydroxyl radical interactions with liquids, biomolecules and cells	65
O1 D2B2	Joseph Lorent -Spatial distribution of cold atmospheric plasma reactive species displaying activity on bacterial cell membranes	66
O2 D2B2	Thomas Thompson -Comparison of the antimicrobial activity of three Cold Plasma jets against S. aureus	67
O3 D2B2	Nagendra Kumar Kaushik -NONTHERMAL BIOCOMPATIBLE PLASMA FOR IMMUNO-MODULATION, SYNERGY WITH NANOMATERIALS, AND CORONA VIRUS INACTIVATION	68
O4 D2B2	Julia Sutter -Nonthermal Plasma as an Antiviral and Immunomodulatory Agent Effective Against HSV-1 Infection	69
O5 D2B2	Ross Duncan -Cold plasma treatment of macrophages and biofilms affects their interaction with free antibiotics and liposomes	70

## Plasma pin-jet for treatment of water: production of reactive species in distilled and tap water

Olivera Jovanović<sup>1</sup>, Nevena Puač<sup>1</sup>, Nikola Škoro<sup>1</sup>

<sup>1</sup> Institute of Physics, University of Belgrade, Pregrevica 118, 11080 Belgrade, Serbia

E-mail: [olivera@ipb.ac.rs](mailto:olivera@ipb.ac.rs)

In two increasingly important fields of plasma application – biomedicine and plasma agriculture, Plasma Activated Liquids (PALs) play a key role [1,2]. These applications caused the development of various designs of atmospheric pressure plasma jets (APPJs) that operate in contact with liquid samples. Despite a significant number of successful investigations involving the use of PALs [3], there are still lot of unknowns that need to be clarified. The first is to completely understand the interaction mechanisms between plasma and liquid, and the creation of a huge number of chemical species. The second, equally challenging problem, is how to standardize a device's performance to produce PAL of required physico-chemical characteristics for different applications.

In this work, we will present the results of the treatment of pure distilled and tap water in order to create Plasma Activated Water (PAW). We have used an atmospheric pressure plasma jet (APPJ) in pin electrode configuration operating at a frequency of 340kHz in contact with aqueous sample. The plasma jet was used with pure argon and an admixture with synthetic air as working gas. Total gas flow was kept constant at 1 slm in all experiments. The distilled water and tap water samples were exposed to the streamer discharge under several treatment conditions in order to investigate the influence of plasma parameters and the target properties on characteristics of the produced PAW. In order to determine the excited species produced in plasma above the liquid, optical emission spectroscopy was employed. Diagnostics of liquid samples were performed to assess the effectiveness of plasma treatment. The analysis of physicochemical parameters was conducted by measuring conductivity, pH, temperature and the amount of deposited RONS ( $H_2O_2$ ,  $NO_3^-$ ,  $NO_2^-$ ).

The results of optical emission spectroscopy showed the existence of oxygen and nitrogen reactive species in the spectrum of argon discharge. Besides the dominant OH radical band, NO $\gamma$  emission was also detected. Measurements of RONS created in plasma and deposited in aqueous samples showed that the sample properties, treatment time, and working gas were parameters that influenced both the type and the amount of produced reactive species.

### Acknowledgment

This work was supported by the Ministry of Education, Science and Technological Development, grant number 451-03-68/2021- 14/200024.

### References

- [1] M. Laroussi, X. Lu, and M. Keidar, *Journal of Applied Physics*, 122, 020901 (2017).
- [2] N. Puač, M. Gherardi and M. Shiratani, *Plasma Processes and Polymers*, 15, 1700174 (2018).
- [3] N. K. Kaushik, B. Ghimire, Y. Li, M. Adhikari, M. Veerana, N. Kaushik, N. Jha, B. Adhikari, S.-J. Lee, K. Masur, T. von Woedtk, K.-D. Weltmann and E. H. Choi, *Biological chemistry*, 400, 39-62, (2019).



# SAPP XXIV

24<sup>th</sup> Symposium on Application of Plasma Processes  
and  
13<sup>th</sup> EU-Japan Joint Symposium on Plasma  
Processing

Book of Contributed Papers

Štrbské Pleso, Slovakia  
27 Jan - 1 Feb, 2023

Edited by J. Országh, B. Stachová, D. Mészáros, P. Papp, Š. Matejčík



Book of Contributed Papers: 24<sup>th</sup> Symposium on Application of Plasma Processes and 13<sup>th</sup> EU-Japan Joint Symposium on Plasma Processing, Štrbské Pleso, Slovakia, 27 January – 1 February 2023.

Symposium organised by Department of Experimental Physics, Faculty of Mathematics, Physics and Informatics, Comenius University in Bratislava and Society for Plasma Research and Applications in hotel SOREA TRIGAN\*\*\*.

Editors: J. Országh, B. Stachová, D. Mészáros, P. Papp, Š. Matejčík

Publisher: Society for Plasma Research and Applications, Bratislava, Slovakia

Issued: January 2023, Bratislava, first issue

ISBN: 978-80-972179-3-8

URL: <https://neon.dpp.fmph.uniba.sk/sapp/>



## Local Organizers

---

### Department of Experimental Physics

Faculty of Mathematics, Physics and Informatics

Comenius University in Bratislava

Mlynská dolina F2

842 48 Bratislava, Slovakia

URL: <http://www.fmph.uniba.sk/>

Tel.: +421 2 602 95 686

Fax: +421 2 654 29 980



### Society for plasma research and applications

Faculty of Mathematics, Physics and Informatics

Comenius University Bratislava

Mlynská dolina F2

842 48 Bratislava, Slovakia

E-mail: [spvap@neon.dpp.fmph.uniba.sk](mailto:spvap@neon.dpp.fmph.uniba.sk)

Tel.: +421 2 602 95 686



## Local Organizing Committee

---

Štefan Matejčík (chair)

František Krčma

Peter Papp

Juraj Országh

Ladislav Moravský

Veronika Medvecká

<b>P-17</b>	Kateřina Šindelková	CHARACTERIZATION OF PLASMA ACTIVATED WATER FOR BIO-APPLICATIONS	156
<b>P-18</b>	Věra Mazánková	PLASMA POLYMERIZATION OF ANTIBACTERIAL THIN FILMS FROM PROPANE-BUTANE MIXTURE IN ATMOSPHERIC PRESSURE DISCHARGE	159
<b>P-19</b>	Zuzana Měšťánková	USE OF DIRECT APPLICATION OF PLASMA FOR THERAPEUTIC PURPOSES	163
<b>P-20</b>	Sandra Ďurčányová	PREPARATION OF PROTECTIVE HYDROPHOBIC LAYERS ON ALUMINUM USING PLASMA POLYMERIZATION AT ATMOSPHERIC PRESSURE	166
<b>P-21</b>	Aranka Derzsi	PROPERTIES OF LOW-PRESSURE RF DISCHARGES SUITABLE FOR TREATMENT OF ABSORBANTS	169
<b>P-22</b>	Martin Kuřka	MODIFICATION OF MICROPOROUS POLYPROPYLENE MEMBRANES BY PLASMA-INITIATED GRAFTING OF ACRYLIC ACID	170
<b>P-23</b>	František Krčma	SURFACE CLEANING OF ARCHEOLOGIC LEAD BY LOW PRESSURE PLASMA	175
<b>P-24</b>	Joanna Pawłat	COLD ATMOSPHERIC PLASMA FOR PRESERVATION OF BREAD	176
<b>P-25</b>	Jana Šimečková	INFLUENCE OF PAW APPLICATION ON WATER AGGREGATE STABILITY OF SOIL – CONTAINER EXPERIMENT	178
<b>P-26</b>	Martin Muller	PLASMA MODIFICATION OF METAL OXIDE NANOWIRES FOR Zn-AIR BATTERIES	182
<b>P-27</b>	Masoomah Mahmoodi-Darian	COMPARISON OF CONTINUOUS AND PULSED LOW POWER DC SPUTTERED Ti THIN FILMS	183
<b>P-28</b>	Nevena Puac	MASS SPECTROMETRY OF LARGE ASYMETRICAL CCP OXYGEN DISCHARGE	184
<b>P-29</b>	Ladislav Moravský	ATMOSPHERIC PRESSURE CHEMICAL IONIZATION STUDY OF SULPHUR-CONTAINING COMPOUNDS BY ION MOBILITY SPECTROMETRY AND MASS-SPECTROMETRY	186
<b>P-30</b>	Emanuel Matáš	DETECTION OF NO <sub>2</sub> GENERATED BY APPJ IN ARGON USING IMS	189
<b>P-31</b>	Bartosz Michalczuk	LOW ENERGY ELECTRON ATTACHEMNT BY FLUOROSILANES	194
<b>P-32</b>	Marija Radmilović-Radjenović	SIMULATION STUDIES OF SURGICAL ELECTRODE DESIGN TO PREVENT SPARKING ENHANCED BURNS	196

# PROPERTIES OF LOW-PRESSURE RF DISCHARGES SUITABLE FOR TREATMENT OF ABSORBANTS

A. Derzsi<sup>1</sup>, B. Horváth<sup>1</sup>, K. Kutasi<sup>1</sup>, K. Spasic<sup>2</sup>, M. Puač<sup>2</sup>, N. Puač<sup>2</sup>  
and N. Škoro<sup>2</sup>

<sup>1</sup>*Wigner Research Centre for Physics, Budapest, Hungary*

<sup>2</sup>*Institute of Physics, Belgrade, Serbia*

E-mail: [derzsi.aranka@wigner.hu](mailto:derzsi.aranka@wigner.hu)

Particle-in-Cell/Monte Carlo Collisions simulations are performed to provide a detailed characterization of low-pressure capacitively coupled radiofrequency gas discharge plasmas suitable for treatment of absorbants. Based on the simulations, discharge characteristics such as particle densities, and particle flux and energy distributions at the surfaces relevant for treatment of Zeolite are determined.

Zeolite has long been recognized as a mineral with excellent absorptive properties. This material, made up of arrays of aluminum, silica, and oxygen, has been recently introduced as a novel microporous material suitable for application in water decontamination. Since it is a porous material, the absorption process results in not only capturing particles between grains, but also insertion of the particles into its pores. Due to its high effective surface area, desorption is typically performed using suitable solutions. However, this way of Zeolite regeneration proved to be ineffective for some adsorbed pharmaceuticals. Experimental investigations performed so far showed that in this case regeneration can be efficiently performed by plasma treatment which also represents an efficient and ecologically responsible procedure. These procedures are based on the interaction of adsorbed particles and chemically active species created in the plasma. However, the desirable effects can be achieved only for a narrow range of treatment conditions. For the reliable, knowledge-based optimization of the applications, a detailed characterization of the plasma reactor used for surface treatment is required, including information on the plasma properties and surface processes. In this work, one-dimensional in space and three dimensional in velocity space (1d3v) Particle-in-Cell/Monte Carlo Collisions (PIC/MCC) simulations are performed in low-pressure capacitively coupled plasmas in Argon, under conditions corresponding to the experiments for treatment of Zeolite (4.5 cm electrode gap, driving frequency of 13.56 MHz, pressures < 600 mTorr, voltage amplitudes < 450 V). For these conditions, the voltage-current characteristics, as well as the power and emission spectrum for the discharge are available from the experiments. In the simulations, electrons, Ar<sup>+</sup> ions, and fast Ar atoms are traced. As surface processes, secondary electron emission due to heavy particles and elastic reflection of electrons are considered. The PIC/MCC simulations provide information on many plasma parameters and distributions of interest, such as densities of the traced particles and their flux and energy distribution at the surfaces, the spatiotemporal distribution of the electric field, the power absorption and energy of particles, as well as the ionization and excitation dynamics in the discharge.

**Acknowledgement:** This work was supported by the grant 2019-2.1.11-TÉT-2020-00162 “Characterization of radiofrequency gas discharges applied for surface treatment” of the Hungarian National Research, Development and Innovation Office and bilateral project Hungary-Serbia (2021-2023).

**9<sup>th</sup> Central European Symposium on  
Plasma Chemistry (CESPC-9)**  
joint with  
**COST Action CA19110 Plasma Applications for  
Smart and Sustainable Agriculture (PIAgri)**

---

Vysoké Tatry, Slovakia  
September 4–9, 2022

# **BOOK OF ABSTRACTS**

including general information and program



Edited by Karol HENSEL, Richard CIMERMAN, Aleksandra LAVRIKOVA,  
Mário JANDA, and Zdenko MACHALA

## Friday, September 9

8 <sup>30</sup>	<b>Intro to WG3 Plasma for Plants - Joanna Pawlat / Vida Mildažienė</b>	
8 <sup>45</sup>	<b>I-17</b>	<b>Sara Di Lonardo</b> <span style="float: right;"><u>Chair: V. Mildažienė</u></span> Cold plasma effects on plants: challenges and future in its use
9 <sup>15</sup>	<b>O-39</b>	<b>František Krčma</b> Cold plasmas application on onion bulbs
9 <sup>30</sup>	<b>O-40</b>	<b>Rasa Žūkienė</b> The evaluation of cold plasma effect on morphometric and biochemical parameters in ...
9 <sup>45</sup>	<b>O-41</b>	<b>Karol Hensel</b> Effect of plasma activated water, its chemically equivalent solutions and arsenic stress on ...
10 <sup>00</sup>	<b>O-42</b>	<b>Sabrinne Bouselmi</b> Effects of plasma treated water on seed germination and growth of blue lupine ( <i>Lupinus angustifolius</i> L. ) ...
10 <sup>15</sup>	Coffee break ☕	
10 <sup>35</sup>	<b>I-18</b>	<b>Milica Milutinović</b> <span style="float: right;"><u>Chair: J. Pawlat</u></span> Molecular response to PAW in model plant species
11 <sup>05</sup>	<b>O-43</b>	<b>Kazunori Koga</b> Development of experimental system for plasma irradiation effects on plants using marchantia polymorpha
11 <sup>20</sup>	<b>O-44</b>	<b>Liutauras Marcinauskas</b> Application of plasma and pulsed electric field for the treatment of microalgae
11 <sup>35</sup>	<b>O-45</b>	<b>Eugen Hnatiuc</b> Preparing for large scale use of cold plasma discharges: Pitfalls and challenges
11 <sup>50</sup>	Closing ceremony	
12 <sup>05</sup>	Lunch	

# ABSTRACTS

## PIAgri Workshop



## Invited Lectures

ID	Presenter – Presentation Title	Page
I-11	<b>Tomislava Vukušić-Pavičić</b> - The effects of direct plasma treatment and indirect (PAW) treatment on physicochemical and functional properties of food	89
I-12	<b>Fernando Alba-Elías</b> - Applications of atmospheric plasma in the food and medical industry	90
I-13	<b>Chedly Tizaoui</b> - Non-thermal plasma and advanced oxidation processes for micropollutants removal in water	91
I-14	<b>Rune Ingels</b> - Do we need the Haber Bosch?	92
I-15	<b>Božena Šerá</b> - Seed treatment with non-thermal plasma from the point of view of seed germination and early seedling growth	93
I-16	<b>Pankaj Attri</b> - Impact of plasma/electric field treated seeds on germination, morphology, gene expression, and biochemical responses	94
I-17	<b>Sara di Lonardo</b> - Cold plasma effects on plants: challenges and future in its use	95
I-18	<b>Milica Milutinović</b> - Molecular response to PAW in model plant species	96

## Oral Presentations

ID	Presenter – Presentation Title	Page
O-27	<b>Filippo Capelli</b> - Plasma decontamination of food packaging material	97
O-28	<b>Klaas De Baerdemaeker</b> - Cold plasma for bacterial decontamination: Impact of food matrix composition and relative humidity of the input gas	98
O-29	<b>Ludmila Čechová</b> - Effect of plasma and plasma activated water on growth media used in hydroponics	99
O-30	<b>Vladimír Scholtz</b> - Comparison of the effect of plasma activated water and artificially prepared activated water on wheat grain properties	100
O-31	<b>Jan Čech</b> - CaviPlasma: A plasma source capable of application-scale generation of plasma treated water for agriculture, aquaculture, and medicine	101
O-32	<b>Elise Vervloessem</b> - Experimental and computational study of nitrogen fixation mechanisms from (humid) air and nitrogen in pulsed plasma	102
O-33	<b>Kinga Kutasi</b> - Role of metals on fixation of NO <sub>2</sub> <sup>-</sup> in plasma-activated liquids	103
O-34	<b>Arijana Filipić</b> - Inactivation of viruses in irrigation waters	104
O-35	<b>Raluca Alina Bisag</b> - On the use of plasma activated water (PAW) for agricultural purposes	105
O-36	<b>Jonas August</b> - From anhydrobiosis to germination: Effect of an air atmospheric cold plasma treatment on Arabidopsis seed dormancy	106
O-37	<b>Plamena Marinova</b> - Cold plasma treatment effect on the germination and seedlings growth of durum wheat genotypes	107

## Molecular response to PAW in model plant species

**M. Milutinović<sup>1</sup>, O. Jovanović<sup>2</sup>, N. Devrnja<sup>1</sup>, M. Todorović<sup>1</sup>, S. Živković<sup>1</sup>, J. Savić<sup>1</sup>,  
M. Skorić<sup>1</sup>, N. Puač<sup>2</sup>, N. Škoro<sup>2</sup>**

<sup>1</sup>Institute for Biological Research "Siniša Stanković" – National Institute of Republic of Serbia,  
University of Belgrade, Belgrade, Serbia

<sup>2</sup>Institute of Physics, National Institute of Republic of Serbia, University of Belgrade, Belgrade, Serbia  
e-mail: milica.milutinovic@ibiss.bg.ac.rs

Non-thermal temperature plasmas (NTPs) have rich chemistry of Reactive Oxygen and Nitrogen Species (RONS) that are formed in gas phase and, in case of water treatment, in gas/liquid interface in liquid [1]. NTPs can be applied in direct treatments of plant samples or indirectly when treated water, called Plasma Activated Water (PAW), is used in treatments. In both cases RONS (short or long-living) are responsible for triggering various mechanisms and effects in plant cells. RONS have a dual role and a dose-dependent effect, they can regulate the normal physiological activities of plants as signaling molecules at the range of physiological concentration, and can trigger damage to lipids, proteins and DNA at too high or too low concentration. Plants integrate RONS with genetic, epigenetic and external signals to regulate developmental processes. RONS signaling is highly integrated with hormonal signaling networks, thereby allowing plants to adjust to environmental cues.

All organisms have adaptive responses to oxidative stress, with antioxidant enzymes (i.e. catalase, peroxidase, superoxide dismutase) being induced by changes in the levels of H<sub>2</sub>O<sub>2</sub> or O<sub>2</sub><sup>•-</sup>, leading to the activation or silencing of genes encoding defensive enzymes and transcription factors [2]. Although various observations have led to the suggestion that cells have the means to sense RONS and to induce specific responses, the underlying mechanisms are still not fully understood. In addition, plants also have non-enzymatic systems known to remove RONS, which are important players in plant processes that use RONS-dependent signaling mechanisms [3]. In this work, we have shown, by using molecular approaches, how PAW treatment affect expression of genes coding for specialized metabolites and hormones, thus regulating development and stress responses in the model plant system *Arabidopsis thaliana*.

*This work was supported by Ministry of Education, Science and Technological Developments of the Republic of Serbia, contact number grants 451-03-68/2022-14/200007 and 451-03-68/2022-14/200024. This publication is based upon work from COST Action CA19110 - PLAGri, supported by COST (European Cooperation in Science and Technology-www.cost.eu).*

### References

- [1] N. Puač, M. Gherardi, M. Shiratani, *Plasma Process Polym.* **15**, 1700174, (2017).
- [2] J. G. Scandalios, *Genome Biol.* **3**, reviews1019.1 (2002).
- [3] T. S. Gechev, F. Van Breusegem, J. M. Stone, I. Denev, C. Laloi, *Bioessays* **28**, 1091–1101 (2006).

**9<sup>th</sup> Central European Symposium on  
Plasma Chemistry (CESPC-9)**  
joint with  
**COST Action CA19110 Plasma Applications for  
Smart and Sustainable Agriculture (PIAgri)**

---

Vysoké Tatry, Slovakia  
September 4–9, 2022

# **BOOK OF ABSTRACTS**

including general information and program



Edited by Karol HENSEL, Richard CIMERMAN, Aleksandra LAVRIKOVA,  
Mário JANDA, and Zdenko MACHALA



P-6	<b>Jiangu Feng</b> - Adhesion improvement of large area flexible PTFE foils by atmospheric pressure plasma	63
P-7	<b>Oleksandr Galmiz</b> - Applications of surface dielectric barrier discharge generated from liquid electrode	64
P-8	<b>Jan Hrudka</b> - Image analysis evaluation of the non-thermal plasma inactivation of dermatophytes	65
P-9	<b>Martina Ilčíková</b> - Plasma-assisted processing of PET waste flakes for use in wood-based composites	66
P-10	<b>Ali Jamaati Kenari</b> - Comparative study of the different cold atmospheric-pressure plasma sources' effects on the surface modification of thermally sensitive BOPP film	67
P-11	<b>Mário Janda</b> - The role of HNO <sub>2</sub> in the generation of plasma activated water	68
P-12	<b>Barbora Konečná</b> - <i>In vivo</i> effect of cold plasma activated water on wound healing	69
P-13	<b>Dušan Kováčik</b> - In-line plasma pre- and post-treatment as parts of technology for manufacturing of nanofiber-based filters with the improved performance properties	70
P-14	<b>Niksa Krstulović</b> - Photocatalysis of laser synthesized colloidal Ag-doped ZnO nanoparticles	71
P-15	<b>Darina Kužmová</b> - The effects of plasma-activated phosphate buffered saline on monolayers and spheroids of cancer cells	72
P-16	<b>Michal Kwiatkowski</b> - Plasma treatment for conditioning of non-pasteurized beverages	73
P-17	<b>Aleksandra Lavrikova</b> - Eradication of bacterial biofilms with atmospheric air pulsed streamer corona discharge	74
P-18	<b>Věra Mazánková</b> - Plasma polymerized oxazoline based thin films for biomedical applications	75
P-19	<b>Zuzana Okruhlicová</b> - Non-thermal plasma and ozone disinfection of FFP2-type respirators	76
P-20	<b>Colin O'Modhrain</b> - Interpreting improved performance of a rotating gliding arc plasma for N <sub>2</sub> -fixation: Insights from a self-consistent, fully-coupled model	77
P-21	<b>Pankaj Pareek</b> - The impact of humidity and circuit parameters in the generation of NO <sub>2</sub> and HNO <sub>2</sub> by transient spark discharge	78
P-22	<b>Mária Petřková</b> - The effect of plasma on germination, oxidative stress response and DNA damage in barley	79
P-23	<b>Sára Pišteková</b> - Genotoxic effects of non-thermal plasma generated by various sources on plasmid DNA	80
P-24	<b>Nevena Puač</b> - Characterization of 1- and 3-pin atmospheric pressure plasma jet used for decontamination of water samples	81
P-25	<b>Rafaela Radičić</b> - Incorporation of ZnO nanoparticles into PVC and HDPE polymers using atmospheric pressure plasma jet	82
P-26	<b>Tomislava Vukušić Pavičić</b> - Polyphenol degradation by high voltage gas discharge plasma	83
P-27	<b>Dawid Zarzeczny</b> - Plasma treatment for conditioning of juice	84
P-28	<b>František Zažimal</b> - Photocatalytic water treatment by nanocomposites processed using low temperature plasma	85

## Characterization of 1- and 3-pin atmospheric pressure plasma jet used for decontamination of water samples

**N. Puač<sup>1</sup>, A. Kumar<sup>1,2</sup>, W. Gernjak<sup>3,4</sup>, N. Škoro<sup>3</sup>**

<sup>1</sup>Institute of Physics, University of Belgrade, Belgrade, Serbia

<sup>2</sup>Universitat de Girona, Girona, Spain

<sup>3</sup>Catalan Institute for Water Research (ICRA), Girona, Spain

<sup>4</sup>Catalan Institution for Research and Advanced Studies (ICREA), Barcelona, Spain

e-mail: nevena@ipb.ac.rs

With growing population more and more issues arise from human influence on the environment and, therefore, on the food chain and the ability to produce enough food. The amounts of organic micropollutants (OMPs) that are released into the water bodies are huge and, in order to deal with this issue, we need more alternative green technologies that can replace (or aid) standard oxidative processes (AOPs). One of such technologies that can be used for non-biodegradable OMPs is non-thermal plasma (NTP) that operates at atmospheric pressure [1]. The NTPs created in gas phase in contact with liquid or in liquid phase are rich source of oxidative species responsible for OMP destruction [2, 3].

Here we will present pin-type atmospheric pressure plasma jet (APPJ) that uses argon as a working gas. We have investigated two different configurations: 1-pin APPJ and 3-pin APPJ. We have performed electrical characterization, temperature measurements, optical emission spectroscopy and ICCD imaging for both experimental setups. The flow of argon was kept constant in all experiments at 1 slm (1-pin APPJ) and 2 slm (3-pin APPJ). As a power supply we have used commercial sine wave resonant type power supply. In our case the resonant frequency for 1-pin APPJ was 330 kHz and for 3-pin it was 350 kHz. The discharge was created in a gas phase and was in contact with water samples in all experiments. The water samples were contaminated either with Acid Blue 25 (AB25) dye, diclofenac (DCF) or 4-chlorobenzoic acid (pCBA). In case of 3-pin APPJ we have performed treatments without mixing (water sample was in crystallizing dish) and with mixing (water sample was circulated by a pump during the plasma treatment). As expected, the removal efficacy increased with decrease in the initial concentration of the contaminants in all cases. When comparing the destruction of the DCF and pCBA in flow mode we saw that plasma removed DCF better. This can be related to the chemical structure of both compounds, whereby pCBA can only be converted by strong oxidants such as the hydroxyl radical, whereas DCF is susceptible to reaction with weaker oxidants, too.

*This work was carried out under NOWELTIES project funded by the European Union's Horizon 2020 research and innovation programme under the Marie Skłodowska-Curie grant agreement No. 812880. N.S. and N.P. are funded by Ministry of Education, Science and Technological Development, grant number 451-03-68/2022-14/200024.*

### References

- [1] A. Kumar, N. Škoro, W. Gernjak, N. Puač, *Eur. Phys. J. D* **75**, 283 (2021)
- [2] V.I. Parvulescu, M. Magureanu, P. Lukes, *Plasma chemistry and catalysis in gases and liquids*, 1st ed., Wiley, New York (2012).
- [3] P. Bruggeman, C. Leys, *J. Phys. D:Appl. Phys.* **42**, 053001 (2009).

**9<sup>th</sup> Central European Symposium on  
Plasma Chemistry (CESPC-9)**

joint with

**COST Action CA19110 Plasma Applications for  
Smart and Sustainable Agriculture (PIAgri)**

---

Vysoké Tatry, Slovakia  
September 4–9, 2022

# **BOOK OF ABSTRACTS**

including general information and program



Edited by Karol HENSEL, Richard CIMERMAN, Aleksandra LAVRIKOVA,  
Mário JANDA, and Zdenko MACHALA

O-38	<b>Vida Mildažienė</b> - The persistence of effects of seed treatment with cold plasma, vacuum and electromagnetic field: 7-years of observations on Norway spruce	108
O-39	<b>František Krčma</b> - Cold plasmas application on onion bulbs	109
O-40	<b>Rasa Žūkienė</b> - The evaluation of cold plasma effect on morphometric and biochemical parameters in <i>Stevia rebaudiana</i> by principal component analysis	110
O-41	<b>Karol Hensel</b> - Effect of plasma activated water, its chemically equivalent solutions and arsenic stress on growth, development of selected seed and plants	111
O-42	<b>Sabrinne Bousselmi</b> - Effects of plasma treated water on seed germination and growth of blue lupine ( <i>Lupinus angustifolius</i> L.) plants under abiotic stress	112
O-43	<b>Kazunori Koga</b> - Development of experimental system for plasma irradiation effects on plants using <i>Marchantia polymorpha</i>	113
O-44	<b>Liutauras Marcinauskas</b> - Application of plasma and pulsed electric field for the treatment of microalgae	114
O-45	<b>Eugen Hnatiuc</b> - Preparing for large scale use of cold plasma discharges: Pitfalls and challenges	115

## Poster Presentations

ID	Presenter – Presentation Title	Page
P-29	<b>Laima Degutyte-Fomins</b> - Influence of radish ( <i>Raphanus Sativus</i> L.) seed coat color on plant secondary metabolites and response to cold plasma treatment	116
P-30	<b>Mostafa E. Hassan</b> - Analysis of the reactive species in the gas-plasma–water interactions	117
P-31	<b>Anatolii Ivankov</b> - Changes in hemp growth and content of cannabinoids after seeds treatment with cold plasma, vacuum, and electromagnetic field	118
P-32	<b>Olivera Jovanović</b> - Investigation of an atmospheric pressure pin-type plasma jet for water treatment - optical diagnostics and temperature measurements	119
P-33	<b>Saeed Kooshki</b> - High flow rate plasma activated water generation using dielectric barrier discharge reactor	120
P-34	<b>Zdenka Kozáková</b> - Characterization of plasma activated water prepared in different plasma systems	121
P-35	<b>Michal Kwiatkowski</b> - GAD impact on selected foods	122
P-36	<b>Danyang Liu</b> - Examining the impact of non-thermal plasma on lipid model systems	123
P-37	<b>Petr Lukeš</b> - PAW properties for agriculture: What we want?	124
P-38	<b>Plamena Marinova</b> - Microwave plasma torch treatment of in vitro plum ( <i>Prunus domestica</i> L.) plants	125
P-39	<b>Ester Marotta</b> - Comparative evaluation of different plasma reactors for PFAS degradation	126
P-40	<b>Márcia D. Oliveira</b> - Atmospheric-pressure plasma for seed germination of lentils and mung bean and its effect on nutritional value	127
P-41	<b>Márcia D. Oliveira</b> - Control of <i>Listeria innocua</i> biofilms on food industrial surfaces with plasma-based technologies	128
P-42	<b>Zuzana Okruhlicová</b> - Direct and indirect effects of cold atmospheric plasma on green moulds	129
P-43	<b>Lokeswari Ramireddy</b> - AgriPlasma – Non-thermal air plasma treatment of multispecies swards seeds for reduction of greenhouse gas emissions	130

## Investigation of an atmospheric pressure pin-type plasma jet for water treatment - optical diagnostics and temperature measurements

**O. Jovanović<sup>1</sup>, N. Puač<sup>1</sup>, A. Petrović<sup>1</sup>, M. Gromov<sup>2</sup>, A. Nikiforov<sup>2</sup>, N. Škoro<sup>1</sup>**

<sup>1</sup>Institute of Physics, University of Belgrade, Belgrade, Serbia

<sup>2</sup>Ghent University, Ghent, Belgium

e-mail: olivera@ipb.ac.rs

In the increasingly important field of plasma agriculture, atmospheric pressure plasmas have proved their excellent potential for the elimination or reduction of organic contaminants and sterilization of microorganisms [1,2]. The exposure of aqueous solutions to plasma induces many reactions occurred in the gaseous phase and introduces reactive species in aqueous phases. One of the most commonly detected chemical species in gas plasma is OH radical because it plays a key role in the reactions of degradation of organic pollutants from water [3]. Another important factor that should be controlled during the plasma wastewater treatment to avoid the evaporation of harmful substances is the gas temperature. From the point of view of plasma physics, it is essential for future applications that the plasma processes and the effects of treatment are correlated, which can only be done by accurate and thorough diagnostics of the plasma sources.

Atmospheric pressure plasma jet (APPJ) in pin-electrode configuration operating in contact with liquid sample has been investigated by two different measurement techniques for gas temperature measurement. Firstly, the gas temperature above the liquid was determined by using the optical emission spectroscopy (OES) method for measurement based on partially rotationally resolved emission from hydroxyl (OH) radical. Another goal was to employ an active method - Rayleigh scattering laser spectroscopy which allows spatially resolved gas temperature measurements and to compare obtained results with OES measurements. Since the plasma jet generates intense streamer discharge, such a detailed analysis of the emission spectrum of plasma radiation and precise measurement of gas temperature was necessary for the potential application in biotechnology and wastewater treatment. Finally, as earlier studies have shown that OH radicals formed in the plasma play an important role in the degradation of pollutants dissolved in water, the absolute values of OH radicals were recorded by laser-induced fluorescence (LIF) technique.

The recorded spectra showed intense emission of OH radicals at wavelengths around 306 nm for discharge generated in pure Ar and an admixture of Ar and synthetic air. Preliminary results showed that the temperature in the plasma core reached values of up to 300°C. Also, it was obtained that the intensity of the LIF signal increases with the increase in the power deposited in the plasma, whether the discharge was in contact with distilled water or tap water.

*This work was supported by a STSM Grant from the COST Action CA19110 PLAGri, supported by the COST Association (European Cooperation in Science and Technology) and the Ministry of Education, Science and Technological Development, grant number 451-03-68/2022- 14/200024.*

### References

- [1] D. Graves, L. Bakken, R. Ingels, *Plasma Chem. Plasma Process.* **39**, 1-19 (2019).
- [2] N. Skoro, N. Puač, S. Zivkovic, D. Krstic-Milosevic, U. Cvelbar, G. Malovic, Z. Lj. Petrovic, *Eur. Phys. J. D* **72**, 1-8 (2018).
- [3] M. Magureanu, C. Bradu, V. I. Parvulescu, *J. Phys. D: Appl. Phys.* **51**, 313002 (2018).

**9<sup>th</sup> Central European Symposium on  
Plasma Chemistry (CESPC-9)**  
joint with  
**COST Action CA19110 Plasma Applications for  
Smart and Sustainable Agriculture (PIAgri)**

---

Vysoké Tatry, Slovakia  
September 4–9, 2022

# **BOOK OF ABSTRACTS**

including general information and program



Edited by Karol HENSEL, Richard CIMERMAN, Aleksandra LAVRIKOVA,  
Mário JANDA, and Zdenko MACHALA

P-44	<b>Nina Recek</b> - Growth of plasma-treated wheat seeds under realistic conditions	131
P-45	<b>Jana Šimečková</b> - Changes of soil properties after plasma activated water application	132
P-46	<b>Pia Starič</b> - Plasma treatment decreases the concentration of elements in pericarp of buckwheat grains	133
P-47	<b>Barbora Tarabová</b> - Bactericidal properties of aminoacids modified by plasma treatment in physiological buffered saline solutions	134
P-48	<b>Ionut Topala</b> - Air plasma exposure of <i>Tagetes erecta</i> seeds: gas phase FTIR monitoring and effects on germination dynamics	135
P-49	<b>Dawid Zarzeczny</b> - GAD impact on selected properties of bread	136
P-50	<b>Suzana Živković</b> - Long term effects in dwarf bearded iris ( <i>Iris reichenbachii</i> Heuff.) calli metabolism induced by plasma treatment	137

---

## Long term effects in dwarf bearded iris (*Iris reichenbachii* Heuff.) calli metabolism induced by plasma treatment

**S. Živković<sup>1</sup>, S. Jevremović<sup>1</sup>, U. Gašić<sup>1</sup>, M. Milutinović<sup>1</sup>, Z. Lj. Petrović<sup>2</sup>, N. Škoro<sup>3</sup>, N. Puač<sup>3</sup>**

<sup>1</sup>Institute for Biological Research "Siniša Stanković"-National Institute of RS,  
University of Belgrade, Belgrade, Serbia

<sup>2</sup>Serbian Academy of Sciences and Arts, Belgrade, Serbia

<sup>3</sup>Institute of Physics-National Institute of RS, University of Belgrade, Belgrade, Serbia  
e-mail: suzy@ibiss.bg.ac.rs

The Plasma Agriculture is a new field of plasma applications where non-thermal (cold) plasmas (NTPs) operating at atmospheric pressure are used as a tool in biotechnology for genetic manipulation of plants, for micropropagation, for studies of plant metabolism and cellular development or a commercial production of natural products that cannot be chemically synthesized. NTPs have rich chemistry of Reactive Oxygen and Nitrogen Species (RONS) that are responsible for triggering various mechanisms and effects in plant cells, such as the induction of somatic embryogenesis, higher and faster seed germination, better water uptake or have an anti-bacterial and anti-viral effects, etc. [1-3]. In the current study plant undifferentiated compact tissue (calli) of Balkan endemic dwarf bearded iris (*Iris reichenbachii* Heuff.) was treated using a RF plasma needle device operating with He as a working gas. The flow of He was kept constant at 1 slm and the power deposited to the plasma was below 2 W. The plasma needle was positioned 3 mm above the callus surface enabling direct contact between the active plasma volume and the surface of the sample. We induced significant morphological alterations in structure of non-embryonic calli that could be attributed to the enhanced cell division of the plant cells at the surface of the calli that was in contact with plasma. The differentiation of the calli cells was stimulated by reactive species created in gas phase of NTP. The morphological changes were then followed by the significant long term alteration in specialized metabolite content in derived calli types. Our results implicate that direct plasma treatment could serve as a significant elicitor of the production of specific metabolites in dwarf bearded iris calli.

*Supported by Ministry of Education, Science and Technological Developments of the Republic of Serbia, contact number grants 451-03-68/2022-14/200007 and 451-03-68/2022-14/200024. This publication is based upon work from COST Action CA19110 - PlAgri, supported by COST (European Cooperation in Science and Technology-www.cost.eu).*

### References

- [1] M. Domonkos, P. Tichá, J. Trejbal, P. Demo, *Appl. Sci.* **11**, 4809 (2021).
- [2] A. Waskow, A. Howling, I. Furno, *Front. Phys.* **8** 174 (2021).
- [3] N. Puač, M. Gherardi, M. Shiratani, *Plasma Process Polym.* **15**, 1700174 (2017).





# SAPP XXIV

24<sup>th</sup> Symposium on Application of Plasma Processes  
and  
13<sup>th</sup> EU-Japan Joint Symposium on Plasma  
Processing

Book of Contributed Papers

Štrbské Pleso, Slovakia  
27 Jan - 1 Feb, 2023

Edited by J. Országh, B. Stachová, D. Mészáros, P. Papp, Š. Matejčík



Book of Contributed Papers: 24<sup>th</sup> Symposium on Application of Plasma Processes and 13<sup>th</sup> EU-Japan Joint Symposium on Plasma Processing, Štrbské Pleso, Slovakia, 27 January – 1 February 2023.

Symposium organised by Department of Experimental Physics, Faculty of Mathematics, Physics and Informatics, Comenius University in Bratislava and Society for Plasma Research and Applications in hotel SOREA TRIGAN\*\*\*.

Editors: J. Országh, B. Stachová, D. Mészáros, P. Papp, Š. Matejčík

Publisher: Society for Plasma Research and Applications, Bratislava, Slovakia

Issued: January 2023, Bratislava, first issue

ISBN: 978-80-972179-3-8

URL: <https://neon.dpp.fmph.uniba.sk/sapp/>

## Local Organizers

---

### Department of Experimental Physics

Faculty of Mathematics, Physics and Informatics

Comenius University in Bratislava

Mlynská dolina F2

842 48 Bratislava, Slovakia

URL: <http://www.fmph.uniba.sk/>

Tel.: +421 2 602 95 686

Fax: +421 2 654 29 980



### Society for plasma research and applications

Faculty of Mathematics, Physics and Informatics

Comenius University Bratislava

Mlynská dolina F2

842 48 Bratislava, Slovakia

E-mail: [spvap@neon.dpp.fmph.uniba.sk](mailto:spvap@neon.dpp.fmph.uniba.sk)

Tel.: +421 2 602 95 686



## Local Organizing Committee

---

Štefan Matejčík (chair)

František Krčma

Peter Papp

Juraj Országh

Ladislav Moravský

Veronika Medvecká

# MASS SPECTROMETRY OF LARGE ASYMETRICAL CCP OXYGEN DISCHARGE

Nevena Puač<sup>1</sup>, Kosta Spasić<sup>1</sup>, Nikola Škoro<sup>1</sup>, Gordana Malović<sup>1</sup>  
and Zoran Lj. Petrović<sup>2</sup>

<sup>1</sup>*Institute of Physics, University of Belgrade, Pregrevica 118, 11080 Belgrade, Serbia*

<sup>2</sup>*Serbian Academy of Sciences and Arts, Knez Mihailova 35, 11000 Belgrade, Serbia*

E-mail: nevena@ipb.ac.rs

We present the results of mass spectrometry of large asymmetrical CCP discharge. The discharge operated at 13.56 MHz with oxygen as working gas at the pressures of 300 mTorr, 450 mTorr and 600 mTorr. Threshold Ionization Mass Spectrometry (TIMS) was used to detect excited and metastable oxygen molecules and oxygen atoms.

## 1. Introduction

Motivation for research of non-thermal low pressure plasmas stems from wide range of possible applications. Due to the possibility of fine tuning of the discharge conditions and ability of the reactive species from the discharge to modify and activate surfaces, low pressure plasmas are being exploited for a long time for applications in fabrication of microelectronic devices, in textile industry, sterilization of medical equipment, cleaning of archaeological samples, nitriding of metals etc. Lately this lists has expanded in the field of plasma agriculture for treatment of seed to increase germination, plant yield or to remove pathogens. In order to satisfy various demands in many different applications in which plasma is used various types of plasma reactors had to be developed.

It is already known that reactive oxygen species (ROS) play important role in metabolism of plants with most of them being also the signalling molecules. [1, 2]. Since ROS are easily created in oxygen containing discharges the effects of these plasmas on plants metabolism is increasingly being studied for discharges in both atmospheric and low pressures [2, 3]. In order to make the first steps towards identifying the mechanisms responsible for triggering of signalling pathways in the treated seeds it is important to determine chemistry produced in the plasma. Here we will present results of mass spectrometry of the oxygen low pressure discharge in the large asymmetric CCP chamber.

## 2. Experimental setup and results

A cylindrically shaped reactor chamber was made of stainless steel. The length of the chamber was 2.5 m with the diameter of 1.17 m. Axially placed aluminium rod served as a powered electrode while the chamber wall was used as a grounded electrode. The power supply unit operated at 13.56 MHz and it was equipped with Variomatch matching network for reducing reflected power. In all measurements the reflected power was kept below 1 % of the forwarded power. Vacuum was achieved by mechanical Pfeiffer Vacuum rotary vane pump. We have used mixture of 99% of O<sub>2</sub> with 1% of Argon added. Flow meters were used to control flow of each gas, in appropriate proportion, so that pressure could be set to selected values of 300, 450 and 600 mTorr. Mass energy HIDEN Analytical EQP analyser was used for mass and energy measurements of plasma species. It was introduced into the chamber side-on, perpendicular to the powered electrode, with its orifice positioned at fixed distance of 31.5 cm from powered electrode. For the detection of neutral species we have used RGA (residual gas analysis) mode. The mass spectra of neutral species was recorded for the range 1 amu to up to 50 amu. In order to determine the amount of oxygen excited and metastable species created in the discharge we have also performed Threshold Ionization Mass Spectrometry (TIMS). We have done this type of measurements for oxygen molecules and atoms with electron energy varied from 4 to 25 eV with resolution of 0.1 eV. In Figure 1(a). Distribution of O<sub>2</sub><sup>+</sup> as a function of the electron energy emitted from the ionising source of the mass spectrometer is shown. We can see that for lower powers there are no excited and metastable species detected by the mass spectrometer.

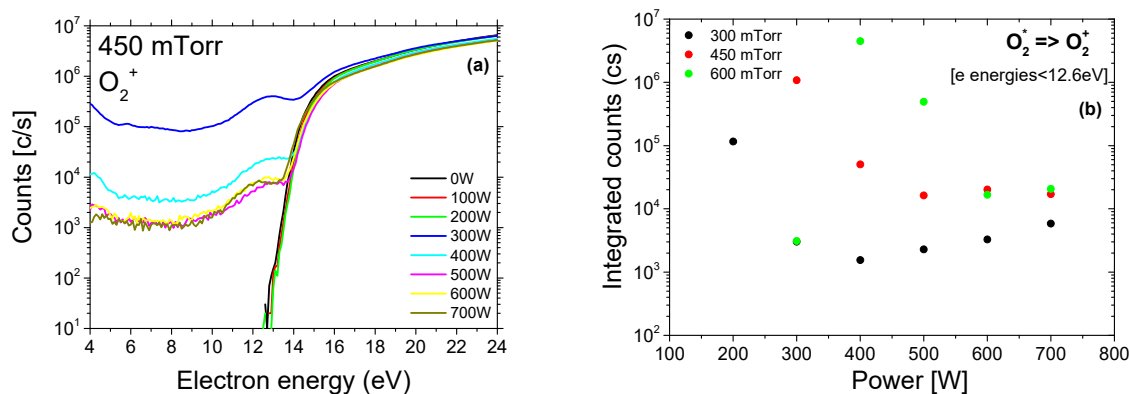


Figure 1. (a) Distribution of  $O_2^+$  molecule detected by mass spectrometer as a function of energies of electrons emitted by analyser's ionising source. (b) Number of excited and metastable  $O_2$  species detected by mass spectrometry as a function of power given by RF power supply.

In Figure 1(b) we present integrated counts obtained by ionizing excited and metastable oxygen molecule coming for the discharge. The integration of the mass spectrometer signals (shown in Figure 1(a)) was performed from 4 eV to 12.5 eV. We have used this range of energies in order to be below the ionization threshold for the neutral oxygen molecule. The maximum of detected excited and metastable oxygen molecules moves towards higher powers given by the RF power supply with the increase of the working pressure. This can be explained by the decrease in the mean free path of the species and the position of the mass spectrometer orifice. Also, with the increase of the power plasma expands towards the wall of the chamber.

### 3. Conclusion

We have presented the mass spectrometry results obtained in a large asymmetric CCP low pressure oxygen discharge. The mass spectrometry was used to detect reactive oxygen species with the emphasis on the excited and metastable species. We have used TIMS to determine the behaviour and abundance of metastable and excited oxygen molecule and oxygen atoms.

Acknowledgement: This work was supported by MSTDI Republic of Serbia grant number 451-03-68/2022-14/200024 and NOWELTIES project - EU H2020 MSCA ITN No. 812880.

### 4. References

- [1] Bailly C 2004 *Seed science research* **14** 93-107.
- [2] Graves D B 2012 *J. Phys. D: Appl. Phys.* **45** 263001 (42pp).
- [3] Puač N, Škoro N, Spasić K, Živković S, Milutinović M, Malović G and Petrović ZLj 2018 *Plasma Processes and Polymers* **15** 1700082.



# GEC 2022

75th Annual Gaseous Electronics Conference



# ICRP-11

11th International Conference on Reactive Plasmas

## PROGRAM BOOK

Date : October 3-7, 2022

Sendai International Center Conference Building

Joint Conference in Sendai, Japan

Supported by  
American Physical Society  
Co-sponsored by  
The Japan Society of Applied Physics



Photo courtesy of Miyagi Prefecture Tourism Promotion Division

## Day 5 *Friday, October 7th, 2022*

<i>Room</i>	<i>Tachibana</i>	<i>Hagi</i>	
8:00 AM - 9:30 AM	<b>DF1</b> Plasmas and Nanotechnology III [Wei-Hung Chiang] - 9:00 AM	<b>EF1</b> Plasma Medical & Agricultural Application I [Dingxin Liu]	
9:30 AM - 10:00 AM	--- Coffee Break ---		
10:00 AM - 12:00 PM	<b>DF2</b> Laser Diagnostics II [Holger Kersten]	<b>EF2</b> Plasma Medical & Agricultural Application II [Kenji Ishikawa] - 11:45 AM	
12:00 PM - 1:30 PM	--- Lunch ---		
1:30 PM - 3:30 PM	<b>DF3</b> Plasma Propulsion III [Andrei Smolyakov]	<b>EF3</b> Plasma Medical & Agricultural Application III [Nevena Puac] - 3:15 PM	
3:30 PM - 4:00 PM	--- Coffee Break ---		
4:00 PM - 5:30 PM	<b>DF4</b> Fundamental Processes - 5:15 PM	<b>EF4</b> Plasma Medical & Agricultural Application IV [Mounir Laroussi]	
5:30 PM - 6:00 PM	<b>DF5</b> <b>Closing Ceremony</b> • Toshiro Kaneko • Julian Schulze • Shahid Rauf		

## Bulletin of the American Physical Society

### 75th Annual Gaseous Electronics Conference

Monday–Friday, October 3–7, 2022; Sendai International Center, Sendai, Japan

The session times in this program are intended for Japan Standard Time zone in Tokyo, Japan (GMT+9)

#### **Session EF3: Plasma Medical & Agricultural Application III**

1:30 PM–3:15 PM, Friday, October 7, 2022

Sendai International Center Room: Hagi

Chair: Jun-Seok Oh, Osaka Metropolitan University

#### **Abstract: EF3.00001 : Role of atmospheric pressure plasma in triggering of cell mechanisms in plant cells\***

1:30 PM–2:00 PM

[Abstract](#) →

#### **Presenter:**

Nevena Puac

(Institute of Physics, National Institute of the Republic of Serbia, University of Belgrade, Pregrevica 118, 11080 Belgrade, Serbia)

#### **Authors:**

Nevena Puac

(Institute of Physics, National Institute of the Republic of Serbia, University of Belgrade, Pregrevica 118, 11080 Belgrade, Serbia)

Olivera Jovanović

(Institute of Physics, National Institute of the Republic of Serbia, University of Belgrade, Pregrevica 118, 11080 Belgrade, Serbia)

Anđelija Petrović

(Institute of Physics, National Institute of the Republic of Serbia, University of Belgrade, Pregrevica 118, 11080 Belgrade, Serbia)

Suzana Živković

(Institute for Biological Research "Siniša Stanković", National Institute of the Republic of Serbia, University of Belgrade, Bulevar despota Stefana 142, 11060 Belgrade, Serbia)

Milica Milutinović

(Institute for Biological Research "Siniša Stanković", National Institute of the Republic of Serbia, University of Belgrade, Bulevar despota Stefana 142, 11060 Belgrade, Serbia)

Gordana Malović

(Institute of Physics, National Institute of the Republic of Serbia, University of Belgrade, Pregrevica 118, 11080 Belgrade, Serbia)

Nikola Skoro

(Institute of Physics, National Institute of the Republic of Serbia, University of Belgrade, Pregrevica 118, 11080 Belgrade, Serbia)

The atmospheric pressure plasmas (APPs) are known to be rich in Reactive Oxygen and Nitrogen Species (RONS) and this rich chemistry is responsible for triggering of cell mechanisms in case of plant or human/animal cells. We can divide this influence in two groups: (1) RONS in gas phase; (2) RONS in liquid phase. Therefore, in order to better understand the reasons for triggered mechanisms and outcomes (better germination percentage and speed, breakout of dormancy, creation of embryos etc.) we need to know and be able to tailor the plasma chemistry both in gas and liquid phase. We have used several APPs for gas phase treatments of plant cells and also for production of Plasma Activated Water (PAW) in order to investigate the influence of liquid RONS chemistry on plant cells. Here we will present different APP sources that are used for production of PAW used for seed imbibition in germination process and direct treatment of meristematic plant cells. Dielectric Barrier Discharge type of APPJ was used for production of PAW, while the plasma needle type was used for direct treatment of meristematic plant cells. The main idea was to check if plasma treatments can be used as for breaking of dormancy and trigger mechanisms in cells even in a normally non-permissive conditions.

\*This work was supported by MESTD RS, grant numbers 451-03-9/2021-14/200007 and 451-03-68/2022-14/200024.

This site uses cookies. To find out more, read our [Privacy Policy](#).





CA20114

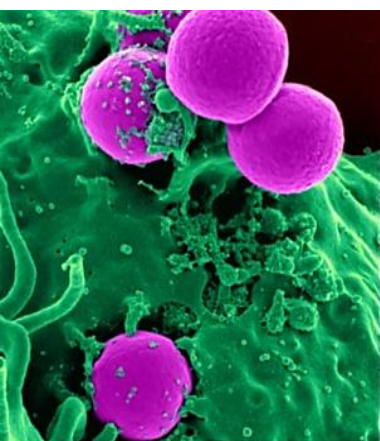
**PlasTHER**

THERAPEUTICAL APPLICATIONS OF COLD PLASMAS



CA19110

Plasma applications  
for smart and  
sustainable agriculture



## 2<sup>nd</sup> Training School

Cold plasmas to fight microorganisms, viruses & toxins for medical and agricultural applications

13<sup>th</sup> - 16<sup>th</sup> February, 2023. Bari (Italy)

**Book of abstracts**



CA20114



CA19110

## *Editors*

### **Eloisa Sardella**

CNR-Institute of Nanotechnology (CNR-NANOTEC)  
Bari, Italy

### **Nikola Škoro**

Institute of Physics Belgrade, University of Belgrade  
Belgrade, Serbia

### **Savino Cosmai**

CNR-Institute of Nanotechnology (CNR-NANOTEC)  
Bari, Italy

### **Pietro Favia**

Department of Chemistry, University of Bari Aldo Moro,  
Bari, Italy

### **Fabio Palumbo**

CNR-Institute of Nanotechnology (CNR-NANOTEC)  
Bari, Italy

### **Vincenza Armenise**

Department of Chemistry, University of Bari Aldo Moro,  
Bari, Italy

This article/publication is based upon work from COST Actions CA19110 PIAgri and CA20114 PlasTher, supported by COST (European Cooperation in Science and Technology).

COST (European Cooperation in Science and Technology) is a funding agency for research and innovation networks. Our Actions help connect research initiatives across Europe and enable scientists to grow their ideas by sharing them with their peers. This boosts their research, career and innovation.

[www.cost.eu](http://www.cost.eu)

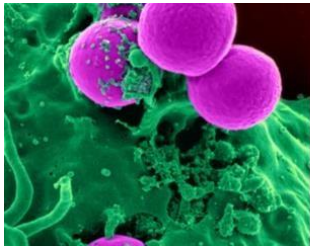
## Poster/Pitches Program

Monday 13th February  
Time 17:00 – 18:30

N.	Name	Institution	Country
P1	Neda Babucic	Institute of Physics Belgrade	Serbia
P2	Neusa Silva	Faculdade de Medicina Dentária da Universidade de Lisboa	Portugal
P3	Olivera Jovanović	Institute of Physics Belgrade	Serbia
P4	Darina Kužmová	Faculty of Mathematics, Physics and Informatics, Comenius University	Slovakia
P5	Mostafa Elsayed Hassan	Institut Pprime	France
P6	Valentina Puca	University G. d'Annunzio Chieti-Pescara	Italy
P7	Aleksandra Nurzyńska	Medical University of Lublin	Poland
P8	Anna Michalicha	Medical University of Lublin	Polska
P9	Pankaj Pareek	Comenius University Bratislava, Slovakia	Slovakia
P10	Domenico Aceto	CNR-ISTP; Instituto Superior Tecnico Lisboa	Italy
P11	Silvia Giuditta Scaltriti	University of Bologna	Italy
P12	Rouillard Amaury	GREMI	France
P13	Francesco Tomelleri	Università di Bologna	Italy
P14	Palma Rosa Rotondo	University of Bari	Italy
P15	Vladyslav Vivcharenko	Medical University of Lublin	Poland
P16	Tijana Lainović	Faculty of Medicine, School of Dental Medicine, University of Novi Sad	Serbia
P17	Alina Maria Holban	University of Bucharest	Romania
P18	Lorenzo Ibba	EPFL	Switzerland

**Tuesday 14th February**  
**Time 12:00 – 13:30**

<b>N.</b>	<b>Name</b>	<b>Institution</b>	<b>Country</b>
<b>P19</b>	Caterina Maccaferri	Università di Bologna	Italy
<b>P20</b>	Leonardo Zampieri	Università degli Studi di Milano Bicocca	Italy
<b>P21</b>	Berrak Kurt	Ankara University Faculty of Veterinary Medicine Department of Biochemistry	Turkey
<b>P22</b>	Dawid Zarzeczny	Lublin University of Technology	Poland
<b>P23</b>	Aleksandra Lavrikova	Comenius University in Bratislava	Slovakia
<b>P24</b>	Rita Agus	EPFL	Switzerland
<b>P25</b>	Marianna Roggio	University of Bari Aldo Moro	Italy
<b>P26</b>	Sara Lotito	University of Bari Aldo Moro	Italy
<b>P27</b>	Regina Del Sole	University of Bari Aldo Moro	Italy
<b>P28</b>	Nikola Milojević	School of Dental Medicine University of Belgrade	Serbia
<b>P29</b>	Kristína Trebulová	Brno University of Technology	Czech Republic
<b>P30</b>	Marwa Balaha	D'Annunzio University of Chieti–Pescara	Italy
<b>P31</b>	Merve Şensöz Turgut	Ankara University Faculty of Veterinary Medicine Department of Biochemistry	Turkey
<b>P32</b>	Sara Covella	Università degli Studi di Perugia	Italy
<b>P33</b>	Zuzana Měšťánková	Brno University of Technology	Czech Republic
<b>P34</b>	Vincenza Armenise	University of Bari Aldo Moro	Italy
<b>P35</b>	Michal Wojcik	Medical University of Lublin	Poland
<b>P36</b>	Marta Trzaskowska	Medical University of Lublin	Poland
<b>P37</b>	Zuzana Okruhlicová	Division of Environmental Physics, Comenius University in Bratislava	Slovakia



# 2<sup>nd</sup> Training School

Cold plasmas to fight microorganisms, viruses & toxins for medical and agricultural applications

P1

## Nonthermal Plasma at atmospheric pressure with aerosols: applications in agriculture

*Neda Babucić<sup>1</sup>, Nikola Škoro<sup>1</sup>, Nevena Puač<sup>1</sup>*

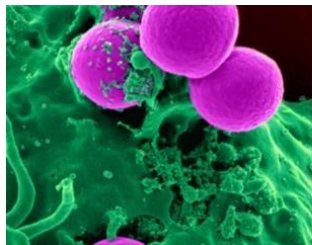
<sup>1</sup>Institute of Physics, University of Belgrade, Pregrevica 118, 11080 Belgrade, Serbiae-mail: nedab@ipb.ac.rs

Applications of low temperature plasma (LTP) are investigated due to its versatile use in water decontamination, wound treatment by using plasma activated water (PAW) and in agriculture. One of the key challenges in plasma-water interaction is to increase flux of reactive species from the plasma. The addition of micrometer-scale droplets of aerosols immersed in plasma provides a high surface-to-volume ratio, increases the contact area for a given amount of water and potentially enhancing the rates for chemical interaction between plasma in gas phase and liquid. Apart from development of plasma-liquid applications, the plasma-aerosol configuration is also enabling greater scientific insights into a complex problem with potentially thousands of transient and non-equilibrium chemical reactions<sup>1</sup>. In this regard, we made the first step in assembling an experiment where microwave (MW) plasma source is used for aerosol treatment. The setup will enable characterization of the plasma, interaction between the plasma and droplets and characterization of treated water in order to better understand gas-liquid reactions of high chemical reactivity. At the moment, MW plasma is operated using Ar flow from 1-7 slm without addition of aerosols. Optical emission spectroscopy together with images of plasma provided information about the distance from the source where role of reactive species is important. After introducing aerosol into the reactive volume, in this setup we will be able to assess the influence of droplets to the plasma. The main idea is to better understand the interaction of plasmas with aerosols as there is potential of plasma-aerosol interaction at atmospheric pressure in treatment of biology samples. This research will be linked to the topics of WG 3 (treatment of plants with PAW made through aerosol) and WG4 (determination of PAW properties) of PIAgri COST action.<sup>2,3</sup>.

**Keywords:** *Nonthermal plasma, aerosols, MW source, activated water*

### References

1. Stancampiano A., Galligani T., Gherardi M., et al., Applied Sciences, 9(18) (2019), 3861, 10.3390/app9183861
2. Kruszelnicki J., Lietz A., Kushner M., journal of Physics D: Applied Physics, 52 (2019), 355207, 29pp, 10.1088/1361-6463/ab25dc
3. Palumbo F., Lo Porto C., Fracassi F., et al., MDPI coatings, 10(5) (2020), 440, 10.3390/coatings10050440



# 2<sup>nd</sup> Training School

Cold plasmas to fight microorganisms, viruses & toxins for medical and agricultural applications

P3

## Varying the plasma-treated liquids' characteristics for applications in biomedicine

*Olivera Jovanović<sup>a</sup>, Nevena Puač<sup>a</sup>, Anđelija Petrović<sup>a</sup>, and Nikola Škoro<sup>a</sup>*

<sup>a</sup>Institute of Physics, University of Belgrade, Pregrevica 118 11080 Belgrade, Serbia.

The development of new plasma sources operating at atmospheric pressure in contact with liquid samples over the past 20 years has mostly been driven by new biomedical applications such as wound healing, cancer treatment, as well as the deactivation of bacteria and viruses and sterilization<sup>1-2</sup>. Recent research is focused on several aspects of plant biology and wastewater treatment<sup>3-4</sup> because low-temperature plasmas are environmentally acceptable and the active gaseous environment is at room temperature.

Plasma Activated Liquids (PALs) are essential in this application. PALs have been used in a substantial number of successful experiments, but there are still many questions regarding the mechanisms governing the interaction between the plasma and liquid including the production of a broad number of chemical species.

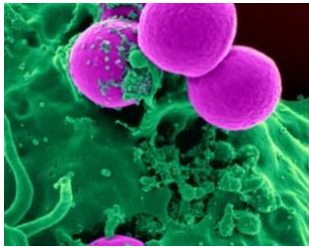
In this work, we utilized atmospheric pressure non-equilibrium plasma jets for the treatment of liquids, and the production of PALs. PALs were employed for the treatment of plant tissue culture, then also for application on wound healing in diabetic mice and finally in a study that tested their toxicity after oral intake by rats. Diagnostics of liquid samples were performed to assess the effectiveness of plasma treatment. The analysis of physicochemical parameters was conducted by measuring conductivity, pH, temperature, and the amount of deposited RONS ( $H_2O_2$ ,  $NO_3^-$ ,  $NO_2^-$ ). The mechanisms of interaction between plasma and liquid samples were determined depending on the conditions in the system. Through this research, we wanted to show that the used plasma systems provide the possibility to adjust the properties of treated liquids for a particular application in biomedicine by changing the treatment conditions.

**Acknowledgements:** This work was supported by MSTDI Republic of Serbia grant number 451-03-68/2022-14/200024, and The Science Fund of the Republic of Serbia, grant No. 3114/2021 - Project APPerTAin-BIOM.

**Keywords:** *plasma jet, plasma biomedicine, plasma activated liquids*

### References

1. Kaushik N.K, Ghimire B, Li Y, et al., *Biological chemistry*, 400 (2019), 39-62 doi.org/10.1515/hsz-2018-0226
2. Tomic S, Petrovic A, Puač N, et al., *Cancers*, 13 (2021), 1626 doi.org/10.3390/cancers13071626
3. Zambon Y, Contaldo N, Laurita R, et al., *Scientific Reports*, 10 (2020), 19211 doi.org/10.1038/s41598-020-76247-3
4. Kumar A, Škoro N, Gernjak W, et al., *Sci. Total Env.*, 864 (2023), 161194 doi.org/10.1016/j.scitotenv.2022.161194



# 2<sup>nd</sup> Training School

Cold plasmas to fight microorganisms, viruses & toxins for medical and agricultural applications

P16

## The influence of Cold Atmospheric Plasma dentin pretreatment on endogenous MMPs activity and bond strength – a pilot study

*T. Lainović<sup>a</sup>, T. Maravić<sup>b</sup>, N. Pecikozić<sup>a</sup>, L. Blažić<sup>a,c</sup>, V. Checchi<sup>d</sup>, L. Generali<sup>d</sup>,  
L. Breschi<sup>b</sup>, A. Mazzoni<sup>b</sup>, U. Josić<sup>b</sup>, N. Škoro<sup>e</sup>, N. Puač<sup>e</sup>*

<sup>a</sup>Faculty of Medicine, School of Dental Medicine, University of Novi Sad, Novi Sad, Serbia

<sup>b</sup>University of Bologna — Alma Mater Studiorum, Bologna, Italy

<sup>c</sup>Dental Clinic of Vojvodina, Novi Sad, Serbia

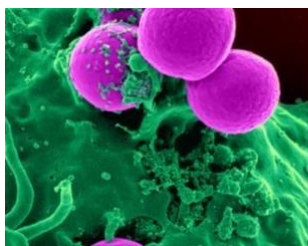
<sup>d</sup>University of Modena & Reggio Emilia, Modena, Italy

<sup>e</sup>Institute of Physics, University of Belgrade, Belgrade, Serbia

The present research aimed to investigate the influence of Cold Atmospheric Plasma (CAP) pretreatment on dentinal endogenous enzymatic activity and dentin-adhesive bond strength, by means of in situ zymography and microtensile bond strength ( $\mu$ TBS) test, respectively. Materials and methods: Sound human extracted molars (N=30) were cut to expose middle/deep dentin. Teeth were randomly assigned to the treatment groups: a) no pretreatment (control – CTR); 15s plasma pretreatment (15s); c) 30s plasma pretreatment (30s). Further, a universal adhesive was applied on dentin surfaces either in the self-etch (SE) or the etch-and-rinse (ER) mode, with or without dentin surface rewetting (RW) after plasma treatment. Hence, 10 different treatment groups were formed: 1) self-etch control – SE-CTR; 2) SE 15s DRY; 3) SE 15s RW; 4) SE 30s DRY; 5) SE 30s RW; 6) etch-and-rinse control – ER-CTR; 7) ER 15s DRY; 8) ER 15s RW; 9) ER 30s DRY; 10) ER 30s RW. Composite resin build-ups (4 mm) were made on all teeth. Bonded specimens were further cut into 1-mm<sup>2</sup>-thick sticks and subjected to  $\mu$ TBS. Dentin slices were obtained from additional 3 teeth (8 slices per tooth) and were treated in the same way as for  $\mu$ TBS to investigate the dentinal endogenous enzymatic activity. Bonded slices were ground down and covered overnight with fluorescein-conjugated gelatin and observed using a confocal microscope. Data were statistically analyzed ( $p < 0.05$ ). Results: Direct dentin treatment with CAP influenced  $\mu$ TBS significantly ( $p < 0.05$ ). The influence was more notable in the ER groups, where 15s RW increased the bond strength results significantly, while 30s DRY led to the complete debonding of all the specimens. The differences in the SE groups did not reach statistical significance. Enzymatic activity was higher in the ER groups compared to SE. Plasma treatment influenced more the ER groups, demonstrating the lowest enzymatic activity in the 15s RW group, which is in accordance with  $\mu$ TBS results. Conclusions: Direct plasma pretreatment could influence bond strength, particularly of ER adhesive systems, possibly also due to the reduction in endogenous enzymatic activity. Adequate CAP treatment duration and dentin moisture level should be further analyzed in detail and applied.

**Acknowledgements:** The work is supported by the PlasTHER COST Action and is in accordance with the topics related to WG1 and WG3. The authors would like to thank the DIBIDEM department from the University of Bologna, for their great hospitality.

**Keywords:** Cold Atmospheric Plasma (CAP), microtensile bond strength, MMPs, dentin



# 2<sup>nd</sup> Training School

Cold plasmas to fight microorganisms, viruses & toxins for medical and agricultural applications

P28

## Title: Examination of the antimicrobial potential of different sources of low-temperature atmospheric plasma *in vitro* against methicillin-resistant *Staphylococcus aureus*

Nikola Milojević<sup>a</sup>, Boško Toljić<sup>b</sup>, Nikola Škoro<sup>c</sup>, Nevena Puač<sup>c</sup>, Dragana Vuković<sup>d</sup>, Maja Miletić<sup>a</sup>

<sup>a</sup> Department of Pathophysiology, School of Dental Medicine, University of Belgrade, Serbia

<sup>b</sup> Department of Physiology, School of Dental Medicine, University of Belgrade, Serbia

<sup>c</sup> Institute of Physics Belgrade, University of Belgrade, Serbia

<sup>d</sup> Institute of Microbiology, Faculty of Medicine, University of Belgrade, Serbia

The growing prevalence of infections caused by multiresistant bacteria represents a global medical problem, given that there is no adequate therapeutic solution for these infections. Infections caused by resistant, multi-resistant, and even pan-resistant bacteria occur primarily in the hospital environment, but their frequency is also increasing in the general population. The emergence and spread of resistance to antibiotics and chemotherapeutics is observed in most medically important bacteria. However, the problem of resistance is particularly significant with Gram-positive bacteria of the genera *Staphylococcus* and *Enterococcus*. Methicillin-resistant *Staphylococcus aureus* (MRSA) is one of the leading nosocomial pathogens, but it is increasingly occurring as a cause of infections in the general population. These strains are resistant to all beta-lactam antibiotics and represent a very big problem today. Abscess is a common form of odontogenic infections and is a reflection of a favorable defensive reaction of the organism that tries to localize the infectious focus. The microbiological flora of odontogenic infections consists of an association of anaerobic and aerobic species with a dominant role of anaerobic species. One of the facultative anaerobes in odontogenic abscesses is MRSA, whose prevalence, according to some studies, ranges from 3.3% and even up to 12%<sup>1</sup>. Previous research shows that low-temperature atmospheric plasma exhibits a strong antimicrobial effect without toxic effects on human stem cells, which is why it could be applied in the field of biomedicine for *in vivo* decontamination of surfaces colonized by bacteria and antimicrobial therapy<sup>2,3,4</sup>. The aim of this research is to examine the antimicrobial effect of different sources of NTAP on the reference strain and clinical isolate of MRSA from an abscess of odontogenic origin and to determine whether resistance to plasma treatment develops, as well as whether plasma treatment increases the sensitivity of MRSA to different antibiotics. **Keywords:** MRSA, low temperature atmospheric plasma, antimicrobial effects

### References

1. M Pokharel, A Dhakal, P Rajbhandari, S K Madhup, L Khadka. A study of Deep Neck Space Infections at Kathmandu University Dhulikhel Hospital Kathmandu *Univ Med J (KUMJ)*. (2021);19: 57-61.
2. Miletić M, Vuković D, Živanović I, Dakić I, Soldatović I, Maletić D, Lazović S, Malović G, Petrović ZLJ, Puač N. Inhibition of methicillin resistant *Staphylococcus aureus* biofilm by a plasma needle. *CEJP* (2014);12(3): 160-167.
3. Lazović S, Puač N, Miletić M, Maletić D, Malović G, Bugarski D, Mojsilović S, Milenković P, Petrović Z. The effect of a plasma needle on bacteria in planktonic samples and on peripheral blood mesenchymal stem cells. *New J Phys* (2010); 12: 083037. DOI 10.1088/1367-2630/12/8/083037
4. Miletić M, Mojsilović S, Okić Djordjević I, Maletić D, Puač N, Lazović S, Malović G, Milenković P, Petrović ZLJ, Bugarski D. Effects of non-thermal atmospheric plasma on human periodontal ligament mesenchymal stem cells. *J Phys D: Appl Phys* (2013); 46: 345401 (9pp). DOI 10.1088/0022-3727/46/34/345401